

IHEP-CEPC-DR-2018-02

IHEP-EP-2018-XX

IHEP-TH-2018-XX

CEPC

Conceptual Design Report

Volume II - Physics & Detector

The CEPC Study Group

Fall 2018

Draft-V2.0

ACKNOWLEDGMENTS

2 The CEPC Physics and Detector Conceptual Design Report (CDR) was prepared and
3 written by the CEPC Study Group. The study was organised and led by scientists from
4 the Institute of High Energy Physics (IHEP) of the Chinese Academy of Sciences (CAS),
5 and from many universities and other institutes in China and abroad.

6 This work was supported by National Key Program for Science and Technology Re-
7 search and Development (GRANT No. 2016YFA0400400, 2018YFA0404300, H92942-
8 0GTD); The General Program of National Natural Science Foundation of China (GRANT
9 No. 11635007, 11535007); The Key Program of National Natural Science Foundation of
10 China (GRANT No. 11675202, 11575221, 11575220, 11675197); The Young Science
11 Program of National Natural Science Foundation of China (GRANT No. 11605217); Yi-
12 fang Wang's Science Studio of the Ten Thousand Talents Project; The National 1000 Tal-
13 ents Program of China (Y6291240S0); Key Research Program of Frontier Sciences, Chi-
14 nese Academy of Science; Center for Excellence in Particle Physics, Chinese Academy
15 of Science; The Hundred Talent programs, Chinese Academy of Science (GRANT No.
16 Y3515540U1, Y71184005C); Key Research Program of Frontier Sciences, Chinese Aca-
17 demy of Science (GRANT No. QYZDY-SSW-SLH002); Scientific innovation plan, Chi-
18 nese Academy of Science (GRANT No. Y6299113K); International Partnership Program,
19 Chinese Academy of Sciences (GRANT No. 113111KYSB20170005); The CAS/SAFEA
20 International Partnership Program for Creative Research Teams (GREAT No. H751S018-
21 S5); The Innovation Grant of Institute of High Energy Physics, Chinese Academy of Sci-
22 ence (GRANT No. Y4545170Y2, Y4545176Y2, Y6515510U1); The Xie Jialin Fund of
23 Institute of High Energy Physics, Chinese Academy of Science (GRANT No. Y8546120U-
24 2), The General Research Program of Taiwan (GRANT No. MOST-106-2112-M-001-
25 023); The Ta-You Wu Memorial Award (GRANT No. 105-2112-M-008-022-MY3); The
26 H2020 Project AIDA2020 (GRANT No. 654168); The Corporation fund of Wuxi Toly
27 Electric Works Co.Ltd, (GRANT No. RD01-201401, RD03-201601).

¹ We are also grateful to Alexandre Glazov (DESY), Charlie Young (SLAC), Sebastian
² Grinstein (Barcelona), Alberto Belloni (Maryland), Jianming Qian (Michigan), Walter
³ Snoeys (CERN), Daniela Bortoletto (Oxford), Franco Grancagnolo (INFN) for their con-
⁴ tribution to the international review of an earlier version of the document.

CONTENTS

2	Acknowledgments	iii
3	1 Executive Summary	1
4	2 Overview of the physics case for CEPC	7
5	2.1 CEPC: the precision frontier	8
6	2.2 Higgs boson and electroweak symmetry breaking	11
7	2.2.1 Naturalness	11
8	2.2.2 Electroweak phase transition	19
9	2.3 Exploring new physics	28
10	2.3.1 Exotic Higgs boson decays	29
11	2.3.2 Exotic Z boson decays	31
12	2.3.3 Dark matter and hidden sectors	34
13	2.3.4 Neutrino connection	50
14	2.3.5 Extended Higgs sector	59
15	2.4 QCD precision measurement	62
16	2.4.1 Precision α_s determination	64
17	2.4.2 Jet rates at CEPC	65
18	2.4.3 Non-global logarithms	65
19	2.4.4 QCD event shapes and light quark Yukawa coupling	67
20	2.5 Flavor Physics with the Z factory of CEPC	68
21	2.5.1 Rare B decays	69
22	2.5.2 Tau decays	74
23	2.5.3 Flavor violating Z decays	75
24	2.5.4 Summary	76
25	3 Experimental Conditions, Physics Requirements and Detector Concepts	111

vi CONTENTS

1	3.1	CEPC Experimental Conditions	112
2	3.1.1	The CEPC beam	112
3	3.1.2	Beam backgrounds	112
4	3.2	Physics Requirements	116
5	3.2.1	Multiplicity	116
6	3.2.2	Tracking	118
7	3.2.3	Charged Leptons	118
8	3.2.4	Charged hadron identification	119
9	3.2.5	Photons	120
10	3.2.6	Jets and Missing energy	121
11	3.2.7	Flavor Tagging	124
12	3.2.8	Requirements on the physics objects: summary	124
13	3.3	Detector concepts	125
14	3.3.1	The baseline detector concept	127
15	3.3.2	Full silicon detector concept	129
16	3.3.3	An alternative low magnetic field detector concept	130
17	4	Tracking system	137
18	4.1	Vertex tracker detector	138
19	4.1.1	Performance Requirements and Detector Challenges	138
20	4.1.2	Baseline design	138
21	4.1.3	Detector performance studies	139
22	4.1.4	Beam-induced Background in the Vertex Detector	142
23	4.1.5	Sensor Technology Options	143
24	4.1.6	Mechanics and Integration	144
25	4.1.7	Critical R&D	146
26	4.1.8	Summary	147
27	4.2	Time Projection Chamber and Silicon tracker	147
28	4.2.1	Time Projection Chamber	147
29	4.2.2	Silicon tracker	162
30	4.2.3	TPC and Silicon tracker performance	166
31	4.3	Full-silicon tracker detector	166
32	4.3.1	Full silicon tracker layout	167
33	4.3.2	Expected Resolution	168
34	4.3.3	Detector simulation and reconstruction	170
35	4.3.4	Tracking performance	173
36	4.3.5	Conclusion	176
37	4.4	Drift chamber tracker detector	177
38	4.4.1	Introduction	177
39	4.4.2	Overview	178
40	4.4.3	Expected performance	178
41	4.4.4	Tracking system simulation results	179
42	4.4.5	Backgrounds in the tracking system	180
43	4.4.6	Constraints on the readout system	181
44	5	Calorimetry	189
45	5.1	Introduction to calorimeters	189
46	5.2	General design considerations for the PFA Calorimetry system	192

1	5.3 Electromagnetic Calorimeter for Particle Flow Approach	192
2	5.3.1 Design Optimization	193
3	5.3.2 Silicon-Tungsten Sandwich Electromagnetic Calorimeter	197
4	5.3.3 Scintillator-Tungsten Sandwich Electromagnetic Calorimeter	201
5	5.4 Hadronic Calorimeter for Particle Flow Approach	207
6	5.4.1 Introduction	207
7	5.4.2 Semi-Digital Hadronic Calorimeter (SDHCAL)	208
8	5.4.3 AHCAL based on Scintillator and SiPM	217
9	5.5 Dual-readout calorimetry	222
10	5.5.1 Introduction	222
11	5.5.2 Principle of dual-readout calorimetry	223
12	5.5.3 Layout and mechanics	225
13	5.5.4 Sensors and readout electronics	228
14	5.5.5 Performance studies with fiber-sampling prototypes	230
15	5.5.6 Monte Carlo simulations	233
16	5.5.7 Final remarks on dual-readout calorimetry	241
17	6 Detector magnet system	245
18	6.1 Magnetic field design	245
19	6.1.1 Main parameters	245
20	6.1.2 Magnetic field calculation	246
21	6.2 Superconducting coil system	246
22	6.3 Ancillaries (cryogenics, power supply, quench protection)	247
23	6.3.1 Cryogenics system	247
24	6.3.2 Power supply	248
25	6.3.3 Quench protection and instrumentation	249
26	6.4 Iron yoke design	250
27	6.5 Alternative designs and R&D	251
28	6.5.1 LTS solenoid for the IDEA detector	251
29	6.5.2 HTS solenoid for IDEA detector	251
30	6.5.3 Dual solenoid design	252
31	6.5.4 Superconducting conductor	252
32	6.5.5 Thermosyphon circuit	252
33	7 Muon system	255
34	7.1 Baseline Design	256
35	7.2 The Resistive Plate Chamber technology	259
36	7.3 The μ -RWELL technology	259
37	7.4 Future R&D	261
38	8 Readout electronics, trigger and data acquisition	265
39	8.1 Trigger strategy	266
40	8.2 Readout electronics	266
41	8.3 Data Acquisition System	267
42	8.3.1 Readout Data Rate Estimation	267
43	8.3.2 Conceptual Design Schema	267
44	9 Machine detector interface and luminosity detectors	271

1	9.1	Interaction region	271
2	9.2	Final focusing magnets	272
3	9.3	Beam pipe	273
4	9.4	Detector backgrounds	273
5	9.4.1	Synchrotron radiation	274
6	9.4.2	Beam-beam interactions	276
7	9.4.3	Off-energy beam particles	277
8	9.4.4	Summary of radiation backgrounds	279
9	9.5	Luminosity instrumentation	281
10	9.5.1	Technological and design options	282
11	9.5.2	Systematic effects	288
12	9.5.3	Summary on LumiCal	289
13	9.6	Detector integration	290
14	10	Simulation, Reconstruction and Physics Object Performance	293
15	10.1	Event simulation and reconstruction	293
16	10.1.1	Event simulation	293
17	10.1.2	Event reconstruction	294
18	10.2	Object Identifications and Performances	297
19	10.2.1	Leptons	297
20	10.2.2	Photons	299
21	10.2.3	Tau Leptons	300
22	10.2.4	Jets	302
23	10.2.5	Jet flavor tagging	304
24	10.2.6	Missing Energies, Momenta and Masses	305
25	10.2.7	Kaon Identification	307
26	10.3	Summary	308
27	11	Physics performance with benchmark processes	311
28	11.1	Higgs Boson Physics	312
29	11.1.1	Higgs boson production and decay	312
30	11.1.2	Higgs boson tagging	314
31	11.1.3	Measurements of $\sigma(ZH)$ and m_H	316
32	11.1.4	Analyses of individual Higgs boson decay modes	317
33	11.1.5	Combination of individual analyses	321
34	11.1.6	Higgs boson width	323
35	11.1.7	Higgs Boson Coupling Measurements	323
36	11.1.8	Tests of Higgs boson spin/ CP	337
37	11.1.9	Summary	339
38	11.2	W and Z Boson Physics	340
39	11.2.1	Z pole measurements	340
40	11.2.2	Measurement of the W boson mass	347
41	11.2.3	Oblique Parameter	351
42	12	Future plans and R&D prospects	367
43	12.1	Tracking	368
44	12.1.1	Vertex	368
45	12.1.2	Silicon tracker	368

1	12.1.3	TPC	368
2	12.1.4	Full-silicon tracker	369
3	12.1.5	Drift Chamber tracker	369
4	12.2	Calorimetry	369
5	12.2.1	PFA-ECAL	369
6	12.2.2	PFA-HCAL	370
7	12.2.3	Dual-readout calorimeter	371
8	12.3	Magnet	371
9	12.4	Muon system	372
10	12.5	DAQ	372
11	12.6	Machine detector interface	372
12	12.7	Simulation, reconstruction and object performance	373
13	12.8	Physics	373
14	13	Summary	375
15	A	HTS solenoid concept for IDEA detector	377
16	A.1	Radiation length of YBCO superconductor	377
17	Glossary		381

Draft-V2.0

CHAPTER 1

EXECUTIVE SUMMARY

¹ The discovery of the Higgs boson in 2012 by the ATLAS and CMS collaborations [1, 2] at CERN’s Large Hadron Collider (LHC) opened a new era in particle physics and raised new opportunities for a large-scale accelerator. Due to the low mass of the Higgs, it is possible to produce it in the relatively clean environment of a circular electron-positron collider with reasonable luminosity, technology, cost and power consumption. The Higgs boson is a crucial cornerstone of the Standard Model (SM). It is at the center of the biggest mysteries of modern particle physics, such as the large hierarchy between the weak scale and the Planck scale, the nature of the electroweak phase transition, and many other related questions. Precise measurements of the properties of the Higgs boson, together with precise measurements of the W and Z bosons, serve as excellent tests of the underlying fundamental physics principles of the SM, and they are instrumental in explorations beyond the SM. Such physics program will be a critical component of any road map for high energy physics in the coming decades.

¹⁴ The Circular Electron Positron Collider (CEPC) is a large international scientific project initiated and hosted by China. It was first presented to the international community at the ICFA Workshop “Accelerators for a Higgs Factory: Linear vs. Circular” (HF2012) in November 2012 at Fermilab. A Preliminary Conceptual Design Report (Pre-CDR) [3, 4] was published in March 2015.

¹⁹ This document is the second volume of the CEPC Conceptual Design Report (CDR). Its main purpose is to address the physics potential of the CEPC, possible detector concepts and the corresponding R&D program. The first volume [5], released in July 2018, describes the CEPC accelerator complex design, associated civil engineering and strategic alternative scenarios.

2 EXECUTIVE SUMMARY

1 The CEPC operation will be staged in a few steps of center-of-mass energy to maximize
2 its physics potential. It is expected the CEPC to start operations at 240 GeV, giving raise
3 to a wealth of Higgs physics, and then move to lower center-of-mass energies and collect
4 large samples of W and Z bosons. This complete program of precision standard-model
5 physics will place stringent constraints on new physics, and it has the potential for direct
6 observation of new physics.

7 This CDR volume presents the essential features of the detectors that are required
8 to extract the full physics potential of the CEPC. The experimental conditions at high-
9 luminosity high-energy circular electron positron colliders present different challenges
10 than those for electron-positron linear colliders due to the higher levels of beam-induced
11 backgrounds, and the high-luminosity required to collect the extremely large samples of
12 Z boson events. A main goal of this report is to demonstrate that, expanding on the on-
13 going R&D program, a wide range of high-precision physics measurements can be made
14 at CEPC with detectors that are feasible to complete in the next 12-15 years.

15 Consequently, part of this report is devoted to understanding the impact of the machine
16 environment on the detector with the aim of demonstrating, with the example of a few
17 realistic detector concepts, that high-precision physics measurements can be made at the
18 CEPC. This document concentrates on the detector requirements and physics measure-
19 ments at the highest CEPC center-of-mass energy of 240 GeV, when the beam induced
20 backgrounds are higher, but consideration is also given to the high-rate operation at the
21 Z -boson mass energy.

22 This volume of the CEPC CDR consists of 12 chapters. The next chapter presents an
23 overview of the physics case for the CEPC, where the physics potential for both SM pre-
24 cision measurement and searches beyond the SM is highlighted. Chapter 3 introduces the
25 CEPC accelerator and the experimental environment and lists the detector requirements
26 that must be met to achieve the CEPC physics goals. This chapter ends with the intro-
27 duction of the CEPC detector concepts proposed to satisfy these physics requirements.
28 The detector subsystems are then described together in more detail in the subsequent
29 chapters. Chapter 4 describes the tracking systems of all detector concepts, including the
30 vertex detectors. Chapter 5 presents the calorimeter options, while Chapter 7 describes
31 the muon system concepts. Results from detailed full simulation and test beam studies
32 are presented when available. The challenges referring to the design of the interaction re-
33 gion are described in Chapter 9, together with the beam backgrounds and details about the
34 plans for the luminosity measurement. The design of the detector solenoid is addressed in
35 Chapter 6, while a summary plan for the readout electronics and data acquisition system
36 is presented in Chapter 8. The overall performance of the CEPC baseline detector concept
37 is presented in Chapters 10 and 11. Chapter 10 introduces the detector software used in
38 the studies and details the physics object performance, taking into account full detector
39 simulation and reconstruction. Chapter 11 demonstrates the full physics potential of the
40 CEPC by emphasizing selected benchmark physics results. Finally, Chapter 12 ends this
41 report with an overview of future plans on detector R&D and physics studies towards the
42 Technical Design Report.

43 In what follows we present a short executive summary of the CDR content, highlighting
44 the CEPC physics case, the collider and experimental environment, the detector concepts,
45 and the physics performance and benchmarks.

Physics Case The precision measurement of Higgs properties will be a critical component of any road map for high energy physics in the coming decades. In addition to motivating new physics beyond the SM, the Higgs provides a uniquely sensitive probe of new physics. New physics beyond the SM can lead to observable deviations in Higgs boson couplings relative to SM expectations. These, and other electroweak physics parameters, can be measured at the CEPC with unprecedented precision. Such measurements can be used to address important open questions of the electroweak symmetry breaking. The most important question about the electroweak symmetry is to explain the size of the weak scale, which is much smaller than some of the fundamental scales, such as the Planck scale. The idea of naturalness has been crucial in constructing solutions of this so called hierarchy problem. At the CEPC, it is possible to test the idea of naturalness to an unprecedented level. They can be used to probe fine-tuning down to the percent level in the conventional scenarios such as Supersymmetry and Composite Higgs. They are also sensitive to the signals of a range of newly developed ideas, from the neutral naturalness to the relaxion. In addition, the precision Higgs coupling measurements can help probing the global feature of the Higgs potential, and reveal the nature of the electroweak phase transition. Understanding electroweak phase transition marks another concrete step forward in our knowledge of the early universe, and it could hold the key to solve the problem of asymmetry between matter and anti-matter in our universe. It is argued that in addition to the triple Higgs coupling, models with first order electroweak phase transition generically predict significant deviations in other Higgs couplings. An important example is the modification of the coupling of the Higgs boson to the Z boson which can be measured with sub-percent level accuracy at the CEPC.

The CEPC can also search for a variety of new physics particles. Running as both a Higgs-boson factory and a Z -boson factory, the exotic decays of Higgs and Z bosons can be used to search for new physics, such as those associated with a light dark sector. The CEPC can also search for dark matter, both through direct production and through its indirect effects on electroweak precision measurements. There is also an exciting possibility of direct producing the right handed neutrino and probe a class of see-saw models. Finally, both direct search and indirect measurement can look for signals of a possible extended Higgs sector.

A lepton collider is an excellent place to perform precise QCD measurement, and further our understanding of the strong interaction. Possible topics, include measurement of α_s , jet, event shapes and their utility in probing light Yukawa couplings. The CEPC can also produce close to 10^{12} Z bosons. Hence, it can be a powerful B -factory and τ -factory with excellent physics potential. At the same time, new flavor physics may show up as rare flavor violating Z decays.

Collider and the Experimental Environment The CEPC is a double-ring e^+e^- collider with 100 km circumference and two interaction points (IP). It will operate in three different modes, corresponding to three different center-of-mass energies (\sqrt{s}): Higgs factory ($e^+e^- \rightarrow ZH$) at $\sqrt{s} = 240$ GeV, Z boson factory ($e^+e^- \rightarrow Z$) at $\sqrt{s} = 91.2$ GeV and W threshold ($e^+e^- \rightarrow W^+W^-$) at $\sqrt{s} = \sim 160$ GeV. The instantaneous luminosities are expected to reach 3×10^{34} , 32×10^{34} and $10 \times 10^{34} \text{ cm}^{-2}\text{s}^{-1}$, respectively, as shown in Table 1.1. The current tentative operation plan will allow the CEPC to collect one million Higgs particles or more, close to one trillion Z boson events, and ten million W^+W^- event pairs.

Operation mode	\sqrt{s} (GeV)	L per IP ($10^{34} \text{ cm}^{-2}\text{s}^{-1}$)	Years	Total $\int L$ (ab^{-1} , 2 IPs)	Event yields
H	240	3	7	5.6	1×10^6
Z	91.2	32 (*)	2	16	7×10^{11}
W^+W^-	158-172	10	1	2.6	2×10^7

Table 1.1: CEPC operation plan at different center-of-mass energies (\sqrt{s}), and corresponding anticipated instantaneous luminosity (L), total integrated luminosity ($\int L$) and event yields. (*) The maximum instantaneous luminosity achievable at the Z pole operation is dependent on the detector solenoid magnet field. The value reported here assumes a 2 Tesla solenoid.

1 The detectors will record collisions in beam conditions presented in Table 3.1. Several
2 of these parameters impose important constraints on the detectors. The bunch spacing
3 of the colliding beams differ greatly in the three operational modes (680 ns, 25 ns, and
4 210 ns, respectively) as do the background levels and event rates. The three most impor-
5 tant sources of radiation backgrounds are (1) synchrotron radiation photons from the last
6 bending dipole magnet, (2) e^+e^- pair production following the beamstrahlung process,
7 and (3) off-energy beam particles lost in the interaction region. These backgrounds gen-
8 erate a hit density in the first vertex detector layer ($r = 1.6$ cm) of about 2.4 hits/cm² per
9 bunch crossing when running at $\sqrt{s} = 240$ GeV and tolerable levels of the total ionizing
10 energy (TID) and non-ionizing energy loss (NIEL). The event rate reaches ~ 32 kHz for
11 Z factory operation from Z boson decays and Bhabha events.

12 **Detector Concepts** The CEPC detector concepts are based on the stringent performance
13 requirements needed to deliver a precision physics program that tests the Standard Model
14 and searches for new physics over a wide range of center-of-mass energies and at high
15 beam luminosities. These specifications include large and precisely defined solid angle
16 coverage, precise track momentum resolution, high efficiency vertex reconstruction, pre-
17 cise photon energy reconstruction, excellent particle identification, excellent jet recon-
18 struction and flavor tagging.

19 The physics program demands that all possible final states from decays of the inter-
20 mediate vector bosons, W and Z , and the Higgs boson need to be separately identi-
21 fied and reconstructed with high resolution. In particular, to clearly discriminate the
22 $H \rightarrow ZZ^* \rightarrow 4j$ and $H \rightarrow WW^* \rightarrow 4j$ final states, the energy resolution of the CEPC
23 calorimetry system for hadronic jets needs to be pushed quite beyond today's limits. The
24 $H \rightarrow \gamma\gamma$ decay and the search for $H \rightarrow$ invisible decays impose additional require-
25 ments on energy and missing energy measurement resolutions. To measure the coupling of the
26 Higgs boson to the charm quark, the CEPC detectors are required to efficiently distin-
27 guish b -jets, c -jets, and light jets from each other. To achieve excellent sensitivity for the
28 $H \rightarrow \mu^+\mu^-$ decay the the momentum resolution is required to achieve a per mille level
29 relative accuracy. The latter two requirements drive the performance of the vertex detector
30 and tracking systems.

31 Two primary detector concepts were studied, a baseline detector concept with two ap-
32 proaches to the tracking systems, and an alternative detector concept with a different
33 strategy for meeting the jet resolution requirements. The baseline detector concept in-

1 incorporates the Particle Flow principle with a precision vertex detector, Time Projection
 2 Chamber and silicon tracker, 3T solenoid, and a high granularity calorimeter followed
 3 by muon chambers. A variant of the baseline detector concept incorporates a full sili-
 4 con tracker. An alternative detector concept is based on dual readout calorimetry with a
 5 precision vertex detector, drift chamber tracker, 2T solenoid, and muon chambers. The
 6 different technologies for each detector sub-system are being pursued actively with R&D
 7 programs and provide many opportunities to leverage leading advances in detector devel-
 8 opment in the coming years.

9 **Performance and Physics Benchmarks** Precise measurements of the Higgs boson prop-
 10 erties and the electroweak observables at the CEPC place stringent requirements on the
 11 performance of the CEPC detectors to identify and measure physics objects such as lep-
 12 tons, photons, jets and their flavors with high efficiencies, purities and precision. The per-
 13 formances of the CEPC baseline detector concept have been investigated with full simula-
 14 tion. Electrons and muons with momenta above 2 GeV and photons with energies above
 15 5 GeV can be identified with efficiencies of nearly 100% and with negligible backgrounds.
 16 Jets from W , Z and Higgs boson decays can be measured with an energy resolution of
 17 3–5%, allowing an average 2σ or better separation of hadronic decays of these bosons.
 18 Heavy-quark jets can be tagged with unprecedented efficiencies and purities. K^\pm can be
 19 distinguished from π^\pm with a significance better than 2σ . These performance results can
 20 be further improved with more optimizations and better calibrations.

21 Many new physics models predict deviations of Higgs boson couplings to particles at
 22 the sub-percent level, beyond those achievable at the (HL-)LHC. The CEPC complements
 23 the LHC and will be able to study the properties of the Higgs boson in great details with
 24 unprecedented precision. With over 10^6 Higgs bosons produced, most of the Higgs boson
 25 couplings can be measured with precision at a percent level or better, in particular the
 26 coupling to the Z boson can be determined with a precision of 0.25%. More importantly,
 27 the CEPC will be able to measure many of the key Higgs boson properties such as the total
 28 width and decay branching ratios model independently. The clean event environment
 29 of the CEPC will allow the identifications of potential unknown decay modes that are
 30 impractical at the LHC.

31 Beyond the Higgs boson physics, the CEPC will reach a new level of precision for
 32 the measurements of the properties of the W and Z bosons. With samples of $10^8 W$
 33 bosons and $10^{12} Z$ bosons at the CEPC, an order of magnitude improvements in precision
 34 are expected for many electroweak observables. Precise measurements of the W and Z
 35 boson masses, widths, and couplings are critical to test the consistency of the SM. These
 36 measurements could discover deviations from the SM predictions and reveal the existence
 37 of new particles that are beyond the reaches of direct searches at the current experiments.
 38 These new particles are predicted by many extensions of the SM.

39 This report provides a snapshot of the current studies, many of them are ongoing and
 40 more analyses are needed to fully explore the physics potential of the CEPC. Neverthe-
 41 less, the performance results presented have either already met or are close to meet the
 42 requirements of the CEPC experiments. Studies of physics benchmark processes suggest
 43 that the CEPC has the potential to “undress” the Higgs boson, similarly to what LEP did
 44 to the Z boson, and significantly improve the precision of electroweak measurements,
 45 ultimately shedding light on new physics.

6 REFERENCES

1 **Future Plans** The CEPC construction is expected to start in 2022 and be completed in
2 2030, followed by the commissioning of the accelerator and detectors. A tentative op-
3 erational plan covers 10 years of physics data: 7 years for Higgs physics, followed by 2
4 years operation in Z mode and 1 year operation in W mode. Prior to the construction
5 there will be a five-year R&D period (2018–2022). During this period, two international
6 collaborations will be formed to produce Technical Design Reports, build and operate
7 two large experiments. Prototypes of key-technical detector components will be built,
8 and worldwide infrastructure established for industrialization and manufacturing of the
9 required components.

10 The CEPC is an important part of the world plan for high-energy particle physics re-
11 search. It will support a comprehensive research program by scientists from all over the
12 world and provide leading educational opportunities for universities and research insti-
13 tutes in China and around the world. Physicists from many countries will work together
14 to explore the science and technology frontiers, and to bring a new level of understanding
15 of the fundamental nature of matter, energy and the universe.

16 References

- 17 [1] The ATLAS Collaboration, G. Aad et al., *Observation of a new particle in the search*
18 *for the Standard Model Higgs boson with the ATLAS detector at the LHC*, **Phys. Lett.**
19 **B 716** (2012) 1–29, [arXiv:1207.7214 \[hep-ex\]](https://arxiv.org/abs/1207.7214).
- 20 [2] The CMS Collaboration, S. Chatrchyan et al., *Observation of a new boson at a mass*
21 *of 125 GeV with the CMS experiment at the LHC*, **Phys. Lett. B716** (2012) 30–61,
22 [arXiv:1207.7235 \[hep-ex\]](https://arxiv.org/abs/1207.7235).
- 23 [3] The CEPC-SPPC Study Group, *CEPC-SPPC Preliminary Conceptual Design*
24 *Report, Volume I - Physics and Detector*, .
25 <http://cepc.ihep.ac.cn/preCDR/volume.html>.
26 IHEP-CEPC-DR-2015-01, IHEP-TH-2015-01, IHEP-EP-2015-01.
- 27 [4] The CEPC-SPPC Study Group, *CEPC-SPPC Preliminary Conceptual Design*
28 *Report, Volume II - Accelerator*, 2015.
29 <http://cepc.ihep.ac.cn/preCDR/volume.html>.
30 IHEP-CEPC-DR-2015-01, IHEP-AC-2015-01.
- 31 [5] The CEPC Study Group, *CEPC Conceptual Design Report, Volume I - Accelerator*, .
32 IHEP-CEPC-DR-2018-01, IHEP-AC-2018-01, to be published.

CHAPTER 2

OVERVIEW OF THE PHYSICS CASE FOR CEPC

After a very brief summary of the projections of the precision of Higgs coupling and electroweak measurements, the next part of this chapter describes the potential of using these measurements to address important open questions of the electroweak symmetry breaking. First, the most important question about the electroweak symmetry is to explain the size of the weak scale, which is much smaller than some of the fundamental scales, such as the Planck scale. The idea of naturalness (Section 2.2.1) has been crucial in constructing solutions of this so called hierarchy problem. At the CEPC, it is possible to test the idea of naturalness to an unprecedented level. They can be used to probe fine-tuning down to the percent level in the conventional scenarios such as Supersymmetry and Composite Higgs. They are also sensitive to the signals of a range of newly developed ideas, from the neutral naturalness to the relaxion. In addition, the precision Higgs coupling measurements can help probing the global feature of the Higgs potential, and reveal the nature of the electroweak phase transition. Understanding electroweak phase transition (Section 2.2.2) marks another concrete step forward in our knowledge of the early universe, and it could hold the key to solve the problem of asymmetry between matter and anti-matter in our universe. It is argued that in addition to the triple Higgs coupling, models with first order electroweak phase transition generically predict significant deviations in other Higgs couplings. An important example is the modification of the coupling of the Higgs boson to the Z boson which can be measured with sub-percent level accuracy at the CEPC. This is demonstrated in a representative scenario of singlet extension of the Higgs sector.

The CEPC can also search for a variety of new physics particles. Section 2.3 contains a set of such examples. Running as both a Higgs factory and a Z -factory, the exotic decays of Higgs boson and Z bosons can be used to search for new physics, such as those associated with a light dark sector. CEPC can also search for dark matter (Section 2.3.3),

8 OVERVIEW OF THE PHYSICS CASE FOR CEPC

1 both through direct production and through its indirect effects on electroweak precision
2 measurements. There is also an exciting possibility of direct producing the right handed
3 neutrino and probe a class of see-saw models (Section 2.3.4). Finally, both direct search
4 and indirect measurement can look for signals of a possible extended Higgs sector.

5 A lepton collider is an excellent place to perform precise QCD measurement, and fur-
6 ther our understanding of the strong interaction. Possible topics, covered in Section 2.4,
7 include measurement of α_s , jet, event shapes and their utility in probing light Yukawa
8 couplings, are summarized in the next part of the section.

9 The CEPC can produce close to $10^{12} Z$ bosons. Hence, it can be a powerful B -factory
10 and τ -factory with excellent potential. At the same time, new flavor physics may show up
11 as rare flavor violating Z decays. Section 2.5 is an overview of such physics, and provides
12 an estimate of the potential of the CEPC.

2.1 CEPC: the precision frontier

14 The discovery of a Higgs boson in 2012 by the ATLAS and CMS collaborations [1, 2] at
15 the Large Hadron Collider (LHC) has opened a new era in particle physics. Subsequent
16 measurements of the properties of this new particle have indicated compatibility with
17 the predictions of the SM. While the SM has been remarkably successful in describing
18 experimental phenomena, it is important to recognize that the SM is not a complete theory.
19 In particular, the SM does not *predict* the parameters in the Higgs potential, such as the
20 Higgs boson mass. The vast difference between the Planck scale and the weak scale
21 remains a major mystery. In addition, there is not a complete understanding of the nature
22 of the electroweak phase transition. The discovery of a spin zero Higgs boson, the first
23 elementary particle of its kind, has only sharpened these questions, and their resolution
24 will necessarily involve new physics beyond the SM. In this respect, the discovery of the
25 Higgs boson marks the beginning of a new era of theoretical and experimental exploration.

26 The precision measurement of Higgs boson properties will be a critical component of
27 any road map for high energy physics in the coming decades. In addition to motivating
28 new physics beyond the SM, the Higgs boson provides a uniquely sensitive probe of new
29 physics. In particular, new physics beyond the SM can lead to observable deviations in
30 Higgs couplings relative to SM expectations. These deviations δ are generically of order

$$\delta = c \frac{v^2}{M_{\text{NP}}^2}, \quad (2.1)$$

31 where v and M_{NP} are the vacuum expectation value of the Higgs field and the typical
32 mass scale of new physics, respectively. The size of the proportionality constant c is
33 model-dependent, but it should not be much larger than $\mathcal{O}(1)$. The current and upcoming
34 LHC runs will measure Higgs couplings to about the 5% level [3], while direct searches
35 at the LHC will test many new physics scenarios from a few hundreds of GeV to at least
36 a TeV. Equation (2.1) implies that probing new physics significantly *beyond* the LHC's
37 reach requires measuring Higgs couplings with sub-percent-level accuracy. Achieving
38 such a level of precision will require new facilities, for which a lepton collider operating
39 as a Higgs factory is a natural candidate.

40 In this section we explore the physics potential of the CEPC, translating the potential
41 precision of Higgs coupling measurements into implications for a variety of motivated sce-
42 narios for physics beyond the SM. Projections for the precision in Higgs coupling mea-

surements and electroweak observables attainable by the CEPC are summarized below.
The details of the analysis underpinning these projections are presented in Section 11.1

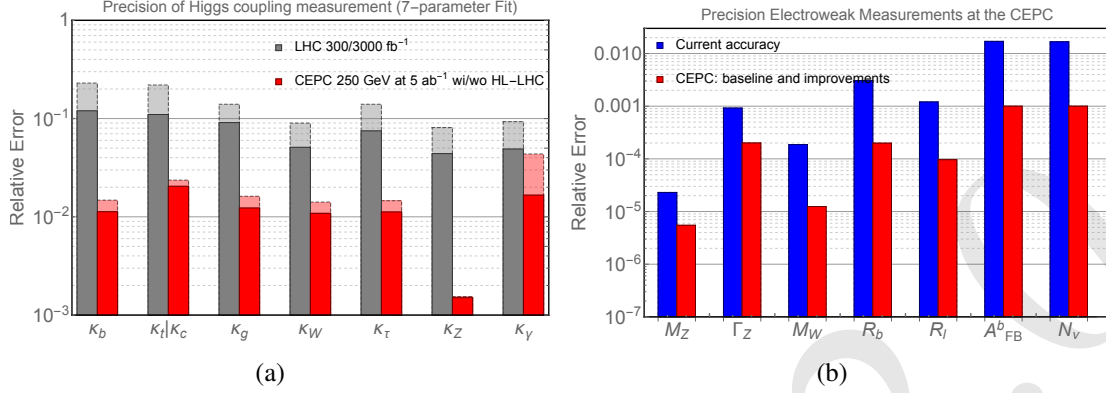


Figure 2.1: (a) Higgs coupling extraction in the κ -framework. (b) Projection for the precision of the Z -pole measurements.

The CEPC will operate primarily at a center-of-mass energy of $\sqrt{s} \sim 240$ GeV. The main mode of Higgs boson production is through $e^+e^- \rightarrow ZH$ process, and with an integrated luminosity of 5.6 ab^{-1} , over one million Higgs bosons will be produced. At CEPC, in contrast to the LHC, Higgs boson candidate events can be identified through a technique known as the recoil mass method without tagging its decay products. This allows Higgs boson production to be disentangled from Higgs boson decay in a model-independent way. Moreover, the cleaner environment at a lepton collider allows much better exclusive measurement of Higgs boson decay channels. All of these give CEPC impressive reach in probing Higgs boson properties. The resulting precision attainable by CEPC in measurements of Higgs couplings is shown in the Figure 2.1(a) in terms of the κ framework.

Several aspects of the precision attainable at CEPC stand out. The CEPC will be able to measure the Higgs coupling to the Z boson with an accuracy of 0.25%, about a factor of 10 better than the reach of the High Luminosity upgrade of the LHC (HL-LHC). Such a precise measurement gives CEPC unprecedented reach into interesting new physics scenarios which are very difficult to probe at the LHC. The CEPC also has strong capability in detecting invisible decays of the Higgs boson. For example, with 5.6 ab^{-1} , it can improve the accuracy of the measurement of the Higgs boson invisible branching ratio to 0.3%. In addition, it is expected to have excellent sensitivity to exotic decay channels which are swamped by backgrounds at the LHC. It is also important to stress that an e^+e^- Higgs factory can perform *model independent* measurement of the Higgs boson width. This unique feature in turn allows for the determination of the Higgs couplings without assumptions about Higgs boson decay channels.

The CEPC is also designed to run at the Z pole and near the W^+W^- threshold (with about 10^7 W pairs). This enables a robust program of electroweak precision measurements to complement the Higgs precision program. The projected precision for a set of such observables is shown in on the Figure 2.1(b). In comparison with the current precision, CEPC can improve by about one order of magnitude.

The combination of precision Higgs and electroweak measurements at CEPC is particularly powerful. This is most readily apparent in the potential for CEPC to constrain

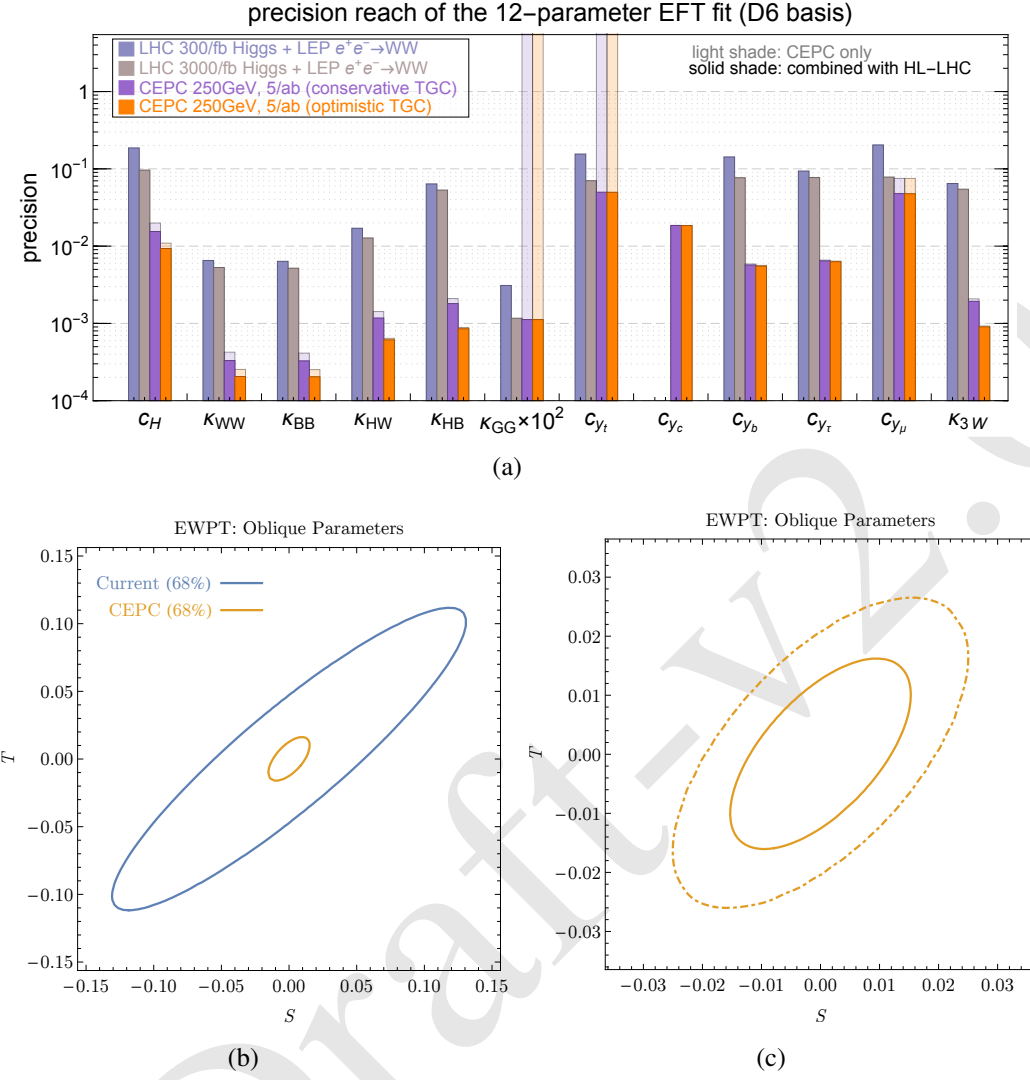


Figure 2.2: (a) The reach of the Higgs measurement on the size of effective field theory operators, normalized as $c_i(\mathcal{O}_i/v^2)$. (b) the CEPC limit on the oblique parameters in comparison with the current precision. (c) 68% (dash-dot) and 95% (solid) contours from CEPC measurement.

departures from the Standard Model parametrized in the language of effective field theory (EFT). The reach of CEPC Higgs measurements in constraining Wilson coefficients of select dimension-6 operators in the SM EFT is shown in Figure 2.2, while the reach of CEPC electroweak precision measurements in terms of the so-called oblique parameters (likewise expressible in terms of Wilson coefficients of dimension-6 operators in the SM EFT) is shown in the lower panel of Figure 2.2. The significant improvement of CEPC relative to both current and projected LHC measurements is apparent. Later in this section, we will explore in detail the implications of the precision measurements at CEPC for important open questions of the Standard Model.

CEPC, running as both Higgs factory and Z -factory, will also probe interesting new physics, offer an excellent opportunity of studying flavor physics, allow precise QCD measurements. We will also elaborate on these later in this section. To set the stage, we briefly comment on the running scenarios assumed in the results presented in this section. While the plan for the Higgs factory has been fixed, the plan for the Z -factory run is

1 still preliminary. The total number of Z s with different options ranging from 0.3×10^{12}
 2 (baseline) to up to 10^{12} Z s. To give an characterization of the full potential of the CEPC,
 3 we will use 10^{12} Z s (Tera Z) in our estimates.

4 2.2 Higgs boson and electroweak symmetry breaking

5 2.2.1 Naturalness

6 The appearance of large numerical hierarchies in fundamental theories has long been a
 7 source of discomfort, articulated in the modern era by Dirac [4] and subsequently refined
 8 in the context of quantum field theory by Wilson [5], Susskind [6], 't Hooft [7], and others.
 9 In the context of quantum field theory, dimensionless parameters of a quantum field theory
 10 are naturally expected to be $\mathcal{O}(1)$, while the dimensional parameters are naturally the size
 11 of the fundamental scale at which the theory is defined. An exception arises when a
 12 symmetry is manifested in the limit that a parameter of the theory is taken to zero. In this
 13 case, it is "technically natural" for some parameters to remain smaller than others, in the
 14 sense that they are protected from large quantum corrections, though even in this case one
 15 is left to find an explanation for the dynamical origin of the small parameter. This notion
 16 of naturalness has been reinforced by the widespread successes of effective field theory
 17 and diverse realizations in both particle physics and condensed matter physics.

18 Famously, all of the observed parameters of the Standard Model satisfy the naturalness
 19 criterion in some form, with the exception of the Higgs boson mass parameter and the
 20 strong CP angle. The naturalness of these parameters remains an open question, and
 21 in each case a natural explanation entails a significant extension of the Standard Model.
 22 Of these, the naturalness of the weak scale is perhaps the most pressing, as it is drawn
 23 into sharp relief by the discovery of an apparently elementary Higgs boson at the LHC.
 24 Evidence for a natural explanation for the value of the weak scale has yet to appear, with
 25 null results across a suite of experimental searches imperiling many preferred candidates.
 26 But the LHC is not capable of decisively deciding the naturalness of the weak scale,
 27 providing strong motivation for colliders that complement LHC sensitivity to natural new
 28 physics.

29 The oft-cited quadratically divergent radiative corrections to the Higgs boson mass pa-
 30 rameter,

$$\delta m_H^2 \sim \frac{3y_t^2}{8\pi^2} \Lambda^2, \quad (2.2)$$

31 are not the naturalness problem in and of themselves, but rather an indication of the prob-
 32 lem. Such divergences indicate that the Higgs boson mass parameter is precisely that –
 33 a parameter – and incalculable in the Standard Model. But the robust expectation is that
 34 the Higgs boson mass and other parameters of the Standard Model are fully calculable in
 35 a fundamental theory. In this case, the quadratically divergent contributions to the Higgs
 36 boson mass parameter in the Standard Model are replaced by finite contributions dictated
 37 by the fundamental theory. The Higgs boson mass in terms of underlying parameters will
 38 take the form

$$m_H^2 = a\Lambda_h^2 + b\frac{3y_t^2}{8\pi^2}\Lambda_h^2 + \dots \quad (2.3)$$

39 where a, b, \dots are dimensionless constants and Λ_h is an underlying mass scale of the fun-
 40 damental theory. If the Higgs boson mass is *natural*, the parameters a and b will be $\mathcal{O}(1)$,

1 up to possible manifestations of technical naturalness associated with symmetries in the
 2 underlying theory. In this case, one expects $m_H \sim \Lambda_h$, corresponding to the appearance
 3 of new physics near the weak scale. Alternately, $m_H \ll \Lambda_h$ points either to *fine-tuning*
 4 among fundamental parameters, or to a correlation between ultraviolet and infrared as-
 5 pects of the theory with no known counterpart in effective field theory.

6 The most promising strategy for rendering the weak scale natural in a more fundamen-
 7 tal theory is to extend the Standard Model to include additional symmetries that render
 8 the Higgs boson mass parameter technically natural. In four dimensions, the available
 9 symmetries are supersymmetry and global symmetry. In the former case, the fields of the
 10 Standard Model are extended into complete supersymmetric multiplets, and supersym-
 11 metry is softly broken to accommodate the non-degeneracy of Standard Model fields and
 12 their partners [8–10]. The Higgs boson is related to a fermionic partner, thereby rendering
 13 the Higgs boson mass technically natural by the same chiral symmetries that protect the
 14 fermion masses. In the latter case, the Higgs boson is a pseudo-Nambu-Goldstone boson
 15 (pNGB) of a spontaneously broken global symmetry, with a mass parameter protected by
 16 the corresponding shift symmetries. The scale of global symmetry breaking in such theo-
 17 ries must itself be rendered natural, leading to e.g. composite Higgs models [11] and little
 18 Higgs models [12] (for an excellent recent review, see [13]).

19 In both cases, these symmetries predict an abundance of new physics near the weak
 20 scale. Although this new physics may be searched for efficiently at the LHC, such searches
 21 typically leverage ancillary properties of the new physics unrelated to the naturalness of
 22 the weak scale. For example, searches for the scalar top partners predicted by supersym-
 23 metry typically leverage QCD quantum numbers of the stop and decay modes unrelated
 24 to the stop-Higgs coupling. The sensitivity of LHC searches to inessential features of the
 25 new physics makes them imperfect probes of electroweak naturalness.

26 In this respect, a Higgs factory provides the ideal context for probing natural new
 27 physics via precision Higgs couplings. The same couplings and diagrams that control the
 28 size of the Higgs boson mass in a natural theory generate radiative corrections to its cou-
 29 plings. As such, precision tests of Higgs boson properties directly probe natural physics
 30 in a way that is complementary to, and less subject to caveats than, direct searches at the
 31 LHC.

32 Signatures of natural new physics in precision Higgs boson measurements take a va-
 33 riety of forms. In most symmetry solutions, there are Higgs coupling deviations due to
 34 tree-level mixing with additional Higgs-like states. However, these tree-level deviations
 35 need not be the leading effect. Radiative corrections are also significant, due to both the
 36 size of Higgs couplings and the proximity of new particles to the weak scale. In theories
 37 where new physics associated with naturalness carries Standard Model quantum numbers,
 38 such as conventional supersymmetric and composite models, the most distinctive radiative
 39 corrections modify loop-induced Higgs couplings to gluons and photons. In addition, all
 40 symmetry solutions – whether or not they involve new states charged under the Standard
 41 Model – radiatively modify Higgs couplings through effective wavefunction renormaliza-
 42 tion of the physical Higgs scalar, an effect that may be observed in loop-level corrections
 43 to tree-level Higgs couplings.

44 Although our discussion of naturalness has focused on symmetries, they are not the
 45 only mechanism for explaining the value of the weak scale. The most notable alternative
 46 is to lower the cutoff in Equation (2.3), the avenue realized by technicolor [6, 14] and
 47 large [15, 16] or warped [17, 18] extra dimensions. However, these solutions typically

1 do not predict a significant mass gap between the Higgs boson and additional degrees
 2 of freedom, making them more susceptible to LHC null results. More recent proposals,
 3 such as relaxation of the weak scale [19], can potentially lead to $m_H \ll \Lambda_h$ without fine-
 4 tuning, and remain interesting targets for exploration. Nonetheless, these alternatives still
 5 involve new particles coupling to the Higgs boson, and may leave their imprint on Higgs
 6 couplings or exotic decays.

7 **Supersymmetry**

8 Supersymmetric extensions of the Standard Model have the virtue of rendering the weak
 9 scale natural with an elementary Higgs scalar, consistent with properties observed thus
 10 far at the LHC. While searches for supersymmetric partner particles at the LHC have
 11 excluded large regions of the natural supersymmetric parameter space, significant blind
 12 spots remain that are best covered by precision Higgs coupling measurements.

13 **Tree-level modifications to Higgs boson properties** Supersymmetric extensions of the
 14 Standard Model necessitate more than one Higgs doublet. Mass mixing between the
 15 CP -even neutral Higgs scalars leads to tree-level deviations in Higgs properties. In the
 16 limit that the additional Higgs scalars are heavy and may be integrated out, this leads to
 17 dimension-six operators that shift Higgs couplings to fermions and dimension-eight op-
 18 erators that shift Higgs couplings to massive vectors. As a result, deviations are largest
 19 in Higgs couplings to fermions, particularly those in the down quark and lepton sectors.
 20 Percent-level CEPC sensitivity to modifications of the Higgs coupling to bottom quark en-
 21 ables indirect tests of the MSSM Higgs sector to the TeV scale, as illustrated in Figure 2.3.
 22 More broadly, CEPC sensitivity to tree-level effects in extended Higgs sectors such as the
 23 MSSM is studied comprehensively in [20]. However, due to the decoupling properties
 24 of the MSSM Higgs sector, heavy Higgs states may remain above the TeV scale without
 25 increasing the fine-tuning of the weak scale. In this respect, tree-level modifications to
 26 Higgs properties arising in supersymmetric theories represent a discovery opportunity but
 27 not an irreducible constraint.

28 **Loop-level modifications to Higgs properties** The plethora of new partner particles pre-
 29 dicted by supersymmetric extensions of the Standard Model leads to a wealth of loop-level
 30 contributions to Higgs couplings. These contributions are typically largest in the stop sec-
 31 tor, due to the large coupling to the Higgs boson required by supersymmetry, but may
 32 be significant for any of the partners of third-generation fermions. The most distinctive
 33 consequences are modifications to the loop-level Standard Model couplings of the Higgs
 34 boson to gluons and photons, though radiative corrections to tree-level couplings arise
 35 as well and may be used to cover blind spots arising in the loop-level couplings. The
 36 potential for CEPC to probe a suite of loop-level corrections to Higgs and electroweak
 37 observables in supersymmetric models is comprehensively studied in [23].

38 For simplicity, here we will focus on the loop-level consequences in the stop sector,
 39 corresponding to the scalar partners of both the right-handed and left-handed top quarks.
 40 In the limit that the stops are significantly heavier than the Higgs boson, the correction to
 41 gluons and photons is proportional to

$$\frac{1}{4} \left(\frac{m_t^2}{m_{\tilde{t}_1}^2} + \frac{m_t^2}{m_{\tilde{t}_2}^2} - \frac{m_t^2 X_t^2}{m_{\tilde{t}_1}^2 m_{\tilde{t}_2}^2} \right) \quad (2.4)$$

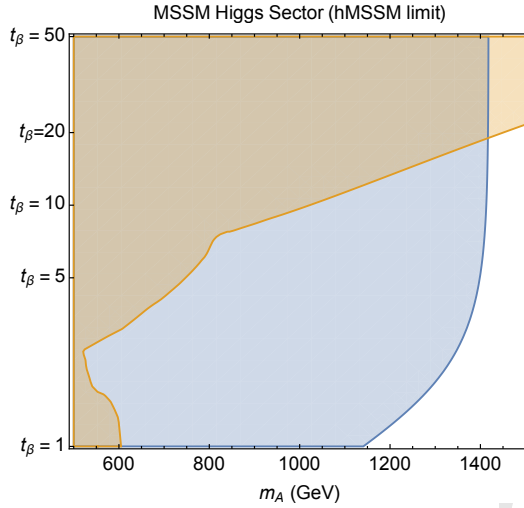


Figure 2.3: Potential coverage of the MSSM Higgs sector in the hMSSM limit [21] at CEPC is shown in blue. Sensitivity is driven largely by modifications of the Higgs coupling to bottom quarks. Projected HL-LHC coverage of the MSSM Higgs sector in the same limit due to direct searches for heavy Higgs states is shown in orange [22].

where $m_{\tilde{t}_1}, m_{\tilde{t}_2}$ are the stop mass eigenstates and $X_t = A_t - \mu \cot \beta$ is the off-diagonal mixing parameter in the stop mass matrix. The mixing parameter is bounded from above by the avoidance of tachyonic stops, and from below by precision measurements of the Higgs coupling to gluons and photons. A robust bound may be placed on the stop sector whenever the minimum value exceeds the maximum value [24]. The strongest constraints arise in the degenerate limit when $m_{\tilde{t}_1} = m_{\tilde{t}_2}$, in which case CEPC is capable of probing stop masses close to the TeV scale; this is illustrated in the Figure 2.4(a). However, the modification of Higgs couplings is highly sensitive to the mixing in the stop sector, and blind spots arise when the mixing leads to vanishing deviations in the Higgs coupling to gluons and photons [23, 25]. However, as illustrated in the Figure 2.4(b), these blind spots may be covered by precision measurements of the ZH cross section, which is sensitive to loop-level corrections to the tree-level HZZ coupling that are generically nonzero in the gluon/photon blind spot [25].

14 Global symmetry

Global symmetry approaches to the weak scale cover a vast array of specific models and UV completions, but share the common features of an approximately elementary Standard Model-like Higgs boson mixing with heavier resonances and further influenced by the presence of light fermionic excitations.

Tree level In global symmetry solutions, the Higgs boson is a pNGB of a spontaneously broken global symmetry. This invariably implies tree-level corrections, which can be interpreted as arising from mixing between the Standard Model-like Higgs boson and heavy states associated with the spontaneously broken global symmetry. This mixing is typically proportional to v^2/f^2 , where f is the decay constant associated with the broken global symmetry (see e.g. [27] for a comprehensive parameterization), although precise corrections may vary between Higgs couplings to fermions and gauge bosons depending on the model. As shown in Figure 2.5, the precision attainable at CEPC probes this mixing

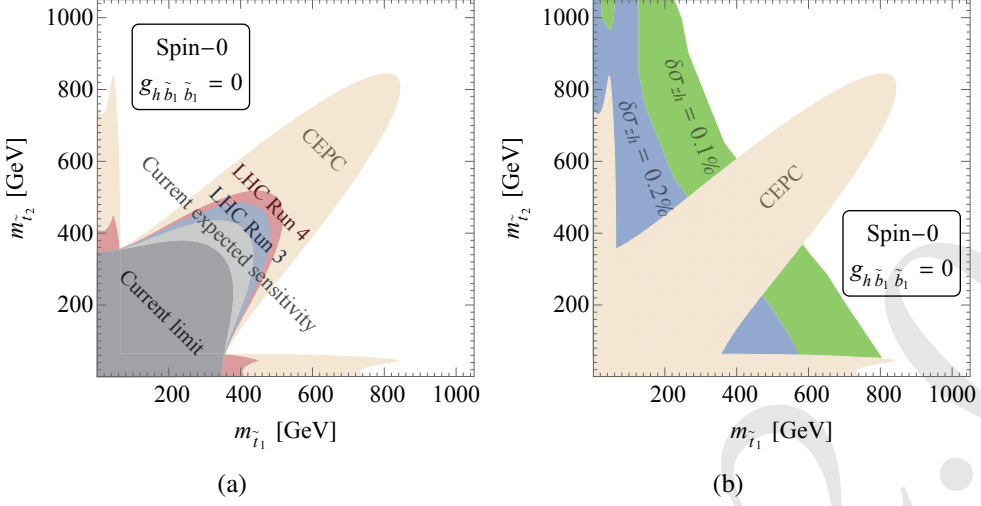


Figure 2.4: (a) LHC and CEPC precision Higgs constraints in the $m_{\tilde{t}_1} - m_{\tilde{t}_2}$ plane from Higgs couplings to gluons and photons. (b) Coverage of blind spots including precision measurement of the ZH cross section. Figures adapted from [26].

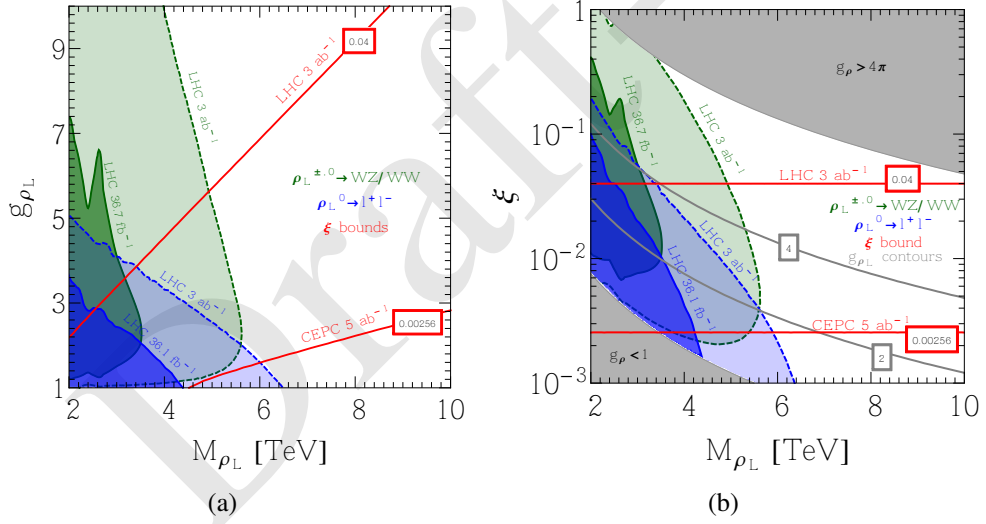


Figure 2.5: Potential coverage of composite-type global symmetry models in terms of resonance mass M_{ρ_L} and coupling parameter g_{ρ_L} (a) or mixing parameter $\xi \equiv v^2/f^2$ (b) via direct searches at the LHC (blue and green shaded regions) and precision Higgs measurement constraints (red lines).

to better than one part in one hundred, translating to an energy reach of several TeV. In the simplest composite realizations of global symmetries, bounds on v^2/f^2 translate directly into lower bounds on the tuning of the electroweak scale, but this tuning may be avoided in Little Higgs models and related constructions. The complementarity between precision measurements of Higgs couplings and direct searches at future colliders in probing global symmetry approaches to the hierarchy problem is explored in detail in e.g. [28].

Loop level Global symmetry approaches to naturalness likewise feature a plethora of new states near the weak scale, albeit with the same statistics as their Standard Model

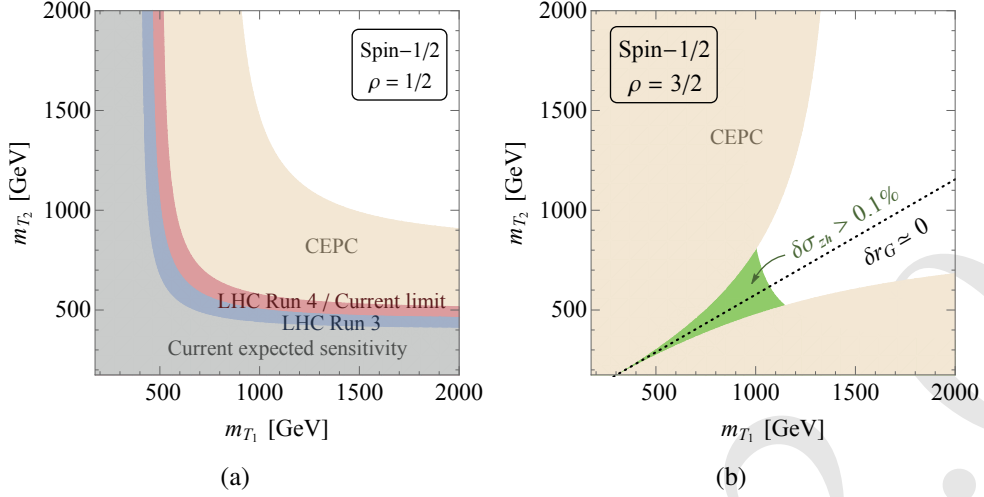


Figure 2.6: (a) LHC and CEPC precision Higgs constraints in the $m_{T_1} - m_{T_2}$ plane from Higgs couplings to gluons and photons assuming equal couplings. (b) Coverage of blind spots including precision measurement of the ZH cross section. Figures adapted from [26].

1 counterparts. While corrections to Higgs couplings from loops of these new particles are
2 typically sub-dominant compared to tree-level corrections, they provide a more immutable
3 test of naturalness. As with supersymmetry, the largest corrections are typically due to the
4 fermionic top partner sector, due to the large coupling of these partners to the Higgs boson
5 and their proximity to the weak scale. As such partners typically carry Standard Model
6 quantum numbers, the most striking corrections are to the loop-level couplings of the
7 Higgs boson to gluons and photons.

8 For the sake of definiteness, consider a theory involving two top partners T_1, T_2 whose
9 couplings are dictated by the global symmetry protecting the Higgs boson mass. In this
10 case corrections to the Higgs coupling to gluons and photons are proportional to [26]

$$-\left(\rho \frac{m_t^2}{m_{T_1}^2} + (1 - \rho) \frac{m_t^2}{m_{T_2}^2}\right) \quad (2.5)$$

11 where ρ parametrizes the fraction of the quadratic divergence cancellation coming from
12 the T_1 field, which is directly reflected in the modification of Higgs couplings. In the case
13 of equal couplings, CEPC is capable of probing fermionic top partners above the TeV
14 scale, as shown in the Figure 2.6(a). Note that the existence of more than one fermionic
15 top partner allows for the possibility of a blind spot to arise when $\rho > 1$, which may be
16 constrained by radiative corrections to the ZH cross section (shown in the Figure 2.6(b))
17 in analogy with the stop blind spot in supersymmetry. A comprehensive exploration of
18 CEPC's potential to constrain radiative corrections to Higgs couplings arising in global
19 symmetry solutions to the hierarchy problem may be found in [26].

20 Neutral naturalness

21 While it is entirely possible that the naturalness of the weak scale is explained by con-
22 ventional symmetries that have thus far evaded LHC detection, LHC null results may
23 indicate that the weak scale is stabilized by less conventional symmetries that do not lead
24 to partner particles carrying Standard Model quantum numbers. This form of "neutral"

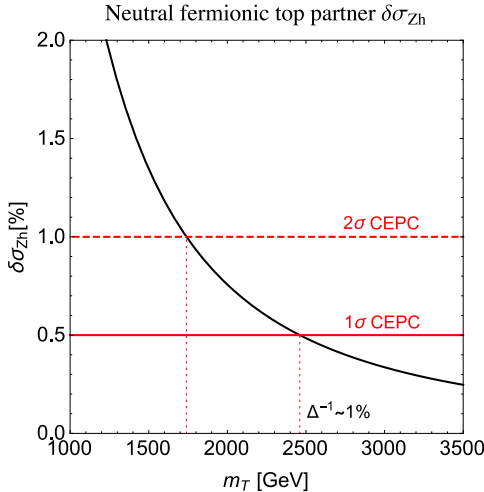


Figure 2.7: CEPC reach in the mass scale of neutral fermionic top partners due to tree-level mixing corrections to σ_{ZH} .

“naturalness” [29] can occur, for example, when only discrete symmetries are operative at the weak scale. To date both opposite-statistics and same-statistics examples of neutral naturalness have been constructed. The former case is exemplified by Folded Supersymmetry [30], which features new partner particles carrying electroweak quantum numbers but no irreducible tree-level corrections. The latter case is exemplified by the Twin Higgs [31], which features new partner particles entirely neutral under the Standard Model, as well as significant tree-level Higgs coupling deviations. Examples also exist of theories with entirely neutral scalar top partners [32] and electroweak-charged fermionic top partners [33], both of which share the tree-level modifications to Higgs couplings of the Twin Higgs.

The primary phenomenological consequences of neutral naturalness are (1) a significant weakening of direct search limits due to the paucity of states charged under the Standard Model, and (2) the reduction of loop-level corrections to loop-level Higgs couplings. However, these models still lead to distinctive patterns of Higgs coupling deviations that may be first revealed at a Higgs factory.

Tree level Many theories of neutral naturalness, most notably the Twin Higgs [31], feature significant tree-level mixing between the Standard Model-like Higgs boson and an additional CP even scalar state. Much as with conventional global symmetries, this leads to $\mathcal{O}(v^2/f^2)$ deviations in Higgs couplings. In contrast to conventional global symmetries, however, these corrections are typically universal in the sense that they are the same for Higgs couplings to both vectors and fermions. Bounds on v^2/f^2 may be translated directly into bounds on the mass of the twin top partner, as shown in Figure 2.7. In such cases, CEPC can probe multi-TeV scales and test the efficacy of neutral naturalness down to the percent level.

Loop level While all models of neutral naturalness feature loop-level corrections to Higgs properties, they are the leading effect in many opposite-statistics models such as folded supersymmetry. New partner particles in these models still carry electroweak quantum numbers, leading to loop-level deviations in the Higgs coupling to photons, as shown

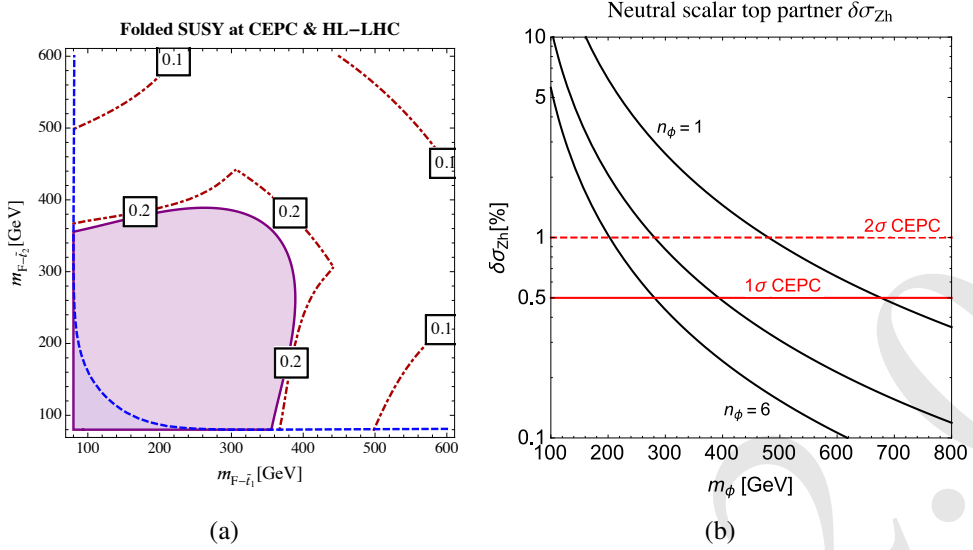


Figure 2.8: (a) CEPC reach for color-neutral folded stops in Folded SUSY from Higgs couplings to photons, from [23]. (b) CEPC reach in the mass scale of neutral scalar top partners due to loop-level corrections to σ_{ZH} , adapted from [34].

in Figure 2.8. This allows CEPC to place constraints on the mass scale of folded partner particles in the hundreds of GeV, probing tuning of the weak scale to the 20% level in these theories.

It is also possible that the weak scale is stabilized by scalar top partners entirely neutral under the Standard Model without accompanying tree-level Higgs coupling deviations. In this case, all of the distinctive direct search channels and corrections to loop-level Higgs couplings are absent. However, a precision measurement of the ZH cross section is still sensitive to the wavefunction renormalization of the physical Higgs scalar induced by loops of the scalar top partners [34]. In general, n_ϕ scalars ϕ_i coupling via the Higgs portal interaction $\sum_i \lambda_\phi |H|^2 |\phi_i|^2$ leads to a correction to the ZH cross section of the form

$$\delta\sigma_{ZH} = \frac{n_\phi |\lambda_\phi|^2}{8\pi^2} \frac{v^2}{m_H^2} \left[1 + \frac{1}{4\sqrt{\tau(\tau-1)}} \log \left(\frac{1 - 2\tau - 2\sqrt{\tau(\tau-1)}}{1 - 2\tau + 2\sqrt{\tau(\tau-1)}} \right) \right] \quad (2.6)$$

where $\tau = m_H^2/4m_\phi^2$. This leads to the sensitivity shown in Figure 2.8, for which CEPC is able to place constraints in the hundreds of GeV on a scenario that is otherwise largely untestable at colliders.

Other solutions

Symmetries are not the only mechanism for explaining the origin of the weak scale, though other solutions may not be manifestly natural in the same way. However, even non-symmetry explanations for the value of the weak scale (excepting anthropic ones) generically entail some degree of coupling between new degrees of freedom and the Higgs boson itself. This typically leads to deviations in Higgs couplings, new exotic decay modes of the Higgs boson, or a combination thereof.

A compelling example of non-symmetry solutions is the relaxion [19], in which the value of the weak scale is set by the evolution of an axion-like particle across its potential in the early universe. The relaxion necessarily couples to the Higgs boson in order for

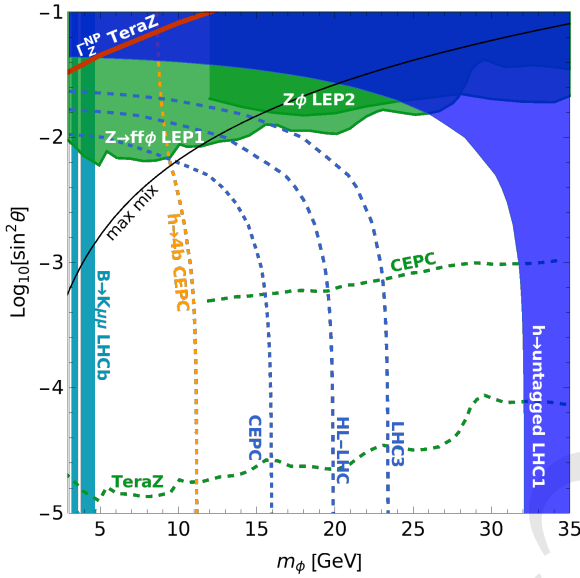


Figure 2.9: Constraints on the relaxion mass m_ϕ and relaxion-Higgs mixing angle $\sin \theta$ from the non-Standard Model decay of the Higgs boson into relaxion pairs, adapted from [35]. Shaded regions indicate current exclusions from LEP and the LHC. Dashed blue lines indicate the reach of CEPC and future operation of the LHC in searches for untagged non-Standard Model decays of the Higgs boson, while the orange dashed line indicates the reach of CEPC in searches for $H \rightarrow \phi\phi \rightarrow 4b$. The green dashed line indicates the reach of CEPC’s Z -pole run in searches for $e^+e^- \rightarrow Z\phi$.

its evolution to influence the Higgs boson mass. This leads to a variety of signatures that may be tested via precision Higgs measurements [35, 36].

The most promising signature is that of new exotic Higgs boson decays, most notably into the relaxion itself. This signature arises in most relaxion models as a generic consequence of the backreaction of electroweak symmetry breaking onto the relaxion potential. The mixing angle between the Higgs boson and relaxion in these scenarios is parametrically of order

$$\sin \theta \approx \frac{\Lambda_{\text{br}}^4}{v f m_H^2} \quad (2.7)$$

where Λ_{br} is the confinement scale inducing a potential for the relaxion (identifiable with Λ_{QCD} in the most minimal models) and f is the relaxion decay constant. This leads to the decay of the Higgs boson into pairs of relaxions ϕ , which in turn decay back into Standard Model states via Higgs-relaxion mixing.

The CEPC can significantly constrain these scenarios through both direct searches for processes such as $H \rightarrow \phi\phi \rightarrow 4b$ and indirect limits on exotic Higgs boson decays coming from precision Higgs measurements, as shown in Figure 2.9. This exemplifies the considerable power of CEPC in identifying natural explanations for the weak scale, even in the absence of additional symmetries, by virtue of its broad sensitivity to new particles interacting with the Higgs boson.

2.2.2 Electroweak phase transition

The discovery of the Higgs boson marks the culmination of a decades-long research program to understand the source of electroweak symmetry breaking (EWSB). We have known since the mid-20th century that this symmetry is not realized in nature and that the

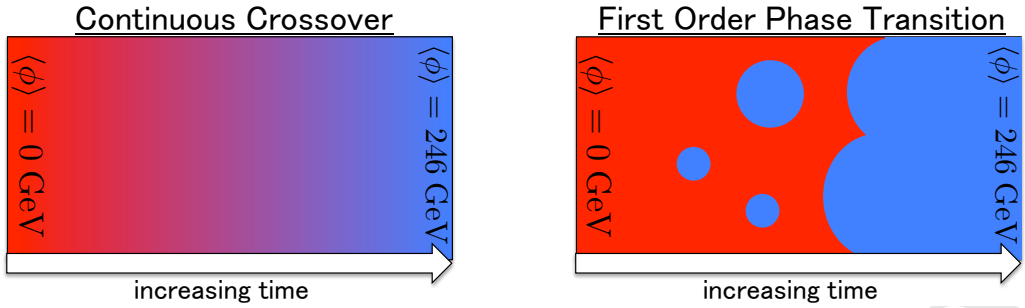


Figure 2.10: An illustration of a continuous crossover (left) and a first order phase transition (right).

weak gauge bosons are massive. Now measurements at the Large Hadron Collider (LHC) have provided overwhelming evidence that EWSB results from the recently-discovered Higgs boson. With the Higgs boson discovery we have learned *why* the electroweak symmetry is broken in nature, but we still do not understand *how* it is broken dynamically — this is the question of the *electroweak phase transition*.

The nature of the electroweak phase transition (EWPT) is controlled by the properties and interactions of the Higgs boson. For instance the Higgs mass sets the temperature scale of the phase transition to be roughly $T \sim m_H \simeq 125 \text{ GeV}$. The more detailed and interesting features of the phase transition depend also upon the interactions of the Higgs boson with itself, with other Standard Model particles, and with possible new physics. The nature of these interactions will not be determined very precisely at the LHC, where we have only just begun to study the Higgs boson. Rather, if we want to understand the nature of the electroweak phase transition, we require precision measurements of Higgs physics at a dedicated Higgs factory experiment like CEPC.

First order phase transition or continuous crossover?

Despite years of careful study at the LHC, we still have such a poor understanding of the Higgs boson that it is impossible to determine even the *order of the electroweak phase transition*. In general, these two scenarios are used to classify symmetry-breaking phase transitions:

- A *first order phase transition* proceeds through the nucleation of *bubbles* that grow, coalesce, and eventually fill the system.
- By contrast, a *continuous crossover* occurs smoothly throughout the system.

See also Figure 2.10. If the phase transition is determined to be first order, there would be profound implications for early-universe cosmology and the origin of the matter-antimatter asymmetry. Moreover, determining the order of the EWPT is simply the first step in a much richer research program that deals with other aspects of the phase transition including its latent heat, bubble wall velocity, and plasma viscosity.

The Higgs potential

The order of the EWPT is intimately connected to the shape of the *Higgs potential energy function*. For each value of the Higgs field, ϕ , there is an associated potential energy density, $V(\phi)$. During the electroweak phase transition, the Higgs field passes from $\phi = 0$ where the electroweak symmetry is unbroken to $\phi = v \simeq 246 \text{ GeV}$ where the electroweak

symmetry is broken and the weak gauge bosons are massive. Thus the order of the phase transition is largely determined by the shape of $V(\phi)$ in the region $0 < \phi < v$.

For instance, if the Higgs potential has a barrier separating $\phi = 0$ from $\phi = v$, then electroweak symmetry breaking is accomplished through a first order phase transition with the associated bubble nucleation that we discussed above. If there is no barrier in $V(\phi)$, the transition may be either first order or a crossover depending on the structure of the *thermal effective potential*, $V_{\text{eff}}(\phi, T)$.

Currently we know almost nothing about the shape of the Higgs potential. This situation is illustrated in Figure 2.11 and the following discussion. When we make measurements of the Higgs boson in the laboratory, we only probe small fluctuations of the potential around $\phi = v$. By measuring the strength of the weak interactions, $G_F = (\sqrt{2}v^2)^{-1} \simeq 1 \times 10^{-5} \text{ GeV}^{-2}$, we learn that the Higgs potential has a local minimum at $v \simeq 246 \text{ GeV}$. By measuring the Higgs boson's mass, we learn that the local curvature of the potential at its minimum is $(d^2V/d\phi^2)|_{\phi=v} = m_H^2 \simeq (125 \text{ GeV})^2$. This is the extent of what we know today about the Higgs potential. Even the third derivative, which is related to the Higgs boson's cubic self-coupling, is completely undetermined!

Measurements of the Higgs boson thus far are consistent with the predictions of the Standard Model of particle physics. The Standard Model asserts that the Higgs potential has the form

$$V(\phi) = \frac{1}{2}\mu^2\phi^2 + \frac{1}{4}\lambda\phi^4, \quad (2.8)$$

which only depends on the two parameters μ^2 and λ . Taking $\lambda > 0$ and $\mu^2 < 0$ induces a vacuum expectation value (VEV) for the Higgs field and triggers electroweak symmetry breaking. At the minimum of the potential $v = \sqrt{-\mu^2/\lambda}$ gives the Higgs field VEV and $m_H^2 = -2\mu^2$ gives the Higgs boson's mass. Thus, having measured both $v \simeq 246 \text{ GeV}$ and $m_H \simeq 125 \text{ GeV}$ in the laboratory, the Standard Model completely predicts the shape of the Higgs potential. For these values of the Higgs boson mass and VEV, the electroweak phase transition is expected to proceed via a continuous crossover in the absence of additional physics beyond the Standard Model.

However the presence of new physics can dramatically change the shape of the Higgs potential without disrupting the measurements of v and m_H . For example, a simple generalization of Equation (2.8) is to include a sextic term and write the Higgs potential as [37–39]

$$V(\phi) = \frac{1}{2}\mu^2\phi^2 + \frac{1}{4}\lambda\phi^4 + \frac{1}{8\Lambda^2}\phi^6. \quad (2.9)$$

A potential of this form arises if new, heavy particles are coupled to the Higgs boson, and then Λ is related to the mass scale of the new particles. This potential has enough structure to support two local minima with a barrier between, which we see in Figure 2.11 for the curve labeled "new physics (1)." The nature of the electroweak phase transition in this model is expected to be very different from the Standard Model due to the barrier [40–42]. Alternatively the new physics can manifest through a non-analytic term in the Higgs potential, such as the one proposed by Coleman and Weinberg [43],

$$V(\phi) = \frac{1}{4}\lambda\phi^4 \log \frac{\phi^2}{\Lambda^2}. \quad (2.10)$$

Such a potential arises when new physics is coupled to the Higgs boson and leads to a strong running in the Higgs quartic self-coupling [44]. As shown by the curve labeled

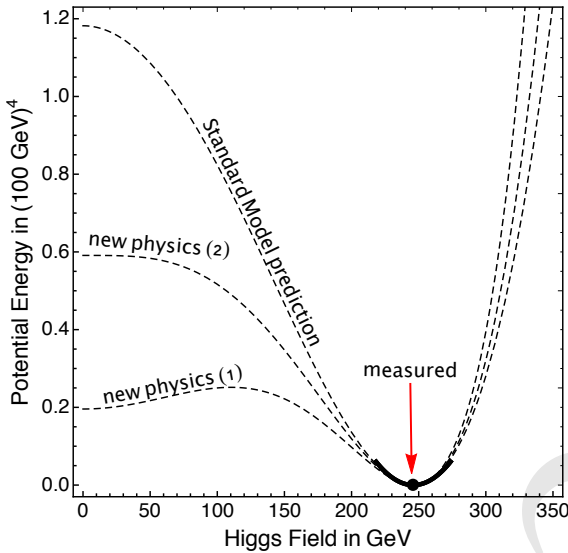


Figure 2.11: The Higgs potential energy function. All we know about the shape of the Higgs potential is the local curvature at its minimum. These observations are consistent with the Standard Model, but they are also consistent with models containing new physics that can dramatically change the nature of the electroweak phase transition.

¹ "new physics (2)" in Figure 2.11, this potential is very flat near the origin allowing thermal
² corrections to induce a barrier and thus a first order phase transition.

³ Precision measurements of the Higgs boson's interactions with itself and other particles
⁴ will probe the shape of the potential energy function and thereby provide much-needed
⁵ experimental input to test the order of the electroweak phase transition.

⁶ Cosmological implications

⁷ Since we cannot reproduce the high-temperature conditions of the electroweak phase transition
⁸ in the laboratory, the question of the EWPT has the most relevance for studies of the
⁹ early universe. Most cosmologists expect that a thermal EWPT occurred soon after
¹⁰ the Big Bang when the universe was filled with a very hot plasma. If the early universe
¹¹ EWPT was first order, it may have left behind interesting cosmological relics that could
¹² be accessible to observations today.

¹³ **Gravitational Waves.** During a first order electroweak phase transition, gravitational waves
¹⁴ are produced from the collisions of bubbles, the decay of magnetohydrodynamic turbulence,
¹⁵ and the damping of sound waves [45]. Today these gravitational waves would look
¹⁶ like a stochastic and isotropic "noise" from all directions on the sky. As we see in Figure
¹⁷ 2.12 the predicted gravitational wave spectrum falls within reach of future space-based
¹⁸ interferometer experiments, including LISA, DECIGO, BBO, Taiji, and TianQin. The de-
¹⁹ tection of these gravitational waves would provide direct evidence that the cosmological
²⁰ EWPT was a first-order one, but a future collider like CEPC is required to uncover the
²¹ new physics that explains *why* the EWPT is first order.

Matter-Antimatter Asymmetry. A first order cosmological EWPT provides the right environment to explain the Universe's excess of matter over antimatter through the mechanism of *electroweak baryogenesis* [46]. This mechanism uses the fact that baryon number is

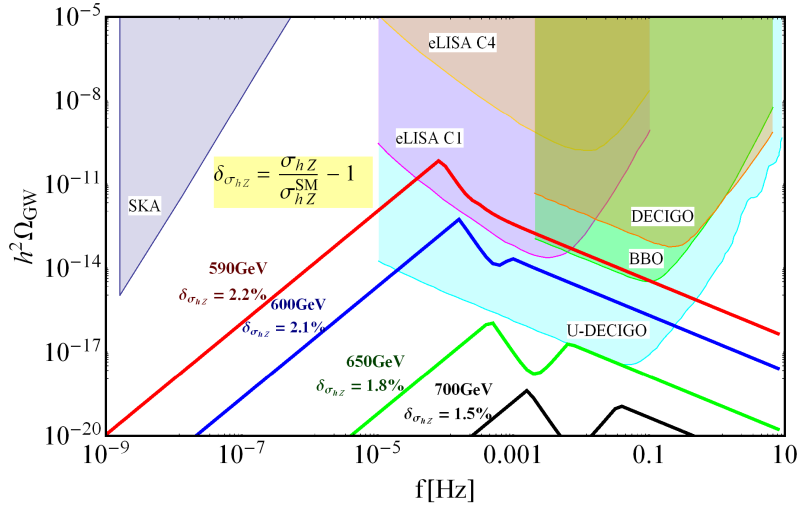


Figure 2.12: The spectrum of gravitational waves generated during a first order electroweak phase transition for the model described in Equation (2.9). Colored curves show the predicted spectrum for different models as the scale of new physics, Λ , is varied. The figure is reproduced from Ref. [42].

violated in the Standard Model through reactions mediated by the electroweak sphaleron. Before the cosmological EWPT, the sphaleron efficiently converts matter into antimatter, but during the electroweak phase transition the sphaleron-mediated reactions are shut off. If this shutoff is sufficiently abrupt, then an excess of matter over antimatter can be generated. This requires that the electroweak phase transition is *strongly first order* in the sense that

$$\frac{v(T_{\text{pt}})}{T_{\text{pt}}} \gtrsim 1.0 \quad (\text{"strongly first order" electroweak phase transition}) \quad (2.11)$$

where $v(T_{\text{pt}})$ is the value of the Higgs field inside of the bubbles during the phase transition at temperature T_{pt} .

Electroweak baryogenesis is not viable in the Standard Model, because the electroweak phase transition is a continuous crossover, $v(T_{\text{pt}}) = 0$, and thus the observed excess of matter over antimatter is an irrefutable motivation for physics beyond the Standard Model. In general the new physics can take many forms, but in the context of electroweak baryogenesis, it is clear that the new physics must couple to the Higgs boson so that the sphaleron-suppression condition in Equation (2.11) is satisfied. Therefore this condition directly quantifies the required departure from Standard Model physics.

New physics and the electroweak phase transition

The Standard Model predicts that the EWPT is a continuous crossover, but we have seen in the discussion of Figure 2.11 that even minimal extensions of the Standard Model can drastically change the predictions for electroweak symmetry breaking. Thus for any model with new physics coupled to the Higgs boson, it is necessary to ask: What is the nature of the electroweak phase transition?

In the years before the LHC started running, much of the work was focused on the *light stop scenario* of the Minimal Supersymmetric Standard Model (MSSM) [47, 48]. Early LHC data determined that this scenario is ruled out [49, 50], because the light stops,

which are colored and charged particles with spin-0, should have been easy to produce and detect at the LHC. However, if the new scalar particles were not charged or colored, the electroweak phase transition could still be first order while evading collider constraints; to leading order, the electroweak phase transition only cares about couplings with the Higgs boson, not quantum numbers [51]. Therefore in order to assess the unique power of CEPC to test new physics that leads to a first order electroweak phase transition, it is useful to consider models with uncharged and uncolored particles, which are very difficult to probe at the LHC [52].

A viable model with a first order EWPT is found in even the most minimal extension of the Standard Model with a real, scalar singlet field S [53–55]. The relevant Lagrangian is written as

$$\begin{aligned} \mathcal{L} = & (D_\mu H)^\dagger (D^\mu H) + \frac{1}{2} (\partial_\mu S) (\partial^\mu S) - \mu_H^2 H^\dagger H - \lambda_H (H^\dagger H)^2 \\ & - \frac{\mu_S^2}{2} S^2 - \frac{a_S}{3} S^3 - \frac{\lambda_S}{4} S^4 - \lambda_{HS} H^\dagger H S^2 - 2a_{HS} H^\dagger H S \end{aligned} \quad (2.12)$$

where $H(x)$ denotes the Higgs doublet field. The last two operators in Equation (2.12) correspond to the so-called Higgs portal interactions. The Higgs field acquires a vacuum expectation value, $\langle H \rangle = (0, v/\sqrt{2})$ that breaks the electroweak symmetry. In general the singlet field may acquire a vacuum expectation value, $\langle S \rangle = v_S$, and it can mix with the Higgs boson, which is parametrized by an angle θ . The spectrum of this theory contains two scalars with masses $m_H \simeq 125$ GeV and m_S .

It is also interesting to consider the model that is obtained by imposing a \mathbb{Z}_2 symmetry on Equation (2.12). This symmetry transformation, $S(x) \rightarrow -S(x)$, enforces $a_{HS} = a_S = 0$, and it is conventional to also assume that $v_S = 0$.

The singlet extension of the Standard Model allows for a first order electroweak phase transition in a variety of ways [51]. If the singlet particle is heavy, $m_S \gg m_H$, then it can be integrated out of the theory generating an effective potential for the Higgs field. In the regime where the a_S and λ_S terms are negligible and $\mu_S^2 \gg \lambda_{HS} v^2$, the Higgs potential takes the form

$$V(\phi) = \frac{1}{2} \mu_H^2 \phi^2 + \frac{1}{4} \left(\lambda_H - \frac{2a_{HS}^2}{\mu_S^2} \right) \phi^4 + \frac{\lambda_{HS} a_{HS}^2}{2m_S^4} \phi^6, \quad (2.13)$$

which has the same structure as the one that we encountered in Equation (2.9). The two potentials are matched by taking $\Lambda^2 = m_S^4/(4\lambda_{HS} a_{HS}^2)$. For smaller Λ the shape of the Higgs potential begins to deviate more from the Standard Model prediction, and the phase transition becomes first order. This example illustrates the intuition that models with a first order electroweak phase transition require new, light particles with a large coupling to the Higgs boson. If the singlet particle is so light that we are not justified to integrate it out ($m_S \sim m_H$) the analysis above is inapplicable, but the phase transition can still be made first order due to the presence of large loop corrections to the Higgs potential [44], large thermal corrections, and/or a multi-step phase transition [56]. Some of these scenarios are illustrated in the Figure 2.13(a) for the \mathbb{Z}_2 -symmetric singlet extension.

In general the presence of new particles coupled to the Higgs boson modifies how strongly the Higgs boson couples to itself and to the other Standard Model particles. It is precisely the goal of Higgs factory experiments, like CEPC, to measure these couplings with high precision. Therefore, if the electroweak phase transition is first order, we ex-

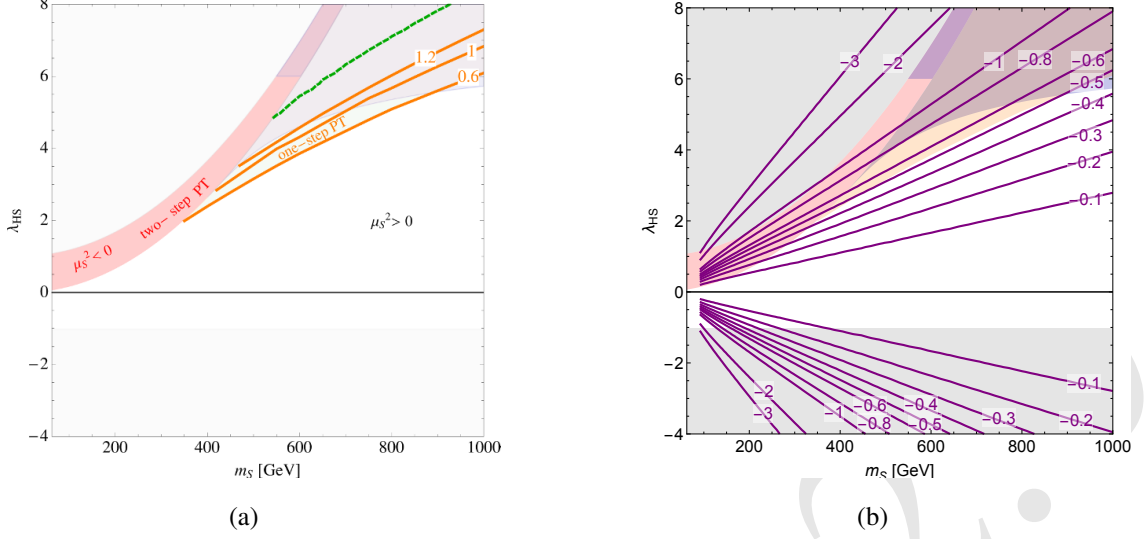


Figure 2.13: Parameter space of the real scalar singlet model with \mathbb{Z}_2 symmetry. (a) Regions of parameter space that lead to a first order electroweak phase transition that proceeds in one or two steps. The orange curves show the strength of the electroweak phase transition, $v(T_c)/T_c$, in the one-step region. (b) Purple curves show the fractional change to the ZH production cross section relative to the SM prediction in percent; these values are $2\delta g_{HZZ}$ using the notation in the text (2.14). The figures are taken from Ref. [57]. (Also see Ref. [58].)

pect that the measurements of these couplings must deviate from their Standard Model predictions.

The coupling that will be measured most precisely at CEPC and future lepton colliders is the Higgs- Z - Z coupling. We can parametrize deviations in this parameter away from the Standard Model prediction with the variable

$$\delta g_{HZZ} \equiv \frac{1}{2} \left(\frac{\sigma(e^+e^- \rightarrow HZ)}{\sigma_{SM}(e^+e^- \rightarrow HZ)} - 1 \right) \Big|_{s=(250 \text{ GeV})^2} = \frac{g_{HZZ}}{g_{HZZ,SM}} - 1 \Big|_{s=(250 \text{ GeV})^2}. \quad (2.14)$$

In the singlet extension model, the strength of the HZZ coupling is suppressed compared to the SM prediction. The leading-order suppression arises from the Higgs-singlet mixing, and the sub-leading effect arises from Higgs wavefunction renormalization [34] and the Higgs triple self-coupling [59]. Combining these effects, the fractional suppression is written as [57, 60]

$$\begin{aligned} \delta g_{HZZ} = & (\cos \theta - 1) - 2 \frac{|a_{HS} + \lambda_{HS} v_S|^2}{16\pi^2} I_B(m_H^2; m_H^2, m_S^2) \\ & - \frac{|\lambda_{HS}|^2 v^2}{16\pi^2} I_B(m_H^2; m_S^2, m_S^2) + 0.006 \left(\frac{\lambda_3}{\lambda_{3,SM}} - 1 \right) \end{aligned} \quad (2.15)$$

where θ is the Higgs-singlet mixing angle, and I_B is a loop function. The Higgs triple self-coupling λ_3 also deviates from the Standard Model prediction due to the Higgs-singlet mixing. Then the self-coupling is predicted to be [61]

$$\begin{aligned} \lambda_3 = & (6\lambda_H v) \cos^3 \theta + (6a_{HS} + 6\lambda_{HS} v_S) \sin \theta \cos^2 \theta \\ & + (6\lambda_{HS} v) \sin^2 \theta \cos \theta + (2a_S + 6\lambda_S v_S) \sin^3 \theta. \end{aligned} \quad (2.16)$$

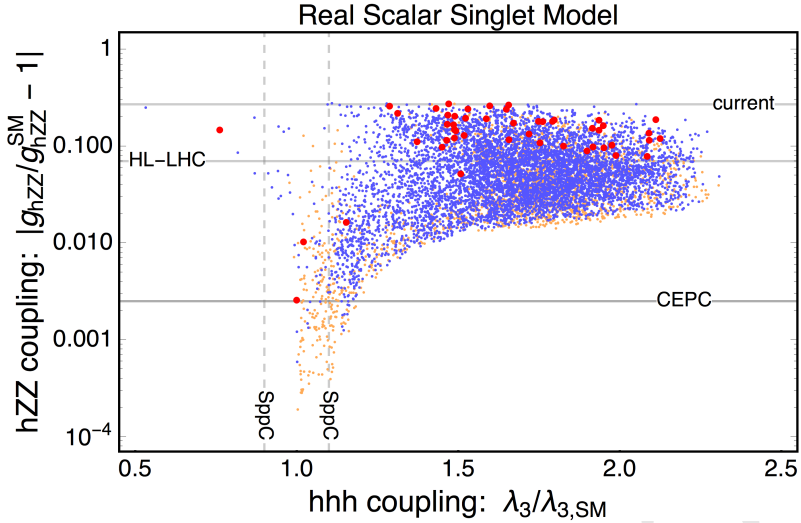


Figure 2.14: Collider observables in the real scalar singlet model. Points in theory space with a first order phase transition are shown in orange, points with a strongly first order phase transition are shown in blue, and points with a strongly first order phase transition that also produces detectable gravitational waves are shown in red. The figure is reproduced from Ref. [60].

In the Standard Model we have $\lambda_3 = \lambda_{3,SM} \equiv 3m_H^2/v \simeq 191$ GeV. If the singlet is light, $m_S < m_H/2$, then the Higgs boson acquires an exotic decay channel, $H \rightarrow SS$, which may be invisible depending on the stability of S . The rate for this decay is

$$\Gamma(H \rightarrow SS) = \frac{\lambda_{211}^2}{32\pi m_H} \sqrt{1 - \frac{4m_S^2}{m_H^2}} \quad (2.17)$$

where

$$\begin{aligned} \lambda_{211} = & (2a_{HS} + 2\lambda_{HSV}v_S) \cos^3 \theta + (4\lambda_{HSV}v - 6\lambda_H v) \sin \theta \cos^2 \theta \\ & + (6\lambda_S v_S + 2a_S - 4\lambda_{HSV}v_S - 4a_{HS}) \sin^2 \theta \cos \theta + (-2\lambda_{HSV}) \sin^3 \theta \end{aligned} \quad (2.18)$$

is the effective tri-linear coupling of the mass eigenstates. Measurements of the Higgs boson at the LHC already strongly constrain the invisible decay channel, which requires $\lambda_{211} \ll 1$ or $m_S > m_H/2$.

The complementarity between a first order electroweak phase transition and precision Higgs observables is shown in Figure 2.14 for the singlet extension of the Standard Model. Orange points correspond to models with a first order phase transition, $v(T_{pt})/T_{pt} \neq 0$. Blue points correspond to models with a strongly first order phase transition, $v(T_{pt})/T_{pt} \gtrsim 1$, which is a necessary requirement for electroweak baryogenesis (2.11). Red points correspond to models with a very strongly first order phase transition that can potentially be probed by the space-based gravitational wave interferometer telescope LISA.

Figure 2.14 shows that the models with a first order phase transition (all colored points) also generally predict large deviations in the HZZ coupling. For the models with a strongly first order phase transition (blue and red points) the effect on g_{HZZ} is large enough to be tested by CEPC. Additionally, most of the parameter points also predict a large enhancement to the Higgs trilinear self-coupling that can be probed by a future 100 TeV hadron collider experiment, like the proposed SppC. The funnel region of orange points at $\lambda_3/\lambda_{3,SM} \approx 1$ corresponds to a "blind spot" where the Higgs-singlet mixing

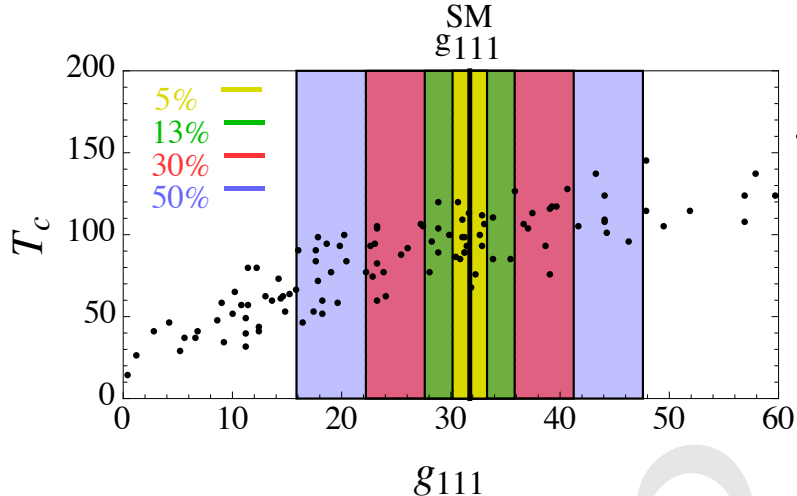


Figure 2.15: A correlation between the cubic self-coupling of the SM-like scalar boson and the critical temperature of the first order electroweak phase transition. To connect with the notation in the text, $g_{111} \rightarrow \lambda_3/(6 \text{ GeV})$ and $T_c \rightarrow T_{\text{pt}}/\text{GeV}$. The figure is reproduced from Ref. [61].

1 vanishes. Thus, apart from the blind spot, *the reach of CEPC is sufficient to probe a first
2 order electroweak phase transition across the entire parameter space.*

3 The blind spot mentioned above corresponds to two scenarios. The Higgs-singlet mix-
4 ing could vanish, because of an accidental cancellation between a_{HS} and $\lambda_{HS}v_S$. This
5 corresponds to an artificially fine-tuned parameter space, that is not theoretically appeal-
6 ing. Alternatively, the mixing vanishes identically in the \mathbb{Z}_2 symmetric limit of the singlet
7 extension. In this case, the relevant parameter space is shown in Figure 2.13. The right
8 panel shows the predicted deviation in the HZZ coupling away from the Standard Model
9 expectation, which is comfortably within reach of CEPC’s projected sensitivity.

10 Another representation of the parameter space appears in Figure 2.15, which shows a
11 correlation between the phase transition temperature and the Higgs cubic self-coupling.
12 For a similar analysis see also Ref. [62], but note that this article was published before the
13 Higgs boson mass was determined.

14 Among all possible new physics that renders the electroweak phase transition to be first
15 order, we focus on the singlet extension here, because it is the most challenging to test
16 with collider experiments. To illustrate this point, one can allow the new scalar particles
17 to carry an electric charge (similar to a two-Higgs doublet model). An analysis of this
18 model has been performed in Ref. [60], and the results are shown in Figure 2.16. The
19 CEPC has enough sensitivity to test the entire interesting parameter space, and much of
20 the space will also be tested by measurements at the LHC.

21 What will we learn from CEPC?

22 The CEPC will probe the Higgs boson with unprecedented precision. While the LHC has
23 taught us that the Higgs field is responsible for electroweak symmetry breaking, measure-
24 ments at CEPC provide a unique opportunity to learn *how* electroweak symmetry breaking
25 occurs. The nature of the electroweak phase transition is a question that we cannot settle
26 using only measurements at the LHC and its upgrades. Simple and compelling extensions
27 of the Standard Model can have a dramatic effect on the nature of the electroweak phase

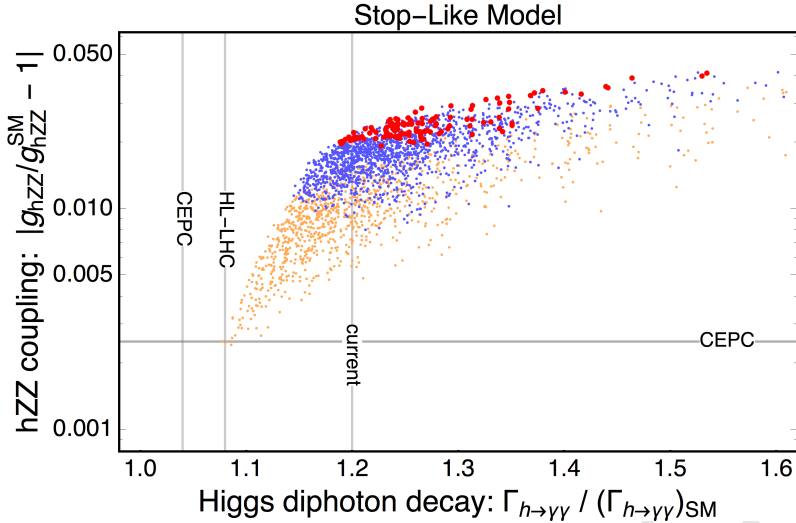


Figure 2.16: A model in which the new scalar particles are charged and uncolored. Such a model can be tested by CEPC, but it is already strongly constrained by the LHC’s measurement of the Higgs diphoton decay width. The figure is reproduced from Ref. [60].

transition, while remaining completely inaccessible to the LHC. However, the presence of new particles coupled to the Higgs boson must affect the way that the Higgs boson couples to itself and to other Standard Model particles, such as the Z -boson. Therefore precision measurements of the Higgs couplings are precisely what’s required to expose the new physics. In particular, the strength of the HZZ coupling, which will be measured at the 0.1% level by CEPC, is an excellent litmus test for a first order electroweak phase transition.

2.3 Exploring new physics

Exotic new physics could interact with the Standard Model in multiple ways that could be tested at CEPC. Here we summarize and classify different possible scenarios, which are discussed in more detail in the following sections:

1. Exotic particles carry Standard Model charges. The classic example in the dark matter context is dark matter in electroweak multiplets: although dark matter must be neutral, it could be part of an $SU(2)$ multiplet that also contains charged particles. Because CEPC is primarily a machine for Higgs and electroweak physics, this is a natural case to consider.
2. Renormalizable Standard Model portals: if there are no new particles with Standard Model gauge interactions and no new gauge groups that the Standard Model particles are charged under, exotic particles in the hidden (dark) sectors can still interact with the Standard Model via the gauge-singlet operators $H^\dagger H$ ("Higgs portal") [63–70], $B_{\mu\nu}$ ("hypercharge portal" or kinetic mixing) [71–77], and HL ("neutrino portal") [78–84].
3. Portals with additional Standard Model sector physics or new gauge groups that the Standard Model is charged under: if some exotic particle itself carries no Standard

Model gauge charges, it may nonetheless interact with the Standard Model via unknown new particles with Standard Model charges. For instance, the existence of a second Higgs doublet that couples dominantly to leptons can make models of "leptophilic" dark matter possible. The second possibility is that there exists some new gauge group, e.g. $U(1)'$, that (some) Standard Model particles are charged under. Then there is a renormalizable coupling between the new gauge boson and the current made of the Standard Model particles. If the new gauge group is anomalous with the Standard Model particle content, there could also be a Wess-Zumino type interaction between the Z and the new gauge boson [85–94].

4. Effective theory and high dimensional operators: this approach is agnostic to which of the above three scenarios we consider. The theory only contains certain light exotic particles and the Standard Model. The other new physics that generates the coupling between them is not identified and is only encoded in Wilson coefficients. Examples include an axion-like particle (ALP) interacting with the Z boson or photon through dimension-five operators [95–107] and magnetic inelastic dark matter and Rayleigh dark matter models [108–112], in which the dark sector interacts with Z via even higher dimensional operators.

These different scenarios may result in modifications to precision Higgs and Z observables or to exotic Higgs and Z boson decays. The first type of signal has been discussed in Section 2.2. In Sections 2.3.1 and 2.3.2, we will discuss the potential of CEPC for measuring exotic Higgs and Z boson decays. Then in Section 2.3.3, we will focus on the implications for dark matter and dark sectors. In Sections 2.3.4 and 2.3.5, we will discuss the potential of measuring exotic physics connected to neutrino and flavor physics.

2.3.1 Exotic Higgs boson decays

Higgs boson can be an important portal to new physics beyond the Standard Model. Such new physics could manifest itself through Higgs boson exotic decays if some of the degrees of freedom are light. The Higgs boson BSM decays have a rich variety of possibilities. Two-body Higgs boson decays into BSM particles $H \rightarrow X_1 X_2$, where the BSM particles X_i are allowed to subsequently decay further, are considered here. These decay modes are classified into four cases, schematically shown in Figure 2.17. These processes are well-motivated by BSM models such as singlet extensions of the SM, two-Higgs-doublet-models, SUSY models, Higgs portals, gauge extensions of the SM, and so on [113–115]. In this study, only prompt decays of the BSM particles are considered. For Higgs decays into long-lived particles, novel search strategies can be developed in future studies utilizing the advancement in detector development [116].

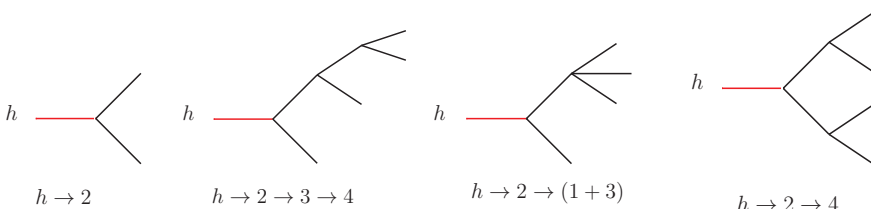


Figure 2.17: The topologies of the SM-like Higgs boson exotic decays.

Decay Mode	95% CL limit on BR		
	LHC	HL-LHC	CEPC
E_T^{miss}	0.23	0.056	0.030
$(b\bar{b}) + E_T^{\text{miss}}$	–	[0.2]	1×10^{-4}
$(jj) + E_T^{\text{miss}}$	–	–	4×10^{-4}
$(\tau^+\tau^-) + E_T^{\text{miss}}$	–	[1]	8×10^{-5}
$b\bar{b} + E_T^{\text{miss}}$	–	[0.2]	2×10^{-4}
$jj + E_T^{\text{miss}}$	–	–	5×10^{-4}
$\tau^+\tau^- + E_T^{\text{miss}}$	–	–	8×10^{-5}
$(b\bar{b})(b\bar{b})$	1.7	(0.2)	6×10^{-4}
$(c\bar{c})(c\bar{c})$	–	(0.2)	8×10^{-4}
$(jj)(jj)$	–	[0.1]	2×10^{-3}
$(b\bar{b})(\tau^+\tau^-)$	[0.1]	[0.15]	4×10^{-4}
$(\tau^+\tau^-)(\tau^+\tau^-)$	[1.2]	[0.2 ~ 0.4]	2×10^{-4}
$(jj)(\gamma\gamma)$	–	[0.01]	1×10^{-4}
$(\gamma\gamma)(\gamma\gamma)$	$[7 \times 10^{-3}]$	4×10^{-4}	8×10^{-5}

Table 2.1: The current and projected limits on Higgs boson exotic decay modes for the (HL-)LHC and CEPC with 5.6 ab^{-1} integrated luminosity, based upon results from Ref. [115]. The projections for the HL-LHC are collected in the third column, where the limits for 100 fb^{-1} and 300 fb^{-1} alone are shown in parentheses and square brackets, respectively.

For CEPC running at the center of mass energy 240 GeV, the most important Higgs boson production mechanism is Z -Higgs associated production $e^+e^- \rightarrow Z^* \rightarrow ZH$. The Z boson with visible decays enables Higgs boson tagging using the "recoil mass" technique. A cut around the peak of the recoil mass spectrum would remove the majority of the SM background. Further selection and tagging on the Higgs boson decay product can hence achieve high signal efficiency, and the major background would be from the Higgs boson SM decays. The details of these analysis can be found in Ref. [115].

The set of Higgs boson exotic decays with their projected LHC constraints and limits from the CEPC with 5.6 ab^{-1} integrated luminosity are summarized in Table 2.1. For the LHC constraints, both the current limits and projected limits on these exotic decay channels from various references are tabulated. The comparison are performed for particular benchmark points to demonstrate the qualitative difference between the (HL-)LHC and CEPC.

The exotic Higgs boson decay channels summarized in Table 2.1 and the corresponding Figure 2.19 are among the most difficult modes to constrain at the LHC and exemplify the considerable sensitivity of the CEPC. The red bars in Figure 2.19 correspond to a recoil mass analysis that only uses leptonic decays of the Z -boson that is produced in association with the Higgs boson. The inclusion of hadronic decays of the Z -boson provides around ten times more statistics and would lead to substantially improved reach. Based upon the study of Higgs boson decays $H \rightarrow WW^*$, ZZ^* and invisible particles, hadronically decaying Z -bosons are conservatively assumed to provide a limit comparable to the limit from leptonic Z -bosons, and hence improve the limits by around 40% when combined. These extrapolated results are shown in yellow bars in Figure 2.18.

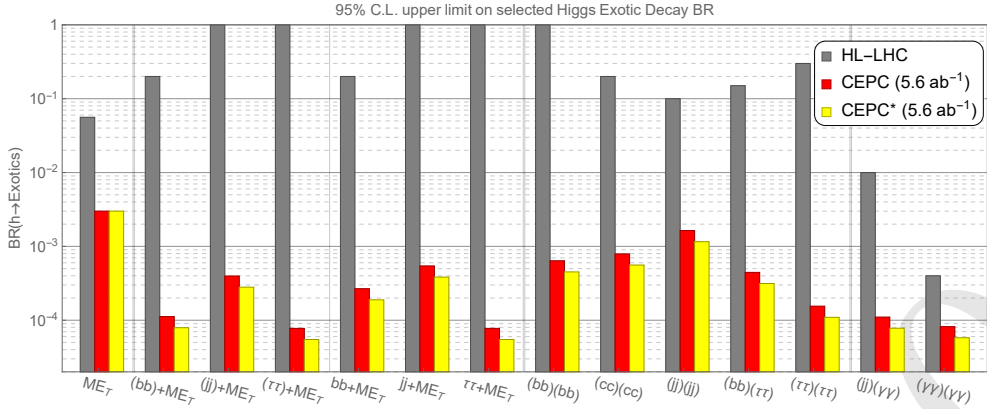


Figure 2.18: The 95% CL upper limit on selected Higgs exotic decay branching fractions at HL-LHC and CEPC, based on Ref. [115]. The benchmark parameter choices are the same as in Table 2.1. The red bars correspond to the results using only leptonic decays of the spectator Z -boson. The yellow bars further include extrapolation with the inclusion of the hadronic decays of the spectator Z -boson. Several vertical lines are drawn in this figure to divide different types of Higgs boson exotic decays.

In comparison with the HL-LHC, the improved coverage of Higgs boson exotic branching fractions is significant, varying from one to four orders of magnitude for the channels under consideration. For the Higgs boson exotic decays into hadronic final states plus missing energy, $b\bar{b} + E_T^{\text{miss}}$, $jj + E_T^{\text{miss}}$ and $\tau^+\tau^- + E_T^{\text{miss}}$, CEPC improves on the HL-LHC sensitivity for these channels by three to four orders of magnitude. These significant improvements benefit from low QCD backgrounds and the Higgs boson tagging from recoil mass reconstruction at CEPC. As for the Higgs boson exotic decays without missing energy, the comparative improvements vary between two to three orders of magnitude, as LHC performance in these channels is improved by reconstruction of the Higgs boson mass from visible final state particles and reduced QCD backgrounds in events with leptons and photons.

2.3.2 Exotic Z boson decays

The CEPC's Z -pole run will offer unique possibilities to test new physics that allows the Z boson to decay through new, exotic channels. Figure 2.19 summarizes the sensitivity of CEPC to exotic Z decays, and it compares CEPC's sensitivity to that of the high-luminosity LHC (HL-LHC) and a proposed Tera Z upgrade. Exotic Z decay channels are classified by final states, the number of intermediate resonances, and different topologies. The final states considered here include $Z \rightarrow \not{E} + \gamma$, $\not{E} + \gamma\gamma$, $\not{E} + \ell^+\ell^-$, $\not{E} + JJ$, $(JJ)(JJ)$ and $\gamma\gamma\gamma$. Each pair of photons, charged leptons, or jets can form a resonance, denoted with (\cdot) . All six categories of final states are represented in Figure 2.19; several representative decay topologies are chosen for each category and correspondingly labeled on the bar-chart. For CEPC and Tera Z , the sensitivity reach for exotic Z decay branching ratios (BR) are plotted as blue and red bars. These projections include kinematic cuts, namely general p_T and angular cuts on reconstructed objects, as well as an appropriate invariant mass cut if there is a resonance in the pair of particles (including dark matter particles). The cuts are optimized for each topology by checking the kinematic variable distributions. The sensitivity reach for the HL-LHC at 13 TeV with $\mathcal{L} = 3 \text{ ab}^{-1}$ has been computed in a similar way. Details of the simulation can be found in Ref. [117].

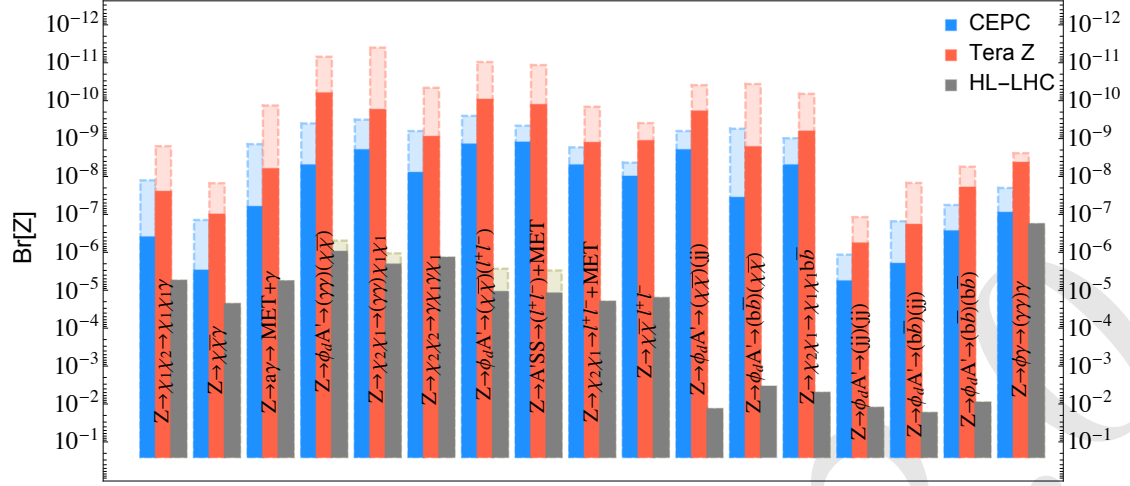


Figure 2.19: The sensitivity reach in the Z branching ratio for various exotic Z decay topologies at CEPC ($10^{10} Z$), a possible extension to Tera Z ($10^{12} Z$), and the high luminosity LHC at 13 TeV with $\mathcal{L} = 3 \text{ ab}^{-1}$. Adapted from Ref. [117].

1 The sensitivity to final states with missing energy reaches branching ratios of 10^{-6} to
2 $10^{-9.5}$ for CEPC and 10^{-7} to $10^{-11.5}$ for Tera Z . For each topology, the light blue and
3 red shaded regions indicate the range from varying the model parameters, like mediator
4 or dark matter mass. The light color regions with dashed boundary show the optimal sen-
5 sitivity, while the dark color regions with solid boundary show the pessimistic benchmark
6 of the model. In all the channels, future Z factories improve the sensitivity by several
7 orders of magnitude above those of the HL-LHC.

8 In general, CEPC has several advantages compared to a hadron collider like the HL-
9 LHC. First, an $e^+ e^-$ collider has a much cleaner environment compared to a hadron col-
10 ller with a huge QCD background. Second, in the Drell-Yan production of a Z boson at
11 a hadron collider, the decay products tends to be soft because the Z boson mass is small
12 compared to the beam energy, which makes them hard to detect at the HL-LHC. There-
13 fore, it is natural that CEPC has better sensitivity compared to the HL-LHC and provides
14 a better opportunity to investigate dark sector physics through exotic Z decays.

15 Two specific benchmark scenarios demonstrate the significant power of exotic Z decays
16 to probe different dark (hidden) sectors [117]. (Further discussion of a variety of exotic Z
17 decays appears in [118].) The first model contains fermionic dark matter interacting with
18 a singlet real scalar S , which mixes with the Standard Model Higgs boson. The possible
19 exotic Z decay channel in this case is $Z \rightarrow \tilde{s}Z^* \rightarrow (\bar{\chi}\chi) + l^+ l^-$, where \tilde{s} is the light scalar
20 mass eigenstate (mostly the dark Higgs S) and χ is the fermionic dark matter. The second
21 model is an axion-like particle a coupling to the Standard Model $U(1)_Y$ gauge field B_μ .
22 Then the exotic Z decay is $Z \rightarrow a\gamma \rightarrow (\gamma\gamma)\gamma$. The final state is 3γ and in the case
23 that m_a is too small to separate the two photons, the final state is 2γ . The sensitivity of
24 exotic Z decays (as well as other possible probes) to key parameters in these two models
25 is summarized in Figure 2.20.

26 Projections for CEPC and Tera Z reach in the first model are shown in the Fig-
27 ure 2.20(a). There are two free parameters, namely the Higgs mixing angle $\sin \alpha$ and dark

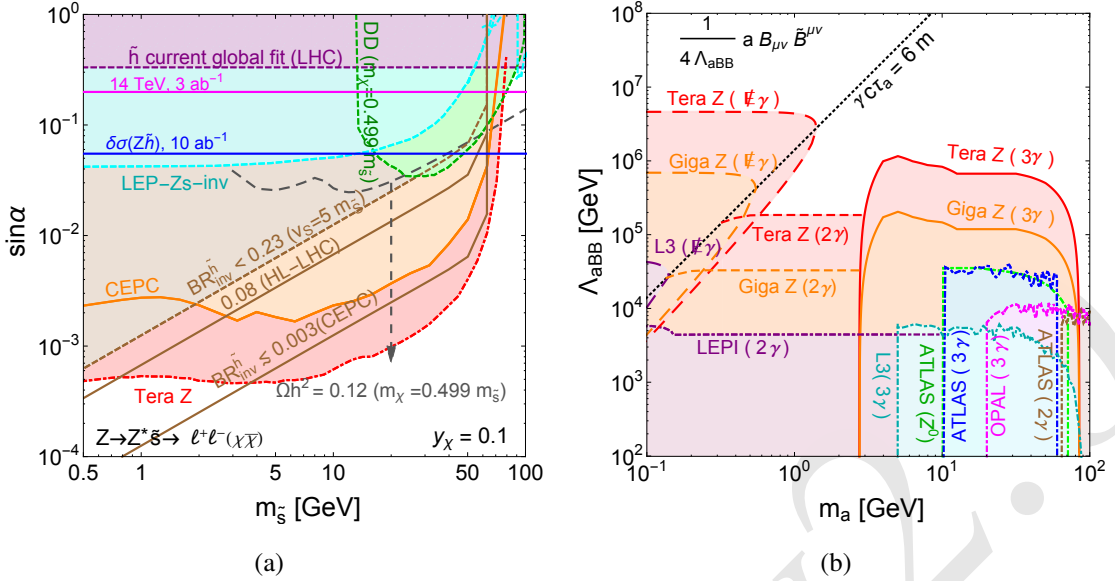


Figure 2.20: The reach for rare Z decays at CEPC in two benchmark scenarios, adapted from Ref. [117]. (a) the sensitivity to the dark Higgs mixing angle $\sin\alpha$ at CEPC ($10^{10} Z$) and at a Tera Z option ($10^{12} Z$) in a Higgs portal dark matter model, using the process $Z \rightarrow \ell^+ \ell^- \tilde{s} \rightarrow \ell^+ \ell^- (\bar{\chi}\chi)$. (b) the sensitivity to the coupling Λ_{aBB} for an axion-like particle (ALP) model as a function of the ALP mass m_a , where B is the hypercharge gauge field. The signal process is $Z \rightarrow \gamma a$, where a can decay to a pair of photons (3γ), be detected as one photon due to high boost (2γ), or be detected as missing energy due to its long lifetime ($\gamma \cancel{E}$).

Higgs boson mass $m_{\tilde{s}}$. The other two parameters related to dark matter are fixed. One is the dark matter mass, fixed close to half of $m_{\tilde{s}}$, which only affects the dark matter relic abundance but not other limits. The other one is the Yukawa coupling between dark matter χ and the dark Higgs \tilde{s} , which is taken to be $y_\chi = 0.1$ for illustrative purposes. Limits are projected for the exotic Z decay process $Z \rightarrow \ell^+ \ell^- \tilde{s} \rightarrow \ell^+ \ell^- (\bar{\chi}\chi)$, which has been labeled as an orange solid line for CEPC ($10^{10} Z$) option and a red dot-dashed line for the Tera Z ($10^{12} Z$) option, and compared with the LEP result with an integrated luminosity 114 pb^{-1} [119] labeled as "LEP-Zs-inv".

The dark Higgs in this benchmark scenario can also be constrained by the modification of SM Higgs couplings proportional to the mixing angle $\sin\alpha$, independent of the scalar mass \tilde{s} . The global fit to Higgs data at the LHC 7 TeV and 8 TeV runs can constrain the single scaling factor to Higgs interactions, giving $\sin\alpha < 0.33$ [120]; this is labeled as " \tilde{h} current global fit (LHC)". The HL-LHC can extend this reach to $\sin\alpha < 0.28$ (0.20) using 300 fb^{-1} (3 ab^{-1}) luminosity [121]. At CEPC, the precision measurement of the Higgs Bremsstrahlung cross-section $\sigma(ZH)$ can reach the accuracy of $\mathcal{O}(0.3\% - 0.7\%)$ expected from $5 - 10 \text{ ab}^{-1}$ [122–124], which can probe the scalar mixing down to $0.055 - 0.084$ [125]; this is labeled as " $\delta\sigma(ZH)$ ". In addition, there are constraints coming from the invisible decay of the SM Higgs boson. The current LHC limits from the Run I combination of ATLAS and CMS data constrains $\text{BR}(h \rightarrow \text{inv}) \leq 0.23$ at 95% CL [126, 127]. Following the \tilde{h} invisible decay branching ratio in the Higgs portal dark matter model, the limit on the mixing angle $\sin\alpha$ is labeled as " $\text{BR}_{\text{inv}}^{\tilde{h}} < 0.23$ ". We also add the HL-LHC (3 ab^{-1}) and future $e^+ e^-$ collider projections on invisible Higgs boson search, which lead to 95% CL limits $\text{BR}_{\text{inv}}^{\tilde{h}} \lesssim 0.08 \sim 0.16$ [128, 129] and

¹ $\text{BR}_{\text{inv}}^{\tilde{h}} \lesssim 0.003$ [123, 130] at ILC and CEPC. There are also constraints based on dark matter assumptions. The dark matter relic abundance [131] is satisfied on the dashed gray line, while the direct detection limits on spin-independent cross-sections (XENON1T [132], LUX [133], PANDAX-II [134], and CRESST-II [135]) exclude the region within the dashed green line.

⁶ Projections for CEPC and Tera Z reach in the second model are illustrated in the Figure 2.20(b), focusing on the exotic Z decay $Z \rightarrow \gamma a$ followed by $a \rightarrow \gamma\gamma$. In the 3γ signal, the ALP mass is heavy enough that the two photons are well separated and detectable. When the mass of the ALP is below $\mathcal{O}(1)$ GeV, the boost of the axion makes the two photons from the axion decay close enough together that they cannot be resolved, leading to signals in the 2γ search channel. The current constraints on the two cases are given by LEP and LHC photon searches. In Figure 2.20, the LEP I [136] constraint uses an inclusive diphoton search $e^+e^- \rightarrow 2\gamma + X$ covering the small mass region. In the higher mass region, the boost of the axion decreases and the 3γ channel is considered. The LEP II (OPAL) constraints have 2γ and 3γ data [137], which are employed to put bounds on the process $e^+e^- \rightarrow \gamma/Z^* \rightarrow a\gamma \rightarrow 2\gamma + \gamma$. ATLAS 3γ and $Z \rightarrow 3\gamma$ [138, 139] searches can be translated to an ALP bound, as derived in [140]. There is also the possibility that the ALP decays outside of the detector, which is relevant for a $\cancel{E} + \gamma$ search. In this case the strongest bound comes from the LEP L3 collaboration with 137 pb^{-1} data at the Z pole [141], which constrains the branching ratio of the exotic decay $Z \rightarrow \gamma\cancel{E}$ down to 1.1×10^{-6} if the photon energy is greater than ~ 30 GeV. It directly excludes $\Lambda_{\text{aBB}} < 4.3 \times 10^4$ GeV for $Z \rightarrow \cancel{E} + \gamma$ decay, and is labeled as "L3 ($\cancel{E}\gamma$)" in the Figure 2.20(b). The sensitivity curves are plotted as an orange solid line for CEPC ($10^{10} Z$) and a red dot-dashed line for a Tera Z ($10^{12} Z$) option, demonstrating the significant reach of CEPC and Tera Z in this scenario.

²⁶ These comparisons show that searches for exotic Z decays at CEPC (and a possible Tera Z extension) can provide the leading sensitivity to a range of motivated extensions of the Standard Model, substantially exceeding the reach of dark matter direct detection experiments, current limits from collider searches, and estimated sensitivities of the high luminosity run of the LHC (HL-LHC).

³¹ 2.3.3 Dark matter and hidden sectors

³² Observations tell us that the majority of matter in the universe is dark matter (DM). Because the abundance of dark matter in the universe is within an order of magnitude of the abundance of ordinary matter, it is natural to suspect that dark matter and ordinary matter should be related in some way. A variety of models, including the classic thermal relic weakly interacting massive particle (WIMP), attempt to explain the abundance of dark matter in terms of its interactions with ordinary matter. In some models, there is a richer "dark sector" consisting not only of dark matter itself but of new force-carrying particles that can mediate self-interactions between dark matter particles or interactions of dark matter with ordinary matter.

⁴¹ Different classes of possibilities for how dark matter interacts with the Standard Model have been summarized in Section 2.3. Below we discuss each of these possibilities in turn. This categorization of studies may be useful in the future for identifying DM scenarios at CEPC that have not yet been fully studied.

1 There are major efforts underway to search for dark matter via direct detection, indirect
 2 detection, and searches at the LHC and lower-energy-but-high-luminosity collider and
 3 fixed-target experiments. It is possible that one of these experiments will discover a dark
 4 matter signal before CEPC operates. Even in that case, CEPC can play a crucial role in
 5 discovering the *nature* of the dark matter particle. Direct detection, for example, may
 6 tell us a spin-independent scattering rate, but without knowledge of the local dark matter
 7 density or whether the particle we are seeing constitutes all of the dark matter or is just a
 8 component, limited knowledge of particle physics would be gleaned from the discovery.
 9 The role of CEPC in such a case could be to tell us that dark matter interacts directly with
 10 the Higgs boson or weak gauge bosons, for instance. Below we will emphasize both cases
 11 in which CEPC can *measure* dark matter properties and supplement other experiments
 12 and cases in which CEPC could play the crucial role in *discovering* a DM signal for the
 13 first time.

14 **Dark matter in electroweak multiplets**

15 The CEPC’s strength is electroweak physics, both through precision measurements of
 16 properties of the W and Z bosons and through its primary role as a Higgs factory. Studies
 17 of CEPC’s capabilities for detecting new electroweak physics include Refs. [20, 23, 40,
 18 142–148]. Hence, the most natural place to begin is with CEPC searches for dark matter
 19 particles that are in electroweak multiplets (e.g. doublets or triplets of $SU(2)_L$) or mixtures
 20 of electroweak multiplets (including admixtures of a singlet). Studies on this topic include
 21 Refs. [149–154].

22 One question is whether other, dedicated dark matter experiments will cover the full
 23 parameter space of dark matter in electroweak multiplets. Dark matter direct detection
 24 experiments, like the currently-operating Xenon1T [132] and PandaX [155], are currently
 25 probing much of the parameter space for spin-independent dark matter scattering on nu-
 26 cleons mediated by Higgs exchange. The current bound on the DM-nucleon cross section
 27 of a few times 10^{-46} cm^2 corresponds to an $h\chi\chi$ coupling in the Lagrangian with coef-
 28 ficient of order 10^{-2} . Future experiments like DARWIN [156] will potentially push the
 29 search down to the neutrino floor, corresponding to $h\chi\chi$ couplings of order 10^{-3} . This
 30 will probe a large swath of the parameter space for electroweak dark matter.

31 As noted above, CEPC could help to measure DM properties even if a direct detection
 32 experiment makes the discovery first. Still more interesting are possibilities in which
 33 electroweak DM could be *missed* by direct detection experiments but seen by CEPC.
 34 There are two main scenarios to consider where this could happen. The first is if DM
 35 is a nearly pure electroweak multiplet, such as a pseudo-Dirac higgsino. Such particles
 36 have very small interactions with the Higgs boson, so their direct detection rate is loop-
 37 suppressed and at about the level of the neutrino floor [157]. These particles would also
 38 be very difficult to detect at the LHC [158]. Indirect detection may constrain them, but at
 39 low mass their thermal abundance is low, and even a significant non-thermal abundance
 40 may fall below current constraints [159, 160]. A second possibility is that DM lies in a
 41 mixed electroweak multiplet with couplings to the Higgs boson, but the coupling of the
 42 lightest mass eigenstate has a small coupling to the Higgs boson, either accidentally or due
 43 to an approximate symmetry. This is referred to as a *blind spot* for direct detection [161,
 44 162]. For instance, a mostly-wino dark matter particle in a supersymmetric theory has
 45 vanishing tree-level coupling to the Higgs boson if $M_2 = -\mu \sin(2\beta)$. In some cases,

1 a spin-independent blind spot may be covered by spin-dependent scattering. Blind spots
 2 might also be uncovered by collider searches [163].

3 Robust blind spots for both spin-dependent and spin-independent scattering arise in
 4 some theories due to approximate *parity* or *custodial* symmetries. In the MSSM, this
 5 occurs for higgsino dark matter at $\tan\beta = 1$ and $\text{sign}(\mu M_{1,2}) < 0$. In closely related
 6 theories, these blind spots have been understood to result from custodial symmetries [150].
 7 These robust direct detection blind spots are excellent opportunities for CEPC to play a
 8 role in dark matter physics, so let us explain the physics in somewhat more detail. They
 9 arise for pseudo-Dirac DM, i.e. theories with a Dirac mass term of the form $\mu\chi_1\chi_2$ which
 10 can be written as a sum of two Majorana mass terms, $\mu(\chi_+\chi_+ - \chi_-\chi_-)$ where $\chi_\pm =$
 11 $(\chi_1 \pm \chi_2)/\sqrt{2}$. In such a theory the Z boson couples off-diagonally, $Z_\mu(\chi_+^\dagger \bar{\sigma}^\mu \chi_- + \text{h.c.})$.
 12 Mixing or higher-dimension operators can split the mass eigenstates, but in the custodially
 13 symmetric limit, the eigenstates remain χ_+ and χ_- rather than mixtures thereof. There is
 14 a parity symmetry under which χ_+ and the Z are odd but χ_- and h are even, which forbids
 15 an $h\chi_+\chi_+$ coupling. Hence when χ_+ is the lighter mass eigenstate, both spin-dependent
 16 and spin-independent scattering are turned off.

17 A number of studies have been carried out on two particular models of electroweak dark
 18 matter, the doublet–singlet and doublet–triplet models (e.g. [164–166]). The doublet–
 19 singlet model introduces a singlet fermion S (with zero hypercharge) with Majorana
 20 mass $-(m_S/2)SS$ and two electroweak doublet Weyl fermions $D_{1,2}$ with opposite hy-
 21 percharges $\mp 1/2$ and Dirac mass $-m_D \epsilon_{ij} D_1^i D_2^j$, together with mixing through the SM
 22 Higgs boson:

$$y_1 H S D_1 - y_2 H^\dagger S D_2 + \text{h.c.} \quad (2.19)$$

23 The doublet–triplet model introduces the same doublet fields as well as an SU(2) triplet
 24 with zero hypercharge, T , with a Majorana mass $-(m_T/2)T^i T^i$ and mixing with the
 25 doublet through the Higgs boson:

$$y_1 (H \sigma^i D_1) T^i - y_2 (H^\dagger \sigma^i D_2) T^i + \text{h.c.} \quad (2.20)$$

26 Both of these models have blind spots for both spin-independent *and* spin-dependent di-
 27 rect detection in the pseudo-Dirac case when $m_D < m_{S,T}$ (all mass parameters taken to
 28 be positive) and $y_1 = y_2$. An explicit rewriting of the Lagrangian that makes a custodial
 29 symmetry manifest in this limit has been given in [150]. This blind spot can also be un-
 30 derstood in terms of a parity symmetry at the point $y_1 = y_2$ along the lines explained in
 31 the previous paragraph.

32 In the SUSY context we can identify the fields S , D , and T with the bino, higgsino,
 33 and wino. In this case the couplings y_1 and y_2 are equivalent to $g^{(i)} \cos\beta$ and $g^{(i)} \sin\beta$ in
 34 the doublet–triplet (doublet–singlet) case. These relatively small couplings tend to lead
 35 to small signals at CEPC. However, it is also interesting to consider extensions of the
 36 MSSM with an *additional* doublet and singlet that mix to serve as dark matter. Such
 37 theories can help to explain why the observed Higgs boson mass is heavier than expected
 38 in the simplest SUSY theories [167], which offers a motivation for considering the larger
 39 values of $y_{1,2}$ that could be probed at CEPC.

40 Precision electroweak physics at the Z pole is most sensitive to the S and T parameters.
 41 Although these operators appear in studying the propagators of gauge fields, they originate
 42 from new physics that couples to the Higgs boson. For instance, in the basis of Ref. [168],
 43 the S parameter is related to the operators $H^\dagger \sigma^i H W_{\mu\nu}^i B^{\mu\nu}$, $(H^\dagger \sigma^i \overleftrightarrow{D}_\mu H) D^\nu W_{\mu\nu}^i$, and

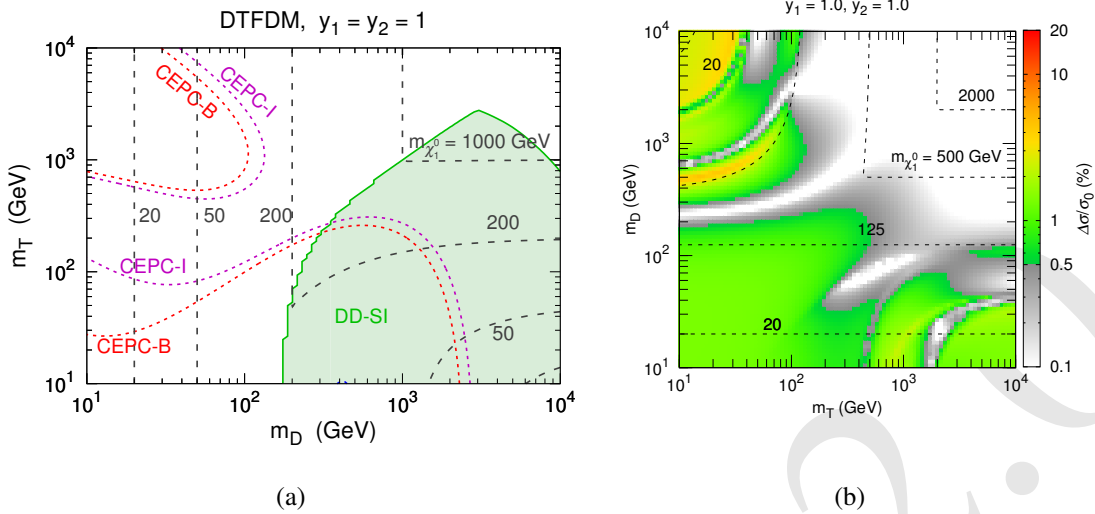


Figure 2.21: (a) The CEPC electroweak precision (S, T) fit probe of the doublet–triplet model at the custodially symmetric point $y_1 = y_2 = 1$, taken directly from Figure 5a of Ref. [150]. When the dark matter particle is mostly triplet ($m_D \gg m_T$), spin-independent direct detection is a powerful probe (shaded green region). When the dark matter particle is mostly doublet, the tree-level direct detection rate vanishes but CEPC’s measurement of the S parameter becomes a powerful probe (dashed contours). (b) CEPC’s sensitivity to the same model via the Higgsstrahlung cross section $\sigma(ZH)$, taken directly from Figure 11b of Ref. [153]. We see that in a large part of parameter space with $m_T \gg m_D$, where the direct detection rate is low due to custodial symmetry, there are observable (percent-level or higher) deviations in the ZH cross section.

¹ $(H^\dagger \overleftrightarrow{D}_\mu H) \partial^\nu B_{\mu\nu}$; the T parameter, to $(H^\dagger \overleftrightarrow{D}_\mu H)^2$. These operators are generated in the doublet–singlet or doublet–triplet model because the fermions mix by coupling to the Higgs boson. On the other hand, for a pure electroweak multiplet like the pseudo-Dirac higgsino, Higgs couplings are very small and S and T are suppressed. The T parameter is also suppressed in models with a good approximate custodial symmetry. In such theories, other electroweak precision observables like the W and Y operators $(D^\mu W_{\mu\nu}^i)^2$ or $(\partial^\mu B_{\mu\nu})^2$ may be relatively important, though they are generated with small coefficients and are harder to probe. In this case, observables at 240 GeV from processes like $e^+ e^- \rightarrow \mu^+ \mu^-$ [169] or $e^+ e^- \rightarrow W^+ W^-$ [151, 170] may be more effective probes of electroweak dark matter than Z -pole observables.

The doublet–singlet and doublet–triplet models at CEPC have been discussed in Ref. [150], which focuses on the S and T parameters (and also discusses a quadruplet–triplet model with similar properties).¹ They have shown that CEPC can probe a large region of parameter space where the dark matter mass is below 200 GeV, and certain regions of parameter space with even larger masses. In particular, the S parameter allows a probe of the custodially symmetric region that is hidden from direct detection. We show some results from this paper in the Figure 2.21(a). A related study in Ref. [153] considers effects of doublet–singlet and doublet–triplet dark matter on Higgs observables, including the ZH cross section, the $h \rightarrow \gamma\gamma$ decay rate, and the Higgs boson invisible width. Away from the

¹Earlier papers discussing electroweak and Higgs constraints on similar models include [171–175].

1 custodially symmetric point in the doublet–singlet model, when $y_1 = 0.5$ and $y_2 = 1.5$,
 2 CEPC’s measurement of the total ZH cross section probes the lightest neutralino mass up
 3 to 200 GeV. For $y_1 = y_2 = 1$, with custodial symmetry, deviations are smaller and m_D
 4 is probed only up to about 125 GeV. In the doublet–triplet case, the region of parameter
 5 space bounded by the ZH measurement is illustrated in the Figure 2.21(b). Aspects of
 6 a slightly different doublet–singlet model, with the singlet taken to be a Dirac fermion,
 7 have also been discussed in Ref. [149]. They focus on the region with mostly singlet DM,
 8 in which case the doublet may be thought of as allowing a completion of a "Higgs portal"
 9 model. In this case, the most important constraints come from the T parameter. They also
 10 present results for a wider range of doublet and singlet masses including cases where dark
 11 matter is mostly doublet.

12 In the case in which DM resides in a nearly pure electroweak multiplet, the S and T
 13 parameters and the $H \rightarrow \gamma\gamma$ rate are no longer useful probes. For the case of nearly pure
 14 higgsinos, Ref. [151] has studied the prospects of an $e^+e^- \rightarrow W^+W^-$ measurement at
 15 CEPC as a constraint. This measurement is sensitive not only to corrections to the photon
 16 and Z propagators but to loop corrections to the triple gauge coupling vertex. Ref. [151]
 17 claims that a 0.1% precision measurement of $e^+e^- \rightarrow W^+W^-$ at CEPC could probe
 18 higgsino dark matter up to about 210 GeV. However, the scatter plot in Figure 1 of that
 19 reference suggests that many models with even heavier higgsinos will be accessible. A
 20 more detailed future exploration of the parameter space probed by the W^+W^- measure-
 21 ment would be useful. The rate of $e^+e^- \rightarrow \mu^+\mu^-$ at 240 GeV can also be a sensitive
 22 probe of deviations in the propagators of photons and Z bosons; in particular, for new
 23 physics contributing to the W and Y parameters but not to S and T , it may be superior
 24 to electroweak precision studies on the Z pole thanks to the larger center-of-mass energy.
 25 A detailed study of this probe of electroweak physics has been carried out in Ref. [169].
 26 Their conclusion is that if systematic uncertainties can be controlled to achieve a 0.1%
 27 precision on the rate, pseudo-Dirac higgsinos may be excluded up to a mass of about
 28 200 GeV. This is encouraging, since pseudo-Dirac doublets are among the most difficult
 29 electroweak particles to probe in any experiment. In particular, the LHC is not expected
 30 to reach far above 200 GeV (though this will depend in part on how well systematic un-
 31 certainties can be understood). The results of Ref. [169] may not apply directly to CEPC
 32 due to their assumptions about beam polarization, so a further dedicated CEPC study of
 33 this process is warranted.

34 Another interesting possibility is that of light singlet dark matter mixing with heavier
 35 electroweak-charged particles. A particular example arises for mostly-bino dark matter in
 36 the MSSM [176], $\tilde{\chi}_1^0$, which could have a non-thermal relic abundance. Because the bino
 37 is a pure singlet, it couples to the Standard Model only through small mixing parameters
 38 and is difficult to detect directly. However, in some cases it can be detected through
 39 the invisible width of the Higgs boson. The parameter space probed by dark matter direct
 40 detection and CEPC is shown in the Figure 2.22(b). This figure illustrates that CEPC could
 41 probe the region allowed by the current direct detection with a sensitivity to $\text{BR}(H \rightarrow$
 42 $\tilde{\chi}_1^0\tilde{\chi}_1^0) \gtrsim 0.24\%$.

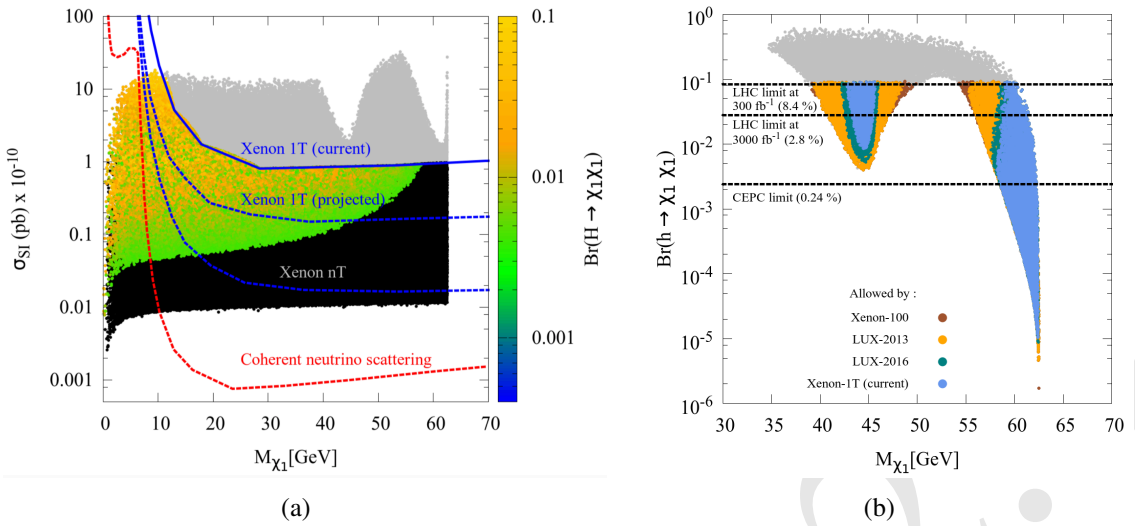


Figure 2.22: These figures, which are adapted from Ref. [176], show constraints on nonthermal neutralino dark matter and invisible Higgs boson decays. (a) The spin-independent WIMP-nucleon cross-section vs $M_{\tilde{\chi}_1^0}$ for all points allowed by collider and relic density constraints. The color code characterizes the value of $\text{BR}(H \rightarrow \tilde{\chi}_1^0 \tilde{\chi}_1^0)$, while black points have $\text{BR}(H \rightarrow \tilde{\chi}_1^0 \tilde{\chi}_1^0) < 0.4\%$. The solid blue line shows the current limit from LUX-2016 [177], and the dashed blue line shows the reach for Xenon1T [178] and Xenon-nT [178]. (b) The Higgs boson to invisible branching ratio $\text{BR}(H \rightarrow \tilde{\chi}_1^0 \tilde{\chi}_1^0)$ vs. the LSP mass $M_{\tilde{\chi}_1^0}$. The gray (colored) points distinguish the points allowed before (after) the Higgs signal strength constraints. Blue, green, yellow, red points are allowed by the current limits on SI WIMP-nucleon cross-section from Xenon1T, LUX-2016, LUX-2013, and Xenon-100. From top to bottom, the black-dashed line represents the reach of the LHC with 300 fb^{-1} , the LHC with 3000 fb^{-1} , and CEPC.

Standard Model portals

- If the dark matter does not reside in an electroweak multiplet, it may still interact with the SM particles through gauge-invariant "portal" operators. The portal operators include

$$H^\dagger H, \quad B^{\mu\nu}, \quad \text{and} \quad HL, \quad (2.21)$$

where H is the SM Higgs doublet, $B^{\mu\nu}$ is the hypercharge field strength tensor, and L is a SM lepton doublet. These three portals are usually referred to as the Higgs portal, the kinetic mixing (or hypercharge) portal, and the lepton (neutrino) portal. These simple portal dark matter scenarios predict rich phenomenology and a plethora of experimental signatures. They have been established as well-defined dark matter benchmarks and experimental targets, in addition to the traditional electroweak WIMP scenario.

The many powerful direct and indirect probes available at the CEPC mean that it could play an important role in detecting and testing these SM portals to dark matter. Below we will present estimates of the CEPC potential for the Higgs and kinetic mixing portals based on the studies in the existing literature. The neutrino portal is discussed further in Section 2.3.4.

In a simple example of the Higgs portal model, the dark matter (DM) is assumed to be either a real scalar (S) or a Majorana fermion (χ), with the following interaction terms

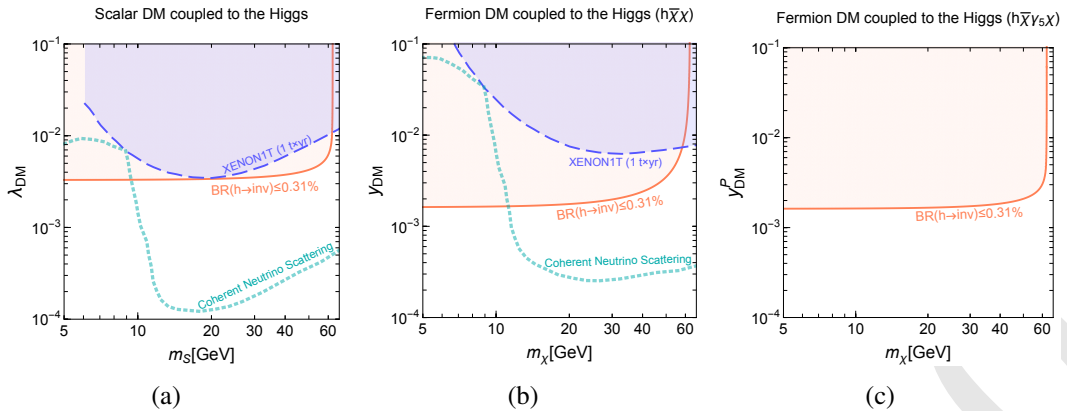


Figure 2.23: The *mass-coupling* plane for the Higgs portal models of Equation (2.23) with a scalar DM (a), a Majorana fermion DM with a scalar coupling y_{DM} (b) and a Majorana fermion DM with a pseudo-scalar coupling y_{DM}^P (c). The orange region is excluded by the invisible Higgs boson decay measurements at the CEPC, which constrains the branching ratio to be below 0.31% at 95% CL. The blue region is excluded by the most recent result from XENON1T [181]. The cyan dotted curve corresponds to the discovery limit set by the coherent-neutrino-scattering background, adapted from Ref. [182].

with the Higgs field [179, 180]

$$\mathcal{L} = -H^\dagger H \left(\frac{\lambda_{\text{DM}}}{4} S^2 + \bar{\chi} \frac{y_{\text{DM}} + iy_{\text{DM}}^P \gamma_5}{\sqrt{2}v} \chi \right). \quad (2.22)$$

² The couplings between a single Higgs boson particle and the dark matter fields are thus given by

$$\mathcal{L} = -\frac{\lambda_{\text{DM}} v}{4} H S^2 - \frac{y_{\text{DM}}}{\sqrt{2}} H \bar{\chi} \chi - \frac{i y_{\text{DM}}^P}{\sqrt{2}} H \bar{\chi} \gamma_5 \chi. \quad (2.23)$$

For dark matter masses smaller than $m_H/2$, the decay channel $H \rightarrow SS/\bar{\chi}\chi$ is open, which produces the signal of Higgs boson invisible decays. As shown in Section 11.1, the CEPC could reach a sensitivity of 0.31% (at 95% CL) on the branching ratio of Higgs boson invisible decays.²

This provides considerable sensitivity to Higgs portal models with a dark matter mass below $m_H/2$, which can be competitive with the reaches of current and future direct detection experiments. To illustrate this, we make a comparison between the reach of the CEPC and the one from the most recent result of XENON1T [181] in the *mass-coupling* plane for both the scalar and Majorana fermion DM. For the fermion DM, we consider two separate scenarios, one with a purely scalar coupling (y_{DM}) and the other with a purely pseudo-scalar coupling (y_{DM}^P), as shown in Equation (2.23). We also assume that the correct relic abundance is achieved regardless of the model parameters. The results are shown in Figure 2.23. For the three scenarios in consideration, the CEPC bound on the Higgs boson invisible branching ratio, 0.31%, corresponds to a sensitivity to the Higgs-DM coupling of around 10^{-3} for DM mass smaller than $m_H/2$. For the scalar DM and Majorana fermion DM with coupling y_{DM} , this clearly surpasses the reach of XENON1T in this mass region.

² Here we only include the Higgs boson invisible decay to BSM particles. If the SM decay $H \rightarrow ZZ \rightarrow \nu\bar{\nu}\nu\bar{\nu}$ is also included, the bound on the Higgs boson invisible branching ratio becomes 0.42% instead. See Section 11.1 for more details.

Even for future direct detection experiments, the reach could not go beyond the so-called "neutrino floor" (shown by the cyan dotted curve) due to the coherent-neutrino-scattering background [182], while the CEPC could still probe a significant part of the region below the neutrino discovery limit in the region $m_{\text{DM}} \lesssim 10 \text{ GeV}$. The pseudo-scalar coupling y_{DM}^P only produces a spin-dependent WIMP-nucleon interaction which is suppressed by the transferred momentum. The constraints on the fermion DM with y_{DM}^P from direct detection experiments are thus much weaker, while the reach of the CEPC still remains strong. In addition to these bounds, the CEPC's sensitivity to fermionic Higgs portal dark matter through exotic Z boson decays has been discussed in Section 2.3.2.

In Figure 2.24, the CEPC coverage of Higgs portal dark matter models for both scalar and fermionic DM (y_{DM}) is converted to the corresponding spin-independent WIMP-nucleon cross-section, and compared to the coverage of direct detection experiments. In addition to the Xenon1T, the sensitivities of other experiments are also presented, including LUX (2017) [133] and PandaX-II (2017) [155], as well as future projections of PandaX4T with $5.6 t \times \text{yr}$ data [183], XENONnT with $20 t \times \text{yr}$ data [178], LUX-ZEPLIN (LZ) with $15.6 t \times \text{yr}$ data [184] and a xenon experiment with $200 t \times \text{yr}$ data [185] that corresponds to either DARWIN [156] or PandaX-30T. The current and future reaches of the LHC Higgs boson invisible decay measurements are also shown. The current bound, $\text{BR}(H \rightarrow \text{inv}) < 24\%$ at 95% CL, comes from the CMS analysis in Ref. [186]. The projection by the ATLAS collaboration on the reach of $\text{BR}(H \rightarrow \text{inv})$ at the HL-LHC is around 10% [187]. A study in Ref. [188] suggests that the reach could be improved to 3.5% with multivariate techniques. Both the current bound (24%) and the optimistic projection (3.5%) are plotted in Figure 2.24, which cover the possible range that the (HL-)LHC could reach in the future. Finally, the cyan dashed curve corresponds to the projected discovery limit from Ref. [182]. The region below this curve is inaccessible by direct detection experiments due to the coherent-neutrino-scattering background.

We see in Figure 2.24 that the sensitivity of the Higgs boson invisible decay measurements to the scalar DM and the Majorana fermion DM have different dependence on the mass. This is due to the following two reasons: first, the Higgs portal interaction with the scalar DM is a dimension-four operator, while the fermion one is of dimension five, which results in different mass dependence of the WIMP-nucleon cross-section; second, the Higgs boson decay rates are also different for the two cases, with $\Gamma(H \rightarrow SS) \propto (1 - 4m_S^2/m_H^2)^{1/2}$ and $\Gamma(H \rightarrow \bar{\chi}\chi) \propto (1 - 4m_\chi^2/m_H^2)^{3/2}$, a result of the s (p)-wave nature of the scalar (fermion). Nevertheless, for both scenarios, it is clear that the Higgs boson invisible decay measurements provide the strongest limit in the dark matter mass region below $\sim 10 \text{ GeV}$. Not only do direct detection experiments become less efficient in this region due to the mass threshold, the "neutrino floor" is also higher in this region, which sets the limit for the reach of direct detection experiments regardless of the size and length of the experiment. For dark matter masses in the region $10 \text{ GeV} \lesssim m_{\text{DM}} < m_H/2$, the sensitivity of the Higgs boson invisible decay measurements is comparable with that of direct detection experiments. In particular, for fermion DM the CEPC still has sensitivity in regions not covered by PandaX4T, XENONnT or LZ. On the other hand, a $200 t \times \text{yr}$ xenon experiment would fully surpass the reach of the CEPC in this region.

It bears emphasizing that, as mentioned earlier, the interaction term between the Higgs boson and the fermion DM in Equation 2.22 is of dimension five. Such a nonrenormalizable operator indicates that the theory is only an effective one, and needs to be UV

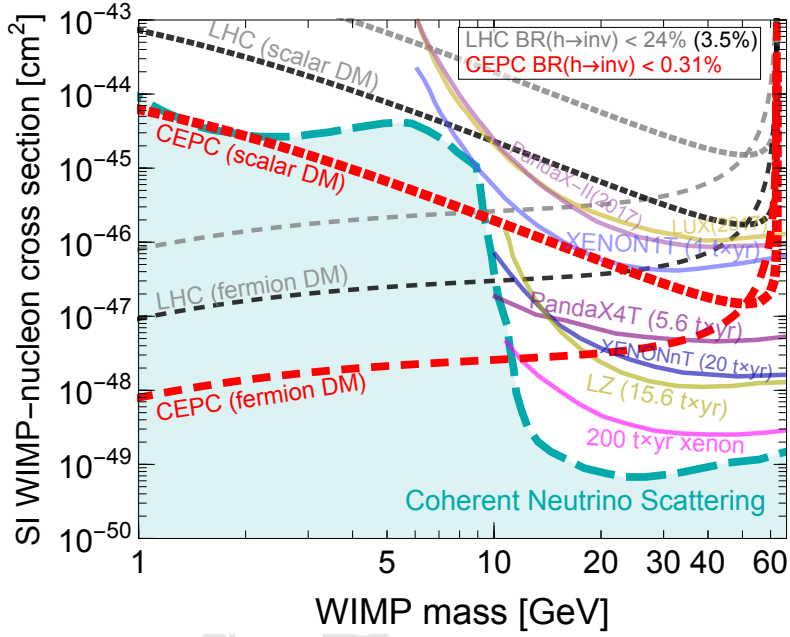


Figure 2.24: The sensitivity to the spin-independent WIMP-nucleon cross-section of current and future direct detection experiments, compared with the reach of Higgs boson invisible decay measurements at the LHC and CEPC in Higgs portal dark matter models. The direct detection limits are shown in solid lines, which include the most recent limits from LUX (2017) [133], PandaX-II (2017) [155], XENON1T [181] and future projections for PandaX4T [183], XENONnT [178], LZ [184] and a 200 $t \times yr$ xenon experiment [185]. For the Higgs portal models, the dark matter is assumed to be either a scalar or a Majorana fermion with a scalar coupling. The red dotted curves show the limits from CEPC which corresponds to a invisible Higgs boson branching ratio of $BR(H \rightarrow \text{inv}) < 0.31\%$ at the 95% CL. The gray dotted curves correspond to $BR(H \rightarrow \text{inv}) < 24\%$, the current limit at the LHC [186], and the black dotted curves correspond to $BR(H \rightarrow \text{inv}) < 3.5\%$, the projected reach at HL-LHC from Ref. [188]. The cyan dashed curve corresponds to the discovery limit set by the coherent-neutrino-scattering background, adapted from Ref. [182].

completed at a higher scale. More specifically, this operator can be generated by integrating out a heavy mediator that connects the Higgs boson and the fermion DM. The validity of the effective theory thus requires the mediator to be heavier than the scale of the interaction. For direct detection experiments, the momentum exchange is in the nonrelativistic regime, and is at the MeV level. For the Higgs boson decay, the interaction scale is at the order of the Higgs boson mass. Our results for the fermion DM are thus only valid if the mediator is at least as heavy as the Higgs boson.

Next, let us consider the kinetic mixing portal scenario, in which the hidden sector containing the dark matter is charged under a broken dark Abelian gauge symmetry, $U(1)_D$. The $U(1)_D$ could mix with the SM hypercharge $U(1)_Y$ through the operator

$$\frac{1}{2} \frac{\epsilon}{\cos \theta} Z_{D\mu\nu} B^{\mu\nu}, \quad (2.24)$$

where ϵ is the (dimensionless) kinetic mixing parameter and θ is the weak mixing angle. The heavy gauge boson associated with $U(1)_D$, often called the dark photon, could be searched for at a lepton collider in a variety of ways. First, the dark photon introduces two effects in the fit of precision electroweak observables: a shift in the Z mass observable and a shift of the Z couplings to SM fermions. The Z -pole program at CEPC could improve the sensitivity to electroweak observables by a factor of 10 compared to LEP and push the reach of ϵ down to $\sim 10^{-3}$ for $m_{Z_D} < 90$ GeV [189]. A more powerful way is to search for dark photons directly through the radiative return processes such as $e^+ e^- \rightarrow \gamma Z_D \rightarrow \gamma \mu^+ \mu^-$. The search can be implemented by simply counting the number of events in the dimuon invariant mass spectrum in both the Z -pole and Higgs programs at CEPC. The direct searches probe $\epsilon \subset (3 \times 10^{-4} - 10^{-3})$ depending on m_{Z_D} in the entire mass range up to 250 GeV that could be covered by CEPC [190], as illustrated in Figure 2.25. Another possible direct probe is the rare Z decay: $Z \rightarrow h_D Z_D \rightarrow Z_D Z_D Z_D$, where h_D is the dark Higgs. The reach of this search has been discussed in Sec. 2.3.2.

In the remainder of this subsection we will discuss a case study of a model with two renormalizable Standard Model–dark sector couplings, the Double Dark Portal model of Ref. [125]. This model rests on the observation that one possible origin for the mass of a $U(1)_D$ dark gauge boson is through the VEV of a dark Higgs scalar Φ carrying $U(1)_D$ charge. The $U(1)_D$ gauge boson kinetically mixes with the photon (with mixing parameter ϵ) while the dark Higgs Φ mixes with the Higgs through a $\lambda_{HP} |\Phi|^2 |H|^2$ quartic potential. A dark fermion χ with Dirac mass m_χ carrying $U(1)_D$ dark charge can play the role of dark matter. We denote the two scalar mass eigenstates of this model by H_0 (mostly Higgs) and S (mostly Φ) with mixing angle α . We denote the vector mass eigenstates by \tilde{Z}_μ (mostly the SM Z boson) and \tilde{K}_μ (mostly the dark photon). Both of the renormalizable portal couplings lead to attractive discovery prospects at CEPC from a variety of channels summarized in Table 2.2.

This model contains several couplings allowing transitions from the Standard Model to the dark sector, proportional to an insertion of a mixing parameter. Vertices proportional to α include $H_0 S S$; $H_0 H_0 S$; $\tilde{K}_\mu \tilde{K}^\mu H_0$; and $\tilde{Z}_\mu \tilde{Z}^\mu S$. Vertices proportional to ϵ include $\tilde{Z}_\mu \tilde{K}^\mu S$ and $\tilde{Z}_\mu \tilde{K}^\mu H_0$. If $4m_\chi < 2m_{\tilde{K}} < m_S$, then both the dark photon \tilde{K} and dark Higgs S will dominantly decay invisibly, with visible branching ratios suppressed by $e^2 \epsilon^2 / g_D^2$ and $\tan^2 \alpha / g_D^2$ respectively. Hence, the Double Dark Portal model contains invisible Higgs boson decay modes $H_0 \rightarrow S S \rightarrow 4\tilde{K} \rightarrow 8\chi$ and $H_0 \rightarrow 2\tilde{K} \rightarrow 4\chi$, in addition to the possible exotic decay $H_0 \rightarrow \tilde{Z} \tilde{K}$ which is either partially visible or invisible

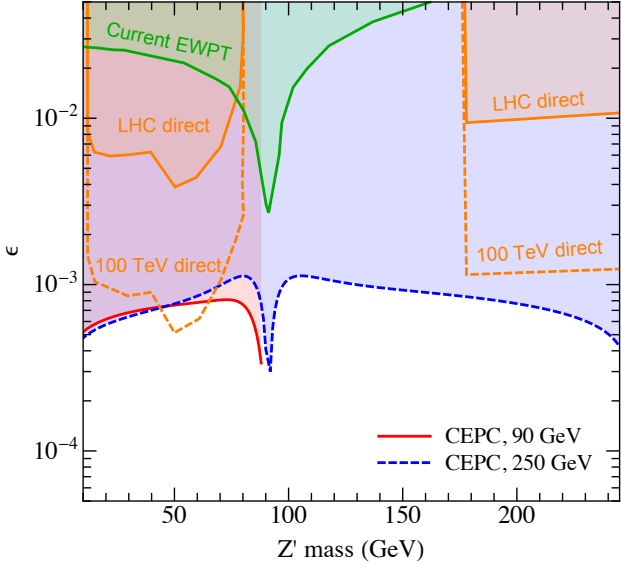


Figure 2.25: This figure illustrates CEPC’s capacity to probe dark photons via radiative return. The red-solid and blue-dashed lines show the 95% CL projected sensitivity to the (hypercharge) mixing parameter, ϵ , as a function of the dark photon’s mass, $m_{Z'}$. The red curve corresponds to $\sqrt{s} = 90$ GeV and $\mathcal{L} = 0.5 \text{ ab}^{-1}$ while the blue curve shows 250 GeV and 5 ab^{-1} . The figure is adapted from Refs. [189, 190].

Parameter	Signal process	Background (pb)	Signal region
ϵ	$\tilde{Z} \tilde{K}$	$\bar{\ell}\ell\bar{\nu}\nu$	$N_\ell \geq 2, m_{\ell\ell} - m_Z < 10 \text{ GeV},$ and $ m_{\text{recoil}} - m_{\tilde{K}} < 2.5 \text{ GeV}$
	$\tilde{Z} \rightarrow \bar{\ell}\ell, \tilde{K} \rightarrow \bar{\ell}\ell$	$\bar{\ell}\ell\bar{\ell}\ell$	$N_\ell \geq 4, m_{\ell\ell} - m_Z < 10 \text{ GeV},$ and $ m_{\ell\ell} - m_{\tilde{K}} < 2.5 \text{ GeV}$
$\tilde{A}\tilde{K}$	\tilde{K} inclusive decay	$\gamma\bar{f}f$	$N_\gamma \geq 1, \text{ and}$ $ E_\gamma - (\frac{\sqrt{s}}{2} - \frac{m_{\tilde{K}}^2}{2\sqrt{s}}) < 2.5 \text{ GeV}$
	$\tilde{K} \rightarrow \bar{\ell}\ell$	$\gamma\bar{\ell}\ell$	$N_\gamma \geq 1, N_\ell \geq 2, E_\gamma - (\frac{\sqrt{s}}{2} - \frac{m_{\tilde{K}}^2}{2\sqrt{s}}) < 2.5 \text{ GeV},$ and $ m_{\ell\ell} - m_{\tilde{K}} < 5 \text{ GeV}$
$\tilde{Z}H_0$	$\tilde{K} \rightarrow \bar{x}\chi$	$\gamma\bar{\nu}\nu$	$N_\gamma \geq 1, E_\gamma - (\frac{\sqrt{s}}{2} - \frac{m_{\tilde{K}}^2}{2\sqrt{s}}) < 2.5 \text{ GeV},$ and $\cancel{E} > 50 \text{ GeV}$
	$H_0 \rightarrow \tilde{K}\tilde{Z}$ with $\tilde{K} \rightarrow \bar{x}\chi, \tilde{Z} \rightarrow \bar{\ell}\ell$	$\bar{\ell}\ell\bar{\ell}\ell\bar{\nu}\nu$	$N_\ell \geq 4, m_{\ell\ell} - m_Z < 10 \text{ GeV},$ and $ m_{\text{recoil}} - m_{\tilde{K}} < 2.5 \text{ GeV}$
$\sin \alpha$	$\tilde{Z}S$	$\bar{\ell}\ell\bar{\nu}\nu$	$N_\ell \geq 2, m_{\ell\ell} - m_Z < 10 \text{ GeV},$ and $ m_{\text{recoil}} - m_S < 2.5 \text{ GeV}$

Table 2.2: Double Dark Portal model: summary of the different vector + scalar and vector + vector production modes studied, along with the most salient cuts to identify the individual signals. All background processes include up to one additional photon to account for initial and final state radiation. Background rates are given for $\sqrt{s} = 250$ GeV, and visible particles are required to satisfy preselection cuts given in the main text of [125].

depending on the \tilde{Z} decay channel. A precision measurement of the invisible branching fractions of the Higgs boson can significantly constrain the model, as summarized in Figure 2.26. Precision observation of the Higgsstrahlung rate with $\mathcal{O}(0.3\% - 0.7\%)$ accuracy [122–124] will constrain the scalar mixing angle at the level $\sin \alpha \lesssim 0.055 - 0.084$. Direct searches for dark sector particles are possible in the channels $\tilde{Z}H_0$, $\tilde{Z}S$, $\gamma\tilde{K}$ and $\tilde{Z}\tilde{K}$. The sensitivity of CEPC searches for these signals and comparisons to existing constraints from BaBar, LEP, and LHC are summarized in Figure 2.27. The $\tilde{Z}\tilde{K}$ final state

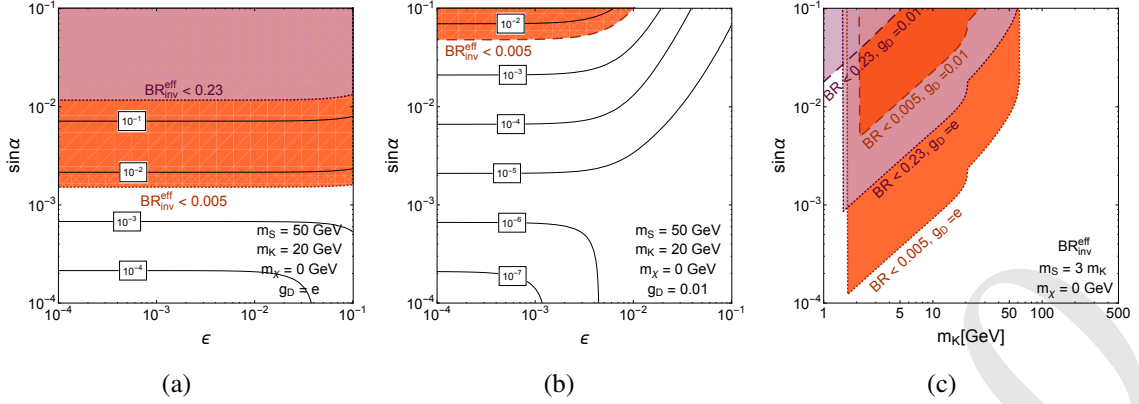


Figure 2.26: This figure shows the reach of CEPC to test the Double Dark Portal model [125] through invisible decay of the SM-like Higgs boson. (a, b) Rates for the invisible branching fraction of the 125 GeV Higgs boson in the $\sin\alpha$ vs. ϵ plane, setting $m_S = 50 \text{ GeV}$, $m_K = 20 \text{ GeV}$, and $g_D = e$ (left) and 0.01 (center). (c) Exclusion regions in the $\sin\alpha$ vs. m_K plane from the search for an invisible decay of the 125 GeV Higgs boson by ATLAS and CMS giving $\text{BR}_{\text{inv}} < 0.23$ [126, 127], and the projected reach from a future e^+e^- machine giving $\text{BR}_{\text{inv}} < 0.005$ [121–123, 191].

can be searched for using the recoil mass in events containing $Z \rightarrow \ell^+\ell^-$. The radiative return process $e^+e^- \rightarrow \gamma \tilde{K}$ allows a search for events with a monochromatic photon together with $\tilde{K} \rightarrow \bar{\chi}\chi, \ell^+\ell^-$. The Figure 2.27(a) shows that searches with invisible \tilde{K} are more effective than those with $\tilde{K} \rightarrow \ell^+\ell^-$, due to the larger branching fraction. The figure also shows that a search for $H_0 \rightarrow \tilde{Z}\tilde{K}(\rightarrow \bar{\chi}\chi)$ is less effective. Finally, the Figure 2.27(b) shows the reach of a search for the S -strahlung process $e^+e^- \rightarrow \tilde{Z}S$ in the mixing angle $\sin\alpha$. This search is exactly analogous to the previous search at LEP-II for a purely invisible decaying Higgs boson [119]. Improved sensitivity could be obtained by varying the \sqrt{s} of the collider to maximize the $\sigma(e^+e^- \rightarrow \tilde{Z}S)$ rate for the test S mass (see also Ref. [192]).

Portals with additional SM-sector physics

While the renormalizable SM portals are simple, they are not the only possibilities. Portals between the dark and visible sectors could be formed by additional particles with Standard Model gauge charges. These can offer interesting variations on the renormalizable portal. One example of such a portal is the leptonic Higgs portal [196]. This model includes an elementary scalar, S , which only couples to the SM leptons, $g_\ell S \bar{l}l$.³ Note that this operator is not SM gauge invariant and has to be UV completed. One possible simple UV completion is to couple a SM singlet to two Higgs doublets with one of the doublets only coupling to leptons and the other one only coupling to quarks. At a lepton collider, assuming that the couplings g_ℓ are proportional to the corresponding lepton mass, S could be produced in association with τ leptons, $e^+e^- \rightarrow \tau^+\tau^- + (S \rightarrow e^+e^-, \mu^+\mu^-, \tau^+\tau^-)$. Current beam dump and lepton colliders only probe m_S to a few GeV. CEPC could be capable of extending the sensitivity to much heavier S up to $m_S \sim 250 \text{ GeV}$. In the particular lepton-specific two Higgs doublet UV completion, the mixing between the

³A variant of the model with S dominantly coupling to the muon and proton with tiny couplings to the electron and neutron might explain the proton radius puzzle and the muon anomalous magnetic moment discrepancy.

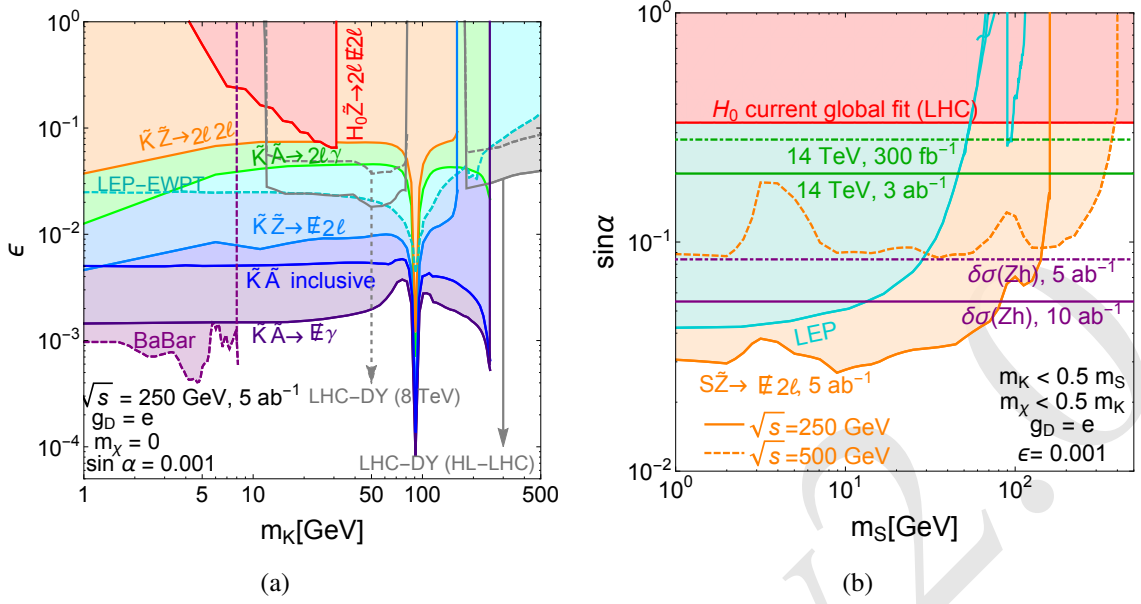


Figure 2.27: This figure shows the reach of CEPC to test the Double Dark Portal model [125] through searches for dark-sector particles. (a) Projected exclusion regions in the ϵ vs. m_K plane from multiple complementary searches of \tilde{K} production. Solid lines enclose expected exclusion regions with $\mathcal{L} = 5 \text{ ab}^{-1}$ of $\sqrt{s} = 250 \text{ GeV } e^+e^-$ machine data. Dashed lines indicate existing limits from the LEP $e^-e^+ \rightarrow \ell^-\ell^+$ contact operator search, the LEP electroweak precision tests (LEP-EWPT), the BaBar \tilde{K} invisible decay search (BaBar), and the LHC Drell-Yan constraints (LHC-DY). The 3 ab^{-1} HL-LHC projection for Drell-Yan constraints is also shown as a solid line. Note that m_K is approximately the $m_{\tilde{K}}$ mass eigenvalue. (b) Exclusion reach from the ZS , $Z \rightarrow \ell^+\ell^-$ search in the recoil mass distribution for invisible S decays in the $\sin \alpha$ vs. m_S plane using 5 ab^{-1} of e^+e^- data at $\sqrt{s} = 250 \text{ GeV}$ or 500 GeV . We also show comparisons to the current fit, $\sin \alpha < 0.33$ [120], future LHC projections of 0.28 (0.20) using 300 fb^{-1} (3 ab^{-1}) luminosity [121], and precision $\delta\sigma(ZH)$ measurements constraining 0.084 (0.055) using 5 ab^{-1} (10 ab^{-1}) [122–124]. We plot the excluded region from LEP searches for invisible low mass Higgs boson in the ZS channel in cyan [119, 193–195].

1 singlet S and the Higgs boson H leads to exotic Higgs boson decays such as $H \rightarrow SS \rightarrow$
2 $4\tau, 2\mu 2\tau$. For the 4τ final state, CEPC could test a branching fraction as small as 10^{-4}
3 at 95% CL, improving the sensitivity by three orders of magnitude compared to even the
4 HL-LHC [197]! This is translated to a factor of 30 improvement in testing the coupling
5 g_ℓ , fixing all the other parameters. Another similar possibility is a leptonic portal arising
6 from some gauge bosons coupling to SM lepton-flavor currents [198].

7 In general, the dark matter portal models could give rise to exotic Higgs boson decays.
8 A thorough review of the models leading to exotic Higgs boson decays and the status of
9 LHC searches can be found in Ref. [113]. Supersymmetric exotic decays of the Higgs
10 boson have been studied in Refs. [197, 199]. The potential of detecting exotic Higgs
11 boson decays in 14 different final states at CEPC has been presented in Ref. [197]. In
12 every final state, we expect at least one order of magnitude improvement in sensitivity
13 compared to the HL-LHC and in quite a few channels, we expect 3-4 orders of magnitude
14 improvement at CEPC. More details are discussed in Section 2.3.1.

15 A characteristic feature of many models that go beyond renormalizable portals is the
16 possibility of new sources of flavor violation. For example, nonrenormalizable (dipole

moment) operators could allow one SM fermion to decay to a dark photon and another SM fermion of different flavor, e.g. $\mu^\pm \rightarrow e^\pm \gamma_d$ or $t \rightarrow c\gamma_d$ [200]. Renormalizable completions of such models introduce new "messenger" particles that interact with the SM gauge groups and the dark photon. The induced flavor-violating decays could be searched for at CEPC.

Another possibility that could be tested at CEPC is flavor-violating dark matter in which dark matter couples dominantly to muons [201]. The dark multiplet contains a scalar and a vector-like fermion and couples to the muon through a Yukawa interaction. The neutral component of the scalar serves as the dark matter candidate. The interaction generates a loop correction to the $\gamma\mu^+\mu^-$ and $Z\mu^+\mu^-$ couplings that could be measured as deviations in the cross section of $e^+e^- \rightarrow \mu^+\mu^-$. Choosing the Yukawa coupling to be $\mathcal{O}(1)$ means that a 2% precision measurement of the cross section can probe dark matter mass within 20 GeV around 120 GeV. Related models include flavored dark matter [202, 203], in which the dark matter particle carries flavor quantum numbers and has renormalizable contact interactions with the SM fields. In particular, electron-flavored dark matter could be produced copiously at a lepton collider associated with a photon if its mass is below ~ 120 GeV.

Effective theory

So far, our discussion of dark matter has been organized based on details of the model. However, one could also take a portal-agnostic or "model-independent" approach, simply searching for a generic signal like a single photon plus missing energy [204]. This could arise if DM is part of an electroweak multiplet, due to loops of the charged $SU(2)_L$ partners of dark matter and W bosons. It could also arise if completely new charged particles, independent of DM, exist and couple to DM. Results can be expressed simply in terms of effective operators, without committing to a particular UV completion. A variety of studies of such signals at e^+e^- colliders have been carried out, e.g. [205–208].

In an effective theory approach, such signals arise from dimension-7 effective operators coupling fermionic dark matter to pairs of SM gauge bosons. The operators that can be efficiently constrained by searches at CEPC are

$$\begin{aligned} \mathcal{L}_S &\supset \frac{1}{\Lambda_{\gamma\gamma}^3} \bar{\chi}\chi A^{\mu\nu} A_{\mu\nu} + \frac{1}{\Lambda_{\gamma Z}^3} \bar{\chi}\chi A^{\mu\nu} Z_{\mu\nu}, \\ \mathcal{L}_P &\supset \frac{1}{\Lambda_{\gamma\gamma}^3} \bar{\chi}i\gamma_5\chi A^{\mu\nu} \tilde{A}_{\mu\nu} + \frac{1}{\Lambda_{\gamma Z}^3} \bar{\chi}i\gamma_5\chi A^{\mu\nu} \tilde{Z}_{\mu\nu}, \end{aligned} \quad (2.25)$$

where the field strengths $A_{\mu\nu}$ and $Z_{\mu\nu}$ and their duals $\tilde{A}_{\mu\nu}$ and $\tilde{Z}_{\mu\nu}$ couple to the scalar (S) and the pseudoscalar (P) fermionic dark matter bilinears. The Λ factors in the coefficients represent the approximate mass scale of new physics (up to loop factors). Similar operators can also be written for the $SU(2)_L$ gauge fields, but the WW couplings may not be as efficiently probed by e^+e^- collisions at the Z pole.

The diphoton operator dominates processes with low momentum transfer because the photon is massless. It is much more stringently constrained by direct detection than its DM- γZ and DM- ZZ counterparts. For DM lighter than half of m_Z , indirect detection using diffuse gamma rays is also more sensitive to the diphoton operator. Collider searches, on the other hand, can more effectively probe Z couplings. The high-luminosity Z -pole run at CEPC offers a unique opportunity to test the DM couplings to the Z boson. For a

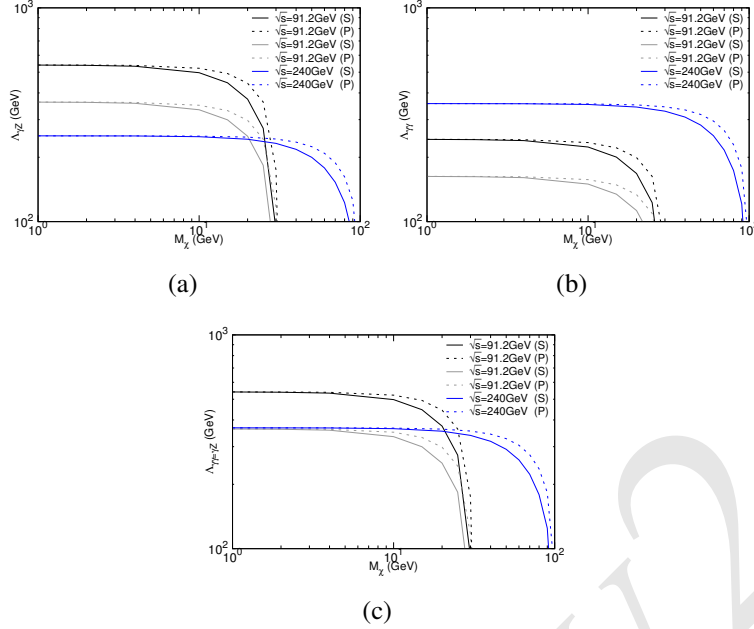


Figure 2.28: CEPC’s capacity to test whether dark matter couples to the SM photon and/or Z boson through the operators in Equation (2.25). From (a) to (c), the three panels correspond to pure $\Lambda_{\gamma Z}$ interaction, pure $\Lambda_{\gamma\gamma}$ interaction, and $\Lambda_{\gamma Z} = \Lambda_{\gamma\gamma}$ interaction. The various curves show CEPC’s 3σ projected sensitivity to the dark matter mass, m_χ , and the energy scale of new physics, Λ . The black, gray, and blue lines refer to $\sqrt{s} = 91.2$ GeV with 2.5 ab^{-1} , 91.2 GeV with 25 fb^{-1} , and 240 GeV with 5 ab^{-1} , respectively. The photon is required to have $|\eta| < 3$ and a $p_T > 25$ (35) GeV for 91.2 (240) GeV collision energy to optimize the sensitivity for a low m_χ . The solid lines are for a scalar operator and the dashed lines for the pseudoscalar case. The figure is adapted from Ref. [209].

1 light DM mass, the resonantly produced $\bar{\chi}\chi\gamma$ system is best searched for in the monophoton
2 + missing energy channel.

3 The proposed Z -pole runs’ prospective limits on effective DM- γZ and $\gamma\gamma$ couplings in
4 the monophoton channel are studied in Ref. [209]. The major SM background, $e^+e^- \rightarrow$
5 $\bar{\nu}\nu\gamma$, can be effectively controlled by optimizing the cut on the single photon’s p_T . The
6 corresponding constraints on Λ are illustrated in Figures. 2.28 and 2.29. The best sensi-
7 tivity is obtained for light dark matter mass. In case only one operator is considered, the
8 projected sensitivity for $\Lambda_{\gamma Z}$ is 360 GeV and 540 GeV for 25 fb^{-1} (giga Z) and 2.5 ab^{-1}
9 (tera Z) luminosities at the Z pole, respectively. In comparison, $\Lambda_{\gamma\gamma}$ is best probed at
10 higher energy runs, and a limit of 360 GeV is obtained for a 5 ab^{-1} run at 240 GeV
11 center-of-mass energy. In general, both $\Lambda_{\gamma Z}$ and $\Lambda_{\gamma\gamma}$ would be present and their relative
12 size is model dependent.

13 Figure 2.29 further shows the direct and indirect detection limits together with CEPC’s
14 constraint in the $\Lambda_{\gamma\gamma} - \Lambda_{\gamma Z}$ plane. For direct detection, we adopt the calculation of the
15 spin-independent scattering rate via the scalar operator from Ref. [111, 214], which takes
16 into account the diphoton exchange that dominates over γZ contributions. We choose
17 benchmark DM masses at 4 and 10 GeV that are accessible to major nuclear recoil exper-
18 iments. For indirect detection, we show the 95% CL constraint from the gamma ray line
19 search at Fermi-LAT [213]. The nonrelativistic DM annihilation cross section into two
20 photons ($\bar{\chi}\chi \rightarrow \gamma\gamma$) is dominated by $\Lambda_{\gamma\gamma}$ for m_χ below $m_Z/2$. The $\Lambda_{\gamma Z}$ dependence only

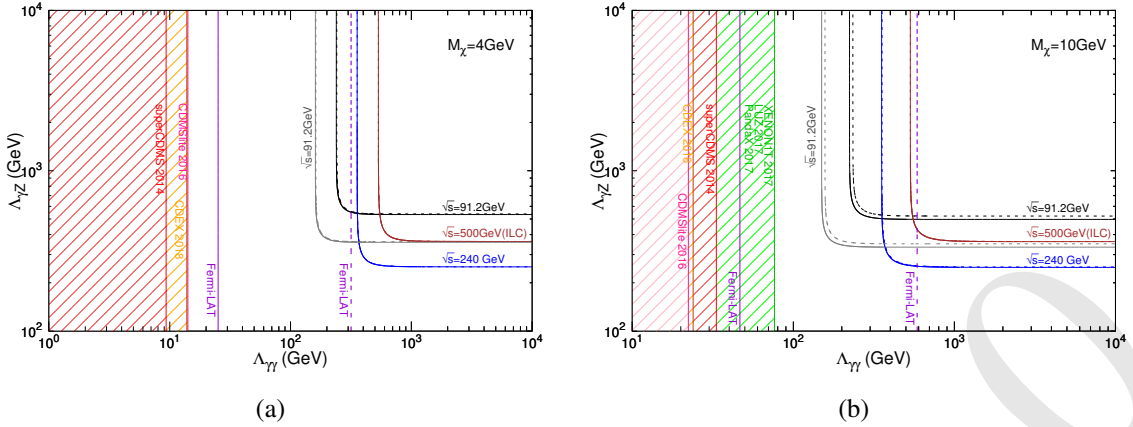


Figure 2.29: CEPC’s capacity to test whether dark matter couples to the SM photon and/or Z boson through the operators in Equation (2.25). The (a) (b) panel shows a DM mass of $m_\chi = 4$ (10) GeV. The CEPC sensitivity is shown by the black, gray, and blue curves, which are defined in the caption of Figure 2.28. The brown line denotes the ILC 3σ sensitivity with an integrated luminosity of 500 fb^{-1} at $\sqrt{s} = 500 \text{ GeV}$ with cuts $10^\circ < \theta_\gamma < 170^\circ$ and $p_T(\gamma) > 90 \text{ GeV}$. Constraints from dark matter direct detection experiments are shown in red for SuperCDMS [210], orange for CDEX [211], pink for CDMSlite [212], and green for XENON1T [132], LUX [133], and PandaX [155] (which are in close proximity to each other). The purple-dashed line denotes the Fermi-LAT bound from the R3 region [213]. Note that the XENON1T/LUX/PandaX limit only appears in the $m_\chi = 10$ GeV case. The figure is adapted from Ref. [209].

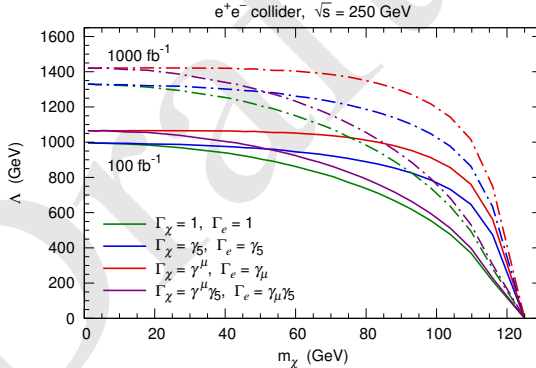


Figure 2.30: CEPC 3σ reach for several effective interactions between dark matter and electrons in the channel of monophoton + missing energy with integrated luminosities of 100 fb^{-1} and 1 ab^{-1} .

emerges in a tiny correction as part of the $\bar{\chi}\chi \rightarrow \gamma(\gamma^*/Z^* \rightarrow \bar{f}f)$ process, and can be ignored at the DM masses shown.

The channel of monophoton + missing energy would also be sensitive to effective interactions between dark matter and electrons. In this case, the photon arises from initial state radiation. The related dimension-6 operators are

$$\mathcal{L}_{\chi e} = \frac{1}{\Lambda^2} \bar{\chi} \Gamma_\chi \chi \bar{e} \Gamma_e e, \quad (2.26)$$

where $\Gamma_\chi, \Gamma_e \in \{1, \gamma_5, \gamma^\mu, \gamma^\mu \gamma_5, \sigma^{\mu\nu}\}$. The CEPC reach at 250 GeV center of mass energy is demonstrated in the $m_\chi - \Lambda$ plane in Figure 2.30. For low masses, limits of $\sim 1.4 \text{ TeV}$ on Λ could be achieved with an integrated luminosity of 1 ab^{-1} .

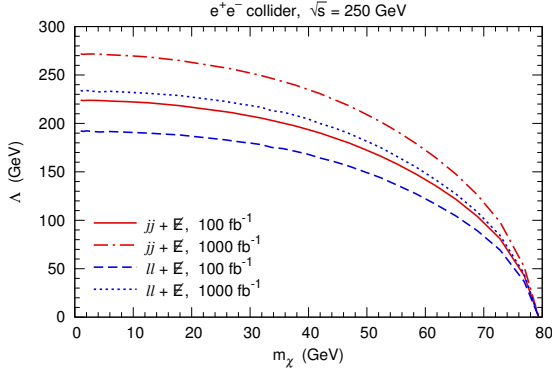


Figure 2.31: CEPC 3σ reach for the effective operator $\mathcal{L}_{\chi Z}$ in the channel of mono- Z + missing energy, adapted from [208]. Both the hadronic ($jj + \cancel{E}$) and the leptonic ($ll + \cancel{E}$) modes are presented with integrated luminosities of 100 fb^{-1} and 1 ab^{-1} .

1 An analogous approach is to search for a signal in the channel of mono- Z + missing
 2 energy. This channel is sensitive to effective operators like

$$\mathcal{L}_{\chi Z} = \frac{1}{\Lambda^3} \bar{\chi} \chi Z^{\mu\nu} Z_{\mu\nu}. \quad (2.27)$$

3 Z bosons can be reconstructed by either two jets or two opposite-sign same-flavor leptons.
 4 Figure 2.31 shows the CEPC reach in the $m_\chi - \Lambda$ plane at 250 GeV center of mass energy.
 5 It is expected that the hadronic modes would provide a better sensitivity than the leptonic
 6 modes.

7 2.3.4 Neutrino connection

8 Neutrino mass models

9 The CEPC is an excellent tool to study the physics of neutrino mass generation as a portal
 10 to unknown new physics during both the 240 GeV and the Z -pole runs. In this respect
 11 it can serve as a discovery machine for new physics that evades detection at hadronic
 12 colliders, including feebly coupled "hidden sector" extensions of the SM that can address
 13 fundamental questions in particle physics and cosmology.

14 The experimental observation of neutrino flavor oscillations [215, 216] indicates that
 15 neutrinos have a nonzero mass. Global fits to neutrino oscillation experiments (see e.g. [217,
 16 218]) are sufficient to fix two neutrino mass-square differences and all mixing angles in
 17 the Pontecorvo-Maki-Nakagawa-Sakata matrix V_ν (assuming it to be unitary), while the
 18 absolute neutrino mass scale is constrained from cosmology to be in the sub-eV range
 19 (see e.g. [219]). These results raise a pair of pressing questions, namely why the neutrinos
 20 are so much lighter than all other fermions, and why the elements of the neutrino mass
 21 mixing matrix are so different from the quark mixing matrix.

22 Since the Standard Model of particle physics cannot account for nonzero neutrino
 23 masses in a renormalizable way, neutrino oscillations provide compelling experimen-
 24 tal evidence for physics beyond the SM. While the origin of mass for the charged SM
 25 fermions (at least of the third generation) is well established by Higgs coupling measure-
 26 ments, the origin of mass for neutrinos is unknown and calls for a more fundamental
 27 theory of nature underlying the Standard Model. Moreover, neutrinos may be Majorana

1 fermions [220], fundamentally different from their charged fermion counterparts, with
 2 consequences related to violation of lepton number that are potentially discoverable at col-
 3 liders [221]. Lepton number violation may also be connected to an open question in cos-
 4 mology, the baryon asymmetry of the universe (BAU), i.e., the tiny excess $\sim 10^{-10}$ [131]
 5 of matter over antimatter.

6 Under the assumption that the scale of new physics Λ associated with the mass of the
 7 lightest new particle involved in the generation of neutrino masses is much larger than the
 8 typical energy $E_\nu \sim \text{MeV}$ in neutrino oscillation experiments,⁴ the neutrino oscillations
 9 can be described in the framework of Effective Field Theory (EFT). The relevant operators
 10 $\mathcal{O}_i^{[n]}$ have mass dimension $n > 4$, are suppressed by powers of Λ^{n-4} , and have Wilson
 11 coefficients $c_i^{[n]}$ that are matrices in flavor space. In this framework the smallness of the
 12 neutrino masses can be a consequence of any combination of the following reasons:

13 I) *High-Scale Seesaw Mechanism*: Large values of Λ automatically lead to small m_i .
 14 The three tree level implementations of the idea [224] are known as: Type-I See-
 15 saw [78, 79, 225–228], involving the SM plus right-handed neutrinos N ; Type-II
 16 Seesaw [228–232], involving the SM plus a scalar $SU(2)_L$ triplet Δ_L ; and Type-III
 17 Seesaw [233], involving the SM plus a fermionic $SU(2)_L$ triplet field Σ_L .

18 II) *Small numbers*: The $\mathcal{O}_i^{[n]}$ can remain small (for all values of Λ , including those acces-
 19 sible to CEPC) if the Wilson coefficients $c_i^{[n]}$ are small. In particular, if the neutrinos
 20 are Dirac particles their masses can be generated by the Higgs mechanism in exactly
 21 the same way as all other fermion masses with tiny Yukawa couplings. Tiny constants
 22 can be avoided e.g. when the neutrino interactions are created dynamically due to the
 23 spontaneous breaking of a flavor symmetry by flavons [234], or when the $\mathcal{O}_i^{[n]}$ are
 24 created radiatively (see e.g. [235–239]).

25 III) *Low-Scale Seesaw Mechanism*: A low scale Λ and $\mathcal{O}(1)$ couplings between the SM
 26 and the new particles can be realized when symmetries give rise to cancellations in
 27 the neutrino mass matrix. For instance the $B - L$ symmetry of the SM can keep the
 28 $\mathcal{O}_i^{[n]}$ small for Λ below the TeV scale [240–242]. Specific models that implement
 29 this idea include the inverse [243–245] and linear [246, 247] seesaw, the Neutrino
 30 Minimal Standard Model [248, 249] and scale invariant models [250].

31 Here the terms "high scale" and "low scale" should be understood with respect to the
 32 CEPC collision energy; for values of Λ far above 240 GeV the EFT treatment intro-
 33 duced here to describe neutrino oscillation experiments can also be applied to CEPC phe-
 34 nomenology, while lower values imply that the new particles can be found at CEPC and
 35 should be described dynamically.

36 The original setting for the seesaw mechanism was grand unified theories, based on
 37 $\text{SO}(10)$ [226], and $\text{SU}(5)$ [225], as well as the minimal Left-Right (LR) symmetric model [78,
 38 79] and flavor/family symmetries [227]. The large scale of grand unification typically sets
 39 the mass scale Λ related to neutrino physics beyond the direct reach of colliders, although
 40 parts of multiplets may lie well below the GUT scale. For example, the minimal $\text{SU}(5)$
 41 model with the addition of a 24_F multiplet requires a light fermionic triplet in order for

⁴Scenarios with $\Lambda < E_\nu$ are in principle feasible (see e.g. Refs. [222, 223] and references therein), but strongly constrained by the success of the high level of consistency in global fits to neutrino oscillation data that assume only three light neutrinos [217, 218].

gauge couplings to unify [251, 252], motivating Type III Seesaw searches at the TeV scale. Other well known examples are for instance $B - L$ symmetry, additional "neutrinoophilic" Higgs doublets, and flavor symmetries. Such neutrino mass physics generally predicts the existence of new particles, which could at least in principle be discovered and studied at CEPC.

6 Lepton number violation

If neutrinos are Majorana particles, the mechanism that generates their mass can mediate lepton-number violating (LNV) processes at colliders if the scale Λ is below or near the collision energy [221]. A variety of signatures arise in specific models for neutrino mass generation.

Type I Seesaw: Observing the violation of lepton number from heavy neutrino mass eigenstates (N_i) in the process $e^+e^- \rightarrow N\nu$ at lepton colliders is possible in principle due to the different kinematics of LNV and LNC processes, as was demonstrated for the ILC [253]. In particular, for heavy neutrino N_i masses $M_i > m_Z$, the process $e^+e^- \rightarrow \nu\ell jj$ is a promising signature at lepton colliders [254–256] and has been studied specifically for CEPC [257]. The subleading production process for heavy neutrinos at lepton colliders $e^+e^- \rightarrow N\ell^\pm W^\mp$ allows for same sign dileptons for $N \rightarrow \ell^\pm W^{(*)}$ and $W \rightarrow$ hadrons [256].

It is worth pointing out, however, that LNV in the Type I Seesaw mechanism is suppressed by the smallness of the light neutrino masses [241, 242]. It has been proposed that the suppression of LNV may be alleviated by the process of heavy neutrino-antineutrino oscillations, which occurs for heavy neutrinos with masses below the W boson's mass, m_W , and with $U^2 < \mathcal{O}(10^{-5})$ [258–260].

Type II Seesaw: The triplet scalar multiplet Δ_L in the Type II Seesaw contains three complex fields, which are respectively neutral, singly charged, and doubly charged under electromagnetism. The appealing feature of the model is the direct connection between neutrino masses and mixing parameters [261, 262] and the Majorana Yukawa matrix $M_\nu = Y_\Delta \langle \Delta_L \rangle$, which may lead to charged lepton flavor violating signals [263].

Collider phenomenology is governed by the final state, which primarily depends on the triplet's vacuum expectation value (VEV) [264] and the mass splittings of its components [265]. If the masses are degenerate, the dominant decay mode is to leptons if the triplet VEV is smaller than $\sim 10^{-4}$ GeV. This decay mode tests the flavor structure of the neutrino mass matrix and leads to significant flavor-dependent bounds on the triplet scalar mass up to 870 GeV at the LHC [266]. For the triplet VEV above $\sim 10^{-4}$ GeV, the states decay to pairs of gauge bosons. A relatively small mass splitting, consistent with precision electroweak constraints, triggers cascade decay modes [265] which produce soft hadronic and multi-lepton final states [267]. Signal in the WW final state lead to weak lower bounds on doubly charged scalars at the LHC, $m_{\Delta_L^{++}} \gtrsim 90$ GeV [268] or less, depending on the lepton's flavor. Similarly, the cascade decays [265, 269] are not easy to look for in hadronic colliders [270]; however, they may be observable in cleaner lepton collisions [271].

At lepton colliders, the triplet components can be produced pair-wise through $e^+e^- \rightarrow S\bar{S}$ (where $S = \Delta_L^0, \Delta_L^\pm, \Delta_L^{\pm\pm}$ are the various charged states in the triplet) or in single production in association with two same-sign leptons $e^+e^- \rightarrow \Delta_L^{\pm\pm}\ell^\mp\ell^\mp$ [272, 273].

¹ Another possible production mode is via vector-boson fusion $e^+e^- \rightarrow \ell\ell'SS'$, where
² $\ell, \ell' = e^\pm, \nu$, as discussed in [274].

³ The doubly charged scalar bosons $\Delta_L^{\pm\pm}$ can couple to the electrons and positrons directly and contribute to Bhabha scattering in the t -channel [272, 275]. Running the lepton colliders with same-sign beams may strongly enhance the production of the doubly charged components in the s -channel [272, 276], see [277] for more recent work.

⁷ **Left-Right Symmetric Model:** The mixing of the SM Higgs doublet with the $SU(2)_R$ triplet Higgs that gives Majorana mass to right-handed neutrinos in the Left-Right Symmetric Model (LRSM) [278–281] may lead to LNV decays of $h \rightarrow NN$ [282]. The subsequent (and possibly displaced) decay of $N \rightarrow \ell^\pm jj$ can lead to a $\Delta L = 2$ LNV and potentially charged lepton flavor violating final state with two same sign-leptons and up to four jets. Due to the soft final states and displacement, such searches may be challenging at the LHC; however lepton colliders are much more suitable to detect such signals due to the absence of triggers and lower QCD backgrounds.

¹⁵ The presence of the mixing also allows for an enhanced production of the $SU(2)_R$ triplet $pp \rightarrow \Delta_R^0 \rightarrow NN$ at the LHC [283] with varying kinematics, depending on its mass. Moreover, one may be able observe a truly exotic Higgs boson decay with $h \rightarrow \Delta_R^0 \Delta_R^0 \rightarrow 4N$, where lepton number can be broken to up to four units [283]. The production at lepton colliders may proceed through the Higgs mixing $e^+e^- \rightarrow Z\Delta_R^0 \rightarrow NNZ$ for $\sqrt{s} \lesssim 100$ GeV and in the vector boson fusion (VBF) channel that produces the $NN\nu\bar{\nu}$ final state with lepton number violation and missing energy [283]. At $\sqrt{s} = 240$ GeV and $\mathcal{L} = 5$ ab, one may expect from a few hundred to more than 5000 NNZ events, depending on the masses of triplets and heavy neutrinos, as well as the Higgs-triplet mixing. Such events are essentially background free at lepton colliders because of the LNV final state, Z tagging, and characteristic displacement. Similarly, the quadruple production of N 's can proceed through the Higgs-triplet triple vertex with the potential of observing $\mathcal{O}(10^4)$ events with the branching ratio of Higgs boson to $\Delta_R^0 \Delta_R^0$ at the 1% level.

²⁸ Charged lepton flavor violation

²⁹ Neutrino oscillations violate lepton flavor, which is transferred to the charged leptons via perturbation theory, such that the violation of the charged lepton flavor (cLFV) is a prediction [284]. This gives rise to a variety of distinctive processes that may be probed at CEPC.

³³ **Mixed flavor leptonic Higgs or Z boson decays:** Observables at high energy that can measure cLFV are exotic decays of the Z boson into two charged leptons of different flavor, $Z \rightarrow e^\pm\mu^\mp, e^\pm\tau^\mp, \mu^\pm\tau^\mp$ [285, 286]. Also the decays of the Higgs boson into two charged leptons of different flavor are possible [287, 288]. The processes $h \rightarrow e^\pm\mu^\mp, e^\pm\tau^\mp, \mu^\pm\tau^\mp$ are lepton flavor violating Higgs boson decays that can be measured at CEPC for branching ratios as small as 1.2×10^{-5} to 1.6×10^{-4} [289].

³⁹ **Lepton universality violation in W boson decays:** The branching ratios of the W bosons should be identical for the three different leptons⁵ due to the lepton flavor universality in the SM. Another probe of lepton universality is given by the decays of the τ lepton.

⁵Current LEP data features a branching $\text{Br}(W \rightarrow \tau\nu)$ that is larger than $\text{Br}(W \rightarrow \ell_{e,\mu}\nu)$ by $\sim 2\sigma$ [290].

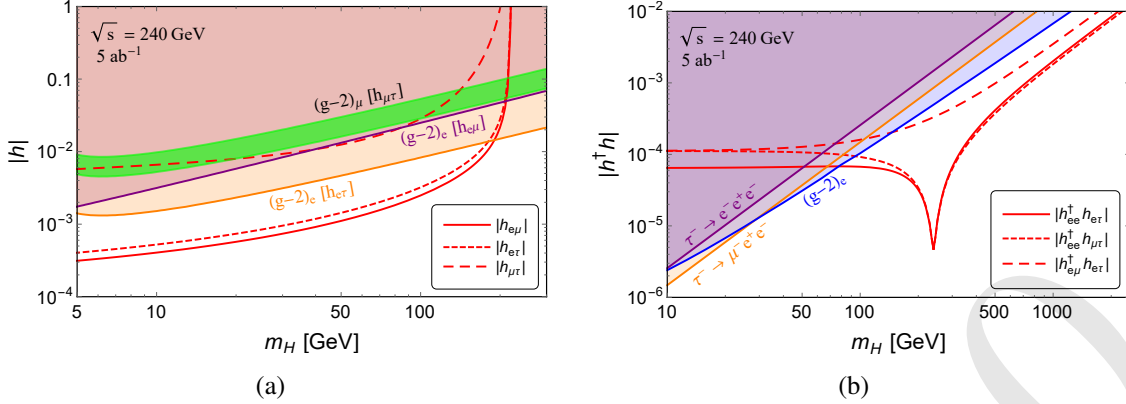


Figure 2.32: The CEPC’s ability to probe charged lepton-flavor violation (cLFV) is illustrated here as a sensitivity to the cLFV couplings, $h_{\alpha\beta}$ ($\alpha \neq \beta$), and the mass of a new, electrically-neutral scalar particle, m_H . Searches for $e^+e^- \rightarrow \ell_\alpha^\pm \ell_\beta^\mp H$ (left) and $e^+e^- \rightarrow \ell_\alpha^\pm \ell_\beta^\mp$ (right) at CEPC with $\sqrt{s} = 240$ GeV and $\mathcal{L} = 5 \text{ ab}^{-1}$ lead to projected sensitivities shown by the red curves (assuming 10 cLFV signal events). In (a) panel, the shaded regions are excluded by electron and muon $g - 2$, but the green band could explain the $(g - 2)_\mu$ discrepancy at the 2σ level. In (b) panel the shaded regions are excluded by rare τ lepton decays, $\tau \rightarrow eee$ and $\tau \rightarrow ee\mu$. See the text and Ref. [293] for more details.

- ¹ Mixing of the active neutrinos with neutral fermions from the Type I or III Seesaw can lead to violations of lepton universality, see e.g. [291]. Charged scalar particles can affect the measurement of lepton-universality observables from W boson branching ratios [292].
- ⁴ **Mixed flavor final states with and without resonance:** In addition to exotic decays of Higgs boson, W , and Z bosons, an observable cLFV process at lepton colliders $e^+e^- \rightarrow \ell_\alpha^\pm \ell_\beta^\mp (+H)$. These processes receive contributions from electrically neutral scalars, for instance from neutrinoophilic Two Higgs Doublet models, Type II-based Seesaw models, $B - L$, or left-right symmetry. A dedicated study of such cLFV processes involving neutral scalars can be found in Ref. [293]. The most stringent constraints and the CEPC prospects in both the on-shell and off-shell modes are collected in Figure 2.32.

¹¹ Higgs boson properties

- ¹² The Higgs boson is a particularly sensitive probe of the mechanism of neutrino mass generation. Higgs boson-based signatures motivated by neutrino mass models include anomalous Higgs boson production mechanisms; invisible or exotic Higgs boson decays; lepton-flavor-violating Higgs couplings; and modified Higgs couplings, all of which may be probed at CEPC.

- ¹⁷ **Anomalous Higgs boson production:** In models with heavy neutrinos, for heavy neutrino masses $M_i > m_H$ additional Higgs bosons can be produced from heavy neutrino decays in processes $e^+e^- \rightarrow Z^* \rightarrow N\nu \rightarrow H\nu\nu$. This can yield an enhancement of the SM mono-Higgs channel of up to $\sim 2\%$ when applying "standard" filters [294, 295]. The CEPC sensitivity via additional Higgs bosons from dedicated analyses is shown by the yellow line in Figure 2.33.

- ²³ **Invisible Higgs boson decays:** The N_i can leave measurable imprints in precision measurements of the Higgs boson branching ratios. In the Type I Seesaw the Higgs boson

1 can decay into a light and a heavy neutrino mass eigenstate when kinematically accessible,
 2 which can account for up to 30% of the Higgs boson decays [296] without violating
 3 present constraints [297]. CEPC sensitivity to this scenario from searches for the Higgs
 4 boson invisible branching ratio, considering the precision from Ref. [124], is shown by
 5 the red line in Figure 2.33.

6 **Leptonic Higgs boson decays with cLFV or LNV:** As mentioned previously, cLFV de-
 7 cays also add loop-induced additional channels to the total Higgs boson decay width,
 8 and processes where the Higgs boson couples to two N_i can give rise to exotic LNV de-
 9 cay channels, all of which may be extensively probed by the precision Higgs program at
 10 CEPC.

11 **Higgs boson decays into two N_i :** In $B - L$ and $L - R$ symmetric models, additional
 12 neutral scalars can mix with the Higgs boson. This can give rise to additional decay
 13 channels into two N_i , which can be observable depending on their masses and lifetimes.
 14 Such signatures were studied in the context of LRSM [282, 283] and $B - L$ models [298,
 15 299].

16 **Anomalous diphoton decays:** In the Type II Seesaw additional scalar particles couple
 17 directly to the Higgs boson, such that the singly and doubly charged components con-
 18 tribute to the loop-induced coupling of the Higgs boson to two photons [265, 300–302].
 19 Similarly, the Type III Seesaw contains additional charged particles that can contribute to
 20 the Higgs-to-diphoton branching ratio, see e.g. [303]. In the LRSM, the doubly charged
 21 component of the $SU(2)_R$ triplet couples rather strongly to the SM Higgs boson, leading
 22 to an $\mathcal{O}(100 \text{ GeV})$ lower bound on its mass [304] from similar radiative corrections. The
 23 Higgs-to-diphoton in the SM could have non-trivial on-shell and off-shell interference ef-
 24 fect [305, 306], which can be used to constrain Higgs boson properties and help resolve
 25 higher dimensional operators.

26 **Modified Higgs self couplings:** In the Type I Seesaw the N_i with masses M_i of a few TeV
 27 can modify the trilinear Higgs self-coupling up to 30 percent [307]. This modification is
 28 also expected for the low-scale Type III Seesaw [308, 309]. CEPC sensitivity to the Higgs
 29 self-coupling via radiative corrections to Higgsstrahlung provides a promising probe of
 30 this effect.

31 **Modifications of electroweak precision observables**

32 Neutrino mass physics can modify the theory predictions for electroweak precision ob-
 33 servables, which may be measurable even if the new mass scale is above the CEPC center-
 34 of-mass energy. These can either occur due to virtual exchange of the new particles (which
 35 may be represented by higher dimensional operators in an EFT approach [313, 314]) or
 36 due to the production of new particles that mix with SM particles (e.g. with the active
 37 neutrinos or the SM Higgs boson).

38 In the context of the Type I Seesaw mechanism the mixings $\theta_{ai} = vY_{ai}/M_i$ of n_s heavy
 39 right handed neutrinos with the SM neutrinos leads to an effective violation of unitarity
 40 in the 3×3 mixing matrix V_ν , which is a submatrix of the $(3 + n_s) \times (3 + n_s)$ leptonic
 41 mixing matrix \mathcal{U} [291, 315–317]. This affects all the electroweak precision observables.
 42 Such tests are mostly independent of the heavy neutrino masses M_i , and they test different

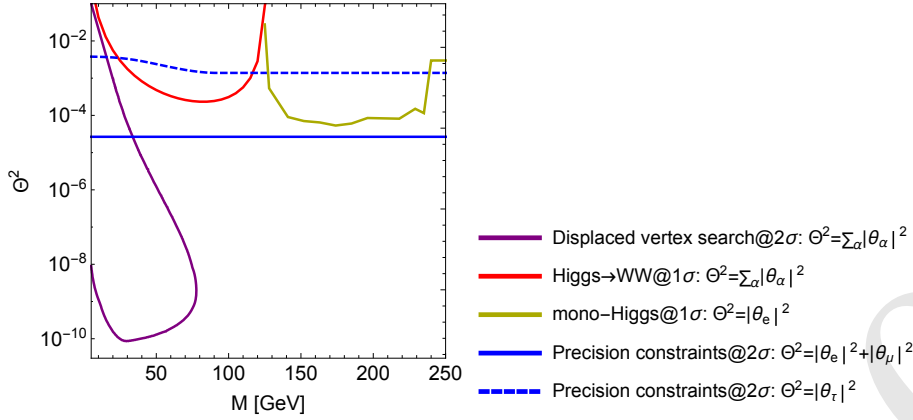


Figure 2.33: The CEPC’s ability to probe heavy sterile neutrinos is expressed as a projected sensitivity on the active-sterile mixing angle, Θ , and the sterile neutrino mass scale, M . The blue (solid and dashed) line denotes electroweak precision measurements [291, 296, 310, 311]. The purple line denotes displaced vertex searches [312] at the Z -pole run with an integrated luminosity of 10 ab^{-1} . The yellow and red lines stem from the measurements of Higgs boson production [294, 295] and decay [296] for an integrated luminosity of 5 ab^{-1} at $\sqrt{s} = 240 \text{ GeV}$.

combinations of the active-sterile mixing parameters [291, 296, 310, 311]. We show the corresponding possible sensitivity of CEPC by solid and dashed blue lines in Figure 2.33, considering a total integrated luminosity of 0.1 ab^{-1} . In addition to the modified precision observables, one also expects violations of lepton universality and (apparent) violations of the unitarity of the Cabibbo-Kobayashi-Maskawa matrix [291, 297, 318–321].

In the context of Type II Seesaw, the electroweak precision observables are affected both by the triplet VEV, as well as by the mass splittings [265] that enter the oblique T parameter. In the minimal LRSM, this splitting is predicted to be large and leads to a lower bound on the entire $SU(2)_L$ triplet multiplet [304].

10 Displaced secondary vertices

The mechanism of neutrino mass generation can also give rise to truly exotic signatures in the form of long-lived particles whose decays produce displaced secondary vertices. Such displaced vertices are often poorly constrained at the LHC due to trigger and background limitations, whereas CEPC can provide significant sensitivity.

15 Single displaced vertex in Type I Seesaw: For masses below the W bosons’s mass, m_W , the lifetime of N_i scales as $\tau_{N_i} \propto |\sum_a |\theta_{ai}|^2|^{-2} G_F^{-2} M_i^{-5}$ and their decays give rise to a visibly displaced secondary vertex in a large part of the allowed parameter space. Displaced vertex signatures have been studied in detail for the case of the Type I Seesaw, and the CEPC specific results from Refs. [260, 312] are shown in Figure 2.33 by the purple line. It is worth noting that with a longer Z -pole run the sensitivity for $M_i < m_Z$ can be significantly increased, see Figure 2.34. The sensitivity of a standard detector could be increased with additional detectors of the MATHUSLA [322, 323] or FASER [324] type.

23 Long lived neutral scalars: Due to mixing with the Higgs boson, the electrically neutral scalars in gauged $U(1)_{B-L}$ [325] or the neutral scalar from $SU(2)_R$ [326] can decay via the SM Yukawa couplings into the SM fermions. For masses in the GeV range, the result-

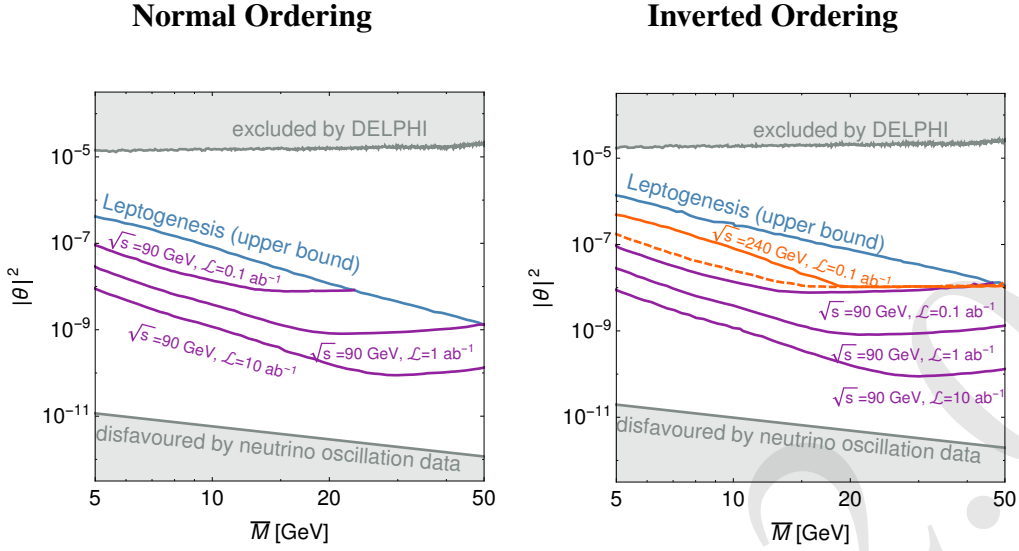


Figure 2.34: CEPC’s capacity to test models of leptogenesis. The parameter space for a minimal Type I Seesaw model with $n_s = 2$ is shown; the two sterile neutrino masses, M_1 and M_2 , are combined to form $\bar{M} = (M_1 + M_2)/2$ (with $|M_2 - M_1|/(M_2 + M_1) < 0.1$), and θ represents the active-sterile mixing angle. Models in the parameter space below the blue line are consistent with the observed baryon asymmetry of the universe through leptogenesis. Models above the orange lines are tested by CEPC at $\sqrt{s} = 240$ GeV, which is expected to observe at least four displaced vertex events. Models above the purple lines are probed by CEPC at the Z pole. The gray areas are ruled out by the DELPHI experiment [327, 328] (top) and current neutrino oscillation data (bottom). The figure is based on Ref. [260]. Note that for $n_s = 3$ heavy neutrinos, the “leptogenesis” upper bound is expected to be much higher [329] and practically identical to the DELPHI constraint, so that CEPC at 240 GeV can enter the cosmologically interesting parameter region for both hierarchies.

ing proper lifetimes can easily be $\mathcal{O}(1 \text{ cm})$, such that their decays give rise to displaced secondary vertices.

Multiple displaced vertices: Pair production of N in exotic Higgs boson decays may lead to two displaced vertices, each containing a lepton and two jets at parton level, as pointed out in the context of LRSM [282, 283] and models with $B - L$ symmetry [298, 299]. Rare exotic decays of the SM-like Higgs boson to a pair of triplets with subsequent decay to 4 N s leads to up to four displaced vertices with rather soft final states, for which the CEPC is likely to be much better suited than the LHC.

Similarly, the associated production of the scalar triplet at $e^+e^- \rightarrow Z^* \rightarrow Z\Delta_R^0$ leads to two displaced vertices when $\Delta_R^0 \rightarrow NN$, while Z decay gives additional prompt leptons/jets or missing energy.

Extra gauge bosons

Extended theoretical frameworks generally predict more and stronger signals from heavy neutrinos. In particular the gauged $B - L$ symmetry, which contains an extra Z' gauge boson, may give rise to a modified rate for the processes $e^+e^- \rightarrow \ell^+\ell^-$ at lepton colliders [330–332].

The Left-Right symmetric model contains the parity-symmetric W_R and Z_{LR} charged and neutral gauge bosons. The charged bosons are strongly constrained by B and K meson mixing and CP -odd observables, (see e.g. [333]), as well as the neutron electric

1 dipole moment constraints [334], with current bounds in the 3 TeV range. The neutral
 2 gauge boson Z_{LR} is typically heavier in minimal LR models.

3 In many instances, the LHC searches are catching up with flavor limits. In particular the
 4 ‘golden channel’ $pp \rightarrow W_R \rightarrow \ell N$ [335] features a dynamic parameter space [336] that
 5 ranges from prompt N production to merged neutrino jets [337–339], displaced vertices
 6 [340, 341] and a single prompt lepton with missing energy, where current bounds range up
 7 to 5 TeV, see [341] for the complete coverage of parameter space of W_R and N masses.

8 Additional gauge bosons can give rise to additional production mechanisms for N_i that
 9 are not suppressed by small Yukawa couplings, but possibly by the large gauge boson
 10 masses or their small couplings to the SM, see e.g. [298].

11 Leptogenesis

12 *Leptogenesis* refers to the idea that a matter-antimatter asymmetry is initially generated in
 13 the lepton sector [342] and then transferred into a baryon asymmetry via sphaleron pro-
 14 cesses [343]. Leptogenesis provides an explanation for the observed *baryon asymmetry of*
 15 *the universe* (BAU), i.e., the tiny excess $\eta_B \sim 10^{-10}$ [131] of matter over antimatter in the
 16 early universe over that formed the origin of the baryonic matter in the universe after mu-
 17 tual annihilation of all other particles and antiparticles, see e.g. [344]. Thus leptogenesis
 18 connects one of the deepest mysteries in cosmology to the properties of neutrinos.

19 **Motivation.** Global fits to present neutrino oscillation data prefer charge-parity (CP) vi-
 20 olation in the leptonic sector at the 2 to 2.5σ level, see [217, 218]. This CP violation in
 21 the leptonic sector may be related [345] to the observed BAU.

22 When the scale of new physics Λ is above the collision energies at CEPC, it is impos-
 23 sible to discover the new particles responsible for the generation of the BAU via direct
 24 production. However, observing a combination of LNV and cLFV signatures at scales
 25 accessible to CEPC could still rule out such “high scale leptogenesis” scenarios because
 26 particles with LNV interactions near the electroweak scale could wash out baryon asym-
 27 metries that were produced at high scales [346, 347].

28 If, in contrast, Λ is within reach of CEPC, one can directly probe the mechanism of
 29 leptogenesis by studying the properties of the new particles [348]. One of the best studied
 30 scenarios that accommodates leptogenesis is based on the low-scale Type I Seesaw model.
 31 The Yukawa couplings Y_{ai} that couple the right-handed neutrinos N_i to the Higgs boson
 32 and the left-handed neutrinos ν_{La} in general are complex and are a potential source of
 33 CP violation. Hence, the N_i may be the common origin on neutrino masses and baryonic
 34 matter in the universe.

35 If the mass range M_i is around or below the collider-accessible TeV scale, leptogenesis
 36 can proceed in two different ways. For M_i above the electroweak scale, the BAU can be
 37 generated during the freeze-out and decay of the N_i [349] (“freeze-out scenario”). For
 38 masses below the electroweak scale the BAU can be generated in CP -violating oscilla-
 39 tions [249, 350] and Higgs decays [351] during the N_i production (“freeze-in scenario”).
 40 The latter effectively also describes leptogenesis in the *Neutrino Minimal Standard Model*
 41 (ν MSM) [248, 249], a complete model where a third heavy neutrino composes the Dark
 42 Matter [80, 81] and does not contribute significantly to neutrino mass generation and lep-
 43 togenesis due to strong observational constraints [352]. Due to its minimality, part of the
 44 relevant parameter space of this model is in principle fully testable at colliders [353, 354],
 45 and significant fractions of the parameter space can be probed with CEPC [260]. For M_i

below the electroweak scale, this analysis could be done with an accuracy on the percent level at the Z pole with 10 ab^{-1} [260].

Lepton-number violation. Lepton number violation is a crucial ingredient of any leptogenesis scenario. Typical signatures at CEPC may involve same sign dilepton final states, either in prompt or displaced decays. An observation of such processes in all three SM flavors or a combination of LNV in some channel and different cLFV signatures could potentially falsify high scale leptogenesis scenarios [346, 347].

Many low scale models rely on an approximate lepton-number conservation to explain the smallness of the neutrino masses in the regime of coupling constants that is accessible to CEPC [240–242], which parametrically suppresses the rate of LNV processes in prompt decays. For particles with quasi-degenerate masses and comparable lifetimes, as they e.g. appear in resonant leptogenesis scenarios of the ν MSM, it has been proposed that this suppression may be overcome by the long time that they have to undergo coherent oscillations within the detector [258, 259, 355]. Since the amount of lepton number violation is proportional to the mass splitting, indirect measurements may be possible from a comparison of the rates for lepton number violating and conserving processes [258, 355] or by observing heavy neutrino-antineutrino oscillations in the detector [259] in displaced vertex searches at CEPC [260]. The reach of such searches at CEPC in the minimal seesaw model is shown in Figure 2.34, see also Figure 2.33.

Lepton-flavor violation. Measurements of cLFV are crucial to test high scale leptogenesis models at CEPC, because an efficient washout of the asymmetries in all flavors at temperatures above the electroweak scale is crucial to rule out such scenarios as the origin of the BAU [347].

Low scale leptogenesis scenarios typically rely on flavor effects and therefore tend to make predictions for the rates of cLFV. In the minimal Type I Seesaw with $n_s = 2$ (or the ν MSM), leptogenesis significantly restricts the flavor mixing pattern of heavy neutrinos N_i with experimentally accessible mixing angles [354]. The accuracy on the percent level at which the flavor mixing pattern can be probed in displaced vertex searches with 10 ab^{-1} at the Z pole are sufficient to probe large fractions of the parameter region for which heavy neutrinos can be discovered.

Displaced decays from long lived heavy neutrinos. For heavy neutrino masses below the electroweak scale, where leptogenesis proceeds in the "freeze in" manner, the N_i couplings should be comparably small to avoid a complete washout of the BAU in the early universe ($|\theta_{ai}|^2 < 10^{-8} \times (10 \text{ GeV}/M_i)$ [356], where larger values can be allowed due to strong hierarchies in their couplings to individual SM flavors [329]). Hence, most of the parameter space of active-sterile neutrino mixing and masses that is compatible with low scale leptogenesis in this scenario gives rise to long lifetimes of the heavy neutrino mass eigenstates, which can be found with high sensitivity via displaced vertex searches at CEPC. The reach of such searches at CEPC is compared to the parameter region where leptogenesis is feasible in the minimal seesaw model in Figure 2.34.

2.3.5 Extended Higgs sector

In many extensions of the Standard Model, the Higgs boson is embedded in a larger Higgs sector. Searching for new Higgs bosons is an important experimental target with a

high priority. One of the most straightforward and well-motivated extensions is the two-Higgs-doublet model (2HDM) [357], in which there are five massive spin-zero states in the spectrum (h, H^0, A^0, H^\pm) after electroweak symmetry breaking. Extensive searches for BSM Higgs bosons have been carried out, especially at the LHC [22, 358–368]. Null results in searches to date imply that either the non-SM Higgs bosons are much heavier and essentially decoupled from the SM, or the lightest CP -even Higgs boson mimics the SM Higgs boson by accident or symmetry while non-SM Higgs bosons are light as well [369–371]. In either case, it would be challenging to observe those states directly in experiments.

Complementary to the direct searches, precision measurements of the SM parameters and Higgs properties could also provide useful probes of new physics. High-precision measurements at future Higgs factories with about 10^6 Higgs bosons, and Z -pole measurements with $10^{10} - 10^{12}$ Z bosons [142, 372–375] would invariably shed light on new physics associated with the electroweak sector such as an extended Higgs sector. There is an extensive literature on the effects of the heavy Higgs states on the SM Higgs couplings, e.g. [20, 357, 376–384]. Identifying the light CP -even Higgs boson h to be the experimentally observed 125 GeV Higgs boson, the couplings of h to the SM fermions and gauge bosons receive two contributions: tree-level values, which are controlled by the mixing angles α of the two CP -even Higgs bosons and $\tan\beta$, ratios of the vacuum expectation values of two Higgs doublets, $\tan\beta = v_1/v_2$, and loop corrections from heavy Higgs bosons running in the loop. Of particular interest is the "alignment limit" with $\cos(\beta - \alpha) = 0$, in which the light CP -even Higgs couplings are identical to the SM ones at the tree-level, regardless of the other scalars' masses. Loop corrections, however, could lead to deviations of the couplings of h to the other SM particles, even in the alignment limit.

We first consider tree-level corrections. The allowed region at 95% CL in the $\cos(\beta - \alpha)$ vs. $\tan\beta$ plane for various types of 2HDM (depending on how the two Higgs doublets are coupled to the quarks and leptons) are shown in Figure 2.35 including only tree-level effects. This is obtained via a global fit to the Higgs rate measurements at the LHC as well as CEPC, assuming that no deviation to the SM values is observed at future measurements. From the figure, one can see that $\cos(\beta - \alpha)$ in all four types is tightly constrained at both small and large values of $\tan\beta$, except for Type-I, in which constraints are relaxed at large $\tan\beta$ due to suppressed Yukawa couplings.

To fully explore the Higgs factory potential, both the tree-level deviation and loop corrections to the SM Higgs couplings need to be taken into account. Figure 2.36 shows the global fit results to all CEPC Higgs rate measurements in the Type-II 2HDM parameter space, including both tree level and loop corrections. Degenerate heavy Higgs masses $m_A = m_H = m_{H^\pm} = m_\Phi$ are assumed so that the Z -pole precision constraints are automatically satisfied. The left panel is in the $\cos(\beta - \alpha)$ vs. $\tan\beta$ plane with regions enclosed by curves allowed if no deviation from the SM prediction is observed. Black, red, blue, and green curves are for $\sqrt{\lambda v^2} = \sqrt{m_\Phi^2 - m_{12}^2}/s_\beta c_\beta = 0, 100, 200$, and 300 GeV, respectively. The global fit result with tree-level only corrections is shown by dashed black lines for comparison. In all scenarios, $|\cos(\beta - \alpha)|$ is typically constrained to be less than about 0.008 for $\tan\beta \sim 1$. For smaller or larger values of $\tan\beta$, the allowed range of $\cos(\beta - \alpha)$ is significantly reduced. Loop effects from the heavy Higgs bosons tilt the allowed $\cos(\beta - \alpha)$ towards negative values, especially when $\tan\beta$ is large.

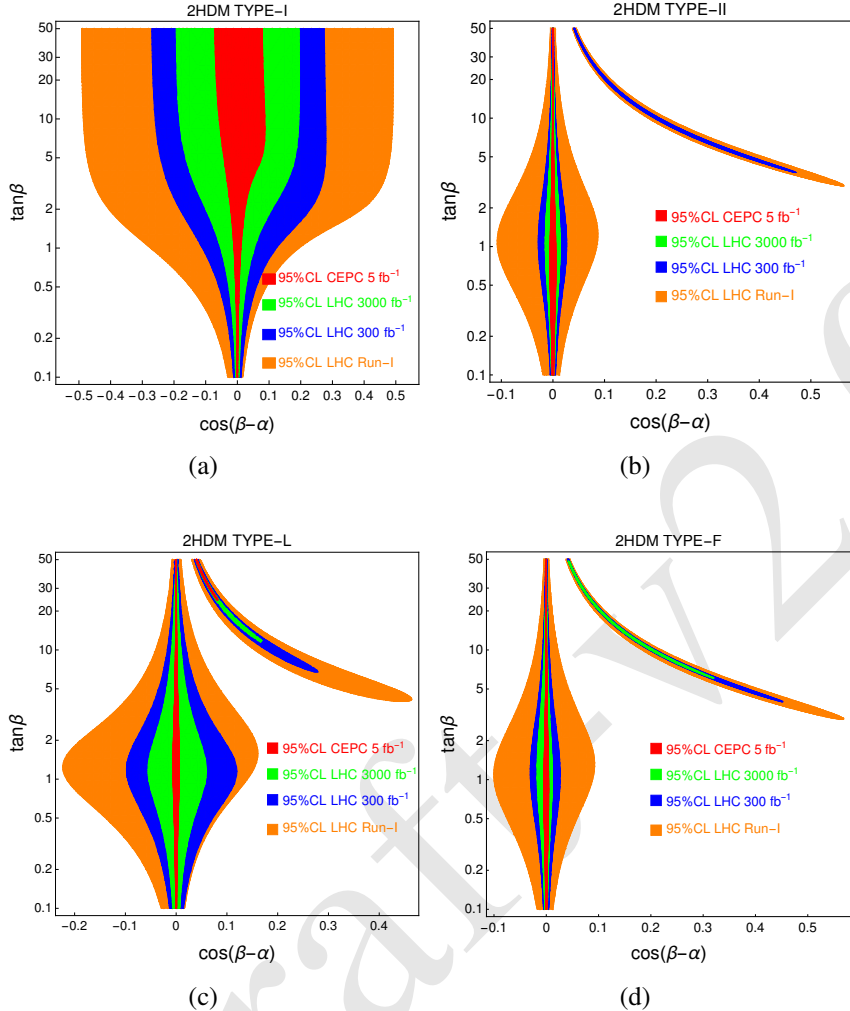


Figure 2.35: This figure shows the CEPC’s capacity to test for new physics in the Higgs sector and its dramatic improvement over existing and projected limits from the LHC. Shaded regions show the viable parameter space assuming that the future measurements agree with SM predictions. The panels show the four types of two-Higgs-doublet models (2HDM). The special “arm” regions for the Type-II, L, and F 2HDMs are the wrong-sign Yukawa regions. Plots are taken from Ref. [20].

- 1 The Figure 2.36(b) shows the allowed region at 95% CL in the m_Φ vs. $\tan \beta$ plane,
 2 with $\cos(\beta - \alpha) = -0.005$ (green), 0 (blue), and 0.005 (red). In the alignment limit with
 3 $\cos(\beta - \alpha) = 0$, the mass of the heavy Higgs bosons $m_\Phi > 500$ GeV is still allowed when
 4 $\tan \beta \lesssim 10$. Once deviating away from the alignment limit, the constraints on the heavy
 5 Higgs mass get tighter. The reach in the heavy Higgs mass and couplings at future Higgs
 6 factories can be complementary to the direct search limits at the LHC [22, 358–368],
 7 especially at intermediate values of $\tan \beta$.
- 8 Going beyond the degenerate mass case, both the Higgs and Z -pole precision mea-
 9 surements are sensitive to the mass splitting between the charged and neutral Higgses,
 10 as well as the splitting between the neutral ones. Figure 2.37 shows the allowed region
 11 of $\Delta m_A = m_A - m_H$ and $\Delta m_C = m_{H^\pm} - m_H$ at 95% CL, for different choices of
 12 $\cos(\beta - \alpha)$. The Higgs and Z -pole precision constraints are presented separately in the left
 13 panel while the combined constraints are shown in the right panel, with $m_H = 600$ GeV

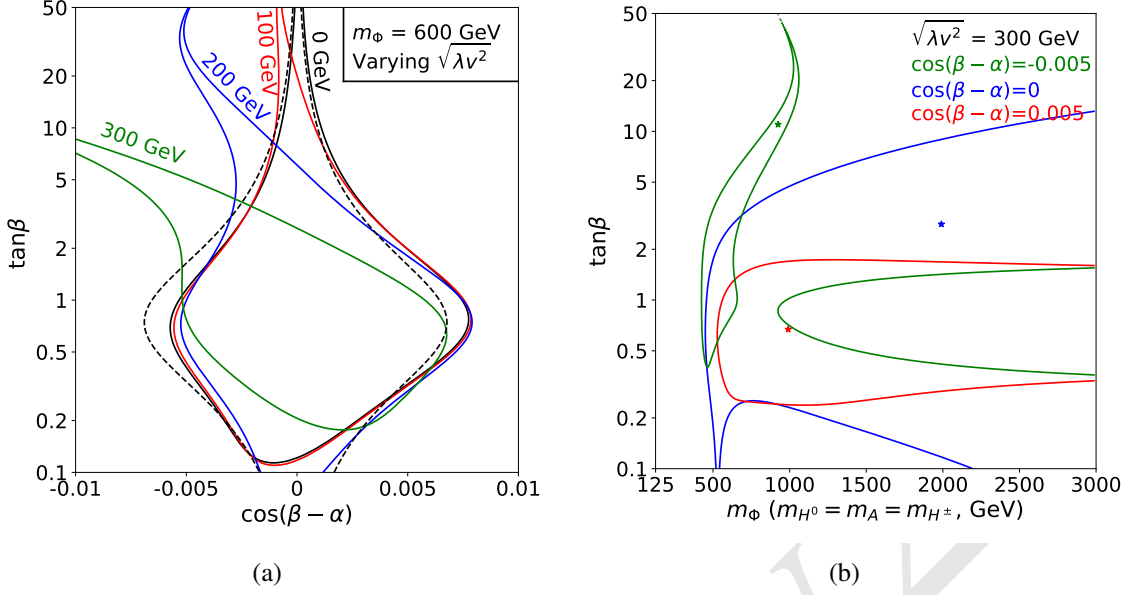


Figure 2.36: The constraining power of the CEPC precision measurements are illustrated here using the Type-II 2HDM parameter space. Assuming that no deviation from SM predictions are observed, the allowed regions of parameter space (at 95% CL) are enclosed by the curves with the same style. These curves are calculated by a fit including both the tree-level and the loop correction to the SM Higgs couplings. The (a) is in the $\cos(\beta - \alpha)$ vs. $\tan\beta$ plane, with $m_A = m_H = m_{H^\pm} = m_\Phi = 600$ GeV. The parameter $\sqrt{\lambda v^2}$ is set to be 0 (black solid), 100 (red solid), 200 (blue solid), and 300 GeV (green solid). The global fit result with tree-level only correction is represented by the dashed black lines for comparison. The (b) is in the m_Φ vs. $\tan\beta$ plane with $\sqrt{\lambda v^2} = 300$ GeV. The values of $\cos(\beta - \alpha)$ are chosen to be -0.005 (green), 0 (blue), and 0.005 (red). The stars represent the corresponding best fit points. These plots are taken from Ref. [384].

and $\sqrt{\lambda v^2} = 300$ GeV. For the Higgs precision fit, in the alignment limit, Δm_A and Δm_C are bounded to be around 0 within a few hundred GeV. Δm_A is constrained to be positive when $\cos(\beta - \alpha)$ takes a (small) positive value, and negative when $\cos(\beta - \alpha)$ is negative. The Z -pole precision measurements constrain either $\Delta m_C \sim 0$ or $\Delta m_C \sim \Delta m_A$, equivalent to $m_{H^\pm} \sim m_{H,A}$. In the small range of $\cos(\beta - \alpha)$ allowed by the current LHC Higgs precision measurements, the change of the Z -pole constraints due to different choices of $\cos(\beta - \alpha)$ is negligible. Combining both the Higgs and Z -pole precisions (right panel), the allowed $\Delta m_{A,C}$ is further constrained to be in a smaller region. From the plots, one can see that Z -pole measurements and Higgs measurements are complementary in constraining the heavy Higgs mass splittings.

2.4 QCD precision measurement

As a fundamental force in nature, the strong force is primarily responsible for the generation of the proton's mass. The discovery in the 1970's of Quantum Chromodynamics (QCD) as a correct theory for describing the strong force marks a great achievement in the history of physics. Despite forty years of intense study and much progress, QCD remains the least understood quantum field theory of nature, particularly in its non-perturbative domain. Even at high energy where the strong force becomes weak due to the property of asymptotic freedom, it is still challenging to obtain a quantitative descrip-

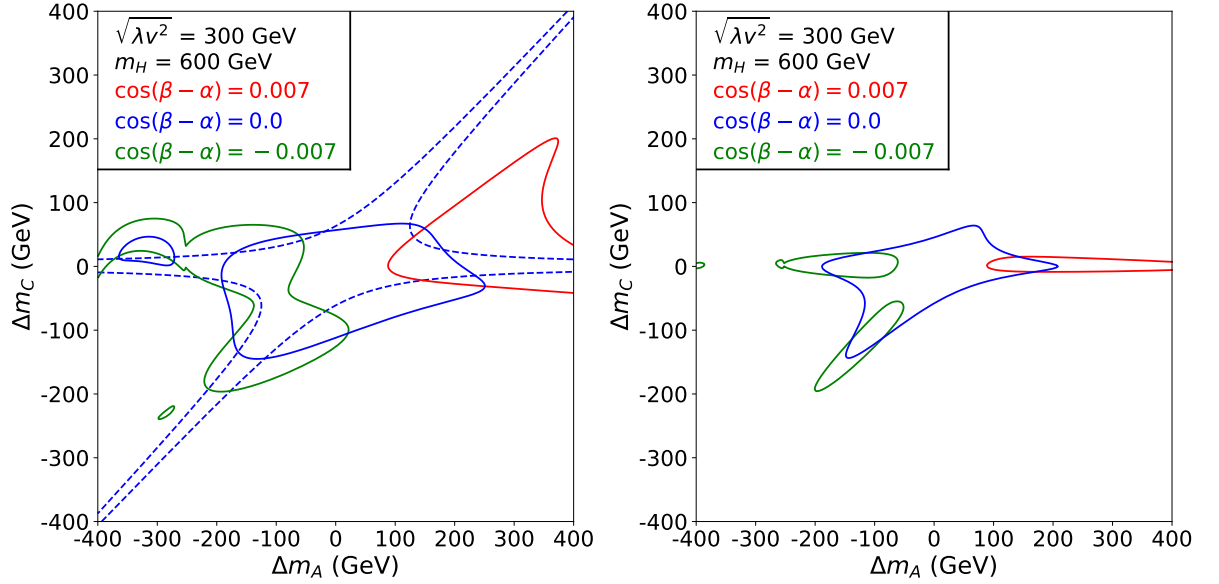


Figure 2.37: Allowed regions of $\Delta m_A = m_A - m_H$ and $\Delta m_C = m_{H^\pm} - m_H$ at 95% CL, for different choices of $\cos(\beta - \alpha)$. Left: Higgs precision constraints for $\cos(\beta - \alpha) = 0.007$ (solid red), 0 (solid blue), and -0.007 (solid green) and Z -pole constraints (dashed blue). Note that the Z -pole constraints are the same for $\cos(\beta - \alpha) = 0.007$, 0, and -0.007 . Right: constraints from combining both the Higgs and Z pole measurements for $\cos(\beta - \alpha) = 0.007$ (solid red), 0 (solid blue), and -0.007 (solid green). Plots are taken from Ref. [385].

tion of QCD phenomena. For example, the "fine structure constant" of QCD, α_s , is eight orders of magnitude less constrained than the fine structure constant of Quantum Electrodynamics (QED). In this respect, QCD is currently the least constrained fundamental force of nature, including gravity. Improving the precision in our understanding of QCD directly impacts our understanding of nature, ranging from the production and decay of the Higgs boson, the partonic structure of proton, and the stability of the Standard Model vacuum.

QCD can be studied at lepton, lepton-hadron, and hadron colliders. Traditionally hadron colliders, such as the Large Hadron Collider (LHC), have been described as QCD machines, because both the initial state and the final state at these colliders are intimately connected to QCD. However, the strongly-interacting nature of the initial state adds additional complications to the description of hard scattering, including the need for the detailed knowledge of Parton Distribution Functions (PDFs), as well as the removal/subtraction of the effects from multiple scattering or underlying events. These complications are absent at a lepton collider, making it an ideal environment for studying QCD at the highest precision. In the past lepton colliders have played an important role in the study of QCD, from the direct observation of gluon jets to the precise extraction of α_s . Compared with LEP, the largest e^+e^- collider ever built, CEPC has substantial improvement in statistics and systematics, therefore allowing QCD to be studied at unprecedented precision. The increase in collision energy will also allow for the exploration of QCD phenomena in territory previously unaccessible at a lepton collider. Besides those well-known problems from the LEP era, many new directions in QCD and jet physics have been opened since the LHC era due increasing attention to the study of jet structure, ei-

ther as a way to disentangle new physics from QCD backgrounds, or as a probe of QCD dynamics. CEPC will be an ideal machine to address many of these questions at high precision, due to the absence of complications from multiple scattering and underlying events.

Combined with the remarkable progress in QCD theory, ranging from new methods for efficient calculation of cross sections, to the development of effective field theory for collider processes, to new ideas for simulating scattering processes on the lattice, it is expected that CEPC will mark a new chapter in QCD research.

2.4.1 Precision α_s determination

The strong coupling constant α_s is perhaps the most important parameter in QCD. It enters the perturbative predictions of QCD in every observable, in particular cross sections for scattering processes involving hadronic final states at CEPC. A precision determination of α_s at CEPC with unprecedented experimental uncertainties will be an important contribution to the world's effort to determine α_s . At a lepton collider, α_s can be measured in a number ways. The represented ones include hadronic Z decay, hadronic τ decay, QCD jet rates, and QCD event shape measurements. A summary of α_s determination from these observables using LEP data can be found in Ref. [290].

A distinct feature of CEPC compared with previous lepton colliders is the increase in center-of-mass energy, Q . The measurements which can benefit from increased energy are event shape observables, for which non-perturbative corrections typically scale as $c\Lambda_{\text{QCD}}/Q$, where c is an $\mathcal{O}(1)$ parameter that can not be calculated from first principle with our current understanding of QCD. There exist two different approaches in the modeling of non-perturbative hadronization effects for event shapes. One approach is based on corrections for non-perturbative hadronization effects using QCD inspired Monte Carlo tools [386–390], and the other is based on analytic modeling of the non-perturbative shape function [391–395]. Neither of the two treatments can be regarded as fully satisfactory. In the Monte Carlo approach, there is mismatch in the parton level definition of a Monte Carlo simulation and the fixed order calculation. In the analytic power correction approach, the associated systematics have not been fully verified. Therefore, by going to higher center-of-mass energy, the impact of hadronization effects and their associated uncertainties can be reduced.

As an example of α_s determination from event shape observables using analytic power correction, we quote the recent determination based on the C parameter from Ref. [395],

$$\alpha_s(m_Z) = 0.1123 \pm 0.0002_{\text{exp}} \pm 0.0007_{\text{hadr}} \pm 0.0014_{\text{pert}}, \quad (2.28)$$

where hadronization effects and perturbative uncertainties are the main source of uncertainties contributing to α_s determination. While the perturbative uncertainties can be expected to be reduced further in the coming years, given the remarkable progress in the calculation of higher order corrections and in the resummation of large logarithms, the reduction of hadronization uncertainty will likely come from an increase of center-of-mass energy.

Currently, for thrust [392, 396], C parameter [394, 395], and heavy-jet-mass distribution [397], the best theoretical predictions are at the level of $N^3\text{LL}$ resummation matched to NNLO in fixed order perturbation theory. A notable recent development is the calculation of Energy-Energy Correlation (EEC) at NNLO. EEC is an event shape observable

which exhibits the so-called rapidity divergence, and leads to additional logarithms to be resummed, compared with thrust and other observables. Very recently, a determination of α_s using NNLL resummation matched to NNLO, and Monte Carlo for the modeling of power corrections, has been done, with the result [398] being

$$\alpha_s(m_Z) = 0.11750 \pm 0.00018_{\text{exp}} \pm 0.00102_{\text{hadr}} \pm 0.00257_{\text{ren}} \pm 0.00078_{\text{res}}, \quad (2.29)$$

where hadronization effects are important source of uncertainties. Since the analysis in Ref. [398] only uses data at or below the Z pole, it is expected that future data from CEPC at 250 GeV can significantly reduce the hadronization uncertainty. Additional scale and resummation uncertainties can also be reduced in the future by incorporating N^3LL resummation [399].

2.4.2 Jet rates at CEPC

Another distinct feature of CEPC compared with LEP is its unprecedented luminosity, in particular above the Z pole. The higher luminosity opens the door for the precision study of multi-jet production at an e^+e^- collider.

As an example, we show in Figure 2.38 the four-jet production cross sections at CEPC ($\sqrt{s} = 250$ GeV) with the Durham jet algorithm as a function of the resolution parameter y_{cut} , calculated using NLOjet++ [400]. The cross sections are at the level of a few pb to tens of pb for the range of y_{cut} considered. The colored bands represent the scale variations calculated by varying the renormalization scale from $\sqrt{s}/2$ to $2\sqrt{s}$. The NLO predictions show a smaller scale variation as compared to the LO ones. The cross sections diverge for small resolution parameter where further QCD resummations are needed to stabilize the theoretical predictions. The right panel shows the projected statistical uncertainties assuming an integrated luminosity of 1 and 5 ab^{-1} . The statistical uncertainties are at the level of one per mille or better for y_{cut} below 10^{-2} due to the large luminosity. The scale uncertainties of the NLO predictions are large in comparison and about 10%, which can be reduced with QCD resummation [400]. The n -jet rate has been employed to measure the strong coupling constant α_s at LEP [401]. The four-jet cross sections are proportional to α_s^2 at leading order, thus the statistical uncertainties in the measurement of α_s are estimated to be well below one per mille. On the other hand, the theoretical uncertainties will play a dominant role and need further investigation. Currently, NNLO predictions for e^+e^- to three jets are available [402–406]. Along this line there has been remarkable progress in the calculation of two-loop amplitudes with five external particles [407, 408] and its associated integrals [409, 410]. Although there is still substantial work to be done, an NNLO calculation for four jet production can be expected in the future. There has also been progress in resumming the large logarithms in jet rates. A Monte Carlo approach for resummation has been proposed and used to resum the large logarithms in two-jet rates in Ref. [411], which can achieve resummation at NNLL level. Ideally this approach can be extended to three and four jet rates.

2.4.3 Non-global logarithms

Besides the precision extraction of α_s from jetty final states, there has also be significant interest in understanding some novel aspects of QCD dynamics from jet processes at a lepton collider. An important example is the study of non-global logarithms (NGL) [412, 413].

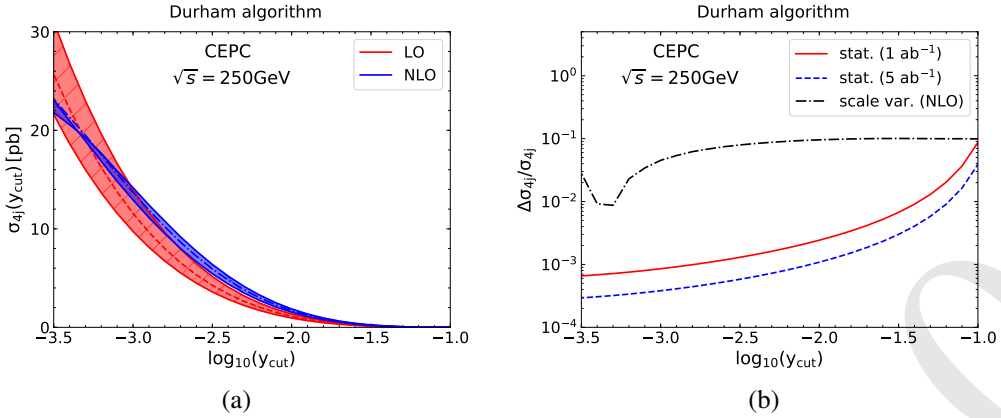


Figure 2.38: (a) The four-jet production cross section at CEPC ($\sqrt{s} = 250$ GeV) with the Durham jet algorithm as a function of the resolution parameter y_{cut} . (b) The scale variation and expected statistical uncertainties for the same cross sections normalized to their central values.

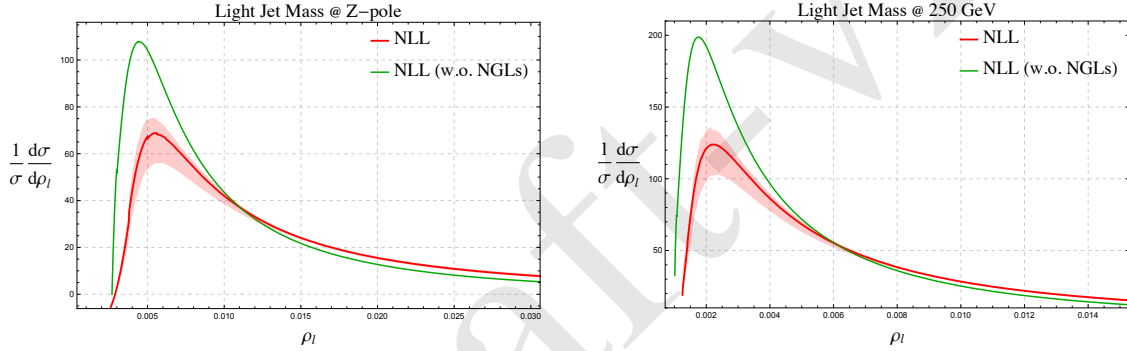


Figure 2.39: The normalized light-jet-mass distribution both at Z -pole (left) and at 250 GeV (right). Green curves are NLL results without NGLs, and red bands are full NLL results with scale uncertainties.

1 Non-global logarithms are significant obstacles in the study of soft physics at high energy
2 energy colliders (jet physics, energy flow measurements, hadronization, and so on). Therefore it is important to develop a theoretical framework to understand their structure. NGLs
3 were first pointed out by Dasgupta and Salam in Ref. [412], where they developed a Monte-Carlo algorithm to resum leading-logarithmic(LL) NGLs in the large N_c limit. After that work, based on the strong energy ordering limit, Banfi, Marchesini and Smye derived an integral-differential evolution equation that can also resum LL NGLs [413]. Since then, there has been a great effort to improve the theoretical predictions [414–419], including the sub-leading N_c effects [420–422] and some fixed-order calculations [423, 424].

10 Recently, there have been several developments in this field [425–433]. One example
11 is the effective field theory developed in Ref. [427]; this reference was the first to write
12 down the factorization formula for non-global observables and to give an any-order renormalization group evolution equation for NGLs.

14 As an electron-positron collider, CEPC will provide new opportunities, which can precisely
15 measure NGLs in many observables. Figure 2.39 shows the normalized light-jet-mass distribution
16 at Z -pole (left) and at 250 GeV (right). Green curves are NLL results without NGLs, and red bands are full NLL results with scale uncertainties. Ob-

$Z(l^+l^-)H(X)$	gg	$b\bar{b}$	$c\bar{c}$	$WW^*(4h)$	$ZZ^*(4h)$	$q\bar{q}$
BR [%]	8.6	57.7	2.9	9.5	1.3	~ 0.02
N_{event}	6140	41170	2070	6780	930	14

Table 2.3: This table shows branching ratios (BR) for decays of the SM Higgs boson in different hadronic channels [435] and the number of expected events (N_{event}) for ZH production at CEPC ($\sqrt{s} = 250$ GeV and $\mathcal{L} = 5 \text{ ab}^{-1}$) with the corresponding hadronic Higgs decay. In this table, H represents the Higgs boson, h represents any of the quarks except the top quark, and q are light quarks.

1 viously, after including NGLs theoretical predictions are reduced significantly, and this
2 reduction is especially magnificent at 250 GeV. Therefore CEPC will give us the first
3 opportunity to measure NGLs.

4 **2.4.4 QCD event shapes and light quark Yukawa coupling**

5 The SM Higgs boson decays dominantly to various hadronic final states with a total
6 branching fraction of more than 80%. These hadronic decays provide a new source for
7 QCD studies at CEPC (in its Higgs factory mode). In particular, Higgs decays produce a
8 unique color-neutral digluon state. Table 2.3 summarizes the estimated number of events
9 for different hadronic decay modes of the Higgs boson, assuming that the tagged Z boson
10 decays into electrons or muons.

11 At CEPC the traditional hadronic event shapes, e.g., thrust distribution, can be well
12 measured due to the high statistics. At a lepton collider one can reconstruct the kine-
13 matics fully and then boost all final states back to the rest frame of the decaying Higgs
14 boson. On the theory side those distributions can be calculated with high precision by
15 QCD resummation matched with fixed-order results. There exist uncertainties from non-
16 perturbative QCD effects, e.g. hadronization modeling, which are usually estimated by
17 Monte Carlo event generators. The Figure 2.40(a) shows the normalized distribution of
18 the variable thrust for several different hadronic decay channels of the Higgs boson, in-
19 cluding gg , $q\bar{q}$, $b\bar{b}$, and $W(q\bar{q})W^*(q\bar{q})$ [434]. The distribution peaks at $\tau \sim 0.02$ for the
20 light-quark decay channel. The peak shifts to $\tau \sim 0.05$ for the gluon channel, corre-
21 sponding to a scaling of roughly C_A/C_F . The distribution is much broader for the gluon
22 case due to the stronger QCD radiation. The distribution for the $b\bar{b}$ channel is very close
23 to the $q\bar{q}$ case, except at very small τ , where the mass and hadronization effects become
24 important. For the WW^* channel there already exist four quarks at leading order and the
25 distribution is concentrated in the large- τ region.

26 Different shapes of the thrust distribution from diquark and digluon final states mo-
27 tivates the idea of using global event shapes to probe the Yukawa couplings of light
28 quarks [434], namely strange, up and down quarks. The provided discrimination can
29 largely reduce background due to Higgs boson decays into two gluons while backgrounds
30 from Higgs boson decays into heavy quarks can be suppressed with the usual heavy-flavor
31 tagging algorithms. It is a great challenge to probe the light-quark Yukawa couplings since
32 they are very small and the expected number of events with CEPC's full luminosity is
33 only 14, as shown in Table 2.3. The expected exclusion limits on decay branching ratios
34 of Higgs boson to light quarks are shown in the right plot of Figure 2.40, indicated by
35 intersections with the vertical line and normalized to the branching ratio to digluon. The

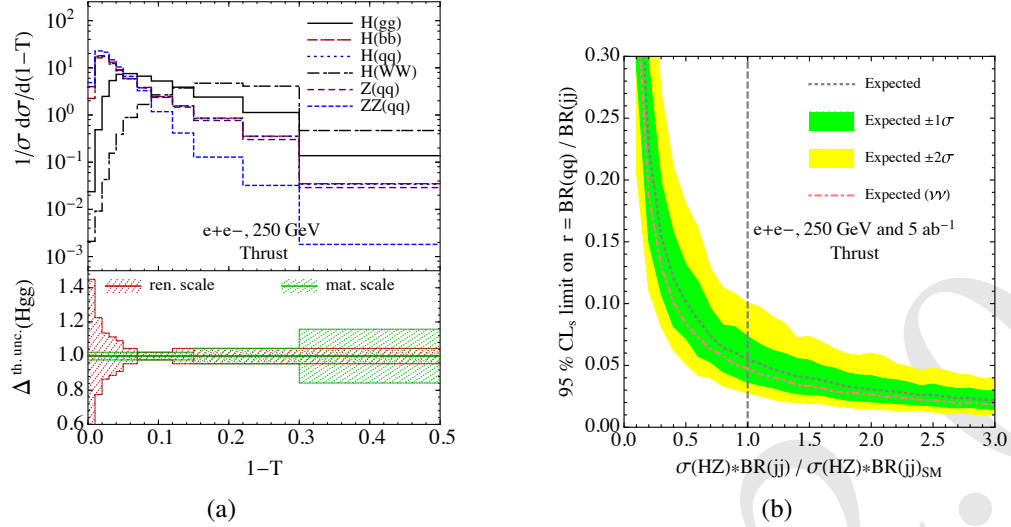


Figure 2.40: (a) The normalized distributions of thrust in hadronic Higgs decay, in $e^+e^- \rightarrow q\bar{q}$ with $\sqrt{s} = 125$ GeV and in $e^+e^- \rightarrow Zq\bar{q}$ with $\sqrt{s} = 250$ GeV. (b) CEPC’s capacity to probe the Higgs boson’s decay into light quarks. The green and yellow bands show the expected 95% CL exclusion limit on $r = BR(q\bar{q})/BR(jj)$ as a function of the total cross section of the Higgs boson decay to jj normalized to the SM value.

1 results can be translated into an upper limit of 0.48% on the decay branching ratios or 5
2 times of the Standard Model value for the Yukawa coupling of strange quark.

3 2.5 Flavor Physics with the Z factory of CEPC

4 A high luminosity Z factory that produces 10^{12} Z bosons provides unique opportunities
5 for various flavor measurements. In particular, the decay of 10^{12} Z bosons will result
6 in approximately 10^{11} b hadrons, which is almost two orders of magnitude larger than
7 the number of B mesons produced at the B factories BaBar and Belle and comparable
8 to the number of B mesons expected at Belle II. As the B factories are running mainly
9 on the $\Upsilon(4S)$ resonance, they mostly produce B^0 and B^\pm mesons; they also produce B_s
10 mesons but in much smaller numbers from shorter runs on $\Upsilon(5S)$. A machine running
11 on the Z -pole on the other hand will not only produce a large number of B_s mesons,
12 but also a large sample of b baryons. In Table 2.4 we compare the expected numbers of
13 produced b -hadrons corresponding to 10^{12} Z -boson decays to those produced with the
14 50 ab^{-1} run on $\Upsilon(4S)$ and the 5 ab^{-1} run on $\Upsilon(5S)$ of Belle II. For the tera- Z we also
15 list number of produced charmed hadrons and tau leptons (we use the known Z branching
16 fractions $BR(Z \rightarrow b\bar{b}) = (15.12 \pm 0.05)\%$, $BR(Z \rightarrow c\bar{c}) = (12.03 \pm 0.21)\%$, and
17 $BR(Z \rightarrow \tau^+\tau^-) = (3.3696 \pm 0.0083)\%$ [290] and the b and c hadronization fractions at
18 the Z pole from Refs. [436–438]). Using the large sample of produced b/c hadrons and
19 taus, the tera- Z factory of CEPC will be able to access many rare decays of these particles,
20 many with a precision beyond any of the ongoing or planned experiments. In addition,
21 the 10^{12} Z bosons would also allow measurements of flavor violating Z decays with an
22 unprecedented precision.

23 A future circular electron–positron collider does not only benefit from its large statistics.
24 Compared to LHCb, an electron–positron collider offers a much cleaner environment

Particle	@ Tera- Z	@ Belle II	
b hadrons			
B^+	6×10^{10}	3×10^{10}	(50 ab^{-1} on $\Upsilon(4S)$)
B^0	6×10^{10}	3×10^{10}	(50 ab^{-1} on $\Upsilon(4S)$)
B_s	2×10^{10}	3×10^8	(5 ab^{-1} on $\Upsilon(5S)$)
b baryons	1×10^{10}		
Λ_b	1×10^{10}		
c hadrons			
D^0	2×10^{11}		
D^+	6×10^{10}		
D_s^+	3×10^{10}		
Λ_c^+	2×10^{10}		
τ^+	3×10^{10}	5×10^{10}	(50 ab^{-1} on $\Upsilon(4S)$)

Table 2.4: Collection of expected number of particles produced at a tera- Z factory from 10^{12} Z -boson decays. We have used the hadronization fractions (neglecting p_T dependences) from Refs. [436, 437] (see also Ref. [438]). For the decays relevant to this study we also show the corresponding number of particles produced by the full 50 ab^{-1} on $\Upsilon(4S)$ and 5 ab^{-1} on $\Upsilon(5S)$ runs at Belle II.

and, therefore, generally smaller background levels. Compared to the Belle II flavor factory, running at the Z -pole leads to a much larger boost of the b hadrons and their decay products, which is in particular useful in constraining decays with missing energy, e.g., decays with neutrinos in the final state.

In section 2.5.1 we discuss the prospects of measuring a number of rare b -hadron decays at the tera- Z factory of CEPC: we cover leptonic decays, semi-leptonic decays, and decays with missing energy. Particular emphasis is laid on rare decays to final states with tau leptons, in which the sensitivity of the tera- Z program of CEPC will be unparalleled. We also comment on possible implications of the current hints for lepton-flavor-universality violation in rare B decays, that have been observed by LHCb. A discussion of tau decays follows in Section 2.5.2, where we discuss the prospects of CEPC to significantly improve lepton universality tests in leptonic tau decays as well as its prospects for measuring rare, lepton-flavor violating tau decays. Flavor violating Z decays are discussed in section 2.5.3.

2.5.1 Rare B decays

2.5.1.1 Leptonic decays $B^0 \rightarrow \ell^+ \ell^-$ and $B_s \rightarrow \ell^+ \ell^-$

The purely leptonic $B_s \rightarrow \ell^+ \ell^-$ and $B^0 \rightarrow \ell^+ \ell^-$ decays are strongly suppressed in the Standard Model and therefore highly sensitive to new-physics contributions. Their

branching ratios are known with high precision in the Standard Model [439]

$$\text{BR}(B_s \rightarrow e^+ e^-)_{\text{SM}} = (8.54 \pm 0.55) \times 10^{-14}, \quad (2.30)$$

$$\text{BR}(B^0 \rightarrow e^+ e^-)_{\text{SM}} = (2.48 \pm 0.21) \times 10^{-15}, \quad (2.31)$$

$$\text{BR}(B_s \rightarrow \mu^+ \mu^-)_{\text{SM}} = (3.65 \pm 0.23) \times 10^{-9}, \quad (2.32)$$

$$\text{BR}(B^0 \rightarrow \mu^+ \mu^-)_{\text{SM}} = (1.06 \pm 0.09) \times 10^{-10}, \quad (2.33)$$

$$\text{BR}(B_s \rightarrow \tau^+ \tau^-)_{\text{SM}} = (7.73 \pm 0.49) \times 10^{-7}, \quad (2.34)$$

$$\text{BR}(B^0 \rightarrow \tau^+ \tau^-)_{\text{SM}} = (2.22 \pm 0.19) \times 10^{-8}. \quad (2.35)$$

- ¹ Presently, LHCb has provided the most sensitive measurement of the $\mu^+ \mu^-$ decays with
- ² a precision at the level of 10^{-9} [440]. The current most stringent bound on the $e^+ e^-$
- ³ modes is still coming from CDF [441]. With 50 fb^{-1} of data, LHCb is expected to reach
- ⁴ sensitivities of approximately 10^{-10} in the muonic modes and $\text{few} \times 10^{-10}$ in the electronic
- ⁵ modes [442].

To estimate the sensitivity of a tera- Z factory for the decays to electrons and muons we rescale the existing bound from the L3 collaboration [443] from the full LEP-I data sample, which corresponds to approximately 3×10^5 , and $9 \times 10^4 B^0$'s, and B_s 's, respectively. A naive rescaling of these bounds accounting for the number of B^0 's and B_s 's produced at a tera- Z factory gives:

$$\text{BR}(B_s \rightarrow e^+ e^-)_{\text{tera-}Z} \lesssim 4 \times 10^{-10}, \quad (2.36)$$

$$\text{BR}(B^0 \rightarrow e^+ e^-)_{\text{tera-}Z} \lesssim 8 \times 10^{-11}, \quad (2.37)$$

$$\text{BR}(B_s \rightarrow \mu^+ \mu^-)_{\text{tera-}Z} \lesssim 3 \times 10^{-10}, \quad (2.38)$$

$$\text{BR}(B^0 \rightarrow \mu^+ \mu^-)_{\text{tera-}Z} \lesssim 7 \times 10^{-11}. \quad (2.39)$$

- ⁶ Note, that this linear scaling with the number of B mesons assumes that backgrounds
- ⁷ can be kept under control also at the CEPC. The comparison with the projections from
- ⁸ LHCb [442] shows that LHCb with 50 fb^{-1} will likely outperform the tera- Z factory by a
- ⁹ factor of few for the muonic modes. For the electronic modes the tera- Z factory may be
- ¹⁰ able to compete with LHCb.

The rare B decays to the $\tau^+ \tau^-$ final state are experimentally still a largely uncharted territory. The existing bound from BaBar [444], $\text{BR}(B^0 \rightarrow \tau^+ \tau^-) < 4.1 \times 10^{-3}$, is orders of magnitude away from the corresponding SM prediction. Measurements of the $\tau^+ \tau^-$ final states are highly challenging at LHCb. The current sensitivities are at the level of $\text{few} \times 10^{-3}$ [445] and could improve down to $\text{few} \times 10^{-4}$ [442]. Also Belle II will likely only reach sensitivities at the level of 10^{-4} for $B^0 \rightarrow \tau^+ \tau^-$ [446]. The decays $B^0 \rightarrow \tau^+ \tau^-$ and $B_s \rightarrow \tau^+ \tau^-$ are thus prime examples of processes to which a circular electron–positron collider running at the Z pole is uniquely sensitive. As no dedicated study exists at them moment for the sensitivity of tera- Z factory to these decays, we estimate it by comparing Belle II's relative sensitivity between the $B^0 \rightarrow \mu^+ \mu^-$ and the $B^0 \rightarrow \tau^+ \tau^-$ modes. The corresponding rough estimates read

$$\text{BR}(B^0 \rightarrow \tau^+ \tau^-)_{\text{tera-}Z} < 4 \times 10^{-6}, \quad (2.40)$$

$$\text{BR}(B_s \rightarrow \tau^+ \tau^-)_{\text{tera-}Z} < 2 \times 10^{-5}. \quad (2.41)$$

- ¹¹ These estimates do not account for the higher boost of the decay products in a Z factory.
- ¹² We thus expected them to be conservative, i.e., CEPC's sensitivity may be even higher. We

thus find that CEPC's tera- Z factory will provide the by far most stringent measurements of the $B_s \rightarrow \tau^+ \tau^-$ and $B^0 \rightarrow \tau^+ \tau^-$ decays, improving the expected sensitivities at LHCb and Belle II by more than an order of magnitude.

2.5.1.2 Semileptonic decays $b \rightarrow s(d)\ell^+\ell^-$

Semileptonic FCNC decays of b -mesons are not as theoretically clean as the $B_{s,d} \rightarrow \ell^+\ell^-$ decays. They are, however, *i*) less rare within the SM, which makes them experimentally more accessible, and *ii*) three-body or four-body decays resulting in multiple observables for a given mode, e.g., invariant-mass and angular distribution observables, CP asymmetries, etc.

In recent years, the exclusive decays $B \rightarrow K^{(*)}e^+e^-$ and $B \rightarrow K^{(*)}\mu^+\mu^-$ have attracted a lot of attention due to the large number of LHCb measurements and in particular due to some persistent $\approx 2 - 3\sigma$ tensions between data and SM expectations in related observables, i.e., $R_{K^{(*)}}$ [447, 448] theoretically clean observables that tests for lepton-flavor-universality violation, and the angular observable P'_5 [449]. The tensions are present in LHCb's Run-1 data set of 3 fb^{-1} , with Run-2 results yet to be announced. We expect significant progress as LHCb collects a data set of 50 fb^{-1} . Belle II will also probe these exclusive modes. Its 50 ab^{-1} run on $\Upsilon(4S)$ will provide measurements of these modes with a precision not much lower than LHCb with its full data set [446]. As the number of B^0 and B^+ mesons produced at the tera- Z factory and at Belle II are approximately the same, we ultimately expect a similar precision at the two machines. In this respect, the CEPC's measurements of these modes will be invaluable, especially if the tensions in the exclusive $B \rightarrow K^{(*)}e^+e^-$ and $B \rightarrow K^{(*)}\mu^+\mu^-$ persist in the full data set of LHCb. In such a case, the CEPC's program will provide a new data set and will be able to independently confirm the existence of new-physics effects in the electronic and muonic decays.

Both Belle II and CEPC will also be able to access the inclusive decays $B \rightarrow X_s e^+e^-$ and $B \rightarrow X_s \mu^+\mu^-$ with comparable precision. Hadronic uncertainties are under better control in the inclusive modes and their measurements will complement the studies of the exclusive decays mentioned above.

Contrary to the ee and $\mu\mu$ modes, little experimental information exists on the semi-tauonic modes $b \rightarrow s(d)\tau^+\tau^-$ so far. The only existing bound from BaBar [450], $\text{BR}(B \rightarrow K\tau^+\tau^-) < 3.3 \times 10^{-3}$, is approximately four orders of magnitude above the SM prediction and it is not clear whether LHCb will be able to improve the sensitivity substantially. The first major improvements are thus expected at Belle II. For instance, its 50 ab^{-1} run will probe the branching ratio of $B^+ \rightarrow K^+\tau^+\tau^-$ at the level of 2×10^{-5} [446]. A dedicated study is required to quantitatively assess the full potential of the tera- Z factory, which is expected to outperform Belle II in modes as the ones in question, in which missing energy from the tau decays is present in the event. A study for the FCC- ee program that investigates the $B^0 \rightarrow K^*\tau^+\tau^-$ decay [451], finds that approximately a thousand cleanly reconstructed events are expected from $10^{13} Z$'s. We thus expect approximately hundred events at the tera- Z factory probing the SM branching ratio of $\sim 10^{-7}$ with a statistical uncertainty of 10%. We see that, similarly to the $B_q \rightarrow \tau^-\tau^+$ mode, also here the tera- Z factory will provide the by far most accurate measurements. With hundred events even a partial angular analysis might be possible. Additionally, the large number of B_s mesons and Λ_b baryons produced at the tera- Z factory will facilitate the first measurements of the corresponding decays, $B_s \rightarrow \phi\tau^+\tau^-$, and $\Lambda_b \rightarrow \Lambda\tau^+\tau^-$ at a similar

level of precision. The measurements of the semi-tauonic decay will also open the path towards measurements of lepton-flavor-universality violation involving not only electrons and muons, but also taus, which will be of particular interest if the present tensions in the muon–electron data persist.

2.5.1.3 Decays with missing energy $b \rightarrow s(d)\nu\bar{\nu}$

The rare FCNC decays $B \rightarrow K^{(*)}\nu\bar{\nu}$ are widely recognized as important flavor probes, as they are not affected by non-factorizable corrections and thus theoretically cleaner compared to $b \rightarrow s\ell\ell$ transitions. The SM predictions for the branching ratios of these decays read [452]

$$\text{BR}(B^+ \rightarrow K^+\nu\bar{\nu})_{\text{SM}} = (4.68 \pm 0.64) \times 10^{-6}, \quad (2.42)$$

$$\text{BR}(B^0 \rightarrow K^0\nu\bar{\nu})_{\text{SM}} = (2.17 \pm 0.30) \times 10^{-6}, \quad (2.43)$$

$$\text{BR}(B^+ \rightarrow K^{*+}\nu\bar{\nu})_{\text{SM}} = (10.22 \pm 1.19) \times 10^{-6}, \quad (2.44)$$

$$\text{BR}(B^0 \rightarrow K^{*0}\nu\bar{\nu})_{\text{SM}} = (9.48 \pm 1.10) \times 10^{-6}, \quad (2.45)$$

with uncertainties in the theoretical predictions of roughly 10%, dominated by parametric and form-factor uncertainties. The accuracy of these predictions in combination with the fact that these modes have not yet been observed (current bounds are typically an order magnitude away from the SM predictions, e.g., see Ref. [453]), is the reason why these modes are prime candidates for disentangling small new-physics contributions. Since the neutrinos are never tagged in the experiments, such modes are not only relevant for searches for heavy new physics, but can also provide the leading constraints in models with light, long-lived particles with small flavor-violating couplings, e.g., the “axi-flavon” [454].

With its full, 50 ab^{-1} dataset run on $\Upsilon(4S)$, Belle II is expected to probe for the first time deviations from the SM predictions at a level of approximately 17% [455]. The dominant uncertainties in such measurements are expected to be due to statistics. The related decays based on the $b \rightarrow d\nu\bar{\nu}$ transition, i.e., $B \rightarrow \pi\nu\bar{\nu}$ and $B \rightarrow \rho\nu\bar{\nu}$, are further suppressed in the SM by a factor of approximately 30. Limits at a level of 10^{-6} are expected at Belle II.

Given that the number of B^0 and B^+ particles produced with 50 ab^{-1} at Belle II are roughly the same at a tera- Z factory, we expect similar statistical uncertainties there. Therefore, at the very least, the tera- Z factory will probe the SM predictions of $B \rightarrow K^{(*)}\nu\bar{\nu}$, $B \rightarrow \pi\nu\bar{\nu}$, and $B \rightarrow \rho\nu\bar{\nu}$ at the same level as Belle II. However, this estimate does not take into account the favourable kinematic environment of a tera- Z factory. The larger, with respect to Belle II, boost of the B mesons in a collider running on the Z pole persists on the neutrino system. This leads to a robuster measurement of missing energy, which is instrumental for the searches of these decays. While a dedicated study would be needed to quantitatively assess this advantage, it may well be the case that this will be enough to tilt the balance in favour of the tera- Z factory.

As illustrated in Table 2.4 the tera- Z factory will produce two orders of magnitude more $B_s^{(*)}$ mesons than a 5 ab^{-1} run of Belle II on $\Upsilon(5S)$. Also, approximately 10^{10} b baryons will be produced at the tera- Z factory, whereas none can be produced at Belle II without (not planned) dedicated runs. The tera- Z factory will thus for the first time have access to decay modes of B_s mesons and Λ_b baryons, like $B_s \rightarrow \phi\nu\bar{\nu}$ and $\Lambda_b \rightarrow \Lambda\nu\bar{\nu}$. Given the large statistical sample, we expect the tera- Z factory to probe these branchings fractions at

1 a level similar to the related B_0 and B^+ modes, i.e., branching fractions of approximately
 2 10^{-6} .

3 More than one higher-dimensional operator of the five-flavor effective theory can in-
 4 duce these decays. By probing multiple members of this whole family of decays, the
 5 measurements of the tera- Z -factory will probe more than a single linear combination of
 6 operators. For instance, the combination of the information from the pseudoscalar to pse-
 7udoscalar transitions ($B \rightarrow K\nu\bar{\nu}$), the pseudoscalar to vector transitions ($B \rightarrow K^*\nu\bar{\nu}$ and
 8 $B_s \rightarrow \phi\nu\bar{\nu}$), as well as the fermion to fermion transition ($\Lambda_b \rightarrow \Lambda\nu\bar{\nu}$) could be a way to
 9 disentangle possible new-physics contributions from right-handed currents.

10 2.5.1.4 Probing new physics with $b \rightarrow s(d)\tau^+\tau^-$ decays

11 There are many new-physics scenarios, e.g., models with extended Higgs sectors, or ex-
 12 tended gauge sectors, or scenarios with leptoquarks, that could give rise to sizable effects
 13 in leptonic or semi-leptonic $\tau^+\tau^-$ modes, without violating constraints from the e^+e^-
 14 and/or $\mu^+\mu^-$ channels. Model independently, tau specific new physics in rare B decays
 15 can be encoded in an effective Lagrangian

$$\mathcal{L}_{\text{NP}} = -\frac{G_F}{\sqrt{2}} V_{tb} V_{tq}^* \frac{e^2}{16\pi^2} \sum_i \left(C_i O_i + C'_i O'_i \right), \quad q = s, d, \quad (2.46)$$

with the operators

$$\begin{aligned} O_7 &= (\bar{q}\sigma_{\mu\nu}P_R b)F^{\mu\nu}, & O'_7 &= (\bar{q}\sigma_{\mu\nu}P_L b)F^{\mu\nu}, \\ O_9 &= (\bar{q}\gamma_\mu P_L b)(\bar{\tau}\gamma^\mu\tau), & O'_9 &= (\bar{q}\gamma_\mu P_R b)(\bar{\tau}\gamma^\mu\tau), \\ O_{10} &= (\bar{q}\gamma_\mu P_L b)(\bar{\tau}\gamma^\mu\gamma_5\tau), & O'_{10} &= (\bar{q}\gamma_\mu P_R b)(\bar{\tau}\gamma^\mu\gamma_5\tau), \\ O_S &= (\bar{q}P_R b)(\bar{\tau}P_L\tau), & O'_S &= (\bar{q}P_L b)(\bar{\tau}P_R\tau). \end{aligned}$$

16 Constraining all possible $\tau^+\tau^-$ operators requires measurements of both the leptonic and
 17 semi-leptonic modes, as they have different blind directions in the parameter space of
 18 Wilson coefficients [456, 457]. Note, that also the decays with neutrinos, $b \rightarrow q\nu\bar{\nu}$, can
 19 constrain the operator-combinations that contain a left-handed tau current $O_9 - O_{10}$ and
 20 $O'_9 - O'_{10}$, due to $SU(2)_L$ invariance. On the other hand, the neutrino modes are blind to
 21 the orthogonal directions $O_9 + O_{10}$ and $O'_9 + O'_{10}$, which contain right-handed tau currents.

22 There are various new-physics models that can lead to non-standard effects in $b \rightarrow$
 23 $(d, s)\tau^+\tau^-$ decays. Interestingly, several models that address the LHCb anomalies in the
 24 $B \rightarrow K^*\mu^+\mu^-$ angular distribution or the hints for lepton-flavor-universality violation in
 25 $R_{K^{(*)}}$ [447, 448] or $R_{D^{(*)}}$ [458] predict characteristic non-standard effects in $b \rightarrow s\tau^+\tau^-$
 26 transitions.

27 The model proposed in Ref. [459] is based on gauging the difference of muon- and
 28 tau-number, $L_\mu - L_\tau$. Given the current anomalies in $b \rightarrow s\mu^+\mu^-$, the model predicts that
 29 all semi-leptonic $b \rightarrow s\mu^+\mu^-$ decays are suppressed by approximately 25% [460]. The
 30 $L_\mu - L_\tau$ symmetry implies that all semi-leptonic $b \rightarrow s\tau^+\tau^-$ decays are instead enhanced
 31 by a similar amount. However, the $B_s \rightarrow \tau^+\tau^-$ decay remains SM-like in the $L_\mu - L_\tau$
 32 framework.

33 In the new-physics scenarios originally introduced in Refs. [461–463], the current B -
 34 physics anomalies are addressed by non-standard left-handed currents involving mainly
 35 the 3rd generation of quarks and leptons. In such scenarios, enhancements of $B_s \rightarrow \tau^+\tau^-$
 36 and $b \rightarrow s\tau^+\tau^-$ rates by an order of magnitude compared to the SM predictions are

possible. Left-handed currents also imply a strong correlation between $b \rightarrow s\tau^+\tau^-$ and $b \rightarrow s\nu\bar{\nu}$ decays, as well as enhanced $b \rightarrow s\nu\bar{\nu}$ rates. On the other hand, enhancements of $b \rightarrow s\tau^+\tau^-$ rates that are independent of $b \rightarrow s\nu\bar{\nu}$ are possible in models with right-handed lepton currents. In such scenarios the current experimental bounds can in principle be saturated.

2.5.2 Tau decays

From Table 2.4 we see that at the tera- Z factory of CEPC we can expect approximately $3 \times 10^{10} \tau^+\tau^-$ pairs produced from Z decays. This is comparable to the expected number of taus produced at Belle II, i.e., roughly 5×10^{10} . This suggests that the sensitivities to lepton-flavor violating decays of taus at CEPC can be similar to the sensitivities expected at Belle II. The large boost of taus from the Z decays is expected to allow CEPC to measure the standard leptonic branching ratios of the tau and to test lepton universality in $\tau \rightarrow \ell\nu\bar{\nu}$ with unprecedented precision.

2.5.2.1 Lepton universality in $\tau \rightarrow \ell\nu\bar{\nu}$

The best measurements of the leptonic branching ratios of the tau, $\text{BR}(\tau \rightarrow \mu\nu_\tau\bar{\nu}_\mu)$ and $\text{BR}(\tau \rightarrow e\nu_\tau\bar{\nu}_e)$, still come from LEP [290]. The most precise individual results are from Aleph [464] and read $\text{BR}(\tau \rightarrow \mu\nu_\tau\bar{\nu}_\mu) = (17.319 \pm 0.070 \pm 0.032)\%$ and $\text{BR}(\tau \rightarrow e\nu_\tau\bar{\nu}_e) = (17.837 \pm 0.072 \pm 0.036)\%$, where the first uncertainty is due to statistics and the second due to systematics. One can see that the measurements were statistics limited with systematic uncertainties at the level of approximately 2 permille. This implies that the larger statistics of a tera- Z program at the CEPC will result in the world best measurement of these branching ratios with uncertainties at the permille level or even much better. Indeed, it is very likely that the much larger number of τ pairs will also allow the experiments to gain a much better control of systematic uncertainties. Assuming that systematics can be reduced by an order of magnitude (which requires exquisite control of the electron and muon efficiencies), the leptonic tau branching ratios could be measured at CEPC with a relative uncertainty of 10^{-4} . Dedicated studies are required to establish the precise sensitivity of CEPC.

The leptonic branching ratios of the tau can in principle be predicted with very high precision in the SM [465]. The SM precision is limited by the uncertainty in the measured tau lifetime, τ_τ . The most precise tau lifetime determination comes currently from Belle [466] and has an uncertainty of approximately 2 permille. Given the much higher statistics expected at Belle II, future measurements may be able to improve the precision of τ_τ by up to an order of magnitude. We expect that CEPC could reach a precision for τ_τ similar to Belle II. The precise relation between the τ lifetime and the leptonic branching ratios in the SM, combined with future precise determinations of $\text{BR}(\tau \rightarrow \mu\nu_\tau\bar{\nu}_\mu)$ and $\text{BR}(\tau \rightarrow e\nu_\tau\bar{\nu}_e)$ at CEPC would allow to scrutinize the weak interactions in tau decays with an unprecedented precision.

Additional information can be extracted from measurements of kinematic distributions in tau decays and the determination of the tau decay parameters (also known as Michel parameters) [290], which are highly sensitive to the structure (spin and chirality) of the current that mediates tau decays. CEPC can be expected to substantially improve the existing (LEP) and expected (Belle II) measurements of tau decay parameters.

1 In addition to measurements of the absolute leptonic branching ratios and their kinematic distributions, it is of particular interest to look at the lepton-flavor universality ratio
 2

$$3 \quad R_\tau = \frac{\text{BR}(\tau \rightarrow \mu\nu_\tau\bar{\nu}_\mu)}{\text{BR}(\tau \rightarrow e\nu_\tau\bar{\nu}_e)}. \quad (2.47)$$

4 This ratio is independent of the tau lifetime and can be predicted with extremely high
 5 precision in the SM, $R_\tau^{\text{SM}} = 0.972559 \pm 0.000005$ [465]. The currently most precise direct
 6 measurement of this ratio comes from BaBar and has an uncertainty of approximately
 7 4 permille, $R_\tau^{\text{BaBar}} = 0.9796 \pm 0.0016 \pm 0.0036$ [467]. A measurement of R_τ with an
 8 uncertainty of 10^{-4} may be possible at CEPC (cf. discussion above about the expected
 9 precision in the absolute branching ratios).

10 Most new-physics models that explain the current hints for lepton-flavor universality
 11 violation in B decays, $R_{K^{(*)}}$ [447, 448] and $R_{D^{(*)}}$ [458] also lead to lepton-flavor univer-
 12 sity violation in $\tau \rightarrow \mu\nu_\tau\bar{\nu}_\mu$ vs. $\tau \rightarrow e\nu_\tau\bar{\nu}_e$ [468, 469]. Typical new-physics effects are
 13 at the level of a few permille and should be well within the reach of CEPC. Therefore,
 14 more accurate measurements of R_τ would be invaluable to scrutinize many motivated
 15 new-physics scenarios.

16 2.5.2.2 Lepton-flavor violating τ decays

17 In the SM without neutrino masses, lepton flavor is conserved and lepton-flavor violating
 18 tau decays are completely absent. While non-zero neutrino masses in principle lead to
 19 lepton-flavor violating tau decays, branching ratios like $\tau \rightarrow \mu\gamma$ are predicted at the level
 20 of 10^{-45} . However, in models of new physics such branching ratios could be enhanced by
 21 many orders of magnitude and could be in reach of experimental searches. In this sense,
 22 any observation of lepton-flavor violating tau decays would be an unambiguous sign of
 23 physics beyond the SM.

24 Lepton-flavor violating tau decays have been searched for in a multitude of channels
 25 at the B factories BaBar and Belle. Among them are the radiative modes $\tau \rightarrow \mu\gamma$ and
 26 $\tau \rightarrow e\gamma$, purely leptonic modes like $\tau \rightarrow 3\mu$, $\tau \rightarrow 3e$, $\tau \rightarrow \mu ee$, etc., as well as many
 27 hadronic modes like $\tau \rightarrow \mu\pi^0$, $\tau \rightarrow e\pi^0$, $\tau \rightarrow \mu K$, etc. Most of these decays have
 28 been constrained at the level of 10^{-8} [436]. Thanks to its increase in statistics, Belle II is
 29 expected to improve the sensitivities to the lepton-flavor violating tau decays by at least
 30 one order of magnitude or even more in very clean modes like $\tau \rightarrow 3\mu$.

31 The clean signature of three muons allows LHCb to search for the decay $\tau \rightarrow 3\mu$ with
 32 high sensitivity. The current limit, which has been obtained with 3 fb^{-1} of the combined
 33 7 TeV and 8 TeV data, reads $\text{BR}(\tau \rightarrow 3\mu)_{\text{LHCb}} < 4.6 \times 10^{-8}$ [470] and is competitive with
 34 the existing bounds from BaBar and Belle. In the high-luminosity phase of LHC, LHCb
 35 will likely improve this bound by one order of magnitude down to few times 10^{-9} .

36 Given the comparable numbers of taus that will be produced at Belle II and that could be
 37 expected from the tera- Z factory at CEPC, we expect similar sensitivities to these decays
 38 at both machines. While dedicated studies would need to be performed to ascertain that
 39 backgrounds would be under control at CEPC, we expect CEPC's sensitivities to lepton-
 40 flavor violating tau decays across the board at the level of 10^{-9} or better.

41 2.5.3 Flavor violating Z decays

42 Rare decays of the Z boson that violate quark flavor, $Z \rightarrow qq'$, are absent in the SM
 43 at tree level and therefore strongly suppressed. The largest branching ratio in the SM is

expected to be $Z \rightarrow bs$ and can be estimated as $\text{BR}(Z \rightarrow bs) \sim \left| \frac{g^2}{16\pi^2} V_{tb} V_{ts}^* \right|^2 \times \text{BR}(Z \rightarrow bb) \sim 10^{-9}$. Even with the statistics expected from 10^{12} Z bosons, a measurement of the SM rate would be extremely challenging as the $Z \rightarrow bs$ events will be buried under an enormous background from $Z \rightarrow q\bar{q}$ and $Z \rightarrow b\bar{b}$ decays. New physics can induce effective quark-flavor violating Z couplings, but such effects are typically constrained by rare meson decays and meson-mixing observables. Rates of $Z \rightarrow qq'$ that are far above SM expectations are therefore unlikely.

Lepton-flavor violating decays are completely absent in the SM without neutrino masses. Including neutrino masses, $Z \rightarrow \ell\ell'$ decays can in principle arise but the branching ratios are suppressed by the tiny neutrino masses and predicted to be in the ballpark of $10^{-50} - 10^{-60}$. However, new physics could enhance these branching ratios by many orders of magnitude.

Searches at LEP established the following upper bounds using few $\times 10^6$ Z bosons [471–473]: $\text{BR}(Z \rightarrow \mu e) < 1.7 \times 10^{-6}$, $\text{BR}(Z \rightarrow \tau e) < 9.8 \times 10^{-6}$, and $\text{BR}(Z \rightarrow \tau \mu) < 1.2 \times 10^{-5}$. Due to the huge numbers of Z bosons produced at the LHC, searches at ATLAS and CMS for the clean $Z \rightarrow \mu e$ decay have recently set limits at the level of few $\times 10^{-7}$ [474, 475]. Searches for the final states with taus are more challenging at the LHC. The current ATLAS limits for $Z \rightarrow \tau e$ and $Z \rightarrow \tau \mu$ are at the level of few $\times 10^{-5}$ [476]. With the high statistics that are expected from the future LHC runs, it is conceivable that the bounds on lepton-flavor violating Z decays will improve by an order of magnitude or more.

Assuming that the sensitivities at the tera- Z factory of CEPC can be scaled from the LEP bounds with the square root of the number of produced Z bosons we find that with 10^{12} Z bosons

$$\text{BR}(Z \rightarrow \mu e)_{\text{CEPC}} \lesssim 3 \times 10^{-9}, \quad (2.48)$$

$$\text{BR}(Z \rightarrow \tau e)_{\text{CEPC}} \lesssim 2 \times 10^{-8}, \quad (2.49)$$

$$\text{BR}(Z \rightarrow \tau \mu)_{\text{CEPC}} \lesssim 2 \times 10^{-8}. \quad (2.50)$$

This is a substantial improvement compared to existing and expected bounds. A more realistic analysis, including explicit background studies from e.g. $Z \rightarrow \tau\tau$ would need to be performed to provide a more precise estimate of the sensitivities [477]. Nevertheless, the above estimates indicate promising sensitivities to new-physics models that induce lepton-flavor violating Z decays, as for example extensions of the SM with heavy sterile neutrinos [285].

2.5.4 Summary

A CEPC that produces 10^{12} Z bosons provides large statistics samples of b and c hadrons as well as tau leptons in a clean experimental environment. This results to unique opportunities for various flavor measurements that are unparalleled in current or any other future machine. For example, the observation of the rare tauonic decays $B \rightarrow K^* \tau^+ \tau^-$ and $B_s \rightarrow \phi \tau^+ \tau^-$ at the SM rate could be achieved at CEPC, whereas the SM rates of such tauonic decays are not in reach of neither LHCb nor Belle II. It appears that sufficient statistics could be accumulated such that even an angular analysis of $B \rightarrow K^{(*)} \tau^+ \tau^-$ may be possible. CEPC should also achieve the world's best sensitivity to the related tauonic decay modes $B_s \rightarrow \tau^+ \tau^-$ and $B \rightarrow K \tau^+ \tau^-$ at a level of 10^{-5} . New physics in the rare

Observable	Current sensitivity	Future sensitivity	Tera- Z sensitivity
$\text{BR}(B_s \rightarrow \tau\tau)$	5.2×10^{-3} (LHCb)	$\sim 5 \times 10^{-4}$ (LHCb)	$\sim 10^{-5}$
$\text{BR}(B \rightarrow K^*\tau\tau)$	–	$\sim 10^{-5}$ (Belle II)	$\sim 10^{-8}$
$\text{BR}(B_s \rightarrow \phi\nu\bar{\nu})$	–	–	$\sim 10^{-6}$
$\text{BR}(\Lambda_b \rightarrow \Lambda\nu\bar{\nu})$	–	–	$\sim 10^{-6}$
$\text{BR}(\tau \rightarrow \mu\gamma)$	4.5×10^{-8} (Belle)	$\sim 10^{-9}$ (Belle II)	$\sim 10^{-9}$
$\frac{\text{BR}(\tau \rightarrow \mu\nu\bar{\nu})}{\text{BR}(\tau \rightarrow e\nu\bar{\nu})}$	3.9×10^{-3} (BaBar)	$\sim 10^{-3}$ (Belle II)	$\sim 10^{-4}$
$\text{BR}(Z \rightarrow \mu e)$	1.7×10^{-6} (LEP)	$\sim 10^{-8}$ (ATLAS/CMS)	$\sim 10^{-9}$
$\text{BR}(Z \rightarrow \tau e)$	9.8×10^{-6} (LEP)	$\sim 10^{-6}$ (ATLAS/CMS)	$\sim 10^{-8}$
$\text{BR}(Z \rightarrow \tau\mu)$	1.2×10^{-5} (LEP)	$\sim 10^{-6}$ (ATLAS/CMS)	$\sim 10^{-8}$

Table 2.5: Order of magnitude estimates of the sensitivity to a number of key observables for which the tera- Z factory at CEPC has unique capabilities. The expected future sensitivities assume luminosities of 50 fb^{-1} at LHCb, 50 ab^{-1} at Belle II, and 3 ab^{-1} at ATLAS and CMS. For the tera- Z factory of CEPC we have assumed the production of $10^{12} Z$ bosons.

¹ tauonic decays is particularly well motivated given the current hints for lepton-flavor universality violation in $R_{K^{(*)}}$ and $R_{D^{(*)}}$. A future circular electron–positron collider is also the only machine that would allow measurements of the rare FCNC decays of B_s mesons and Λ_b baryons to neutrinos, i.e., $B_s \rightarrow \phi\nu\bar{\nu}$ and $\Lambda_b \rightarrow \Lambda\nu\bar{\nu}$, with sensitivities of $\sim 10^{-6}$, thus complementing the sensitivity of Belle II to $B \rightarrow K^{(*)}\nu\bar{\nu}$.

⁶ A tera- Z factory of CEPC will also likely reach sensitivities to lepton-flavor violation in tau decays at a level of 10^{-9} , which is comparable to the sensitivities expected at Belle II. The leptonic decays of taus, $\tau \rightarrow \mu\nu\nu$ and $\tau \rightarrow e\nu\nu$ would be measured at CEPC with unprecedented precision, providing extremely sensitive tests of the weak interaction in tau decays. Furthermore, it may be possible to test lepton universality in $\tau \rightarrow \ell\nu\nu$ at the level of 10^{-4} . Many new-physics explanations of the observed anomalies in $R_{K^{(*)}}$ and $R_{D^{(*)}}$ predict violation of lepton-flavor universality in tau decays at the permille level and could, therefore, be scrutinized at CEPC. Finally, the CEPC measurements would improve the bounds on lepton-flavor violating Z decays by orders of magnitude compared to the current best bounds from LEP, down to a level of 10^{-8} and better.

¹⁶ Table 2.5, we summarize a number of key observables. All listed sensitivities are rough estimates only and need to be followed up by dedicated sensitivity studies that carefully take into account detection efficiencies, background systematics, etc.

19 References

- ²⁰ [1] The ATLAS Collaboration, G. Aad et al., *Observation of a new particle in the*

- 1 *search for the Standard Model Higgs boson with the ATLAS detector at the LHC,*
2 *Phys. Lett. B* **716** (2012) 1–29, [arXiv:1207.7214 \[hep-ex\]](https://arxiv.org/abs/1207.7214).
- 3 [2] The CMS Collaboration, S. Chatrchyan et al., *Observation of a new boson at a*
4 *mass of 125 GeV with the CMS experiment at the LHC*, *Phys. Lett. B* **716** (2012)
5 30–61, [arXiv:1207.7235 \[hep-ex\]](https://arxiv.org/abs/1207.7235).
- 6 [3] ATLAS Collaboration, P. Glaysher, *ATLAS Higgs physics prospects at the high*
7 *luminosity LHC*, PoS **EPS-HEP2015** (2015) 160.
- 8 [4] P. A. M. Dirac, *New basis for cosmology*, *Proc. Roy. Soc. Lond. A* **165** (1938)
9 199–208.
- 10 [5] K. G. Wilson, *The Renormalization Group and Strong Interactions*, *Phys. Rev. D* **3**
11 (1971) 1818.
- 12 [6] L. Susskind, *Dynamics of Spontaneous Symmetry Breaking in the Weinberg-Salam*
13 *Theory*, *Phys. Rev. D* **20** (1979) 2619–2625.
- 14 [7] G. ’t Hooft, *Naturalness, chiral symmetry, and spontaneous chiral symmetry*
15 *breaking*, *NATO Sci. Ser. B* **59** (1980) 135–157.
- 16 [8] P. Fayet, *Supersymmetry and Weak, Electromagnetic and Strong Interactions*,
17 *Phys. Lett. 64B* (1976) 159.
- 18 [9] P. Fayet, *Spontaneously Broken Supersymmetric Theories of Weak,*
19 *Electromagnetic and Strong Interactions*, *Phys. Lett. 69B* (1977) 489.
- 20 [10] S. Dimopoulos and H. Georgi, *Softly Broken Supersymmetry and SU(5)*, *Nucl.*
21 *Phys. B* **193** (1981) 150–162.
- 22 [11] D. B. Kaplan, H. Georgi, and S. Dimopoulos, *Composite Higgs Scalars*, *Phys.*
23 *Lett. 136B* (1984) 187–190.
- 24 [12] N. Arkani-Hamed, A. G. Cohen, E. Katz, A. E. Nelson, T. Gregoire, and J. G.
25 Wacker, *The Minimal moose for a little Higgs*, *JHEP 08* (2002) 021,
26 [arXiv:hep-ph/0206020 \[hep-ph\]](https://arxiv.org/abs/hep-ph/0206020).
- 27 [13] *Composite Higgses*, *Eur. Phys. J. C* **74** (2014) no. 5, 2766, [arXiv:1401.2457 \[hep-ph\]](https://arxiv.org/abs/1401.2457).
- 28 [14] S. Weinberg, *Implications of Dynamical Symmetry Breaking*, *Phys. Rev. D* **13**
29 (1976) 974–996. [Addendum: *Phys. Rev.D19*,1277(1979)].
- 30 [15] N. Arkani-Hamed, S. Dimopoulos, and G. R. Dvali, *The Hierarchy problem and*
31 *new dimensions at a millimeter*, *Phys. Lett. B* **429** (1998) 263–272,
32 [arXiv:hep-ph/9803315 \[hep-ph\]](https://arxiv.org/abs/hep-ph/9803315).
- 33 [16] I. Antoniadis, N. Arkani-Hamed, S. Dimopoulos, and G. R. Dvali, *New*
34 *dimensions at a millimeter to a Fermi and superstrings at a TeV*, *Phys. Lett. B* **436**
35 (1998) 257–263, [arXiv:hep-ph/9804398 \[hep-ph\]](https://arxiv.org/abs/hep-ph/9804398).
- 36 [17] L. Randall and R. Sundrum, *A Large mass hierarchy from a small extra dimension*,
37 *Phys. Rev. Lett. 83* (1999) 3370–3373, [arXiv:hep-ph/9905221 \[hep-ph\]](https://arxiv.org/abs/hep-ph/9905221).

- [18] L. Randall and R. Sundrum, *An Alternative to compactification*, *Phys. Rev. Lett.* **83** (1999) 4690–4693, [arXiv:hep-th/9906064](https://arxiv.org/abs/hep-th/9906064) [hep-th].
- [19] P. W. Graham, D. E. Kaplan, and S. Rajendran, *Cosmological Relaxation of the Electroweak Scale*, *Phys. Rev. Lett.* **115** (2015) no. 22, 221801, [arXiv:1504.07551](https://arxiv.org/abs/1504.07551) [hep-ph].
- [20] J. Gu, H. Li, Z. Liu, S. Su, and W. Su, *Learning from Higgs Physics at Future Higgs Factories*, *JHEP* **12** (2017) 153, [arXiv:1709.06103](https://arxiv.org/abs/1709.06103) [hep-ph].
- [21] A. Djouadi, L. Maiani, G. Moreau, A. Polosa, J. Quevillon, and V. Riquer, *The post-Higgs MSSM scenario: Habemus MSSM?*, *Eur. Phys. J.* **C73** (2013) 2650, [arXiv:1307.5205](https://arxiv.org/abs/1307.5205) [hep-ph].
- [22] J. Baglio, A. Djouadi, and J. Quevillon, *Prospects for Higgs physics at energies up to 100 TeV*, *Rept. Prog. Phys.* **79** (2016) no. 11, 116201, [arXiv:1511.07853](https://arxiv.org/abs/1511.07853) [hep-ph].
- [23] J. Fan, M. Reece, and L.-T. Wang, *Precision Natural SUSY at CEPC, FCC-ee, and ILC*, *JHEP* **08** (2015) 152, [arXiv:1412.3107](https://arxiv.org/abs/1412.3107) [hep-ph].
- [24] J. Fan and M. Reece, *A New Look at Higgs Constraints on Stops*, *JHEP* **06** (2014) 031, [arXiv:1401.7671](https://arxiv.org/abs/1401.7671) [hep-ph].
- [25] N. Craig, M. Farina, M. McCullough, and M. Perelstein, *Precision Higgsstrahlung as a Probe of New Physics*, *JHEP* **03** (2015) 146, [arXiv:1411.0676](https://arxiv.org/abs/1411.0676) [hep-ph].
- [26] R. Essig, P. Meade, H. Ramani, and Y.-M. Zhong, *Higgs-Precision Constraints on Colored Naturalness*, *JHEP* **09** (2017) 085, [arXiv:1707.03399](https://arxiv.org/abs/1707.03399) [hep-ph].
- [27] G. F. Giudice, C. Grojean, A. Pomarol, and R. Rattazzi, *The Strongly-Interacting Light Higgs*, *JHEP* **06** (2007) 045, [arXiv:hep-ph/0703164](https://arxiv.org/abs/hep-ph/0703164) [hep-ph].
- [28] A. Thamm, R. Torre, and A. Wulzer, *Future tests of Higgs compositeness: direct vs indirect*, *JHEP* **07** (2015) 100, [arXiv:1502.01701](https://arxiv.org/abs/1502.01701) [hep-ph].
- [29] N. Craig, S. Knapen, and P. Longhi, *Neutral Naturalness from Orbifold Higgs Models*, *Phys. Rev. Lett.* **114** (2015) no. 6, 061803, [arXiv:1410.6808](https://arxiv.org/abs/1410.6808) [hep-ph].
- [30] G. Burdman, Z. Chacko, H.-S. Goh, and R. Harnik, *Folded supersymmetry and the LEP paradox*, *JHEP* **02** (2007) 009, [arXiv:hep-ph/0609152](https://arxiv.org/abs/hep-ph/0609152) [hep-ph].
- [31] Z. Chacko, H.-S. Goh, and R. Harnik, *The Twin Higgs: Natural electroweak breaking from mirror symmetry*, *Phys. Rev. Lett.* **96** (2006) 231802, [arXiv:hep-ph/0506256](https://arxiv.org/abs/hep-ph/0506256) [hep-ph].
- [32] T. Cohen, N. Craig, G. F. Giudice, and M. McCullough, *The Hyperbolic Higgs*, *JHEP* **05** (2018) 091, [arXiv:1803.03647](https://arxiv.org/abs/1803.03647) [hep-ph].
- [33] H. Cai, H.-C. Cheng, and J. Terning, *A Quirky Little Higgs Model*, *JHEP* **05** (2009) 045, [arXiv:0812.0843](https://arxiv.org/abs/0812.0843) [hep-ph].

- [34] N. Craig, C. Englert, and M. McCullough, *New Probe of Naturalness*, Phys. Rev. Lett. **111** (2013) no. 12, 121803, [arXiv:1305.5251 \[hep-ph\]](#).
- [35] T. Flacke, C. Fruguele, E. Fuchs, R. S. Gupta, and G. Perez, *Phenomenology of relaxion-Higgs mixing*, JHEP **06** (2017) 050, [arXiv:1610.02025 \[hep-ph\]](#).
- [36] K. Choi and S. H. Im, *Constraints on Relaxion Windows*, JHEP **12** (2016) 093, [arXiv:1610.00680 \[hep-ph\]](#).
- [37] X.-m. Zhang, *Operators analysis for Higgs potential and cosmological bound on Higgs mass*, Phys. Rev. **D47** (1993) 3065–3067, [arXiv:hep-ph/9301277 \[hep-ph\]](#).
- [38] C. Grojean, G. Servant, and J. D. Wells, *First-order electroweak phase transition in the standard model with a low cutoff*, Phys. Rev. **D71** (2005) 036001, [arXiv:hep-ph/0407019 \[hep-ph\]](#).
- [39] C. Delaunay, C. Grojean, and J. D. Wells, *Dynamics of Non-renormalizable Electroweak Symmetry Breaking*, JHEP **04** (2008) 029, [arXiv:0711.2511 \[hep-ph\]](#).
- [40] Q.-H. Cao, F. P. Huang, K.-P. Xie, and X. Zhang, *Testing the electroweak phase transition in scalar extension models at lepton colliders*, Chin. Phys. **C42** (2018) no. 2, 023103, [arXiv:1708.04737 \[hep-ph\]](#).
- [41] F. P. Huang, P.-H. Gu, P.-F. Yin, Z.-H. Yu, and X. Zhang, *Testing the electroweak phase transition and electroweak baryogenesis at the LHC and a circular electron-positron collider*, Phys. Rev. **D93** (2016) no. 10, 103515, [arXiv:1511.03969 \[hep-ph\]](#).
- [42] F. P. Huang, Y. Wan, D.-G. Wang, Y.-F. Cai, and X. Zhang, *Hearing the echoes of electroweak baryogenesis with gravitational wave detectors*, Phys. Rev. **D94** (2016) no. 4, 041702, [arXiv:1601.01640 \[hep-ph\]](#).
- [43] S. R. Coleman and E. J. Weinberg, *Radiative Corrections as the Origin of Spontaneous Symmetry Breaking*, Phys. Rev. **D7** (1973) 1888–1910.
- [44] J. R. Espinosa and M. Quiros, *Novel Effects in Electroweak Breaking from a Hidden Sector*, Phys. Rev. **D76** (2007) 076004, [arXiv:hep-ph/0701145 \[hep-ph\]](#).
- [45] C. Caprini et al., *Science with the space-based interferometer eLISA. II: Gravitational waves from cosmological phase transitions*, JCAP **1604** (2016) no. 04, 001, [arXiv:1512.06239 \[astro-ph.CO\]](#).
- [46] A. G. Cohen, D. Kaplan, and A. Nelson, *Progress in electroweak baryogenesis*, Ann. Rev. Nucl. Part. Sci. **43** (1993) 27–70, [arXiv:hep-ph/9302210 \[hep-ph\]](#).
- [47] M. Carena, M. Quiros, and C. E. M. Wagner, *Opening the window for electroweak baryogenesis*, Phys. Lett. **B380** (1996) 81–91, [arXiv:hep-ph/9603420 \[hep-ph\]](#).

- [48] J. R. Espinosa, *Dominant two loop corrections to the MSSM finite temperature effective potential*, Nucl. Phys. **B475** (1996) 273–292, arXiv:hep-ph/9604320 [hep-ph].
- [49] T. Cohen, D. E. Morrissey, and A. Pierce, *Electroweak Baryogenesis and Higgs Signatures*, Phys. Rev. **D86** (2012) 013009, arXiv:1203.2924 [hep-ph].
- [50] D. Curtin, P. Jaiswal, and P. Meade, *Excluding Electroweak Baryogenesis in the MSSM*, JHEP **08** (2012) 005, arXiv:1203.2932 [hep-ph].
- [51] D. J. H. Chung, A. J. Long, and L.-T. Wang, *125 GeV Higgs boson and electroweak phase transition model classes*, Phys. Rev. **D87** (2013) no. 2, 023509, arXiv:1209.1819 [hep-ph].
- [52] M. Carena, Z. Liu, and M. Riembau, *Probing the electroweak phase transition via enhanced di-Higgs boson production*, Phys. Rev. **D97** (2018) no. 9, 095032, arXiv:1801.00794 [hep-ph].
- [53] J. R. Espinosa and M. Quiros, *The Electroweak phase transition with a singlet*, Phys. Lett. **B305** (1993) 98–105, arXiv:hep-ph/9301285 [hep-ph].
- [54] J. Choi and R. R. Volkas, *Real Higgs singlet and the electroweak phase transition in the Standard Model*, Phys. Lett. **B317** (1993) 385–391, arXiv:hep-ph/9308234 [hep-ph].
- [55] J. McDonald, *Electroweak baryogenesis and dark matter via a gauge singlet scalar*, Phys. Lett. **B323** (1994) 339–346.
- [56] S. Profumo, M. J. Ramsey-Musolf, and G. Shaughnessy, *Singlet Higgs phenomenology and the electroweak phase transition*, JHEP **08** (2007) 010, arXiv:0705.2425 [hep-ph].
- [57] D. Curtin, P. Meade, and C.-T. Yu, *Testing Electroweak Baryogenesis with Future Colliders*, JHEP **11** (2014) 127, arXiv:1409.0005 [hep-ph].
- [58] D. Curtin, P. Meade, and H. Ramani, *Thermal Resummation and Phase Transitions*, arXiv:1612.00466 [hep-ph].
- [59] M. McCullough, *An Indirect Model-Dependent Probe of the Higgs Self-Coupling*, Phys. Rev. **D90** (2014) no. 1, 015001, arXiv:1312.3322 [hep-ph]. [Erratum: Phys. Rev.D92,no.3,039903(2015)].
- [60] P. Huang, A. J. Long, and L.-T. Wang, *Probing the Electroweak Phase Transition with Higgs Factories and Gravitational Waves*, Phys. Rev. **D94** (2016) no. 7, 075008, arXiv:1608.06619 [hep-ph].
- [61] S. Profumo, M. J. Ramsey-Musolf, C. L. Wainwright, and P. Winslow, *Singlet-catalyzed electroweak phase transitions and precision Higgs boson studies*, Phys. Rev. **D91** (2015) no. 3, 035018, arXiv:1407.5342 [hep-ph].
- [62] A. Noble and M. Perelstein, *Higgs self-coupling as a probe of electroweak phase transition*, Phys. Rev. **D78** (2008) 063518, arXiv:0711.3018 [hep-ph].

- [63] V. Silveira and A. Zee, *Scalar Phantoms*, Phys. Lett. **161B** (1985) 136–140.
- [64] J. McDonald, *Gauge singlet scalars as cold dark matter*, Phys. Rev. **D50** (1994) 3637–3649, arXiv:hep-ph/0702143 [HEP-PH].
- [65] C. P. Burgess, M. Pospelov, and T. ter Veldhuis, *The Minimal model of nonbaryonic dark matter: A Singlet scalar*, Nucl. Phys. **B619** (2001) 709–728, arXiv:hep-ph/0011335 [hep-ph].
- [66] B. Patt and F. Wilczek, *Higgs-field portal into hidden sectors*, arXiv:hep-ph/0605188 [hep-ph].
- [67] Y. G. Kim and K. Y. Lee, *The Minimal model of fermionic dark matter*, Phys. Rev. **D75** (2007) 115012, arXiv:hep-ph/0611069 [hep-ph].
- [68] V. Barger, P. Langacker, M. McCaskey, M. J. Ramsey-Musolf, and G. Shaughnessy, *LHC Phenomenology of an Extended Standard Model with a Real Scalar Singlet*, Phys. Rev. **D77** (2008) 035005, arXiv:0706.4311 [hep-ph].
- [69] Y. G. Kim, K. Y. Lee, and S. Shin, *Singlet fermionic dark matter*, JHEP **05** (2008) 100, arXiv:0803.2932 [hep-ph].
- [70] J. M. Cline, K. Kainulainen, P. Scott, and C. Weniger, *Update on scalar singlet dark matter*, Phys. Rev. **D88** (2013) 055025, arXiv:1306.4710 [hep-ph]. [Erratum: Phys. Rev.D92,no.3,039906(2015)].
- [71] L. B. Okun, *Limits of Electrodynamics: Paraphotons?*, Sov. Phys. JETP **56** (1982) 502. [Zh. Eksp. Teor. Fiz.83,892(1982)].
- [72] B. Holdom, *Two U(1)'s and Epsilon Charge Shifts*, Phys. Lett. **166B** (1986) 196–198.
- [73] K. R. Dienes, C. F. Kolda, and J. March-Russell, *Kinetic mixing and the supersymmetric gauge hierarchy*, Nucl. Phys. **B492** (1997) 104–118, arXiv:hep-ph/9610479 [hep-ph].
- [74] M. Pospelov, A. Ritz, and M. B. Voloshin, *Secluded WIMP Dark Matter*, Phys. Lett. **B662** (2008) 53–61, arXiv:0711.4866 [hep-ph].
- [75] N. Arkani-Hamed and N. Weiner, *LHC Signals for a SuperUnified Theory of Dark Matter*, JHEP **12** (2008) 104, arXiv:0810.0714 [hep-ph].
- [76] N. Arkani-Hamed, D. P. Finkbeiner, T. R. Slatyer, and N. Weiner, *A Theory of Dark Matter*, Phys. Rev. **D79** (2009) 015014, arXiv:0810.0713 [hep-ph].
- [77] M. Pospelov, *Secluded U(1) below the weak scale*, Phys. Rev. **D80** (2009) 095002, arXiv:0811.1030 [hep-ph].
- [78] P. Minkowski, $\mu \rightarrow e\gamma$ at a Rate of One Out of 10^9 Muon Decays?, Phys. Lett. **67B** (1977) 421–428.
- [79] R. N. Mohapatra and G. Senjanovic, *Neutrino Mass and Spontaneous Parity Violation*, Phys. Rev. Lett. **44** (1980) 912.

- [80] S. Dodelson and L. M. Widrow, *Sterile-neutrinos as dark matter*, *Phys. Rev. Lett.* **72** (1994) 17–20, [arXiv:hep-ph/9303287](https://arxiv.org/abs/hep-ph/9303287) [hep-ph].
- [81] X.-D. Shi and G. M. Fuller, *A New dark matter candidate: Nonthermal sterile neutrinos*, *Phys. Rev. Lett.* **82** (1999) 2832–2835, [arXiv:astro-ph/9810076](https://arxiv.org/abs/astro-ph/9810076) [astro-ph].
- [82] D. E. Kaplan, M. A. Luty, and K. M. Zurek, *Asymmetric Dark Matter*, *Phys. Rev. D* **79** (2009) 115016, [arXiv:0901.4117](https://arxiv.org/abs/0901.4117) [hep-ph].
- [83] A. Falkowski, J. Juknevich, and J. Shelton, *Dark Matter Through the Neutrino Portal*, [arXiv:0908.1790](https://arxiv.org/abs/0908.1790) [hep-ph].
- [84] J. F. Cherry, A. Friedland, and I. M. Shoemaker, *Neutrino Portal Dark Matter: From Dwarf Galaxies to IceCube*, [arXiv:1411.1071](https://arxiv.org/abs/1411.1071) [hep-ph].
- [85] J. A. Harvey, C. T. Hill, and R. J. Hill, *Standard Model Gauging of the Wess-Zumino-Witten Term: Anomalies, Global Currents and pseudo-Chern-Simons Interactions*, *Phys. Rev. D* **77** (2008) 085017, [arXiv:0712.1230](https://arxiv.org/abs/0712.1230) [hep-th].
- [86] R. J. Hill, *Some new implications of the anomalous baryon current in the Standard Model*, in *Proceedings, 43rd Rencontres de Moriond on Electroweak Interactions and Unified Theories: La Thuile, Italy, March 1-8, 2008*, pp. 355–362. 2008. [arXiv:0806.3673](https://arxiv.org/abs/0806.3673) [hep-ph].
http://lss.fnal.gov/cgi-bin/find_paper.pl?conf=08-202.
- [87] A. Dedes and K. Suxho, *Heavy Fermion Non-Decoupling Effects in Triple Gauge Boson Vertices*, *Phys. Rev. D* **85** (2012) 095024, [arXiv:1202.4940](https://arxiv.org/abs/1202.4940) [hep-ph].
- [88] B. Batell, P. deNiverville, D. McKeen, M. Pospelov, and A. Ritz, *Leptophobic Dark Matter at Neutrino Factories*, *Phys. Rev. D* **90** (2014) no. 11, 115014, [arXiv:1405.7049](https://arxiv.org/abs/1405.7049) [hep-ph].
- [89] J. A. Dror, R. Lasenby, and M. Pospelov, *New constraints on light vectors coupled to anomalous currents*, *Phys. Rev. Lett.* **119** (2017) no. 14, 141803, [arXiv:1705.06726](https://arxiv.org/abs/1705.06726) [hep-ph].
- [90] A. Ismail, A. Katz, and D. Racco, *On dark matter interactions with the Standard Model through an anomalous Z'* , *JHEP* **10** (2017) 165, [arXiv:1707.00709](https://arxiv.org/abs/1707.00709) [hep-ph].
- [91] J. A. Dror, R. Lasenby, and M. Pospelov, *Dark forces coupled to nonconserved currents*, *Phys. Rev. D* **96** (2017) no. 7, 075036, [arXiv:1707.01503](https://arxiv.org/abs/1707.01503) [hep-ph].
- [92] A. Ismail and A. Katz, *Anomalous Z' and Diboson Resonances at the LHC*, [arXiv:1712.01840](https://arxiv.org/abs/1712.01840) [hep-ph].
- [93] A. Ekstedt, R. Enberg, G. Ingelman, J. Löfgren, and T. Mandal, *Minimal anomalous U(1) theories and collider phenomenology*, [arXiv:1712.03410](https://arxiv.org/abs/1712.03410) [hep-ph].

- [94] M. Fabbrichesi, E. Gabrielli, and B. Mele, *Z boson decay into light and darkness*, [arXiv:1712.05412 \[hep-ph\]](https://arxiv.org/abs/1712.05412).
- [95] R. D. Peccei and H. R. Quinn, *CP Conservation in the Presence of Instantons*, Phys. Rev. Lett. **38** (1977) 1440–1443.
- [96] S. Weinberg, *A New Light Boson?*, Phys. Rev. Lett. **40** (1978) 223–226.
- [97] F. Wilczek, *Problem of Strong p and t Invariance in the Presence of Instantons*, Phys. Rev. Lett. **40** (1978) 279–282.
- [98] J. M. Frere, D. R. T. Jones, and S. Raby, *Fermion Masses and Induction of the Weak Scale by Supergravity*, Nucl. Phys. **B222** (1983) 11–19.
- [99] A. E. Nelson and N. Seiberg, *R symmetry breaking versus supersymmetry breaking*, Nucl. Phys. **B416** (1994) 46–62, [arXiv:hep-ph/9309299 \[hep-ph\]](https://arxiv.org/abs/hep-ph/9309299).
- [100] J. Bagger, E. Poppitz, and L. Randall, *The R axion from dynamical supersymmetry breaking*, Nucl. Phys. **B426** (1994) 3–18, [arXiv:hep-ph/9405345 \[hep-ph\]](https://arxiv.org/abs/hep-ph/9405345).
- [101] J. P. Conlon, *The QCD axion and moduli stabilisation*, JHEP **05** (2006) 078, [arXiv:hep-th/0602233 \[hep-th\]](https://arxiv.org/abs/hep-th/0602233).
- [102] P. Svrcek and E. Witten, *Axions In String Theory*, JHEP **06** (2006) 051, [arXiv:hep-th/0605206 \[hep-th\]](https://arxiv.org/abs/hep-th/0605206).
- [103] Y. Nomura and J. Thaler, *Dark Matter through the Axion Portal*, Phys. Rev. **D79** (2009) 075008, [arXiv:0810.5397 \[hep-ph\]](https://arxiv.org/abs/0810.5397).
- [104] A. Arvanitaki, S. Dimopoulos, S. Dubovsky, N. Kaloper, and J. March-Russell, *String Axiverse*, Phys. Rev. **D81** (2010) 123530, [arXiv:0905.4720 \[hep-th\]](https://arxiv.org/abs/0905.4720).
- [105] J. Jaeckel and A. Ringwald, *The Low-Energy Frontier of Particle Physics*, Ann. Rev. Nucl. Part. Sci. **60** (2010) 405–437, [arXiv:1002.0329 \[hep-ph\]](https://arxiv.org/abs/1002.0329).
- [106] B. S. Acharya, K. Bobkov, and P. Kumar, *An M Theory Solution to the Strong CP Problem and Constraints on the Axiverse*, JHEP **11** (2010) 105, [arXiv:1004.5138 \[hep-th\]](https://arxiv.org/abs/1004.5138).
- [107] A. Ringwald, *Exploring the Role of Axions and Other WISPs in the Dark Universe*, Phys. Dark Univ. **1** (2012) 116–135, [arXiv:1210.5081 \[hep-ph\]](https://arxiv.org/abs/1210.5081).
- [108] K. Sigurdson, M. Doran, A. Kurylov, R. R. Caldwell, and M. Kamionkowski, *Dark-matter electric and magnetic dipole moments*, Phys. Rev. **D70** (2004) 083501, [arXiv:astro-ph/0406355 \[astro-ph\]](https://arxiv.org/abs/astro-ph/0406355). [Erratum: Phys. Rev.D73,089903(2006)].
- [109] E. Masso, S. Mohanty, and S. Rao, *Dipolar Dark Matter*, Phys. Rev. **D80** (2009) 036009, [arXiv:0906.1979 \[hep-ph\]](https://arxiv.org/abs/0906.1979).
- [110] S. Chang, N. Weiner, and I. Yavin, *Magnetic Inelastic Dark Matter*, Phys. Rev. **D82** (2010) 125011, [arXiv:1007.4200 \[hep-ph\]](https://arxiv.org/abs/1007.4200).

- [111] N. Weiner and I. Yavin, *How Dark Are Majorana WIMPs? Signals from MiDM and Rayleigh Dark Matter*, Phys. Rev. **D86** (2012) 075021, arXiv:1206.2910 [hep-ph].
- [112] N. Weiner and I. Yavin, *UV completions of magnetic inelastic and Rayleigh dark matter for the Fermi Line(s)*, Phys. Rev. **D87** (2013) no. 2, 023523, arXiv:1209.1093 [hep-ph].
- [113] D. Curtin et al., *Exotic decays of the 125 GeV Higgs boson*, Phys. Rev. **D90** (2014) no. 7, 075004, arXiv:1312.4992 [hep-ph].
- [114] LHC Higgs Cross Section Working Group Collaboration, D. de Florian et al., *Handbook of LHC Higgs Cross Sections: 4. Deciphering the Nature of the Higgs Sector*, arXiv:1610.07922 [hep-ph].
- [115] Z. Liu, L.-T. Wang, and H. Zhang, *Exotic decays of the 125 GeV Higgs boson at future e^+e^- lepton colliders*, Chin. Phys. **C41** (2017) no. 6, 063102, arXiv:1612.09284 [hep-ph].
- [116] J. Liu, Z. Liu, and L.-T. Wang, *Long-lived particles at the LHC: catching them in time*, arXiv:1805.05957 [hep-ph].
- [117] J. Liu, L.-T. Wang, X.-P. Wang, and W. Xue, *Exposing Dark Sector with Future Z-Factories*, arXiv:1712.07237 [hep-ph].
- [118] W.-F. Chang, J. N. Ng, and G. White, *Prospects for Detecting light bosons at the FCC-ee and CEPC*, arXiv:1803.00148 [hep-ph].
- [119] L3 Collaboration, M. Acciarri et al., *Search for neutral Higgs boson production through the process $e^+ e^- \rightarrow Z^* H 0$* , Phys. Lett. **B385** (1996) 454–470.
- [120] ATLAS, CMS Collaboration, G. Aad et al., *Measurements of the Higgs boson production and decay rates and constraints on its couplings from a combined ATLAS and CMS analysis of the LHC pp collision data at $\sqrt{s} = 7$ and 8 TeV*, JHEP **08** (2016) 045, arXiv:1606.02266 [hep-ex].
- [121] S. Dawson et al., *Working Group Report: Higgs Boson*, in *Proceedings, 2013 Community Summer Study on the Future of U.S. Particle Physics: Snowmass on the Mississippi (CSS2013): Minneapolis, MN, USA, July 29-August 6, 2013*. 2013. arXiv:1310.8361 [hep-ex].
<http://inspirehep.net/record/1262795/files/arXiv:1310.8361.pdf>.
- [122] TLEP Design Study Working Group Collaboration, M. Bicer et al., *First Look at the Physics Case of TLEP*, JHEP **01** (2014) 164, arXiv:1308.6176 [hep-ex].
- [123] CEPC-SPPC Study Group Collaboration, *CEPC-SPPC Preliminary Conceptual Design Report. 1. Physics and Detector*, .
http://cepc.ihep.ac.cn/preCDR/main_preCDR.pdf.
- [124] M. Ruan, *Higgs Measurement at e^+e^- Circular Colliders*, Nucl. Part. Phys. Proc. **273-275** (2016) 857–862, arXiv:1411.5606 [hep-ex].

- [125] J. Liu, X.-P. Wang, and F. Yu, *A Tale of Two Portals: Testing Light, Hidden New Physics at Future e^+e^- Colliders*, *JHEP* **06** (2017) 077, [arXiv:1704.00730 \[hep-ph\]](https://arxiv.org/abs/1704.00730).
- [126] ATLAS Collaboration, G. Aad et al., *Constraints on new phenomena via Higgs boson couplings and invisible decays with the ATLAS detector*, *JHEP* **11** (2015) 206, [arXiv:1509.00672 \[hep-ex\]](https://arxiv.org/abs/1509.00672).
- [127] CMS Collaboration, V. Khachatryan et al., *Searches for invisible decays of the Higgs boson in pp collisions at $\sqrt{s} = 7, 8,$ and 13 TeV*, *JHEP* **02** (2017) 135, [arXiv:1610.09218 \[hep-ex\]](https://arxiv.org/abs/1610.09218).
- [128] *Projections for measurements of Higgs boson cross sections, branching ratios and coupling parameters with the ATLAS detector at a HL-LHC*, ATL-PHYS-PUB-2013-014, CERN, Geneva, Oct, 2013.
<http://cds.cern.ch/record/1611186>.
- [129] CMS Collaboration, *Projected Performance of an Upgraded CMS Detector at the LHC and HL-LHC: Contribution to the Snowmass Process*, in *Proceedings, 2013 Community Summer Study on the Future of U.S. Particle Physics: Snowmass on the Mississippi (CSS2013): Minneapolis, MN, USA, July 29-August 6, 2013.* 2013. [arXiv:1307.7135 \[hep-ex\]](https://arxiv.org/abs/1307.7135).
<https://inspirehep.net/record/1244669/files/arXiv:1307.7135.pdf>.
- [130] K. Fujii et al., *Physics Case for the 250 GeV Stage of the International Linear Collider*, [arXiv:1710.07621 \[hep-ex\]](https://arxiv.org/abs/1710.07621).
- [131] Planck Collaboration, P. A. R. Ade et al., *Planck 2015 results. XIII. Cosmological parameters*, *Astron. Astrophys.* **594** (2016) A13, [arXiv:1502.01589 \[astro-ph.CO\]](https://arxiv.org/abs/1502.01589).
- [132] XENON Collaboration, E. Aprile et al., *First Dark Matter Search Results from the XENON1T Experiment*, *Phys. Rev. Lett.* **119** (2017) no. 18, 181301, [arXiv:1705.06655 \[astro-ph.CO\]](https://arxiv.org/abs/1705.06655).
- [133] LUX Collaboration, D. S. Akerib et al., *Results from a search for dark matter in the complete LUX exposure*, *Phys. Rev. Lett.* **118** (2017) no. 2, 021303, [arXiv:1608.07648 \[astro-ph.CO\]](https://arxiv.org/abs/1608.07648).
- [134] PandaX-II Collaboration, A. Tan et al., *Dark Matter Results from First 98.7 Days of Data from the PandaX-II Experiment*, *Phys. Rev. Lett.* **117** (2016) no. 12, 121303, [arXiv:1607.07400 \[hep-ex\]](https://arxiv.org/abs/1607.07400).
- [135] CRESST Collaboration, G. Angloher et al., *Results on light dark matter particles with a low-threshold CRESST-II detector*, *Eur. Phys. J.* **C76** (2016) no. 1, 25, [arXiv:1509.01515 \[astro-ph.CO\]](https://arxiv.org/abs/1509.01515).
- [136] J. Jaeckel and M. Spannowsky, *Probing MeV to 90 GeV axion-like particles with LEP and LHC*, *Phys. Lett.* **B753** (2016) 482–487, [arXiv:1509.00476 \[hep-ph\]](https://arxiv.org/abs/1509.00476).

- [137] OPAL Collaboration, G. Abbiendi et al., *Multiphoton production in $e+e-$ collisions at $s^{**}(1/2) = 181\text{-GeV}$ to 209-GeV* , *Eur. Phys. J.* **C26** (2003) 331–344, [arXiv:hep-ex/0210016 \[hep-ex\]](https://arxiv.org/abs/hep-ex/0210016).
- [138] ATLAS Collaboration, G. Aad et al., *Search for Scalar Diphoton Resonances in the Mass Range $65 - 600 \text{ GeV}$ with the ATLAS Detector in pp Collision Data at $\sqrt{s} = 8 \text{ TeV}$* , *Phys. Rev. Lett.* **113** (2014) no. 17, 171801, [arXiv:1407.6583 \[hep-ex\]](https://arxiv.org/abs/1407.6583).
- [139] ATLAS Collaboration, G. Aad et al., *Search for new phenomena in events with at least three photons collected in pp collisions at $\sqrt{s} = 8 \text{ TeV}$ with the ATLAS detector*, *Eur. Phys. J.* **C76** (2016) no. 4, 210, [arXiv:1509.05051 \[hep-ex\]](https://arxiv.org/abs/1509.05051).
- [140] S. Knapen, T. Lin, H. K. Lou, and T. Melia, *Searching for Axionlike Particles with Ultraperipheral Heavy-Ion Collisions*, *Phys. Rev. Lett.* **118** (2017) no. 17, 171801, [arXiv:1607.06083 \[hep-ph\]](https://arxiv.org/abs/1607.06083).
- [141] L3 Collaboration, M. Acciarri et al., *Search for new physics in energetic single photon production in e^+e^- annihilation at the Z resonance*, *Phys. Lett.* **B412** (1997) 201–209.
- [142] J. Fan, M. Reece, and L.-T. Wang, *Possible Futures of Electroweak Precision: ILC, FCC-ee, and CEPC*, *JHEP* **09** (2015) 196, [arXiv:1411.1054 \[hep-ph\]](https://arxiv.org/abs/1411.1054).
- [143] L. Bian, J. Shu, and Y. Zhang, *Prospects for Triple Gauge Coupling Measurements at Future Lepton Colliders and the 14 TeV LHC*, *JHEP* **09** (2015) 206, [arXiv:1507.02238 \[hep-ph\]](https://arxiv.org/abs/1507.02238).
- [144] J. Ellis and T. You, *Sensitivities of Prospective Future $e+e-$ Colliders to Decoupled New Physics*, *JHEP* **03** (2016) 089, [arXiv:1510.04561 \[hep-ph\]](https://arxiv.org/abs/1510.04561).
- [145] S.-F. Ge, H.-J. He, and R.-Q. Xiao, *Probing new physics scales from Higgs and electroweak observables at e^+e^- Higgs factory*, *JHEP* **10** (2016) 007, [arXiv:1603.03385 \[hep-ph\]](https://arxiv.org/abs/1603.03385).
- [146] S.-F. Ge, H.-J. He, and R.-Q. Xiao, *Testing Higgs coupling precision and new physics scales at lepton colliders*, *Int. J. Mod. Phys.* **A31** (2016) no. 33, 1644004, [arXiv:1612.02718 \[hep-ph\]](https://arxiv.org/abs/1612.02718). [,55(2017)].
- [147] G. Durieux, C. Grojean, J. Gu, and K. Wang, *The leptonic future of the Higgs*, *JHEP* **09** (2017) 014, [arXiv:1704.02333 \[hep-ph\]](https://arxiv.org/abs/1704.02333).
- [148] W. H. Chiu, S. C. Leung, T. Liu, K.-F. Lyu, and L.-T. Wang, *Probing 6D operators at future e^-e^+ colliders*, *JHEP* **05** (2018) 081, [arXiv:1711.04046 \[hep-ph\]](https://arxiv.org/abs/1711.04046).
- [149] M. A. Fedderke, T. Lin, and L.-T. Wang, *Probing the fermionic Higgs portal at lepton colliders*, *JHEP* **04** (2016) 160, [arXiv:1506.05465 \[hep-ph\]](https://arxiv.org/abs/1506.05465).
- [150] C. Cai, Z.-H. Yu, and H.-H. Zhang, *CEPC Precision of Electroweak Oblique Parameters and Weakly Interacting Dark Matter: the Fermionic Case*, *Nucl. Phys.* **B921** (2017) 181–210, [arXiv:1611.02186 \[hep-ph\]](https://arxiv.org/abs/1611.02186).

- [151] N. Liu and L. Wu, *An indirect probe of the higgsino world at the CEPC*, *Eur. Phys. J.* **C77** (2017) no. 12, 868, [arXiv:1705.02534 \[hep-ph\]](#).
- [152] C. Cai, Z.-H. Yu, and H.-H. Zhang, *CEPC Precision of Electroweak Oblique Parameters and Weakly Interacting Dark Matter: the Scalar Case*, *Nucl. Phys.* **B924** (2017) 128–152, [arXiv:1705.07921 \[hep-ph\]](#).
- [153] Q.-F. Xiang, X.-J. Bi, P.-F. Yin, and Z.-H. Yu, *Exploring Fermionic Dark Matter via Higgs Boson Precision Measurements at the Circular Electron Positron Collider*, *Phys. Rev.* **D97** (2018) no. 5, 055004, [arXiv:1707.03094 \[hep-ph\]](#).
- [154] J.-W. Wang, X.-J. Bi, Q.-F. Xiang, P.-F. Yin, and Z.-H. Yu, *Exploring triplet-quadruplet fermionic dark matter at the LHC and future colliders*, *Phys. Rev.* **D97** (2018) no. 3, 035021, [arXiv:1711.05622 \[hep-ph\]](#).
- [155] PandaX-II Collaboration, X. Cui et al., *Dark Matter Results From 54-Ton-Day Exposure of PandaX-II Experiment*, *Phys. Rev. Lett.* **119** (2017) no. 18, 181302, [arXiv:1708.06917 \[astro-ph.CO\]](#).
- [156] DARWIN Collaboration, J. Aalbers et al., *DARWIN: towards the ultimate dark matter detector*, *JCAP* **1611** (2016) 017, [arXiv:1606.07001 \[astro-ph.IM\]](#).
- [157] R. J. Hill and M. P. Solon, *WIMP-nucleon scattering with heavy WIMP effective theory*, *Phys. Rev. Lett.* **112** (2014) 211602, [arXiv:1309.4092 \[hep-ph\]](#).
- [158] M. Low and L.-T. Wang, *Neutralino dark matter at 14 TeV and 100 TeV*, *JHEP* **08** (2014) 161, [arXiv:1404.0682 \[hep-ph\]](#).
- [159] J. Kawamura and Y. Omura, *Study of dark matter physics in non-universal gaugino mass scenario*, *JHEP* **08** (2017) 072, [arXiv:1703.10379 \[hep-ph\]](#).
- [160] R. Krall and M. Reece, *Last Electroweak WIMP Standing: Pseudo-Dirac Higgsino Status and Compact Stars as Future Probes*, *Chin. Phys.* **C42** (2018) no. 4, 043105, [arXiv:1705.04843 \[hep-ph\]](#).
- [161] C. Cheung, L. J. Hall, D. Pinner, and J. T. Ruderman, *Prospects and Blind Spots for Neutralino Dark Matter*, *JHEP* **05** (2013) 100, [arXiv:1211.4873 \[hep-ph\]](#).
- [162] P. Huang and C. E. M. Wagner, *Blind Spots for neutralino Dark Matter in the MSSM with an intermediate m_A* , *Phys. Rev.* **D90** (2014) no. 1, 015018, [arXiv:1404.0392 \[hep-ph\]](#).
- [163] T. Han, F. Kling, S. Su, and Y. Wu, *Unblinding the dark matter blind spots*, *JHEP* **02** (2017) 057, [arXiv:1612.02387 \[hep-ph\]](#).
- [164] R. Mahbubani and L. Senatore, *The Minimal model for dark matter and unification*, *Phys. Rev.* **D73** (2006) 043510, [arXiv:hep-ph/0510064 \[hep-ph\]](#).
- [165] T. Cohen, J. Kearney, A. Pierce, and D. Tucker-Smith, *Singlet-Doublet Dark Matter*, *Phys. Rev.* **D85** (2012) 075003, [arXiv:1109.2604 \[hep-ph\]](#).

- [166] A. Dedes and D. Karamitros, *Doublet-Triplet Fermionic Dark Matter*, Phys. Rev. **D89** (2014) no. 11, 115002, [arXiv:1403.7744 \[hep-ph\]](https://arxiv.org/abs/1403.7744).
- [167] A. Basirnia, S. Macaluso, and D. Shih, *Dark Matter and the Higgs in Natural SUSY*, JHEP **03** (2017) 073, [arXiv:1605.08442 \[hep-ph\]](https://arxiv.org/abs/1605.08442).
- [168] J. Elias-Miró, C. Grojean, R. S. Gupta, and D. Marzocca, *Scaling and tuning of EW and Higgs observables*, JHEP **05** (2014) 019, [arXiv:1312.2928 \[hep-ph\]](https://arxiv.org/abs/1312.2928).
- [169] K. Harigaya, K. Ichikawa, A. Kundu, S. Matsumoto, and S. Shirai, *Indirect Probe of Electroweak-Interacting Particles at Future Lepton Colliders*, JHEP **09** (2015) 105, [arXiv:1504.03402 \[hep-ph\]](https://arxiv.org/abs/1504.03402).
- [170] J. D. Wells and Z. Zhang, *Status and prospects of precision analyses with $e^+e^- \rightarrow W^+W^-$* , Phys. Rev. **D93** (2016) no. 3, 034001, [arXiv:1507.01594 \[hep-ph\]](https://arxiv.org/abs/1507.01594). [Phys. Rev.D93,034001(2016)].
- [171] M. Drees, K. Hagiwara, and A. Yamada, *Process independent radiative corrections in the minimal supersymmetric standard model*, Phys. Rev. **D45** (1992) 1725–1743.
- [172] S. P. Martin, K. Tobe, and J. D. Wells, *Virtual effects of light gauginos and higgsinos: A Precision electroweak analysis of split supersymmetry*, Phys. Rev. **D71** (2005) 073014, [arXiv:hep-ph/0412424 \[hep-ph\]](https://arxiv.org/abs/hep-ph/0412424).
- [173] A. Joglekar, P. Schwaller, and C. E. M. Wagner, *Dark Matter and Enhanced Higgs to Di-photon Rate from Vector-like Leptons*, JHEP **12** (2012) 064, [arXiv:1207.4235 \[hep-ph\]](https://arxiv.org/abs/1207.4235).
- [174] N. Arkani-Hamed, K. Blum, R. T. D’Agnolo, and J. Fan, *2:1 for Naturalness at the LHC?*, JHEP **01** (2013) 149, [arXiv:1207.4482 \[hep-ph\]](https://arxiv.org/abs/1207.4482).
- [175] C. Englert and M. McCullough, *Modified Higgs Sectors and NLO Associated Production*, JHEP **07** (2013) 168, [arXiv:1303.1526 \[hep-ph\]](https://arxiv.org/abs/1303.1526).
- [176] R. K. Barman, G. Belanger, B. Bhattacherjee, R. Godbole, G. Mendiratta, and D. Sengupta, *Invisible decay of the Higgs boson in the context of a thermal and nonthermal relic in MSSM*, Phys. Rev. **D95** (2017) no. 9, 095018, [arXiv:1703.03838 \[hep-ph\]](https://arxiv.org/abs/1703.03838).
- [177] LUX, LZ Collaboration, M. Szydagis, *The Present and Future of Searching for Dark Matter with LUX and LZ*, PoS **ICHEP2016** (2016) 220, [arXiv:1611.05525 \[astro-ph.CO\]](https://arxiv.org/abs/1611.05525).
- [178] XENON Collaboration, E. Aprile et al., *Physics reach of the XENON1T dark matter experiment*, JCAP **1604** (2016) no. 04, 027, [arXiv:1512.07501 \[physics.ins-det\]](https://arxiv.org/abs/1512.07501).
- [179] A. De Simone, G. F. Giudice, and A. Strumia, *Benchmarks for Dark Matter Searches at the LHC*, JHEP **06** (2014) 081, [arXiv:1402.6287 \[hep-ph\]](https://arxiv.org/abs/1402.6287).

- [180] A. Beniwal, F. Rajec, C. Savage, P. Scott, C. Weniger, M. White, and A. G. Williams, *Combined analysis of effective Higgs portal dark matter models*, *Phys. Rev.* **D93** (2016) no. 11, 115016, [arXiv:1512.06458 \[hep-ph\]](https://arxiv.org/abs/1512.06458).
- [181] XENON Collaboration, E. Aprile et al., *Dark Matter Search Results from a One Tonne×Year Exposure of XENON1T*, [arXiv:1805.12562 \[astro-ph.CO\]](https://arxiv.org/abs/1805.12562).
- [182] J. Billard, L. Strigari, and E. Figueroa-Feliciano, *Implication of neutrino backgrounds on the reach of next generation dark matter direct detection experiments*, *Phys. Rev.* **D89** (2014) no. 2, 023524, [arXiv:1307.5458 \[hep-ph\]](https://arxiv.org/abs/1307.5458).
- [183] PANDA-X Collaboration, H. Zhang et al., *Dark matter direct search sensitivity of the PandaX-4T experiment*, [arXiv:1806.02229 \[physics.ins-det\]](https://arxiv.org/abs/1806.02229).
- [184] LZ Collaboration, D. S. Akerib et al., *LUX-ZEPLIN (LZ) Conceptual Design Report*, [arXiv:1509.02910 \[physics.ins-det\]](https://arxiv.org/abs/1509.02910).
- [185] J. Liu, X. Chen, and X. Ji, *Current status of direct dark matter detection experiments*, *Nature Phys.* **13** (2017) no. 3, 212–216, [arXiv:1709.00688 \[astro-ph.CO\]](https://arxiv.org/abs/1709.00688).
- [186] CMS Collaboration, C. Collaboration, *Search for invisible decays of the Higgs boson produced through vector boson fusion at $\sqrt{s} = 13$ TeV*, .
- [187] *Projections for measurements of Higgs boson signal strengths and coupling parameters with the ATLAS detector at a HL-LHC*, ATL-PHYS-PUB-2014-016, CERN, Geneva, Oct, 2014. <http://cds.cern.ch/record/1956710>.
- [188] C. Bernaciak, T. Plehn, P. Schichtel, and J. Tattersall, *Spying an invisible Higgs boson*, *Phys. Rev.* **D91** (2015) 035024, [arXiv:1411.7699 \[hep-ph\]](https://arxiv.org/abs/1411.7699).
- [189] D. Curtin, R. Essig, S. Gori, and J. Shelton, *Illuminating Dark Photons with High-Energy Colliders*, *JHEP* **02** (2015) 157, [arXiv:1412.0018 \[hep-ph\]](https://arxiv.org/abs/1412.0018).
- [190] M. Karliner, M. Low, J. L. Rosner, and L.-T. Wang, *Radiative return capabilities of a high-energy, high-luminosity e^+e^- collider*, *Phys. Rev.* **D92** (2015) no. 3, 035010, [arXiv:1503.07209 \[hep-ph\]](https://arxiv.org/abs/1503.07209).
- [191] ILC Collaboration, G. Aarons et al., *International Linear Collider Reference Design Report Volume 2: Physics at the ILC*, [arXiv:0709.1893 \[hep-ph\]](https://arxiv.org/abs/0709.1893).
- [192] L.-B. Jia, *Study of WIMP annihilations into a pair of on-shell scalar mediators*, *Phys. Rev.* **D94** (2016) no. 9, 095028, [arXiv:1607.00737 \[hep-ph\]](https://arxiv.org/abs/1607.00737).
- [193] L3 Collaboration, M. Acciarri et al., *Missing mass spectra in hadronic events from $e+e-$ collisions at $s^{**}(1/2) = 161\text{-GeV} - 172\text{-GeV}$ and limits on invisible Higgs decay*, *Phys. Lett.* **B418** (1998) 389–398.
- [194] DELPHI Collaboration, P. Abreu et al., *A Search for invisible Higgs bosons produced in $e+e-$ interactions at LEP-2 energies*, *Phys. Lett.* **B459** (1999) 367–381.

- [195] OPAL, DELPHI, LEP Higgs Working for Higgs boson searches, L3 CERN, ALEPH Collaboration, *Searches for invisible Higgs bosons: Preliminary combined results using LEP data collected at energies up to 209-GeV*, in *Lepton and photon interactions at high energies. Proceedings, 20th International Symposium, LP 2001, Rome, Italy, July 23-28, 2001.* 2001.
arXiv:hep-ex/0107032 [hep-ex].
https://inspirehep.net/record/559835/files/arXiv:hep-ex_0107032.pdf.
- [196] B. Batell, N. Lange, D. McKeen, M. Pospelov, and A. Ritz, *Muon anomalous magnetic moment through the leptonic Higgs portal*, Phys. Rev. **D95** (2017) no. 7, 075003, arXiv:1606.04943 [hep-ph].
- [197] T. Liu and C. T. Potter, *Exotic Higgs Decay $h \rightarrow a_1 a_1$ at the International Linear Collider: a Snowmass White Paper*, in *Proceedings, 2013 Community Summer Study on the Future of U.S. Particle Physics: Snowmass on the Mississippi (CSS2013): Minneapolis, MN, USA, July 29-August 6, 2013.* 2013.
arXiv:1309.0021 [hep-ph].
<https://inspirehep.net/record/1252062/files/arXiv:1309.0021.pdf>.
- [198] J. Kile, A. Kobach, and A. Soni, *Lepton-Flavored Dark Matter*, Phys. Lett. **B744** (2015) 330–338, arXiv:1411.1407 [hep-ph].
- [199] J. Huang, T. Liu, L.-T. Wang, and F. Yu, *Supersymmetric Exotic Decays of the 125 GeV Higgs Boson*, Phys. Rev. Lett. **112** (2014) no. 22, 221803, arXiv:1309.6633 [hep-ph].
- [200] E. Gabrielli, B. Mele, M. Raidal, and E. Venturini, *FCNC decays of standard model fermions into a dark photon*, Phys. Rev. **D94** (2016) no. 11, 115013, arXiv:1607.05928 [hep-ph].
- [201] Q.-H. Cao, Y. Li, B. Yan, Y. Zhang, and Z. Zhang, *Probing dark particles indirectly at the CEPC*, Nucl. Phys. **B909** (2016) 197–217, arXiv:1604.07536 [hep-ph].
- [202] P. Agrawal, S. Blanchet, Z. Chacko, and C. Kilic, *Flavored Dark Matter, and Its Implications for Direct Detection and Colliders*, Phys. Rev. **D86** (2012) 055002, arXiv:1109.3516 [hep-ph].
- [203] P. Agrawal, Z. Chacko, E. C. F. S. Fortes, and C. Kilic, *Skew-Flavored Dark Matter*, Phys. Rev. **D93** (2016) no. 10, 103510, arXiv:1511.06293 [hep-ph].
- [204] A. Birkedal, K. Matchev, and M. Perelstein, *Dark matter at colliders: A Model independent approach*, Phys. Rev. **D70** (2004) 077701, arXiv:hep-ph/0403004 [hep-ph].
- [205] Y. J. Chae and M. Perelstein, *Dark Matter Search at a Linear Collider: Effective Operator Approach*, JHEP **05** (2013) 138, arXiv:1211.4008 [hep-ph].

- [206] H. Dreiner, M. Huck, M. Krämer, D. Schmeier, and J. Tattersall, *Illuminating Dark Matter at the ILC*, Phys. Rev. **D87** (2013) no. 7, 075015, arXiv:1211.2254 [hep-ph].
- [207] Z.-H. Yu, Q.-S. Yan, and P.-F. Yin, *Detecting interactions between dark matter and photons at high energy e^+e^- colliders*, Phys. Rev. **D88** (2013) no. 7, 075015, arXiv:1307.5740 [hep-ph].
- [208] Z.-H. Yu, X.-J. Bi, Q.-S. Yan, and P.-F. Yin, *Dark matter searches in the mono-Z channel at high energy e^+e^- colliders*, Phys. Rev. **D90** (2014) no. 5, 055010, arXiv:1404.6990 [hep-ph].
- [209] Y. Gao and M. Jin, *Z-pole test of effective dark matter diboson interactions at the CEPC*, arXiv:1712.02140 [hep-ph].
- [210] SuperCDMS Collaboration, R. Agnese et al., *Search for Low-Mass Weakly Interacting Massive Particles with SuperCDMS*, Phys. Rev. Lett. **112** (2014) no. 24, 241302, arXiv:1402.7137 [hep-ex].
- [211] CDEX Collaboration, H. Jiang et al., *Limits on Light Weakly Interacting Massive Particles from the First 102.8 kg × day Data of the CDEX-10 Experiment*, Phys. Rev. Lett. **120** (2018) no. 24, 241301, arXiv:1802.09016 [hep-ex].
- [212] SuperCDMS Collaboration, R. Agnese et al., *New Results from the Search for Low-Mass Weakly Interacting Massive Particles with the CDMS Low Ionization Threshold Experiment*, Phys. Rev. Lett. **116** (2016) no. 7, 071301, arXiv:1509.02448 [astro-ph.CO].
- [213] Fermi-LAT Collaboration, M. Ackermann et al., *Updated search for spectral lines from Galactic dark matter interactions with pass 8 data from the Fermi Large Area Telescope*, Phys. Rev. **D91** (2015) no. 12, 122002, arXiv:1506.00013 [astro-ph.HE].
- [214] M. T. Frandsen, U. Haisch, F. Kahlhoefer, P. Mertsch, and K. Schmidt-Hoberg, *Loop-induced dark matter direct detection signals from gamma-ray lines*, JCAP **1210** (2012) 033, arXiv:1207.3971 [hep-ph].
- [215] SNO Collaboration, Q. R. Ahmad et al., *Direct evidence for neutrino flavor transformation from neutral current interactions in the Sudbury Neutrino Observatory*, Phys. Rev. Lett. **89** (2002) 011301, arXiv:nucl-ex/0204008 [nucl-ex].
- [216] Super-Kamiokande Collaboration, Y. Fukuda et al., *Evidence for oscillation of atmospheric neutrinos*, Phys. Rev. Lett. **81** (1998) 1562–1567, arXiv:hep-ex/9807003 [hep-ex].
- [217] NuFIT 3.2 (2018), <HTTP://WWW.NU-FIT.ORG/>.
- [218] I. Esteban, M. C. Gonzalez-Garcia, M. Maltoni, I. Martinez-Soler, and T. Schwetz, *Updated fit to three neutrino mixing: exploring the accelerator-reactor complementarity*, JHEP **01** (2017) 087, arXiv:1611.01514 [hep-ph].

- [219] M. Lattanzi and M. Gerbino, *Status of neutrino properties and future prospects - Cosmological and astrophysical constraints*, *Front.in Phys.* **5** (2018) 70, [arXiv:1712.07109 \[astro-ph.CO\]](https://arxiv.org/abs/1712.07109).
- [220] E. Majorana, *Teoria simmetrica dell'elettrone e del positrone*, *Nuovo Cim.* **14** (1937) 171–184.
- [221] Y. Cai, T. Han, T. Li, and R. Ruiz, *Lepton-Number Violation: Seesaw Models and Their Collider Tests*, [arXiv:1711.02180 \[hep-ph\]](https://arxiv.org/abs/1711.02180).
- [222] K. N. Abazajian et al., *Light Sterile Neutrinos: A White Paper*, [arXiv:1204.5379 \[hep-ph\]](https://arxiv.org/abs/1204.5379).
- [223] M. Drewes, *The Phenomenology of Right Handed Neutrinos*, *Int. J. Mod. Phys. E* **22** (2013) 1330019, [arXiv:1303.6912 \[hep-ph\]](https://arxiv.org/abs/1303.6912).
- [224] E. Ma, *Pathways to naturally small neutrino masses*, *Phys. Rev. Lett.* **81** (1998) 1171–1174, [arXiv:hep-ph/9805219 \[hep-ph\]](https://arxiv.org/abs/hep-ph/9805219).
- [225] S. L. Glashow, *The Future of Elementary Particle Physics*, *NATO Sci. Ser. B* **61** (1980) 687.
- [226] M. Gell-Mann, P. Ramond, and R. Slansky, *Complex Spinors and Unified Theories*, *Conf. Proc. C* **790927** (1979) 315–321, [arXiv:1306.4669 \[hep-th\]](https://arxiv.org/abs/1306.4669).
- [227] T. Yanagida, *Horizontal Symmetry and Masses of Neutrinos*, *Prog. Theor. Phys.* **64** (1980) 1103.
- [228] J. Schechter and J. W. F. Valle, *Neutrino Masses in $SU(2) \times U(1)$ Theories*, *Phys. Rev.* **D22** (1980) 2227.
- [229] M. Magg and C. Wetterich, *Neutrino Mass Problem and Gauge Hierarchy*, *Phys. Lett.* **94B** (1980) 61–64.
- [230] T. P. Cheng and L.-F. Li, *Neutrino Masses, Mixings and Oscillations in $SU(2) \times U(1)$ Models of Electroweak Interactions*, *Phys. Rev. D* **22** (1980) 2860.
- [231] G. Lazarides, Q. Shafi, and C. Wetterich, *Proton Lifetime and Fermion Masses in an $SO(10)$ Model*, *Nucl. Phys.* **B181** (1981) 287–300.
- [232] R. N. Mohapatra and G. Senjanovic, *Neutrino Masses and Mixings in Gauge Models with Spontaneous Parity Violation*, *Phys. Rev. D* **23** (1981) 165.
- [233] R. Foot, H. Lew, X. G. He, and G. C. Joshi, *Seesaw Neutrino Masses Induced by a Triplet of Leptons*, *Z. Phys.* **C44** (1989) 441.
- [234] C. D. Froggatt and H. B. Nielsen, *Hierarchy of Quark Masses, Cabibbo Angles and CP Violation*, *Nucl. Phys.* **B147** (1979) 277–298.
- [235] A. Zee, *A Theory of Lepton Number Violation, Neutrino Majorana Mass, and Oscillation*, *Phys. Lett.* **93B** (1980) 389. [Erratum: *Phys. Lett.* **95B**, 461 (1980)].
- [236] E. Witten, *Neutrino Masses in the Minimal $O(10)$ Theory*, *Phys. Lett.* **91B** (1980) 81–84.

- [237] A. Zee, *Quantum Numbers of Majorana Neutrino Masses*, *Nucl. Phys.* **B264** (1986) 99–110.
- [238] K. S. Babu, *Model of 'Calculable' Majorana Neutrino Masses*, *Phys. Lett.* **B203** (1988) 132–136.
- [239] E. Ma, *Verifiable radiative seesaw mechanism of neutrino mass and dark matter*, *Phys. Rev.* **D73** (2006) 077301, [arXiv:hep-ph/0601225](https://arxiv.org/abs/hep-ph/0601225) [hep-ph].
- [240] M. Shaposhnikov, *A Possible symmetry of the nuMSM*, *Nucl. Phys.* **B763** (2007) 49–59, [arXiv:hep-ph/0605047](https://arxiv.org/abs/hep-ph/0605047) [hep-ph].
- [241] *Right-Handed Neutrinos at CERN LHC and the Mechanism of Neutrino Mass Generation*, *Phys. Rev.* **D76** (2007) 073005, [arXiv:0705.3221](https://arxiv.org/abs/0705.3221) [hep-ph].
- [242] K. Moffat, S. Pascoli, and C. Weiland, *Equivalence between massless neutrinos and lepton number conservation in fermionic singlet extensions of the Standard Model*, [arXiv:1712.07611](https://arxiv.org/abs/1712.07611) [hep-ph].
- [243] R. N. Mohapatra, *Mechanism for Understanding Small Neutrino Mass in Superstring Theories*, *Phys. Rev. Lett.* **56** (1986) 561–563.
- [244] R. N. Mohapatra and J. W. F. Valle, *Neutrino Mass and Baryon Number Nonconservation in Superstring Models*, *Phys. Rev.* **D34** (1986) 1642.
- [245] J. Bernabeu, A. Santamaria, J. Vidal, A. Mendez, and J. W. F. Valle, *Lepton Flavor Nonconservation at High-Energies in a Superstring Inspired Standard Model*, *Phys. Lett.* **B187** (1987) 303–308.
- [246] E. K. Akhmedov, M. Lindner, E. Schnapka, and J. W. F. Valle, *Left-right symmetry breaking in NJL approach*, *Phys. Lett.* **B368** (1996) 270–280, [arXiv:hep-ph/9507275](https://arxiv.org/abs/hep-ph/9507275) [hep-ph].
- [247] E. K. Akhmedov, M. Lindner, E. Schnapka, and J. W. F. Valle, *Dynamical left-right symmetry breaking*, *Phys. Rev.* **D53** (1996) 2752–2780, [arXiv:hep-ph/9509255](https://arxiv.org/abs/hep-ph/9509255) [hep-ph].
- [248] T. Asaka, S. Blanchet, and M. Shaposhnikov, *The nuMSM, dark matter and neutrino masses*, *Phys. Lett.* **B631** (2005) 151–156, [arXiv:hep-ph/0503065](https://arxiv.org/abs/hep-ph/0503065) [hep-ph].
- [249] T. Asaka and M. Shaposhnikov, *The nuMSM, dark matter and baryon asymmetry of the universe*, *Phys. Lett.* **B620** (2005) 17–26, [arXiv:hep-ph/0505013](https://arxiv.org/abs/hep-ph/0505013) [hep-ph].
- [250] V. V. Khoze and G. Ro, *Leptogenesis and Neutrino Oscillations in the Classically Conformal Standard Model with the Higgs Portal*, *JHEP* **10** (2013) 075, [arXiv:1307.3764](https://arxiv.org/abs/1307.3764) [hep-ph].
- [251] B. Bajc and G. Senjanovic, *Seesaw at LHC*, *JHEP* **08** (2007) 014, [arXiv:hep-ph/0612029](https://arxiv.org/abs/hep-ph/0612029) [hep-ph].
- [252] B. Bajc, M. Nemevsek, and G. Senjanovic, *Probing seesaw at LHC*, *Phys. Rev.* **D76** (2007) 055011, [arXiv:hep-ph/0703080](https://arxiv.org/abs/hep-ph/0703080) [hep-ph].

- [253] F. del Aguila, J. A. Aguilar-Saavedra, A. Martinez de la Ossa, and D. Meloni, *Flavor and polarisation in heavy neutrino production at e+ e- colliders*, *Phys. Lett.* **B613** (2005) 170–180, [arXiv:hep-ph/0502189 \[hep-ph\]](https://arxiv.org/abs/hep-ph/0502189).
- [254] T. Saito, M. Asano, K. Fujii, N. Haba, S. Matsumoto, T. Nabeshima, Y. Takubo, H. Yamamoto, and K. Yoshioka, *Extra dimensions and Seesaw Neutrinos at the International Linear Collider*, *Phys. Rev.* **D82** (2010) 093004, [arXiv:1008.2257 \[hep-ph\]](https://arxiv.org/abs/1008.2257).
- [255] A. Das and N. Okada, *Inverse seesaw neutrino signatures at the LHC and ILC*, *Phys. Rev.* **D88** (2013) 113001, [arXiv:1207.3734 \[hep-ph\]](https://arxiv.org/abs/1207.3734).
- [256] S. Banerjee, P. S. B. Dev, A. Ibarra, T. Mandal, and M. Mitra, *Prospects of Heavy Neutrino Searches at Future Lepton Colliders*, *Phys. Rev.* **D92** (2015) 075002, [arXiv:1503.05491 \[hep-ph\]](https://arxiv.org/abs/1503.05491).
- [257] W. Liao and X.-H. Wu, *Signature of heavy sterile neutrinos at CEPC*, *Phys. Rev.* **D97** (2018) no. 5, 055005, [arXiv:1710.09266 \[hep-ph\]](https://arxiv.org/abs/1710.09266).
- [258] G. Anamiati, M. Hirsch, and E. Nardi, *Quasi-Dirac neutrinos at the LHC*, *JHEP* **10** (2016) 010, [arXiv:1607.05641 \[hep-ph\]](https://arxiv.org/abs/1607.05641).
- [259] S. Antusch, E. Cazzato, and O. Fischer, *Heavy neutrino-antineutrino oscillations at colliders*, [arXiv:1709.03797 \[hep-ph\]](https://arxiv.org/abs/1709.03797).
- [260] S. Antusch, E. Cazzato, M. Drewes, O. Fischer, B. Garbrecht, D. Gueter, and J. Klaric, *Probing Leptogenesis at Future Colliders*, [arXiv:1710.03744 \[hep-ph\]](https://arxiv.org/abs/1710.03744).
- [261] E. J. Chun, K. Y. Lee, and S. C. Park, *Testing Higgs triplet model and neutrino mass patterns*, *Phys. Lett.* **B566** (2003) 142–151, [arXiv:hep-ph/0304069 \[hep-ph\]](https://arxiv.org/abs/hep-ph/0304069).
- [262] J. Garayoa and T. Schwetz, *Neutrino mass hierarchy and Majorana CP phases within the Higgs triplet model at the LHC*, *JHEP* **03** (2008) 009, [arXiv:0712.1453 \[hep-ph\]](https://arxiv.org/abs/0712.1453).
- [263] M. L. Swartz, *Limits on Doubly Charged Higgs Bosons and Lepton Flavor Violation*, *Phys. Rev.* **D40** (1989) 1521.
- [264] P. Fileviez Perez, T. Han, G.-y. Huang, T. Li, and K. Wang, *Neutrino Masses and the CERN LHC: Testing Type II Seesaw*, *Phys. Rev.* **D78** (2008) 015018, [arXiv:0805.3536 \[hep-ph\]](https://arxiv.org/abs/0805.3536).
- [265] A. Melfo, M. Nemevsek, F. Nesti, G. Senjanovic, and Y. Zhang, *Type II Seesaw at LHC: The Roadmap*, *Phys. Rev.* **D85** (2012) 055018, [arXiv:1108.4416 \[hep-ph\]](https://arxiv.org/abs/1108.4416).
- [266] ATLAS Collaboration, M. Aaboud et al., *Search for doubly charged Higgs boson production in multi-lepton final states with the ATLAS detector using proton-proton collisions at $\sqrt{s} = 13 \text{ TeV}$* , *Eur. Phys. J.* **C78** (2018) no. 3, 199, [arXiv:1710.09748 \[hep-ex\]](https://arxiv.org/abs/1710.09748).

- [267] M. Mitra, S. Niyogi, and M. Spannowsky, *Type-II Seesaw Model and Multilepton Signatures at Hadron Colliders*, *Phys. Rev.* **D95** (2017) no. 3, 035042, [arXiv:1611.09594 \[hep-ph\]](https://arxiv.org/abs/1611.09594).
- [268] S. Kanemura, M. Kikuchi, K. Yagyu, and H. Yokoya, *Bounds on the mass of doubly-charged Higgs bosons in the same-sign diboson decay scenario*, *Phys. Rev.* **D90** (2014) no. 11, 115018, [arXiv:1407.6547 \[hep-ph\]](https://arxiv.org/abs/1407.6547).
- [269] M. Aoki, S. Kanemura, and K. Yagyu, *Testing the Higgs triplet model with the mass difference at the LHC*, *Phys. Rev.* **D85** (2012) 055007, [arXiv:1110.4625 \[hep-ph\]](https://arxiv.org/abs/1110.4625).
- [270] Z.-L. Han, R. Ding, and Y. Liao, *LHC phenomenology of the type II seesaw mechanism: Observability of neutral scalars in the nondegenerate case*, *Phys. Rev.* **D92** (2015) no. 3, 033014, [arXiv:1506.08996 \[hep-ph\]](https://arxiv.org/abs/1506.08996).
- [271] P. Agrawal, M. Mitra, S. Niyogi, S. Shil, and M. Spannowsky, *Probing the Type-II Seesaw Mechanism through the Production of Higgs Bosons at a Lepton Collider*, [arXiv:1803.00677 \[hep-ph\]](https://arxiv.org/abs/1803.00677).
- [272] T. G. Rizzo, *Doubly Charged Higgs Bosons and Lepton Number Violating Processes*, *Phys. Rev.* **D25** (1982) 1355–1364. [Addendum: *Phys. Rev.* D27,657(1983)].
- [273] M. Lusignoli and S. Petrarca, *EXOTIC HIGGS PRODUCTION AT E+ E-COLLIDERS*, *Phys. Lett.* **B226** (1989) 397–400.
- [274] J. F. Gunion, J. Grifols, A. Mendez, B. Kayser, and F. I. Olness, *Higgs Bosons in Left-Right Symmetric Models*, *Phys. Rev.* **D40** (1989) 1546.
- [275] S. Atag and K. O. Ozansoy, *Realistic constraints on the doubly charged bilepton couplings from Bhabha scattering with LEP data*, *Phys. Rev.* **D68** (2003) 093008, [arXiv:hep-ph/0310046 \[hep-ph\]](https://arxiv.org/abs/hep-ph/0310046).
- [276] V. D. Barger, J. F. Beacom, K.-m. Cheung, and T. Han, *Production of weak bosons and Higgs bosons in e- e- collisions*, *Phys. Rev.* **D50** (1994) 6704–6712, [arXiv:hep-ph/9404335 \[hep-ph\]](https://arxiv.org/abs/hep-ph/9404335).
- [277] W. Rodejohann and H. Zhang, *Higgs triplets at like-sign linear colliders and neutrino mixing*, *Phys. Rev.* **D83** (2011) 073005, [arXiv:1011.3606 \[hep-ph\]](https://arxiv.org/abs/1011.3606).
- [278] J. C. Pati and A. Salam, *Lepton Number as the Fourth Color*, *Phys. Rev.* **D10** (1974) 275–289. [Erratum: *Phys. Rev.* D11,703(1975)].
- [279] R. N. Mohapatra and J. C. Pati, *Left-Right Gauge Symmetry and an Isoconjugate Model of CP Violation*, *Phys. Rev.* **D11** (1975) 566–571.
- [280] G. Senjanovic and R. N. Mohapatra, *Exact Left-Right Symmetry and Spontaneous Violation of Parity*, *Phys. Rev.* **D12** (1975) 1502.
- [281] G. Senjanovic, *Spontaneous Breakdown of Parity in a Class of Gauge Theories*, *Nucl. Phys.* **B153** (1979) 334–364.

- [282] A. Maiezza, M. Nemevsek, and F. Nesti, *Lepton Number Violation in Higgs Decay at LHC*, Phys. Rev. Lett. **115** (2015) 081802, arXiv:1503.06834 [hep-ph].
- [283] M. Nemevsek, F. Nesti, and J. C. Vasquez, *Majorana Higgses at colliders*, JHEP **04** (2017) 114, arXiv:1612.06840 [hep-ph].
- [284] F. del Aguila and J. A. Aguilar-Saavedra, *Distinguishing seesaw models at LHC with multi-lepton signals*, Nucl. Phys. **B813** (2009) 22–90, arXiv:0808.2468 [hep-ph].
- [285] A. Abada, V. De Romeri, S. Monteil, J. Orloff, and A. M. Teixeira, *Indirect searches for sterile neutrinos at a high-luminosity Z-factory*, JHEP **04** (2015) 051, arXiv:1412.6322 [hep-ph].
- [286] S. Antusch, E. Cazzato, and O. Fischer, *Sterile neutrino searches at future e^-e^+ , pp , and e^-p colliders*, Int. J. Mod. Phys. **A32** (2017) no. 14, 1750078, arXiv:1612.02728 [hep-ph].
- [287] S. Banerjee, B. Bhattacherjee, M. Mitra, and M. Spannowsky, *The Lepton Flavour Violating Higgs Decays at the HL-LHC and the ILC*, JHEP **07** (2016) 059, arXiv:1603.05952 [hep-ph].
- [288] E. Arganda, M. J. Herrero, X. Marcano, and C. Weiland, *Imprints of massive inverse seesaw model neutrinos in lepton flavor violating Higgs boson decays*, Phys. Rev. **D91** (2015) no. 1, 015001, arXiv:1405.4300 [hep-ph].
- [289] *Charged lepton flavor violating Higgs decays at the CEPC*, arXiv:1711.07243 [hep-ph].
- [290] Particle Data Group Collaboration, C. Patrignani et al., *Review of Particle Physics*, Chin. Phys. **C40** (2016) no. 10, 100001.
- [291] S. Antusch and O. Fischer, *Non-unitarity of the leptonic mixing matrix: Present bounds and future sensitivities*, JHEP **10** (2014) 094, arXiv:1407.6607 [hep-ph].
- [292] J.-h. Park, *Lepton non-universality at LEP and charged Higgs*, JHEP **10** (2006) 077, arXiv:hep-ph/0607280 [hep-ph].
- [293] P. S. B. Dev, R. N. Mohapatra, and Y. Zhang, *Lepton Flavor Violation Induced by a Neutral Scalar at Future Lepton Colliders*, Phys. Rev. Lett. **120** (2018) no. 22, 221804, arXiv:1711.08430 [hep-ph].
- [294] S. Antusch, E. Cazzato, and O. Fischer, *Higgs production from sterile neutrinos at future lepton colliders*, JHEP **04** (2016) 189, arXiv:1512.06035 [hep-ph].
- [295] S. Antusch, E. Cazzato, and O. Fischer, *Higgs production through sterile neutrinos*, Int. J. Mod. Phys. **A31** (2016) no. 33, 1644007. [93(2017)].
- [296] S. Antusch and O. Fischer, *Testing sterile neutrino extensions of the Standard Model at future lepton colliders*, JHEP **05** (2015) 053, arXiv:1502.05915 [hep-ph].

- [297] *Combining experimental and cosmological constraints on heavy neutrinos*, *Nucl. Phys.* **B921** (2017) 250–315, [arXiv:1502.00477 \[hep-ph\]](#).
- [298] E. Accomando, L. Delle Rose, S. Moretti, E. Olaiya, and C. H. Shepherd-Themistocleous, *Extra Higgs boson and Z' as portals to signatures of heavy neutrinos at the LHC*, *JHEP* **02** (2018) 109, [arXiv:1708.03650 \[hep-ph\]](#).
- [299] F. F. Deppisch, W. Liu, and M. Mitra, *Long-lived Heavy Neutrinos from Higgs Decays*, [arXiv:1804.04075 \[hep-ph\]](#).
- [300] A. G. Akeroyd and S. Moretti, *Enhancement of H to gamma gamma from doubly charged scalars in the Higgs Triplet Model*, *Phys. Rev.* **D86** (2012) 035015, [arXiv:1206.0535 \[hep-ph\]](#).
- [301] P. S. Bhupal Dev, D. K. Ghosh, N. Okada, and I. Saha, *125 GeV Higgs Boson and the Type-II Seesaw Model*, *JHEP* **03** (2013) 150, [arXiv:1301.3453 \[hep-ph\]](#). [Erratum: JHEP05,049(2013)].
- [302] D. Das and A. Santamaria, *Updated scalar sector constraints in the Higgs triplet model*, *Phys. Rev.* **D94** (2016) no. 1, 015015, [arXiv:1604.08099 \[hep-ph\]](#).
- [303] L. Basso, O. Fischer, and J. J. van der Bij, *A singlet-triplet extension for the Higgs search at LEP and LHC*, *EPL* **101** (2013) no. 5, 51004, [arXiv:1212.5560 \[hep-ph\]](#).
- [304] A. Maiezza, M. Nemevsek, and F. Nesti, *Perturbativity and mass scales in the minimal left-right symmetric model*, *Phys. Rev.* **D94** (2016) no. 3, 035008, [arXiv:1603.00360 \[hep-ph\]](#).
- [305] L. J. Dixon and Y. Li, *Bounding the Higgs Boson Width Through Interferometry*, *Phys. Rev. Lett.* **111** (2013) 111802, [arXiv:1305.3854 \[hep-ph\]](#).
- [306] J. Campbell, M. Carena, R. Harnik, and Z. Liu, *Interference in the $gg \rightarrow h \rightarrow \gamma\gamma$ On-Shell Rate and the Higgs Boson Total Width*, *Phys. Rev. Lett.* **119** (2017) no. 18, 181801, [arXiv:1704.08259 \[hep-ph\]](#). [Addendum: *Phys. Rev. Lett.* 119,no.19,199901(2017)].
- [307] *The triple Higgs coupling: A new probe of low-scale seesaw models*, *JHEP* **04** (2017) 038, [arXiv:1612.06403 \[hep-ph\]](#).
- [308] I. Gogoladze, N. Okada, and Q. Shafi, *Higgs Boson Mass Bounds in the Standard Model with Type III and Type I Seesaw*, *Phys. Lett.* **B668** (2008) 121–125, [arXiv:0805.2129 \[hep-ph\]](#).
- [309] B. He, N. Okada, and Q. Shafi, *125 GeV Higgs, type III seesaw and gauge Higgs unification*, *Phys. Lett.* **B716** (2012) 197–202, [arXiv:1205.4038 \[hep-ph\]](#).
- [310] S. Antusch and O. Fischer, *Testing sterile neutrino extensions of the Standard Model at the Circular Electron Positron Collider*, *Int. J. Mod. Phys.* **A30** (2015) no. 23, 1544004.

- [311] S. Antusch and O. Fischer, *Probing the nonunitarity of the leptonic mixing matrix at the CEPC*, *Int. J. Mod. Phys. A* **31** (2016) no. 33, 1644006, [arXiv:1604.00208 \[hep-ph\]](https://arxiv.org/abs/1604.00208). [,83(2017)].
- [312] S. Antusch, E. Cazzato, and O. Fischer, *Displaced vertex searches for sterile neutrinos at future lepton colliders*, *JHEP* **12** (2016) 007, [arXiv:1604.02420 \[hep-ph\]](https://arxiv.org/abs/1604.02420).
- [313] A. Abada, C. Biggio, F. Bonnet, M. B. Gavela, and T. Hambye, *Low energy effects of neutrino masses*, *JHEP* **12** (2007) 061, [arXiv:0707.4058 \[hep-ph\]](https://arxiv.org/abs/0707.4058).
- [314] R. Ruiz, *Lepton Number Violation at Colliders from Kinematically Inaccessible Gauge Bosons*, *Eur. Phys. J.* **C77** (2017) no. 6, 375, [arXiv:1703.04669 \[hep-ph\]](https://arxiv.org/abs/1703.04669).
- [315] S. Antusch, C. Biggio, E. Fernandez-Martinez, M. B. Gavela, and J. Lopez-Pavon, *Unitarity of the Leptonic Mixing Matrix*, *JHEP* **10** (2006) 084, [arXiv:hep-ph/0607020 \[hep-ph\]](https://arxiv.org/abs/hep-ph/0607020).
- [316] F. del Aguila, J. de Blas, and M. Perez-Victoria, *Effects of new leptons in Electroweak Precision Data*, *Phys. Rev.* **D78** (2008) 013010, [arXiv:0803.4008 \[hep-ph\]](https://arxiv.org/abs/0803.4008).
- [317] S. Parke and M. Ross-Lonergan, *Unitarity and the three flavor neutrino mixing matrix*, *Phys. Rev.* **D93** (2016) no. 11, 113009, [arXiv:1508.05095 \[hep-ph\]](https://arxiv.org/abs/1508.05095).
- [318] A. Atre, T. Han, S. Pascoli, and B. Zhang, *The Search for Heavy Majorana Neutrinos*, *JHEP* **05** (2009) 030, [arXiv:0901.3589 \[hep-ph\]](https://arxiv.org/abs/0901.3589).
- [319] *Global Constraints on a Heavy Neutrino*, *Phys. Rev.* **D93** (2016) no. 3, 033005, [arXiv:1511.00683 \[hep-ph\]](https://arxiv.org/abs/1511.00683).
- [320] E. Fernandez-Martinez, J. Hernandez-Garcia, and J. Lopez-Pavon, *Global constraints on heavy neutrino mixing*, *JHEP* **08** (2016) 033, [arXiv:1605.08774 \[hep-ph\]](https://arxiv.org/abs/1605.08774).
- [321] F. J. Escrihuela, D. V. Forero, O. G. Miranda, M. Tortola, and J. W. F. Valle, *On the description of nonunitary neutrino mixing*, *Phys. Rev.* **D92** (2015) no. 5, 053009, [arXiv:1503.08879 \[hep-ph\]](https://arxiv.org/abs/1503.08879). [Erratum: *Phys. Rev.* D93,no.11,119905(2016)].
- [322] J. P. Chou, D. Curtin, and H. J. Lubatti, *New Detectors to Explore the Lifetime Frontier*, *Phys. Lett.* **B767** (2017) 29–36, [arXiv:1606.06298 \[hep-ph\]](https://arxiv.org/abs/1606.06298).
- [323] Mathusla Collaboration, C. Alpigiani, *Ultra Long-Lived Particles with MATHUSLA*, *PoS EPS-HEP2017* (2017) 772.
- [324] F. Kling and S. Trojanowski, *Heavy Neutral Leptons at FASER*, [arXiv:1801.08947 \[hep-ph\]](https://arxiv.org/abs/1801.08947).
- [325] P. S. B. Dev, R. N. Mohapatra, and Y. Zhang, *Long Lived Light Scalars as Probe of Low Scale Seesaw Models*, *Nucl. Phys.* **B923** (2017) 179–221, [arXiv:1703.02471 \[hep-ph\]](https://arxiv.org/abs/1703.02471).

- [326] P. Bhupal Dev, R. N. Mohapatra, and Y. Zhang, *Displaced photon signal from a possible light scalar in minimal left-right seesaw model*, *Phys. Rev.* **D95** (2017) no. 11, 115001, [arXiv:1612.09587 \[hep-ph\]](https://arxiv.org/abs/1612.09587).
- [327] DELPHI Collaboration, P. Abreu et al., *Searches for heavy neutrinos from Z decays*, *Phys. Lett.* **B274** (1992) 230–238.
- [328] DELPHI Collaboration, P. Abreu et al., *Search for neutral heavy leptons produced in Z decays*, *Z. Phys.* **C74** (1997) 57–71. [Erratum: *Z. Phys.* C75, 580(1997)].
- [329] *Probing leptogenesis with GeV-scale sterile neutrinos at LHCb and Belle II*, *Phys. Rev.* **D90** (2014) no. 12, 125005, [arXiv:1404.7114 \[hep-ph\]](https://arxiv.org/abs/1404.7114).
- [330] A. Freitas, *Weakly coupled neutral gauge bosons at future linear colliders*, *Phys. Rev.* **D70** (2004) 015008, [arXiv:hep-ph/0403288 \[hep-ph\]](https://arxiv.org/abs/hep-ph/0403288).
- [331] S. Iso, N. Okada, and Y. Orikasa, *The minimal B-L model naturally realized at TeV scale*, *Phys. Rev.* **D80** (2009) 115007, [arXiv:0909.0128 \[hep-ph\]](https://arxiv.org/abs/0909.0128).
- [332] L. Basso, A. Belyaev, S. Moretti, and G. M. Pruna, *Probing the Z-prime sector of the minimal B-L model at future Linear Colliders in the $e^+ e^- \rightarrow \mu^+ \mu^-$ process*, *JHEP* **10** (2009) 006, [arXiv:0903.4777 \[hep-ph\]](https://arxiv.org/abs/0903.4777).
- [333] S. Bertolini, A. Maiezza, and F. Nesti, *Present and Future K and B Meson Mixing Constraints on TeV Scale Left-Right Symmetry*, *Phys. Rev.* **D89** (2014) no. 9, 095028, [arXiv:1403.7112 \[hep-ph\]](https://arxiv.org/abs/1403.7112).
- [334] A. Maiezza and M. Nemevsek, *Strong P invariance, neutron electric dipole moment, and minimal left-right parity at LHC*, *Phys. Rev.* **D90** (2014) no. 9, 095002, [arXiv:1407.3678 \[hep-ph\]](https://arxiv.org/abs/1407.3678).
- [335] W.-Y. Keung and G. Senjanovic, *Majorana Neutrinos and the Production of the Right-handed Charged Gauge Boson*, *Phys. Rev. Lett.* **50** (1983) 1427.
- [336] M. Nemevsek, F. Nesti, G. Senjanovic, and Y. Zhang, *First Limits on Left-Right Symmetry Scale from LHC Data*, *Phys. Rev.* **D83** (2011) 115014, [arXiv:1103.1627 \[hep-ph\]](https://arxiv.org/abs/1103.1627).
- [337] A. Ferrari, J. Collot, M.-L. Andrieux, B. Belhorma, P. de Saintignon, J.-Y. Hostachy, P. Martin, and M. Wielers, *Sensitivity study for new gauge bosons and right-handed Majorana neutrinos in pp collisions at $s = 14\text{-TeV}$* , *Phys. Rev.* **D62** (2000) 013001.
- [338] M. Mitra, R. Ruiz, D. J. Scott, and M. Spannowsky, *Neutrino Jets from High-Mass W_R Gauge Bosons in TeV-Scale Left-Right Symmetric Models*, *Phys. Rev.* **D94** (2016) no. 9, 095016, [arXiv:1607.03504 \[hep-ph\]](https://arxiv.org/abs/1607.03504).
- [339] O. Mattelaer, M. Mitra, and R. Ruiz, *Automated Neutrino Jet and Top Jet Predictions at Next-to-Leading-Order with Parton Shower Matching in Effective Left-Right Symmetric Models*, [arXiv:1610.08985 \[hep-ph\]](https://arxiv.org/abs/1610.08985).
- [340] G. Cottin, J. C. Helo, and M. Hirsch, *Searches for light sterile neutrinos with multitrack displaced vertices*, *Phys. Rev.* **D97** (2018) no. 5, 055025, [arXiv:1801.02734 \[hep-ph\]](https://arxiv.org/abs/1801.02734).

- [341] M. Nemevsek, F. Nesti, and G. Popara, *Keung-Senjanović process at LHC: from LNV to displaced vertices to invisible decays*, arXiv:1801.05813 [hep-ph].
- [342] M. Fukugita and T. Yanagida, *Baryogenesis Without Grand Unification*, Phys. Lett. **B174** (1986) 45–47.
- [343] V. A. Kuzmin, V. A. Rubakov, and M. E. Shaposhnikov, *On the Anomalous Electroweak Baryon Number Nonconservation in the Early Universe*, Phys. Lett. **B155** (1985) 36.
- [344] L. Canetti, M. Drewes, and M. Shaposhnikov, *Matter and Antimatter in the Universe*, New J. Phys. **14** (2012) 095012, arXiv:1204.4186 [hep-ph].
- [345] A. Sakharov, *Violation of CP Invariance, c Asymmetry, and Baryon Asymmetry of the Universe*, Pisma Zh.Eksp.Teor.Fiz. **5** (1967) 32–35.
- [346] F. F. Deppisch, J. Harz, and M. Hirsch, *Falsifying High-Scale Leptogenesis at the LHC*, Phys. Rev. Lett. **112** (2014) 221601, arXiv:1312.4447 [hep-ph].
- [347] *Falsifying High-Scale Baryogenesis with Neutrinoless Double Beta Decay and Lepton Flavor Violation*, Phys. Rev. **D92** (2015) no. 3, 036005, arXiv:1503.04825 [hep-ph].
- [348] E. J. Chun et al., *Probing Leptogenesis*, Int. J. Mod. Phys. **A33** (2018) no. 05n06, 1842005, arXiv:1711.02865 [hep-ph].
- [349] A. Pilaftsis and T. E. J. Underwood, *Resonant leptogenesis*, Nucl. Phys. **B692** (2004) 303–345, arXiv:hep-ph/0309342 [hep-ph].
- [350] E. K. Akhmedov, V. A. Rubakov, and A. Yu. Smirnov, *Baryogenesis via neutrino oscillations*, Phys. Rev. Lett. **81** (1998) 1359–1362, arXiv:hep-ph/9803255 [hep-ph].
- [351] T. Hambye and D. Teresi, *Higgs doublet decay as the origin of the baryon asymmetry*, Phys. Rev. Lett. **117** (2016) no. 9, 091801, arXiv:1606.00017 [hep-ph].
- [352] M. Drewes et al., *A White Paper on keV Sterile Neutrino Dark Matter*, JCAP **1701** (2017) no. 01, 025, arXiv:1602.04816 [hep-ph].
- [353] *Testable Baryogenesis in Seesaw Models*, JHEP **08** (2016) 157, arXiv:1606.06719 [hep-ph].
- [354] M. Drewes, B. Garbrecht, D. Gueter, and J. Klaric, *Testing the low scale seesaw and leptogenesis*, JHEP **08** (2017) 018, arXiv:1609.09069 [hep-ph].
- [355] C. O. Dib, C. S. Kim, K. Wang, and J. Zhang, *Distinguishing Dirac/Majorana Sterile Neutrinos at the LHC*, Phys. Rev. **D94** (2016) no. 1, 013005, arXiv:1605.01123 [hep-ph].
- [356] L. Canetti, M. Drewes, T. Frossard, and M. Shaposhnikov, *Dark Matter, Baryogenesis and Neutrino Oscillations from Right Handed Neutrinos*, Phys. Rev. **D87** (2013) 093006, arXiv:1208.4607 [hep-ph].

- [357] G. C. Branco, P. M. Ferreira, L. Lavoura, M. N. Rebelo, M. Sher, and J. P. Silva, *Theory and phenomenology of two-Higgs-doublet models*, *Phys. Rept.* **516** (2012) 1–102, [arXiv:1106.0034 \[hep-ph\]](https://arxiv.org/abs/1106.0034).
- [358] ATLAS Collaboration, M. Aaboud et al., *Search for additional heavy neutral Higgs and gauge bosons in the ditau final state produced in 36 fb^{-1} of pp collisions at $\sqrt{s} = 13\text{ TeV}$ with the ATLAS detector*, *JHEP* **01** (2018) 055, [arXiv:1709.07242 \[hep-ex\]](https://arxiv.org/abs/1709.07242).
- [359] CMS Collaboration, C. Collaboration, *Search for additional neutral MSSM Higgs bosons in the di-tau final state in pp collisions at $\sqrt{s} = 13\text{ TeV}$* , .
- [360] ATLAS Collaboration, M. Aaboud et al., *Search for heavy resonances decaying into WW in the $e\nu\mu\nu$ final state in pp collisions at $\sqrt{s} = 13\text{ TeV}$ with the ATLAS detector*, *Eur. Phys. J.* **C78** (2018) no. 1, 24, [arXiv:1710.01123 \[hep-ex\]](https://arxiv.org/abs/1710.01123).
- [361] ATLAS Collaboration, M. Aaboud et al., *Search for heavy ZZ resonances in the $\ell^+\ell^-\ell^+\ell^-$ and $\ell^+\ell^-\nu\bar{\nu}$ final states using proton-proton collisions at $\sqrt{s} = 13\text{ TeV}$ with the ATLAS detector*, [arXiv:1712.06386 \[hep-ex\]](https://arxiv.org/abs/1712.06386).
- [362] CMS Collaboration, C. Collaboration, *Search for a new scalar resonance decaying to a pair of Z bosons in proton-proton collisions at $\sqrt{s} = 13\text{ TeV}$* , .
- [363] ATLAS Collaboration, M. Aaboud et al., *Search for new phenomena in high-mass diphoton final states using 37 fb^{-1} of proton–proton collisions collected at $\sqrt{s} = 13\text{ TeV}$ with the ATLAS detector*, *Phys. Lett.* **B775** (2017) 105–125, [arXiv:1707.04147 \[hep-ex\]](https://arxiv.org/abs/1707.04147).
- [364] ATLAS Collaboration, M. Aaboud et al., *Search for heavy resonances decaying into a W or Z boson and a Higgs boson in final states with leptons and b -jets in 36 fb^{-1} of $\sqrt{s} = 13\text{ TeV}$ pp collisions with the ATLAS detector*, [arXiv:1712.06518 \[hep-ex\]](https://arxiv.org/abs/1712.06518).
- [365] ATLAS Collaboration, T. A. collaboration, *Search for charged Higgs bosons in the $H^\pm \rightarrow tb$ decay channel in pp collisions at $\sqrt{s} = 13\text{ TeV}$ using the ATLAS detector*, .
- [366] ATLAS Collaboration, T. A. collaboration, *Search for charged Higgs bosons in the $\tau + \text{jets}$ final state using 14.7 fb^{-1} of pp collision data recorded at $\sqrt{s}=13\text{ TeV}$ with the ATLAS experiment*, .
- [367] *Beyond Standard Model Higgs boson searches at a High-Luminosity LHC with ATLAS*, ATL-PHYS-PUB-2013-016, CERN, Geneva, Oct, 2013.
<http://cds.cern.ch/record/1611190>.
- [368] CMS Collaboration, C. Collaboration, *2HDM Neutral Higgs Future Analysis Studies*, .
- [369] M. Carena, I. Low, N. R. Shah, and C. E. M. Wagner, *Impersonating the Standard Model Higgs Boson: Alignment without Decoupling*, *JHEP* **04** (2014) 015, [arXiv:1310.2248 \[hep-ph\]](https://arxiv.org/abs/1310.2248).

- [370] P. S. Bhupal Dev and A. Pilaftsis, *Maximally Symmetric Two Higgs Doublet Model with Natural Standard Model Alignment*, *JHEP* **12** (2014) 024, [arXiv:1408.3405 \[hep-ph\]](https://arxiv.org/abs/1408.3405). [Erratum: JHEP11,147(2015)].
- [371] J. Bernon, J. F. Gunion, H. E. Haber, Y. Jiang, and S. Kraml, *Scrutinizing the alignment limit in two-Higgs-doublet models: $m_h=125\text{ GeV}$* , *Phys. Rev.* **D92** (2015) no. 7, 075004, [arXiv:1507.00933 \[hep-ph\]](https://arxiv.org/abs/1507.00933).
- [372] G. P. Lepage, P. B. Mackenzie, and M. E. Peskin, *Expected Precision of Higgs Boson Partial Widths within the Standard Model*, [arXiv:1404.0319 \[hep-ph\]](https://arxiv.org/abs/1404.0319).
- [373] M. Baak et al., *Working Group Report: Precision Study of Electroweak Interactions*, in *Proceedings, 2013 Community Summer Study on the Future of U.S. Particle Physics: Snowmass on the Mississippi (CSS2013): Minneapolis, MN, USA, July 29-August 6, 2013*. 2013. [arXiv:1310.6708 \[hep-ph\]](https://arxiv.org/abs/1310.6708). <http://www.slac.stanford.edu/econf/C1307292/docs/EnergyFrontier/Electroweak-19.pdf>.
- [374] Gfitter Group Collaboration, M. Baak, J. Cúth, J. Haller, A. Hoecker, R. Kogler, K. Mönig, M. Schott, and J. Stelzer, *The global electroweak fit at NNLO and prospects for the LHC and ILC*, *Eur. Phys. J.* **C74** (2014) 3046, [arXiv:1407.3792 \[hep-ph\]](https://arxiv.org/abs/1407.3792).
- [375] Z. Liang, *Z and W Physics at CEPC*, <http://indico.ihep.ac.cn/getFile.py/access?contribId=32&sessionId=2&resId=1&materialId=slides&confId=4338>.
- [376] B. Coleppa, F. Kling, and S. Su, *Constraining Type II 2HDM in Light of LHC Higgs Searches*, *JHEP* **01** (2014) 161, [arXiv:1305.0002 \[hep-ph\]](https://arxiv.org/abs/1305.0002).
- [377] V. Barger, L. L. Everett, H. E. Logan, and G. Shaughnessy, *Scrutinizing the 125 GeV Higgs boson in two Higgs doublet models at the LHC, ILC, and Muon Collider*, *Phys. Rev.* **D88** (2013) no. 11, 115003, [arXiv:1308.0052 \[hep-ph\]](https://arxiv.org/abs/1308.0052).
- [378] G. Belanger, B. Dumont, U. Ellwanger, J. F. Gunion, and S. Kraml, *Global fit to Higgs signal strengths and couplings and implications for extended Higgs sectors*, *Phys. Rev.* **D88** (2013) 075008, [arXiv:1306.2941 \[hep-ph\]](https://arxiv.org/abs/1306.2941).
- [379] P. M. Ferreira, J. F. Gunion, H. E. Haber, and R. Santos, *Probing wrong-sign Yukawa couplings at the LHC and a future linear collider*, *Phys. Rev.* **D89** (2014) no. 11, 115003, [arXiv:1403.4736 \[hep-ph\]](https://arxiv.org/abs/1403.4736).
- [380] X.-F. Han and L. Wang, *Wrong sign Yukawa coupling of 2HDM with a scalar dark matter confronted with dark matter and Higgs data*, [arXiv:1708.06882 \[hep-ph\]](https://arxiv.org/abs/1708.06882).
- [381] S. Kanemura, M. Kikuchi, and K. Yagyu, *Fingerprinting the extended Higgs sector using one-loop corrected Higgs boson couplings and future precision measurements*, *Nucl. Phys.* **B896** (2015) 80–137, [arXiv:1502.07716 \[hep-ph\]](https://arxiv.org/abs/1502.07716).

- [382] S. Kanemura, M. Kikuchi, and K. Yagyu, *Radiative corrections to the Yukawa coupling constants in two Higgs doublet models*, *Phys. Lett.* **B731** (2014) 27–35, [arXiv:1401.0515 \[hep-ph\]](https://arxiv.org/abs/1401.0515).
- [383] S. Kanemura, Y. Okada, E. Senaha, and C. P. Yuan, *Higgs coupling constants as a probe of new physics*, *Phys. Rev.* **D70** (2004) 115002, [arXiv:hep-ph/0408364 \[hep-ph\]](https://arxiv.org/abs/hep-ph/0408364).
- [384] N. Chen, T. Han, S. Su, W. Su, and Y. Wu, *Type-II 2HDM under the Precision Measurements at the Z-pole and a Higgs Factory*, [arXiv:1808.02037 \[hep-ph\]](https://arxiv.org/abs/1808.02037).
- [385] N. Chen, T. Han, S. Su, W. Su, and Y. Wu, *Type-II 2HDM under the Precision Measurements at the Z-pole and a Higgs Factory*, [arXiv:1808.02037 \[hep-ph\]](https://arxiv.org/abs/1808.02037).
- [386] JADE Collaboration, S. Bethke, S. Kluth, C. Pahl, and J. Schieck, *Determination of the Strong Coupling alpha(s) from hadronic Event Shapes with O(alpha**3(s)) and resummed QCD predictions using JADE Data*, *Eur. Phys. J.* **C64** (2009) 351–360, [arXiv:0810.1389 \[hep-ex\]](https://arxiv.org/abs/0810.1389).
- [387] G. Dissertori, A. Gehrmann-De Ridder, T. Gehrmann, E. W. N. Glover, G. Heinrich, G. Luisoni, and H. Stenzel, *Determination of the strong coupling constant using matched NNLO+NLLA predictions for hadronic event shapes in e+e- annihilations*, *JHEP* **08** (2009) 036, [arXiv:0906.3436 \[hep-ph\]](https://arxiv.org/abs/0906.3436).
- [388] G. Dissertori, A. Gehrmann-De Ridder, T. Gehrmann, E. W. N. Glover, G. Heinrich, and H. Stenzel, *Precise determination of the strong coupling constant at NNLO in QCD from the three-jet rate in electron–positron annihilation at LEP*, *Phys. Rev. Lett.* **104** (2010) 072002, [arXiv:0910.4283 \[hep-ph\]](https://arxiv.org/abs/0910.4283).
- [389] OPAL Collaboration, G. Abbiendi et al., *Determination of alpha_s using OPAL hadronic event shapes at $\sqrt{s} = 91 - 209$ GeV and resummed NNLO calculations*, *Eur. Phys. J.* **C71** (2011) 1733, [arXiv:1101.1470 \[hep-ex\]](https://arxiv.org/abs/1101.1470).
- [390] JADE Collaboration, J. Schieck, S. Bethke, S. Kluth, C. Pahl, and Z. Trocsanyi, *Measurement of the strong coupling alpha_S from the three-jet rate in e+e- - annihilation using JADE data*, *Eur. Phys. J.* **C73** (2013) no. 3, 2332, [arXiv:1205.3714 \[hep-ex\]](https://arxiv.org/abs/1205.3714).
- [391] R. A. Davison and B. R. Webber, *Non-Perturbative Contribution to the Thrust Distribution in e+ e- Annihilation*, *Eur. Phys. J.* **C59** (2009) 13–25, [arXiv:0809.3326 \[hep-ph\]](https://arxiv.org/abs/0809.3326).
- [392] R. Abbate, M. Fickinger, A. H. Hoang, V. Mateu, and I. W. Stewart, *Precision Thrust Cumulant Moments at N^3LL* , *Phys. Rev.* **D86** (2012) 094002, [arXiv:1204.5746 \[hep-ph\]](https://arxiv.org/abs/1204.5746).
- [393] T. Gehrmann, G. Luisoni, and P. F. Monni, *Power corrections in the dispersive model for a determination of the strong coupling constant from the thrust distribution*, *Eur. Phys. J.* **C73** (2013) no. 1, 2265, [arXiv:1210.6945 \[hep-ph\]](https://arxiv.org/abs/1210.6945).

- [394] A. H. Hoang, D. W. Kolodrubetz, V. Mateu, and I. W. Stewart, *C-parameter distribution at N^3LL including power corrections*, *Phys. Rev.* **D91** (2015) no. 9, 094017, [arXiv:1411.6633 \[hep-ph\]](https://arxiv.org/abs/1411.6633).
- [395] A. H. Hoang, D. W. Kolodrubetz, V. Mateu, and I. W. Stewart, *Precise determination of α_s from the C-parameter distribution*, *Phys. Rev.* **D91** (2015) no. 9, 094018, [arXiv:1501.04111 \[hep-ph\]](https://arxiv.org/abs/1501.04111).
- [396] T. Becher and M. D. Schwartz, *A precise determination of α_s from LEP thrust data using effective field theory*, *JHEP* **07** (2008) 034, [arXiv:0803.0342 \[hep-ph\]](https://arxiv.org/abs/0803.0342).
- [397] Y.-T. Chien, R. Kelley, M. D. Schwartz, and H. X. Zhu, *Resummation of Jet Mass at Hadron Colliders*, *Phys. Rev.* **D87** (2013) no. 1, 014010, [arXiv:1208.0010 \[hep-ph\]](https://arxiv.org/abs/1208.0010).
- [398] A. Kardos, S. Kluth, G. Somogyi, Z. Tulipánt, and A. Verbytskyi, *Precise determination of $\alpha_S(M_Z)$ from a global fit of energy-energy correlation to NNLO+NNLL predictions*, [arXiv:1804.09146 \[hep-ph\]](https://arxiv.org/abs/1804.09146).
- [399] I. Moult and H. X. Zhu, *Simplicity from Recoil: The Three-Loop Soft Function and Factorization for the Energy-Energy Correlation*, [arXiv:1801.02627 \[hep-ph\]](https://arxiv.org/abs/1801.02627).
- [400] Z. Nagy and Z. Trocsanyi, *Next-to-leading order calculation of four jet observables in electron positron annihilation*, *Phys. Rev.* **D59** (1999) 014020, [arXiv:hep-ph/9806317 \[hep-ph\]](https://arxiv.org/abs/hep-ph/9806317). [Erratum: *Phys. Rev.* **D62**, 099902(2000)].
- [401] OPAL Collaboration, G. Abbiendi et al., *Determination of alpha(s) using jet rates at LEP with the OPAL detector*, *Eur. Phys. J.* **C45** (2006) 547–568, [arXiv:hep-ex/0507047 \[hep-ex\]](https://arxiv.org/abs/hep-ex/0507047).
- [402] A. Gehrmann-De Ridder, T. Gehrmann, E. W. N. Glover, and G. Heinrich, *Second-order QCD corrections to the thrust distribution*, *Phys. Rev. Lett.* **99** (2007) 132002, [arXiv:0707.1285 \[hep-ph\]](https://arxiv.org/abs/0707.1285).
- [403] A. Gehrmann-De Ridder, T. Gehrmann, E. W. N. Glover, and G. Heinrich, *NNLO corrections to event shapes in $e+e-$ annihilation*, *JHEP* **12** (2007) 094, [arXiv:0711.4711 \[hep-ph\]](https://arxiv.org/abs/0711.4711).
- [404] S. Weinzierl, *NNLO corrections to 3-jet observables in electron-positron annihilation*, *Phys. Rev. Lett.* **101** (2008) 162001, [arXiv:0807.3241 \[hep-ph\]](https://arxiv.org/abs/0807.3241).
- [405] V. Del Duca, C. Duhr, A. Kardos, G. Somogyi, and Z. Trócsányi, *Three-Jet Production in Electron-Positron Collisions at Next-to-Next-to-Leading Order Accuracy*, *Phys. Rev. Lett.* **117** (2016) no. 15, 152004, [arXiv:1603.08927 \[hep-ph\]](https://arxiv.org/abs/1603.08927).
- [406] V. Del Duca, C. Duhr, A. Kardos, G. Somogyi, Z. Szőr, Z. Trócsányi, and Z. Tulipánt, *Jet production in the CoLoRFulNNLO method: event shapes in*

- 1 *electron-positron collisions*, Phys. Rev. **D94** (2016) no. 7, 074019,
 2 arXiv:1606.03453 [hep-ph].
- 3 [407] S. Badger, C. Brønnum-Hansen, H. B. Hartanto, and T. Peraro, *First look at
 4 two-loop five-gluon scattering in QCD*, Phys. Rev. Lett. **120** (2018) no. 9, 092001,
 5 arXiv:1712.02229 [hep-ph].
- 6 [408] S. Abreu, F. Febres Cordero, H. Ita, B. Page, and M. Zeng, *Planar Two-Loop
 7 Five-Gluon Amplitudes from Numerical Unitarity*, arXiv:1712.03946
 8 [hep-ph].
- 9 [409] T. Gehrmann, J. M. Henn, and N. A. Lo Presti, *Analytic form of the two-loop
 10 planar five-gluon all-plus-helicity amplitude in QCD*, Phys. Rev. Lett. **116** (2016)
 11 no. 6, 062001, arXiv:1511.05409 [hep-ph]. [Erratum: Phys. Rev.
 12 Lett.116,no.18,189903(2016)].
- 13 [410] C. G. Papadopoulos, D. Tommasini, and C. Wever, *The Pentabox Master Integrals
 14 with the Simplified Differential Equations approach*, JHEP **04** (2016) 078,
 15 arXiv:1511.09404 [hep-ph].
- 16 [411] A. Banfi, H. McAslan, P. F. Monni, and G. Zanderighi, *The two-jet rate in e^+e^- at
 17 next-to-next-to-leading-logarithmic order*, Phys. Rev. Lett. **117** (2016) no. 17,
 18 172001, arXiv:1607.03111 [hep-ph].
- 19 [412] M. Dasgupta and G. P. Salam, *Accounting for coherence in interjet $E(t)$ flow: A
 20 Case study*, JHEP **03** (2002) 017, arXiv:hep-ph/0203009 [hep-ph].
- 21 [413] A. Banfi, G. Marchesini, and G. Smye, *Away from jet energy flow*, JHEP **08** (2002)
 22 006, arXiv:hep-ph/0206076 [hep-ph].
- 23 [414] R. B. Appleby and M. H. Seymour, *Nonglobal logarithms in interjet energy flow
 24 with kt clustering requirement*, JHEP **12** (2002) 063,
 25 arXiv:hep-ph/0211426 [hep-ph].
- 26 [415] M. Rubin, *Non-Global Logarithms in Filtered Jet Algorithms*, JHEP **05** (2010)
 27 005, arXiv:1002.4557 [hep-ph].
- 28 [416] A. Banfi, M. Dasgupta, K. Khelifa-Kerfa, and S. Marzani, *Non-global logarithms
 29 and jet algorithms in high- pT jet shapes*, JHEP **08** (2010) 064,
 30 arXiv:1004.3483 [hep-ph].
- 31 [417] R. Kelley, M. D. Schwartz, and H. X. Zhu, *Resummation of jet mass with and
 32 without a jet veto*, arXiv:1102.0561 [hep-ph].
- 33 [418] A. Hornig, C. Lee, I. W. Stewart, J. R. Walsh, and S. Zuberi, *Non-global Structure
 34 of the $O(\alpha_s^2)$ Dijet Soft Function*, JHEP **08** (2011) 054, arXiv:1105.4628
 35 [hep-ph]. [Erratum: JHEP10,101(2017)].
- 36 [419] A. J. Larkoski and I. Moult, *Nonglobal correlations in collider physics*, Phys. Rev.
 37 **D93** (2016) no. 1, 014012, arXiv:1510.05657 [hep-ph].
- 38 [420] H. Weigert, *Nonglobal jet evolution at finite $N(c)$* , Nucl. Phys. **B685** (2004)
 39 321–350, arXiv:hep-ph/0312050 [hep-ph].

- [421] Y. Hatta and T. Ueda, *Resummation of non-global logarithms at finite N_c* , *Nucl. Phys.* **B874** (2013) 808–820, [arXiv:1304.6930 \[hep-ph\]](https://arxiv.org/abs/1304.6930).
- [422] Y. Hagiwara, Y. Hatta, and T. Ueda, *Hemisphere jet mass distribution at finite N_c* , *Phys. Lett.* **B756** (2016) 254–258, [arXiv:1507.07641 \[hep-ph\]](https://arxiv.org/abs/1507.07641).
- [423] M. D. Schwartz and H. X. Zhu, *Nonglobal logarithms at three loops, four loops, five loops, and beyond*, *Phys. Rev.* **D90** (2014) no. 6, 065004, [arXiv:1403.4949 \[hep-ph\]](https://arxiv.org/abs/1403.4949).
- [424] K. Khelifa-Kerfa and Y. Delenda, *Non-global logarithms at finite N_c beyond leading order*, *JHEP* **03** (2015) 094, [arXiv:1501.00475 \[hep-ph\]](https://arxiv.org/abs/1501.00475).
- [425] S. Caron-Huot, *Resummation of non-global logarithms and the BFKL equation*, *JHEP* **03** (2018) 036, [arXiv:1501.03754 \[hep-ph\]](https://arxiv.org/abs/1501.03754).
- [426] A. J. Larkoski, I. Moult, and D. Neill, *Non-Global Logarithms, Factorization, and the Soft Substructure of Jets*, *JHEP* **09** (2015) 143, [arXiv:1501.04596 \[hep-ph\]](https://arxiv.org/abs/1501.04596).
- [427] T. Becher, M. Neubert, L. Rothen, and D. Y. Shao, *Effective Field Theory for Jet Processes*, *Phys. Rev. Lett.* **116** (2016) no. 19, 192001, [arXiv:1508.06645 \[hep-ph\]](https://arxiv.org/abs/1508.06645).
- [428] D. Neill, *The Edge of Jets and Subleading Non-Global Logs*, [arXiv:1508.07568 \[hep-ph\]](https://arxiv.org/abs/1508.07568).
- [429] T. Becher, M. Neubert, L. Rothen, and D. Y. Shao, *Factorization and Resummation for Jet Processes*, *JHEP* **11** (2016) 019, [arXiv:1605.02737 \[hep-ph\]](https://arxiv.org/abs/1605.02737). [Erratum: JHEP05,154(2017)].
- [430] A. J. Larkoski, I. Moult, and D. Neill, *The Analytic Structure of Non-Global Logarithms: Convergence of the Dressed Gluon Expansion*, *JHEP* **11** (2016) 089, [arXiv:1609.04011 \[hep-ph\]](https://arxiv.org/abs/1609.04011).
- [431] T. Becher, B. D. Pecjak, and D. Y. Shao, *Factorization for the light-jet mass and hemisphere soft function*, *JHEP* **12** (2016) 018, [arXiv:1610.01608 \[hep-ph\]](https://arxiv.org/abs/1610.01608).
- [432] D. Neill, *The Asymptotic Form of Non-Global Logarithms, Black Disc Saturation, and Gluonic Deserts*, *JHEP* **01** (2017) 109, [arXiv:1610.02031 \[hep-ph\]](https://arxiv.org/abs/1610.02031).
- [433] T. Becher, R. Rahn, and D. Y. Shao, *Non-global and rapidity logarithms in narrow jet broadening*, *JHEP* **10** (2017) 030, [arXiv:1708.04516 \[hep-ph\]](https://arxiv.org/abs/1708.04516).
- [434] J. Gao, *Probing light-quark Yukawa couplings via hadronic event shapes at lepton colliders*, [arXiv:1608.01746 \[hep-ph\]](https://arxiv.org/abs/1608.01746).
- [435] LHC Higgs Cross Section Working Group Collaboration, J. R. Andersen et al., *Handbook of LHC Higgs Cross Sections: 3. Higgs Properties*, [arXiv:1307.1347 \[hep-ph\]](https://arxiv.org/abs/1307.1347).
- [436] HFLAV Collaboration, Y. Amhis et al., *Averages of b-hadron, c-hadron, and τ -lepton properties as of summer 2016*, *Eur. Phys. J.* **C77** (2017) no. 12, 895, [arXiv:1612.07233 \[hep-ex\]](https://arxiv.org/abs/1612.07233).

- [437] L. Gladilin, *Fragmentation fractions of c and b quarks into charmed hadrons at LEP*, *Eur. Phys. J.* **C75** (2015) no. 1, 19, [arXiv:1404.3888 \[hep-ex\]](https://arxiv.org/abs/1404.3888).
- [438] M. Lisovyi, A. Verbytskyi, and O. Zenaiev, *Combined analysis of charm-quark fragmentation-fraction measurements*, *Eur. Phys. J.* **C76** (2016) no. 7, 397, [arXiv:1509.01061 \[hep-ex\]](https://arxiv.org/abs/1509.01061).
- [439] C. Bobeth, M. Gorbahn, T. Hermann, M. Misiak, E. Stamou, and M. Steinhauser, $B_{s,d} \rightarrow l^+l^-$ in the Standard Model with Reduced Theoretical Uncertainty, *Phys. Rev. Lett.* **112** (2014) 101801, [arXiv:1311.0903 \[hep-ph\]](https://arxiv.org/abs/1311.0903).
- [440] LHCb Collaboration, R. Aaij et al., *Measurement of the $B_s^0 \rightarrow \mu^+\mu^-$ branching fraction and effective lifetime and search for $B^0 \rightarrow \mu^+\mu^-$ decays*, *Phys. Rev. Lett.* **118** (2017) no. 19, 191801, [arXiv:1703.05747 \[hep-ex\]](https://arxiv.org/abs/1703.05747).
- [441] CDF Collaboration, T. Aaltonen et al., *Search for the Decays $B_s^0 \rightarrow e^+\mu^-$ and $B_s^0 \rightarrow e^+e^-$ in CDF Run II*, *Phys. Rev. Lett.* **102** (2009) 201801, [arXiv:0901.3803 \[hep-ex\]](https://arxiv.org/abs/0901.3803).
- [442] J. Albrecht, F. Bernlochner, M. Kenzie, S. Reichert, D. Straub, and A. Tully, *Future prospects for exploring present day anomalies in flavour physics measurements with Belle II and LHCb*, [arXiv:1709.10308 \[hep-ph\]](https://arxiv.org/abs/1709.10308).
- [443] L3 Collaboration, M. Acciarri et al., *Search for neutral B meson decays to two charged leptons*, *Phys. Lett.* **B391** (1997) 474–480.
- [444] BaBar Collaboration, B. Aubert et al., *A search for the rare decay $B^0 \rightarrow \tau^+\tau^-$ at BABAR*, *Phys. Rev. Lett.* **96** (2006) 241802, [arXiv:hep-ex/0511015 \[hep-ex\]](https://arxiv.org/abs/hep-ex/0511015).
- [445] LHCb Collaboration, R. Aaij et al., *Search for the decays $B_s^0 \rightarrow \tau^+\tau^-$ and $B^0 \rightarrow \tau^+\tau^-$* , *Phys. Rev. Lett.* **118** (2017) no. 25, 251802, [arXiv:1703.02508 \[hep-ex\]](https://arxiv.org/abs/1703.02508).
- [446] E. Kou et al., *The Belle II Physics Book*, 2018.
<http://inspirehep.net/record/1117445/files/arXiv:1206.1230.pdf>.
- [447] LHCb Collaboration, R. Aaij et al., *Test of lepton universality using $B^+ \rightarrow K^+\ell^+\ell^-$ decays*, *Phys. Rev. Lett.* **113** (2014) 151601, [arXiv:1406.6482 \[hep-ex\]](https://arxiv.org/abs/1406.6482).
- [448] LHCb Collaboration, R. Aaij et al., *Test of lepton universality with $B^0 \rightarrow K^{*0}\ell^+\ell^-$ decays*, *JHEP* **08** (2017) 055, [arXiv:1705.05802 \[hep-ex\]](https://arxiv.org/abs/1705.05802).
- [449] LHCb Collaboration, R. Aaij et al., *Angular analysis of the $B^0 \rightarrow K^{*0}\mu^+\mu^-$ decay using 3 fb^{-1} of integrated luminosity*, *JHEP* **02** (2016) 104, [arXiv:1512.04442 \[hep-ex\]](https://arxiv.org/abs/1512.04442).
- [450] BaBar Collaboration, K. Flood, *New results in radiative electroweak penguin decays at BaBar*, *PoS ICHEP2010* (2010) 234.

- [451] J. F. Kamenik, S. Monteil, A. Semkiv, and L. V. Silva, *Lepton polarization asymmetries in rare semi-tauonic $b \rightarrow s$ exclusive decays at FCC-ee*, *Eur. Phys. J.* **C77** (2017) no. 10, 701, [arXiv:1705.11106 \[hep-ph\]](https://arxiv.org/abs/1705.11106).
- [452] M. D. Straub, *$B \rightarrow K^{(*)}\nu\bar{\nu}$ SM predictions*, BELLE2-MEMO-2016-007 (2015) .
- [453] BaBar Collaboration, J. P. Lees et al., *Search for $B \rightarrow K^{(*)}\nu\bar{\nu}$ and invisible quarkonium decays*, *Phys. Rev.* **D87** (2013) no. 11, 112005, [arXiv:1303.7465 \[hep-ex\]](https://arxiv.org/abs/1303.7465).
- [454] L. Calibbi, F. Goertz, D. Redigolo, R. Ziegler, and J. Zupan, *Minimal axion model from flavor*, *Phys. Rev.* **D95** (2017) no. 9, 095009, [arXiv:1612.08040 \[hep-ph\]](https://arxiv.org/abs/1612.08040).
- [455] P. Urquijo, *Extrapolation of $B \rightarrow K^{(*)}\nu\bar{\nu}$ to the full Belle II dataset*, BELLE2-MEMO-2016-008 (2016) .
- [456] C. Bobeth and U. Haisch, *New Physics in Γ_{12}^s : ($\bar{s}b$) $(\bar{\tau}\tau)$ Operators*, *Acta Phys. Polon.* **B44** (2013) 127–176, [arXiv:1109.1826 \[hep-ph\]](https://arxiv.org/abs/1109.1826).
- [457] U. Haisch, *(No) New physics in B_s mixing and decay*, in *2012 Electroweak Interactions and Unified Theories: Proceedings of the 47th Rencontres de Moriond on Electroweak Interactions and Unified Theories, La Thuile, March 3-10, 2012*, pp. 219–226. 2012. [arXiv:1206.1230 \[hep-ph\]](https://arxiv.org/abs/1206.1230). <http://inspirehep.net/record/1117445/files/arXiv:1206.1230.pdf>.
- [458] BaBar Collaboration, J. P. Lees et al., *Evidence for an excess of $\bar{B} \rightarrow D^{(*)}\tau^-\bar{\nu}_\tau$ decays*, *Phys. Rev. Lett.* **109** (2012) 101802, [arXiv:1205.5442 \[hep-ex\]](https://arxiv.org/abs/1205.5442).
- [459] W. Altmannshofer, S. Gori, M. Pospelov, and I. Yavin, *Quark flavor transitions in $L_\mu - L_\tau$ models*, *Phys. Rev.* **D89** (2014) 095033, [arXiv:1403.1269 \[hep-ph\]](https://arxiv.org/abs/1403.1269).
- [460] W. Altmannshofer and I. Yavin, *Predictions for lepton flavor universality violation in rare B decays in models with gauged $L_\mu - L_\tau$* , *Phys. Rev.* **D92** (2015) no. 7, 075022, [arXiv:1508.07009 \[hep-ph\]](https://arxiv.org/abs/1508.07009).
- [461] S. L. Glashow, D. Guadagnoli, and K. Lane, *Lepton Flavor Violation in B Decays?*, *Phys. Rev. Lett.* **114** (2015) 091801, [arXiv:1411.0565 \[hep-ph\]](https://arxiv.org/abs/1411.0565).
- [462] B. Bhattacharya, A. Datta, D. London, and S. Shivashankara, *Simultaneous Explanation of the R_K and $R(D^{(*)})$ Puzzles*, *Phys. Lett.* **B742** (2015) 370–374, [arXiv:1412.7164 \[hep-ph\]](https://arxiv.org/abs/1412.7164).
- [463] A. Greljo, G. Isidori, and D. Marzocca, *On the breaking of Lepton Flavor Universality in B decays*, *JHEP* **07** (2015) 142, [arXiv:1506.01705 \[hep-ph\]](https://arxiv.org/abs/1506.01705).
- [464] ALEPH Collaboration, S. Schael et al., *Branching ratios and spectral functions of tau decays: Final ALEPH measurements and physics implications*, *Phys. Rept.* **421** (2005) 191–284, [arXiv:hep-ex/0506072 \[hep-ex\]](https://arxiv.org/abs/hep-ex/0506072).

- [465] A. Pich, *Precision Tau Physics*, Prog. Part. Nucl. Phys. **75** (2014) 41–85, arXiv:1310.7922 [hep-ph].
- [466] Belle Collaboration, K. Belous et al., *Measurement of the τ -lepton lifetime at Belle*, Phys. Rev. Lett. **112** (2014) no. 3, 031801, arXiv:1310.8503 [hep-ex].
- [467] BaBar Collaboration, B. Aubert et al., *Measurements of Charged Current Lepton Universality and $|V_{us}|$ using Tau Lepton Decays to $e^- \bar{\nu}_e \nu_\tau$, $\mu^- \bar{\nu}_\mu \nu_\tau$, $\pi^- \nu_\tau$ and $K^- \nu_\tau$* , Phys. Rev. Lett. **105** (2010) 051602, arXiv:0912.0242 [hep-ex].
- [468] F. Feruglio, P. Paradisi, and A. Pattori, *Revisiting Lepton Flavor Universality in B Decays*, Phys. Rev. Lett. **118** (2017) no. 1, 011801, arXiv:1606.00524 [hep-ph].
- [469] C. Cornellà, F. Feruglio, and P. Paradisi, *Low-energy Effects of Lepton Flavour Universality Violation*, arXiv:1803.00945 [hep-ph].
- [470] LHCb Collaboration, R. Aaij et al., *Search for the lepton flavour violating decay $\tau^- \rightarrow \mu^- \mu^+ \mu^-$* , JHEP **02** (2015) 121, arXiv:1409.8548 [hep-ex].
- [471] L3 Collaboration, O. Adriani et al., *Search for lepton flavor violation in Z decays*, Phys. Lett. **B316** (1993) 427–434.
- [472] OPAL Collaboration, R. Akers et al., *A Search for lepton flavor violating Z0 decays*, Z. Phys. **C67** (1995) 555–564.
- [473] DELPHI Collaboration, P. Abreu et al., *Search for lepton flavor number violating Z0 decays*, Z. Phys. **C73** (1997) 243–251.
- [474] ATLAS Collaboration, G. Aad et al., *Search for the lepton flavor violating decay $Z \rightarrow e\mu$ in pp collisions at \sqrt{s} TeV with the ATLAS detector*, Phys. Rev. **D90** (2014) no. 7, 072010, arXiv:1408.5774 [hep-ex].
- [475] CMS Collaboration, *Search for Lepton Flavor Violation in Z decays in pp collisions at $\sqrt{s} = 8$ TeV*, CMS-PAS-EXO-13-005, CERN, Geneva, 2015. <http://cds.cern.ch/record/2019863>.
- [476] ATLAS Collaboration, M. Aaboud et al., *A search for lepton-flavor-violating decays of the Z boson into a τ -lepton and a light lepton with the ATLAS detector*, Submitted to: Phys. Rev. (2018), arXiv:1804.09568 [hep-ex].
- [477] S. Monteil, *Flavour Physics beyond the current foreseen programs. A closer look at Future Circular Colliders*, PoS **BEAUTY2016** (2016) 058.
- Equation

CHAPTER 3

EXPERIMENTAL CONDITIONS, PHYSICS REQUIREMENTS AND DETECTOR CONCEPTS

¹ The CEPC physics program spans a wide range of center-of-mass energies and beam luminosities to achieve the highest yields of Z , W and Higgs bosons produced in the exceptionally clean environment of an e^+e^- collider. As described in Chapter 2, the CEPC data will provide new levels of high precision tests of the Standard Model and in the search for new physics. This chapter describes the design requirements for the CEPC detectors to achieve these physics goals, taking into account the CEPC collision environment and the related backgrounds. The CEPC precision physics program places stringent requirements on the detector performance. These include large and precisely defined solid angle coverage, precise track momentum measurement, high efficiency for vertex reconstruction, precise photon energy reconstruction, excellent particle identification, excellent jet reconstruction and flavor tagging.

¹² Three preliminary CEPC detector concepts are introduced in this chapter. They derive from detector concepts introduced for the International Linear Collider project, benefiting from a long period of prior development, and incorporate modifications motivated by the circular collider experimental environment and by the higher luminosity. Although the overall design and main building blocks of the three concepts are similar, the particular technology choices are different. The CEPC baseline detector is based on a 3 Tesla solenoid magnetic field and follows closely the International Large Detector (ILD) design. It is guided by particle flow principles and it includes an ultra high granularity calorimeter system and a Time Projection Chamber (TPC). An alternative proposal substitutes the TPC with a full-silicon tracker (FST). A third design based on a lower magnetic field of 2 Tesla, a drift chamber, and dual readout calorimetry is also presented. While the baseline concept detector is used for the physics performance studies in this Conceptual Design Report, the other two designs are considered fully valid alternatives. The final two CEPC

1 detectors are likely to be composed of the detector technologies included in any of these
 2 three concepts.

3 3.1 CEPC Experimental Conditions

4 The CEPC is an electron-positron collider with 100 km circumference and two interaction
 5 points (IP). The details of the full CEPC accelerator complex are described in the CDR
 6 Volume I [1]. The final stage of the CEPC complex is a double-ring collider. Electron
 7 and positron beams circulate in opposite directions in separate beam pipes. They collide
 8 at two IPs which house large detectors, the specifications of which are presented in this
 9 volume.

10 The detectors must operate in three primary sets of conditions, corresponding to three
 11 different center-of-mass energies (\sqrt{s}): Higgs factory ($e^+e^- \rightarrow ZH$) at $\sqrt{s} \sim 240$ GeV, Z
 12 boson factory ($e^+e^- \rightarrow Z$) at $\sqrt{s} \sim 91.2$ GeV and W threshold scan ($e^+e^- \rightarrow W^+W^-$)
 13 at $\sqrt{s} \sim 160$ GeV. The instantaneous luminosities are expected to reach 3×10^{34} , 32×10^{34}
 14 and $10 \times 10^{34} \text{ cm}^{-2}\text{s}^{-1}$, respectively, as shown in Table 3.2, and will remain relatively
 15 constant throughout operation through a process of full-energy top-up injection by the
 16 CEPC accelerator complex. The current tentative operation plan will allow the detectors
 17 to collect one million Higgs bosons or more, close to one trillion Z boson events, and ten
 18 million W^+W^- events.

19 The detector designs must comprehensively meet the requirements imposed by the
 20 CEPC experimental conditions and the physics program. Each of the beam conditions
 21 and corresponding detector implications are presented below.

22 3.1.1 The CEPC beam

23 The detectors will record collisions in beam conditions presented in Table 3.1. Several of
 24 these parameters impose important constraints on the detectors. The bunch spacing of the
 25 colliding beams differ greatly in the three operational modes (25 ns, 210 ns, and 680 ns,
 26 respectively) as does the power dissipated into synchrotron radiation (16.5 MW for Z
 27 factory and 30 MW for W threshold scan and Higgs factory). Other important differences
 28 are also present in the expected beam backgrounds, described in more detail below, and,
 29 most importantly, in the event rates and types of events to be recorded, according to the
 30 cross sections shown in Figure 3.1 for different center-of-mass energies.

31 3.1.2 Beam backgrounds

32 Three most important sources of radiation backgrounds are evaluated for the CEPC:

- 33 1. synchrotron radiation photons from the last bending dipole magnet;
- 34 2. e^+e^- pair production following the beamstrahlung process;
- 35 3. off-energy beam particles lost in the interaction region.

36 3.1.2.1 Synchrotron radiation

37 Synchrotron radiation (SR) photons are prevalent at circular machines. A large flux SR
 38 photons are generated in the last bending dipole magnets. They are then transported to the
 39 interaction region with the BDSim software [2]. They can hit the central beam pipe, either

	Higgs	W	Z (3T)	Z (2T)
Number of IPs	2			
Beam energy (GeV)	120	80	45.5	
Circumference (km)	100			
Synchrotron radiation loss/turn (GeV)	1.73	0.34	0.036	
Crossing angle at IP (mrad)	16.5×2			
Piwinski angle	3.48	7	23.8	
Bunch number	242	1524	12000 (10% gap)	
Bunch spacing (ns)	680	210	25	
No. of particles/bunch $N_e(10^{10})$	15	12	8	
Beam current (mA)	17.4	87.9	461	
Synch. radiation power (MW)	30	30	16.5	
Bending radius (km)	10.7			
β function at IP: β_x^* (m)	0.36	0.36	0.2	0.2
β_y^* (m)	0.0015	0.0015	0.0015	0.001
Emittance: x (nm)	1.21	0.54	0.18	0.18
y (nm)	0.0024	0.0016	0.004	0.0016
Beam size at IP: σ_x (μm)	20.9	13.9	6.0	6.0
σ_y (μm)	0.06	0.049	0.078	0.04
Beam-beam parameters: ξ_x	0.018	0.013	0.004	0.004
ξ_y	0.109	0.123	0.06	0.079
RF voltage V_{RF} (GV)	2.17	0.47	0.1	
RF frequency f_{RF} (MHz)	650			
Natural bunch length σ_z (mm)	2.72	2.98	2.42	
Bunch length σ_z (mm)	4.4	5.9	8.5	
Natural energy spread (%)	0.1	0.066	0.038	
Energy spread (%)	0.134	0.098	0.08	
Photon number due to beamstrahlung	0.082	0.05	0.023	
Lifetime (hour)	0.43	1.4	4.6	2.5
F (hour glass)	0.89	0.94	0.99	
Luminosity/IP ($10^{34} \text{ cm}^{-2}\text{s}^{-1}$)	3	10	17	32

Table 3.1: Main beam parameters for the CEPC operation at three center-of-mass energies. The detector solenoid magnetic field affects the beam quality in the Z -factory operation mode. The last two columns compare the beam parameters for the case of a two- or three-Tesla detector solenoid.

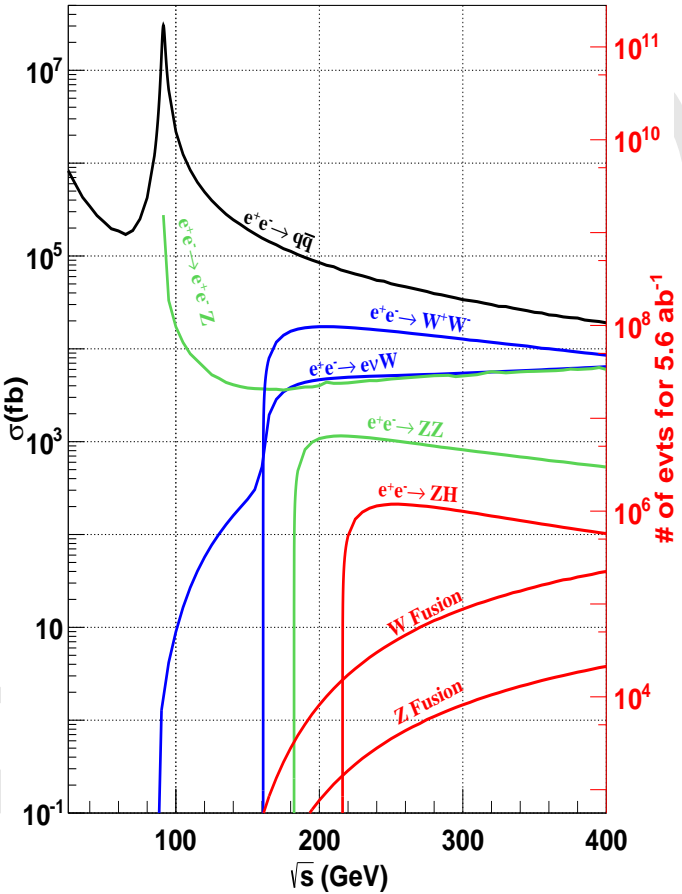


Figure 3.1: Cross sections of the leading Standard Model processes for unpolarized electron-positron collisions and the numbers of events expected in 5.6 ab^{-1} the data of a integrated luminosity. They are Higgs production: Higgs Bremsstrahlung, W fusion, and Z fusion; The dominant 2-fermions background: $e^+e^- \rightarrow q\bar{q}$; The 4-fermions backgrounds: $e^+e^- \rightarrow W^+W^-$, ZZ , $e^+\nu W$, and $e^+e^- Z$, etc.

Operation mode	Z factory	W threshold scan	Higgs factory
\sqrt{s} (GeV)	91.2	158 - 172	240
L ($10^{34} \text{cm}^{-2}\text{s}^{-1}$)	16-32	10	3
Running time (years)	2	1	7
Integrated Luminosity (ab^{-1})	8 - 16	2.6	5.6
Higgs yield	-	-	10^6
W yield	-	10^7	10^8
Z yield	10^{11-12}	10^9	10^9

Table 3.2: Instantaneous and integrated luminosities at different values of center-of-mass energy (\sqrt{s}) and anticipated corresponding boson yields at the CEPC. The range of luminosities for the Z factory correspond to the two possible solenoidal magnetic fields, 3 or 2 Tesla.

directly or after scattered by the beam pipe in the forward region. SR photons can also be generated in the final focusing magnets but contribute little to the detector backgrounds because they are produced with extremely small polar angles and can leave the interaction region without interacting in the beam pipe. To suppress the SR photons, three sets of mask tips made with high- Z material are introduced at $|z| = 1.51, 1.93$ and 4.2 m away from the interaction point. The studies prove that the masks can reduce effectively the number of SR photons hitting the central beam pipe, from almost 40,000 to below 80 from one of the two beams per bunch crossing. Further optimization may suppress SR photons even more and make this particular background well controlled.

3.1.2.2 Pair production

Electron-positron pairs are produced via the interaction of beamstrahlung photons with the strong electromagnetic fields of the colliding bunches. Pair production, in particular the incoherent pair production, represents the most important detector background at CEPC. The process is simulated with GUINEAPIG [3] and interfaced to GEANT4 [4–6] for detector simulation. Despite of the magnitude of beam squeezing being different in x and y directions, the hit distribution is almost uniform in the azimuthal (ϕ) direction. The resulting hit density at the first vertex detector layer ($r = 1.6$ cm) is about 2.2 hits/ cm^2 per bunch crossing when running at $\sqrt{s} = 240$ GeV. The total ionizing energy (TID) and non-ionizing energy loss (NIEL) are 620 kRad/year and $1.2 \times 10^{12} 1$ MeV $n_{eq}/\text{cm}^2 \cdot \text{year}$, respectively. For the background estimation, safety factors of ten are applied to cope with the uncertainties on the event generation and the detector simulation.

3.1.2.3 Off-energy beam particles

Beam particles after loosing a certain amount of energy, *i.e.* 1.5% of the nominal beam energy, can be kicked off their orbit. Such off-energy beam particles may hit machine and/or detector elements close to the interaction region and give rise to important backgrounds. The three main scattering process are radiative Bhabha scattering, beamstrahlung and beam-gas interaction. After the introduction of two sets of collimators upstream of the IPs, backgrounds due to beamstrahlung and beam-gas interaction become negligible. The residual backgrounds due to radiative Bhabha scattering yields hit densities of about 0.22

1 hits/cm² per bunch crossing when operating at $\sqrt{s} = 240$ GeV. The corresponding TID
 2 and NIEL are 310 kRad/year and 9.3×10^{11} 1 MeV $n_{eq}/\text{cm}^2 \cdot \text{year}$, respectively.

3 3.1.2.4 Backgrounds at different energies

4 When operating the machine at the center-of-mass energy of $\sqrt{s} = 240$ GeV, the main
 5 detector backgrounds come from the pair-production and off-energy beam particles. At
 6 lower operational energies, *i.e.* $\sqrt{s} = 160$ GeV for W and $\sqrt{s} = 91$ GeV for Z , the back-
 7 ground particles are usually produced with lower energies but with higher rates given the
 8 higher machine luminosities. The pair-production becomes dominant, while contributions
 9 from other sources tend to be negligible.

10 3.2 Physics Requirements

11 As Higgs, Z , and W boson factories, the CEPC should be equipped with detectors that
 12 can identify all the corresponding physics objects with high efficiency, high purity and
 13 measure them with high precision. In addition, the CEPC physics program requires a
 14 precise determination of the instantaneous luminosity, a precise control and monitoring of
 15 the beam energy. Generally, the CEPC detector is required to:

- 16 1 Operate reliably at high efficiency in the CEPC collision environment. The detector
 17 should be fast enough to record all the physics events with excellent efficiency and
 18 meet the performance requirements throughout the CEPC operation, including being
 19 robust against beam backgrounds.
- 20 2 Provide highly hermetic coverage for physics events. The detector should provide a
 21 solid angle coverage of $|\cos(\theta)| < 0.99$.
- 22 3 Accurately record the integrated luminosity. The luminosity should be measured to
 23 a relative accuracy of 0.1% for the Higgs factory operation, and 10^{-4} for the Z line
 24 shape scan.
- 25 4 The beam energy should be measured to an accuracy of the order of 1 MeV for the
 26 Higgs factory operation, and 100 keV for the Z pole and W mass threshold scan,
 27 following the methods described in [7].

28 The requirements on the physics objects reconstruction are briefly quantified with bench-
 29 mark physics analyses, see discussion below.

30 3.2.1 Multiplicity

31 In each physics event, the visible final state particles include the electrons, muons, photons,
 32 charged and neutral hadrons. The multiplicities of these basic ingredients, with the
 33 charged particles collectively referred to as tracks, are shown in Figure 3.2 for the WW ,
 34 ZZ , and ZH processes (the leading SM processes) at the CEPC Higgs factory operation.

35 The charged tracks and the photons carry most of the visible energies and are much nu-
 36 merous than the neutral hadrons. They follow a similar distribution of multiplicity, which
 37 can be as high as $\mathcal{O}(10^2)$. These final state particles can have extremely small angles
 38 in between, especially for those produced in high energy jets. An efficient separation of
 39 these final state particles provides a solid basis for the reconstruction of all the physics
 40 objects, which is addressed explicitly by the Particle Flow Principle.

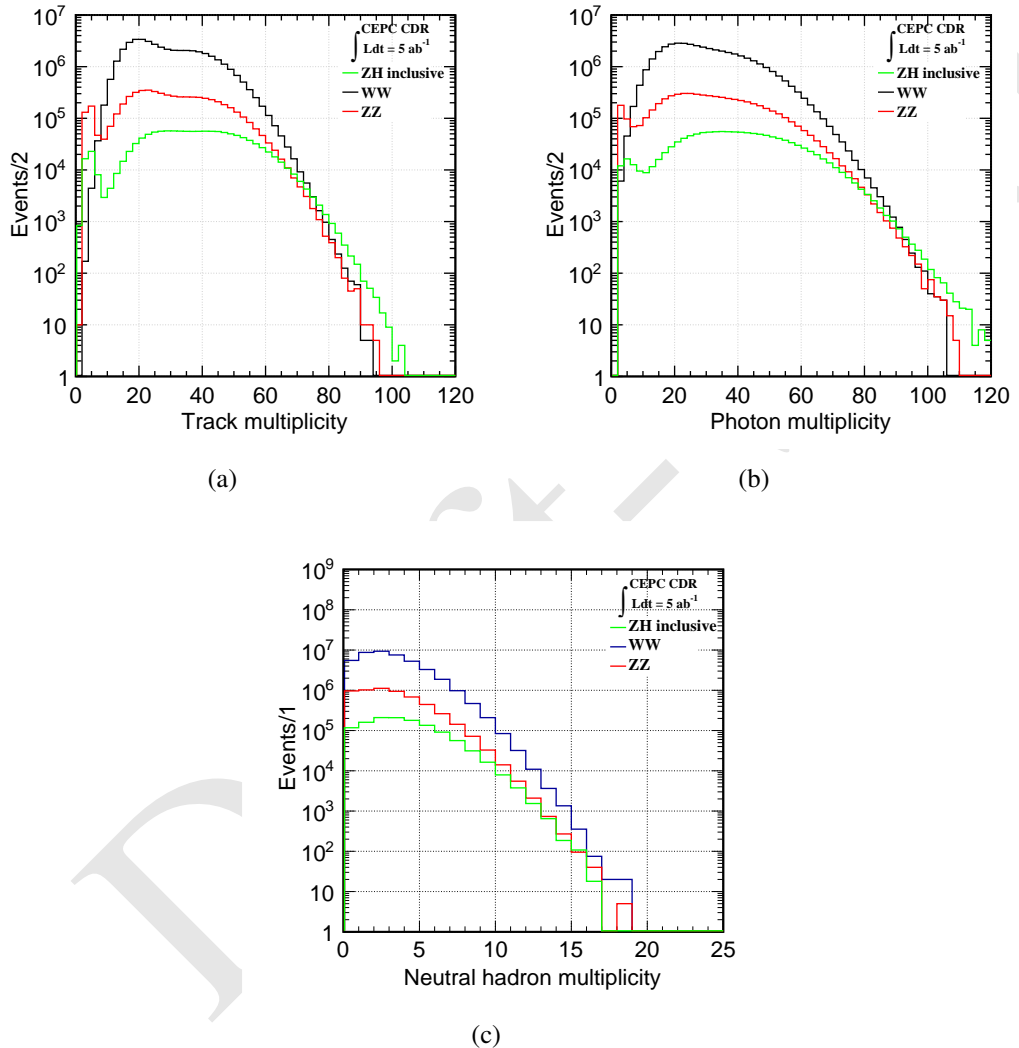


Figure 3.2: The multiplicities of charged particles, photons, and neutral hadrons from the WW , ZZ , and ZH events at the CEPC Higgs operation (corresponding to non-polarized electron positron collision at 240 GeV center of mass energy), normalized to 5 ab^{-1} integrated luminosity. The multiplicities of tracks and photons in some events can be as high as one hundred, 5 times larger than that of neutral hadrons. These physics events with large multiplicity require a detector that can efficiently separate the final state particles.

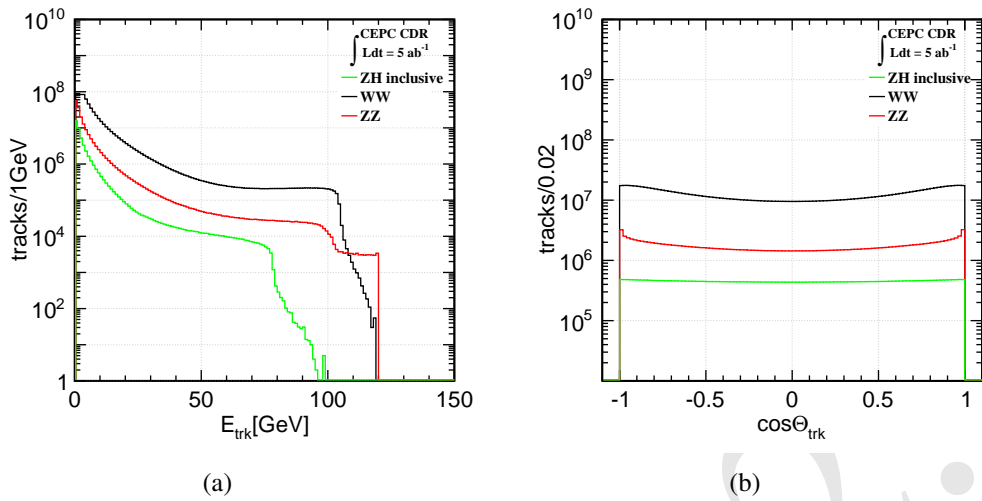


Figure 3.3: The energy and polar angle distributions of charged particles from the WW , ZZ , and ZH events at the CEPC Higgs operation, normalized to 5 ab^{-1} integrated luminosity. The ZH events are flatly distributed along the $\cos(\theta)$ while the other two processes are peaked at forward region.

3.2.2 Tracking

² The CEPC detector should have excellent track finding efficiency and track momentum
³ resolution. Corresponding to the WW , ZZ and the ZH processes at the CEPC Higgs
⁴ factory operation, the energy and polar angle distributions of the charged particles are
⁵ shown in Figure 3.3.

In the polar angle distribution, the ZH process is almost flat in the polar angle direction, while the other two processes are more forward region dominated. A large solid angle coverage is essential to characterize and to distinguish different physics processes, and a coverage of $|\cos(\theta)| = 0.99$ is benchmarked. In the energy distribution, these three processes share the same pattern. For energies below 20 GeV, these distributions follow an exponential distribution, while in the high energy side there is a flat plateau with a steep cliff. Therefore, the CEPC detector should have a high efficiency track reconstruction, especially for these low energy tracks. Meanwhile, it should have an excellent momentum resolution and linearity for a wide energy range (0.1–120 GeV).

For tracks within the detector acceptance and transverse momenta larger than 1 GeV, we request an track finding efficiency better than 99%. In order to measure the $H \rightarrow \mu^+ \mu^-$ signal and to reconstruct precisely the Higgs boson mass from the recoil mass distribution at $\ell^+ \ell^- H$ events, the momentum resolution is required to achieve a per mille level relatively.

3.2.3 Charged Leptons

21 The charged lepton is one of the most important physics signatures and it plays a crucial
22 role in the classification of different physics events. A high efficiency and high purity
23 charged lepton identification is fundamental for the CEPC physics program.

At the CEPC Higgs factory operation, roughly 7% of the Higgs bosons are generated with a pair of charged leptons. These $\ell^+ \ell^- H$ samples are the golden signal for the Higgs

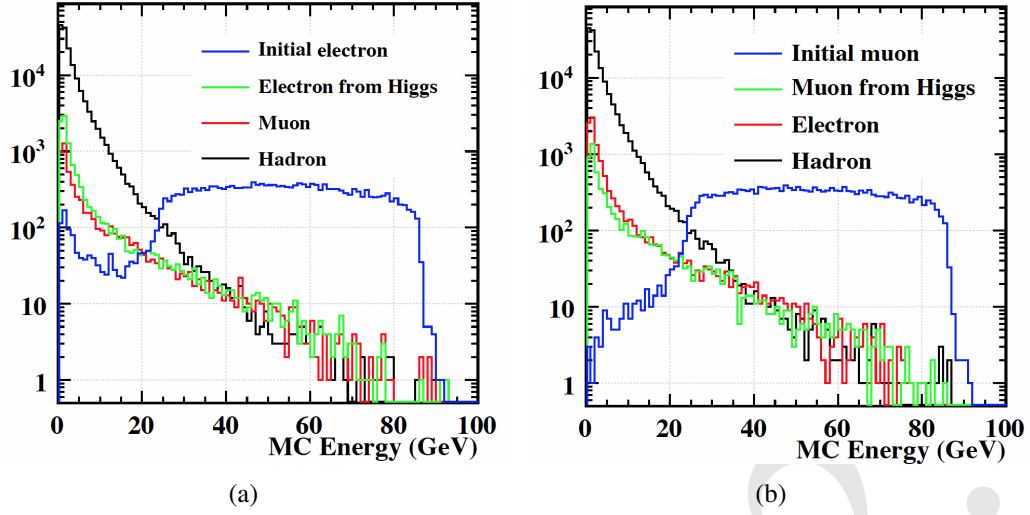


Figure 3.4: The energy spectrum of the prompt leptons and the charged particles in the e^+e^-H events (a) and the $\mu^+\mu^-H$ events (b). Most of the prompt leptons are generated from the Z boson decay in the ZH , $Z \rightarrow \ell^+\ell^-$ events, therefore, their energy spectrum exhibits a flat plateau from 20 to 90 GeV. Therefore, the CEPC detector is required to identify those leptons with high efficiency and high purity. The prompt electron/positron energy spectrum in the e^+e^-H events (the left plot) exhibit a tiny low energy peak, which is induced from the Z fusion events.

boson recoil mass analyses. Figure 3.4 shows the energy distribution of the prompt leptons and these generated in Higgs boson decay cascade. The prompt muons in $\mu^+\mu^-H$ events have a flat energy distribution within the kinematic range (20–100 GeV) and a low energy tail induced by the Z boson width and final state radiation (FSR). The prompt electron-positron pair in e^+e^-H events follows a similar pattern, except the population increases at energy smaller than 10 GeV. This low-energy peak is mainly induced by the Z fusion events where one of the two scattered electrons is produced with low momentum.

The Higgs boson decay also generates leptons, which is mostly concentrated in the low energy side, but can have energies as high as 70 GeV. These high energy leptons are mainly generated from $H \rightarrow \tau^+\tau^-$, ZZ^* , WW^* decay cascades.

The basic requirements on the lepton identification for the CEPC detector is, to identify the prompt charged leptons with high efficiency and high purity. Therefore, we require a lepton identification with efficiency higher than 99% and misidentification rate smaller than 2% for energetic isolated leptons (energetic means energy higher than 5 GeV). These requirements are also essential for the identification of $H \rightarrow \tau^+\tau^-$ events and the semi-leptonic/leptonic decays modes of $H \rightarrow ZZ^*$, WW^* events.

The charged leptons produced in the numerous jets generated in the Higgs boson decay cascades can be crucial for the jet flavor tagging and jet charge reconstruction. Therefore, a good identification of leptons in jets is highly advantageous. More detailed study is needed to quantify the requirements on the lepton-in-jet identification.

3.2.4 Charged hadron identification

The particle identification, especially the identification of charged kaons, is crucial for the flavor physics. Similar to the jet leptons, the identification of charged kaon is highly

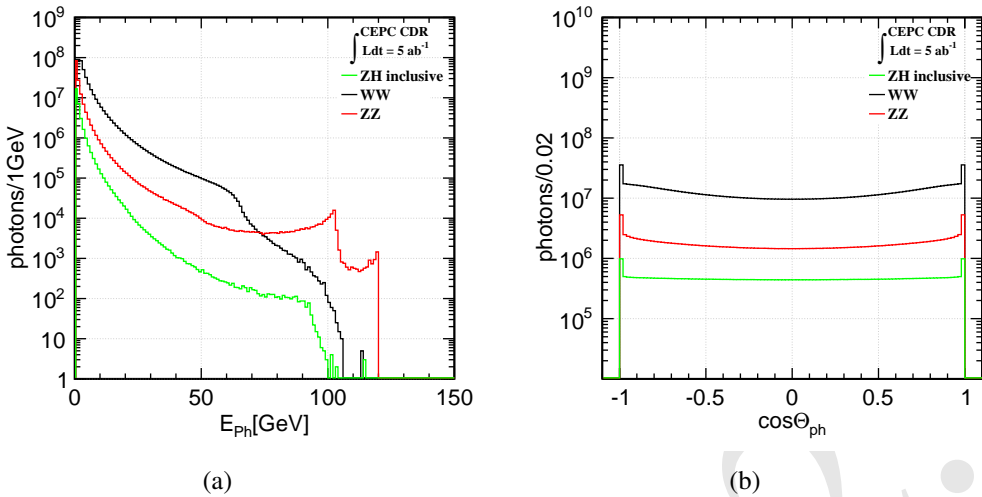


Figure 3.5: The energy and polar angle distributions of all photons from WW , ZZ , and ZH events at the CEPC Higgs operation, normalized to 5 ab^{-1} integrated luminosity. In the energy spectra, the distribution corresponding to ZZ events exhibits a peak near 100 GeV, which is induced from the ISR return events. The tiny peak at the polar angle distribution at the very forward region is corresponding to the ISR photons, see also the next plot.

appreciated for the jet flavor tagging and jet charge reconstruction. Typically, we request the efficiency and purity of the kaon identification at the inclusive Z pole sample to be better than 90%.

3.2.5 Photons

The photons are crucial for the jet energy resolution, the $H \rightarrow \gamma\gamma$ branching ratio measurements, radiative processes and the physics with τ final states. Figure 3.5 shows the energy and polar angle distributions for the inclusive photons, and the initial-state radiation (ISR) photons in Figure 3.6, from these benchmark physics processes at the CEPC Higgs factory operation.

As for the photon reconstruction, we request a photon identification efficiency higher than 99% and a misidentification rate smaller than 5%, for unconverted, isolated photons with energy higher than 1 GeV. To observe at least 50% of diphoton resonances with a pair of unconverted photons, the material budget in front of the calorimeter should be less than $0.35X_0$ averaged over all solid angle. To identify the τ leptons with different decay modes, the photons should be identified from the π^0 with an efficiency and purity higher than 95% from the $Z \rightarrow \tau^+\tau^-$ event sample at CEPC Z factory operation. To fully exploit the hadronic decays of the Z , W , and Higgs bosons, the requirements on the jet energy resolution, described in the next section, impose a photon energy resolution requirement of better than $20\%/\sqrt{E} \oplus 1\%$. This photon energy resolution requirement for jets is sufficient to meet the needs of the measurement of the Higgs boson coupling to photons at CEPC due to the low background environment for the diphoton final state. Further evaluation of photon energy resolution requirements for radiative processes need to be carefully studied.

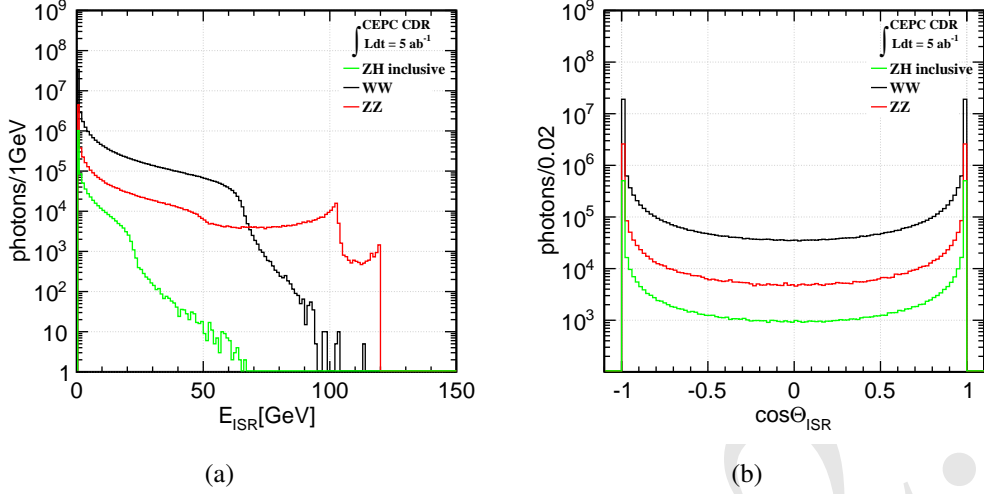


Figure 3.6: The energy and polar angle distributions of ISR photons from WW , ZZ , and ZH events at the CEPC Higgs operation, normalized to 5 ab^{-1} integrated luminosity. These ISR photons are concentrated at forward region (see the right hand plot).

3.2.6 Jets and Missing energy

The reconstruction of jets is essential for the CEPC physics program, since the majority of W , Z , and Higgs bosons decay into hadronic final states. Jets are measured with particles that interact with the full range of sub-detector systems. The Particle Flow principle and corresponding particle flow algorithms (PFA), based upon it, are an overarching approach to reconstructing and interpreting measurements into a form that identifies and optimally measures the properties and kinematic quantities of all individual final state particles produced in the high-energy collision. For Particle Flow oriented detectors, the jet is constructed from a list of final state particles produced by the PFA. Therefore, the jet reconstruction is determined by the reconstruction of final state particles and the jet clustering algorithm. Consequently, the jet reconstruction performance should be evaluated at two stages.

The first is the Boson Mass Resolution (BMR) for massive SM bosons. The boson mass resolution represents the jet energy resolution with perfect jet clustering, or more accurately, a perfect identification of the color singlet. The BMR is defined as the relative resolution of the visible mass on the $\nu\bar{\nu}H, H \rightarrow gg$ events with a standard cleaning procedure. The cleaning procedure has a typical efficiency of 65%, it vetoes the events with energetic visible ISR photon(s), energetic neutrinos generated in the Higgs boson decay, and jets pointing to the very forward regions. Since the width of the SM Higgs boson (4 MeV) is negligible comparing to the jet energy resolution (GeV), BMR is equivalently the Higgs boson mass resolution with cleaned $\nu\bar{\nu}H, H \rightarrow gg$ event sample.

Figure 3.7 shows the reconstructed W , Z , and Higgs boson masses with different BMR. In order to distinguish the W , Z , and the Higgs boson from their hadronic decay final state, a boson mass resolution better than 4% is required. It should be remarked that an efficient separation of individual W , Z , and Higgs boson is a prerequisite for a clear separation of

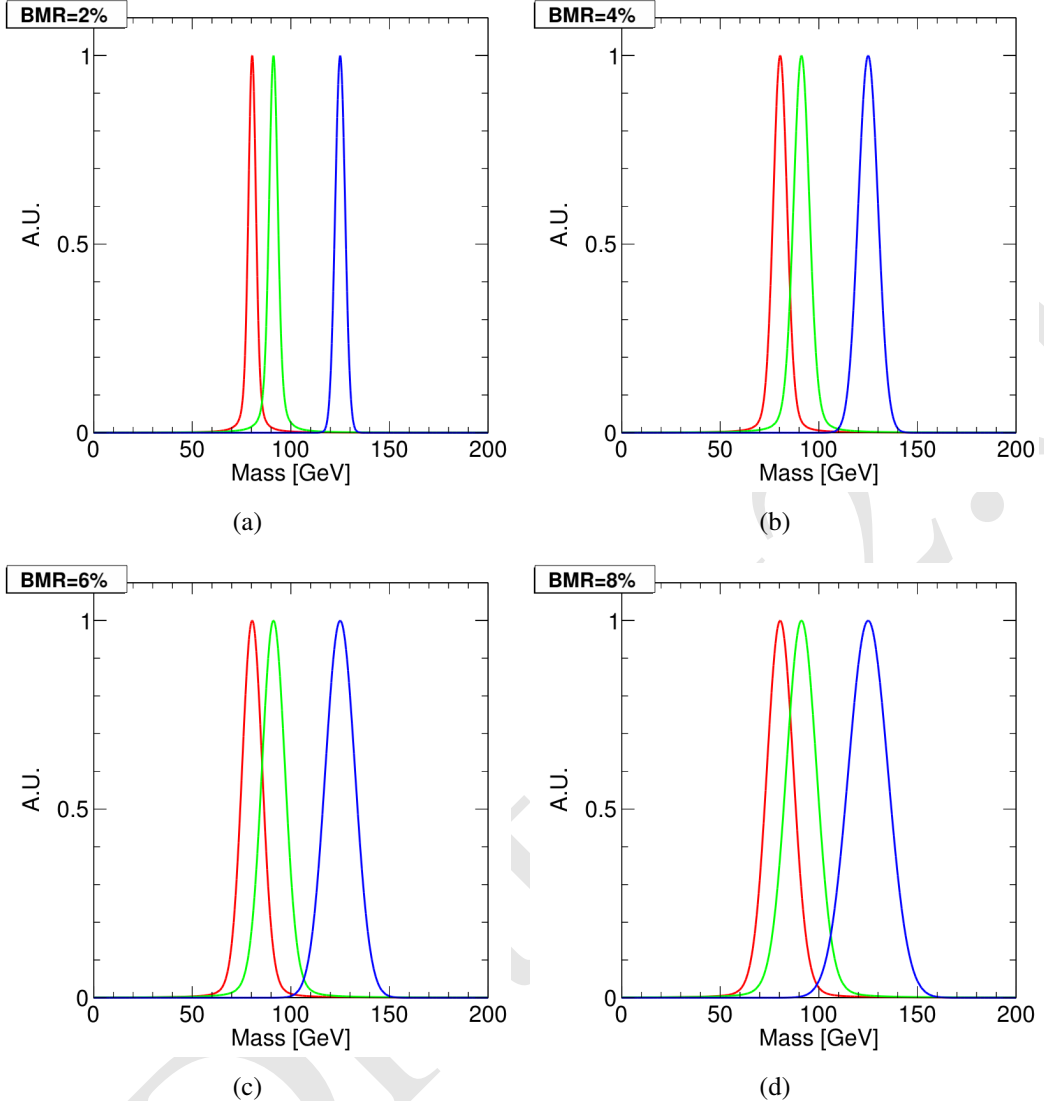


Figure 3.7: The invariant mass distributions of W , Z and Higgs bosons for different Boson Mass Resolutions (BMR), corresponding to the red, the green and the blue curves. Normalized to unit height. The distributions of the W and Z bosons are modeled with an Breit-Wigner Distribution with 2 and 2.5 GeV the width, convoluted with the relative BMR.

¹ WW , ZZ , and ZH events in the 4-jet final states, since the latter strongly depends on the jet clustering performance.

³ The missing energy measurement with jet final states can also be characterized by the BMR. The physics benchmark for the missing energy-momentum measurement is the $BR(H \rightarrow \text{invisible})$ measurement with $q\bar{q}H$ final states. The signal has a Higgs boson mass peak in the missing mass spectrum. The dominant SM background, the $ZZ \rightarrow \nu\bar{\nu}q\bar{q}$ process, exhibits a peak at the Z boson mass. Meanwhile, because the initial state radiation and the heavy flavor component of the $Z \rightarrow q\bar{q}$ decay, both missing mass distributions exhibit a high mass tail. The missing mass distributions at different BMR are displayed in Figure 3.8. At a BMS worse than 4%, the Z recoil mass peak of the background be-

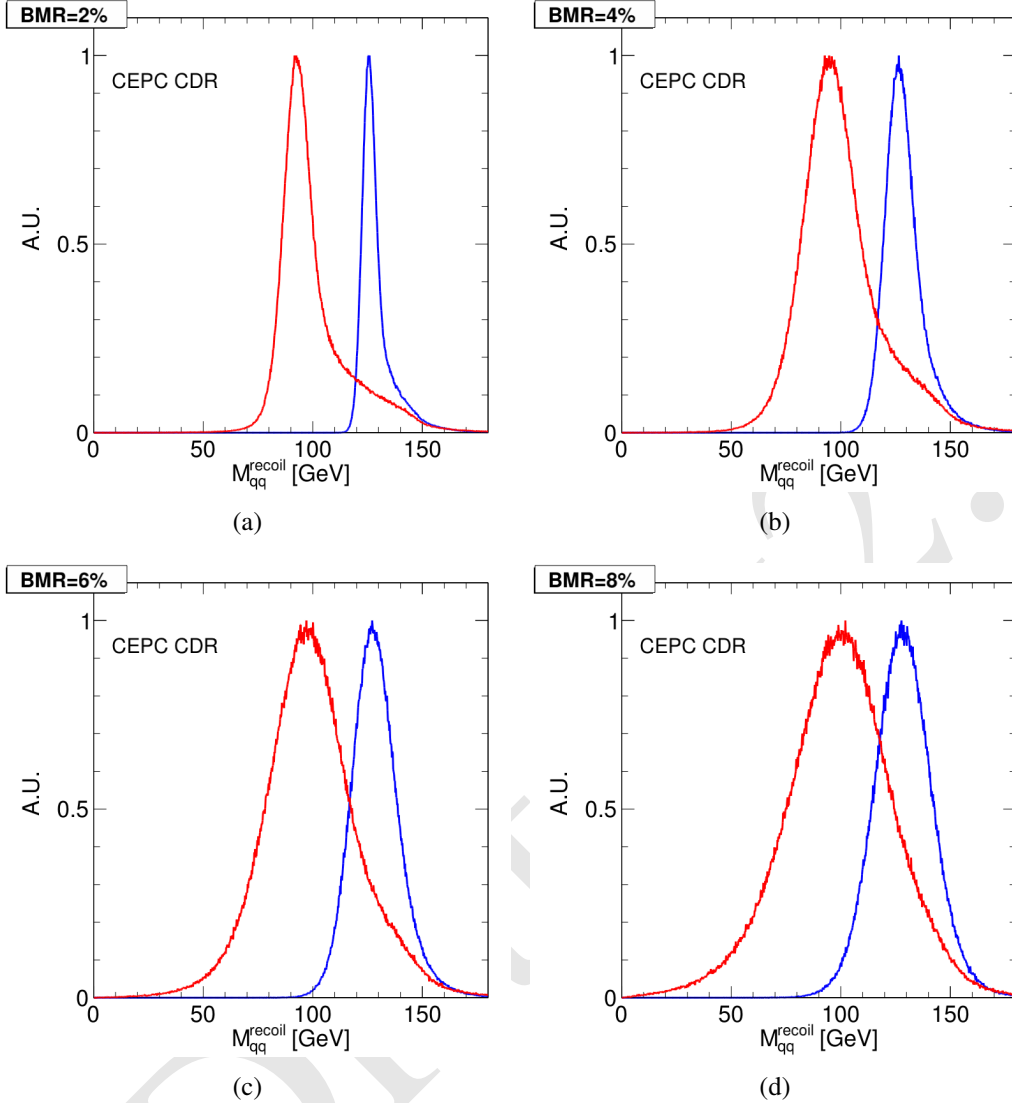


Figure 3.8: The dijet recoil mass distribution of $ZZ \rightarrow v\bar{v}q\bar{q}$ events and ZH events with Z decays into a pair of quarks and the Higgs boson decaying invisibly at different Boson Mass Resolution (BMR). The red/blue curve is corresponding to the ZZ/ZH events, respectively. Each distribution is normalized to an unit height. At a BMR equal or smaller than 4%, the ZZ events exhibit a high recoil mass tail induced by the heavy flavor jets and the ISR photons; while at large BMR, this high mall tail got absorbed into the main peak with large intrinsic width.

¹ comes so wide that it starts to overlap with the Higgs boson mass peak. Therefore, for this
² benchmark, a boson mass resolution better than 4% is certainly advantageous.

³ The identification of individual jets, and its energy-momentum reconstruction is crucial
⁴ for the CEPC physics measurements. The individual jet energy response is highly depend-
⁵ ing on the event topology and the jet clustering algorithms. Detailed analyses are required
⁶ to disentangle the actual physics requirement, which need to be analyzed carefully.

1 **3.2.7 Flavor Tagging**

2 One of the key physics objectives of the CEPC Higgs program is to measure the Higgs
 3 boson coupling to c -quarks. The CEPC detector is therefore required to efficiently dis-
 4 tinguish the b -jets, the c -jets, and the light jets from each other. High performance flavor
 5 tagging is also highly advantageous in EW precision measurements.

6 Benchmarked with the $Z \rightarrow q\bar{q}$ sample at 91.2 GeV c.m.s, we require the b -jets to
 7 be identified with a efficiency and purity higher than 80%, and a c -jet identification effi-
 8 ciency/purity better than 60%.

9 The classification of different kinds of jets depends strongly on the reconstruction of
 10 secondary vertex, where the performance of the vertex system is crucial. The clean col-
 11 lision environment of the CEPC allows much aggressive vertex system design, a detailed
 12 vertex optimization study can be found in Section 4.1.

13 **3.2.8 Requirements on the physics objects: summary**

14 The discussion above quantifies the physics requirements on the physics object recon-
 15 struction. It can be summarized as:

16 1 Tracking performance: For tracks with transverse momenta greater than 1 GeV and
 17 within the detector acceptance, a reconstruction efficiency of better than 99% is re-
 18 quired. The relative resolution of the track momentum should achieve per mille level,
 19 required by the $H\mu\mu$ coupling measurements and the Higgs boson recoil mass analy-
 20 ses of $\ell^+\ell^-H$ events.

21 2 Excellent lepton identification. For isolated leptons with momenta larger than 5 GeV,
 22 we request an identification efficiency of 99% and a misidentification rate smaller than
 23 2%. Leptons inside jets also need to be identified well, as they provide information
 24 on the jet flavor and jet charge.

25 3 Capability to identify charged kaons, which enhances the rich flavor physics program
 26 at CEPC Z factory operation. For the inclusive $Z \rightarrow q\bar{q}$ sample at $\sqrt{s} = 91.2$ GeV,
 27 we request a charged kaon identification with efficiency and purity to be both higher
 28 than 90%.

29 4 Precise reconstruction of photons. Required by the $H\gamma\gamma$ coupling measurement and
 30 the jet energy reconstruction, the photon energy should be measured to a precision
 31 better than $20\%/\sqrt{E} \oplus 1\%$. Meanwhile, to identify the τ leptons with different decay
 32 modes, the photons should be identified from the π^0 with an efficiency and purity
 33 higher than 95% in the $Z \rightarrow \tau^+\tau^-$ event sample at CEPC Z factory operation.

34 5 Excellent Jet/Missing Energy reconstruction. The jet/missing energy reconstruction
 35 is essential for the CEPC since most of the physics events are generated with one or
 36 more of these physics objects. To avoid the complication from jet clustering perfor-
 37 mance, we characterize the jet and missing energy reconstruction with Boson Mass
 38 Resolution. Benchmarked with the separation of massive SM bosons (W , Z , and
 39 Higgs boson) and the $\text{BR}(H \rightarrow \text{invisible})$ measurements, a BMR better than 4% is
 40 identified.

41 6 Capability to separate b -jets, c -jets and light jets (uds and gluon jets): required by the
 42 measurements of the Higgs boson couplings to b -quarks, c -quarks and gluons as well

as the EW measurements. Benchmarked with the $Z \rightarrow q\bar{q}$ sample at $\sqrt{s} = 91.2$ GeV, we require the b -jets to be identified with an efficiency and purity higher than 80%, and a c -jet identification efficiency/purity better than 60%.

Most of the above-mentioned requirements are driven by the precision Higgs measurements. However, it also applies to the precise EW measurements as the W and Z bosons decay into similar physics objects.

3.3 Detector concepts

To address the physics requirements at the CEPC, three preliminary detector concepts are proposed. Two options differ currently only on the main tracking system, although it is conceivable that further optimizations would cause them to diverge in the future. In particular, they share a high-magnetic field solenoid of 3 Tesla. The third option is thoroughly different, and it is designed to take advantage of a lower-magnetic field solenoid of 2 Tesla.

The first two detector concepts are guided by the Particle Flow Principle. The Particle Flow principle interprets all the detector signals as originating from final state particles. For each physics event, all the physics objects are reconstructed from an unique list of final state particles. The single particle level physics objects, for example the leptons, the photons, and the kaons, are identified directly from the final state particle list. The compound physics objects, for example the converted photons, the K_S^0 , the τ lepton and the jets, are identified using dedicated finding algorithms such as the τ finder and jet clustering algorithms. Subtracting the total visible four-momentum of all the final state particles from the initial four momentum determines the missing four-momentum. This global interpretation of the final state particles leads to high efficiency and high purity reconstruction of all the physics objects. In addition, the Particle Flow algorithm in principle associates the detector hits to each individual particle, therefore, the final state particle could be measured in the most-suited sub-detector system. For the charged particles, the relative accuracy of track momentum resolution from the tracking system is usually much better than the energy resolution from the calorimeter system. Therefore, the Particle Flow algorithm also significantly improves the accuracies on the energy reconstruction of compound objects, especially for the τ lepton and the jets.

The CEPC baseline detector concept was initially developed from the concept of the International Large Detector (ILD). It is optimized for the CEPC collision environments, and enhances the particle identification performance which is essential for flavor physics. The baseline detector uses an ultra high granularity calorimeter system to efficiently separate the final state particle showers, low material tracking system to limit the probability of interaction of final state particles in the tracking material, and a large volume solenoid that hosts the entire ECAL and HCAL inside. There are two options for its tracking system, the time-projection chamber (TPC) and the full silicon tracking (FST).

An alternative detector concept, IDEA, is also proposed. IDEA uses a dual readout calorimeter to achieve excellent energy resolution for both electromagnetic and hadronic showers. Comparing to the baseline detector, IDEA uses a lower field solenoid (2 Tesla) but compensates with a large tracker volume. The IDEA is also used as a reference detector for FCC-ee studies.

The main detector parameters of both concepts are summarized in Table 3.3.

Concept	ILD	CEPC baseline	IDEA
Tracker	TPC/Silicon	TPC/Silicon or FST	Drift Chamber/Silicon
Solenoid B-Field (T)	3.5	3	2
Solenoid Inner Radius (m)	3.4	3.2	2.1
Solenoid Length (m)	8.0	7.8	6.0
L^* (m)	3.5	2.2	2.2
VTX Inner Radius (mm)	16	16	16
Tracker Outer Radius (m)	1.81	1.81	2.05
Calorimeter	PFA	PFA	Dual readout
Calorimeter λ_I	6.6	5.6	7.5
ECAL Cell Size (mm)	5	10	-
ECAL Time resolution (ps)	-	200	-
ECAL X_0	24	24	-
HCAL Layer Number	48	40	-
HCAL Absorber	Fe	Fe	-
HCAL λ_I	5.9	4.9	-
DRCAL Cell Size (mm)	-	-	6.0
DRCAL Time resolution (ps)	-	-	100
DRCAL Absorber	-	-	Pb or Cu or Fe
Overall Height (m)	14.0	14.5	11.0
Overall Length (m)	13.2	14.0	13.0

Table 3.3: Comparison of detector parameters. The main difference of the CEPC detectors from the ILD is smaller in size since they will work at 90-240 GeV energy region. And the differences among the CEPC detectors are on technology and size of the trackers and the field solenoid.

3.3.1 The baseline detector concept

From inner to outer, as shown in Figure 3.9, the baseline concept is composed of a silicon pixel vertex system, a silicon internal tracker, a TPC main tracker, a Silicon-tungsten sampling ECAL, an Iron-Glass Resistive Plate Chamber HCAL, a solenoid, and a return yoke.

The baseline concept has a dedicated design in the forward region and machine-detector interface (MDI). The L* of the baseline concept has a length of 2.2 meters, and a compensation solenoid system is installed at a z position of 1100–6000 mm. A luminosity calorimeter (LumiCal) is installed at the end of this nose structure. A compact, forward tracking system composed of 5 pairs of tracking disks is installed in between a z position of 200–1000 mm.

The solenoid B-Field of the baseline is 3 Tesla. The CEPC uses a double ring configuration, with a crossing angle of 33 mrad at the interaction point. Each time the bunch passing through the detector, the beam emittance increases via the coupling to the detector solenoid B-Field (especially the vertical emittance). In order to achieve a high luminosity, this solenoid B-Field needs to be compensated locally. Therefore, a compensating solenoid is installed in the forward region of the CEPC detector. Considering the technology challenge of the compensating solenoid and the physics requirements at the CEPC, the baseline concept uses a solenoid of 3 Tesla for CEPC Higgs factory operation, and the central solenoid may have to be ramped down to 2 Tesla for CEPC Z factory operation.

The baseline concept uses the Time Projection Chamber (TPC) as its main tracker. The TPC provides good energy resolution, excellent track reconstruction efficiency, low material budgets, and its dE/dx measurement is important for particle identification, see Section 10.2.7. On the other hand, compared to the silicon tracking, the TPC is a slow technology: the drift time of ions is of the order of one second in the CEPC TPC. In the TPC, both primary ionization of charged tracks and ion backflow from the amplification procedure generates ions, which accumulate in the gas volume. These ions will distort the drift electric field and eventually limit the precision of track momentum measurement. The physics event rate at the CEPC Z factory operation is of the order of 10^{3-4} Hz. Therefore, ions generated from thousands of events pile up in the gas volume. The control of backflow ion is then essential for the TPC operation.

Iterated with the hardware R&D, dedicated simulation studies are performed in the CEPC TPC study. Using a double amplification layer, the ion backflow could be controlled to per mille level without gating [8]. On the other hand, the simulation analysis shows that at this level of ion backflow control, the degrading of spatial point resolution is smaller than the intrinsic TPC spatial resolution. The TPC occupancy is also analyzed at the CEPC Z factory. Those studies lead to the conclusion that the TPC is a feasible technology option for the CEPC [9].

The TPC in the baseline has an inner radius of 0.3 meters, an outer radius of 1.8 meters, and a length of 4.7 meters. It is divided into 220 radial layers, each has a thickness of 6 mm. Along the ϕ direction, each layer is segmented into 1 mm wide cells. In total, the TPC has 1 million readout channels in each endcap. Operating in 3 Tesla solenoid B-Field, the TPC provides a spatial resolution of 100 μm in the $R - \phi$ plane and 500 μm resolution in the Z direction for each tracker hit. The TPC reaches a standalone momentum resolution of $\Delta(1/p_T) \sim 10^{-4} \text{ GeV}^{-1}$.

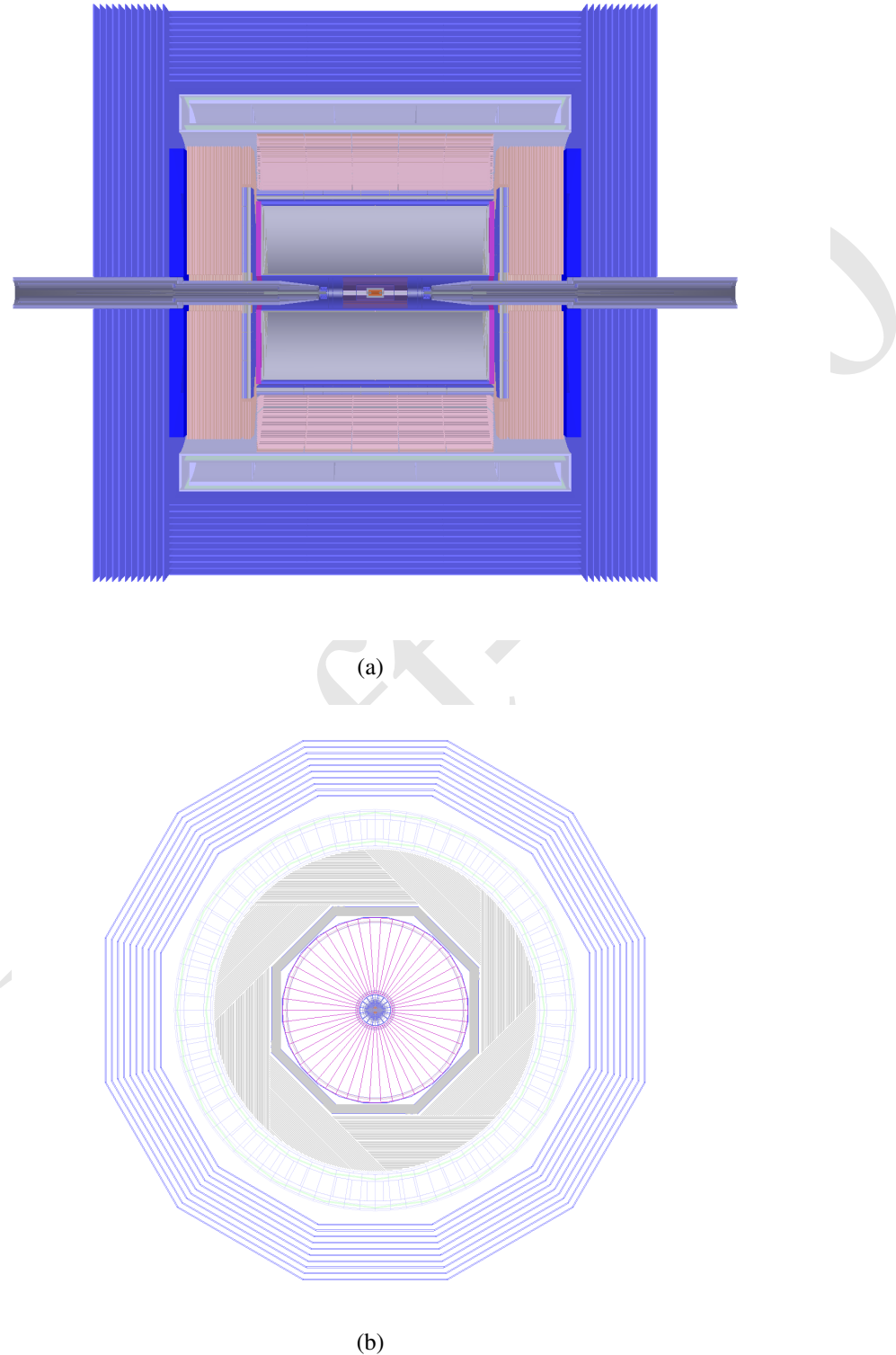


Figure 3.9: The RZ (a) and R- ϕ (b) view of the baseline detector concept. The baseline concept uses a double beam with 33 mrad crossing angle, and has a short L^* of 2.2 meter. In the central Barrel, from inner to outer, the baseline concept is composed of a Vertex system, a Silicon Inner Tracker, a TPC, a Silicon External Tracker, an ECAL, an HCAL, a Solenoid of 3 Tesla and a Return Yoke. In the forward region, 5 pairs of tracking disks are installed to enlarge the tracker acceptance (from $|\cos(\theta)| < 0.99$ to $|\cos(\theta)| < 0.996$).

1 The baseline is equipped with large-area silicon tracking devices, including the pixel
 2 vertex system, the forward tracking system, and the silicon inner/external tracking layers located at the boundary of the TPC. Combining the measurements from the silicon tracking system and the TPC, the track momentum resolution could be improved
 3 to $\Delta(1/p_T) \sim 2 \times 10^{-5} \text{ GeV}^{-1}$. In fact, the TPC is mainly responsible for the pattern
 4 recognition and track finding, while the silicon tracking devices dominate the momentum
 5 measurement. The silicon pixel vertex system also provides precise impact parameter resolution
 6 ($\sim 5 \mu\text{m}$), which is highly advantageous for the τ lepton reconstruction and the jet flavor tagging.
 7

8 The baseline concept uses a high granular sampling Electromagnetic Calorimeter (ECAL)
 9 and Hadronic Calorimeter (HCAL). The calorimeter is responsible for separating final
 10 state particle showers, measuring the neutral particle energy, and providing information
 11 for the lepton identification [10, 11]. The entire ECAL and HCAL are installed inside the
 12 solenoid, providing 3-dimensional spatial position and the energy information. The ECAL
 13 geometry parameters were determined by a dedicated optimization study [12]. The ECAL
 14 is composed of 30 layers of alternating silicon sensors and tungsten absorber. It has a total
 15 absorber thickness of 84 mm. Transversely, each sensor layer is segmented into 10 mm by
 16 10 mm cells. The HCAL uses Resistive Plate Chamber sensor and Iron absorber. It has 40
 17 longitudinal layers, each consists of a 25 mm Iron absorber. Transversely, it is segmented
 18 into 10 mm by 10 mm cells.
 19

20 This calorimeter system provides good energy measurement for the neutral particles
 21 (i.e. roughly $16\%/\sqrt{E/\text{GeV}}$ for the photons and $60\%/\sqrt{E/\text{GeV}}$ for the neutral hadrons).
 22 More importantly, it records enormous information of the shower spatial development,
 23 ensuring efficient separation between nearby showers and providing essential information
 24 for the lepton identification, see Section 10.2.1. In addition, the silicon-tungsten ECAL
 25 could provide precise time measurements. Requesting a cluster level time resolution of
 26 50 ps, the ECAL Time-of-Flight (ToF) measurement plays a complementary role to the
 27 TPC dE/dx measurement, leading to good charged Kaon identification performance, see
 28 Section 10.2.7.
 29

30 As will be introduced in the following chapter, the baseline concept maintains the same
 31 performance for the CEPC Higgs boson measurements comparing to the ILD. Mean-
 32 while, the total cost, the total weight, and the calorimeter thickness have been signifi-
 33 cantly optimized (by 25%, 50% and 20% respectively). In addition, the baseline concept
 34 has good performance for charged kaon identification, which is highly advantageous for
 35 flavor physics and in the jet flavor/charge reconstruction.

36 3.3.2 Full silicon detector concept

37 Silicon detectors provide at present the most precise tracking for charged particles in high
 38 energy physics experiments. They have an excellent space point resolution and granular-
 39 ity to cope track separation in dense jets and hits from the high luminosity beam related
 40 background. A full-silicon tracker (FST) would offer a competitive choice of detector
 41 concepts for CEPC that provides excellent tracking efficiency, momenta resolution, and
 42 vertexing capability for charged particles from the interaction point as well as from the
 43 decay of secondary particles. The challenge is to build it with minimal material to pre-
 44 serve the momentum resolution and being covered hermetically down to the dip angle of
 45 $|\cos\theta| < 0.992$ from the beam pipe.

1 Here we will demonstrate that the full-silicon tracking concept is a viable option for
 2 CEPC by replacing the TPC with additional silicon stereo-strip layers while keeping the
 3 rest of detector unchanged under the same detector boundary conditions used by the CEPC
 4 baseline concept described above. We so far have not changed the detector boundary con-
 5 ditions such as the B field and the track volume in order to provide a cost-optimized
 6 detector since the performance may not matter. However, within these boundary con-
 7 ditions, we have optimized the layout with the number of silicon layers, single- versus
 8 double-sided layers, and support materials using a toy simulation. This concept option is
 9 described below in Section 4.3.

10 Two approaches are considered for the design: the first is to keep the silicon detectors
 11 (VXD, SIT, FTD) in the CEPC baseline detector and replacing TPC with additional silicon
 12 detectors , as shown in Figure 3.10 for 3D view of a full and zoomed detector; the second
 13 is to optimize the ILC-SID tracker to fulfill the CEPC tracking volume in order to achieve
 14 the excellent momentum resolution using 3 Tesla B field. The new detector geometry has
 15 been implemented in the simulation and the track reconstruction has also been adopted
 16 for the full silicon tracker. The initial study of the tracking performance looks promising.
 17 There are still many improvements needed in the simulation and reconstruction in order
 18 to explore the full potential of the full-silicon tracker.

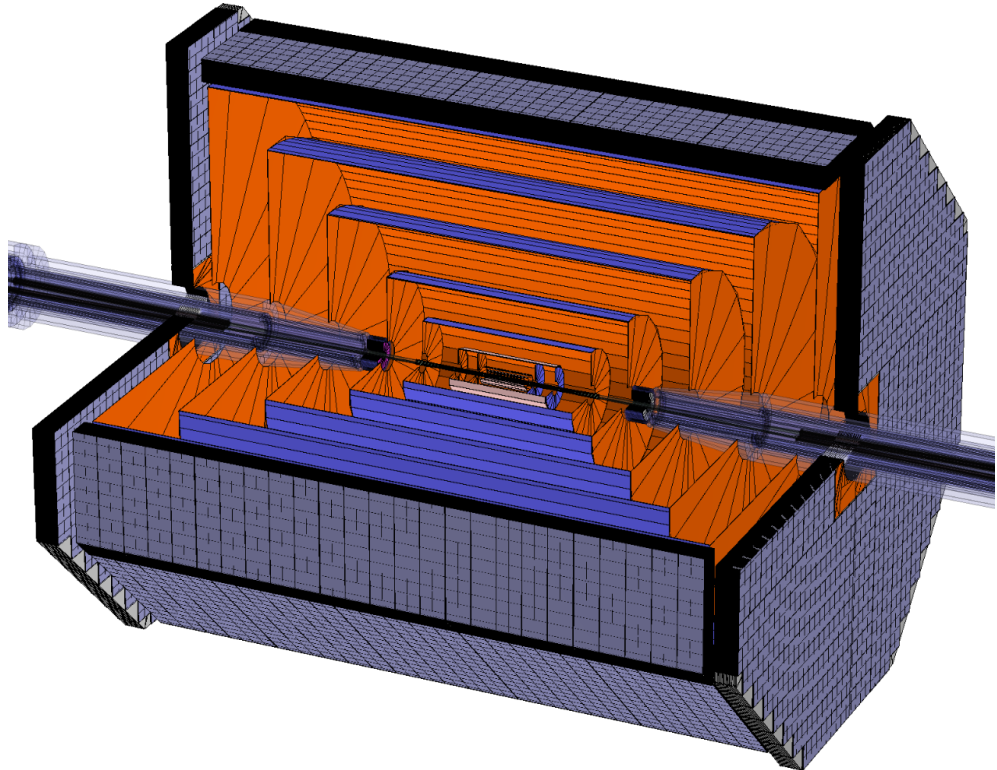


Figure 3.10: Schematic 3-D view of the FST detector and the zoomed full-silicon tracker.

19 3.3.3 An alternative low magnetic field detector concept

20 The baseline detector described in this CDR is a very straightforward evolution of the
 21 ILD detector originally conceived for the International Linear Collider (ILC) [13]. We

1 propose here a new detector concept, IDEA (Innovative Detector for Electron-positron
 2 Accelerator), that is specifically designed for a circular electron-positron collider and also
 3 attempts to economize on the overall cost of the detector.

4 While most detector requirements needed for detectors at ILC are very similar to those
 5 for CEPC [14], there are however some notable differences. First of all the typical lumi-
 6 nosity expected both at the Z pole ($\sqrt{s} = 90$ GeV) and above the ZH threshold ($\sqrt{s} =$
 7 240 GeV) is expected to be one or two orders of magnitude larger, with a much shorter
 8 bunch spacing and no large time gaps in the beam structure. This places severe con-
 9 straints on the tracking system. In particular one would prefer an intrinsically fast main
 10 tracker to fully exploit the cleanliness of the e^+e^- environment while integrating as little
 11 background as possible, and a very low-power vertex detector, since power pulsing is not
 12 allowed by the bunch spacing. Additional issues of emittance preservation, typical of cir-
 13 cular machines, set limits on the maximum magnetic field usable for the tracker solenoid,
 14 especially when running at lower center-of-mass energies. This could be a problem for a
 15 large volume TPC, due to the resolution degradation, and also for a silicon tracker, since
 16 it would require more layers at a large radius, thus significantly increasing the cost.

17 Additional specific requirements on a detector for CEPC come from precision physics
 18 at the Z pole, where the statistical accuracy on various electroweak parameters is expected
 19 to be over an order of magnitude better than at the ILC. This calls for a very tight control
 20 of the systematic error on the acceptance, with a definition of the acceptance boundaries
 21 at the level of a few μm , and a very good $e - \gamma - \pi_0$ discrimination to identify τ leptons
 22 efficiently and measure their polarization. A layer of silicon microstrip detectors around
 23 the main tracker can provide the needed acceptance control for charged tracks, while
 24 also improving the tracking resolution. Similarly, the acceptance accuracy and improved
 25 identification efficiency of γ 's can be obtained with a preshower based on micro-pattern
 26 gas detectors (MPGD) located just outside the detector magnet, which serves as a radiator.

27 The particle flow calorimeters, currently proposed for both ILC and CLIC, feature an
 28 extremely large number of readout channels and require significant data processing to
 29 obtain the optimal performance. A less expensive and more effective calorimeter can
 30 be made using the dual readout technique [15], which has been extensively studied and
 31 demonstrated in over ten years of R&D by the DREAM/RD52 collaboration [16, 17].
 32 With this technology the electromagnetic and hadronic calorimeters come in a single pack-
 33 age that plays both functions and allows an excellent discrimination between hadronic and
 34 electromagnetic showers [18]. Since all the readout electronics is located in the back of the
 35 calorimeter, its cooling is greatly simplified relative to the case of particle flow calorime-
 36 ters.

37 Finally recent developments in micro-pattern gas detector technology, such as μRwell [19],
 38 can significantly reduce the cost of large area tracking chambers to be used for tracking
 39 muons outside the calorimeter volume.

40 **The IDEA detector** The structure of the IDEA detector is outlined in Figure 3.11, which
 41 also shows its overall dimensions.

42 A key element of IDEA is a thin, ~ 30 cm, and low mass, $\sim 0.8 X_0$, solenoid with
 43 a magnetic field of 2 Tesla. This field is optimal, according to studies done for FCC-
 44 ee, as it minimizes the impact on emittance growth and allows for manageable fields
 45 in the compensating solenoids [20], but it is certainly not optimal for a large TPC or a
 46 silicon tracker of reasonable size. The low mass and thickness of the solenoid allows

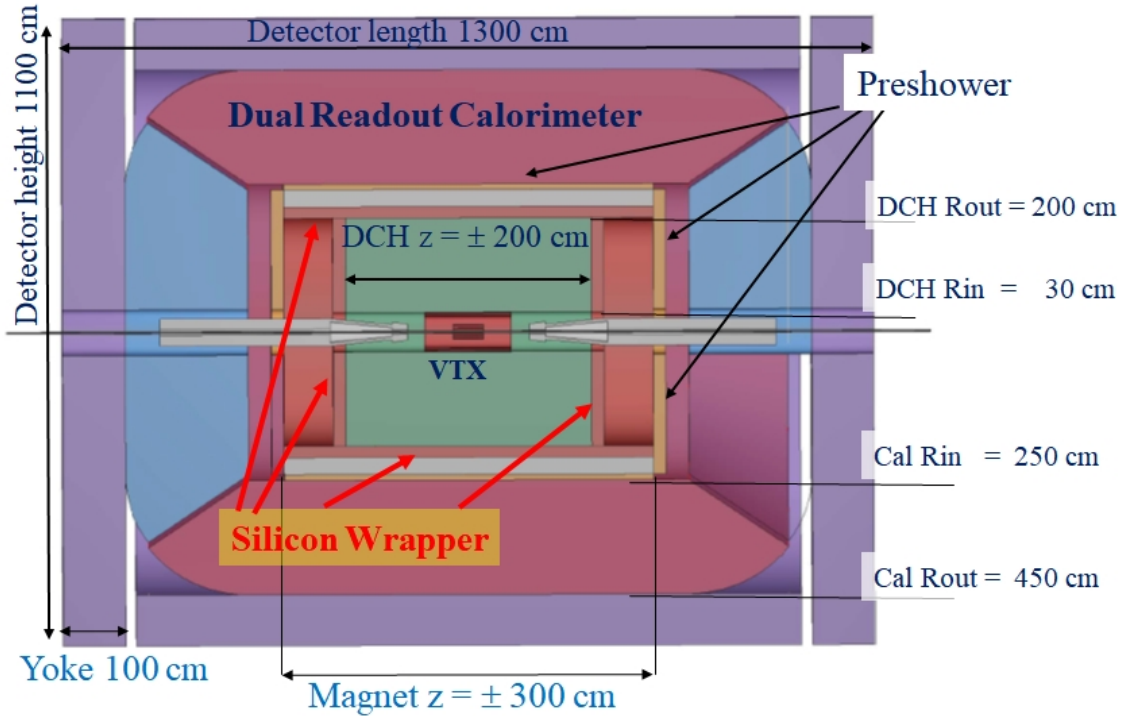


Figure 3.11: Schematic layout of the IDEA detector.

it to be located between the calorimeter and the tracking volume without a significant performance loss.

The innermost detector, surrounding the 1.5 cm radius beam pipe, is a silicon pixel detector for the precise determination of the impact parameter of charged particle tracks. Recent test beam results on the detectors planned for the ALICE inner tracker system (ITS) upgrade, based on the ALPIDE readout chip [21], indicate an excellent resolution, $\sim 5 \mu\text{m}$, and high efficiency at low power and dark noise rate [22]. This looks like a good starting point for the IDEA vertex detector and a similar approach is proposed for the CEPC baseline detector (see Section 4.1). The two detector concepts could then share the same pixel technology as well as profit from the electronic and mechanical work of the ALICE ITS.

Outside the vertex detector we have a 4 m long cylindrical drift chamber starting from a radius of ~ 35 cm and extending until 2 m. The chamber can be made extremely light, with low mass wires and operation using 90% helium gas; less than 1% X_0 is considered feasible for 90° tracks. Additional features of this chamber, which is described in detail in Section 4.4, are a good spatial resolution, $< 100 \mu\text{m}$, dE/dx resolution at the 2% level and a maximum drift time of only 400 ns. A layer of silicon microstrip detectors surrounds the drift chamber in both barrel and forward/backward regions. Track momentum resolution of less than 0.5% for 100 GeV tracks is expected when vertex detector and silicon wrapper information is included in the track fit. It is worth noting that the design of this chamber is the evolution of work done over many years on two existing chambers, that of the KLOE detector [23] and that of the recent MEG experiment upgrade [24]; major R&D work was done also for the 4th concept detector at ILC [25] and then for the Mu2E tracker [26].

1 A preshower is located between the solenoid magnet and the calorimeter in the barrel
 2 region and between the drift chamber and the endcap calorimeter in the forward region.
 3 This detector consists of two passive material radiators each followed by a layer of MPGD
 4 detectors. In the barrel region the solenoidal magnet plays the role of the first radiator,
 5 while in all other cases the radiators are made of lead. The actual thickness of the radiators
 6 are still being optimized based on test beams currently in progress. In the extreme case
 7 of using a total of two radiation lengths about 75% of the π^0 's can be tagged by having
 8 both γ 's from their decay identified by the preshower. Additional π^0 identification power
 9 comes from the high granularity of the calorimeter.

10 A solenoidal magnet surrounds the tracking system and the first preshower layer. Presently
 11 planned dimensions are 6 m of length and 4.2 m inner diameter. The relatively low two
 12 Tesla field and the small dimensions have important implications on the overall magnet
 13 package thickness, that can be kept at the 30–40 cm level, and on the size of the flux
 14 return yoke, which scales linearly with the field and the square of the coil diameter. With
 15 the given dimensions a yoke thickness of less than 100 cm of iron is sufficient to com-
 16 pletely contain the magnetic flux and provide adequate shielding and support for the muon
 17 chambers.

18 A dual readout fiber calorimeter (see Section 5.5) is located behind the second preshower
 19 layer. We assume a total calorimeter depth of 2 m, corresponding to approximately seven
 20 pion interaction lengths. The detector resolution is expected to be about $10.5\%/\sqrt{E}$ for
 21 electrons and $35\%/\sqrt{E}$ for isolated pions with negligible constant terms, as obtained from
 22 extrapolations from test beam data using GEANT4 without including the preshower. This
 23 detector has very good intrinsic discrimination between muons, electrons/photons and
 24 hadrons for isolated particles [18]. This discrimination power is further enhanced when
 25 the information of the preshower and the muon chambers is added, extending the sepa-
 26 ration power also into hadronic jets and making it suitable for the application of particle
 27 flow algorithms. The intrinsic high transverse granularity provides a good matching of
 28 showers to tracks and preshower signals.

29 The muon system consists of layers of muon chambers embedded in the magnet yoke.
 30 The area to be covered is substantial, several hundreds of square meters, requiring an
 31 inexpensive chamber technology. Recent developments in the industrialization of μ Rwell
 32 based large area chambers, as planned for the CMS Phase II upgrade, are very promising
 33 (see Section 7.3).

34 **Conclusions** A different concept for a detector at CEPC has been proposed. This de-
 35 tector is designed specifically for CEPC and its specific running conditions and physics
 36 goals. In particular it is safe with respect to interaction between the detector solenoid field
 37 and the beam. Although additional R&D to optimize performance, reduce costs and come
 38 to a detailed engineered design of the detector is still necessary, this detector is based on
 39 technologies which are established after many years of R&D and whose feasibility has
 40 by large been established. Furthermore several choices are made to simplify the detector
 41 structure and reduce the cost, which in the end should be smaller than for an ILD-like
 42 detector.

43 References

- 44 [1] The CEPC-SPPC Study Group, *CEPC-SPPC Conceptual Design Report, Volume I -*

- 1 Accelerator, IHEP, Beijing, China, Rep. IHEP-CEPC-DR-2018-01 (2018) .
- 2 [2] I. Agapov, G. A. Blair, S. Malton, and L. Deacon, *BDSIM: A particle tracking code*
3 *for accelerator beam-line simulations including particle-matter interactions*, *Nucl.*
4 *Instrum. Meth.* **A606** (2009) 708–712.
- 5 [3] D. Schulte, *Beam-beam simulation with GUINEA-PIG*, In 5th International
6 Computational Accelerator Physics Conference (1998) . CLIC-NOTE 387.
- 7 [4] GEANT4 Collaboration, S. Agostinelli et al., *GEANT4: A Simulation toolkit*, *Nucl.*
8 *Instrum. Meth.* **A506** (2003) 250–303.
- 9 [5] J. Allison et al., *Geant4 developments and applications*, *IEEE Trans. Nucl. Sci.* **53**
10 (2006) 270.
- 11 [6] Geant4 Collaboration, M. Asai et al., *Recent developments in Geant4*, *Annals Nucl.*
12 *Energy* **82** (2015) 19–28.
- 13 [7] L. Arnaudon, B. Dehning, P. Grosse-Wiesmann, R. Jacobsen, M. Jonker,
14 J. Koutchouk, J. Miles, R. Olsen, M. Placidi, R. Schmidt, et al., *Accurate*
15 *determination of the LEP beam energy by resonant depolarization*, *Zeitschrift für*
16 *Physik C Particles and Fields* **66** (1995) no. 1-2, 45–62.
- 17 [8] H. Qi, *Status and progress of TPC module and prototype R&D for CEPC*, 2017.
- 18 [9] M. Zhao, M. Ruan, H. Qi, and Y. Gao, *Feasibility study of TPC at electron positron*
19 *colliders at Z pole operation*, *Journal of Instrumentation* **12** (2017) no. 07, P07005.
20 <http://stacks.iop.org/1748-0221/12/i=07/a=P07005>.
- 21 [10] M. Ruan, D. Jeans, V. Boudry, J.-C. Brient, and H. Videau, *Fractal Dimension of*
22 *Particle Showers Measured in a Highly Granular Calorimeter*, *Phys. Rev. Lett.* **112**
23 (2014) 012001.
24 <https://link.aps.org/doi/10.1103/PhysRevLett.112.012001>.
- 25 [11] D. Yu, M. Ruan, V. Boudry, and H. Videau, *Lepton identification at Particle Flow*
26 *oriented detector for the future e^+e^- Higgs factories*, *The European Physical*
27 *Journal C* **77** (2017) no. 9, 591.
28 <https://doi.org/10.1140/epjc/s10052-017-5146-5>.
- 29 [12] H. Zhao, C. Fu, D. Yu, Z. Wang, T. Hu, and M. Ruan, *Particle flow oriented*
30 *electromagnetic calorimeter optimization for the circular electron positron collider*,
31 *JINST* **13** (2018) no. 03, P03010, [arXiv:1712.09625](https://arxiv.org/abs/1712.09625)
32 [*physics.ins-det*].
- 33 [13] H. Abramowicz et al., *The International Linear Collider Technical Design Report -*
34 *Volume 4: Detectors*, [arXiv:1306.6329](https://arxiv.org/abs/1306.6329) [*physics.ins-det*].
- 35 [14] CEPC-SPPC Study Group, *CEPC-SPPC Preliminary Conceptual Design Report. 1.*
36 *Physics and Detector*, IHEP, Beijing, China, Rep. IHEP-CEPC-DR-2015-01,
37 IHEP-TH-2015-01, IHEP-EP-2015-01 (2015).
38 <http://cepc.ihep.ac.cn/preCDR/volume.html>.
- 39 [15] DREAM Collaboration, R. Wigmans, *The DREAM project: Towards the ultimate in*
40 *calorimetry*, *Nucl. Instrum. Meth.* **A617** (2010) 129–133.

- [16] N. Akchurin et al., *The electromagnetic performance of the RD52 fiber calorimeter*, Nucl. Instrum. Meth. **A735** (2014) 130–144.
- [17] RD52 (DREAM) Collaboration, R. Wigmans, *New results from the RD52 project*, Nucl. Instrum. Meth. **A824** (2016) 721–725.
- [18] N. Akchurin et al., *Particle identification in the longitudinally unsegmented RD52 calorimeter*, Nucl. Instrum. Meth. **A735** (2014) 120–129.
- [19] M. Poli Lener, G. Bencivenni, R. de Olivera, G. Felici, S. Franchino, M. Gatta, M. Maggi, G. Morello, and A. Sharma, *The μ -RWELL: A compact, spark protected, single amplification-stage MPGD*, Nucl. Instrum. Meth. **A824** (2016) 565–568.
- [20] M. Koratzinos et al., *Progress in the FCC-ee Interaction Region Magnet Design*, <http://inspirehep.net/record/126211/files/wepik034.pdf> (2017), IPAC2017.
- [21] ALICE Collaboration, M. Mager, *ALPIDE, the Monolithic Active Pixel Sensor for the ALICE ITS upgrade*, Nucl. Instrum. Meth. **A824** (2016) 434–438.
- [22] ALICE Collaboration, G. Aglieri Rinella, *The ALPIDE pixel sensor chip for the upgrade of the ALICE Inner Tracking System*, Nucl. Instrum. Meth. **A845** (2017) 583–587.
- [23] KLOE Collaboration, A. Calcaterra, *The KLOE drift chamber*, Nucl. Instrum. Meth. **A367** (1995) 104–107.
- [24] MEG Collaboration, Y. Uchiyama, *Upgrade of MEG experiment*, PoS **EPS-HEP2013** (2013) 380.
- [25] A. Mazzacane, *The 4th concept detector for the ILC*, Nucl. Instrum. Meth. **A617** (2010) 173–176.
- [26] L. De Lorenzis, F. Grancagnolo, A. L’Erario, A. Maffezzoli, A. Miccoli, S. Rella, M. Spedicato, and G. Zavarise, *Analysis and Characterization of the Mechanical Structure for the I-Tracker of the Mu2e Experiment*, Nucl. Phys. Proc. Suppl. **248-250** (2014) 134–136.

Draft-V2.0

CHAPTER 4

TRACKING SYSTEM

¹ The CEPC physics program demands a robust and highly performance charged particle tracking system. Charged particles are used directly in physics analyses; they are input to determine primary and secondary vertices; and they are crucial input to particle flow calorimetry.

⁵ The tracking system has two major components. The vertex tracker has excellent spatial resolution and is optimized for vertex reconstruction. The main tracker is optimized for tracking efficiency and resolution required for the CEPC physics program.

⁸ This Chapter introduces all tracking systems options of the detector concepts discussed in this report. Section 4.1 describes the CEPC baseline vertex tracker, the inner tracker, which can be paired with one of the outer tracker options discussed in the subsequent three sections, albeit vertex tracker alternatives are also considered later. An outer tracker system, composed of a Time Projection Chamber (TPC) and Silicon Tracker, is discussed in Section 4.2. This system, together with the vertex detector from Section 4.1 composes the tracking system of the baseline detector concept. Section 4.3 discusses in some detail the option of a Full-Silicon Tracker that could substitute the tracking system described above for the CEPC baseline detector. Finally, in Section 4.4 a Drift Chamber Tracker is proposed as an option for the CEPC main outer tracker. This chamber, together with a layer of silicon microstrip detectors that wraps it in both barrel and forward/backward regions, and the inner vertex detector, constitute the tracking system of the CEPC alternative detector concept.

1 4.1 Vertex tracker detector

2 The identification of heavy-flavor (b - and c -) quarks and τ leptons is essential for the CEPC
 3 physics program. It requires precise determination of the track parameters of charged par-
 4 ticles in the vicinity of the interaction point (IP), permitting reconstruction of the displaced
 5 decay vertices of short-lived particles. This drives the need for a vertex detector with low
 6 material budget and high spatial resolution. The baseline design of the CEPC vertex de-
 7 tector is a cylindrical barrel with six silicon pixel layers and optimized for the energy
 8 regime and utilizes modern sensors.

9 4.1.1 Performance Requirements and Detector Challenges

10 As required for the precision physics program, the CEPC vertex detector is designed to
 11 achieve excellent impact parameter resolution, which in the $r\phi$ plane can be parametrized
 12 by:

$$13 \sigma_{r\phi} = a \oplus \frac{b}{p(\text{GeV}) \sin^{3/2} \theta} \quad (4.1)$$

14 where $\sigma_{r\phi}$ denotes the impact parameter resolution, p the track momentum, and θ the
 15 polar track angle. The first term describes the intrinsic resolution of the vertex detector
 16 in the absence of multiple scattering and is independent of the track parameters, while
 17 the second term reflects the effects of multiple scattering. The parameters $a = 5 \mu\text{m}$ and
 18 $b = 10 \mu\text{m} \cdot \text{GeV}$ are taken as the design values for the CEPC vertex detector. The main
 19 physics performance goals can be achieved with a three concentric cylinders of double-
 layer pixelated vertex detector with the following characteristics:

- 20 ▪ Single-point resolution of the first layer better than $3 \mu\text{m}$;
- 21 ▪ Material budget below $0.15\% X_0$ per layer;
- 22 ▪ First layer located close to the beam pipe at a radius of 16 mm , with a material budget
 23 of $0.15\% X_0$ for the beam pipe;
- 24 ▪ Detector occupancy not exceeding 1% .

25 The power consumption of the sensors and readout electronics should be kept below
 26 50 mW/cm^2 , if the detector is air cooled. The readout time of the pixel sensor needs to
 27 be shorter than $10 \mu\text{s}$, to minimize event accumulation from consecutive bunch crossings.
 28 The radiation tolerance requirements, which are critical for the innermost detector layer,
 29 are driven by the beam-related backgrounds as described in Chapter 9.

30 4.1.2 Baseline design

31 The baseline layout of the CEPC vertex detector consists of six concentric cylindrical
 32 layers of high spatial resolution silicon pixel sensor located between 16 and 60 mm from
 33 the beam line (see Figure 4.1), providing six precise space-points for charged particles
 34 traversing the detector. The main mechanical structure is called a ladder. Each ladder
 35 supports sensors on both sides; thus, there are three sets of ladders for the vertex detector.
 36 The material budget of each detector layer amounts to $\sim 0.15\% X_0$. Extensive simulation
 37 studies (see Section 4.1.3) show that this configuration with the single-point resolutions
 38 listed in Table 4.1 achieves the required impact parameter resolution.

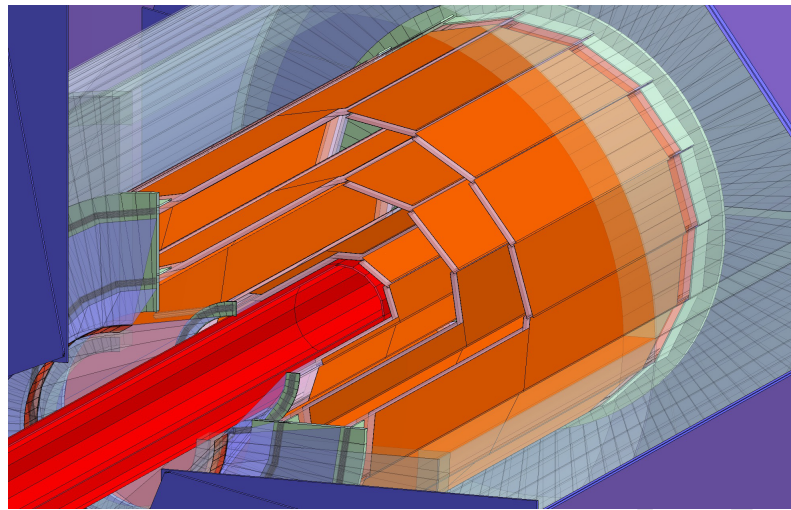


Figure 4.1: Schematic view of pixel detector. Two layers of silicon pixel sensors (in orange) are mounted on both sides of each of three ladders to provide six space points. The vertex detector surrounds the beam pipe (red).

	R (mm)	$ z $ (mm)	$ \cos \theta $	σ (μm)
Layer 1	16	62.5	0.97	2.8
Layer 2	18	62.5	0.96	6
Layer 3	37	125.0	0.96	4
Layer 4	39	125.0	0.95	4
Layer 5	58	125.0	0.91	4
Layer 6	60	125.0	0.90	4

Table 4.1: The baseline design parameters of CEPC vertex detector including position and single-point resolution. The values of single-point resolution for layer 1 and layer 2 are considered from the double-sided ladder concept based on a high resolution sensor on one side, and a faster sensor on the other side to provide necessary time-stamp for tracking.

4.1.3 Detector performance studies

- The identification of b/c -quark jets (called "flavor-tagging") is essential in physics analysis where signal events with b/c -quark jets in the final state have to be separated from one another and from light-quark jets. Flavor tagging requires the precise determination of the trajectory of charged tracks embedded in the jets. For CEPC operation at the center-of-mass energy of 240 GeV, those tracks are often of low momentum, for which the multiple scattering effect dominates the tracking performance as illustrated by Eq. 4.1.
- The CEPC vertex detector layout has been fully implemented in the GEANT4-based simulations framework MOKKA [1]. In addition, the LiC Detector TOY fast simulation and reconstruction framework (LDT) [2] have been used for detector performance evaluation and layout optimization. The preliminary studies for optimization to evaluate the sensitivity of the results on the chosen parameters have been done, for the purpose of assessing the impact of the detector geometries and material budgets on required flavor-

1 tagging performance. However, beam-induced background was not included at the moment.

3 4.1.3.1 Performance of the Baseline Configurations

4 The impact parameter resolution following from the single-point resolutions provided in
5 the Table 4.1 is displayed in Figure 4.2 as a function of the particle momentum, showing
that the ambitious impact parameter resolution is achievable.

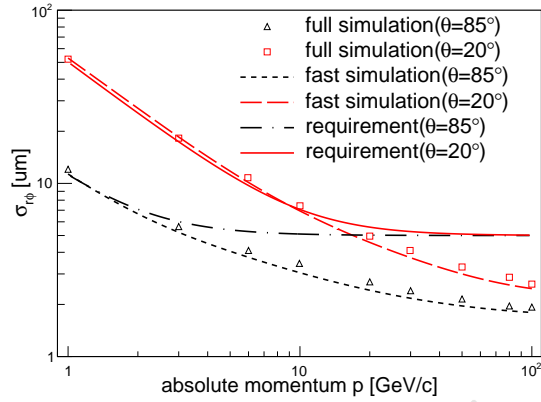


Figure 4.2: Transverse impact-parameter resolutions for single muon events as a function of momentum for two polar angles 20° and 85° . The results are shown for both fast simulation and full simulation method.

6

7 4.1.3.2 Material Budget

8 The baseline design includes very small material budget for the beam pipe as well as
9 for the sensor layers and their support. To assess the sensitivity of the performance on the
10 amount of material, the material budget of the beam pipe and the vertex detector layers has
11 been varied. The resulting transverse impact-parameter resolutions for low-momentum
12 tracks are shown in Figure 4.3. When increasing the material of the detector layers by a
13 factor of two, the resolution degrades by approximately 20%.

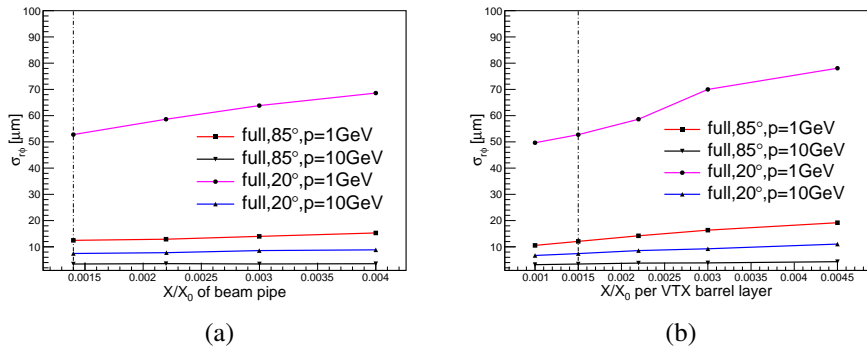


Figure 4.3: Transverse impact-parameter resolution as function of the amount of material in beam pipe (a) and in each vertex detector barrel layer (b), as obtained from the simulation. The results are shown for 1 GeV and 10 GeV muon tracks and for polar angles of $\theta = 20$ degrees and of $\theta = 85$ degrees. The material budget corresponding to the baseline configuration is indicated by dashed lines.

4.1.3.3 Dependence on Single-Point Resolution

The dependence of the transverse impact-parameter resolution on the pixel size was studied by worsening the single-point resolution of the vertex layers by 50% w.r.t. the baseline values. The resulting impact parameter resolution for high and low momentum tracks as function of the polar angle θ is shown in Figure 4.4. The impact parameter resolution for track momenta of 100 GeV is found to change by approximately 50% in the barrel region, which is expected. They are better than the target value for the high-momentum limit of $a \sim 5 \mu\text{m}$ in both cases, as expected from the corresponding single-point resolutions. For 1 GeV, where multiple-scattering effects dominate, the corresponding variation of the transverse impact-parameter resolution is only 10% larger. The target value for the multiple-scattering term of $b \sim 10 \mu\text{m} \cdot \text{GeV}$ is approximately reached in both cases. It should be noted, however, that the pixel size is also constrained by the background occupancies (see Section 4.1.4) and the ability to separate adjacent tracks in very dense jets in the presence of such backgrounds.

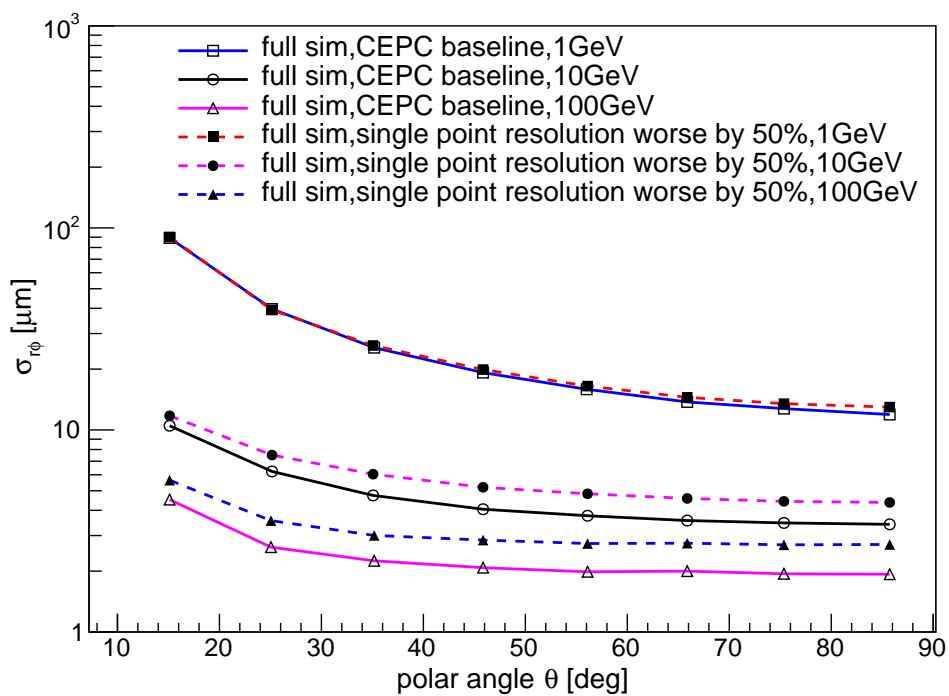


Figure 4.4: Transverse impact-parameter resolutions as function of the polar angle θ for different values of the single-point resolution of the CEPC vertex detector. Shown are the resolutions for 1 GeV, 10 GeV and 100 GeV tracks.

4.1.3.4 Distance to Beam Line

The distance of the first two vertex layers, which are supported by a single ladder, from the interaction point (IP) was varied by $\pm 4 \text{ mm}$ relative to baseline geometry of the CEPC vertex detector. When the radius of the innermost layer is considered to be 12 mm, the ra-

radius of the beam pipe was reduced to 10.5 mm.¹ Figure 4.5 shows the resulting transverse impact parameter resolution at $\theta=85$ degrees as function of the momentum and for different radial distances of the innermost barrel vertex layer from the IP. For low momentum tracks, the transverse impact-parameter resolution is proportional to the inner radius, as expected from the parameter formula.

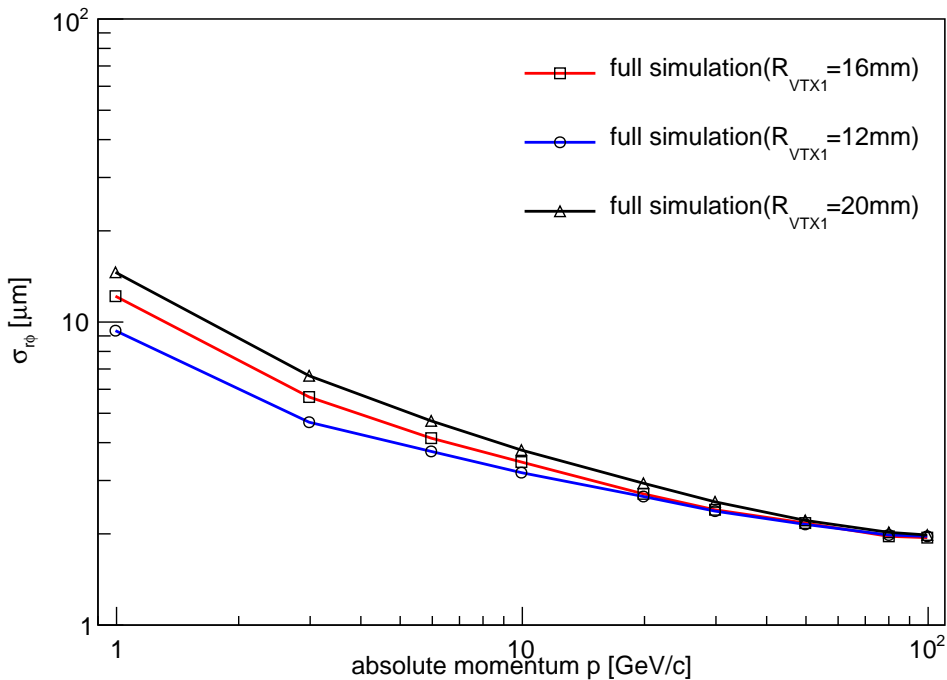


Figure 4.5: Transverse impact-parameter resolution at $\theta = 85$ degrees as function of the momentum for different values of inner most layer radius R_{VTX1} . The red curve indicates the baseline configuration of $R_{VTX1} = 16$ mm.

5

6 4.1.4 Beam-induced Background in the Vertex Detector

7 Pair-production and off-energy beam particles are expected to be the dominating source of
8 detector backgrounds originating from the interaction region. These processes have been
9 studied with detailed Monte Carlo simulation in Chapter 9. For the first vertex detector
10 layer, the maximum annual values of the Total Ionizing Dose (TID) and Non-Ionizing En-
11 ergy Loss (NIEL) are estimated to be 3.4 MRad and 6.2×10^{12} 1 MeV n_{eq}/cm² per year,
12 respectively, with a safety factor of 10 included (see Table 9.4 in Chapter 9). This hap-
13 pens when the machine is operating at the Z -pole energy, and imposes radiation tolerance
14 requirements on the silicon pixel sensor and associated readout electronics.

15 The beam-induced background will have impacts on vertex detector occupancy, which
16 is critical for the innermost detector layer. Table 4.2 shows the expected hit density and
17 occupancies of the first vertex detector layer at different machine operation energies. The
18 result of occupancies depends on assumptions of detector readout time and average cluster

¹This beam pipe radius size is smaller than the current baseline beam pipe, and it poses challenges regarding beam backgrounds and mechanical assembly that would require further studies to demonstrate its feasibility.

	H(240)	W(160)	Z(91)
Hit density ($\text{hits} \cdot \text{cm}^{-2} \cdot \text{BX}^{-1}$)	2.4	2.3	0.25
Bunching spacing (μs)	0.68	0.21	0.025
Occupancy (%)	0.08	0.25	0.23

Table 4.2: Occupancies of the first vertex detector layer at different machine operation energies: 240 GeV for ZH production, 160 GeV near W -pair threshold and 91 GeV for Z -pole.

size. Here we assume 10 μs of readout time for the silicon pixel sensor and an average cluster size of 9 pixels per hit, where a pixel is taken to be $16 \times 16 \mu\text{m}^2$. The resulting maximal occupancy at each machine operation mode is below 1%.

4.1.5 Sensor Technology Options

Significant progress has been made since the first silicon pixel detector was first used in high-energy physics experiments, and considerable R&D efforts have taken place to develop pixel sensors for vertex tracking at future particle physics experiments [3], driven by track density, single-point resolution and radiation level.

As outlined in Section 4.1.1, the detector challenges for the CEPC include high impact-parameter resolution, low material budget, low occupancy and sufficient radiation tolerance (mild comparing to LHC but not necessarily easy to achieve). To fulfill these requirements at system level, sensor technologies which achieve fine pitch, low power and fast readout must be selected. These considerations present unique challenges to the CEPC vertex detector. CEPC has a bunch spacing of 0.68 μs , and power pulsing cannot be utilized to reduce average power as is planned at the ILC. Experiments such as the STAR [4], BELLEII [5] and ALICE upgrade [6] readout continuously as the CEPC. However, they have less stringent requirements in terms of impact-parameter resolution and material budget.

The monolithic pixel sensor has the potential to satisfy the low-material and high-resolution requirements of the CEPC vertex detector. This technology has been developing fast. The 1st generation MAPS-based vertex detector for the STAR HFT upgrade [4, 7] just completed 3-year physics run successfully, while the new generation HR CMOS Pixel Sensor for ALICE-ITS upgrade [6] is in mass production. In the previous 0.35 μm double-well process, only N-MOS transistors can be used in the pixel design. This constraint is removed in the new 0.18 μm quadruple-well process. Both N- and P-MOS transistors could be used in the pixel design. Combining with the smaller feature size, it becomes a very appealing technology. A good start point for the CEPC vertex would be the ALPIDE design [8], which is developed for the aforementioned ALICE-ITS upgrade and has achieved performances very close to the requirements of the CEPC. Further R&Ds are needed to shrink the pixel pitch to 16 μm (binary readout) in order to accomplish the required 2.8 μm single-point resolution. Another monolithic option is the Silicon On Insulator (SOI) pixel sensor. After more than 10 years of evolution, SOI has entered a new stage of maturity. Fundamental issues, including the transistor shielding [9] and the TID tolerance [10], have been addressed and wafer thinning [11] has been demonstrated. In the meanwhile, R&Ds for the ILC and CLIC [12, 13] are exploring time stamping and analog

1 readout schemes. The SOI has a unique feature of a fully-depleted substrate as the active
 2 silicon. And its $0.2\text{ }\mu\text{m}$ CMOS process provides the necessary density of transistors as the
 3 $0.18\text{ }\mu\text{m}$ CMOS in HR CMOS does. Therefore it is envisaged that the readout design for
 4 the CEPC vertex may be adapted for both processes and to exploit each ones potentials.

5 Depleted P-channel Field Effect Transistor (DEPFET) is referred to as semi-monolithic
 6 because the first amplification stage can be integrated into the pixel combined with subse-
 7 quent processing circuit in separate readout ASICs. The BELLE II is anticipating its full
 8 detector operation with a DEPFET-based vertex detector [5] installed at the end of 2018.
 9 It is very helpful to have the readout ASICs, as the major heat sources, located outside
 10 the detector acceptance area, while keeping the sensors exceptionally low power and low
 11 material. The challenge is to periodically sample the modulated current over a large pixel
 12 array within required intervals, $20\text{ }\mu\text{s}/\text{frame}$ or even less.

13 Hybrid pixel has been used at hadron colliders for the past decades, and now CLIC
 14 R&D is pushing for $50\text{ }\mu\text{m}$ thinned sensors, bump-bonded on $25\text{ }\mu\text{m}$ pitch to $50\text{ }\mu\text{m}$
 15 thinned ASICs [14]. The hybrid approach evolves constantly and profits from industrial
 16 technology developments. Apart from the Very Deep Sub-Micron (VDSM) ASIC tech-
 17 nology that enables complex functionalities and superior performances, a close watch on
 18 industrial developments of the vertical and lateral inter-connection technologies will also
 19 be very helpful to meet the material budget.

20 **4.1.6 Mechanics and Integration**

21 The design of the vertex detector is conceived as a barrel structure with three concentric
 22 cylinders of double-sided layers. Each double-sided layer is equipped with pixel sensors
 23 on both sides, and has a common support frame. In the azimuthal direction, each layer is
 24 segmented in elements called ladders. The ladder, which extends over the whole length of
 25 the layer, is the basic building block of the detector. It contains all structural and functional
 26 components, such as chips, flex cable, support frame and cold plate if it is necessary. Pixel
 27 chips in a row are connected to flex cable by wire bonding or other bonding techniques,
 28 and then glued to the support frame, which is composed of low- Z materials, such as
 29 carbon fiber and silicon carbide, providing stable mechanical support. The other side of
 30 the support frame is equipped with another layer of pixel sensors.

31 The design of the ladders should take into account the specifications of the vertex de-
 32 tector. In order to reduce a small multiple Coulomb scattering contribution to the charged-
 33 track vertex resolution and control deformations from gravity and cooling forces for the
 34 sensor position stability, the ladder mechanical support must fulfill stringent requirements
 35 in terms of minimum material budget and highest stiffness. Ladder designs similar to
 36 the STAR pixel detector, the ALICE ITS, the BELLE II PXD, and the ILD double-sided
 37 ladder are under consideration.

38 The ladder mechanical support is inherently linked to the layout of the cooling system
 39 that will be adopted to remove the heat dissipated by the pixel sensors since the cooling
 40 system is integrated in the mechanical structure. The cooling system of the CEPC vertex
 41 detector must balance the conflicting demands of efficient heat dissipation with a minimal
 42 material budget. Therefore a suitable, high thermal conductivity and low material budget,
 43 cold plate coupled with pixel sensors should be implemented in the ladder design. There
 44 are two main types of cooling methods in particle physics experiments, air cooling and
 45 active cooling. Table 4.3 gives a list of cooling methods and the corresponding material

of each layer of the aforementioned experiments. The upgrade of ALICE ITS [6] adopts water cooling with respect to a chips power dissipation value of 300 mW/cm^2 . Polyimide cooling pipes fully filled with water are embedded in the cold plate. STAR-PXL [15] uses air cooling according to its chips power consumption of 170 mW/cm^2 . For ILD [16] vertex system, two different cooling options are considered, depending on the sensor technology. The sensors and SWITCHER chips of BELLE II PXD [17] require air cooling, while active cooling will be used for readout chips on each end of the detector, which is out of the sensitive region of the detector. For the CEPC vertex detector, the suitable cooling method will be determined according to the sensor option and the power consumption.

Vertex detector	Power dissipation	Cooling method	Material budget requirement/layer
Alice ITS	300 mW/cm^2	water	0.3%
STAR PXL	170 mW/cm^2	air	0.39%
ILD vertex	$< 120 \text{ mW/cm}^2$ (CPS and DEPFET)	air or N_2	0.15%
	35 W inside cryostat (FPCCD)	two-phase CO_2	
BELLE-II PXD	20 W for sensor and SWITCHER	Air	0.2%
	180 W on each end	CO_2	

Table 4.3: Cooling methods for several vertex detector designs. The chip power dissipation, coolant type and corresponding material budget requirement per sensor layer are indicated. The active CO_2 cooling adds additional material in the forward region, outside the sensitive area. For the ILD FPCCD option, this additional material budget is $0.3\% X_0$ averaged over the end-plate region, while for the BELLE-II PXD, it is $\sim 0.1 - 0.2\% X_0$ per layer.

Simulation and module prototype studies will be carried out to find suitable designs that can meet requirements of stability, cooling and the performance of the vertex detector. For the design of the whole mechanical structure of the vertex detector, some criteria must be taken into account. Firstly, minimum material has to be used in the sensitive region to reduce multiple Coulomb scattering. Secondly, to ensure high accuracy in the relative position of the detector sensors and provide an accurate position of the detector with respect to the central tracker of TPC and the beam pipe, a mechanical connector or locating pin at each end of the ladder should be considered to allow the fixation and alignment of the ladder itself on the end rings. Thirdly, the cooling system should be arranged reasonably to ensure stable heat dissipation. Lastly, to reduce the dead region caused by the boundary of each ladder, neighboring ladders should be partially superimposed.

In addition, the main mechanical support structures of the vertex should also meet the requirements of the integration with the other detectors, such as time-projection chamber (TPC) and forward tracking disks.

4.1.7 Critical R&D

The inner most layers have to fulfill the most demanding requirements imposed by the physics program. In addition, the system is bounded by stringent running constraints. The technology options in Section 4.1.5 are able to meet each individual requirement, including single-point resolution, low material budget, fast readout, low power consumption and radiation tolerance, but R&D is needed to select the specific design which can achieve the combination of all these criteria. Due to the limited manpower and availability of process, presently R&D efforts have been put into CMOS and SOI pixel sensor development to address the challenges concerning single-point resolution and low power consumption. Further developments are foreseen to follow in the future, including enhancement of density, radiation hardness and ultra-light module assembly.

The current R&D activities have access to two advanced processes. The TowerJazz 0.18 μm quadruple-well process enables the full CMOS pixel circuit, while Lapis 0.2 μm double-SOI process has properly solved the crosstalk between sensor and digital part, and improved TID tolerance significantly.

In order to exploit the potential of these new developments, two design teams have started chip designs using HR CMOS and SOI technologies, respectively. Two designs have been submitted to the TowerJazz foundry. The first one uses simple three transistor (3T) analog amplification circuit to carry out the optimization of sensing diode and evaluate the influence of radiation damage [18]. The second one implements a well-proved rolling shutter readout as well as an innovative data-driven readout [19, 20]. Another two designs that adopt the SOI technology have also been submitted [21]. With the amplifier and discriminator integrated into each pixel, the pixel size has been shrunk to 16 μm pitch. The chip has been thinned to 75 μm successfully and an infrared laser test has shown that a single-point resolution of 2.8 μm is achievable with that pitch [11]. All the designs for current R&D are in line with the same principle of in-pixel discrimination even though each one has its own implementation. An in-pixel discriminator can reduce analog current therefore lead to reduced power consumption.

Enhancements of the TowerJazz 0.18 μm process or Lapis 0.2 μm process are possible by migrating to a smaller feature size, 0.13 μm for example, or combining with a micro-bump 3D integration process. The latter is able to attach a second layer of pixel circuit on top of the existing layer of the sensing diode and front-end circuit. The upper tier can be the fully digital part that implements data-driven readout architecture, while the lower tier can be HR CMOS or SOI pixel matrix. A promising result has been demonstrated by the successful formation of 2.5 μm Au cone bump with NpD (Nano-particle deposition) technique [22]. However, the throughput needs further improvement and the thinning of sensors has to be compatible with micro-bump 3D integration.

The TowerJazz process is expected to be sufficiently radiation hard for the expected TID. An N-type plain implant has recently been added to improve the charge collection efficiency [23], which therefore will benefit the non-ionization radiation damage. In terms of the SOI process, the weak point is the BOX layer of SiO_2 . Although the TID tolerance of the SOI process has been improved dramatically by the introduction of Double-SOI and the optimization of transistor doping recipe (LDD, lightly doped drain) [10], SOI needs carefully study on the irradiation of large scale chips and of low power designs.

Sensor thinning and ultra-low material construction of modules are subject to the constraint of 0.15% X_0/layer . HR CMOS wafer thinned to 50 μm is routine in semiconductor

1 industry nowadays. SOI wafers thinned to 75 μm with backside implant have also been
 2 demonstrated by current R&D. However, low material detector modules need to integrate
 3 mechanical support, power and signal connections, and have sufficient stiffness to avoid
 4 vibration.

5 A pixel detector prototype will be built with full-size pixel sensors to develop and test
 6 some of these critical aspects, including the mechanical design of low-mass support struc-
 7 tures, cooling, fast readout and radiation tolerance.

8 **4.1.8 Summary**

9 The basic concept of the CEPC Vertex detector, including the detector layout, the material
 10 budget per layer, and the pixel sensors specifications required by the impact parameter
 11 resolution are implemented in the baseline detector simulation. This is an essential re-
 12 quirement for the detailed mechanical design. Small pixel sensor prototypes that can
 13 satisfy some of the CEPC requirements have already been produced.

14 It will be crucial to continue the pixel sensor R&D program and develop pixel sensors
 15 with radiation tolerance, lower power consumption and fast readout electronics because
 16 of continuous colliding mode and strong beam-related background. Detailed designs for
 17 low-mass mechanical supports, cooling, cabling, and power conversion are also necessary.
 18 Most of these issues will be addressed by R&D for the CEPC and by exploring synergies
 19 with experiments which have similar requirements.

20 **4.2 Time Projection Chamber and Silicon tracker**

21 The Time Projection Chamber (TPC) is one of the options being considered for the CEPC
 22 outer tracker. The high density of space points provides unparalleled pattern recognition
 23 capability. The TPC is complemented by an envelope of silicon detectors to improve its
 24 momentum resolution. The silicon detectors are also useful for monitoring possible field
 25 distortions in the TPC and for alignment purposes.

26 **4.2.1 Time Projection Chamber**

27 Time Projection Chambers have been extensively studied and used in different fields, es-
 28 pecially in particle physics experiments such as STAR [24] and ALICE [25]. The technol-
 29 ogy directly provides three-dimensional space points; the gaseous detector volume gives
 30 a low material budget; and the high density of such space points enables excellent pattern
 31 recognition capability. However, care must be taken to address space charge distortion
 32 resulting from the accumulation of positive ions in the drift volume [26]. This issue is
 33 especially important in high rate conditions.

34 There have been extensive R&D on readout modules to optimize position resolution
 35 and to control ion backflow. These studies will continue for the next few years in order to
 36 understand and resolve several critical technology challenges.

37 **4.2.1.1 CEPC Time Projection Chamber**

38 The TPC consists of a field cage, which is made with advanced composite materials, and
 39 two readout end-plates that are self-contained including the gas amplification, readout
 40 electronics, supply voltage, and cooling. The CEPC TPC consists of a cylindrical drift
 41 volume with an inner radius of 0.3 m and an outer radius of 1.8 m, and it has a full length

of 4.7 m. The central cathode plane is held at a potential of 50 kV, and the two anodes at the two end-plates are at ground potential. The cylindrical walls of the volume form the field cage, which ensures a highly homogeneous electrical field between the electrodes of 300 V/cm. The drift volume is filled with Ar/CF₄/iC₄H₁₀ in the ratio of 95/3/2. Ionization electrons released by charged particle tracks drift along the electric field to the anodes where they are amplified in an electron avalanche and readout using a micro-pattern gaseous detector (MPGD).

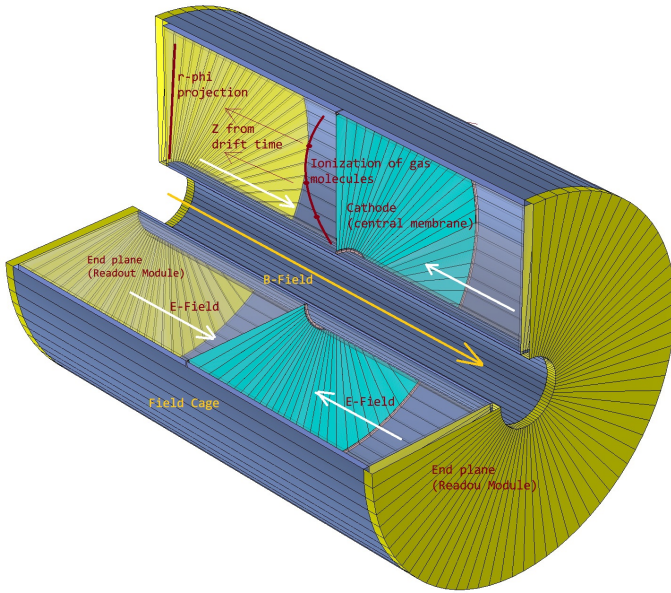


Figure 4.6: Sketch of the TPC detector structure. The TPC is a cylindrical gas detector with an axial electric field formed between the end-planes (yellow) and a central cathode plane/membrane (light blue). The cylindrical walls of the volume form the electric field cage (dark blue). Charged particles passing through the chamber are bent by the axial magnetic field and gas ionization electrons drift to the end plates where they are collected by readout modules (yellow).

The CEPC TPC is operated at atmospheric pressure resulting in a material budget of less than 1% X_0 in the central region. The 3-Tesla solenoidal magnetic field suppresses transverse diffusion and improves position resolution. It also curls up low-momentum tracks resulting in higher occupancy near the beam line. The readout modules are attached to the end-plates from the inside to minimize the dead area between adjacent readout modules. Thus, a particular mounting technique is required to enable rotation and tilting of the readout modules during installation.

The chamber's cylindrical inner and outer walls serve multiple functions. They hold the field forming strips, which are attached to a divider chain of non-magnetic resistors. Since the central cathode will be held at approximately 50 kV, the walls must withstand this enormous potential. The field cage will be designed to maintain the electric field uniform over the whole active TPC volume. Advanced composite material will be used for the cylindrical walls because of its low mass.

The MPGD detector on each end-plate is divided into many independent readout modules to facilitate construction and maintenance. The modules are mounted closely together on the end-plate to provide nearly full coverage. Power cables, electronic connectors, cooling pipes, PCB boards and support brackets wall are also mounted on the end-plate.

The end-plate needs to be constructed from a lightweight material in order not to compromise the jet energy resolution in the forward region but should also be sufficiently rigid to maintain stable positioning of the detector modules with a position accuracy better than 50 μm . The endcap structure has a thickness of $8\%X_0$, 7% of which originate from the material for the readout planes, front-end electronics and cooling. Adding power cables and connectors, the total thickness increases from $8\%X_0$ up to $10\%X_0$.

The CEPC TPC provides 220 space points per track with a single-point resolution in $r - \phi$ of 100 μm . In addition to position information, the TPC measures the energy loss on each readout pad. This can be combined with the measurement of momentum in the magnetic field to provide particle identification.

4.2.1.2 Baseline design and technology challenges

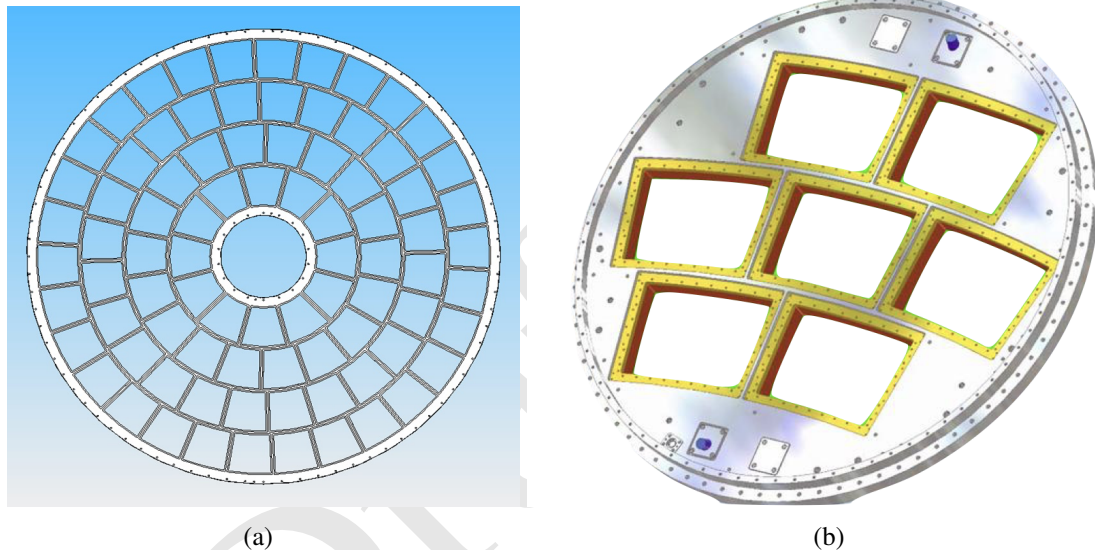


Figure 4.7: Mechanical support (TPC endwall) for mounting the readout modules. Each opening will take a readout module of roughly 170 mm \times 210 mm. (a) Full size design of TPC endwall; (b) Small prototype of the endwall showing details of the openings for the module insertion. The readout modules will be inserted, and installed on the inside of the endwall to minimize dead space.

The readout structure is designed to be modular to facilitate construction and maintenance. Each module will consist of gas amplification system, readout plane and the associated front-end electronics. An MPGD-based gas amplification system will be necessary to achieve the required performance, and the charge from the amplification system will be collected on the readout board. The readout module will also have to provide all necessary power and cooling. Each module will be approximately 170 mm in width and 200 mm in height.

Figure 4.7 shows the design of the mechanical support for the mounting of the readout modules on the inside of the TPC endwall developed by the LC-TPC international collaboration group. Figure 4.7(b) shows the details of the mounting openings from a small endwall prototype. Readout modules are inserted at an angle through openings in the endwall (white in Figure 4.7(b)) into the drift volume. They are then rotated to the proper orientation, pulled back against the mounting frame (yellow in the figure), and bolted into

1 place from the outside. This approach allows the active areas of adjacent readout modules
 2 to be very close to one another and therefore minimizes dead space between them.

3 **Gas amplification detector module**

4 The required physics performance can be achieved with amplification technologies with
 5 gain in the range of $10^3 - 10^4$ combined with a spatial granularity of approximately 1 mm^2 .
 6 Gas Electron Multiplier (GEM) [27] and Micro-Mesh Gaseous Structure (MicroMegas)
 7 detector [28] of the MPGD family of detectors [29] are both viable technologies for the
 8 large-area application in the CEPC TPC readout module. They can generate the very
 9 high fields necessary for gas amplification with modest voltages (300–400 V) across 50–
 10 $100 \mu\text{m}$ structures. In the case of GEM, two or three will be stacked together to achieve
 11 sufficient charge amplification while MicroMegas have enough amplification in a single
 12 stage.

13 Micro-pattern gaseous devices such as GEM and MicroMegas provide:

- 14 1. High gain
- 15 2. High rate capability: MPGDs provide a rate capability over 10^5 Hz/mm^2 without dis-
 16 charges that can damage electronics.
- 17 3. Intrinsic ion backflow suppression: Most of the ions produced in the amplification
 18 region will be neutralized on the mesh or GEM foil and do not go back to the drift
 19 volume.
- 20 4. A direct electron signal, which gives good time resolution ($< 100 \text{ ps}$) and spatial
 21 resolution ($100 \mu\text{m}$).

22 The baseline gas amplification and readout module for the CEPC TPC is a novel con-
 23 figuration detector module: a combination of GEM and a MicroMegas. This detector will
 24 be called a GEM-MM detector for short throughout this paper. This device aims to deliver
 25 gains around 5000 with ion backflow at 0.1% level.

26 **Optimization readout strip size**

27 Signals are read out in two orthogonal sets of strips. The readout strips in the X direction
 28 are $193 \mu\text{m}$ wide with a pitch of $752 \mu\text{m}$. The readout strips in the Y direction are $356 \mu\text{m}$
 29 wide with a pitch of $457 \mu\text{m}$. The difference in strip widths is to improve signal sharing
 30 between adjacent strips. Strips are approximately 6 mm long, and each strip is connected
 31 to one electronic channel to process the signal. Each readout unit contains 267 channels
 32 for the X direction and 437 channels for the Y direction.

33 Figure 4.8 is a typical layout of the X and Y readout strips, and two representative
 34 electron clusters are also superimposed. Each X-Y strip crossing has an area about 1 mm^2 .
 35 Thus each cluster spans a large number of such crossings, allowing the use of the Center-
 36 of-Gravity method to reach a position resolution finer than the strip pitches.

37 **Operation gas**

38 The choice of chamber gas strongly affects the properties and eventually the perfor-
 39 mance of a TPC. Desirable characteristics are:

- 40 1. High drift velocity (to avoid accumulation of too many events inside the chamber)
- 41 2. Low electron capture probability (to preserve signal size)

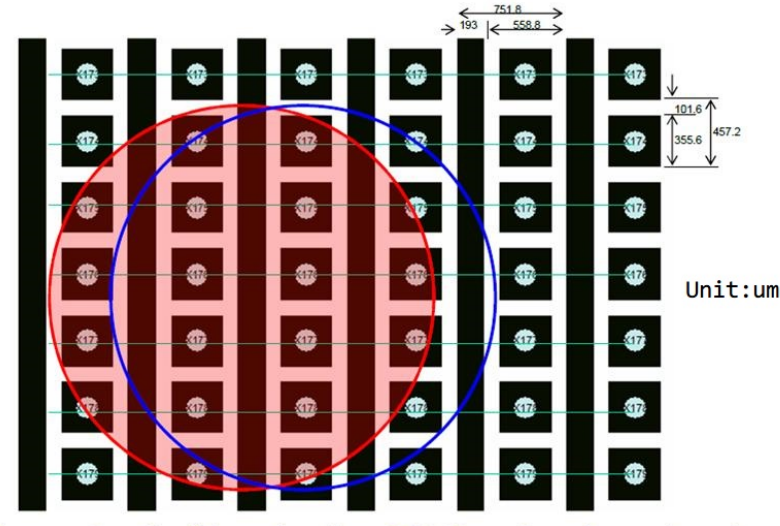


Figure 4.8: The profile of an electron cluster in Triple GEMs. Vertical black lines are the strips in the X direction with a pitch of 752 μm . The light blue horizontal lines connect electrodes to form strips in the Y direction. The red and blue circles are two representative clusters.

- 1 3. Low transverse and longitudinal diffusion coefficients (to prevent deterioration of the spatial resolution)
- 2 4. Large specific energy loss dE/dx (to improve particle identification)
- 3 5. Stability against electrical breakthroughs (to allow reliable operation of the amplification device)
- 4 6. Nonhazardous chemical properties (to address safety concerns like inflammability and damages to the hardware)

8 Due to the long drift distance of ~ 3.0 m and the fact that ions are more massive and
9 much slower than electrons, a large number of ions can accumulate in the chamber. This
10 effect can lead to electric field distortions and should be minimized. To decrease this
11 effect, the structure of the readout chambers is generally designed to avoid ions from es-
12 caping into the gas volume. A gas with a large drift velocity is also chosen in experiments
13 with large interaction rate.

14 In a given working gas, the drift velocity of the electron is a function of E/P where
15 E denotes the electric field and P the gas pressure. Figure 4.9 shows the drift velocity
16 obtained in two different gas mixtures. The mixture of Ar/CF₄/iC₄H₁₀ (95%/3%/2%) is
17 widely used in a number of experiments and is the default for CEPC. At atmospheric pres-
18 sure, this mixture has a saturated drift velocity of approximately 8 cm/ μs in a drift field
19 of ~ 300 V/cm. In addition, the gas has a transverse diffusion coefficient of 30 $\mu\text{m}/\sqrt{\text{cm}}$.

20 The bunch spacing at the CEPC in Higgs factory operation is 0.68 μs , and 25 ns in Z
21 factory operation. Since the ion backflow (IBF) problem scales with the number of colli-
22 sions within the maximum drift time, a working gas with a higher saturated drift velocity
23 would be beneficial and should be considered. The mixture Ar/CF₄/C₂H₆ (92%/7%/1%)
24 is a candidate: its saturated drift velocity is roughly 20% higher than the default gas mix-
25 ture and the diffusion coefficients are lower. Further R&D is needed to confirm that its
26 other properties are compatible with CEPC needs.

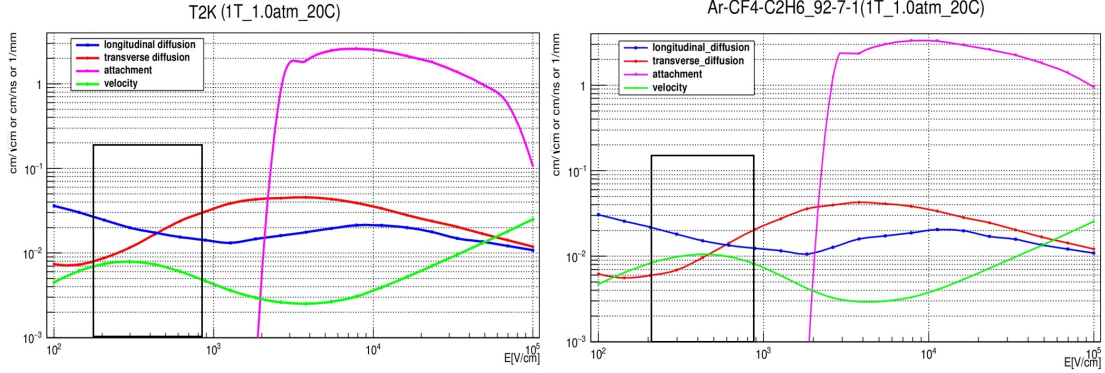


Figure 4.9: Drift velocity study of gas mixtures. Left: Ar/CF₄/iC₄H₁₀ (95%/3%/2%) - the default CEPC gas (T2K gas); Right: Ar/CF₄/C₂H₆ (92%/7%/1%) - the gas mixture with the highest drift velocity. The plots show the drift velocity (green line), transverse diffusion coefficient (red), longitudinal diffusion coefficient (blue) and attachment coefficient (purple) as a function of the electric field. The black rectangle indicates the possible operation range.

1 Low-power consumption readout electronics

2 Small readout pads of a few square millimeters (e.g. 1 mm × 6 mm, there are 3 pads in
3 the electron cluster size, see Figure 4.8) are needed to achieve high spatial and momentum
4 resolution in TPC, demanding about 1 million channels of readout electronics per end-
5 cap. The total power consumption of the front-end electronics is limited by the cooling
6 system to be several kilo-watts in practice. The architecture of the TPC readout electronics
7 is shown in Figure 4.10, selected from a broad range of survey on current electronics
8 installed or under development during past decades, including ALTRO/S-ALTRO and
9 more recently SAMPA for ALICE, AFTER/GET for T2K and Timepix for ILC. It consists
10 of the front-end electronics on the detector panel and the data acquisition system several
meters away from the detector.

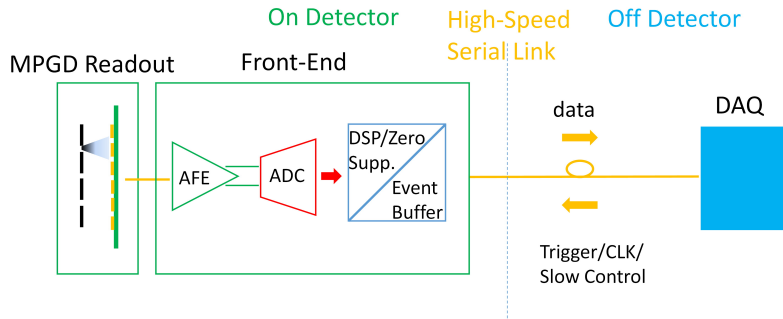


Figure 4.10: Architecture of the TPC readout electronics. The front-end electronics will be mounted directly on the MPGD readout board. It includes the analog front-end (AFE), with a preamplifier and shaper, followed by an analog-to-digital convert (ADC), and a dedicated signal processing (DSP) unit. Signals are sent through high-speed serial links to the off-detector DAQ system.

11
12 The waveform sampling front-end is the preferable option, including a preamplifier
13 and shaper as the analog front-end (AFE), a waveform sampling ADC operating at \geq
14 20 MSPS, a dedicated digital signal processing (DSP) and zero-suppression unit, and a
15 de-randomize event buffer for each channel. To satisfy the stringent requirements on the
16 integration and the power consumption, a front-end ASIC will be developed in 65 nm

Total number of channels		1 million per endcap
AFE (Analog Front-End)	ENC (Equivalent Noise Charge)	500e @ 10pF input capacitance
	Gain	10 mV/fC
	Shaper	CR-RC
	Peaking time	100 ns
ADC	Sampling rate	≥ 20 MSPS
	Resolution	10 bit
Power consumption		≤ 5 mW per channel
Output data bandwidth		300–500 MB/s
Channel number		32
Process		TSMC 65 nm LP

Table 4.4: Key specifications of the front-end readout ASIC for TPC. Each endcap has a total of about 1 million channels that will be readout by over 30,000 ASICs with 32 channels each.

¹ CMOS process. The key specifications of the front-end ASIC are summarized in Table ² [4.4](#).

³ The power consumption of CMOS digital circuits decreases with the reduction of the ⁴ feature size, while the density of the circuitry increases. Digital circuits usually use ⁵ minimum sized transistors, hence part of the ADC, digital filter, control logics and data buffer ⁶ dimensions will be reduced by 1/4 when migrating the same design from a 130 nm to ⁷ 65 nm process. The power consumption is also reduced since it is proportional to the gate ⁸ capacitance of the transistor. Therefore, the 4 mW/ch power consumption of the DSP cir- ⁹ cuits in the 130 nm process reported in Ref. [27] can be reduced by a factor of at least two ¹⁰ by migrating the same design to 65 nm. For the analog circuitry, the transistor size is deter- ¹¹ mined by performance factors, including noise, dynamic range, and bandwidth, hence the ¹² power consumption does not benefit from the smaller feature size of the 65 nm process. ¹³ In this case, the development of a low-power analog front-end, with a design strategy to ¹⁴ keep it as simple as possible, is essential. The block diagram of the analog front-end and ¹⁵ the Successive Approximation Register (SAR) ADC are shown in Figures [4.11](#) and [4.12](#), ¹⁶ respectively. The CR-RC shaper and the SAR ADC instead of a pipeline ADC will be ¹⁷ used for their simplicity in analog circuits and hence the higher power-efficiency.

¹⁸ Dedicated digital filters will be applied to the continuously digitized input signals to ¹⁹ suppress the pedestal perturbations caused by the non-ideal effects such as temperature ²⁰ variation and environmental disturbance. The data will then be compressed by only stor- ²¹ ing the data packets above a programmable threshold with a specified number of pre- and ²² post-samples. A data head will be added to each packet with its timestamp and other in- ²³ formation for reconstruction afterward. The buffered data are readout through high-speed ²⁴ serial links to the DAQ system. The front-end electronics can support both external trigger ²⁵ and self-trigger mode.

²⁶ Even with state of the art technology, the TPC front-end electronics on the end-plate ²⁷ needs a cooling system to keep the temperature stable. Two-phase CO₂ cooling [30] is

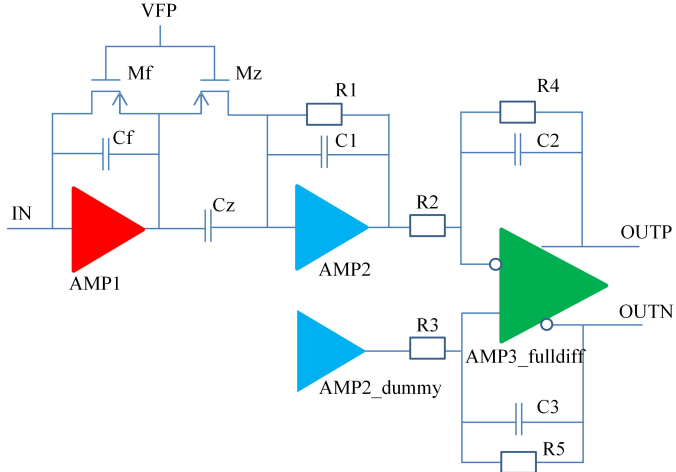


Figure 4.11: Block diagram of the analog front-end component of the TPC on-detector readout electronics. AMP1 is the core amplifier of the preamplifier; AMP2/AMP_dummy amplifiers compose the first stage shaper; AMP3_fulldiff is the fully differential amplifier of the second stage shaper; Feedback for the preamplifier is adjusted by the bias voltage (VFP).

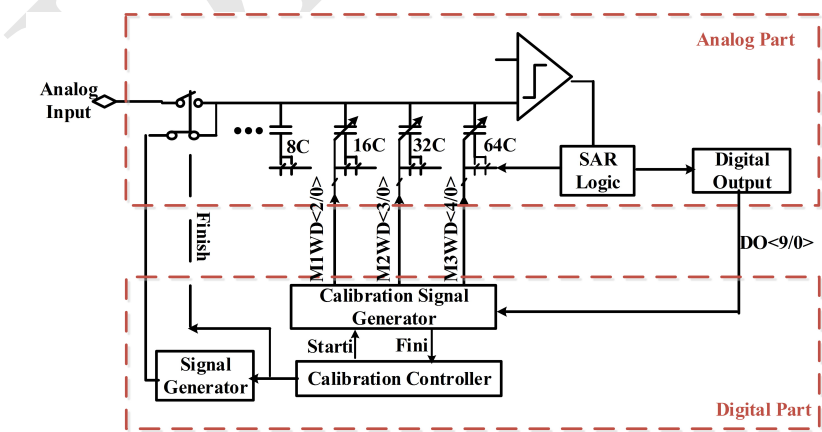


Figure 4.12: Block diagram of the analog-to-digital converter (ADC) using Successive Approximation Registers (SAR). Both analog and digital parts are shown.

1 a well-developed technology and can be used as a baseline solution to extract the heat
 2 generated by the front-end electronics and to keep the temperature of the TPC chamber
 3 stable at 20 °C. Micro-channel CO₂ cooling has lower mass and may be studied further as
 4 an alternative technique to copper pipes [31].

5 The TPC readout electronics are a few meters away from the collision point, and the ra-
 6 diation dose is rather low (< 1 krad) at CEPC, which allows the use of standard, radiation
 7 soft technologies. On the other hand, energetic particles can always produce instantaneous
 8 failure (SEU or SEL) from time to time. Hence, a radiation sophisticated design needs
 9 to be considered such that the overall system performance will not be affected or even
 10 irreversibly damaged by These rare events.

11 Critical technology challenges of TPC detector

12 It will be challenging to design and manufacture the support structure with a relatively
 13 light material, and at the same time very rigid. It is required to maintain accuracy, ro-
 14 bustness in all directions, and stability over long time periods. As the field cage is not
 15 strong enough due to the limited material budget, the end-plates become the only choice,
 16 where the support structure connects to. In the current stage of design, the TPC end-plate
 17 support scheme has not yet been finalized. A promising solution is to suspend it from the
 18 solenoid, in which a number of spokes run radically along the faces of the calorimeter to
 19 the TPC end-plates.

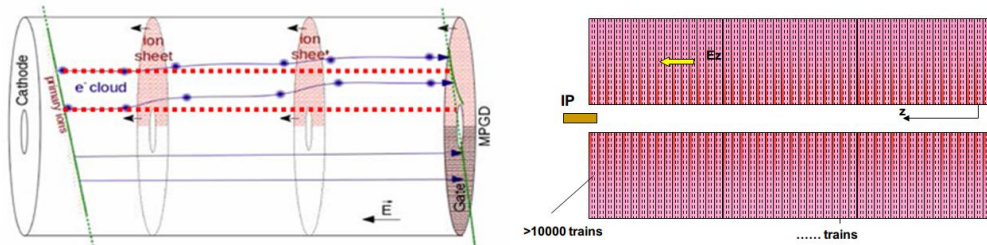


Figure 4.13: Ion backflow effects on the TPC tracking within the CEPC beam conditions. Left: Diagram of the distortion effects on TPC tracks caused by the ion backflow disks. The electrons from gas ionization originated by a track crossing the TPC (green line), in the absence of ion backflow, would drift directly towards the end planes following the red dotted lines. The ion disk clouds cause distortions in their path (blue lines) degrading the track measurement. (The lower part of the diagram shows the operation in case of the usage of a gating grid, a solution adopted for ILC but that is not applicable to the CEPC due to the short bunch space.) Right: The profile of the ions disks under the beam structure of a high-luminosity circular machine such as the CEPC.

20 Ions in the drift volume of the TPC move towards the cathode at a much lower velocity
 21 than electrons, and they can accumulate in this volume to build up a significant space
 22 charge in the form of 'ion discs' that distort the trajectory of electrons moving towards the
 23 anodes.² In the CEPC TPC, the majority of ions inside the drift volume are created in the

²With the electron drift velocity of 5 cm/μs, it takes ~ 40 μs for all the electrons to drift 2 m to reach the end-plate. On the other hand, ions drift with a velocity of only 5 m/s. This leads to ions from hundreds of thousands of events overlapping in the TPC volume.

amplification region and backflow to the drift region. It is therefore important to suppress this ion backflow in order to minimize the deteriorating influence on spatial resolution.

Figure 4.13 shows a diagram of the distortion due to ion backflow and ion disks in CEPC. An often used method of backflow suppression is a so-called gating grid;³ however, it is not applicable here because the bunch spacing of 25 – 680 ns is short compared with the maximum electron drift time ($\sim 40 \mu\text{s}$). Another promising option is to exploit the ‘built-in’ ion backflow suppression of GEMs or MicroMegas. In next section, the R&D study of an hybrid detector module that has been proposed to control ions continuously, and its updated results will be described.

4.2.1.3 Simulation and estimation of key issues

Occupancy requirement from Higgs and Z pole run

The TPC occupancy has been studied for both the WZ and Z -pole CEPC runs at the nominal instantaneous luminosities for the 3 Tesla solenoid. Using a sample of nine thousand fully simulated $Z \rightarrow q\bar{q}$ events at center of mass energy of 91.2 GeV [32], we studied the voxel occupancy and the local charge density of the TPC at the Z pole operation, considering instantaneous luminosity values from $2 \times 10^{34} \text{ cm}^{-2}\text{s}^{-1}$ to $2 \times 10^{36} \text{ cm}^{-2}\text{s}^{-1}$.

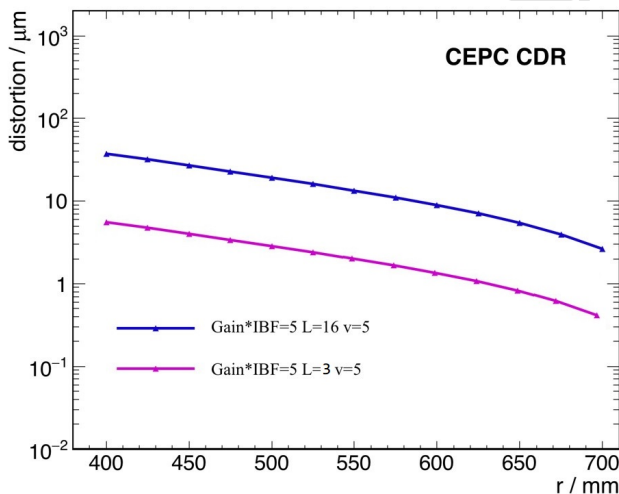


Figure 4.14: Distortion as a function of the electron initial radial position r for different parameters: Gain for the GEM-MicroMegas hybrid, IBF is the ions backflow reducing rate, L is the luminosity, and v is the drift velocity of the ions in m/s.

Given the fact that the beam bunches are evenly distributed along the accelerator circumference, the voxel occupancy is extremely low ($1.4 \times 10^{-5}/1.4 \times 10^{-7}$ for the innermost layer and $3.4 \times 10^{-6}/3.4 \times 10^{-8}$ on average) and poses no problem to the TPC operation. The distortion on the TPC hit positions induced by the ion charges is estimated with a dedicated program and calculation. At instantaneous luminosity of $1 \times 10^{36} \text{ cm}^{-2}\text{s}^{-1}$

³Early TPCs were equipped with multi-wire proportional chambers (MPWCs) as gas amplification devices. The IBF ratio in a standard MWPC is 30–40%, so a gating grid is essential to prevent ions from reaching the drift volume. In the presence of a trigger, the gating grid switches to the open state to allow ionization electrons to travel into the gas amplification region. After a maximum drift time of about 100 μs the gating grid is closed to prevent positive ions from drifting back into the drift volume. Since it must remain closed until the ions have been collected on the grid wires, the ionization electrons are also blocked during this time and dead time is consequently generated.

(~ 6 times larger than nominal) and an ion backflow control of percent level, the distortion can be as significant as 10 mm at the innermost TPC layer, which is two orders of magnitude larger than the intrinsic TPC spatial resolution.

A few approaches are proposed to reduce the effects caused by distortions:

1. Ion backflow control technology; the ion backflow should be controlled to per mille level, in other words, only 1–10 backflow ions are allowed for each primary ionization.
2. Dedicated distortion correction algorithm, for the innermost layers, which should result in a mitigation of the hit position distortion by one order of magnitude.
3. Adequate track finding algorithm that could link the TPC track fragments to vertex tracks at high efficiency and purity.

Figure 4.14 shows the distortion as a function of the electron initial radial position r for the nominal luminosities of the WZ and Z -pole runs. Considering a good ion backflow control, with $\text{Gain} \times \text{IBF} = 5$, the maximal distortion would be about 40 μm . Taking all of the above approaches into account, the distortion can be mitigated to reasonable levels given the TPC position resolution requirement. To conclude, the pad occupancy and distortion posses little pressure on the TPC operation if the above items can be achieved.

4.2.1.4 Feasibility study of TPC detector module and future work

Hybrid structure TPC detector module

TPC readout with MPGDs, especially GEM and MicroMegas, is very attractive, because the IBF of those detectors is intrinsically low, usually around a few percent. GEM detectors have been extensively proved in the last decade to be the prime candidate, as they offer excellent results for spatial resolution and low IBF. Numerous GEM foils can be cascaded, allowing multilayer GEM detectors to be operated at an overall gas gain above 10^4 in the presence of highly ionized particles. MicroMegas is another kind of MPGD that is likely to be used as endcap detectors for the TPC readout. It is a parallel plate device, composed of a very thin metallic micromesh which separates the detector region into a drift and amplification volumes. The IBF of this detector is equal to the inverse of the field ratio between the amplification and the drift electric fields. Low IBF, therefore, favors high gain. However, the high gain will make it particularly vulnerable to sparking. The idea of combining GEM with MicroMegas was first proposed with the goal of reducing the spark rate of MicroMegas detectors. Pre-amplification using GEMs also extends the maximum achievable gain.

This hybrid configuration, GEM-MM is currently the baseline readout module for the CEPC TPC. Figure 4.15 shows a small prototype of $100 \times 100 \text{ mm}^2$ that has been produced and tested. The device has a 4 mm drift region GEM, followed by a 1.4 mm transfer region and a MicroMegas with an avalanche region of 0.128 mm. The preliminary results of this detector module in what regards IBF and laser calibration tests are described next.

The IBF tests have been carried out with a ^{55}Fe X-ray source and several gas mixtures: Ar/CO₂ (90/10), Ar/iC₄H₁₀ (95/5) and T2K gas. The currents on the anode and drift cathode were measured precisely with an electrometer.

The ^{55}Fe X-ray source has a characteristic energy of 5.9 keV. In Ar/CO₂ (90/10) gas, a typically pulse height spectrum for a GEM or MicroMegas detector contains one major

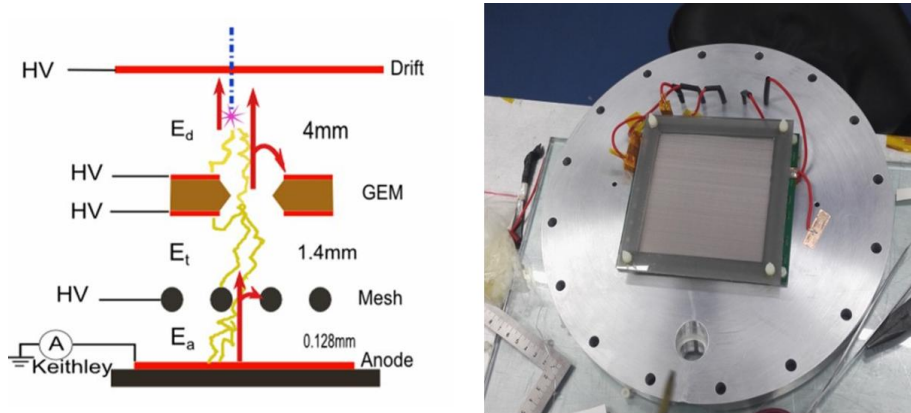


Figure 4.15: Left: Schematic diagram of the GEM-MM hybrid detector module. The device has a GEM with 4 mm drift region, followed by a 1.4 mm transfer region and a MicroMegas with an avalanche region of 0.128 mm. Right: Photo of the detector prototype with 100 cm^2 active area designed based on this concept.

peak corresponding to the 5.9 keV X-rays and an Escape electron peak at lower pulse height corresponding to the ionization energy of an electron from the argon K-shell.

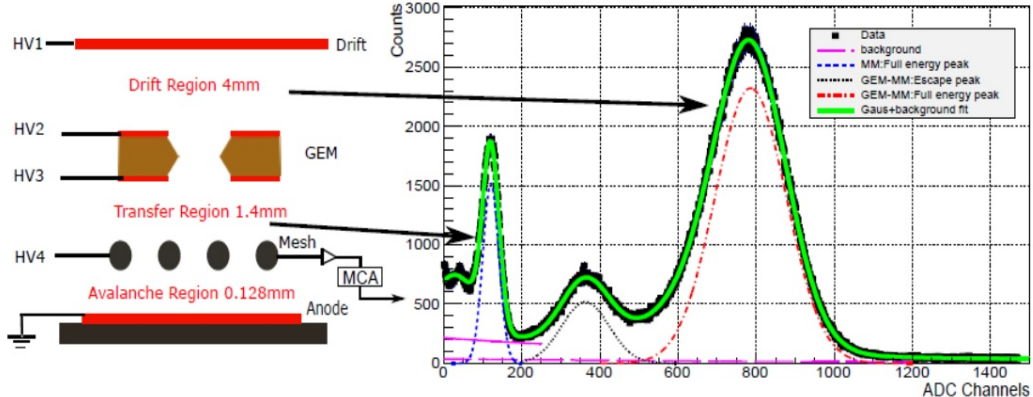


Figure 4.16: Energy spectrum of the ^{55}Fe radioactive source in Ar/CO₂ (90/10) as measured by the GEM-MM hybrid module. The green curve is the whole energy spectrum from the module. The last two peaks correspond to the GEM and MicroMegas amplification in tandem. The first two peaks are from MicroMegas amplification only.)

In the GEM-MM detector, the situation is different. There are two amplification stages inside the detector. The primary ionization created by photon absorption can be in the drift region or in the transfer region (Figure 4.16). Photoelectrons starting from the drift region get amplified by both the GEM detector and the MicroMegas detector before they are collected in the anode. If the photons are absorbed in the transfer region, the primary electrons will be amplified only once (by the MicroMegas).

Figure 4.16 depicts a typical ^{55}Fe pulse height spectrum obtained by the GEM-MM detector. Four peaks are seen in the pulse height spectrum. From left, the first peak and the second peak are the escape peak and the full energy peak of the stand alone MicroMegas. The last two peaks are created by photons with their energy deposited in the drift region.

These primary electrons show combination amplification. The pre-amplification effect of GEM foil has been thus demonstrated in this energy spectrum measurement. The effective gain of the GEM can be measured even when it is relatively low. The energy resolution of the GEM-MM detector is measured to be 27% (FWHM). The gain properties of the device were also measured. A gain up to about 5000 can be achieved without any apparent discharge behavior. Finally, the IBF was measured to be reduced to $\sim 0.1\%$ at this gain.

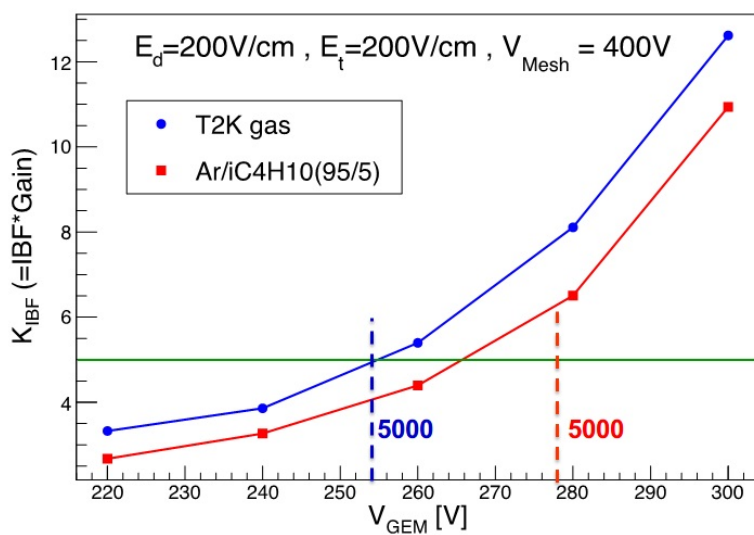


Figure 4.17: IBF Result of the GEM-MM module operating in two different gas mixtures: T2K gas and Ar/iC₄H₁₀. The nominal gain of 5000 is reached at different GEM operating voltage for the two gas mixtures. At that nominal gain, the Gain \times IBF is about 5 for T2K gas, and about 7 for Ar/iC₄H₁₀ gas. Thus the T2K gas mixture has lower ion backflow for the same operational gain.

Different operational parameters are being investigated, including different gas mixtures, with the goal of optimizing the TPC functionality. The gas Gain \times IBF for the T2K and Ar/iC₄H₁₀ (95/5) gas mixtures are shown in Figure 4.17. The T2K gas reaches the nominal gain of 5000 at a lower GEM amplification voltage, corresponding also to a lower Gain \times IBF value, when compared with the Ar/iC₄H₁₀ gas mixture. Thus, T2K results in lower ion backflow and it is therefore considered the baseline gas for the hybrid module.

Space charge effects could disturb the IBF measurement and result in reduced IBF measured values. To quantify these one can study the IBF value as a function of the space-charge density by varying the X-ray's voltage and current as shown in Figure 4.18. The IBF results reported here were obtained in the green rectangle area. There is no obvious discharge or spark, and there is no large number of electrons to lead the high space charge to reduce the value of IBF. We conclude the measurements should not be affected by this issue.

20 **Laser calibration and alignment system**

A laser calibration system with narrow laser beams inside the drift volume to simulate ionizing tracks at predefined locations will be used for calibration and distortion measurements. The goal is to map the uniformity of the TPC drift field within a reasonable relative error corresponding to a spacial resolution of $\sigma_{r\phi} = 100 \mu\text{m}$. The system can be used for tests and calibration either outside or during normal data taking with the aim of

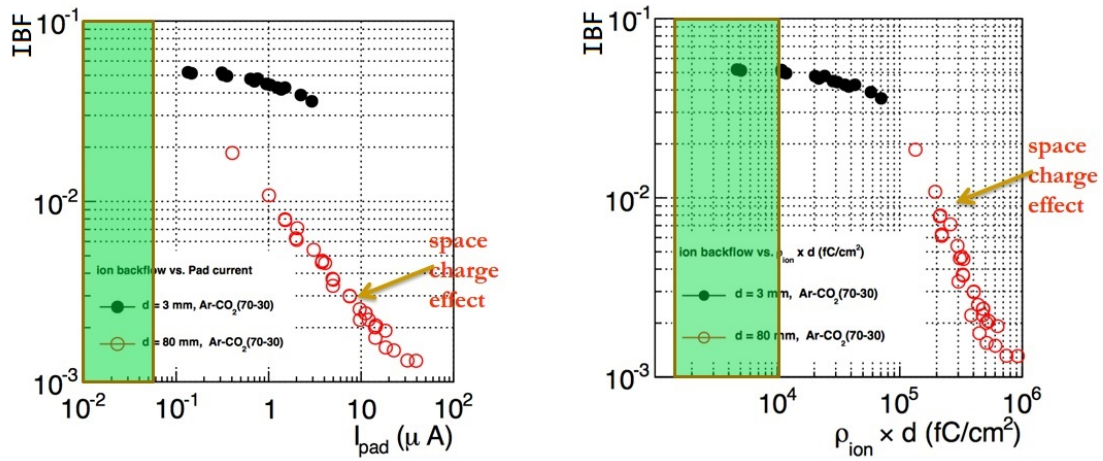


Figure 4.18: Comparison of the IBF with the different X-ray's voltage and current. The test results of the GEM-MM detector prototype appear in the green area where there is no space charge effect.

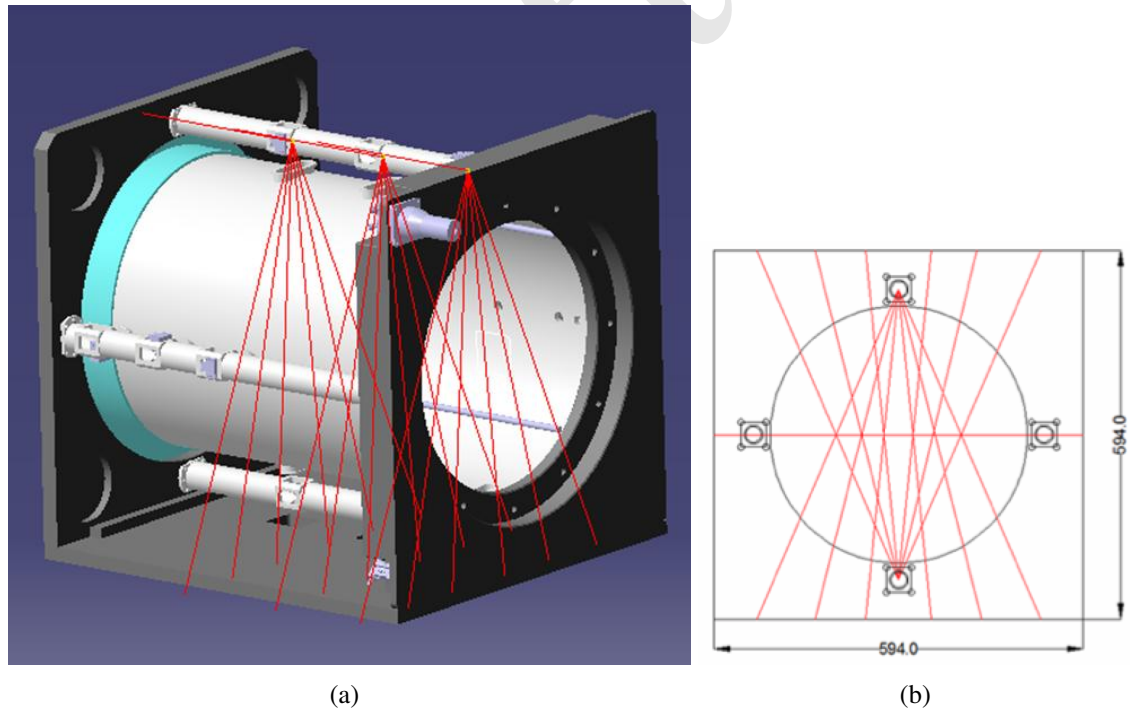


Figure 4.19: (a) Schematic diagram of the detector module with the 266 nm laser system. The red lines show the split laser beam injection into drift chamber; There are several laser beam planes (b), each composed of 6 downward beams, and 6 upwards beams. Several single horizontal laser beams also transverse the chamber.

understanding the chamber performance and control track distortions. Of particular interest is the testing of electronics, alignment of the readout modules, and monitoring of the drift velocity variations due to mechanical imperfections and non-uniformities in the gas, temperature and electric and magnetic fields.

The laser system will be composed of a UV laser beam, such as a Nd:YAG laser with a wavelength of 266 nm, split by transmission and reflection mirrors into several laser planes, as shown in Figure 4.19. The laser entrance window into the chamber will likely be made of fused silica as it has $\sim 99\%$ transmission efficiency at 266 nm. There are several laser beam planes distributed longitudinally throughout the chamber. Each laser plane is composed of 6 downward beams, and 6 upwards beams. Several single-laser beams also transverse the chamber horizontally. Ionization in the gas volume occurs along the laser path via two-photon absorption by organic impurities.

A prototype of this laser calibration system has been built with one readout module and a Nd:YAG laser device. The complete optical path and the laser power is split into planes of 6 laser beams. The laser power reaches over $\sim 10 \mu\text{J/mm}^2$ that is equivalent to $\sim 10 \text{ MIP}$. Tests of the laser system and prototype have been performed at gain of 3000 and 5000. Figure 4.20 reports the response of the prototype readout module as a function of the laser beam size. At the nominal gain of 5000, the desired output signal range of 300 mV – 500 mV can be obtained with a small beam diameter. Ultimately, the beam incident spot area will be in the range of 0.8 mm^2 to 1.0 mm^2 . Larger beam diameters eventually result in the saturation of the signal response from the readout module, but no damage has been observed.

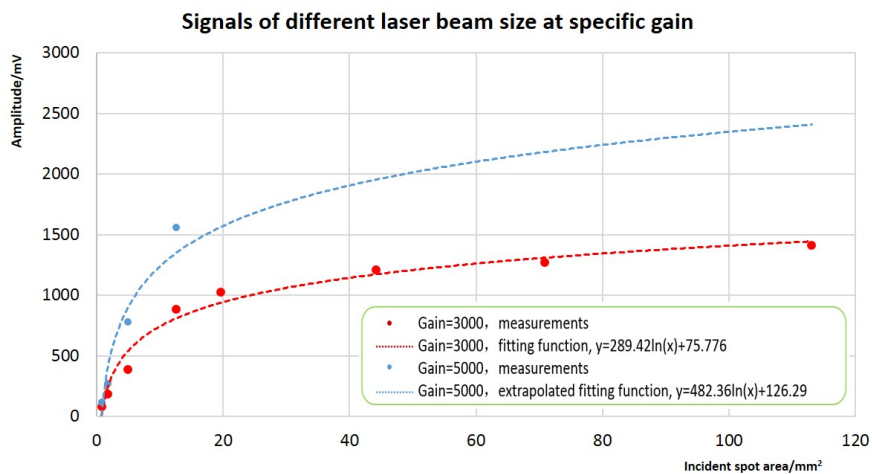


Figure 4.20: Signal amplitude collected by the readout module as a function of the incident area of the laser beam. Measurements have been done for gain of 3000 and 5000. At the nominal gain of 5000, the desired output signal range of 300 mV – 500 mV can be obtained with a laser beam diameter of 0.8 mm. The detector response saturates for larger laser beam sizes without damaging the readout module.

An additional UV-lamp can generate additional ions in the prototype volume via photoelectric effect. A Deuterium lamp with 160–400 nm of the wavelength illuminates a smooth Aluminum film cathode, and produces photoelectrons to study and monitor distortions. To mimic the bunch structure and the ions distortion from CEPC, the UV light lamp can be controlled with a specific time structure and create more than 10000 electrons/s · mm².

4.2.1.5 Conclusion

The Time Projection Chamber presented here provides an excellent starting point for TPC research and development in the context of the CEPC beam environment. Several studies have already been performed and many more are foreseen. Modifications are still expected due to the performance requirements and severe experimental conditions at the CEPC. Several critical R&D issues have been identified in pre-studies. Possible solutions to these issues have been suggested and will continue to be verified with the TPC prototype: The hybrid-structure MPGD detector module has been developed, and preliminary results have been obtained and analyzed. Further studies will be done from this combination detector module; Another small TPC prototype with 266 nm laser calibration system and UV photoelectric function has been designed and assembled. This calibration experiment will continue to be further studied for CEPC.

4.2.2 Silicon tracker

The silicon tracker and the TPC (Time Projection Chamber, see Section 4.2.1) together with the vertex detector form the complete baseline tracking system of CEPC. With sufficiently low material budget to minimize the multi-scattering effect, the silicon tracker provides additional high-precision hit points along trajectories of charged particles, improving tracking efficiency and precision significantly. In addition to complementary tracking, it also provides the following functionalities:

- monitoring possible field distortion in the TPC,
- contributing detector alignment,
- separating events between bunch crossings with relative time-stamping,
- potentially dE/dx measurement.

The CEPC physics requirements put a required performance on the central tracker as

$$\sigma_{1/p_T} = a \oplus \frac{b}{p \sin^{3/2} \theta} \quad [\text{GeV}^{-1}] \quad (4.2)$$

with p and p_T in GeV and θ the polar angle with

$$a \sim 2 \times 10^{-5} \text{ GeV}^{-1} \quad \text{and} \quad b \sim 1 \times 10^{-3}. \quad (4.3)$$

At low momenta, less than 50 GeV for perpendicular tracks, the resolution is dominated by the multiple scattering effect, and at high momenta, the resolution is dominated by the single-point resolution. Hence, stringent constraint has to be put on material budget.

4.2.2.1 Baseline design

The silicon tracker consists of four components: the Silicon Inner Tracker (SIT), the Silicon External Tracker (SET), the Endcap Tracking Detector (ETD) and the Forward Tracking Detector (FTD). The overall layout is shown in Figure 4.21, and the main parameters are summarized in Table 4.5.

The barrel components SIT and SET provide precise hit points before and after the TPC, improving the overall tracking performance in the central region. The SIT helps the link between the vertex detector and the TPC, enhancing the reconstruction efficiency,

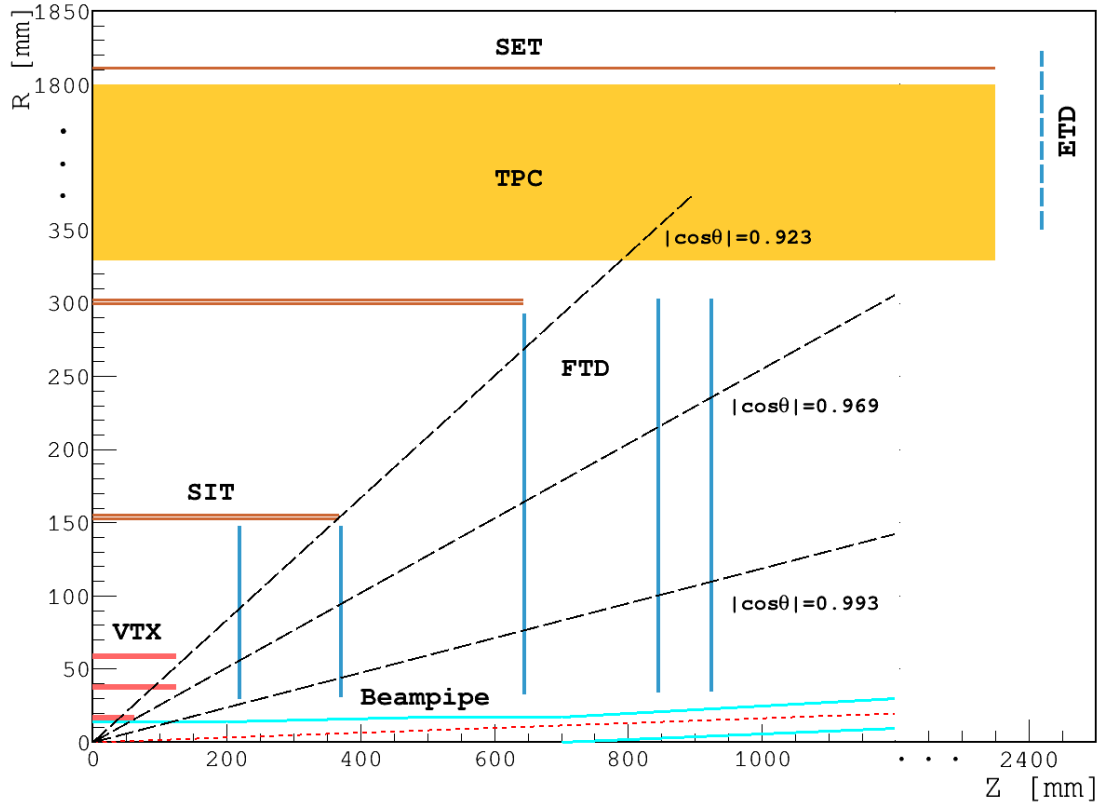


Figure 4.21: Preliminary layout of the CEPC silicon tracker. The red lines indicate positions of the vertex detector layers, orange lines for the SIT and SET components of the silicon tracker, the gray-blue lines for the FTD and ETD components of the silicon tracker, and the cyan lines for the beam pipe. The ETD line is a dashed line because it is not in the present full simulation.

Detector	Radius R [mm]		z [mm]	Material budget [X_0]
SIT	Layer 1:	153	371.3	0.65%
	Layer 2:	300	664.9	0.65%
SET	Layer 3:	1811	2350	0.65%
FTD	Disk 1: $R_{in} = 39$	$R_{out} = 151.9$	220	0.50%
	Disk 2: $R_{in} = 49.6$	$R_{out} = 151.9$	371.3	0.50%
ETD	Disk 3: $R_{in} = 70.1$	$R_{out} = 298.9$	644.9	0.65%
	Disk 4: $R_{in} = 79.3$	$R_{out} = 309$	846	0.65%
	Disk 5: $R_{in} = 92.7$	$R_{out} = 309$	1057.5	0.65%
	Disk: $R_{in} = 419.3$	$R_{out} = 1822.7$	2420	0.65%

Table 4.5: Main parameters of the CEPC silicon tracker.

particularly for low-momentum charged particles. The SET sits between the TPC and the calorimeter and helps in extrapolating from the TPC to the calorimeter. In addition, the good timing resolution of silicon sensors provides time-stamping for bunch separation.

The ETD is positioned in the gap between the endplate of the TPC and the endcap calorimeter. It helps to reconstruct charged particles with a reduced path in the TPC. The SIT, SET and ETD covers the central tracking region. They form the complete silicon envelope and help in calibrating the tracking system. The ETD has not been included in the current version of full simulation.

The FTD is installed between the beam pipe and the inner cage of the TPC, covering the very forward region. It consists of five silicon disks on each side. The FTD is essential for precise and efficient tracking down to very small (or large) polar angles, where a number of challenges exist: the magnetic field approaching zero along the beam pipe, significantly larger occupancies due to forward going jets and high backgrounds from the interaction region. To achieve the best tracking performance, the FTD needs precise space points, a large lever arm, but low material budget.

4.2.2.2 Sensor technologies

The basic sensor technology is silicon microstrips for all tracker components except the two innermost FTD disks where silicon pixels are foreseen. Requirements of the single point resolution vary with positions of tracker components, but a general condition of $\sigma_{SP} < 7 \mu\text{m}$ is required for high precision tracking. The microstrip sensors have proven to be capable of the resolution, taking into account material budget and power consumption. The baseline features of microstrip sensors will be a large detection area of $10 \times 10 \text{ cm}^2$, a fine pitch of $50 \mu\text{m}$ and the thickness $< 200 \mu\text{m}$ to minimize the multi-scattering effect.

An alternative that is being investigated is a fully pixelated silicon tracker. Although the choice of pixel technologies is open, the CMOS pixel sensors (CPS) have gained particular interest because of two main performance advantages compared to the microstrip sensors:

- Granularity. The CPS provides better single-point spatial resolution and significantly reduces the ambiguity caused by multiple hits in a single strip.
- Material budget. The CPS can be thinned to less than $50 \mu\text{m}$, whereas the strip sensor is usually a few hundred microns.

In addition, production cost could be significantly reduced for fabricating large area sensors because CPS is based on standard CMOS procedure in industry. And it's possible to embed circuits in the pixel to simplify the tracker readout circuitry. Initial R&D on large area CPS has been carried out.

The pixelated silicon tracker alternative is used to set data acquisition requirements because it is more demanding. Table 4.6 estimates the pixel occupancy of SIT-L1 and FTD-D1 based on a few assumptions.

1. The pixel dimension is assumed to be $50 \mu\text{m} \times 350 \mu\text{m}$, with which at least in one dimension spatial resolution can reach $7 \mu\text{m}$ by implementing in-pixel ADC with multiple bits.
2. The track multiplicities in different operation modes are inferred from hit densities in Table 9.4.
3. Readout time of pixel sensors is set as $10 \mu\text{s}$, the same as that of VTX.

- ¹ 4. Cluster size is set as 9 hits per track.

operation mode	H (240)	W (160)	Z (91)
track multiplicity (BX^{-1})	310	300	32
bunching spacing (ns)	680	210	25
SIT-L1 occupancy (%)	0.19	0.58	0.52
FTD-D1 occupancy (%)	0.17	0.54	0.48

Table 4.6: Pixel occupancy of SIT-L1 and FTD-D1. See context for explanations.

² 4.2.2.3 Front-End electronics

³ The Front-End (FE) electronics will depend on the choice of sensor, namely microstrips
⁴ or pixels.

⁵ For the microstrips, custom designed ASICs with deep sub-micron CMOS technology
⁶ will be used. The chips will provide functions of the analogue to digital conversion
⁷ (ADC), zero suppression, sparcification and possibly time stamping, together with necessary
⁸ control circuitry. The high degree digitization is for relaxing the data processing
⁹ pressure on downstream electronics.

¹⁰ As for the pixels, all FE functions can be realized in a pixel chip, even with some functions,
¹¹ e.g., ADC on pixels themselves. Particular concerns are readout time and electronic
¹² channels.

¹³ Commonly, the FE chip will be developed in mind with low noise, low power consumption
¹⁴ and high radiation tolerance. New developments, such as in the SiLC collaboration
¹⁵ and the LHC experiment upgrades, will be good references.

¹⁶ 4.2.2.4 Powering and cooling

¹⁷ Powering and cooling are a challenge for the CEPC silicon tracker. It is important to investigate
¹⁸ the novel powering scheme based on DC-DC converters, which has been already
¹⁹ actively pursued by the ATLAS and CMS experiments for silicon detector upgrades [33–
²⁰ 35]. It allows significant reduction in material budget for the low-voltage power cables
²¹ and gives less power dissipation in the delivery system. Cooling is another critical issue.
²² Although cooling based on forced cooled gas flow might be still feasible to efficiently conduct
²³ away the heat generated by the sensors, ASICs and other electronics, it is important
²⁴ to look into other cooling techniques, such as silicon micro-channel cooling [36], which
²⁵ are being investigated by several other experiments. The technique chosen will have to
²⁶ provide sufficient cooling without compromising the detector performance.

²⁷ 4.2.2.5 Mechanics and integration

²⁸ There will always be additional challenging aspects of the mechanical design for a large
²⁹ area silicon tracker. A lightweight but stiff support structure can be built based on Carbon
³⁰ fiber Reinforced Plastic material [37]. The support structure, cable routing and electronics
³¹ common to other sub-detectors need to be carefully designed to minimize the overall quantity
³² of material and make easy construction and integration possible. Precise and quick system
³³ alignment might be achieved with dedicated laser monitoring systems,

1 while the final alignment will be accomplished using tracks from well-understood physics
 2 events [38].

3 **4.2.2.6 Critical R&D**

4 Silicon technology for large-area tracking detectors will continue to evolve over the next
 5 few years [39]. There are ongoing R&D activities conducted by the ATLAS and CMS
 6 experiments to develop advanced silicon detectors for the High Luminosity LHC as well
 7 as several pioneering R&D projects by the SiLC (Silicon tracking for the Linear Collider)
 8 collaboration. Despite the rather different operation conditions and requirements, it is
 9 always important to exploit synergies with existing R&D from other experiments to share
 10 expertise. During the preliminary studies, several critical R&D items have been identified
 11 for the CEPC silicon tracker. All of them, as listed below, will be pursued in the R&D
 12 phase of the CEPC project and made available for engineering construction.

- 13 ▪ Alternative pixelated strip sensors with CMOS technologies;
- 14 ▪ p^+ -on-n silicon microstrip sensors with slim-edge structure;
- 15 ▪ Front-end electronics with low power consumption and low noise, fabricated with
 CMOS technologies of small feature size;
- 16 ▪ Efficient powering with low material budget and CO₂ cooling techniques;
- 17 ▪ Lightweight but robust support structure and related mechanics;
- 18 ▪ Detector layout optimization, in particular in the forward region.

20 It will be vital to develop necessary instrumentation for the module assembly and to
 21 verify the detector module performance with beam tests. Prototypes of support structures,
 22 including cooling solutions, shall be also built for mechanical and thermal tests.

23 **4.2.3 TPC and Silicon tracker performance**

24 The performance study described in the section is based on the vertex detector and the
 25 silicon tracker.

26 While the tracking performance in the central region has been extensively studied, the
 27 performance in the forward region, which has been designed to cope with the rather short
 28 L^* , requires additional careful evaluation. Figure 4.22 shows the estimated transverse
 29 momentum resolution for single muon tracks for two polar angles $\theta = 20^\circ$ and 85° , and
 30 the analytical results from Equation (4.2) and Equation (4.3). Due to the reduced lever arm
 31 of the tracks and fewer FTD disks in the forward region ($\theta = 20^\circ$), the resolution is worse.

32 **4.3 Full-silicon tracker detector**

33 A full-silicon tracker is also an option for the CEPC Main Tracker. It offers a well known
 34 technology that provides excellent space point resolution and granularity to cope with
 35 track separation in dense jets and hits from the high luminosity beam related background.
 36 Potential drawbacks include the relatively high material density within the tracking sys-
 37 tem, fewer space points available for pattern recognition, and limited dE/dx measure-
 38 ments.

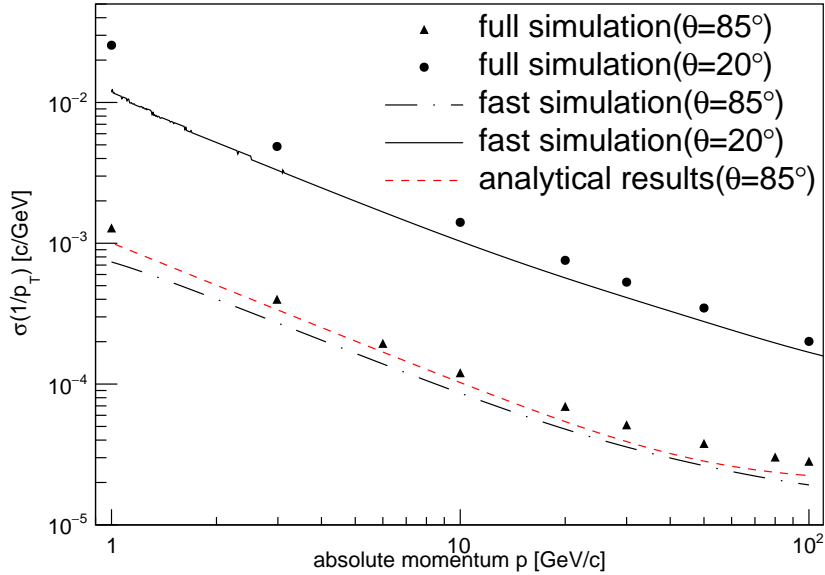


Figure 4.22: Transverse momentum resolution for single muon tracks as a function of the track momentum estimated for the CEPC baseline design with full simulation (dots) and fast simulation (black triangles) compared to the analytical results obtained with Eqs. 4.2 and 4.3 (red line).

This Section will demonstrate that the full-silicon tracking concept is a viable option for CEPC. The layout presented here is constrained to fit within the main tracker detector envelope in the CEPC baseline layout of TPC and silicon tracker in the previous section. Thus, they share the same vertex tracker as well as the same calorimeter. While the boundary conditions are held fixed in this study, we have optimized the layout with the number of silicon layers, single vs double sided, and support material. Relaxing these constraints are expected to yield further optimization. The parameters used in this simplified simulation study are summarized in the following:

- the solenoid B field is set to 3 Tesla,
- the tracking envelope consists of a cylinder with a radius of 1.83 m and a length of 4.6 m,
- the tracker covers down to 7.25 degree from the beam pipe,
- the Be beam pipe has a radius of 1.45 cm and 14 cm long.

4.3.1 Full silicon tracker layout

Two layouts have been investigated in this study.

The first, referred to as FST, has six double-strip layers in the barrel region and five double-strip layers in the endcap region. The barrel strips are labeled SOT and the endcap strips are labeled EOT. Together with the six vertex tracker pixel hits, this layout provides 12 precisely measured points for all tracks in the central region, and at least 7 points down to a polar angle of about 7.25 degree, as shown in Figure 4.24. The six vertex tracker pixel hits and the forward disks of FST are capable of excellent track finding on their own. The outer FST strip layers provide additional track-finding constraints at large radii where the

hit density is low while improving the momentum measurement over a large lever arm with excellent hit resolution in the transverse plane.

The second alternative, referred to as FST2, provides information on the effect of having fewer hits. This layout has five single-sided strip layers in the barrel and four double-sided strip layers in the endcap as shown in Figure 4.23. The number of expected hits on the track from FST2 is also shown in Figure 4.24. Combined with the vertex tracker pixel hits, FST2 provides ten space points in the barrel region.

Tables 4.7 and 4.8 summarize the geometry parameters of the layer and disk configurations that were investigated for both FST and FST2. The total radiation length for all-silicon tracking systems, including dead material such as readout, cables and supports, is about 5-7% for FST and 7-10% for FST2, respectively.

VXD	FST		FST2	
	R (m)	$\pm z$ (m)	R (m)	$\pm z$ (m)
Layer 1	0.016	0.078	0.016	0.173
Layer 2	0.025	0.125	0.030	0.173
Layer 3	0.037	0.150	0.054	0.173
Layer 4	0.038	0.150	0.077	0.173
Layer 5	0.058	0.175	0.100	0.173
Layer 6	0.059	0.175		
EIT	R_{in} (m)	R_{out} (m)	$\pm z$ (m)	R_{in} (m)
Disk 1	0.030	0.151	0.221	0.015
Disk 2	0.051	0.151	0.368	0.016
Disk 3				0.018
Disk 4				0.021
Disk 5				0.028
Disk 6				0.076
Disk 7				0.118
				0.074
				0.130
				0.074
				0.171
				0.074
				0.247
				0.163
				0.290
				0.163
				0.745
				0.163
				1.145

Table 4.7: Geometry parameters for the pixel layers of the two full-silicon-tracker detectors (FST and FST2) discussed in the text. The vertex detector in the barrel region (VXD) has either 5 or 6 layers depending on the configuration. The Endcap Inner Tracker (EIT) is composed of two pixel disks in the FST case, and seven pixel disks in the FST2 case.

4.3.2 Expected Resolution

For each layout, we use the semi-analytical program IdRes, developed by the ATLAS experiment [40], to calculate the expected tracking resolution as function of track momentum for a given incident angle θ , in which the effects of multiple scattering due to the material are taken into account. The results are cross checked using LDT program [41], which gives a consistent result. The coverage of the full-silicon tracking system is shown in Figure 4.24 as function of track pesudo-rapidity.

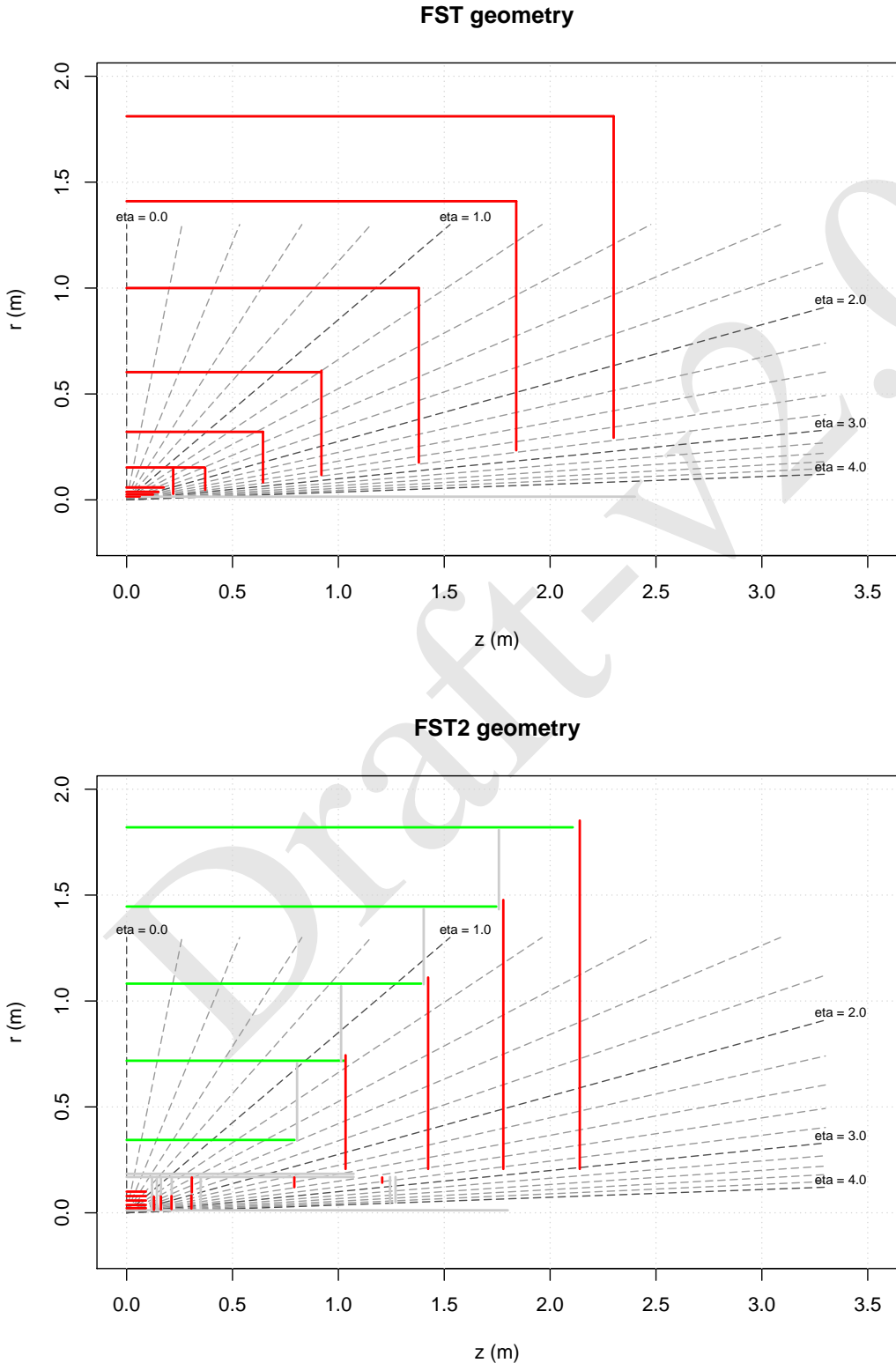


Figure 4.23: The R-Z view of the full silicon tracker proposed for FST (top) and FST2 (bottom).

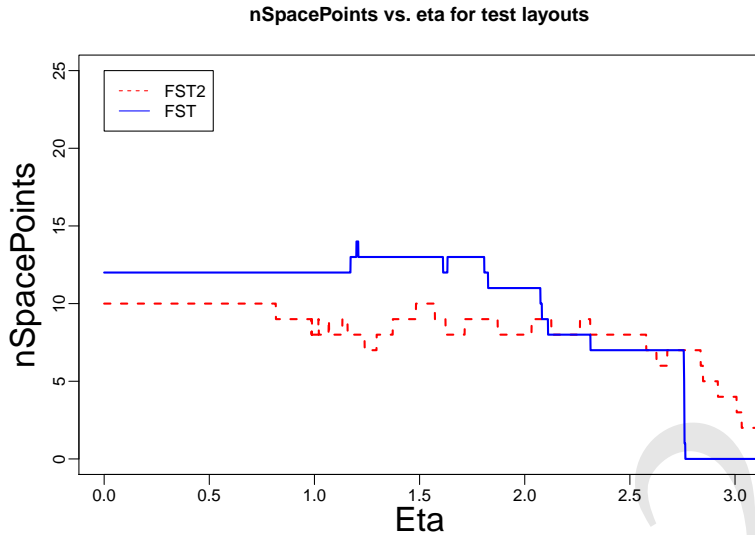


Figure 4.24: The number of expected hits are shown as function of track pseudo-rapidity.

1 The expected transverse momentum (p_T) and impact parameters (d_0 , and z_0) resolutions
2 are compared as function of track p_T for tracks with $\theta = 85$ and 20 degree, respectively,
3 as shown in Figure 4.25. The z_0 resolution is better for FST than for FST2 due to extra
4 stereo-strip layers while the p_T and d_0 resolutions in the barrel region are similar.

5 **4.3.3 Detector simulation and reconstruction**

6 In order to optimize the full silicon tracker detector for CEPC, we generate several bench-
7 mark processes that include single muon events, $e^+e^- \rightarrow ZH \rightarrow \nu\bar{\nu}\mu^+\mu^-$, and $e^+e^- \rightarrow$
8 $ZH \rightarrow \nu\bar{\nu}gg$ (two gluon jets). The events are then simulated and reconstructed using
9 different detector geometries, which are then used for the tracking performance studies.

10 **4.3.3.1 FST tracker**

11 The performance of the FST tracker is studied using the same Mokka simulation tool
12 used to study the CEPC baseline detector by substituting the FST tracker for the baseline
13 tracker while keeping all other detector elements unchanged.

14 In order to improve the flexibility of design, a new package of SiTracker is implemented
15 in Mokka which represents the silicon tracker by planar structure, which consists of a
16 thin layer of silicon with 150 μm thickness and 50 μm pitch size. For VXD and SOT,
17 they are composed by several layers, and each layer is composed by several ladders, and
18 each ladder is divided to several sensors. The SOT layer consist of double silicon layers
19 mounted back to back with a stereo-angle of 7 degree. The endcap tracker is composed
20 by several pixel disks EIT and several double-side strip disks EOT that are composed
21 by petals. The strip EOT disks have two sensitive silicon sub-layers on each side with
22 a stereo-angle of 5 degree. The material budget of the whole tracker is about 5% in the
23 barrel region and about 8% in the endcap region as shown in Figure 4.26, which also
24 shows the contributions of each part of the tracker. In the endcap region, the zigzags are
25 caused by the alternation and overlap of layers.

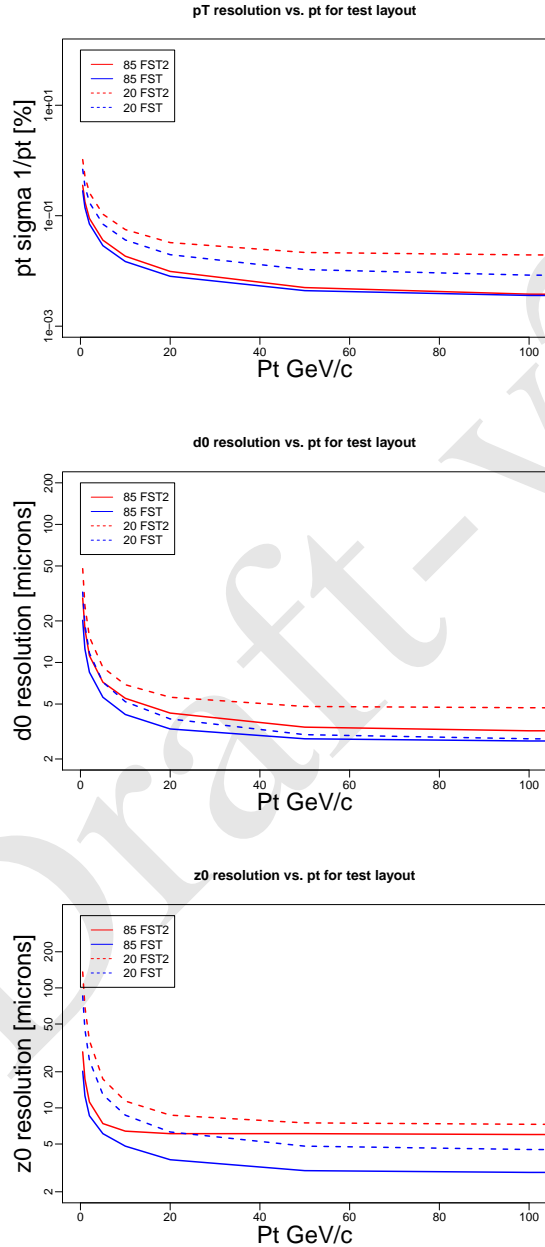


Figure 4.25: The expected p_T , d_0 , and z_0 resolutions from the toy simulation (Idres) are compared as function of track p_T in GeV for tracks with $\theta = 85$ and 20 degree, respectively.

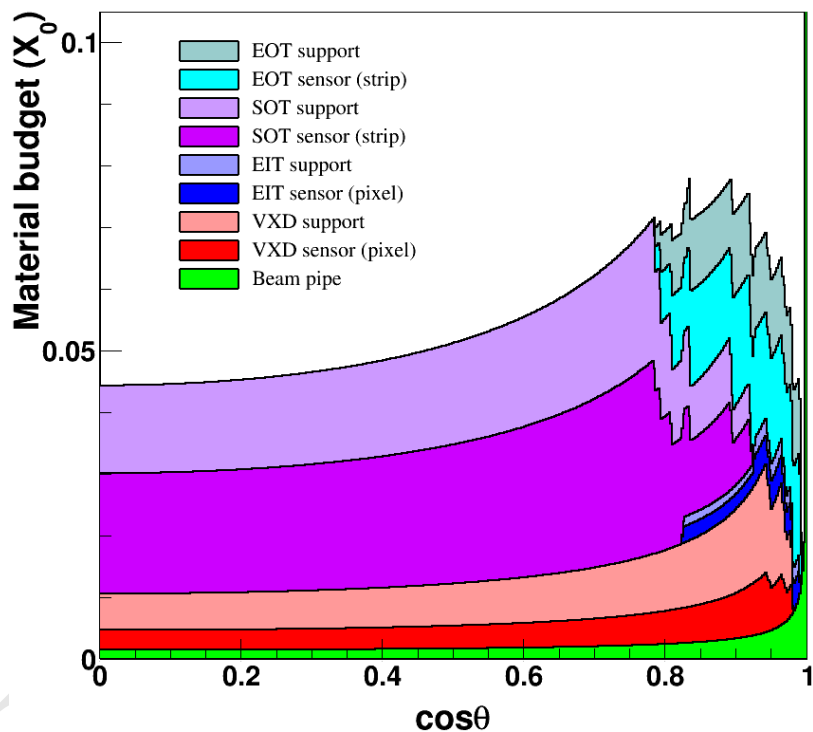


Figure 4.26: Material budget for the FST highlighting the contributions from the vertex detector (VXD) and strip detector (SOT) in the barrel region, and the pixel disks (EIT) and strip disks (EOT) in the endcap region. Comparing to the baseline detector, there are some differences on the thickness of the silicon layers and support materials considered.

SOT	FST			FST2				
	R (m)	$\pm z$ (m)	Type	R (m)	$\pm z$ (m)	Type		
Layer 1	0.153	0.368	D	0.344	0.793	S		
Layer 2	0.321	0.644	D	0.718	1.029	S		
Layer 3	0.603	0.920	D	1.082	1.391	S		
Layer 4	1.000	1.380	D	1.446	1.746	S		
Layer 5	1.410	1.840	D	1.820	2.107	S		
Layer 6	1.811	2.300	D					
EOT	R_{in} (m)	R_{out} (m)	$\pm z$ (m)	Type	R_{in} (m)	R_{out} (m)	$\pm z$ (m)	Type
Disk 1	0.082	0.321	0.644	D	0.207	0.744	1.034	D
Disk 2	0.117	0.610	0.920	D	0.207	1.111	1.424	D
Disk 3	0.176	1.000	1.380	D	0.207	1.477	1.779	D
Disk 4	0.234	1.410	1.840	D	0.207	1.852	2.140	D
Disk 5	0.293	1.811	2.300	D				

Table 4.8: Geometry parameters for the strip layers of the two Full Silicon Tracker detectors (FST and FST2) discussed in the text, where D and S stand for double and single-sided strip layers. The Silicon Outer Tracker (SOT) has either 5 or 6 layers depending on the configuration. The Endcap Outer Tracker (EOT) is composed of either 4 or 5 disks, all double-sided.

1 A conformal tracking algorithm developed for CLIC [42] has been adapted for use with
2 the full silicon tracker here. Through the conformal transform $u = \frac{x}{x^2+y^2}$ and $v = \frac{y}{x^2+y^2}$,
3 where x and y are the positions of the track hits in the detector space, the positions of
4 the track hits in the conformal space lie at a straight line for the track in a magnetic field.
5 Therefore, track finding becomes straight line searching in the pattern recognition. Cur-
6 rently, a cellular automaton is used as pattern recognition for the straight line searching.

7 **4.3.3.2 FST2 tracker**

8 In the case of FST2, events were simulated and reconstructed using software developed for
9 the International Linear Collider (ILC) [43, 44]. The track reconstruction was performed
10 with the LCSIM 4.0 package [42] using the “seed tracker” algorithm developed for the
11 SiD detector simulation. Track candidates with at least six hits in the silicon pixel and mi-
12 crostrip layers were considered. Only tracks with a minimum transverse momentum (p_T)
13 of 100 MeV were accepted. The track-fitting was performed with the following require-
14 ments; maximum distance of closest approach (DCA) is $|DCA| < 6$ mm, $|z_0| < 10$ mm,
15 and fit $\chi^2 < 10$. The reconstruction includes particle-flow algorithms (PFA) which enable
16 identification and reconstruction of individual particles. The PFA objects can be recon-
17 structed using the software algorithms implemented in the PANDORA package [45, 46].

18 **4.3.4 Tracking performance**

19 After the detector simulation and reconstruction, the tracking performances are measured
20 in terms of efficiencies, fake rates, momentum resolution, and the impact parameter res-

olutions using single muons or $e^+e^- \rightarrow ZH$ events. The tracking efficiency is defined as a fraction of stable charged particles that can be matched to well reconstructed tracks. The stable particles are defined as those charged particles with $p_T > 1$ GeV in the detector fiducial region ($9 < \theta < 170$ degree), originated from the interaction point, and lived long enough to reach the calorimeter. A well reconstructed track is defined as sharing more than 50% of its assigned silicon hits originating from a single particle (truth hits). We define a truth hit fraction as ratio of truth hits over total assigned hits of the track using silicon hits only. A poorly reconstructed track is defined to have the truth hit fraction less than 50%. The fake rate is defined as the fraction of poorly reconstructed tracks out of total reconstructed tracks, but this requires a realistic detector simulation, which we are not there yet. Since the CEPC baseline and the CEPC-FST detectors are sharing the common software and design, we will focus on their tracking performance comparisons to demonstrate that the full-silicon tracking concept is a viable option for CEPC.

4.3.4.1 Single muon particle

Figure 4.27 shows the tracking efficiency for single muons in CEPC-FST as function of p_T . The tracking efficiency is close to 100% at high p_T and slightly lower at small p_T . The trend is the same for CEPC baseline (v_4) , which indicate both trackers are capable of finding tracks efficiently in the detector fiducial region.

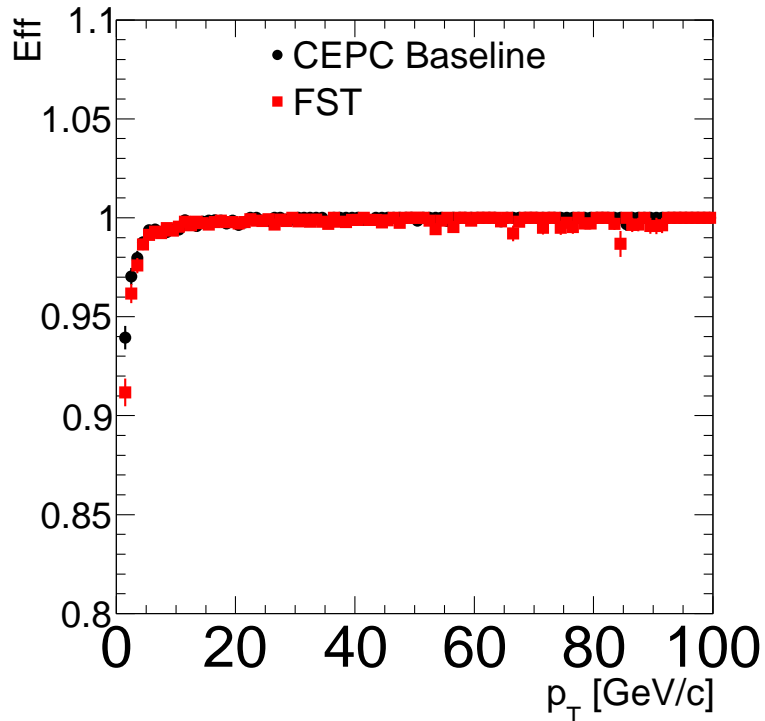


Figure 4.27: The tracking efficiencies are measured as function of p_T for single muons using CEPC baseline and CEPC-FST detectors.

Since the track resolution depends on the track angle θ , we divide the tracks in the barrel region with $40 < \theta < 140$ degree and in the endcap region with $7.25 < \theta < 40$ degree or $140 < \theta < 172.75$ degree. Figure 4.28 shows the track resolutions of p_T , d0, and z0

as function of track p_T in the barrel and endcap region. The resolutions seem comparable to each other, but they seem slightly better for the low momentum tracks in the baseline detector (TPC+Silicon) than CEPC-FST due to extra material in the detector while they are compatible at the high p_T .

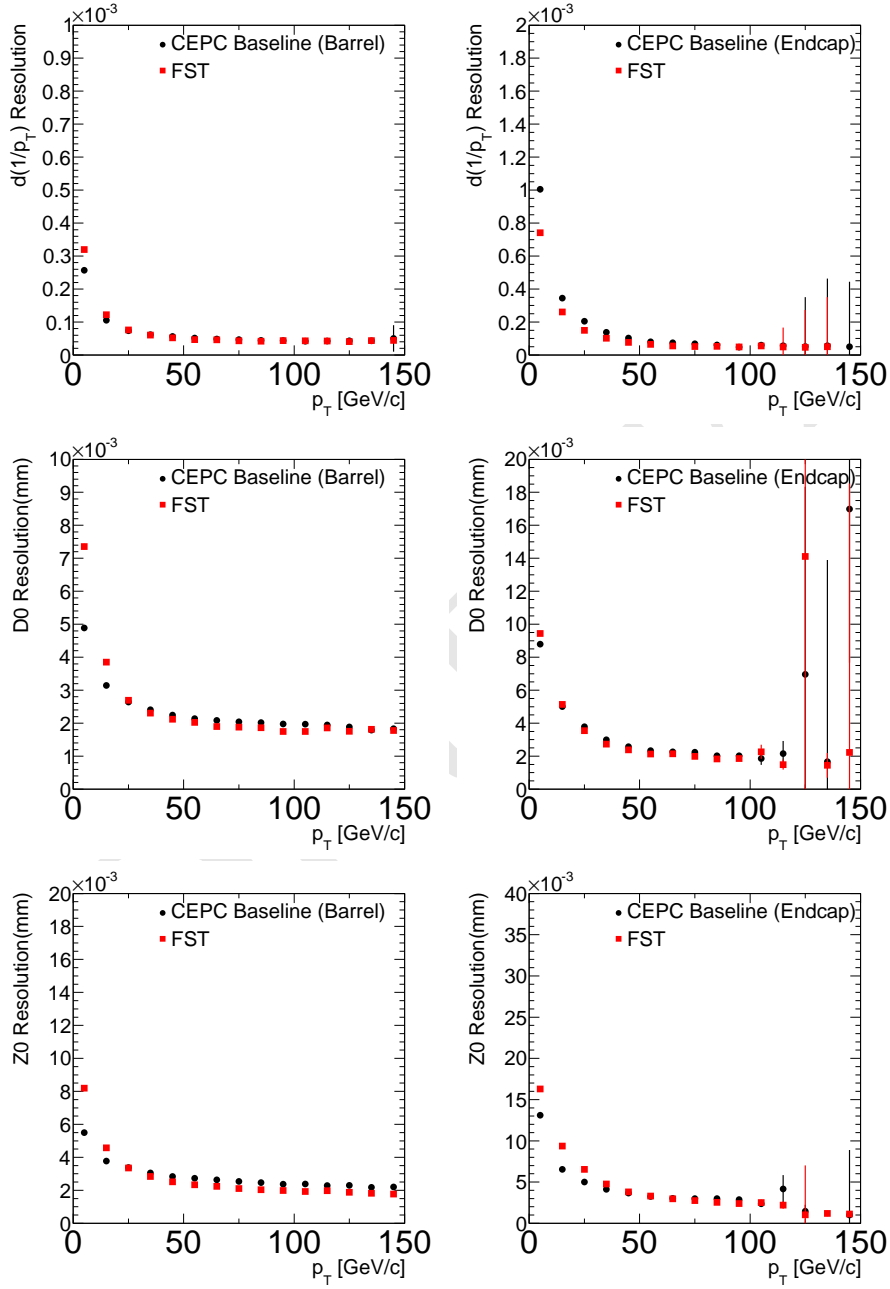


Figure 4.28: The tracking p_T , d0, and z0 resolutions are measured as function of p_T using single muons, left in the barrel region and right in the endcap region. They are compared between CEPC v_4 and CEPC-FST detectors. The resolutions for the low momentum tracks in the CEPC baseline detector seems slightly better than CEPC-FST, due to extra material in the detector. **Let's make sure the baseline numbers are consistent with what we presented earlier in the baseline subsection!**

4.3.4.2 Dimuon mass resolution

Figure 4.29 shows the dimuon invariant mass distributions from $ZH \rightarrow \nu\bar{\nu}\mu^+\mu^-$ decay between different detector configurations. The Higgs mass used in the simulation is 125 GeV. The dimuon mass resolution from CEPC-FST has $\sigma = 0.21$ GeV and seems 14% better than ones obtained from CEPC baseline detector.

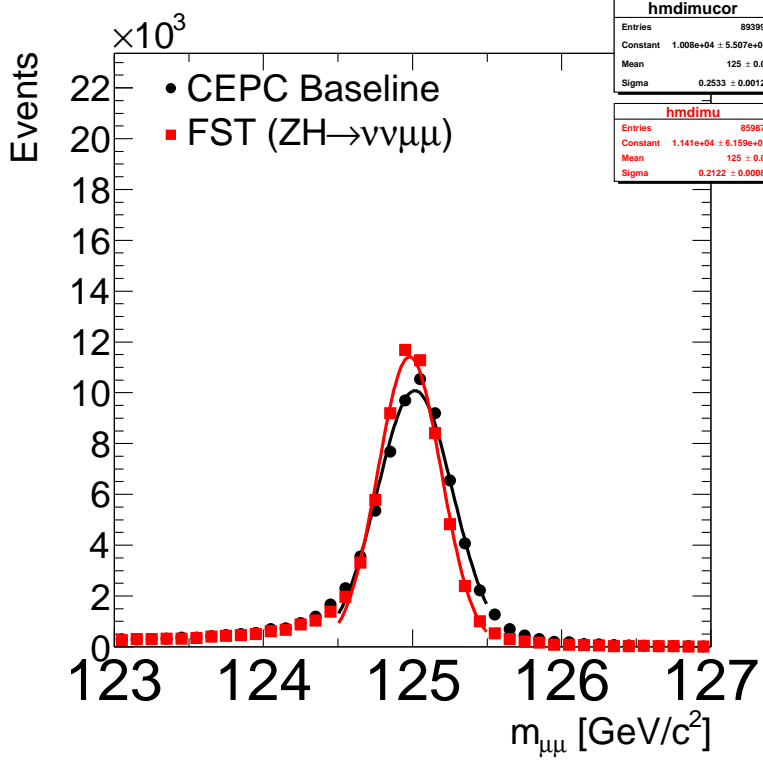


Figure 4.29: The di-muon mass distribution is compared from CEPC baseline and CEPC-FST detectors.

4.3.4.3 Tracking inside the jets

In order to study the tracking performance inside the jets, we generated and simulated some Higgs decaying into two gluon jets in $ZH \rightarrow \nu\bar{\nu}gg$ events. Figure 4.30 shows the tracking efficiency inside the jets as function of track momentum. The efficiency of finding tracks inside the jets is very similar between the CEPC baseline and the CEPC-FST detectors, which is close to 97%.

4.3.5 Conclusion

We present a preliminary study of full silicon tracker option as an alternative design for CEPC tracker. Two approaches are considered for the design: the first is to keep the silicon detectors (VXD, SIT, FTD) in the CEPC baseline detector and replacing TPC with additional silicon detectors, the second is to optimize the ILC-SID tracker to fulfill the CEPC tracking volume in order to achieve the excellent momentum resolution using 3 Tesla B field. The new detector geometry has been implemented in the simulation and the track reconstruction has also been adopted for the full silicon tracker. The initial study of

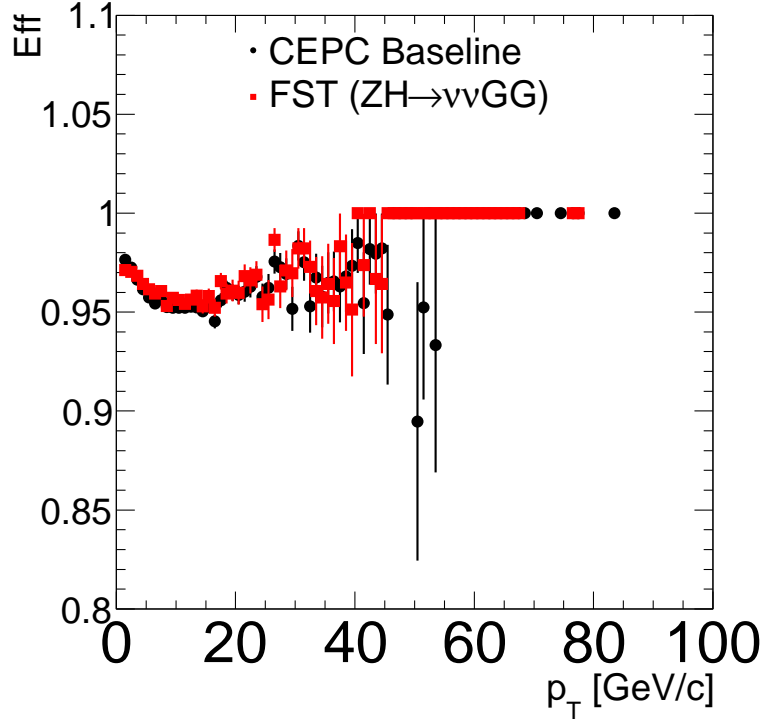


Figure 4.30: The tracking efficiencies for the stable particles inside the gluon jets as function of track p_T with CEPC baseline and CEPC-FST.

the tracking performance looks promising. There are still many improvements needed in the simulation and reconstruction in order to explore the full potential of the full-silicon tracker.

4.4 Drift chamber tracker detector

The drift chamber (DCH) is another option for the CEPC main outer tracker, and it is being purposed in conjunction with the alternative detector concept using a 2-Tesla magnet. It is designed to provide good tracking, high precision momentum measurement and excellent particle identification by cluster counting. In addition, a layer of silicon microstrip detectors surrounds the drift chamber in both barrel and forward/backward regions, and together with the vertex detector, improve the momentum resolution to better than 0.5% for 100 GeV tracks.

4.4.1 Introduction

The special feature of this drift chamber is its high transparency, in terms of radiation lengths, obtained thanks to the novel approach adopted for the wiring and assembly procedures. The design concept originated with the KLOE experiment [47], and more recently culminated in the realization of the MEG2 [48] drift chamber. As implemented here for the CEPC main tracker, the total amount of material in radial direction, towards the barrel calorimeter, is of the order of 1.6% X_0 , whereas, in the forward and backward

1 directions, this is equivalent to about 5.0% X_0 , including the endplates instrumented with
 2 front end electronics. The high transparency is particularly relevant for precision elec-
 3 troweak physics at the Z pole and for flavor physics, where the average charged particles
 4 momenta are in a range over which the multiple scattering contribution to the momentum
 5 measurement is significant.

6 4.4.2 Overview

7 The DCH is a unique volume, high granularity, all stereo, low mass cylindrical drift cham-
 8 ber, co-axial to the 2 T solenoid field. It extends from an inner radius $R_{in} = 0.35$ m to an
 9 outer radius $R_{out} = 2$ m, for a length $L = 4$ m and consists of 112 co-axial layers, at alter-
 10 nating sign stereo angles (in the range from 50 mrad to 250 mrad), arranged in 24 identical
 11 azimuthal sectors. The square cell size (5 field wires per sense wire) varies between 12.0
 12 and 14.5 mm for a total of 56,448 drift cells. Thanks to the peculiar design of the wiring
 13 procedures, successfully applied to the recent construction of the MEG2 drift chamber,
 14 such a large number of wires poses no particular concern.

15 A system of tie-rods directs the wire tension stress to the outer endplate rim, where a
 16 cylindrical carbon fiber support structure bearing the total load is attached. Two thin car-
 17 bon fiber domes, suitably shaped to minimize the stress on the inner cylinder and free to
 18 deform under the gas pressure without affecting the wire tension, enclose the gas volume.
 19 The angular coverage, for infinite momentum tracks originated at the interaction point and
 20 efficiently reconstructed in space, extends down to approximately 13° . In order to facil-
 21 itate track finding, the sense wires are read out from both ends to allow for charge division
 22 and time propagation difference measurements. The chamber is operated with a very light
 23 gas mixture, 90%He-10%iC4H10, corresponding to about 400 ns maximum drift time for
 24 the largest cell size. The number of ionization clusters generated by a *m.i.p.* in this gas
 25 mixture is about 12.5 cm^{-1} , allowing for the exploitation of the cluster counting/timing
 26 techniques for improving both spatial resolution ($\sigma_x < 100 \mu\text{m}$) and particle identification
 27 ($(\sigma(dN_{cluster}/dx)/(dN_{cluster}/dx)) \approx 2\%$).

28 4.4.3 Expected performance

29 The expected performance of the drift chamber has been studied with a MEG2 drift cham-
 30 ber prototype with 7 mm cell size and very similar electrostatic configuration and gas
 31 mixture [49]. Figure 4.31 indicates a $100 \mu\text{m}$ drift distance resolution, averaged over all
 32 drift times. A better resolution is expected for the drift chamber proposed here because
 33 of the longer drift distances. Cluster timing technique may further improve it. Analytical
 34 calculations for the expected transverse momentum and angular resolutions are plotted in
 35 Figure 4.32.

36 Based on the assumption that one can, in principle, reach a relative resolution on the
 37 measurement of the number of primary ionization clusters, N_{cl} , equal to $1/\sqrt{N_{cl}}$, the
 38 expected performance relative to particle separation in number of units of standard devi-
 39 ations is presented in Figure 4.33 as a function of the particle momentum. Solid curves
 40 refer to cluster counting technique applied to a 2 m track length with 80% cluster iden-
 41 tification efficiency and negligible (a few percent) fake clusters contamination. Dashed
 42 curves refer to the best theoretical prediction attainable with the dE/dx technique for the
 43 same track length and same number of samples. For the whole range of momenta, particle
 44 separation with cluster counting outperforms dE/dx technique by more than a factor of

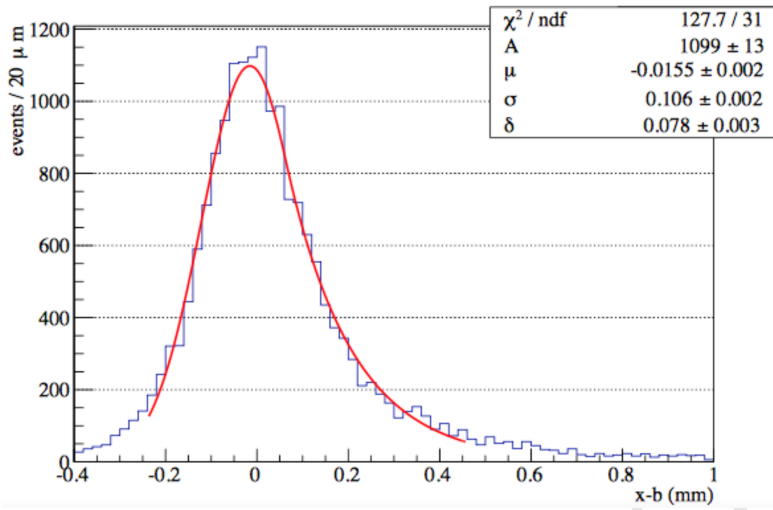


Figure 4.31: Measured drift distance residual distribution in the MEG2 drift chamber prototype using a 85%He-15% $i\text{C}_4\text{H}_{10}$ gas mixture. Cosmic rays tracks indicate a resolution better than $110 \mu\text{m}$, averaged over all drift times and in a wide range of track angles.

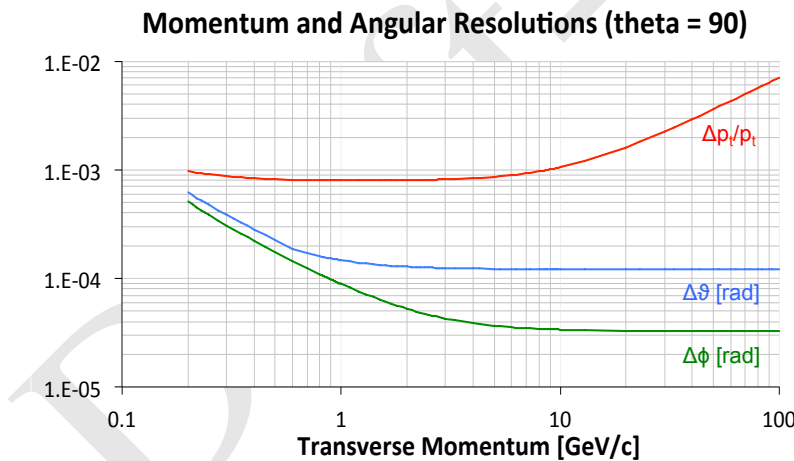


Figure 4.32: Analytical calculations for the expected transverse momenta (pink) and angular resolutions (blue/green) as a function of the particle momentum for $\theta = 90^\circ$.

- ¹ two, estimating an expected pion/kaon separation better than three standard deviations for
- ² all momenta below 850 MeV and slightly above 1.0 GeV.

³ 4.4.4 Tracking system simulation results

- ⁴ For the purpose of optimizing the track reconstruction performance, a vertex detector (dif-
- ⁵ ferent from the baseline choice) made of seven cylindrical layers, inside the drift chamber
- ⁶ inner radius, and of five forward disks, has been simulated together with a layer of silicon
- ⁷ microstrip detectors surrounding the drift chamber both in the barrel and in the forward
- ⁸ regions, followed by a preshower detector system within a homogeneous 2 T longitudinal
- ⁹ magnetic field. Details of ionization clustering for cluster counting/timing analysis
- ¹⁰ have not been included in the simulations, limiting the drift chamber performance both in

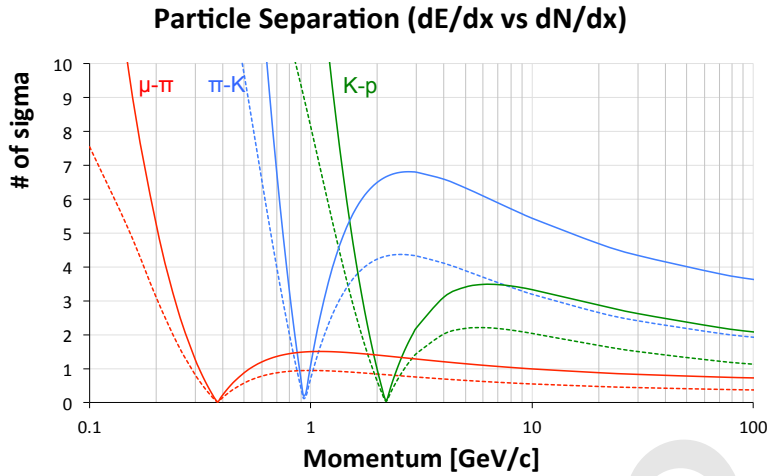


Figure 4.33: Particle type separation in units of standard deviations, with cluster counting (solid lines) and with dE/dx (broken lines) as a function of the particle momentum. A cluster counting efficiency of 80% and a dE/dx resolution of 4.2% have been assumed.

1 spatial resolution (a $100\ \mu\text{m}$ Gaussian smeared point resolution has been assumed) and in
 2 particle separation (no dN_{cl}/dx analysis has been simulated). A simplified track finding
 3 algorithm in its preliminary stage of development has been used to feed the space points
 4 to the fitter interface for the ultimate track fit. Figure 4.34 shows the momentum and
 5 angle resolutions as a function of the track momentum obtained by the tracking system
 6 simulation. No optimization has been tried yet. Momentum resolutions $\Delta p/p = 4 \times 10^{-3}$
 7 at $p = 100\ \text{GeV}$, for $\theta = 65^\circ$, and angular resolutions $\leq 0.1\ \text{mrad}$ for $p \geq 10\ \text{GeV}$, are
 8 within reach. Lastly, Figure 4.34 shows the z_0 and d_0 impact parameter resolutions ob-
 9 tained from the same simulation. A fit to the right plot in Figure 4.35 gives a d_0 impact
 10 parameter resolution:

$$\sigma_{d_0} = a \oplus \frac{b}{p \sin^{3/2} \theta}$$

11 with $a = 3\ \mu\text{m}$ and $b = 15\ \mu\text{m} \cdot \text{GeV}/c$.

12 **4.4.5 Backgrounds in the tracking system**

13 The main sources of backgrounds in the tracking system come from incoherent pair pro-
 14 duction, synchrotron radiation and $\gamma\gamma$ to hadrons. The incoherent pair production back-
 15 ground is dominant among these, however, only very few of the primary e^\pm particles will
 16 have a transverse momentum large enough to reach the inner radius of the drift cham-
 17 ber. The majority of the hits will be generated by secondary particles (mainly photons
 18 of energy below 1 MeV) produced by scattering off the material at low radii. Based on
 19 experience from the very similar MEG2 drift chamber, which has a smaller number of
 20 hits per track and a much more complicated event topology, occupancies of up to several
 21 percent will not affect tracking efficiency and single track momentum resolution. The
 22 level of occupancy here is expected to be even smaller with the use of the drift chamber
 23 timing measurement. As opposed to charged particles that leave a string of ionization in
 24 the drift cells they traverse, photons are characterized by a localized energy deposition.
 25 Signals from photons can therefore be effectively suppressed at the data acquisition level

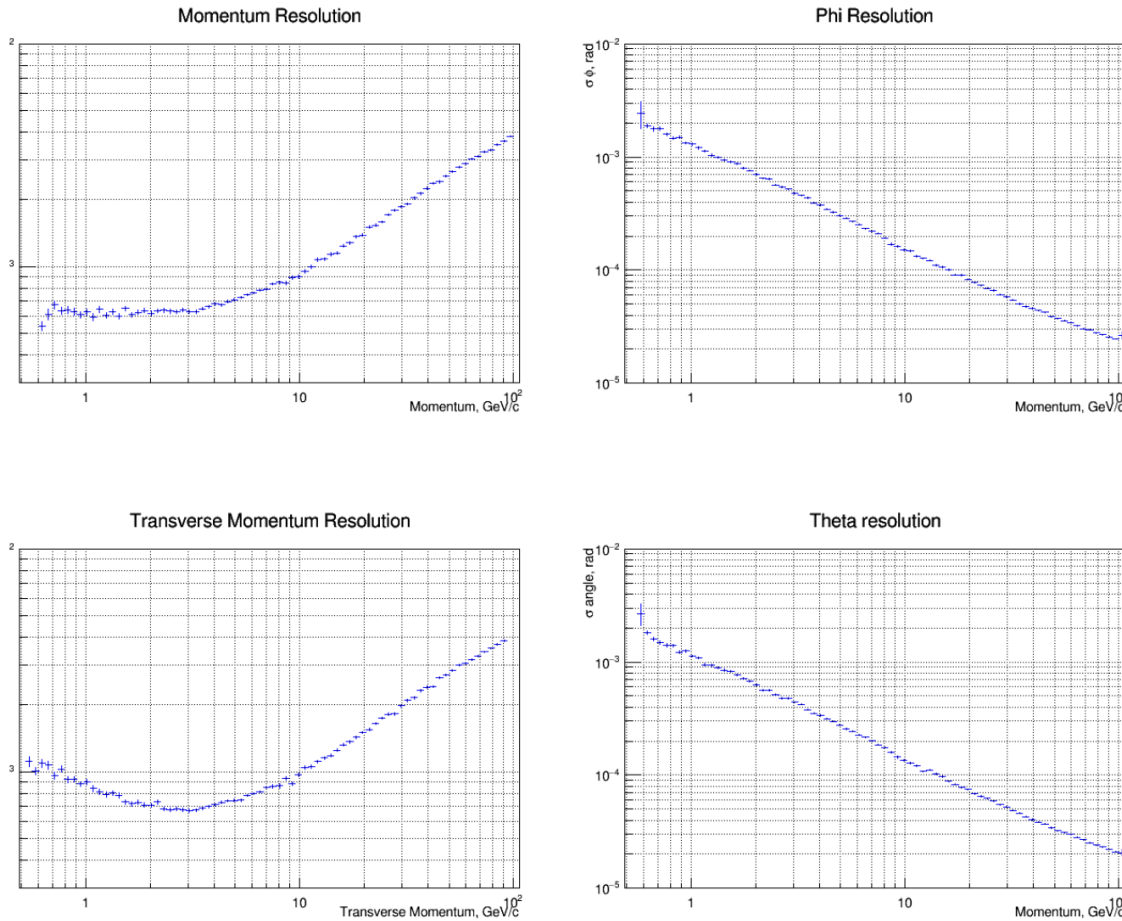


Figure 4.34: Momentum and transverse momentum resolutions (left) and angular ϕ and θ resolutions (right) (in μm) versus track momentum, from simulation of isolated tracks and a preliminary track finding algorithm.

1 by requiring that a threshold be reached by the number of ionization clusters within a
 2 reasonable time window. In addition, charge strings with holes longer than the average
 3 cluster separation can be interpreted as due to separate signals, thus avoiding piling up
 4 of any remaining photon induced background. With this effective suppression of photon
 5 induced signals, the background from incoherent pair production is expected to remain
 6 low and is unlikely to cause adverse issues for the track reconstruction.

7 **4.4.6 Constraints on the readout system**

8 With a drift chamber, all digitized hits generated at the occurrence of a trigger are usually
 9 transferred to data storage. The IDEA drift chamber transfers 2 B/ns from both ends of
 10 all wires hit, over a maximum drift time of 400 ns. With 20 tracks/event and 130 cells
 11 hit for each track, the size of a hadronic Z decay in the DCH is therefore about 4 MB,
 12 corresponding to a bandwidth of 40 GB/s at the Z pole (at a trigger rate of approximately
 13 10 kHz). The contribution from $\gamma\gamma$ to hadrons amounts to 6 GB/s. As mentioned in
 14 the previous paragraph, the incoherent pair production background causes the read-out of

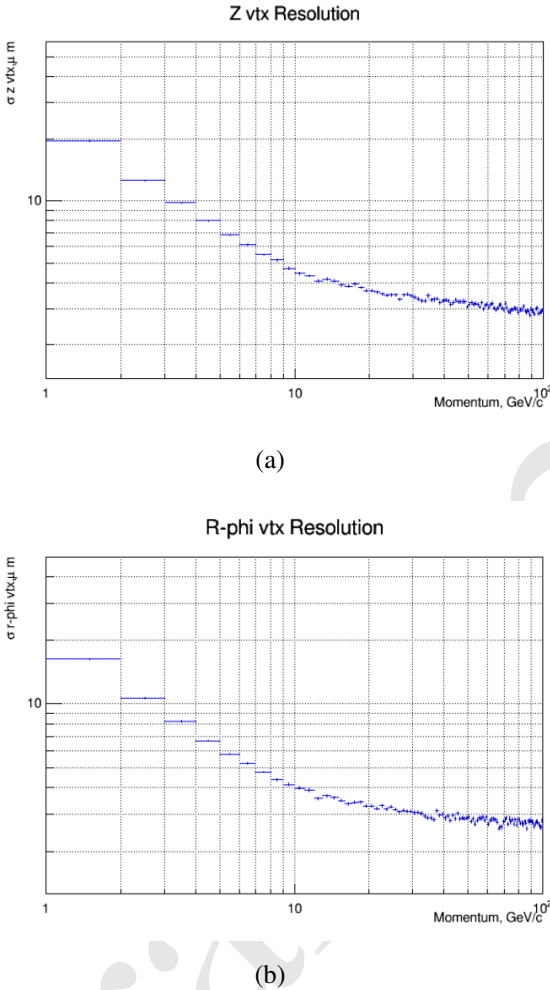


Figure 4.35: Impact parameters, z_0 and d_0 , resolution (in μm) versus track momentum, from simulation of isolated tracks and a preliminary track finding algorithm.

1 additional 1400 wires on average for every trigger, which translates into a bandwidth of
 2 25 GB/s. A similar bandwidth is taken by the noise induced by the low single electron
 3 detection threshold necessary for an efficient cluster counting. Altogether, the various
 4 contributions sum up to a data rate of about 0.1 TB/s. Reading out these data and sending
 5 them into an "event builder" would not be a challenge, but the data storage requires a
 6 large reduction. Such a reduction can be achieved by transferring, for each hit drift cell,
 7 the minimal information needed by the cluster timing/counting, i.e., the amplitude and
 8 the arrival time of each peak associated with each individual ionization electron, each
 9 encoded in 1 Byte, instead of the full signal spectrum. The data generated by the drift
 10 chamber, subsequently digitized by an ADC, can be analyzed in real time by a fast read-
 11 out algorithm implemented in a FPGA[50]. This algorithm identifies, in the digitized
 12 signal, the peaks corresponding to the different ionization electrons, stores the amplitude
 13 and the time for each peak in an internal memory, filters out spurious and isolated hits and
 14 sends these reduced data to the acquisition system at the occurrence of a trigger. Each hit
 15 cell integrates the signal of up to 30 ionization electrons, which can thus be encoded within
 16 60 B per wire end instead of the aforementioned 800 B. Because the noise and background

1 hits are filtered out by the FPGA algorithm, the data rate induced by Z hadronic decays is
 2 reduced to 3 GB/s, for a total bandwidth of about 3.6 GB/s, roughly a factor 30 reduction.

3 References

- 4 [1] P. M. De Freitas and H. Videau, *Detector simulation with MOKKA/GEANT4: Present and future*, in *International Workshop on Linear Colliders (LCWS 2002), Jeju Island, Korea*, pp. 26–30. 2002.
- 5 [2] M. Regler, M. Valentan, and R. Frühwirth, *The LiC detector toy program*, Nuclear Instruments and Methods in Physics Research Section A: Accelerators, Spectrometers, Detectors and Associated Equipment **581** (2007) no. 1, 553–556.
- 6 [3] M. Battaglia et al., *R&D Paths of Pixel Detectors for Vertex Tracking and Radiation Imaging*, Nucl. Instrum. Meth. **A716** (2013) 29–45, arXiv:1208.0251 [physics.ins-det].
- 7 [4] G. Contin et al., *The MAPS based PXL vertex detector for the STAR experiment*, JINST **10** (2015) no. 03, C03026.
- 8 [5] DEPFET Collaboration, C. Lacasta, *The DEPFET pixel detector for the Belle II experiment at SuperKEKB*, PoS **Vertex2013** (2013) 005.
- 9 [6] ALICE Collaboration, B. Abelev et al., *Technical Design Report for the Upgrade of the ALICE Inner Tracking System*, J. Phys. **G41** (2014) 087002.
- 10 [7] I. Valin et al., *A reticle size CMOS pixel sensor dedicated to the STAR HFT*, Journal of Instrumentation **7** (2012) no. 01, C01102. <http://stacks.iop.org/1748-0221/7/i=01/a=C01102>.
- 11 [8] G. A. Rinella, *The ALPIDE pixel sensor chip for the upgrade of the ALICE Inner Tracking System*, Nuclear Instruments and Methods in Physics Research Section A: Accelerators, Spectrometers, Detectors and Associated Equipment **845** (2017) 583 – 587. <http://www.sciencedirect.com/science/article/pii/S0168900216303825>. Proceedings of the Vienna Conference on Instrumentation 2016.
- 12 [9] Y. Lu, Q. Ouyang, Y. Arai, Y. Liu, Z. Wu, and Y. Zhou, *First results of a Double-SOI pixel chip for X-ray imaging*, Nuclear Instruments and Methods in Physics Research Section A: Accelerators, Spectrometers, Detectors and Associated Equipment **831** (2016) 44 – 48. <http://www.sciencedirect.com/science/article/pii/S0168900216301851>. Proceedings of the 10th International Hiroshima Symposium on the Development and Application of Semiconductor Tracking Detectors.
- 13 [10] I. Kurachi, K. Kobayashi, M. Mochizuki, M. Okihara, H. Kasai, T. Hatsui, K. Hara, T. Miyoshi, and Y. Arai, *Tradeoff Between Low-Power Operation and Radiation Hardness of Fully Depleted SOI pMOSFET by Changing LDD Conditions*, IEEE Transactions on Electron Devices **63** (2016) no. 6, 2293–2298.

- [11] Z. Wu, *A prototype SOI pixel sensor for CEPC vertex*,
https://indico.cern.ch/event/577879/contributions/2741627/attachments/1575067/2486910/A_prototype_SOI_pixel_sensor_for_CEPC_vertex.pdf.
- [12] S. Ono, M. Togawa, R. Tsuji, T. Mori, M. Yamada, Y. Arai, T. Tsuboyama, and K. Hanagaki, *Development of a pixel sensor with fine space-time resolution based on SOI technology for the ILC vertex detector*, *Nuclear Instruments and Methods in Physics Research Section A: Accelerators, Spectrometers, Detectors and Associated Equipment* **845** (2017) 139 – 142. <http://www.sciencedirect.com/science/article/pii/S0168900216303783>. Proceedings of the Vienna Conference on Instrumentation 2016.
- [13] M. Idzik, *SOI-Cracow*, https://agenda.linearcollider.org/event/7450/contributions/38595/attachments/31561/47538/2017_LCVertex_Idzik.pdf.
- [14] S. Spannagel, *Silicon technologies for the CLIC vertex detector*, *Journal of Instrumentation* **12** (2017) no. 06, C06006.
<http://stacks.iop.org/1748-0221/12/i=06/a=C06006>.
- [15] H. H. Wieman, E. Anderssen, L. Greiner, H. S. Matis, H. G. Ritter, X. Sun, and M. Szelezniak, *STAR PIXEL detector mechanical design*, *JINST* **4** (2009) P05015.
- [16] H. Abramowicz et al., *The International Linear Collider Technical Design Report - Volume 4: Detectors*, [arXiv:1306.6329 \[physics.ins-det\]](https://arxiv.org/abs/1306.6329).
- [17] Belle-II Collaboration, T. Abe et al., *Belle II Technical Design Report*, [arXiv:1011.0352 \[physics.ins-det\]](https://arxiv.org/abs/1011.0352).
- [18] Y. Zhang, H. Zhu, L. Zhang, and M. Fu, *Charge collection and non-ionizing radiation tolerance of CMOS pixel sensors using a $0.18\mu\text{m}$ CMOS process*, *Nuclear Instruments and Methods in Physics Research Section A: Accelerators, Spectrometers, Detectors and Associated Equipment* **831** (2016) 99 – 104. <http://www.sciencedirect.com/science/article/pii/S0168900216300481>. Proceedings of the 10th International Hiroshima Symposium on the Development and Application of Semiconductor Tracking Detectors.
- [19] Y. Zhou, *Development of highly compact digital pixels for the vertex detector of the future e^+e^- collider*, <https://indico.cern.ch/event/577879/contributions/2740073/>.
- [20] Y. Zhang, *A Monolithic Active Pixel Sensor prototype for the CEPC vertex detector*, https://indico.cern.ch/event/577879/contributions/2740125/attachments/1574470/2485730/P15_ZY_POSTER_Final.pdf.
- [21] Y. Lu, *Study of SOI Pixel for the Vertex*, <http://indico.ihep.ac.cn/event/6433/>.

- [22] M. Motoyoshi, T. Miyoshi, M. Ikebec, and Y. Arai, *3D integration technology for sensor application using less than 5 μm-pitch gold cone-bump connpdfection*, Journal of Instrumentation **10** (2015) no. 03, C03004. <http://stacks.iop.org/1748-0221/10/i=03/a=C03004>.
- [23] W. Snoeys, G. A. Rinella, H. Hillemanns, T. Kugathasan, M. Mager, L. Musa, P. Riedler, F. Reidt, J. V. Hoorne, A. Fenigstein, and T. Leitner, *A process modification for CMOS monolithic active pixel sensors for enhanced depletion, timing performance and radiation tolerance*, Nuclear Instruments and Methods in Physics Research Section A: Accelerators, Spectrometers, Detectors and Associated Equipment **871** (2017) 90 – 96. <http://www.sciencedirect.com/science/article/pii/S016890021730791X>.
- [24] F. Shen, S. Wang, C. Yang, and Q. Xu, *MWPC prototyping and testing for STAR inner TPC upgrade*, JINST **12** (2017) no. 06, C06008.
- [25] ALICE Collaboration, D. Rohr, *Tracking performance in high multiplicities environment at ALICE*, in *5th Large Hadron Collider Physics Conference (LHCP 2017) Shanghai, China, May 15-20, 2017*. 2017. [arXiv:1709.00618 \[physics.ins-det\]](https://inspirehep.net/record/1621494/files/arXiv:1709.00618.pdf). <https://inspirehep.net/record/1621494/files/arXiv:1709.00618.pdf>.
- [26] P. Bhattacharya, S. S. Sahoo, S. Biswas, B. Mohanty, N. Majumdar, and S. Mukhopadhyay, *Numerical Investigation on Electron and Ion Transmission of GEM-based Detectors*, EPJ Web Conf. **174** (2018) 06001.
- [27] M. Posik and B. Surrow, *Construction of a Triple-GEM Detector Using Commercially Manufactured Large GEM Foils*, 2018. [arXiv:1806.01892 \[physics.ins-det\]](https://arxiv.org/abs/1806.01892).
- [28] ATLAS Muon Collaboration, D. Sampsonidis, *Study of the performance of Micromegas detectors in magnetic field*, EPJ Web Conf. **174** (2018) 05003.
- [29] S. Dalla Torre, E. Oliveri, L. Ropelewski, and M. Titov, *R&D Proposal: RD51 Extension Beyond 2018*, [arXiv:1806.09955 \[physics.ins-det\]](https://arxiv.org/abs/1806.09955).
- [30] D. S. Bhattacharya, D. Attié, P. Colas, S. Mukhopadhyay, N. Majumdar, S. Bhattacharya, S. Sarkar, A. Bhattacharya, and S. Ganjour, *Measurement and simulation of two-phase CO₂ cooling in Micromegas modules for a Large Prototype of Time Projection Chamber*, JINST **10** (2015) no. 08, P08001, [arXiv:1801.00304 \[physics.ins-det\]](https://arxiv.org/abs/1801.00304).
- [31] M. Vos, *Micro-channel cooling in high energy physics*, PoS Vertex**2016** (2017) 037.
- [32] M. Zhao, M. Ruan, H. Qi, and Y. Gao, *Feasibility study of TPC at electron positron colliders at Z pole operation*, JINST **12** (2017) no. 07, P07005, [arXiv:1704.04401 \[physics.ins-det\]](https://arxiv.org/abs/1704.04401).
- [33] A. Affolder et al., *DC-DC converters with reduced mass for trackers at the HL-LHC*, JINST **6** (2011) C11035.

- [34] S. Diez, *System Implications of the Different Powering Distributions for the ATLAS Upgrade Strips Tracker*, *Phys.Procedia* **37** (2012) 960–969.
- [35] K. Klein et al., *DC-DC conversion powering schemes for the CMS tracker at Super-LHC*, *JINST* **5** (2010) C07009.
- [36] A. Nomerotski et al., *Evaporative CO₂ cooling using microchannels etched in silicon for the future LHCb vertex detector*, *JINST* **8** (2013) P04004, [arXiv:1211.1176 \[physics.ins-det\]](https://arxiv.org/abs/1211.1176).
- [37] The ATLAS Collaboration, A. Affolder, *Silicon Strip Detectors for the ATLAS HL-LHC Upgrade*, *Phys.Procedia* **37** (2012) 915–922.
- [38] V. Blobel, *Software alignment for tracking detectors*, *Nucl.Instrum.Meth.* **A566** (2006) 5–13.
- [39] A. Savoy-Navarro, *Large Area Silicon Tracking: New Perspectives*, [arXiv:1203.0736 \[physics.ins-det\]](https://arxiv.org/abs/1203.0736).
- [40] N. Calace and A. Salzburger, *ATLAS Tracking Detector Upgrade studies using the Fast Simulation Engine*, in *Journal of Physics Conference Series*, vol. 664 of *Journal of Physics Conference Series*, p. 072005. Dec., 2015.
- [41] M. Regler, W. Mitaroff, M. Valentan, R. Fruhwirth, and R. Hofler, *The 'LiC Detector Toy' program*, *J. Phys. Conf. Ser.* **119** (2008) 032034.
- [42] N. Graf and J. McCormick, *LCSIM: A detector response simulation toolkit*, in *2012 IEEE Nuclear Science Symposium and Medical Imaging Conference Record (NSS/MIC)*, p. 1016. Oct, 2012.
- [43] C. Adolphsen et al., *The International Linear Collider Technical Design Report - Volume 3. II: Accelerator Baseline Design*, 2013. [arXiv:1306.6328 \[physics.acc-ph\]](https://arxiv.org/abs/1306.6328).
- [44] H. Abramowicz et al., *The International Linear Collider Technical Design Report - Volume 4: Detectors*, 2013. [arXiv:1306.6329 \[physics.ins-det\]](https://arxiv.org/abs/1306.6329).
- [45] M. J. Charles, *PFA Performance for SiD*, in *Linear colliders. Proceedings, International Linear Collider Workshop, LCWS08, and International Linear Collider Meeting, ILC08, Chicago, USA, November 16-20, 2008*. 2009. [arXiv:0901.4670 \[physics.data-an\]](https://arxiv.org/abs/0901.4670).
- [46] J. S. Marshall and M. A. Thomson, *Pandora Particle Flow Algorithm*, in *Proceedings, International Conference on Calorimetry for the High Energy Frontier (CHEF 2013)*, pp. 305–315. 2013. [arXiv:1308.4537 \[physics.ins-det\]](https://arxiv.org/abs/1308.4537).
- [47] M. Adinolfi et al., *The tracking detector of the KLOE experiment*, *Nucl. Instrum. Meth.* **A488** (2002) 51–73.
- [48] A. M. Baldini et al., *MEG Upgrade Proposal*, [arXiv:1301.7225 \[physics.ins-det\]](https://arxiv.org/abs/1301.7225).

- ¹ [49] A. M. Baldini et al., *Single-hit resolution measurement with MEG II drift chamber prototypes*, arXiv:1605.07970 [physics.ins-det].
- ²
- ³ [50] G. Chiarello, C. Chiri, G. Cocciole, A. Corvaglia, F. Grancagnolo, M. Panareo, A. Pepino, and G. F. Tassielli, *The Use of FPGA in Drift Chambers for High Energy Physics Experiments*, 2017.
- ⁴
- ⁵

Draft-V2.0

Draft-V2.0

CHAPTER 5

CALORIMETRY

5.1 Introduction to calorimeters

A calorimetry system is employed in the CEPC detector to provide hermetic coverage for high-resolution energy measurements of electrons, photons, taus and hadronic jets. To fully exploit the potential of the CEPC physics program for Higgs and electroweak physics, all possible final states from decays of the intermediate vector bosons, W and Z , and the Higgs boson need to be separately identified and reconstructed with high sensitivity. In particular, to clearly discriminate the $H \rightarrow ZZ^* \rightarrow 4j$ and $H \rightarrow WW^* \rightarrow 4j$ final states, the energy resolution of the CEPC calorimetry system for hadronic jets needs to be pushed quite beyond today's limits. Indeed, in order to distinguish the hadronic decays of W and Z bosons, a 3%-4% invariant mass resolution for two-jet systems is required. Such a performance needs a jet energy resolution of $\sim 30\%/\sqrt{E}$, at energies below 100 GeV. This would be about a factor of two better than that provided by the LEP detectors and the currently operating calorimeters at the LHC, and would significantly improve the separation of the W and Z bosons in their hadronic decays, as shown in Figure 5.1. Two different technology approaches are pursued for the CEPC calorimetry system, the first one aiming to measure individual particles in a jet using a calorimetry system with very high granularity based on the particle flow concept, while the second aiming at a homogeneous and integrated solution based on the dual-readout concept. Both approaches will be described in this chapter, while the first approach is the current baseline for the design of the CEPC calorimetry system in that it is integrated in the full CEPC detector simulation.

The particle flow algorithm (PFA [1]) is a very promising approach to achieve the unprecedented jet energy resolution of 3%-4%. The basic idea of the PFA is to make use

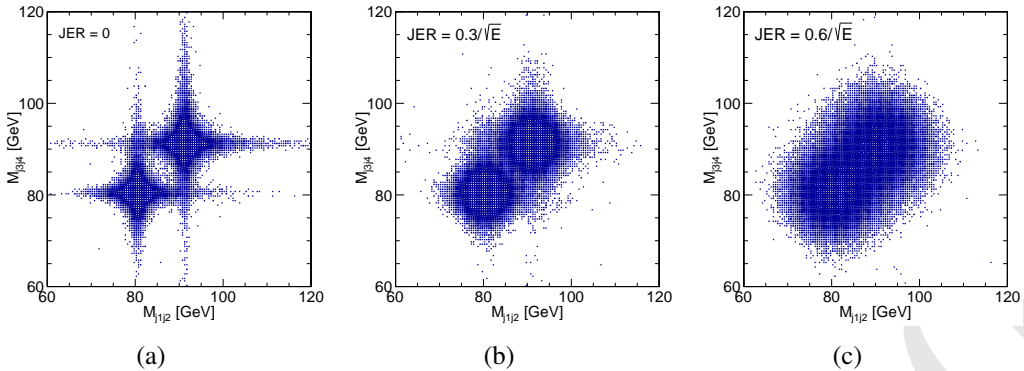


Figure 5.1: Separation of W and Z bosons in their hadronic decays with different jet energy resolutions: $0/\sqrt{E}$ (a), $30\%/\sqrt{E}$ (b), and $60\%/\sqrt{E}$ (c). A jet energy resolution of $30\%/\sqrt{E}$ is required to separate the hadronic decays of W and Z bosons.

of the optimal sub-detector in a detector system to determine the energy/momentum of each particle in a jet. An essential prerequisite for realization of this idea is to distinguish among energy deposits of individual particles from a jet in the calorimetry system. High, three-dimensional spatial granularity is required for the calorimetry system to achieve this. Therefore, PFA calorimeters feature finely segmented, three-dimensional granularity and compact, spatially separated, particle showers to facilitate the reconstruction and identification of every single particle shower in a jet. It is for this feature PFA calorimeters are usually also called imaging calorimeters. A PFA calorimetry system generally consists of an electromagnetic calorimeter (ECAL), optimized for measurements of photons and electrons, and a hadronic calorimeter (HCAL) to measure hadronic showers.

In a typical jet, 65% of its energy is carried by charged particles, 25% by photons, and 10% by neutral hadrons. The charged particles in a jet can be precisely measured with a tracking system, especially for low momentum particles where the relatively small, multiple scattering term dominates in the resolution, and their tracks can be matched to their energy deposits in a PFA calorimetry system. This combination maximizes the overall resolution of the jet energy measurement by compensating for the worsening of calorimeter-only energy resolution for low energy particles by leveraging the improved resolution from the tracking system. Energy deposits in the PFA calorimetry system without matched tracks are considered to originate from the neutral particles of photons and neutral hadrons in the jet. Among these neutral particles, photons are measured using the ECAL with good energy resolution, while only the neutral hadrons are primarily measured using a combination of the ECAL and HCAL with a limited energy resolution. Therefore, in the PFA, the jet energy is determined by combining the best measurement in a detector system of each single particle in the jet: the track momenta of charged particles measured using the tracking system, the energies of photons measured using the ECAL and the energies of neutral hadrons measured primarily using the HCAL.

Extensive studies have been carried out within the CALICE collaboration [2] to develop compact PFA calorimeters. Various detector technology options have been explored to address challenges from stringent performance requirements as shown in Figure 5.2. Prototypes with high granularity using several technological options have been developed and exposed to particle beams, which have demonstrated the in-depth understanding of

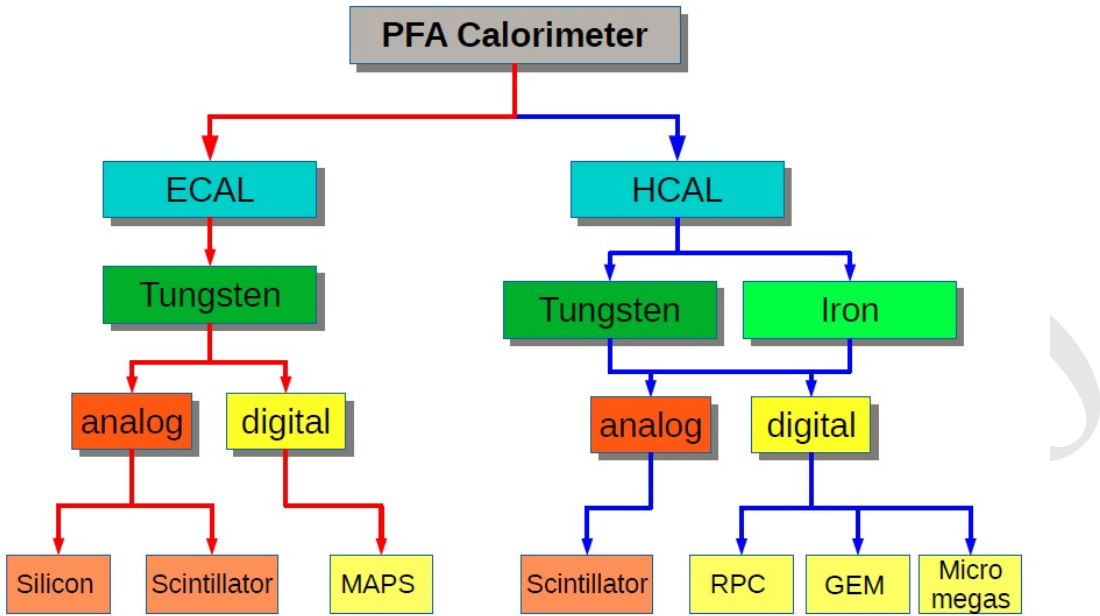


Figure 5.2: PFA: Overview of development of imaging calorimeters in the CALICE collaboration. Various technology options have been explored in aspects including absorber material, active medium and readout scheme.

1 the PFA calorimetry performance.

2

3 An alternative approach for a combined, high-performance, electromagnetic and hadronic
 4 calorimeter aims at reaching an even better (standalone) hadronic resolution, without
 5 spoiling the electromagnetic one, by exploiting the dual-readout (DR) technique. Indeed
 6 the main limiting factor to the energy resolution in hadron calorimetry arises from the fluc-
 7 tuations of the electromagnetic component (f_{em}) that each hadronic shower develops as
 8 consequence of π^0 and η production. Since typically the detector response to the hadronic
 9 and em components is very different ($h/e \neq 1$), the reconstructed signal heavily depends
 10 on the actual value of f_{em} . By using two independent processes (namely, scintillation and
 11 Čerenkov light production) that have a very different sensitivity to the hadronic and em
 12 components, it is possible to reconstruct f_{em} , event by event, and eliminate the effects of
 13 its fluctuations.

14 Among the possible DR implementations, a fiber-sampling DR calorimeter, based on
 15 either copper or lead as absorber material, looks the most suitable to provide the required
 16 performance in a cost-effective way. Preliminary results of GEANT4 simulations point to
 17 possible resolutions better than 15% and around 30% – 40% (over \sqrt{E}), for electromag-
 18 netic and hadronic showers, respectively (see Section 5.5.6).

19 Moreover, if the fibers are readout with Silicon PhotoMultipliers (SiPMs), the high de-
 20 tector granularity and the possibility of longitudinal segmentation will make this solution
 21 easily compatible with Particle Flow Algorithms.

22 In the following sections, several possible concrete implementations of a calorimeter
 23 system are discussed in sufficient detail to describe the readiness of the technologies and
 24 the performance of these systems in current test beams and prototypes and their corre-

1 sponding general implementation in the simulation performance studies of the physics
 2 objects and benchmarks presented in subsequent chapters.

3 **5.2 General design considerations for the PFA Calorimetry system**

4 The CEPC PFA calorimetry system is longitudinally composed of two separate sampling
 5 calorimeters: ECAL and HCAL, both of which are installed inside the solenoid coil of
 6 the CEPC detector system to minimize the inactive material in front of the calorimetry
 7 system and to reliably associate tracks to energy deposits. Following the geometry of the
 8 CEPC detector, each of two calorimeters is organized into one cylindrical barrel and two
 9 disk-like endcap sections.

10 The ECAL, considered here, has analog readout, consisting of sensitive layers of ei-
 11 ther silicon pads or scintillator tiles interleaved with tungsten absorber plates. As for the
 12 HCAL, steel plates are adopted as absorber, and both digital and analog readout is consid-
 13 ered. The digital HCAL (DHCAL) uses either Glass Resistive Plate Chambers (GRPC)
 14 or Thick Gas Electron Multiplier detectors (THGEM) as the active medium, while the
 15 analog HCAL (AHCAL) uses scintillator tiles coupled to SiPMs.

16 The calorimeters for these options are all highly segmented both transversely and longi-
 17 tudinally, which is driven by the requirement from the particle flow algorithm of excellent
 18 particle shower separation capability. The baseline technology options for the CEPC PFA
 19 ECAL and HCAL that have been integrated into the full CEPC detector simulation are
 20 silicon-tungsten and steel-GRPC, respectively.

21 In the baseline designs of the calorimeters, the ECAL is segmented into 30 longitudinal
 22 layers with a total thickness of tungsten of 84 mm (corresponding to a total depth of
 23 $24 X_0$), and the silicon plate in each layer is 0.5 mm thick, divided into square cells each
 24 of $10 \times 10 \text{ mm}^2$. The 30 ECAL layers are split into 2 sections with different thickness of
 25 absorber layers. The first section contains 20 layers of 2.1 mm thick tungsten plates and
 26 the second contains 10 layers of 4.2 mm tungsten plates (see section 5.3.2.2 for details).
 27 The HCAL consists of 40 longitudinal layers each containing 2 cm thick steel with a thin
 28 layer of GRPCs read out in a cell size of $10 \times 10 \text{ mm}^2$. The above design parameters
 29 of both the ECAL and HCAL are a result of dedicated optimization studies based on
 30 simulation that will be presented in the subsequent sections.

31 **5.3 Electromagnetic Calorimeter for Particle Flow Approach**

32 The particle flow paradigm has tremendous impact on the design of the ECAL. With ex-
 33 cellent capability of pattern recognition, the ECAL is expected to identify photons from
 34 close-by showers, reconstruct detailed properties of a shower (i.e. shower shape, starting
 35 point and energy distribution), and distinguish electromagnetic showers from hadronic
 36 ones. Thus, shower imaging capability of the calorimeter is more important than its in-
 37 trinsic energy resolution, although the latter is still important to the particle flow perfor-
 38 mance for electrons, photons and jets. Due to the fact that about half of hadronic showers
 39 start inside the ECAL, excellent three dimensional granularity is of primary importance to
 40 the ECAL. In order to have the power of separating close-by showers in the calorimeter,
 41 absorber material with small Moliere radius is required for the ECAL. And a large ratio
 42 of the interaction length over the radiation length of the absorber material is advantageous
 43 to separation between electromagnetic and hadronic showers because a short radiation

length makes an electromagnetic shower start early in the ECAL, while a long interaction length reduces the fraction of a hadronic shower in the ECAL. A short radiation length also makes a compact ECAL, which is highly desirable from the cost saving point of view.

In short, requirements for the ECAL on high granularity, compactness and shower separation lead to the choice of a sampling calorimeter with tungsten (the radiation length $X_0 = 3.5$ mm, the Molière Radius=9 mm and the interaction length $\lambda_I = 99$ mm) as absorber material. This ensures a compact ECAL with a sufficient depth to contain high-energy showers.

Two options for active material are considered for the ECAL: silicon and scintillator. The silicon option is taken as the baseline, while the scintillator option is also being investigated as alternative. Both options are presented in this section.

5.3.1 Design Optimization

ECAL design parameters including total thickness of absorber, thickness and transverse size of silicon sensors, number of sampling layers have been optimized based on simulation with a simplified and standalone ECAL geometry. There is no material in front of the ECAL and no gaps or dead area between modules in this geometry. In addition, all absorber layers adopt the same thickness and the same is for all sensitive layers.

The Higgs mass resolution in the $\nu\bar{\nu}H$ ($\rightarrow \gamma\gamma$) process was used as a figure of merit in optimizing the total thickness of absorber. The total thickness of absorber was scanned by coherently varying the thickness of each absorber layer at a very fine step for the Higgs mass resolution performance. The number of sampling layers was fixed to 30 in the scanning and the thickness of silicon sensors was fixed to 0.5 mm. The result from the scanning is shown in Figure 5.3. The best Higgs mass resolution is achieved when the total thickness of tungsten absorber is 84 mm. The number of sampling layers was then varied with the total thickness of absorber fixed to 84 mm, and the energy resolution for single photons was examined as a function of photon energy for different numbers of sampling layers as shown in Figure 5.4(a). The energy resolution degrades by 11% and 26% when the number of sampling layers is reduced from 30 to 25 and 20, respectively. However, such degradation in energy resolution can be compensated by increasing the thickness of silicon sensors. As shown in Figure 5.4(b), the ECAL energy resolution for 20 (25) layers with 1.5 mm (1 mm) thick silicon sensors is about the same as that for 30 layers with 0.5 mm thick silicon sensors. Considering potential challenges in use of very thick silicon sensors, 0.5 mm was chosen as the thickness of silicon sensors. As indicated in Figure 5.4(a), to preserve a good energy resolution , a reasonably large number of sampling layers is required for the ECAL with relatively thin silicon sensors. And it is about 30 for 0.5 mm thick silicon sensors.

In the ECAL baseline design, silicon sensors are in square shape, and the transverse size of silicon sensors is a very critical parameter given its significant impact on the shower separation power as well as the number of readout channels of the ECAL. The latter has strong implications on both the cost and power consumption of the ECAL. It is highly desirable to have a large sensor size to reduce the number of readout channels as long as physics performance of the ECAL is not significantly compromised in the context of the CEPC. The sensor size is not expected to have significant effect on photon energy resolution, and its relevance to the performance of the ECAL is primarily on the shower separation power of the ECAL, which could be severely compromised due to a large sen-

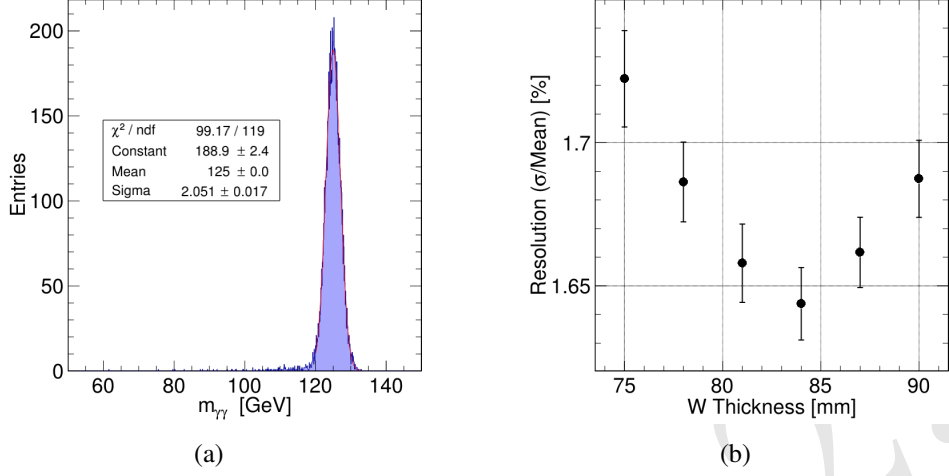


Figure 5.3: A typical distribution of Higgs boson mass reconstructed with the ECAL alone for $\nu\nu H(\rightarrow \gamma\gamma)$ events (a) and the resolution of the reconstructed Higgs boson mass for different total tungsten absorber thickness of the ECAL (b). The mass resolution is extracted from a Gaussian fit to the mass distribution. The best Higgs mass resolution is achieved when the total thickness of tungsten absorber of the ECAL is 84 mm.

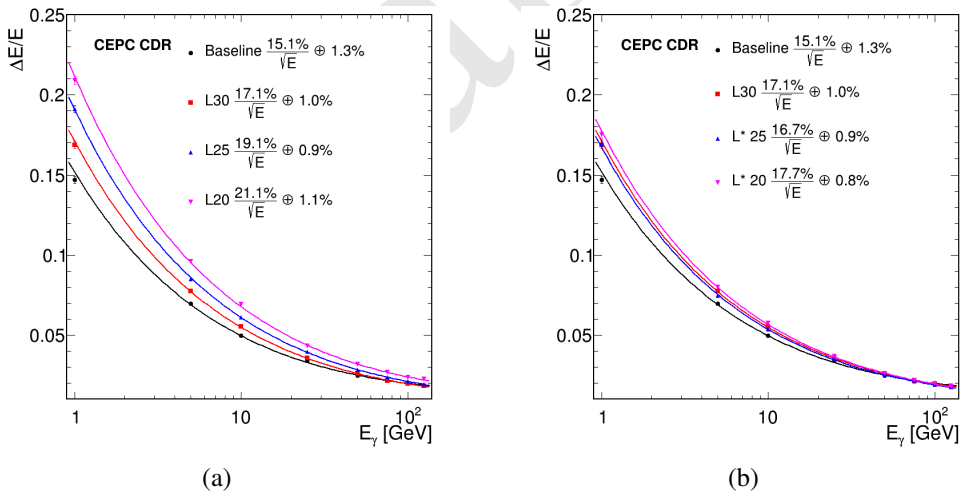


Figure 5.4: Photon energy resolution of the silicon-tungsten ECAL as a function of photon energy for different numbers of sampling layers of the ECAL(a) and together with different thicknesses of silicon sensors (b), where the thickness of silicon sensors for 30 layers is 0.5 mm, while they are 1.5 mm and 1.0 mm for 20 and 25 layers, respectively. The baseline geometry uses inhomogeneous absorber thickness, 2.1 mm tungsten for first 20 layers and 4.2 mm for last 10 layers, which is same with the CEPCv4). This design can improve the energy resolution of low energy photons. Photons are incident randomly for 4π sterad. The photon energy resolution degrades by 12% and 23% when the number of sampling layers is reduced from 30 to 25 and 20, respectively. The resolution degradation can be compensated by increasing the thickness of silicon sensors.

1 sor size. So the sensor size was optimized in two performance aspects: Higgs boson mass
 2 resolution in Higgs hadronic decays and capability of identifying photons from close-by
 3 showers.

4 The Higgs boson mass resolution in the $\nu\nu H$, $H \rightarrow gg$ process was examined for the
 5 first aspect. Showers induced by the photons in the gluon jets need to be well separated
 6 from the rest of the jets in the ECAL for precise mass measurement of the two-jet system
 7 of $H \rightarrow gg$. The sensor size of the ECAL determines the shower separation power of the
 8 ECAL, and hence expects to have an impact on the Higgs boson mass resolution in this
 9 process. Table 5.1 gives the Higgs mass resolution in the process for different sensor sizes.
 10 There is no significant effect on the Higgs mass resolution in the $H \rightarrow gg$ decay mode
 11 when the sensor size changes from 5 mm to 10 mm, and there is only 5% degradation in
 12 the resolution when even increasing to 20 mm.

Silicon sensor size (mm)	Higgs boson mass resolution (with statistic error)
5	$3.74 \pm 0.02 \%$
10	$3.75 \pm 0.02 \%$
20	$3.93 \pm 0.02 \%$

Table 5.1: Higgs mass resolution for the $\nu\nu H$, $H \rightarrow gg$ events for different ECAL sensor sizes. No significant impact of the sensor size on the Higgs mass resolution is found in the $\nu\nu H$, $H \rightarrow gg$ process.

13 The impact of sensor size on identification of close-by photons was evaluated using
 14 events simulated for two parallel photons with different distance between the two photons.
 15 Figure 5.5 shows the reconstruction efficiency of the di-photon events as a function of the
 16 distance between the two photons for different sensor sizes. The di-photon events can
 17 be successfully reconstructed once the sensor size is smaller than half of the distance
 18 between the two photons. This demonstrates the strong correlation between sensor size
 19 and photon shower separation power. And a small ECAL sensor size has to be adopted
 20 if separating close-by photon showers is required. This is most relevant for τ physics
 21 studies using $Z \rightarrow \tau\tau$ events, where there are photons that are very close to each other or
 22 other particles in the τ decays. Table 5.2 presents the percentage of photons in τ decays
 23 that can't be well reconstructed due to overlapping with other showers in the ECAL for
 24 different sensor sizes. The percentage remains very low when the sensor size is within
 25 10 mm, but jumps to 20% once going beyond that.

26 Having taken into account the both aspects of Higgs mass resolution and identification
 27 of close-by photons, the ECAL sensor size between 5 mm and 10 mm looks promising.

28 It should be noted that the above set of optimization studies were performed for the
 29 Silicon-Tungsten ECAL option. The same set of studies were performed for the Scintillator-
 30 Tungsten ECAL option as well, and quite consistent results were obtained except the
 31 thickness of its sensors (scintillator strips) is much larger than the silicon sensors.

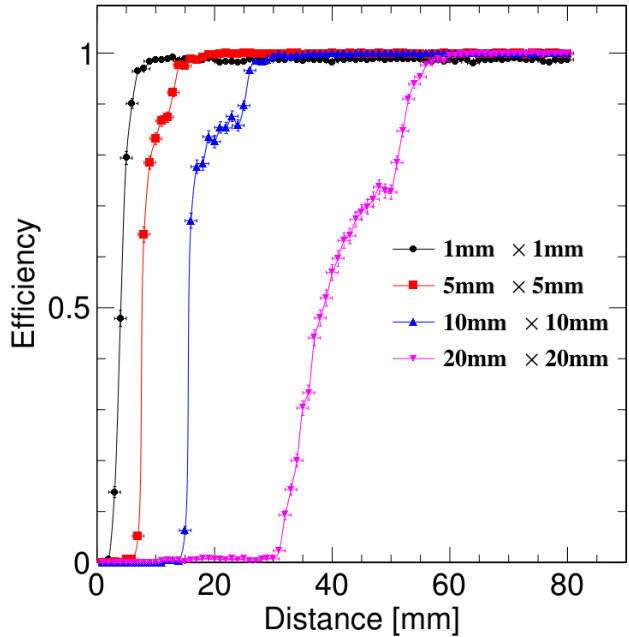


Figure 5.5: Reconstruction efficiency of events with two parallel 5 GeV photons as a function of the distance between the two photons for different ECAL sensor sizes. The reconstruction of the di-photon events is fully efficient once the sensor size is smaller than half of the distance between the two photons.

Cell size (mm)	Percentage of inseparable photons
1	0.07%
5	0.30%
10	1.70%
20	19.6%

Table 5.2: Percentage of photons in τ decays that can't be separated from neighboring particles in the ECAL for $Z \rightarrow \tau\tau$ events for different ECAL sensor sizes. Almost all photons in the τ decays can be well reconstructed for a ECAL sensor size up to 10 mm. A significant portion of the photons fail to be separated from other particles in the ECAL when the sensor size exceeds 10 mm.

5.3.2 Silicon-Tungsten Sandwich Electromagnetic Calorimeter

5.3.2.1 Silicon sensors

Among several sensor techniques, silicon PIN diodes with high resistivity offer several unique intrinsic advantages as follows.

- Stability: under a reasonable bias voltage, a completely depleted silicon PIN diode has unity gain, and a signal response to a Minimum Ionizing Particle (MIP) mostly defined by the sensor thickness, with a relatively low dependence on the operating environment including temperature, humidity, etc.
- Uniformity: the control of the sensor thickness within large production batches (typically to less than a percent) ensures uniform responses within a wafer and between different wafers. The non-sensitive area between wafers has recently been reduced by the use of laser cutting, thinned guard-ring design [3], and would benefit from the use of larger ingot size (8" becoming the standard).
- Flexibility: the dimension and geometry of the cells can be flexibly defined. The readout pads on the PCB need to be compatible.
- High signal-to-noise (S/N) ratio: for a MIP, the most probable number of electron-hole pairs generated in 1 μm thick silicon is around 76 (while the average number is 108), which yields an excellent S/N ratio of silicon sensors. Thus, MIP tracks can be easily tracked in the calorimeter, which is critical to the good performance of the ECAL.

One concern with the silicon sensors is the price, which could be very high.

By integrating the silicon sensors with tungsten plates and carbon fiber structures, the SiW-ECAL offers an excellent option for the PFA optimized calorimetry.

5.3.2.2 Geometry and mechanical design

A key requirement for the calorimeter system is to ensure the best possible hermeticity. Three regions need to be considered, including the boundaries of mechanical modules, the overlap region between the barrel and endcap sections, and very forward regions near forward detectors. A design with large ECAL modules is preferred to minimize crack regions in the barrel section, and the inter-module boundaries should not point back to the interaction point (IP). As shown in Figure 5.6, an octagonal shape is adopted to approximate the cylindrical symmetry and the modules are designed in such a way that the cracks are at a large angle with respect to the radial direction. One eighth of the barrel ECAL is called a stave. Each stave is fastened to the HCAL front face with a precise system of rails. Some space is left between the ECAL and HCAL to accommodate services including cooling, power and signal cabling. Along the beam direction, a stave is divided into five modules. The two ECAL endcap sections are fastened to the front face of HCAL endcap sections using a similar rail system.

Longitudinal arrangement The ECAL is composed of 30 layers in the longitudinal direction. To improve performance on low energy photons (< 5 GeV), the 30 layers are split into 2 sections with different thickness of absorber layers. The first section contains 20 layers of $0.6X_0$ (or 2.1 mm) thick tungsten plates corresponding to 12 radiation lengths. It is followed by the second section with 10 layers of $1.2X_0$ thick (4.2 mm) tungsten plates

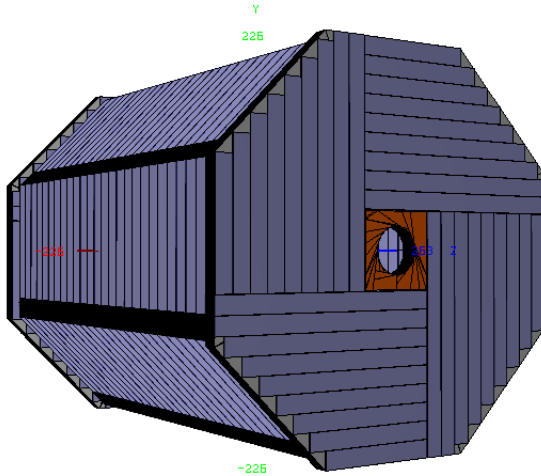


Figure 5.6: Schematic of the CEPC ECAL layout in its baseline design. The ECAL is organized into one cylindrical barrel and two disk-like endcap sections, with 30 layers in each section. The barrel section is arranged into 8 staves, each consisting of 5 trapezoidal modules. Each of the two endcap sections is made of four quadrants, each consisting of 2 modules. The ECAL barrel overall radius is 2028 mm in X-Y plane, the two endcaps are located at ± 2635 mm.

1 corresponding to another 12 radiation lengths. The ECAL starts with an sensitive layer.
 2 Each sensitive layer is equipped with 0.5 mm thick silicon sensors. The granularity of
 3 sensitive layers is determined by the silicon sensor size which is 10×10 mm² for all
 4 layers. The two longitudinal sections are both held on a 20 mm thick base plate made of
 5 carbon-fiber.

6 **Structures** The ECAL barrel section consists of 8 staves, each composed of 5 trapezoidal modules as shown in Figure 5.7. A barrel module contains 5 columns. The numbers of modules and columns are positioned along the beam line and chosen to be odd in number and symmetrically placed in order to avoid any pointing-like dead regions at the azimuthal plane perpendicular to the beam direction at the IP. The column size is 186 mm by mechanical limits and by cost optimization considerations, in order to contain exactly two 6-inch wafers or one and a half 8-inch wafers. Integrating the column size, walls of modules and contingencies, the barrel length adds up to 4700 mm in the beam direction. A gap of typically 100 mm is left between the barrel sides and endcap front faces. The precise dimension will depend on the amount of services for the ECAL, the HCAL and the tracker system (including power and DAQ cabling, cooling pipes, patch panels, etc.).

7 The two endcap sections are made up of 4 quadrants, each of which is then made up of
 8 2 modules with one of the modules containing 4 columns and other other 3 columns. The
 9 endcap inner radius is fixed by the ECAL ring at 400 mm. With 7 columns, the endcap
 10 outer radius is 2088 mm. An overshoot of 32 mm is kept between the outer radii of the
 11 barrel and of the endcaps, in order to contain the EM shower impinging the overlap region.
 12 This fixes the inner radius of the barrel section to 1843 mm. For the above structures,
 13 summing up all barrel and endcap sections, 256 ECAL columns are needed.

14 **Active Sensor Unit** Each ECAL column is made up of several ECAL slabs. Each
 15 slab consists of two symmetric sensitive layers and one tungsten plate. Each sensitive
 16 layer contains a layer of silicon sensors glued on a PCB, equipped with readout ASICs,

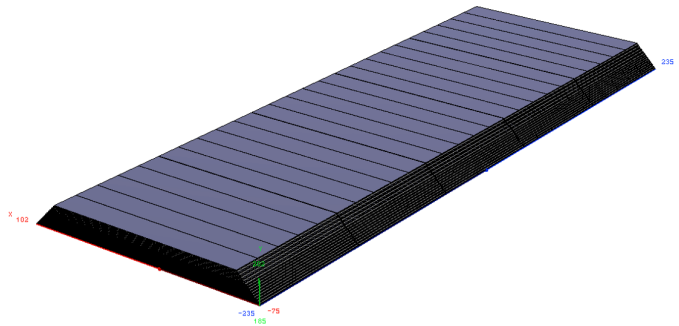


Figure 5.7: Schematic of the structure of one ECAL stave. Each stave is made up of 5 trapezoidal modules, and each module contains up to 5 columns.

1 a high voltage distribution by a Kapton foil and copper layers for passive cooling. The
 2 components are attached on both sides of an H-shaped carbon fiber cradle, with a tungsten
 3 core, and shielded by an aluminum cover. To insure scalability and industrial production,
 4 the design has been made as modular as possible: each basic unit is an ASU (Active Sensor
 5 Unit), which currently has a $18 \times 18 \text{ mm}^2$ PCB glued with 4 pieces of $90 \times 90 \text{ mm}^2$
 6 silicon wafers. Each ASU will handle 256 silicon pads with 4 ASIC chips, for the cell
 7 size of $10 \times 10 \text{ mm}^2$. The ASUs are chained together for the clock and configuration
 8 distributions and data collection.

9 5.3.2.3 SiW-ECAL electronics

10 One of the most critical elements of the CEPC calorimeters is the readout electronics
 11 which is defined by the dynamic range, the effective digitization, mode of trigger, the rate
 12 of working and power consumption per channel.

13 **Dynamic range:** A MIP going through a $500 \mu\text{m}$ silicon diode will produce around
 14 60000 electron-pairs holes (or a charge of 9.6 fC) as the most probable value (MPV).
 15 To record MIPs with an efficiency higher than 95%, this determines the lower limit of
 16 the dynamic range to a 1/3 of the MPV. The higher limit is given by the number of MIP
 17 equivalents at the core of the high-energy EM showers, which can reach up to 10000 MIPs
 18 (or 96 pC) within a $11 \times 11 \text{ mm}^2$ cell.

19 **Timing:** Time measurements of energy depositions in the calorimeters can be useful
 20 to Particle Flow algorithms to help disambiguate particle contributions. For the CEPC as
 21 a lepton collider, normally with a single primary vertex, precision timing of individual
 22 cells - or group of cells - could still be useful to reduce the confusion in the calorimeters
 23 and improve the energy resolution, which however needs further studies to quantitatively
 24 explore this potential. A SiW-ECAL ASIC with the most recent version (SKIROC2A) has
 25 been tested on a test board and reached a measure of timing resolution close to 1.1 ns for
 26 a signal amplitude corresponding to 5 MIPs [4].

27 **Power consumption:** The running conditions of a circular collider exclude pulsed op-
 28 eration as is planned for the linear colliders. As a point of reference, the current power
 29 consumption for the SKIROC2 chip is around 5 mW per channel in the continuous oper-
 30 ating mode.

31 **Occupancy:** The occupancy of the calorimeters is expected to be very low. This offers
 32 room for an ultra-low power electronics design when there is no signal.

5.3.2.4 SiW-ECAL power consumption and cooling

To the first order, the amount of the power dissipation scales up with the number of electronics channels. One critical issue for the calorimeters is the cooling scheme. As for now there are two options. The CEPC ECAL is at the boundary of both options, with a limit for the purely passive option of the order of $20 \times 20 \text{ mm}^2$ cells for a increase of temperature limited to $\Delta T \sim 10^\circ\text{C}$ at the far end of the slab.

Passive cooling: this option requires a reduced number of channels in order to use only passive cooling at the rear of the detector. As an example, a $400 \mu\text{m}$ thick copper sheet will drain the heat to the end of an ECAL slab, where it is then removed by an active cooling system installed near boundaries between barrel and endcap parts. A leakless water cooling system can be such an option to extract the heat at the end of each slab from the copper. Details of implementation can be found in [5]. Full simulation studies based on PFA should be performed to provide the quantitative impact from a reduced granularity and the corresponding calorimeter performance.

Active cooling: this option is the baseline high granularity design and requires the cooling system to provide cooling near the sensors and front-end electronics throughout the entire calorimeter system. A two-phase, low mass CO_2 cooling system is a promising option, which can be embedded in the absorber plates. There are already some simulation studies on a similar system adapted to the SiW-ECAL [6], where 3 mm thick copper plates, equipped with 1.6 mm inner diameter pipes for CO_2 circulation, with the ASICs glued on both sides of the slab. The study assumed a fully transversely isolated system, with ASICs as the primary heat source at equilibrium dissipating 0.64 W (10 mW per channel times 64 channels), and a fixed working point of 20°C for CO_2 (i.e. assuming perfect heat absorption). A doubled-sided module of $252 \times 252 \text{ mm}^2$ holding 32 chips cooled by 2×2 pipes was simulated. Preliminary simulations in "ideal conditions" show a difference of $\Delta T \sim 2^\circ\text{C}$ mostly centered on the ASICs (and only 0.3°C in the heat exchanger).

5.3.2.5 SiW-ECAL R&D status

The performances of a SiW-ECAL have been explored using the "physical prototype" developed within the CALICE collaboration, with extensive beam tests during the years 2005- 2011 [7–9]. Some ASUs have been operated in beam test campaigns: first at CERN in 2015, where 3 ASUs were mounted on test boards which behaved as expected [10]; a signal to noise ratio (SNR) (defined as the Most Probable Value of a Landau fit on data, divided by the Gaussian width of the noise) reached typical values of 15-18, with a very limited number of masked channels.

In a recent a beam test at DESY with 1-5 GeV electrons, "short slabs" (featuring all the elements as required but limited to a single ASU on a single side) could reach a SNR of around 20 on average [11].

The collected data is still under analysis, but they are expected to be similar to the SiW-ECAL physical prototype. The construction of a "long slab" is being actively pursued, and should be completed toward the end of year 2019; the R&D involves all the power, cooling and front-end electronics issues. The results and design will have to be optimized for a circular collider, where the power-pulsing operation is not allowed.

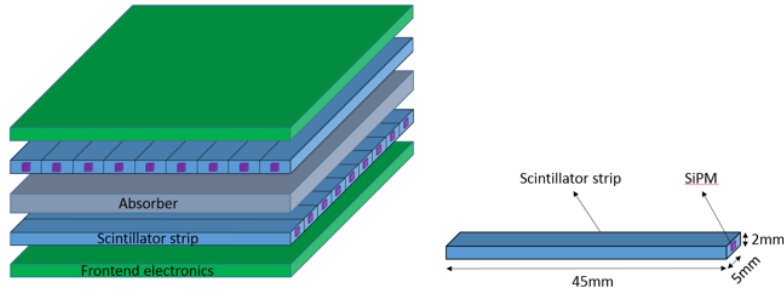


Figure 5.8: Layout of a scintillator-tungsten ECAL module and dimensions of a scintillator strip. The scintillator strips in adjacent layers are perpendicular to each other to achieve a small effective transverse readout cell size.

5.3.3 Scintillator-Tungsten Sandwich Electromagnetic Calorimeter

5.3.3.1 Introduction

Alternatively, a sampling calorimeter with scintillator-tungsten structure is proposed. It can be built in a compact and cost effective way. The layout and structure of the scintillator-tungsten ECAL is very similar to that of the silicon-tungsten ECAL. Major design parameters for the scintillator-tungsten ECAL were also studied and optimized, with an outcome quite similar to that of the silicon-tungsten ECAL. The primary difference is in the thickness of the active layers, and another difference being in the sensor shape of the active layers. The active layers of the scintillator-tungsten ECAL consists of 2 mm thick and $5 \times 45 \text{ mm}^2$ large scintillator strips. The scintillator strips in adjacent layers are perpendicular to each other to achieve a small effective transverse readout cell size. Each strip is covered by a reflector film to increase light collection efficiency and improve the uniformity of scintillation light yield w.r.t. incident position by a particle on the strip. Photons from each scintillator strip are read out by a very compact photo-sensor, SiPM, attached to the strip. The SiPM and highly integrated readout electronics make the dead area in the scintillator-tungsten ECAL almost negligible. Figure 5.8 shows the schematic structure of a scintillator-tungsten ECAL module in the above configuration. Although a SiPM is coupled to a scintillator strip by side in this schematic, it should be pointed out that various schemes for coupling the SiPM to the scintillator strip are considered for optimum performance.

Plastic scintillator is a robust material which has been used in many high energy physics experiments. Production of scintillator strips can be made at low cost by the extrusion method. And prices for SiPMs on the market have also been falling constantly with the rapid development of the SiPM technology. Moreover, the number of readout channels can also be significantly reduced due to the strip readout configuration. So the total construction cost of the scintillator-tungsten ECAL is expected to be lower than that of the silicon-tungsten ECAL. Some key aspects of the scintillator-based ECAL technology were studied and optimized.

5.3.3.2 SiPM dynamic range

Because each pixel on a SiPM can only detect one photon at a time and a few nanoseconds are needed before it is recovered, a SiPM is not a linear photon detection device, particularly when illuminated with high intensity light. Therefore, the dynamic range

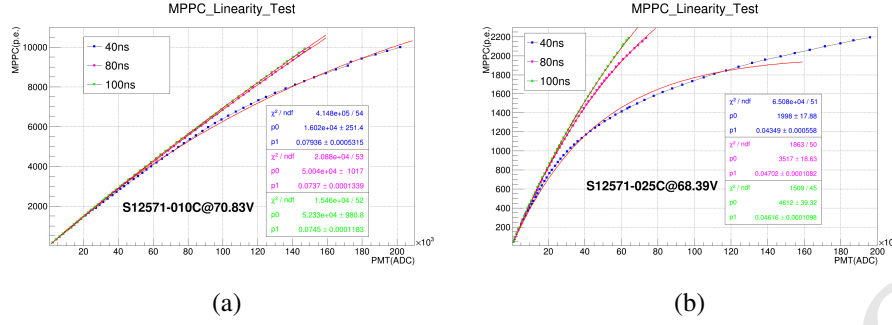


Figure 5.9: Response linearity (the number of photo-electrons detected with a SiPM as a function of the number of incident photons) of SiPMs with different numbers of pixels [(a): 10000-pixel SiPM, (b): 1600-pixel SiPM] for light pulses with different widths (blue: 40ns, red: 80ns and green: 100ns). The linearity of SiPM response with 10000 pixels is better than that with 1600 pixels. And the range for linear response of SiPM gets larger for a wider light pulse.

- 1 and linearity of SiPM needs to be addressed for its application in the scintillator-tungsten ECAL.
- 2 For a very short light pulse , the response of a SiPM can be formulated as

$$N_{\text{fired}} = N_{\text{pixel}}(1 - e^{-N_{\text{pe}}/N_{\text{pixel}}}) \quad (5.1)$$

- 4 Where N_{fired} is the number of fired pixels of a SiPM and N_{pixel} is the number of total
5 pixels. However, light pulses produced in plastic scintillator last long enough for some
6 pixels of a SiPM to detect more than one photon in one event of light generation. The
7 response function of a SiPM is then modified in this case as

$$N_{\text{fired}} = N_{\text{eff}}(1 - e^{-N_{\text{pe}}/N_{\text{eff}}}) \quad (5.2)$$

- 8 Where N_{eff} stands for the effective number of pixels on a SiPM, which is a function
9 of the width of incident light pulse. The response curve of a 10000-pixel (10 μm pitch
10 size) and a 1600-pixel (25 μm pitch size) SiPMs with an active area of $1 \times 1 \text{ mm}^2$ were
11 measured for light pulses with different widths, as shown in Figure 5.9. The dynamic
12 range of the 10000-pixel SiPM is much larger than that of the 1600-pixel one, as expected,
13 and can reach 4000 photon-electrons with very good linearity for short light pulses and
14 much beyond if saturation correction is made. Also the linearity of response of SiPMs is
15 improved with increasing of the width of incident light pulses. So care has to be taken if
16 operation of SiPMs reaches saturated regions and correction is required. Rough estimation
17 suggests a SiPM dynamic range of at least up to 10000 photon-electrons is needed for a
18 scintillator-tungsten ECAL at the CEPC experiment for $H \rightarrow \gamma\gamma$ measurement. So large-
19 area SiPMs with a large number of pixels are favored for use in the CEPC scintillator-
20 tungsten ECAL because of high dynamic ranges. This is also becoming increasingly
21 practical as the SiPM price per cm^2 has been dropping significantly.

22 5.3.3.3 Performance of scintillator sensitive unit

- 23 A scintillator sensitive unit is a scintillator strip coupled with a SiPM. When a SiPM is
24 coupled to a scintillator at one position, the light output is expected to depend on the
25 scintillation light propagation distance along the strip to the SiPM coupling point. This
26 dependence would introduce non-uniformity of light output, hence affecting the ECAL

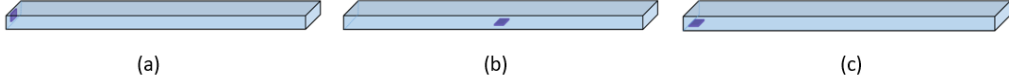


Figure 5.10: Three configurations of the SiPM-scintillator coupling explored for the design of scintillator-tungsten ECAL: (a) a SiPM is embedded in a scintillator strip on one side (side), (b) a SiPM is embedded in a scintillator strip at the center of the bottom face (bottom-center), (c) a SiPM is embedded in a scintillator strip at one end of the bottom face (bottom-end).

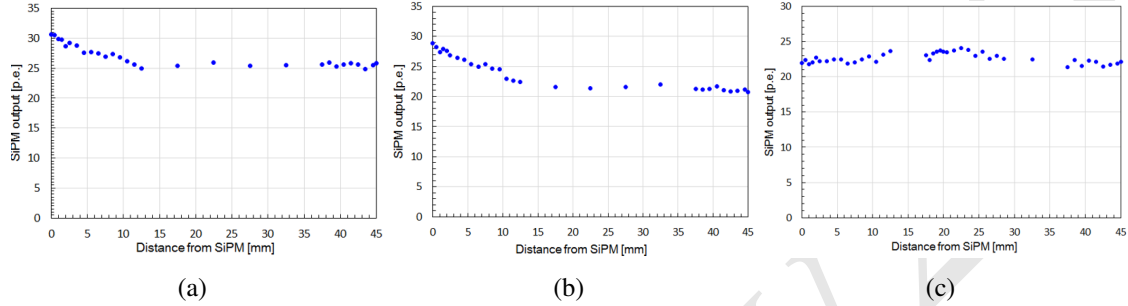


Figure 5.11: Light output of a scintillator sensitive unit with three SiPM coupling configurations: side (a), bottom-end (b), bottom-center (c). The bottom-center configuration gives the best uniformity of 10% without reduction of light output.

1 performance. Three configurations of a SiPM coupling to a scintillator strip were ex-
2 plored as shown in Figure 5.10, to minimize the non-uniformity of light output. And
3 the uniformity of light output was measured with a Sr90 source for the three SiPM cou-
4 pling configurations, respectively, where the pitch size of the SiPM is 10 μm . Figure 5.11
5 shows the measured uniformities. The side and bottom-end configurations give a similar
6 uniformity of 30%, while the bottom-center configuration presents a very good unifor-
7 mity of 10% without reduction of light output. Furthermore, such a configuration has
8 additional advantages of completely eliminating dead areas between scintillator strips due
9 to mounting of SiPMs and allowing to use SiPMs with very large areas which is essential
10 for meeting the requirement on dynamic range of SiPMs. For these attractive features, the
11 bottom-center SiPM coupling configuration is adopted for the scintillator-tungsten ECAL.

12 Light output of scintillator sensitive unit was also studied with the scintillator strip
13 wrapped with different reflectors as shown in Figure 5.12. ESR reflector gives much
14 higher light out than Tyvek reflector.

15 Light output of scintillator sensitive unit would depend on the pitch size of the SiPM
16 due to different photon detection efficiency. Figure 5.13 shows the light output of scintil-
17 lator sensitive units with SiPMs that have the same sensitive area ($1 \times 1 \text{ mm}^2$) but with
18 different pitch sizes (25 μm vs. 10 μm). The light output with the 10 μm SiPM is only
19 about 1/3 of that with the 25 μm SiPM due to its much lower photodetection efficiency.
20 So light output should be taken into account when choosing small-pitch SiPMs for a high
21 dynamic range. It has to be ensured the scintillator sensitive unit is sensitive to M.I.Ps.
22 Figure 5.14 shows the pulse height distribution for cosmic-ray signals of the scintilla-
23 tor sensitive unit with a 10 μm SiPM using the readout electronics described in 5.3.3.4.
24 Cosmic-ray signals are seen well separated from noise demonstrating the sensitivity to
25 M.I.Ps.

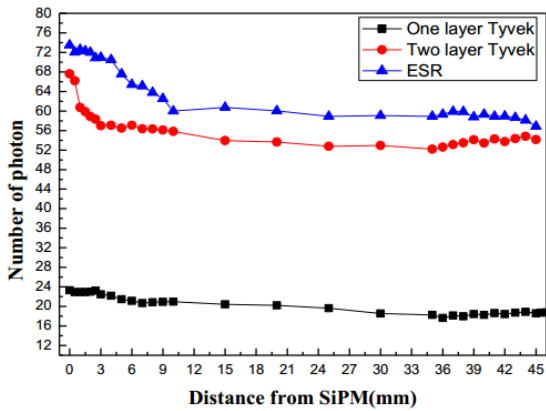


Figure 5.12: Light yields of scintillator strips with different reflectors versus the distance of an incident particle from SiPM . The scintillator with ESR gives the highest light yield.

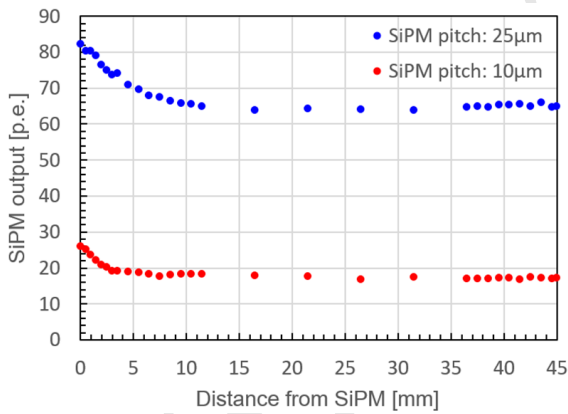


Figure 5.13: Light yields of scintillator strips coupled with SiPMs with different pitch sizes (red: 10 μm , blue: 25 μm). The SiPM with the larger pitch size of 25 μm has a significant higher light yield (about 65 p.e.) than that with the smaller pitch size of 10 μm (about 18 p.e.) due to a higher photon detection efficiency.

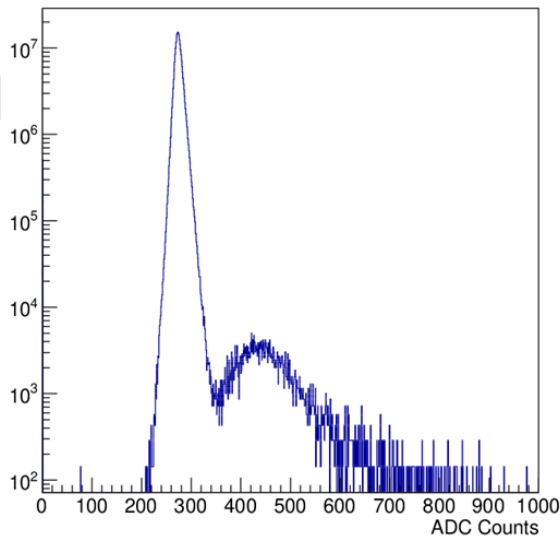


Figure 5.14: The pulse height distribution for cosmic-ray signals of the scintillator sensitive unit with a 10 μm SiPM. Cosmic-ray signals can be found well separated from noise demonstrating the sensitivity of the scintillator sensitive unit to M.I.Ps.

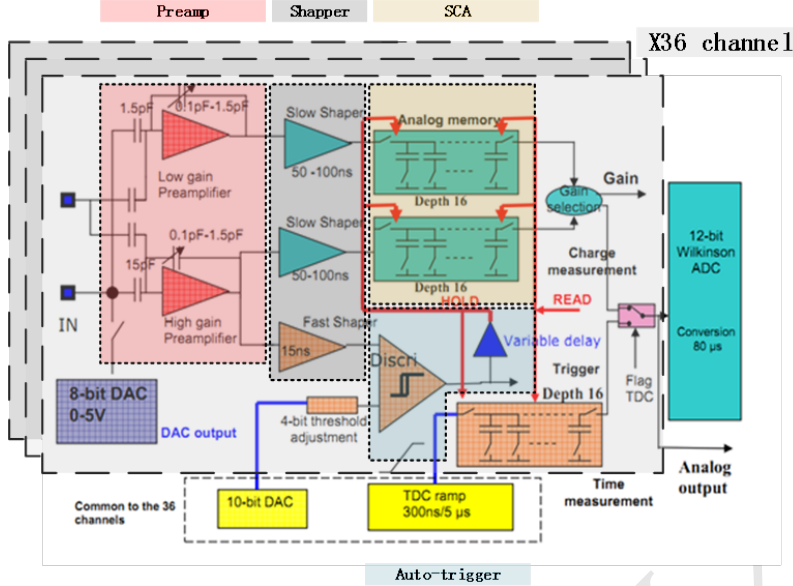


Figure 5.15: Schematic of the SPIROC2b ASIC chip. It consists of a readout chain with an amplifier-shaper using a RCnCRp filter, then the discriminator sends trigger to a Switched-Capacitor-Array (SCA). A 12-bit Wilkinson ADC is used for digitizing the analog voltage in the SCA.

5.3.3.4 SiPM readout electronics

The readout electronics of the ECAL has to provide high dynamic range for energy measurements. A 100 GeV photon shower may leave an energy deposit of 1~800 MIP-equivalent in a single cell. A high spatial granularity of the ECAL readout, typically 10 mm, is required for the Particle Flow Algorithm (PFA). This, in turn, results in a large total channel count and a high density of channels. For this reason, multi-channel readout chips are considered.

The full readout chain of the electronics consists of two parts: Front-End and Back-End. The Front-End electronics (FE) is embedded into the layers of ECAL. It performs amplification, auto-triggering, digitization and zero-suppression, with local storage of data between the working phases. The Back-End electronics (BE) collects data and configures the readout chips before system running.

Several studies and existing calorimeter readout electronics have shown that one can obtain optimized energy resolutions using a preamplifier-shaper and digitizing the pulse at the peak amplitude. For instance, a preamp-shaper-SCA structure of analog circuit was applied on an ILC HCAL and implemented in an ASIC named SPIROC2b. A similar approach can be applied for the CEPC-ECAL. The analog part of the SPIROC2b is schematically depicted in Figure 5.15. This ASIC is presently under consideration for the CEPC-ECAL.

The basic principle consists of a readout chain with an amplifier-shaper using a RCnCRp filter delivering a pulse length of about 50-200ns duration for a SiPM pulse signal. This signal is also shaped by a fast shaper in parallel to generate fast and narrow pulse for pulse discrimination. Then, the discriminator sends the trigger to a Switched-Capacitor-Array (SCA) for locking the peak value of the slowly shaped signal. The locked voltage value corresponds to the charge that the circuit received. A 12bit Wilkinson ADC is used for digitizing the analog voltage in the SCA. Future detailed implementations of the

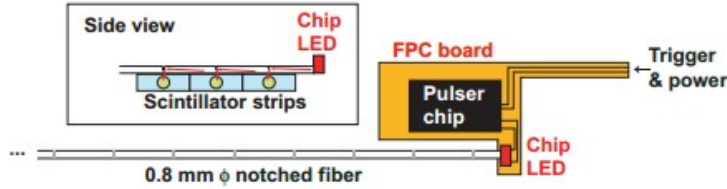


Figure 5.16: Schematic of the SiPM gain monitoring system with LED and notched fiber. Light pulses from the LED are scattered and distributed into each strip.

1 calorimeter front-end electronics for CEPC is still considered using the ROC series ASIC
2 but newer versions.

3 The maximum data rate to the Back-End electronics can be estimated as follows. As-
4 suming continuous operation, the SPIROC2b will be switched between three states called
5 Acquisition, AD Converting and Readout. Only in the Acquisition state can SPIROC2b
6 receive signal from the SiPM and store in received charge in the SCA at a rate of about
7 5 MHz. The two other states contribute to the “dead-time” status. There is depth of 16
8 in the SCA corresponding to 4 μ s for Acquisition, and an additional \sim 4 ms for ADC and
9 Readout. Therefore, the maximum data rate is 16 events per 4 ms which corresponds to
10 4 kHz. Each data package is 2 kBytes in size.

11 The number of chips readout in series in a single layer will multiply the duration of
12 Readout. Assuming that there are 4 chips in one layer, there is 16 ms for Readout. The
13 maximum events rate is reduced to 1 kHz and leads to about a transmission of 5 Mbyte/s.
14 This can easily be managed with 100 Mbps links.

15 The power consumption with 100% duty cycle in the front-end will be dominated by
16 the ASIC and more specifically by the analog part of the ASIC. One SPIROC2b consumes
17 250.8 mW of which about 150 mW is consumed by the analog part. In actual use, most
18 of the cycle is in ADC and Readout. This leads to about 150 mW power consumption per
19 chip and 4 mW per channel.

20 The electronic calibration and cosmic ray tests have been done. From these electronic
21 calibrations we have obtained that the noise of readout system is 46 fC in RMS. The least-
22 significant bit of the ADC in high gain and low gain is 151/pC and 10.3/pC, respectively,
23 while the maximum ADC range is 4096. A dynamic range of 100 fC - 300 pC of the
24 readout system is measured with this method. Cosmic ray results show that the system
25 can distinguish a MIPs signal from pedestal well with a measured charge of approximately
26 1 pC.

27 **5.3.3.5 Calibration System**

28 The Scintillator-Tungsten ECAL consists of about 8 million channels of scintillator strip
29 units. The stability of the light output has to be monitored. A light distribution system is
30 under study to monitor possible gain drifts of the SiPMs by monitoring photon-electron
31 peaks. The system consists of a pulse generator, a chip LED, and a notched fiber. A
32 schematic structure of the system is shown in Figure 5.16. The pulse generator circuit and
33 chip LED are arranged on a thin FPC board. The chip LED is directly connected to the
34 notched fiber to distribute light to about 80 strips through its notches.

5.4 Hadronic Calorimeter for Particle Flow Approach

5.4.1 Introduction

High-granularity hadronic calorimetry is an essential concept in PFA-based experiments such as those proposed for CEPC. The high spatial granularity provides a means to separate the deposits of charged and neutral hadrons and to precisely measure the energy of the neutrals. The contribution of the neutrals to the jet energy, around 10% on average, fluctuates in a wide range from event-to-event, and the accuracy of the measurement is the dominant contribution to the particle flow resolution for jet energies up to about 100 GeV. For higher energies, the performance is dominated by a term in the PFA resolution called the confusion term. This term originates from failures in both the topological pattern recognition and energy information that are important for correct track cluster assignment. A high-granularity hadronic calorimeter is thus needed to achieve excellent jet energy resolution.

The HCAL systems considered here are sampling calorimeters with steel as the absorber and scintillator tiles or gaseous devices with embedded electronics for the active part. The steel was chosen due to its rigidity which allows to build self-supporting structures without auxiliary supports (dead regions). Moreover, the moderate ratio of hadronic interaction length ($\lambda_I = 17$ cm) to electromagnetic radiation length ($X_0 = 1.8$ cm) of iron, allows a fine longitudinal sampling in terms of X_0 with a reasonable number of layers in λ_I , thus keeping the detector volume and readout channel count small. This fine sampling is beneficial both for the measurement of the sizable electromagnetic energy part in hadronic showers and for the topological resolution of shower substructure, needed for particle separation.

The active detector element has finely segmented readout pads, with 1×1 cm² or 3×3 cm² size, for the entire HCAL volume. Each readout pad is readout individually, so the readout channel density is approximately $4 \times 10^{4-5}/\text{m}^3$. For the entire HCAL, with ~ 100 m³ total volume, the total number of channels will be $4 \times 10^{6-7}$ which is one of the biggest challenges for the HCAL system. On the other hand, simulation suggests that, for a calorimeter with cell sizes as small as 1×1 cm², a simple hit counting is already a good energy measurement for hadrons. As a result, the readout of each channel can be greatly simplified and just record 'hit' or 'no hit' according to a single threshold (equivalent to a '1-bit' ADC). A hadron calorimeter with such kind of simplified readout is called a Digital Hadron Calorimeter (DHCAL). In a DHCAL, each readout channel is used to register a 'hit', instead of measure energy deposition, as in traditional HCAL systems. In this context, gas detectors (such as RPC, GEM) become excellent candidates for the active element of a DHCAL. Another technology option is the Analog Hadron Calorimeter (AHCAL) which is based on scintillator coupled with SiPMs as the active sensor.

A drawing of the HCAL structure is shown in Figure 5.17, the barrel part is made of 5 independent and self-supporting wheels along the beam axis. The segmentation of each wheel in 8 identical modules is directly linked with the segmentation of the ECAL barrel. A module is made of 40 stainless steel absorber plates with independent readout cassettes inserted between the plates. The absorber plates consist of a total of 20 mm stainless steel: 10 mm absorber from the welded structure and 10 mm from the mechanical support of the detector layer. Each wheel is independently supported by two rails on the inner wall of

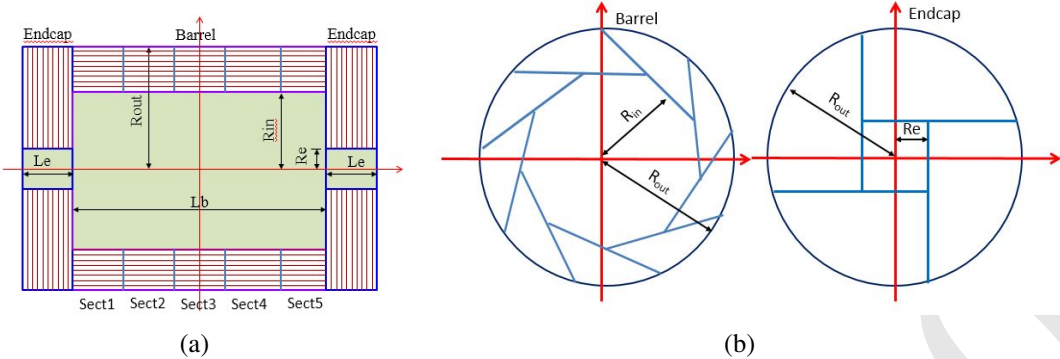


Figure 5.17: HCAL layout in $Y - Z$ plane in panel (a), HCAL Barrel layout in $X - Y$ plane and HCAL Endcap layout in $X - Y$ plane in panel (b). The inner radius in $X - Y$ plane is 2300 mm, the outer radius is 3340 mm. The inner and outer of HCAL endcaps in Z -axis are 2670 mm and 3710 mm, respectively.

- 1 the cryostat of the magnet coil. The cables as well the cooling pipes will be routed outside
- 2 the HCAL in the space left between the outer side of the barrel HCAL and the inner side
- 3 of the cryostat.

4 **5.4.2 Semi-Digital Hadronic Calorimeter (SDHCAL)**

5 **5.4.2.1 Introduction**

6 For the CEPC, a SDHCAL based on gaseous detector is proposed. This is motivated by the
7 excellent efficiency and very good homogeneity the gaseous detectors could provide. An-
8 other important advantage of gaseous detectors is the possibility to have very fine lateral
9 segmentation. Indeed, in contrast to scintillator tiles, the lateral segmentation of gaseous
10 devices is determined by the readout electronics and not by the detector itself. Active
11 layer thickness is also of importance for what concerns the CEPC hadronic calorimeter to
12 be placed inside the magnetic field. Highly efficient gaseous detectors can indeed be built
13 with a thickness of less than 3 mm. While other detectors could achieve such performance,
14 gaseous detectors have the advantage of being cost-effective and discharge free. They are
15 also known for their fast timing performance which could be used to perform 4D con-
16 struction of the hadronic showers. Such a construction can improve on hadronic shower
17 separation by better associating the energy deposits belonging to the same shower from
18 those of other showers. It can also improve on the energy reconstruction by identifying
19 the delayed neutrons and assigning them a different weight.

20 To obtain excellent resolution in the hadronic shower energy measurement a binary
readout of the gaseous detector is the simplest and most effective scenario. However, a
22 lateral segmentation of a few millimeters is needed to ensure good linearity and resolu-
tion of the reconstructed energy. Such a lateral segmentation leads to a huge number of
24 electronic channels resulting in a complicated readout system design and excessive power
consumption. A cell size of $1 \times 1 \text{ cm}^2$ are found to be a good compromise that still pro-
vides a very good resolution at moderate energies. However, simulation studies show that
27 saturation effects are expected to show up at higher energies ($> 40 \text{ GeV}$). This happens
28 when many particles cross one cell in the center of the hadronic shower. To reduce these
29 effects, multi-threshold electronics (Semi-Digital) readout is chosen to improve on the

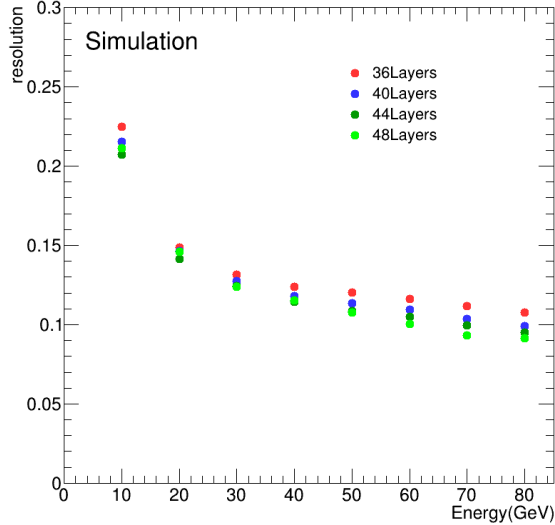


Figure 5.18: The energy resolution of SDHCAL with different number of layers versus simulated pion energy ranging from 10 GeV to 80 GeV. Energy resolution of SDHCAL with 48-layer, 44-layer, 40-layer, 36-layer are shown in light green, green, blue and red dots, respectively. It indicates that SDHCAL with 40-layer yields decent energy resolution, about 15% and 10% with pion energy of 20 GeV and 80 GeV, respectively.

1 energy resolution by exploiting the particle density in a more appropriate way. These ele-
2 ments were behind the development of a Semi-Digital Hadronic CALorimeter (SDHCAL)
3 that we propose to equip one of the CEPC future experiments.

4 Even with a $1 \times 1 \text{ cm}^2$ lateral granularity of the readout system, a large number of ele-
5 tronic channels is still needed. This has two important consequences. The first is the
6 power consumption and the resulting increase of temperature which affects the behavior
7 of the active layers. The other consequence is the number of service cables needed to
8 power and readout these channels. These two aspects can deteriorate the performance of
9 the HCAL and destroy the principle of PFA if they are not addressed properly.

10 The R&D pursued by the CALICE SDHCAL groups has succeeded to pass almost
11 all the technical hurdles of the PFA-based HCAL. The SDHCAL groups have succeeded
12 to build the first technological prototype [12] of these new-generation calorimeters with
13 48 active layers of GReP, 1m^2 each. The prototype validates the concept of the high-
14 granularity gaseous detector and permits to study the energy resolution of hadrons one
15 can obtain with such calorimeter. Figure 5.18 shows the energy resolution of SDHCAL
16 with different numbers of layers using simulated pion samples. It indicates that SDHCAL
17 with 40 layers yield decent performance with pion energies up to 80 GeV which is suitable
18 for a CEPC detector.

19 A baseline detector of SDHCAL has been designed with 40 layers in total. Each layer
20 contains 20 mm thick stainless steel, 3 mm thick GReP and 3 mm for readout electronics
21 with $1 \times 1 \text{ cm}^2$ readout pads on PCB board.

22 In order to investigate appropriate options for the active detector of the SDHCAL,
23 two parallel detector schemes, the Glass Resistive Plate Chamber (GReP) and the Thick
24 Gaseous Electron Multiplier (THGEM) are proposed for the active layers of the SDHCAL.

5.4.2.2 GRPC based SDHCAL

The GRPC scheme The structure of GRPC proposed as an active layer of the HCAL for CEPC is shown in Figure 5.19. It is made out of two glass plates of 0.7 mm and 1.1 mm thickness. The thinner plate is used to form the anode while the the thicker one forms the cathode. Ceramic balls of 1.2 mm diameter are used as spacers between the glass plates. The balls are glued on only one of the glass plates. In addition to those balls, 13 cylindrical fiber-glass buttons of 4 mm diameter are also used. Contrary to the ceramic balls the buttons are glued to both plates ensuring thus a robust structure. Special spacers (ceramic balls) were used to maintain uniform gas gap of 1.2 mm. Their number and distribution were optimized to reduce the noise and dead zones (0.1%).

The distance between the spacers (10 cm) was fixed so that the deviation of the gap distance between the two plates under the glass weight and the electric force does not exceed 45 microns. The choice of these spacers rather than fishing lines was intended to reduce the dead zones (0.1%). It was also aimed at reducing the noise contribution observed along the fishing lines in standard GRPC chambers. The gas volume is closed by a 1.2 mm thick and 3 mm wide glass-fiber frame glued on both glass plates. The glue used for both the frame and the spacers was chosen for its chemical passivity and long term performance. The resistive coating on the glass plates which is used to apply the high voltage and thus to create the electric field in the gas volume was found to play important role in the pad multiplicity associated to a MIP [13]. A product based on colloids containing graphite was developed. It is applied on the outer faces of the two electrodes using the silk screen print method, which ensures very uniform surface quality. The measured surface resistivity at various points over a 1m^2 glass coated with the previous paint showed a mean value of $1.2 \text{ M}\Omega/\text{cm}^2$ and a ratio of the maximum to minimum values of less than 2 ensuring a good homogeneity of the detector.

Another important aspect of this development concerns the gas circulation within the GRPC taking into account that for the CEPC SDHCAL, gas outlets should all be on one side. A realization of this system was developed. It is based on channeling the gas along one side of the chamber and releasing it into the main gas volume at regular intervals. A similar system is used to collect the gas on the opposite side. A finite element model has been established to check the gas distribution. The simulation confirms that the gas speed is reasonably uniform over most of the chamber area. The GRPC and its associated electronics are housed in a special cassette which protects the chamber and ensures that the readout board is in close contact with the anode glass. The cassette is a thin box consisting of 2.5 mm thick stainless steel plates separated by 6 mm wide stainless steel spacers. Its plates are also a part of the absorber.

The electronics board is assembled with a polycarbonate spacer which is also used to fill the gaps between the readout chips and to improve the overall rigidity of the detector. The electronics board is fixed on the small plate of the cassette with tiny screws. The assembled set is fixed on the other plate which hosts the detector and the spacers. The total thickness of the cassette is 11 mm with 6 mm of which due to the sensitive medium including the GRPC detector and the readout electronics.

GRPC technological prototype An SDHCAL prototype fulfilling the efficiency, robustness and the compactness requirements of the future PFA-based leptonic collider experiments [12] was built. A total of 48 cassettes as the one described above were built. They

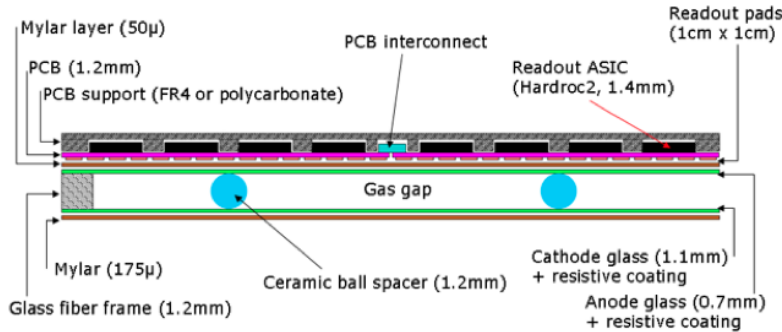


Figure 5.19: Cross-sectional view of an active layer with GRPC and readout layer. The GRPC gas gap is 1.2 mm, with two glass plates of 1.1 mm (cathode plate) and 0.7 mm (anode plate) thickness. The thickness of PCB is 1.2 mm and that of readout ASIC is 1.4 mm.

fulfilled a stringent quality control. It is worth mentioning that 10500 HR ASICs were produced and tested using a dedicated robot for this purpose. The yield was found to be higher than 92%. The ASICs were then fixed on the PCBs over a surface area of 1m^2 and then subsequently fixed on the cassette cover once successfully tested. The cassettes were inserted in a self-supporting mechanical structure that was conceived and built in collaboration with the Spanish group of CIEMAT. The structure is made of Stainless Steel plates of 1.5 cm each. The plates were machined to have an excellent flatness and well controlled thickness. The flatness of the plates was measured using a laser-based interferometer system. It was found that the flatness of the plates are less than 500 microns. In April 2012 the prototype was exposed to pion, muon, electron beams of both the PS and the SPS of CERN as shown in Figure 5.20. The data were collected continuously in a triggerless mode. Figure 5.21 shows the efficiency (a) and pad multiplicity (b) of the prototype GRPC chambers measured using the muon beam. Figure 5.22 shows a display of two events collected in the SDHCAL. One is produced by a pion interaction (a) and the other by an electron interaction (b).

The SDHCAL prototype results obtained with a minimum data treatment (no gain correction) show clearly that excellent linearity and good resolution [14] could be achieved on large energy scale as can be shown in Figure 5.23 where results obtained in two different beam lines are obtained using the same detector configurations. As is clearly demonstrated from this data, the high granularity of the SDHCAL allows one to study thoroughly the hadronic showers topology and to improve on the energy resolution by, among others, separating the electromagnetic and the hadronic contribution. The separation between close-by showers will also benefit from the high granularity on the one hand and the very clean detector response ($< 1 \text{ Hz/cm}^2$) on the other. The results obtained with the SDHCAL [15] confirm the excellent efficiency of such separation due to the SDHCAL performance.

The quality of data obtained during several campaigns of data taking at the CERN PS and SPS beam lines validates completely the SDHCAL concept. This is especially encouraging since no gain correction was applied to the electronics channels to equalize their response. Still, improvement was further achieved by applying gain and threshold correction schemes in terms of the calorimeter response homogeneity.

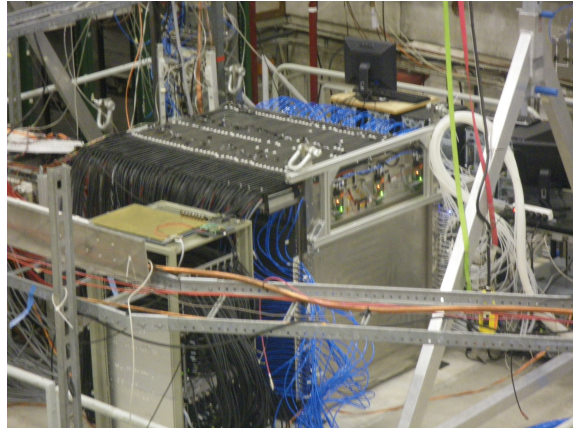


Figure 5.20: The SDHCAL prototype in beam test at CERN.

1 A digitizer describing the response of the G_RPC within the SDHCAL was developed
 2 [16]. It allows to study the SDHCAL behavior in a realistic manner in the future
 3 experiments.

4 In parallel to the prototype construction, a single cassette was tested in a magnetic field
 5 of 3 Tesla (H2 line at CERN) applying the power-pulsed mode. The test beam results [17]
 6 indicated clearly that the use of the power-pulsed mode in such a magnetic field is possible.
 7 The behavior of the detector in terms of efficiency, multiplicity, and other factors was
 8 found to be similar to those obtained in the absence of both the magnetic field and the
 9 power-pulsed mode.

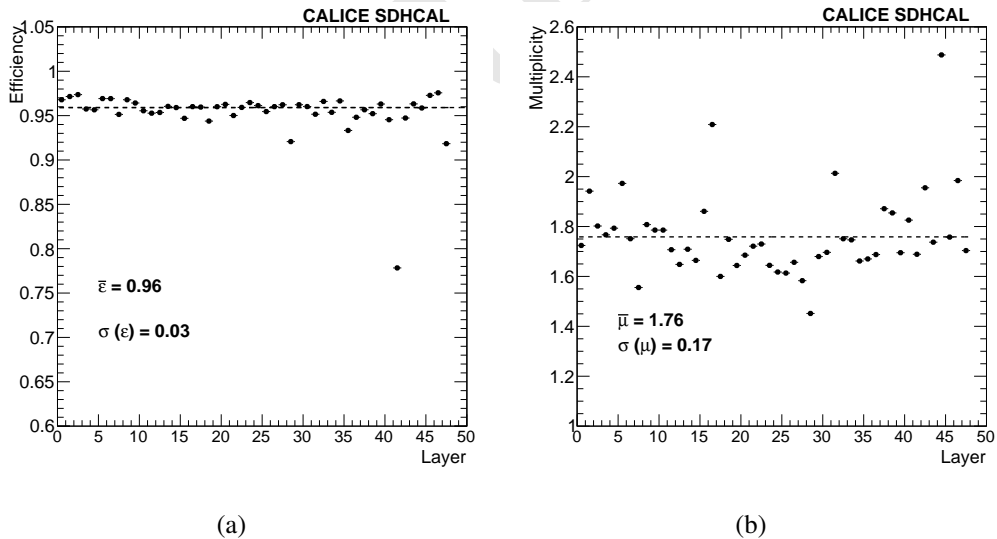


Figure 5.21: (a) Efficiency of the G_RPC detectors of the SDHCAL, the average efficiency is 0.96 ± 0.03 . (b) The pad multiplicity of the G_RPCs, it is 1.76 ± 0.17 . (Note: Figures taken from [14].)

10 **Current SDHCAL R&D** Large G_RPC of 1m^2 were developed and built for the technolog-
 11 ical prototype. However, larger G_RPC are needed in the SDHCAL proposed for future
 12 leptonic collider experiments. These large chambers with gas inlet and outlet on one side
 13 need a dedicated study to guarantee a uniform gas gap everywhere notwithstanding the

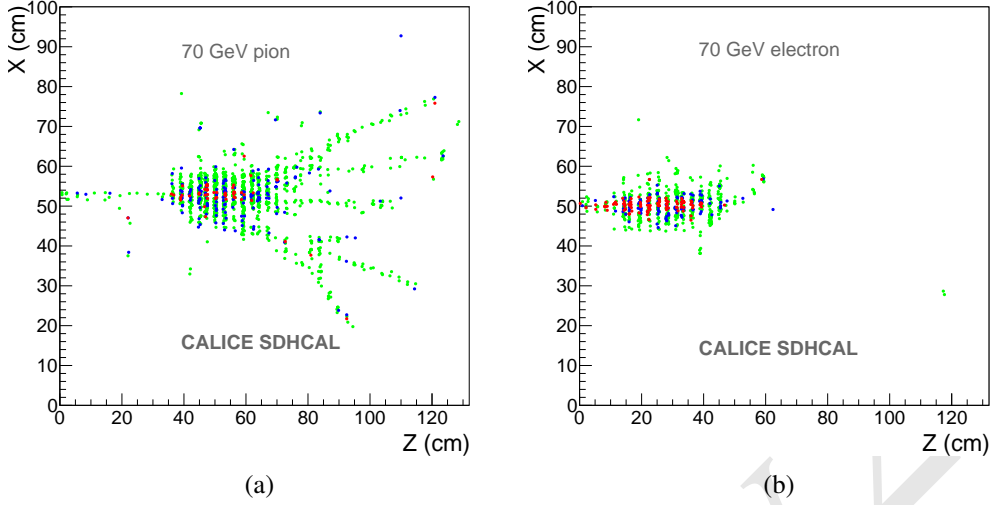


Figure 5.22: (a) Event display of an 70 GeV pion interaction in the SDHCAL prototype. (b) Event display of a 70 GeV electron interaction in the SDHCAL prototype. (Note: Figures taken from [14].)

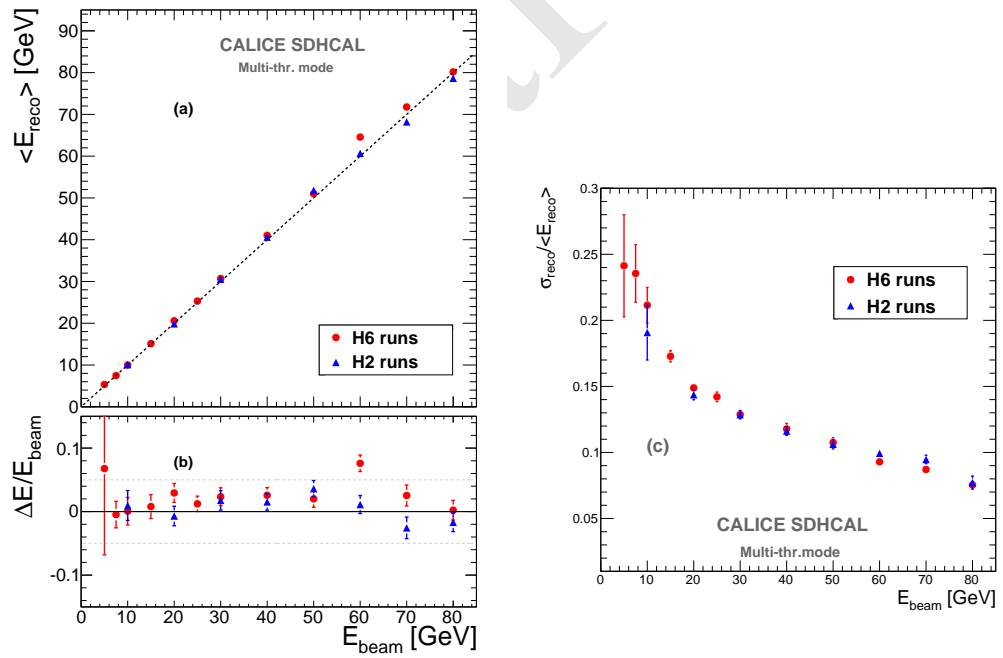


Figure 5.23: (a) Reconstructed energy of the hadronic showers collected in both H2 and H6 SPS beamlines. (b) The relative deviation of the reconstructed energy with respect to the beam energy. Right: Relative energy resolution of the reconstructed hadronic shower. The pion beam of H6 beamline is largely contaminated by protons at high energy (>50 GeV). (Note: Figures taken from [14].)

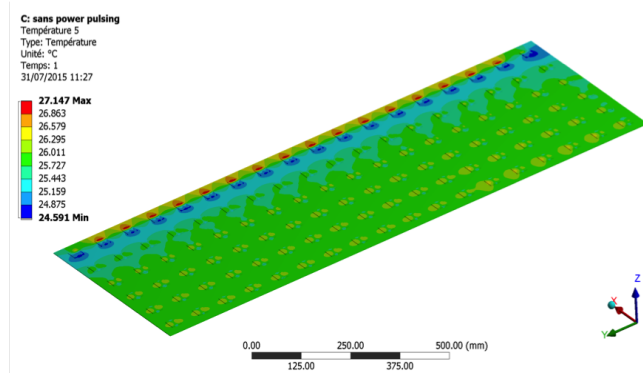


Figure 5.24: Temperature distribution in an active layer of the SDHCAL operated at continuous mode. The cooling system is based on circulating water inside copper tubes in contact with the ASICs.

angle of the plate. It is necessary also to ensure an efficient gas distribution as it was done for the 1 m^2 chambers. To obtain this different gas distribution systems were studied. A new scheme with two gas inlets and one outlet was found to ensure an excellent homogeneity of the gas distribution. This system will be used in the near future to build large detectors exceeding 2 m^2 .

To cope with the heating produced by the embedded readout system in case of limited or even the absence of use of the Power Pulsing system, a new active cooling system is being studied. Figure 5.24 shows a study of a water-based cooling system to absorb the excess of heat in the SDHCAL. The cooling system is very simple but very effective as well. It allows to keep the average temperature as well as the temperature dispersion of the GPC well under control.

5.4.2.3 THGEM-based DHCAL

The THGEM scheme The THGEM can be built in large quantities at low cost, which might make them suitable for the large CEPC HCAL. THGEM detectors can provide flexible configurations, which allow small anode pads for high granularity. They are robust and fast, with only a few nano-seconds rise time, and have a short recovery time which allows a higher rate capability compared to other detectors. They are operated at a relatively low voltage across the amplification layer with stable high gain. The ionization signal from charged tracks passing through the drift section of the active layer is amplified using a single layer or WELL-type THGEM structure. The amplified charge is collected at the anode layer with pads at zero volts. As the HCAL is located within the coil, WELL-THGEM, a single layer structure with thinner thickness, as shown in Figure 5.25, can be considered as the sensitive medium, to keep the HCAL compact.

Digital readout has been proposed to limit the total amount of data, which simplifies the data treatment without comprising the energy resolution performance. The readout electronics of the DHCAL will be integrated into the sensitive layer of the system, thus minimizing dead areas. Large electronics boards are assembled together to form extra large boards before being attached to the THGEM. The board assembly will utilize a mechanical structure made of 4 mm stainless steel plates. In addition, to keep the HCAL as compact as possible, the fully equipped electronic boards are designed to be less than 2 mm thick in total.

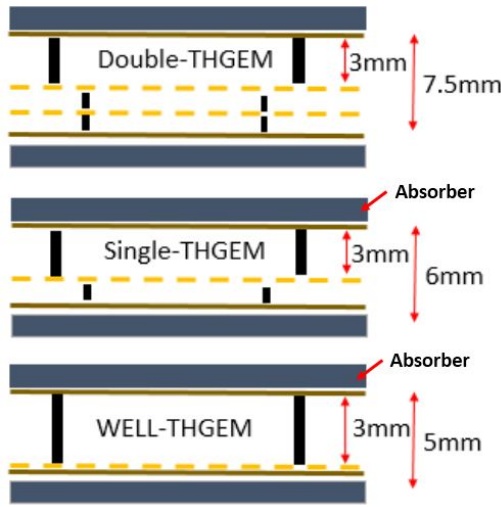


Figure 5.25: Schematic of three different types of THGEMs, eg. doubly-THGEM with thickness of 7.5 mm (top plot), single-THGEM with thickness of 6 mm (middle plot) and well-THGEM with thickness of 5 mm (bottom plot).

1 A THGEM based detector for DHCAL has been designed with 40 layers in total. Each
 2 layer contains 2.0 cm thick stainless steel, 0.8 cm thick THGEM and readout electronics
 3 with $1 \times 1 \text{ cm}^2$ readout pads. As THGEM production technology matures, the maximum
 4 area of THGEM is limited only by the size of the CNC drilling area. The low cost of ma-
 5 terials and fabrication, robustness against occasional discharges, high gain and count rate
 6 capability of up to 10 MHz/cm^2 make THGEM very attractive for building the DHCAL.
 7 As illustrated in Figure 5.25, the total thickness of the sensitive medium is 5 mm, which
 8 consists of 3 mm drift gap, 1 mm transfer gap and 1 mm induction gap. The absorber
 9 between the active layers is made of 20 mm thick stainless steel. The thickness of the
 10 readout electronics board is about 3 mm, and the total thickness of a single sensitive layer
 11 is less than 10 mm. Each layer corresponds to about 1.2 radiation lengths and 0.65 nuclear
 12 interaction lengths. The whole DHCAL detector is evenly divided into 40 layers, with a
 13 total stainless steel absorber thickness of 4.7 nuclear interaction lengths.

14 **THGEM prototype** A THGEM with an area of $40 \times 40 \text{ cm}^2$ has been successfully fab-
 15 ricated, as shown in Figure 5.27, and a gain of 2×10^5 has been achieved with a double
 16 THGEM, with an energy resolution of about 20% for an ^{55}Fe source. The THGEM pro-
 17 duced has the following features:

- 18 1. Standard PCB processes are used, which keeps the cost low;
- 19 2. Excellent performance in terms of energy resolution, gas gain and stability (as shown
 20 in Figure 5.26);
- 21 3. Rim around the hole formed by full-etching process, the size of which can be var-
 22 ied between $10 \mu\text{m}$ and $90 \mu\text{m}$, as depicted in Figure 5.26 - this allows adjustment
 23 according to gas requirements.

24 Figure 5.28 shows the schematic diagram of a new THGEM detector, where a micro-
 25 plate directly attached to the readout plate. Since the micro-porous structure is similar in
 26 shape to a well, these detectors are known as well-type THGEM (WELL-THGEM). This

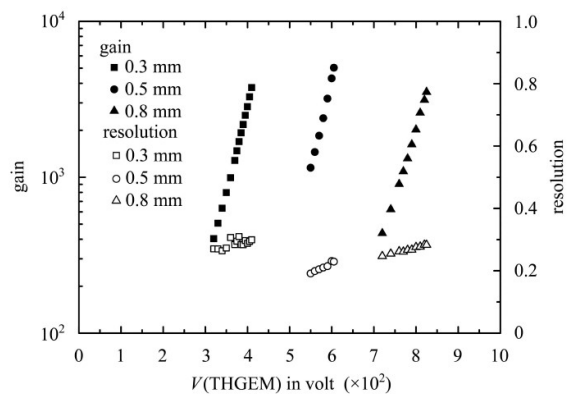


Figure 5.26: Gain and energy resolution of THGEM detector obtained with ^{55}Fe source. Black boxes (0.3 mm thick), dots (0.5 mm thick) and triangles (0.8 mm thick) represent THGEM gain versus voltage, gain is achieved up to 8000. Hollow boxes, dots and triangles show energy resolution, typically around 20% to 25%.

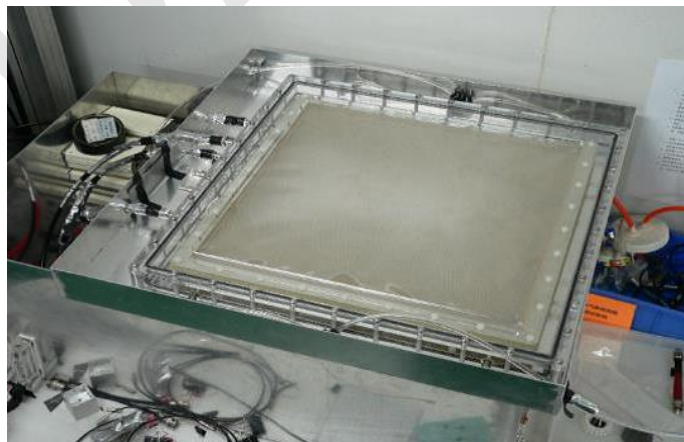


Figure 5.27: A double THGEM was produced with a size of $40 \times 40 \text{ cm}^2$.

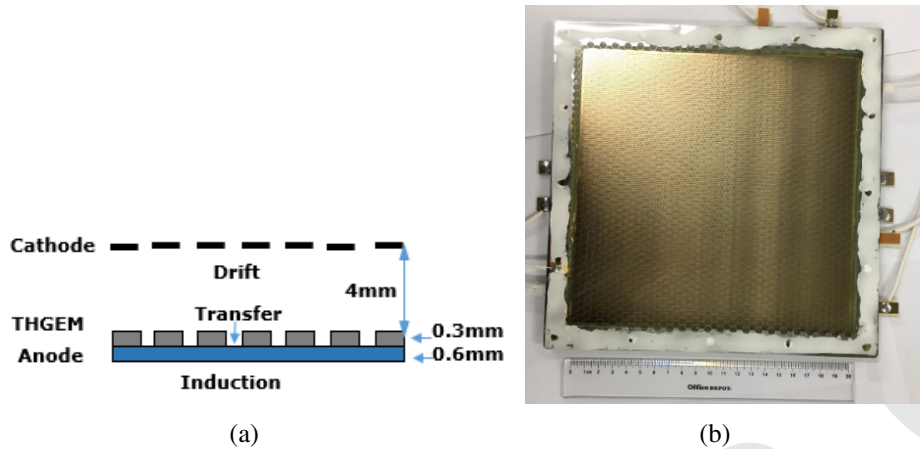


Figure 5.28: The schematic diagram of the WELL-THGEM (a), the thickness is 5 mm. A 20 cm × 20 cm WELL-THGEM detector was produced (b).

1 structure contains a single-layer THGEM, so that the thickness of detector can be reduced
 2 to 4 ~ 5 mm, and the total thickness of the detector including ASIC electronics could
 3 be lowered to about 6 mm. A 20 cm × 20 cm WELL-THGEM detector using thin-type
 4 THGEM has been developed as shown in the right plot of Figure 5.28

5 In addition, large THGEM detectors have been studied. Single THGEM detectors and
 6 WELL-THGEM detectors are being developed to reduce detector instability and ineffi-
 7 ciency. Gas recycling systems are built to lower gas consumption and pollution. The
 8 achieved THGEM detection rates of 1 MHz/cm² with efficiencies greater than 95% al-
 9 ready meet the CEPC requirements.

10 **THGEM digital readout system** A MICRO-mesh gaseous structure Read-Out Chip (MI-
 11 CROROC), which is developed at IN2P3 by OMEGA/LAL and LAPP microelectron-
 12 ics groups was used to readout the THGEM-based SDHCAL. The MICROROC is a 64-
 13 channel mixed-signal integrated circuit based on 350 nm SiGe technology. Each channel
 14 of the MICROROC chip contains a very low noise fixed gain charge preamplifier which is
 15 optimized to cover a dynamic range from 1 fC to 500 fC and allow an input detector capac-
 16 itance of up to 80 pF, two gain-adjustable shapers, three comparators for triple-threshold
 17 readout and a random access memory used as a digital buffer. In addition, the chip has a
 18 10-bit DAC, a configuration register, a bandgap voltage reference, a LVDS receiver shared
 19 by 64 channels and other features. A 1.4 mm total thickness is achieved by using the Thin
 20 Quad-Flat Packaging (TQFP) technology.

21 **5.4.3 AHCAL based on Scintillator and SiPM**

22 The AHCAL (Analog Hadron CALorimeter) is a sampling calorimeter with steel as the
 23 absorber and scintillator tiles with embedded electronics. The moderate ratio of hadronic
 24 interaction length ($\lambda_I=17\text{cm}$) to electromagnetic radiation length ($X_0 = 1.8 \text{ cm}$) of steel,
 25 allows a fine longitudinal sampling in terms of X_0 with a reasonable number of layers.
 26 Within the CALICE collaboration, a large technological prototype [18] using scintillator
 27 tiles and SiPMs has been built to demonstrate the scalability to construct a final detector

1 via automated mass assembly. The outcome of CALICE-AHCAL R&D activities can be
 2 an essential input for the conceptual design of the hadron calorimeter system at CEPC.

3 5.4.3.1 AHCAL geometry and simulation

4 The AHCAL will consist of 40 sensitive and absorber layers, and the total thickness is
 5 about 100 cm. The AHCAL barrel consists of 32 super modules, each super module con-
 6 sists of 40 layers (Figure 5.29 shows the AHCAL structure). Figure 5.30 shows the single
 7 layer structure of AHCAL. The scintillator tiles wrapped by reflective foil are used as
 8 sensitive medium, interleaved with stainless steel absorber. The thickness of active layer
 9 including the scintillator and electronics is about 4 ~ 5 mm. Assuming the scintillator
 10 cell size of $3 \times 3 \text{ cm}^2$, the total readout channels for AHCAL is about 4×10^6 .

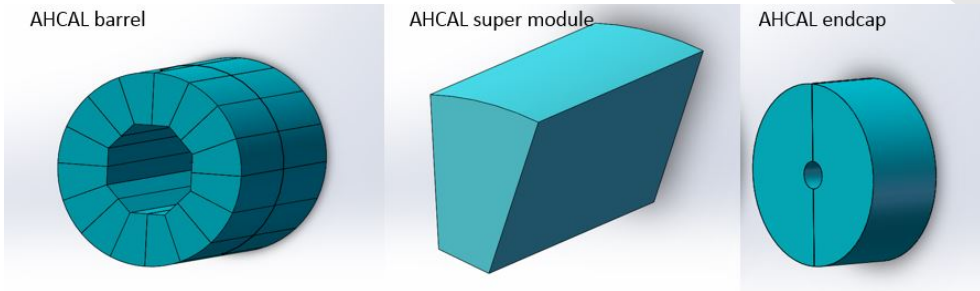


Figure 5.29: The layout of AHCAL barrel (left plot) and endcap regions (right plot), the middle plot shows a super module of AHCAL. The total thickness of AHCAL is about 100 cm. The AHCAL barrel consists of 32 super modules, each with 40 layers.

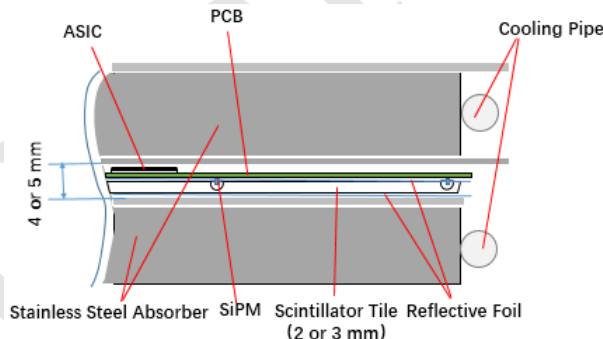


Figure 5.30: Cross-sectional view of a single layer of AHCAL with stainless steel absorber. The thickness of active layer including scintillator and readout electronics is about 5 mm.

11 The structure of scintillator tiles is shown in Figure 5.31. A dome-shaped cavity was
 12 processed in the center of the bottom surface of each tile by injection molding technology.
 13 The diameter and height of the cavity [19] are 6 mm, 1.5 mm, respectively, as shown in
 14 Figure 5.31 (right). The "SiPM-on-Tile" design has advantage to mount SiPMs on PCB so
 15 that automated mass assembly of all components can be achieved. Good response unifor-
 16 mity and low dead area will be achieved by the design of the cavity. More optimizations
 17 of the cavity structure will be done by GEANT4 simulation.

18 The AHCAL prototype detector was simulated by GEANT4 to show the expected
 19 performance of combined ECAL and HCAL using single hadrons. The detector model
 20 used here was the CEPC_v1 detector model. The geometry information was extracted by
 21 Mokka at runtime and the generated events were stored in Slcio, which contains primary

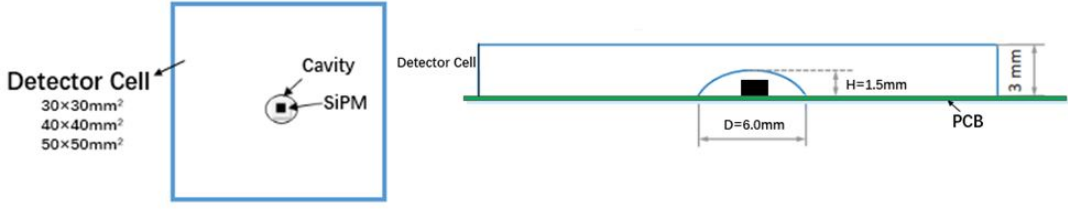


Figure 5.31: Top view of a detector cell (left plot) and cross-sectional view of a detector cell with a dome-shaped cavity (right plot). The detector cell size varies from 30×30 mm², 40×40 mm² to 50×50 mm². The height of dome-shaped cavity in the center of detector cell is 1.5 mm with diameter of 6 mm.

1 information regarding the energy deposition, hit position, time and Monte Carlo particle
 2 causing the energy deposition. The ECAL was simulated with 30 layers, and the HCAL
 3 has 40 active layers interleaved with 20 mm stainless steel as absorber plates. Each active
 4 layer consists of plastic scintillator (3 mm) and readout layer (2 mm PCB). The detector
 5 cell size is 30×30×3 mm³, as shown in Figure 5.32.
 6

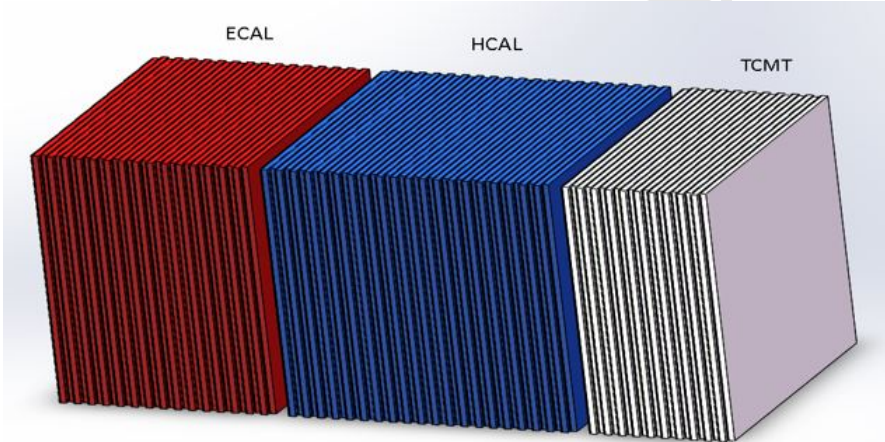


Figure 5.32: The structure of simulated calorimeters which is a part of the simplified geometry. Red part is the Silicon ECAL (30-layer), Blue part is the scintillator AHCAL (40-layer), Gray part is the tail catcher (20-layer).

7 In order to obtain the resolution of calorimeters (ECAL and AHCAL) as shown in
 8 figure 5.32, the energy reconstruction formula 5.3 is employed [20], the coefficients a and
 9 b in this formula represent ECAL and HCAL calibration constants, respectively. After
 10 optimization, the calibration constants are $a = 44.4$ and $b = 44.2$, respectively, which
 11 were corrected to the energy scale of 60 GeV pions. The calibration constants compensate
 12 for the energy leakage from the calorimeters. The formula 5.4 [20] is used to fit for the
 13 energy resolution, as shown in Figure 5.33.

$$E_{REC} = a \times E_{ECAL} + b \times E_{HCAL} \quad (5.3)$$

$$\frac{\sigma}{E} = \frac{p_0}{\sqrt{E}} + p_1 \quad (5.4)$$

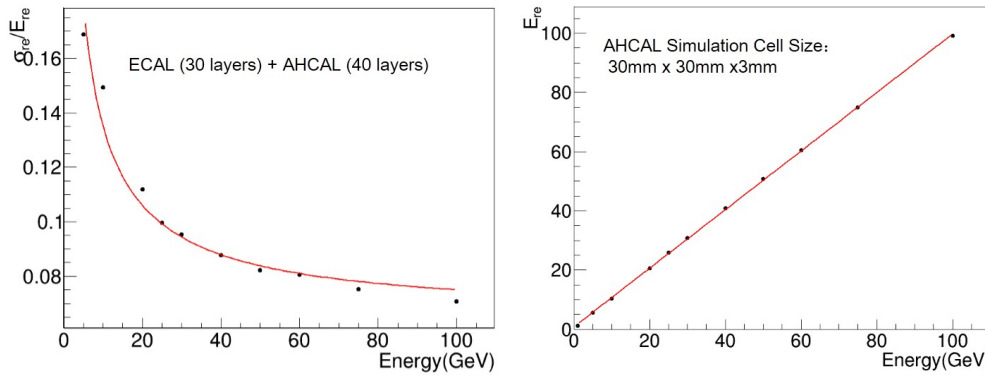


Figure 5.33: The left plot is the energy resolution from the SiW-ECAL and AHCAL for pions. The right plot is the corresponding results of reconstruction energy linearity. The energy resolution is 11% and 8% for energy at 20 GeV and 80 GeV, respectively.

5.4.3.2 Plastic Scintillator detector cell design and test

According to studies by the CALICE collaboration, a scintillator detector cell size of $30 \times 30 \text{ mm}^2$ is an optimal size. The simulation results of the CALICE collaboration [21] also suggest that it is possible to use the detector cells of larger sizes. A large detector cell size of $40 \times 40 \text{ mm}^2$ would reduce by nearly half the number of electronics channels compared to the $30 \times 30 \text{ mm}^2$ size. Therefore, the construction costs can be greatly reduced if the larger detector cells can meet the physics requirements. Two larger sizes of detector cells were considered. Four kinds of scintillator tiles with different sizes were fabricated and tested.

The SiPM is soldered onto a readout Printed Circuit Board (PCB) and the scintillator tile wrapped by ESR reflective foil is directly glued onto the PCB. A cavity design provides enough space for the SiPM package and improves collection efficiency of the light produced by incident particles penetrating the tile at different positions.

A strongly non-uniform tile response can lead to a distortion of the energy reconstruction in a complete calorimeter, and also compromises the calibration of the detector cells based on single particle signals. Three different sizes tiles ($30 \times 30 \times 3 \text{ mm}^3$, $30 \times 30 \times 2 \text{ mm}^3$ and $50 \times 50 \times 3 \text{ mm}^3$) were tested with the Hamamatsu MPPC S12571-025P and S13360-025PE. The spatial distribution of photon equivalents number (p.e.) with different detector cell areas are shown in Figure 5.34. The result shows that the number of p.e. in the center area is slightly larger than that of the surrounding area. The three detector cells show good response uniformity, within 10% deviation from their mean response.

Seven detector cells of different sizes, polishing methods and wrapping foil types were measured. The larger the area of the cell is, the less p.e. are detected, and the results of same size cells varied greatly because of the polishing methods.

The detection efficiency of $30 \times 30 \times 3 \text{ mm}^3$ and $50 \times 50 \times 3 \text{ mm}^3$ were measured with cosmic rays. The detection efficiency of $30 \times 30 \times 3 \text{ mm}^3$ and $50 \times 50 \times 3 \text{ mm}^3$ cells are 99% and 98.2%, respectively. According the cosmic-ray test result, the detection efficiency of $30 \times 30 \times 2 \text{ mm}^3$ with S13360-025PE MPPC also can reach 98%.

The good response uniformity and high detection efficiency results indicate that scintillator detector cells are acceptable for AHCAL. The size of $30 \times 30 \times 3 \text{ mm}^3$ detector cell

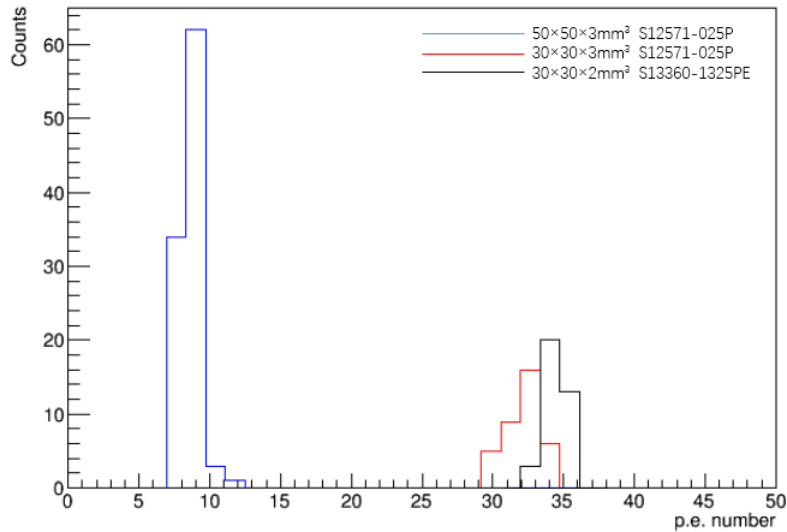


Figure 5.34: The uniformity measurement result of $30 \times 30 \times 3 \text{ mm}^3$ (red histogram, p.e. is about 30–34), $50 \times 50 \times 3 \text{ mm}^3$ (blue histogram, p.e. is about 8–10) and $30 \times 30 \times 2 \text{ mm}^3$ (black histogram, p.e. is about 34–36) detector cell.

¹ is the baseline of AHCAL and more optimization of the detector cell size will be done by
² the simulation and test beam measurements.

³ 5.4.3.3 Development of SiPM

⁴ Several kinds of SiPM were developed by Hamamatsu and other companies, they have
⁵ been used for scintillator ECAL systems. The SiPM with epitaxial quenching resistors
⁶ (EQR SiPM) is one of the main SiPM technologies under development in China. As
⁷ shown in Figure 5.35, each APD cell (pixel) forms a high electric field, composing an en-
⁸ riched region between N-type epitaxial silicon substrate and P++ cap layer, and it employs
⁹ the un-depleted region in the epitaxial silicon layer below P/N junction as the quenching
¹⁰ resistor. Compared to conventional SiPM configurations that employ poly-silicon quen-
¹¹ ching resistors on the device surface, it is easier to achieve high density and small micro-
¹² APD cells, thus obtaining a small junction capacitor; the EQR SiPMs are expected to have
short recovery time and high counting rate capability.

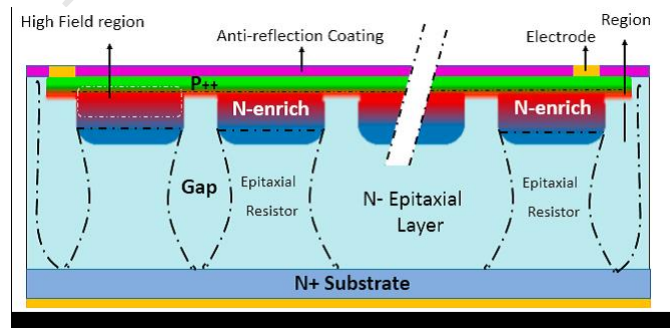


Figure 5.35: Schematic structure of EQR SiPM. APD cell consists of N-enriched regions forming high electric fields between the N-type epitaxial silicon wafer and the P++ surface layer, the un-depleted region in the epitaxial silicon layer below the P/N junction as the quenching resistor. The APD cells are isolated from each other by the Gap depletion region.

5.4.3.4 Electronics and DAQ

Front-end electronics ASIC: High-density electronics is indispensable to the instrumentation of high-granularity calorimetry. An ASIC chip named SPIROC, developed by the OMEGA group, is capable of handling 36 SiPMs. For each channel, it can be operated in an auto-trigger mode and has a dual-gain charge preamplifier with high dynamic range. It allows to measure the charge from 1 to 2000 photo-electron and the time to within 1 ns using a 12-bit digitizing circuit. With one 8-bit 5V input DAC per channel, the bias voltage for each SiPM can be adjusted to reach its optimum. In each channel, there are 16 analog memory cells that can buffer both charge and timing signals to be digitized afterwards consecutively. The digitization circuit is shared for both charge and timing measurements to minimize the power consumption, which needs to be as low as $25 \mu\text{W}$ per channel.

DAQ system is also required to be compatible to the final detector layout, where two hardware parts are essential. One part is so-called LDA (Link to Data Aggregator), which collects all the data via DIFs from active layers in an HCAL segment and transmit them to a back-end PC for further processing or storage. Smart units like FPGAs are equipped on this board for data packaging and transmission. Modern FPGAs integrated with RAMs are an ideal option to have a capability of data buffering and some advanced feature like system on chip.

5.4.3.5 Cooling system

Inside the active layers of the calorimeter, the total power consumption of SPIROC ASIC chip and SiPM is about 5 mW/channel [22]. The scintillator detector cell size is $30 \times 30 \text{ mm}^2$, and the total channel number is about 5 million. For whole AHCAL, the total power consumption from ASIC chips is about 30kW. The copper cooling water pipes are expected to embedded in the stainless steel absorber. The cooling pipes are in the layer structure, as shown in Figure 5.30. Detailed design and optimization of a cooling system is needed.

5.5 Dual-readout calorimetry

5.5.1 Introduction

The dual-readout approach envisages designing a combined, homogeneous, detector with excellent performance for both electromagnetic and hadronic particle showers.

With conventional calorimeters, the performance obtained in hadronic energy measurements is by far worse than for the electromagnetic ones. The origin of this disparity is in the showers from single hadrons or jets of hadrons. Hadronic showers develop an electromagnetic component, from π^0 and η production, that exhibits large event-by-event fluctuations and dependence on the particle type and energy [23]. The *em* and non-*em* components of a hadronic shower are normally sampled with very different sensitivity, producing large differences in the measured signals, heavily affecting the energy resolution capability.

The variation of the *em* fraction is intrinsic to hadronic showers. As a matter of fact, the *em* fraction depends on the kind of particle initiating the shower (e.g., π , K , p) since, for example, impinging π^\pm mesons can undergo a charge-exchange reaction with a nucleon as first interaction and generate a pure *em* shower, while a p cannot do the same due to baryon number conservation. Moreover, since π^0 production happens at any stage

of shower development, the average em fraction $\langle f_{em} \rangle$ increases with the energy as well as with the depth ("age") of the shower.

To overcome the problem two methods have been exploited: compensation and dual readout (DR). The first relies on equalizing the detector response to electromagnetic (e) and non-electromagnetic (h) shower particles (i.e. $h/e = 1$), but this requires a fixed ratio of absorber-to-sensor volumes, which limits the electromagnetic energy resolution, and the integration of the signals over large volumes and long times, to increase the response to the h component. The dual-readout method avoids these limitations by directly measuring f_{em} on an event-by-event basis. The showers are sampled through two independent processes, namely scintillation (S) and Čerenkov (C) light emissions. The former is sensitive to all ionizing particles, while the latter is produced by highly relativistic particles only, almost exclusively found inside the em shower component. By combining the two measurements, energy and f_{em} of each shower can be simultaneously reconstructed. The performance in hadronic calorimetry may be boosted toward its ultimate limit.

The results obtained so far with prototypes, support the statement that fiber-sampling DR calorimeters may reach resolutions of the order of $10\%/\sqrt{E}$ or better for em showers and around $30 - 40\%/\sqrt{E}$ for hadronic showers and jets, coupled with strong standalone particle identification (PID) capabilities. One of the strengths of a DR calorimeter is that it achieves excellent jet energy resolution while not sacrificing performance in electromagnetic energy measurements. This would allow $W \rightarrow jj$ separation from $Z \rightarrow jj$ by invariant mass, high-precision missing three-momentum reconstruction by subtraction, $e-\mu-\pi$ separation and particle tagging.

While the dual-readout concept has been extensively demonstrated and experimentally validated in a series of beam tests, the use of standard PhotoMultiplier (PM) tubes to readout the S and C light has so far limited its development towards a full-scale system compliant with the integration in a particle detector at a colliding beam machine. These limitations should be overcome using SiPMs, low-cost solid-state sensors of light with single photon sensitivity, magnetic field insensitivity and design flexibility.

As it will be shown in the following, the high readout granularity in the plane perpendicular to the shower development and few other signal properties will probably make redundant or even inessential the need of a longitudinal segmentation into em and hadronic compartments (that is anyway possible). In case of a segmented calorimeter, both compartments need to provide dual-readout signals, in order to allow for the measurement of $\langle f_{em} \rangle$.

5.5.2 Principle of dual-readout calorimetry

The independent sampling of hadronic showers, through scintillation and Čerenkov light emission, allows one to fully reconstruct, at the same time, energy and f_{em} of hadronic showers. In fact, the total detected signals, measured with respect to the electromagnetic energy scale, can be expressed as:

$$S = E [f_{em} + \eta_S \cdot (1 - f_{em})] \quad (5.5)$$

$$C = E [f_{em} + \eta_C \cdot (1 - f_{em})] \quad (5.6)$$

where $\eta_S = (h/e)_S$ is the ratio of the average S response for the non- em component to the em component in hadronic showers. The response being defined as the average signal

per unit of deposited particle energy. The parameter $\eta_C = (h/e)_C$ is the response ratio for the C signal. In a typical dual-readout calorimeter, $\eta_S \approx 0.7$ and $\eta_C \approx 0.2$. These two equations are easily solved giving:

$$\frac{C}{S} = \frac{[f_{em} + \eta_C \cdot (1 - f_{em})]}{[f_{em} + \eta_S \cdot (1 - f_{em})]} \quad (5.7)$$

$$E = \frac{S - \chi C}{1 - \chi} \quad (5.8)$$

where:

$$\chi = \frac{1 - \eta_S}{1 - \eta_C} = \cot \theta \quad (5.9)$$

This is the simplest formulation of hadronic calorimeter response: an em part with relative response of unity, and a non- em part with relative response η .

There are two unknowns for each shower, E and f_{em} , and two measurements, S and C . The electromagnetic fraction, f_{em} , is determined entirely by the ratio C/S , and the shower energy calculated as in Eq. 5.8. Both, S and C , $\eta = (h/e)$ ratios have event-by-event fluctuations and should be considered stochastic variables, nevertheless the average $\langle h/e \rangle$ values are essentially independent of hadron energy and species [24–26]. The global parameter χ can be extracted with a fit to calibration data:

$$\chi = \frac{E_0 - S}{E_0 - C} \quad (5.10)$$

$$S = (1 - \chi)E_0 + \chi C \quad (5.11)$$

where E_0 is the beam energy.

The geometrical meaning of the θ angle in Eq. 5.9 can be understood by looking at the scatter plot of C versus S signals in Figure 5.36. An illustration of the prediction for the scatter plot for protons and pions is shown in Figure 5.36(a) and the scatter plot for 60 GeV pions measured in the RD52 lead-fiber calorimeter is shown in Figure 5.36(b).

The plot in Figure 5.36(b) shows that the data points are located on a locus, clustered around a line that intersects the $C/S = 1$ line at the beam energy of 60 GeV. In first approximation, the signal generated in the Čerenkov fibers is produced only by the em components of the hadron showers. The smaller the em fraction f_{em} , the smaller the C/S signal ratio. All signals are relative to the em scale meaning that both the Čerenkov and the scintillation responses are calibrated with beam electrons only, i.e. no hadronic calibration is required. This is one of the most qualifying and important points of dual-readout calorimetry.

The effectiveness of this approach has been demonstrated by the DREAM/RD52 collaboration over a 15-year research program with a variety of detector solutions. Results and simulations [27–32] provide, so far, confidence that a fiber-sampling calorimeter, even without longitudinal segmentation, may meet the requirements of the CEPC physics program in a cost-effective way. Linearity and energy resolution, for both em and hadronic showers, $e/\pi/\mu$ separation, spatial resolution, all show adequate performance.

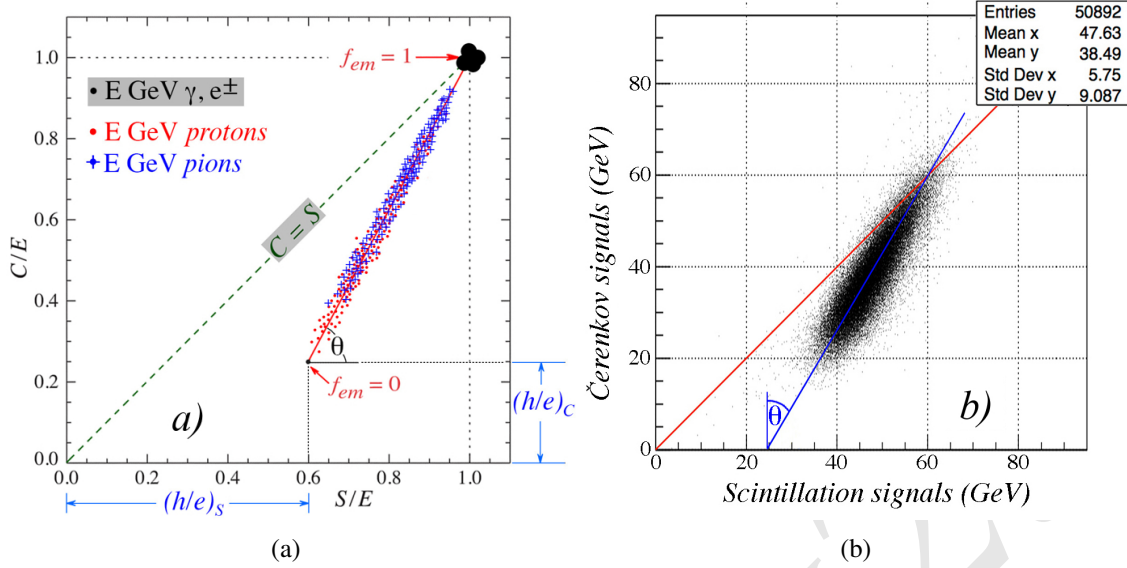


Figure 5.36: (a) Scatter plot of C/E versus S/E in a dual-readout calorimeter for p and π ; (b) scatter plot of C and S signals for 60 GeV pions in the RD52 lead-fiber calorimeter.

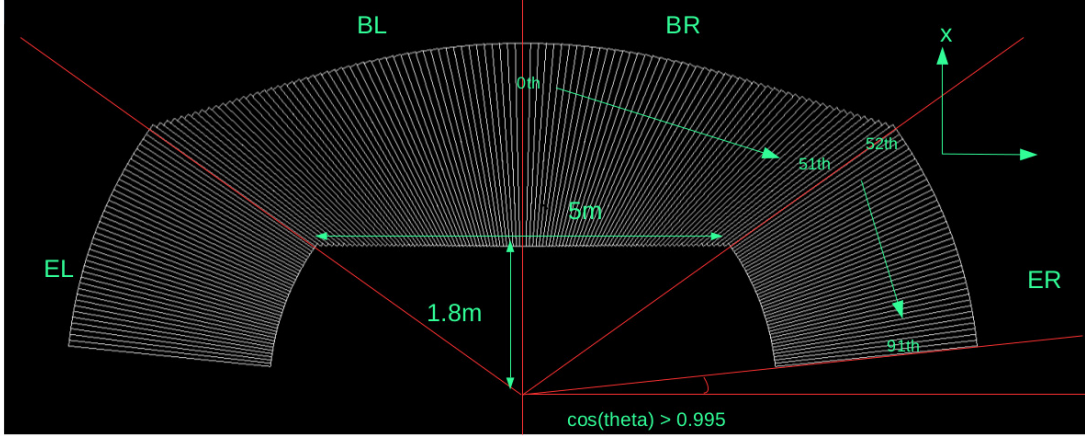


Figure 5.37: A possible 4π solution (called "wedge" geometry).

5.5.3 Layout and mechanics

5.5.3.1 Layout

A possible projective layout ("wedge" geometry, Figure 5.37) has been implemented in the simulations. Based on the work done for the 4th Detector Collaboration (described in its Letter of Intent [33]), it covers, with no cracks, the full volume up to $|\cos(\theta)| = 0.995$, with 92 different types of towers (wedges). A typical one in the barrel region is shown in Figure 5.38(b), together with the fiber arrangement (Figure 5.38(a)): it has a granularity of $\Delta\theta \times \Delta\phi = 1.27^\circ \times 1.27^\circ$, a depth of about 250 cm ($\sim 10 \lambda_{\text{Int}}$), and contains a total of about 4000 fibers. The sampling fraction is kept constant by fibers starting at different depths inside each tower. This layout has been already imported in the simulations for the CEPC detector. Preliminary results on performance are shown in the next chapters.

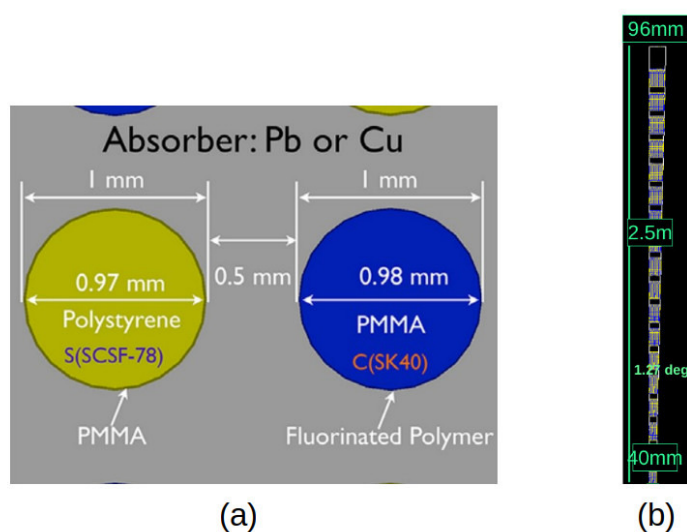


Figure 5.38: (a) Fiber arrangement inside the modules. (b) Dimensions of a module in the barrel region (at $\eta = 0$): from inside to outside the number of fibers more than doubles.

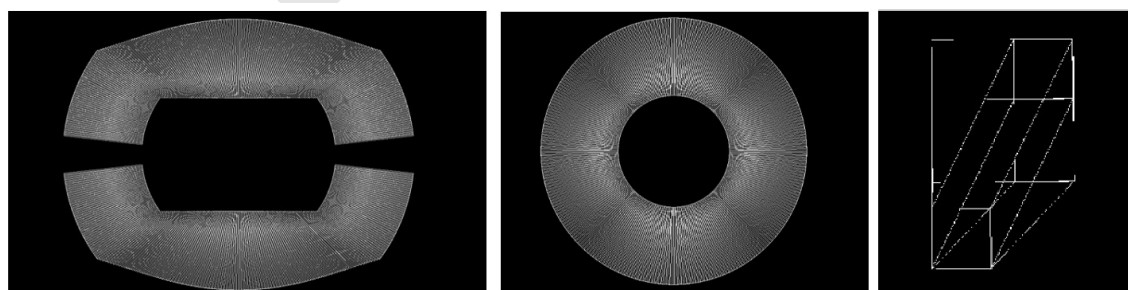


Figure 5.39: An alternative 4π solution (called "wing" geometry).

1 A different layout implementing the "wing" geometry (see Figure 5.39) is also un-
 2 der study and preliminary results on the *em* performance will also been shown in the
 3 next chapters. In this case, the calorimeter is made of rectangular towers coupled with
 4 triangular ones.

5 In both cases, the total number of fibers is of the order of 10^8 for a complete 4π
 6 calorimeter.

7 5.5.3.2 Mechanics (material choice and machining)

8 Copper, lead and brass (Cu260) have been used as absorber materials by the DREAM/RD52
 9 collaboration. Their main properties are shown in the Table 5.3, that also reports the cal-
 10 culation for the RD52 lead-prototype geometry. The values for iron are also shown, for
 11 comparison. From the table it can be seen that, for hadronic showers, a full-coverage solu-
 12 tion with lead will give 6% broader and longer showers and a total mass 56% heavier than
 13 using brass. A full-containment $3 \times 3 \times 10 \lambda^3$ prototype will need ~ 5 tons of material
 14 with lead and ~ 3.2 tons with brass.

Material	ρ (g/cm ³)	X_0 (cm)	$R_{\text{Molière}}$ (cm)	λ_{Int} (cm)	$\rho \times \lambda_{\text{Int}}^3$ (kg)
Copper (Cu)	8.96	1.44	1.57	15.3	32.2
Brass (Cu260)	8.53	1.49	1.64	16.4	37.8
Lead (Pb)	11.35	0.56	1.60	17.6	61.8
Iron (Fe)	7.874	1.76	1.72	16.8	37.1
Fibers:Copper (38:62)	5.98	2.26	2.28	21.9	62.8
Fibers:Brass (38:62)	5.72	2.35	2.38	23.3	72.1
Fibers:Lead (38:62)	7.46	0.90	2.33	24.7	112.8
Fibers:Iron (38:62)	5.31	2.75	2.48	23.7	70.8

Table 5.3: Main properties of lead, copper, brass and iron absorber material and of fiber sampling matrices (RD52 lead-fiber prototype geometry).

15 A possibly stronger reason in favor of copper/brass is the fact that, since the e/MIP
 16 ratio is 50% higher for copper than for lead, the Čerenkov light (almost exclusively pro-
 17 duced by the *em* component of the shower) has a larger yield for copper, resulting in a
 18 better hadronic resolution [23]. However this statement needs to be quantified since it
 19 depends on the absolute level of the Čerenkov light yield(s).

20 On the other hand, lead is easily and accurately extruded, whereas forming copper
 21 into the desired shape, either by extrusion, molding, or machining, with the required tol-
 22 erances in planarity and groove parallelism, is not yet an established industrial process.
 23 A variety of techniques (extrusion, rolling, scraping, and milling) for forming the con-
 24 verter layers have been tested. None has been qualified for a large-scale production and
 25 identifying an industrial and cost-effective process, including moulding, is a key point.

26 Alternative copper alloys (e.g. bronze) and/or materials (e.g. iron) may be investi-
 27 gated as well, both for addressing the production process issues and for optimizing the
 28 detector performance.

5.5.4 Sensors and readout electronics

To separately read out the signals from the S and C fiber forest and avoid oversampling of late developing showers is an issue that may be successfully addressed through the use of Silicon PhotoMultipliers (SiPMs). They would allow the separate reading of each fiber and provide magnetic field insensitivity. In principle, assuming powering and cooling do not pose issues, the transverse segmentation could be made as small as a fiber spacing, or 1.5 mm.

SiPMs are low-cost solid state light sensors with single photon sensitivity that underwent an impressive development over the last few years. Tests done in the last two years by the RD52 collaboration indicate that effective solutions for small-scale prototypes are very close already now. Thanks to their higher photon detection efficiency with respect to a standard PM, the higher number of Čerenkov (pe) should result in an improved resolution for both em and hadronic showers. On the other hand, the scintillation light spans a very large dynamic range and saturation and non-linearity effects were observed already for low-energy em showers.

In Figure 5.40, the number of photoelectrons per GeV (pe/GeV) measured, in July 2017, with a very small module ($\sim 1.44 \text{ cm}^2$ cross section, 32 + 32 fibers), is shown. The most relevant sensor characteristics are 1600, $25 \times 25 \mu\text{m}^2$, cells, and a 25% nominal PDE. Due to the large S light yield, the data for the S signal were obtained at an (ultra low) PDE of $\sim 2\%$, and corrected for non-linearity. Rescaled to a 25% efficiency, the yield of S photoelectrons results in $\sim 108 \times 12.5 = 1350 \text{ pe/GeV}$. By removing from the sum the hottest fiber, more heavily affected by non-linearity effects, the estimate grows to $\sim 1530 \text{ pe/GeV}$.

The C signals show a linear response at $\sim 30 \text{ pe/GeV}$. It should be mentioned that the shower containment was estimated from GEANT4 simulations to be $\sim 45\%$. In addition, the problem of large light leaks from the S fibers into the neighboring C SiPM channels, observed in the 2016 tests, seems to be largely but not completely solved by a staggered readout of the S and C fibers (Figure 5.41). The contamination of the C signal was estimated to be $\sim 16\% \pm 6\%$.

5.5.4.1 Sensor choice

As far as the scintillation light detection is concerned, saturation and non-linearity should be solvable using higher density devices (e.g. with 10000, $10 \times 10 \mu\text{m}^2$, cells) in combination with some light filtering. The definition of the optimal dynamic range and the qualification of existing SiPMs in that regard, will be likely addressed in a short-term R&D phase.

For the Čerenkov light, improvements of the photon collection are possible with the use of an aluminized mirror on the upstream end of the fibers. The acceptance cone may also be enlarged with the use of cladding with a different refractive index. Over a longer term, it could be possible that the R&D on new devices, such as Silicon Carbide (SiC) sensors, expected to provide exclusive UV sensitivity (i.e. visible-light blindness), will allow us to obtain significantly larger pe yields.

5.5.4.2 Front-end electronics and readout

Concerning the front-end, the development shall certainly evaluate the use of Application Specific Integrated Circuits (ASIC) to handle and reduce the information to be transferred

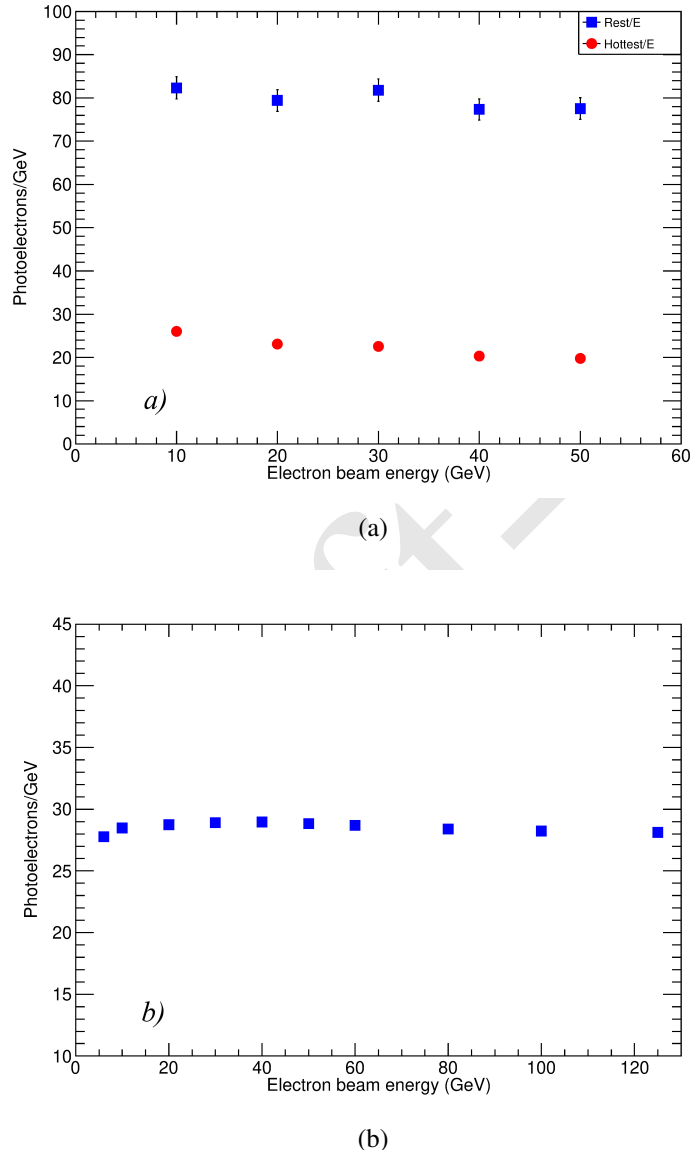


Figure 5.40: Number of photoelectrons per GeV (pe/GeV) for (a) S and (b) C signals, as a function of the electron energy, from 10 to 50 GeV, in a small 64-fiber brass module. In (a), the results are shown separately for the hottest fiber and for the sum of the signals measured by the other 31 scintillating fibers obtained at the (ultra low) PDE of $\sim 2\%$. The main sensor specifications were: 1600, $25 \times 25 \mu\text{m}^2$, cells, and a 25% nominal PDE.

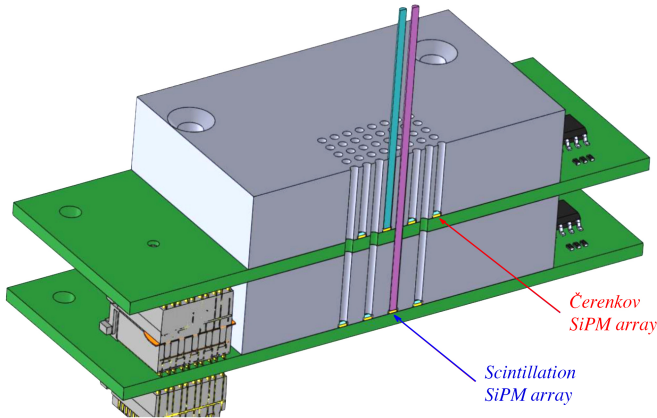


Figure 5.41: Staggered readout scheme: the scintillation and Čerenkov fibers are readout at different planes to minimize light leakage into neighboring channels.

to the DAQ system. A major question is finding the optimal way for summing signals from a plurality of sensors into a single output channel. A dedicated feature-extracting processor, capable of extracting timing information such as time-over-threshold, peaking, leading and/or falling times, may allow to disentangle overlapping *em* and hadronic showers without the need for longitudinal segmentation. With the present fibers, a resolution of the order of 100 ps corresponds to a spatial resolution of about ~ 6 cm along the fiber axis (relativistic particles take 200 ps to cover 6 cm while light needs 300 ps).

5.5.5 Performance studies with fiber-sampling prototypes

Different prototypes were built and studied by the DREAM/RD52 collaboration, with copper or lead as absorber and photomultipliers as light sensors [27–32]. With electrons and pions, in the range of ~ 10 –150 GeV, the response linearity was found at the level of 1% for both the *em* and the hadronic energy reconstruction (having applied the dual-readout formula, equation 5.8, for hadronic showers). The *em* resolution was estimated to be close to $\sim 10\%/\sqrt{E}$, while the hadronic resolution was found to be at the level of 60–70%/ \sqrt{E} , to be corrected for the fluctuations introduced by lateral leakage and light attenuation in the fibers. None of the prototypes built thus far were large enough to substantially contain hadronic showers and an R&D program to assess the hadronic performance of a real detector, is under way. Preliminary simulations of standalone modules indicate a possible ultimate resolution of ~ 30 –40%/ \sqrt{E} . More details can be found in the next paragraphs.

5.5.5.1 Electromagnetic performance

Figure 5.42(a) and 5.42(b) show the radial shower profile and the sensitivity to the impact point: the core of the signal spans just a few mm. Figure 5.42(c) shows the dependence of the *S* signal on the impact point for particles entering parallel to the fibers. This introduces a constant term in the resolution that can be avoided with a small tilt of the fiber axis. In the *C* fibers, the problem does not show up since the early (collimated) part of the shower produces photons outside the fiber numerical aperture.

For the reconstruction of the energy of *em* showers, *S* and *C* signals provide independent uncorrelated measurements, with different sensitivity of the response. They are affected by different problems: *S* signals have photoelectron statistics one or two orders

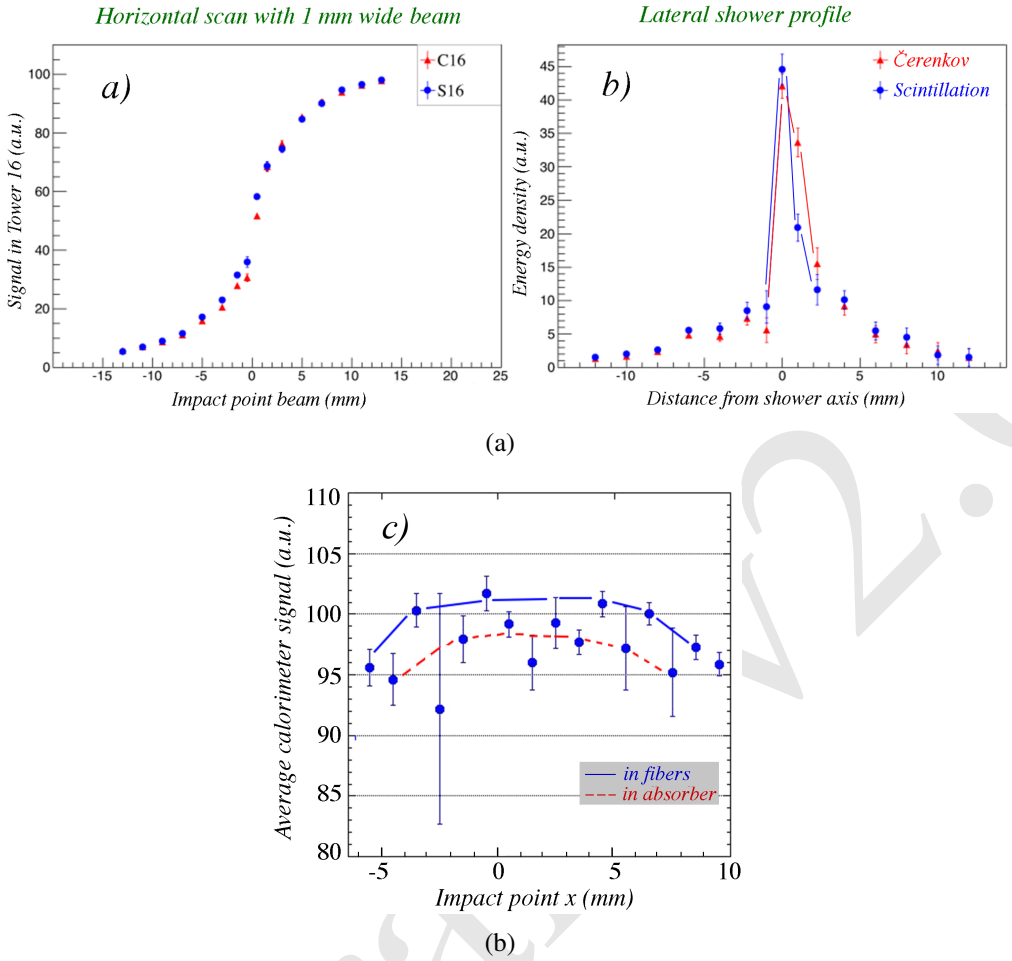


Figure 5.42: (a) The signal from a 1 mm wide beam of 100 GeV electrons, in the RD52 lead-fiber prototype, as a function of the impact point; (b) the lateral shower profiles derived from this measurement; (c) the dependence of the scintillation signal on impact point for a beam impinging parallel to the fibers.

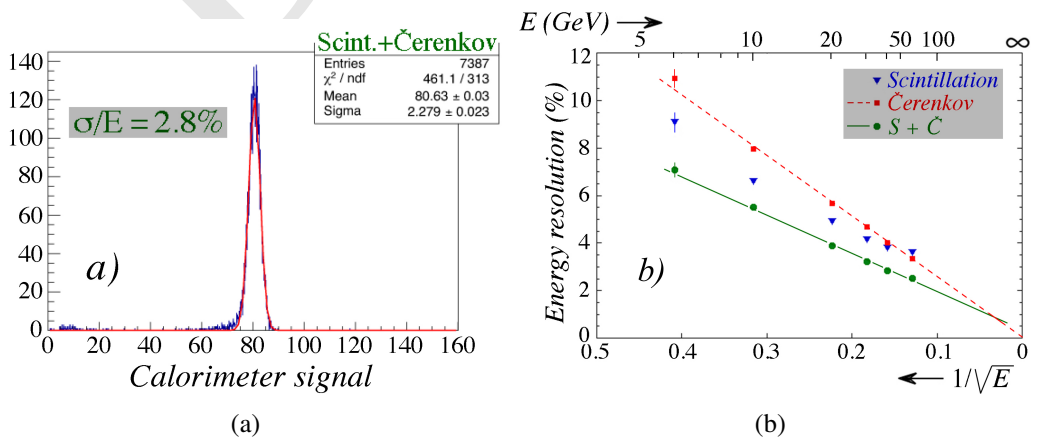


Figure 5.43: In the RD52 copper-fiber module: (a) signal distribution of the sum of all fibers for 40 GeV electrons; (b) the *em* energy resolution as a function of the beam energy. Shown are the results for the two types of fibers, and for the average combined signal.

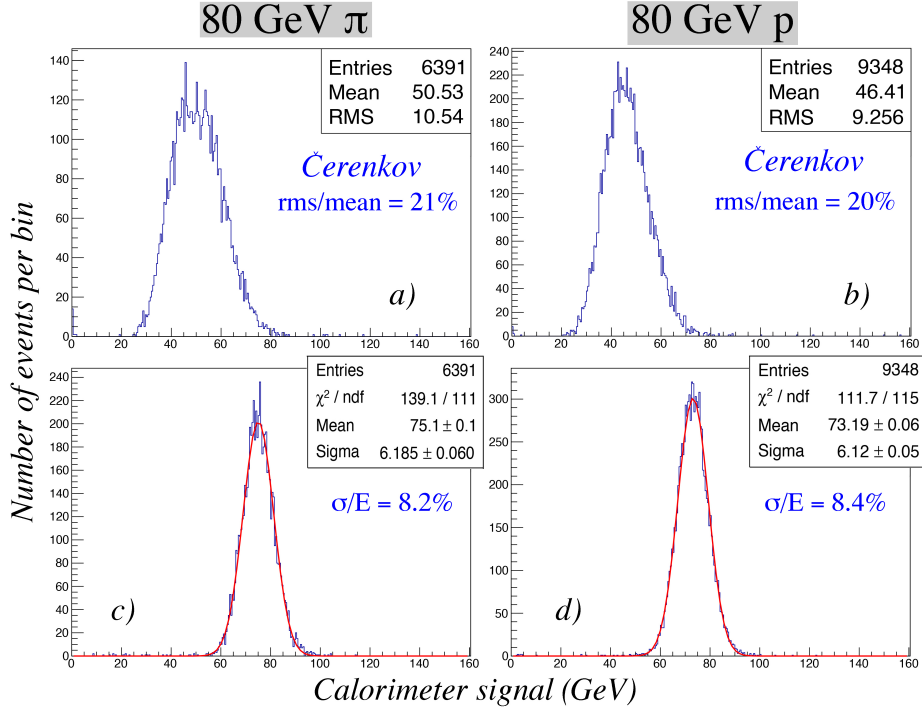


Figure 5.44: Signal distributions for 80 GeV pions and protons measured with the RD52 lead-fiber calorimeter. Shown are the distributions for the Čerenkov signals from 80 GeV (a) π^+ and (b) protons, as well as the dual-readout total signals for 80 GeV(c) π^+ and (d) protons. The dual-readout signals were obtained by applying Equation 5.8 with $\chi = 0.45$.

of magnitude higher than C signals, and their fluctuations are largely dominated by the sampling fluctuation of the energy deposits. C signal fluctuations are generally dominated by the limited photoelectron statistics, especially at low energies. Nevertheless, at high energies, the constant term for C signals is negligible, giving a better resolution. Averaging the two measurements improves the resolution up to a factor of $\sqrt{2}$. For the copper matrix, in Figure 5.43(a) the sum of S and C signals for 40 GeV electrons is plotted, while Figure 5.43(b) shows the em resolution, for S , C and the (average) combined signal.

5.5.5.2 Hadronic performance

The response of a lead-fiber matrix was studied with pion and proton beams [32]. The energy was reconstructed with the dual-readout relation (Eq. 5.8) and shows a restored Gaussian response function (Figure 5.44) and linearity of the mean response.

The comparison of p and π^+ signals confirms that the dual-readout method largely compensates for the differences in shower composition, i.e., differences in the electromagnetic fraction, f_{em} , and between baryon-initiated and pion-initiated hadronic showers.

Due to the limited lateral size of the matrix (the effective diameter was $\sim 1\lambda_{\text{Int}}$), the containment for hadronic showers was $\sim 90\%$ so that leakage fluctuations dominated the energy resolution. Selecting contained showers improved the resolution by a factor of ~ 2 . Although that selection was introducing a bias in favor of high f_{em} showers, a significant improvement is expected for a realistic-size module.

The resolution was also affected by the finite light attenuation length of the fibers, causing early starting showers to be observed at lower signal values. The hadronic resolution, yet to be corrected for both effects, was reconstructed to be $\sim 70\%/\sqrt{E}$.

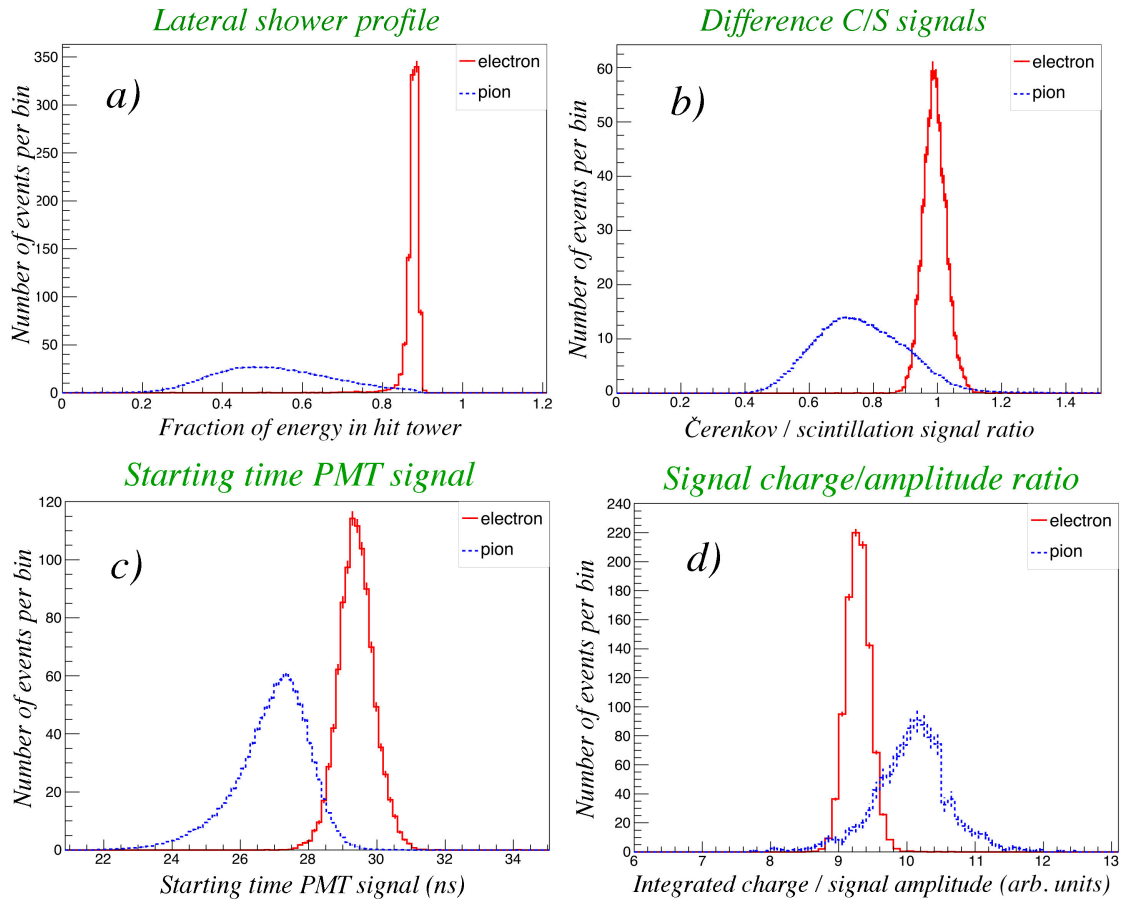


Figure 5.45: Distribution of four discriminating variables for 60 or 80 GeV electrons and pions, as measured with the RD52 lead-fiber prototype: (a) energy fraction deposited in the hit tower; (b) C/S signal ratio in the hit tower; (c) starting time of the PM signal; (d) ratio of the integrated charge and the amplitude of the signals.

1 5.5.5.3 e/π separation

2 Four discriminating variables were identified for implementing e/π separation: the fraction
 3 of energy in the central tower, the C/S signal ratio, the signal starting time and the
 4 total charge/amplitude ratio, shown in Figure 5.45. The plots are relative to test beam data
 5 taken with the RD52 lead-fiber prototype [27].

6 A multivariate neural network analysis showed that the best e/π separation achiev-
 7 able for 60 GeV beams was 99.8% electron identification efficiency with 0.2% pion
 8 misidentification. Further improvements may be expected by including the full time struc-
 9 ture information of the pulses, especially if the upstream ends of the fibers are made re-
 10 flective.

11 5.5.6 Monte Carlo simulations

12 GEANT4 simulations¹ are under development and analysis for understanding the perfor-
 13 mance of both test beam modules and a 4π calorimeter integrated in a detector, with
 14 magnetic field, tracking and preshower elements.

¹version 10.02.p01-10.03.p01, with FTFP_BERT_HP physics list

<i>fibers used</i>	Fitted Gaussian <i>em</i> energy resolution
S-fibers only	$\sigma/E = 10.1\%/\sqrt{E} \oplus 1.1\%$
C-fibers only	$\sigma/E = 17.3\%/\sqrt{E} \oplus 0.1\%$
S-fibers and C-fibers	$\sigma/E = 10.1\%/\sqrt{E} \oplus 0.4\%$

Table 5.4: Fit to the *em* resolution (MC simulations)

5.5.6.1 Electromagnetic performance

A Cu matrix of dimensions $\sim 31 \times 31 \times 100 \text{ cm}^3$, with 1 mm fibers at 1.4 mm distance, compatible with the RD52 prototypes, has been simulated for the evaluation of the electromagnetic performance. PMMA clear fibers and Polystyrene scintillating fibers, with a 3% thick cladding (C_2F_2 Fluorinated Polymer for clear and PMMA for scintillating fibers), were the sensitive elements.

A small ($\lesssim 1^\circ$) tilt angle was introduced to avoid large non-Gaussian tails in the scintillation signal due to channeling.

The energy containment for 20 GeV electrons was estimated to be $\geq 99\%$, with sampling fractions of 5.3% and 6.0% for scintillating and clear fibers, respectively.

Given the integral sampling fraction of 11.3% and the 1 mm diameter fibers, the contribution to the energy resolution due to sampling fluctuations can be estimated to be $\sim 9\%/\sqrt{E}$, ultimate limit on the *em* resolution for this detector.

The scintillation light yield is so large ($\sim 5500 \text{ pe/GeV}$) that the fluctuations of the *S* signals are dominated by the energy sampling process (Figure 5.46(a)). This is not true for the Čerenkov signals (Figure 5.46(b)), whose sensitivity is estimated to be $\sim 100 \text{ pe/GeV}$.

In the simulations, the process of generation and propagation of the scintillation light was switched off and the energy deposited in the fibers was taken as signal since this does not introduce any bias to the detector performance. This statement does not apply to the Čerenkov photons for which a parameterization that convolutes the effect of light attenuation, angular acceptance and PDE, was introduced.

In Figure 5.47 the resolutions are shown for both *C* and *S* signals, separately, and for the unweighted average value of the two. The variable on the horizontal axis and in the formulae for the fitted resolutions is the beam energy. The results of the fit to the data points are shown in Table 5.4. A slightly better result may be obtained with a weighted average.

5.5.6.2 Hadronic performance

A simulation of larger ($\sim 72 \times 72 \times 250 \text{ cm}^3$) matrices was implemented in order to get a hadronic shower containment of $\sim 99\%$. Calibration was done with 40 GeV electron beams.

In Figure 5.48 GEANT4 predictions for the hadronic energy resolution, with copper absorber, are shown. Table 5.5 lists the results of the fit to the curves.

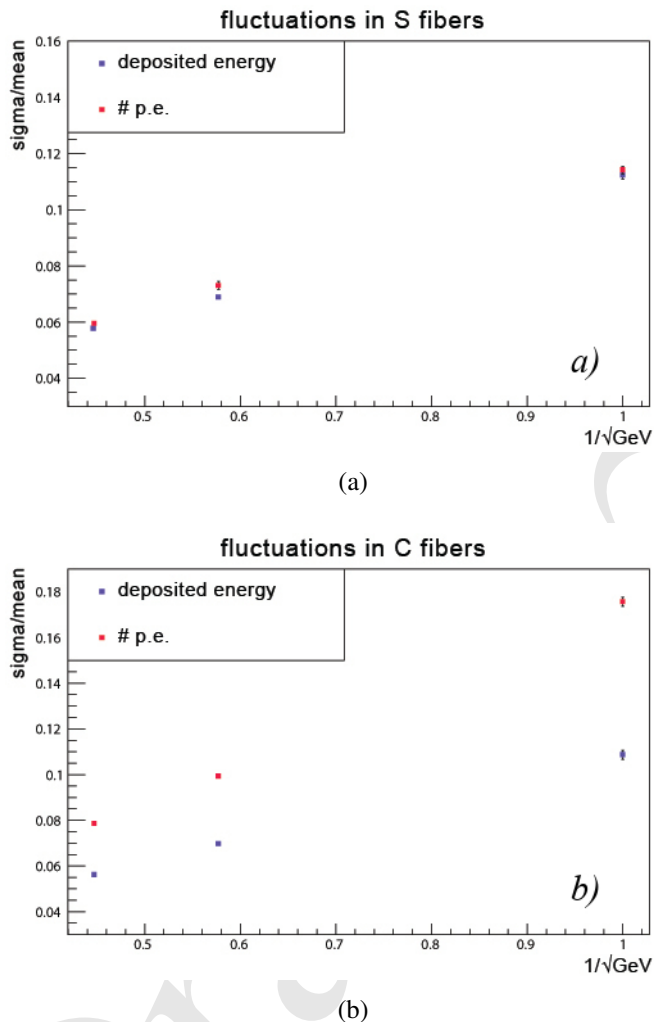


Figure 5.46: Relative fluctuation of the total signal detected in the (a) scintillating and (b) Čerenkov fibers, for both the energy deposit and the number of photoelectrons (MC simulations).

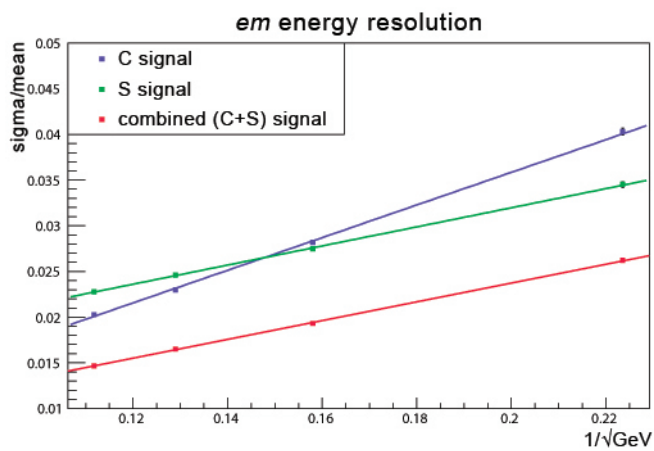


Figure 5.47: Relative resolution for em showers for the C and S signals, independently, and for the average of the two (MC simulations).

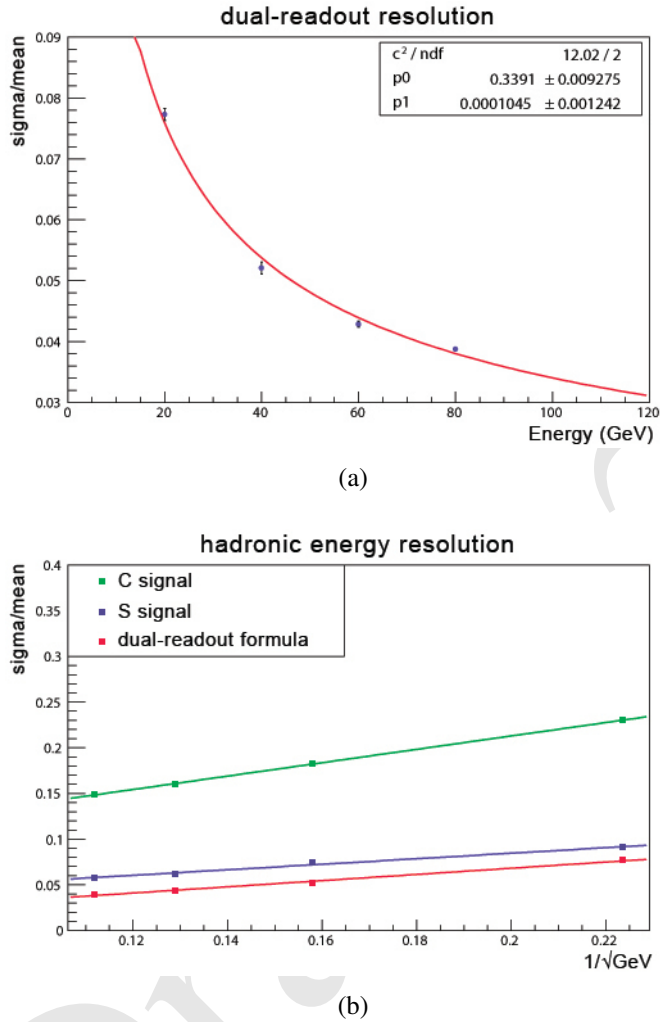


Figure 5.48: Monte Carlo simulations showing: (a) the relative hadronic resolution as reconstructed with the dual-readout formula; (b) the relative hadronic resolution independently for the C and S signals and for the dual-readout combination of the two.

<i>fibers used</i>	Fitted Gaussian hadronic energy resolution
S-fibers only	$\sigma/E = 30\%/\sqrt{E} \oplus 2.4\%$
C-fibers only	$\sigma/E = 73\%/\sqrt{E} \oplus 6.6\%$
Dual-readout S-fibers and C-fibers	$\sigma/E = 34\%/\sqrt{E} \oplus (\text{negligible})\%$

Table 5.5: Fit to the hadronic resolution (MC simulations)

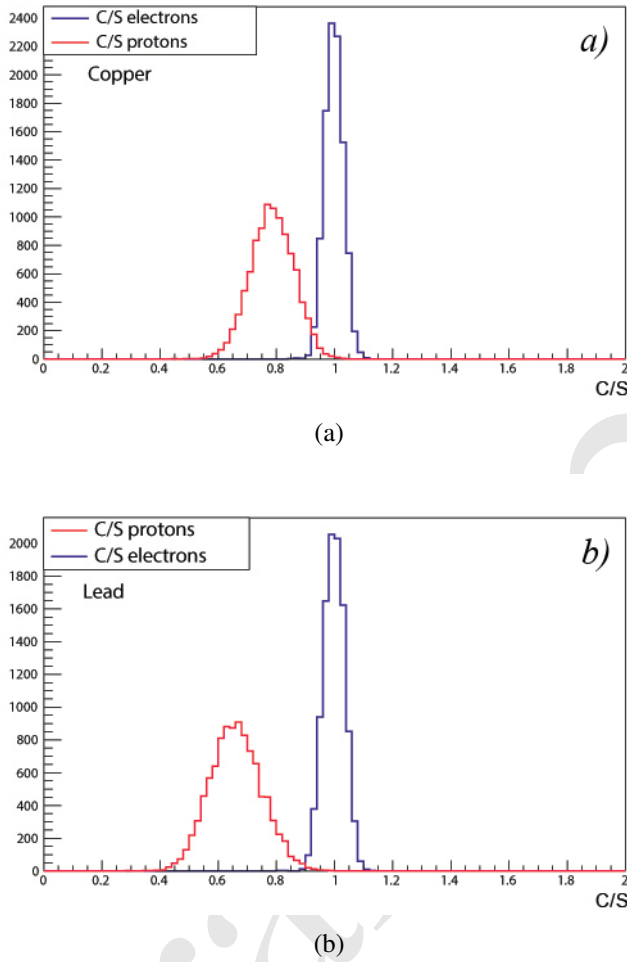


Figure 5.49: C/S ratio (MC simulations) for 80 GeV e^- and protons in (a) copper and (b) lead.

The large constant terms, for both S and C signals, are generated by the f_{em} correlated fluctuations. Simulations with lead absorber give equivalent but even slightly better results. The energy E in the plot (and in the expressions for the fitted resolutions) is the beam energy, corresponding in average to the energy reconstructed with the Equation 5.8 when the containment is properly accounted for (i.e., the reconstructed energy corresponds, in average, to the beam energy times the average containment). The fact that the experimental resolution was, so far, about a factor of two worse than simulations, is in our understanding, largely due to the small lateral size of the prototypes. In order to fully validate the MC predictions, an R&D program is being pursued.

The correlation of the invisible energy with all the other components of hadronic showers was also analyzed. Preliminary results seem to indicate that the most appropriate variable to account for the fluctuations of the invisible energy component is, by far, the f_{em} , with correlation coefficients of 90%, 92%, 94%, for copper, iron and lead respectively. The kinetic energy of the neutrons is predicted to be, at best, correlated at the 76% level. If confirmed, this would prove that compensation through neutron signal pickup or amplification will anyway give worse results than the dual-readout method [34].

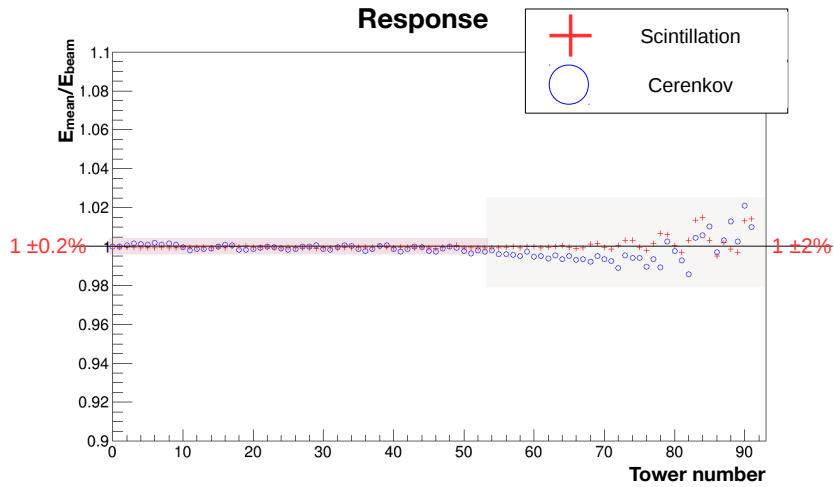


Figure 5.50: Ratio of reconstructed energy to the beam energy for 20 GeV e^- , as a function of the tower number, in the wedge geometry (MC simulations).

In terms of particle ID capabilities, in Figure 5.49 the C/S ratio is shown for 80 GeV e^- and protons in copper (a) and lead (b). For an electron efficiency of $\sim 98\%$, the rejection factor for protons is ~ 50 in copper and ~ 600 in lead. Of course, this is an ideal detector and in reality it is likely that the numbers will be worse. On the other hand, there are more variables that can be easily used in order to enhance the particle ID performance (namely the lateral shower profile, the starting time of the signal, the charge-to-amplitude ratio).

5.5.6.3 Projective geometry

Each tower, in the wedge geometry implementation, was exposed to 20 GeV electron beams, with an incident angle of $(1^\circ, 1.5^\circ)$, and the calibration constants calculated as the average deposit energy (in each tower) divided by the average C or S signal (of each tower). The response to an electron beam of the same energy is plotted in Figure 5.50. In the barrel region the response of all towers is within 0.2%, while in the forward the systematics are within 2%. All results were obtained with the quantum efficiency for the Čerenkov channel of each tower tuned to a light yield of ~ 30 pe/GeV, as estimated in the RD52 beam tests.

The performance of a few towers was studied with electron beams in the range of 10–100 GeV. Figure 5.51 shows the linearity and em energy resolutions for towers #0 and #45. In both cases, the combined S and C signal shows a resolution of $\sim 14\%/\sqrt{E}$ with a constant term of $\sim 0.1\%$ while the average response is constant within 0.4%.

The hadronic resolution was studied with pions in the same energy range. A χ value of 0.29, the value measured for the DREAM calorimeter [35], was used to reconstruct the shower energy with Eq. 5.8. In the linearity plots for both tower #0 and #45 in Figure 5.52, the C and S responses to single pions increase non-linearly as the pion beam energy increases. On the other hand, the value reconstructed with the dual-readout formula shows a constant response to single pions $\sim 8\%$ lower than that to electrons (the reason being the shower containment). This effect in the GEANT4 simulations is described in reference [36]. In addition, the energy resolution after the correction (shown in Figure 5.52 for towers #0 and #45) is $\sim 26\%/\sqrt{E}$, with a constant term of less than 1%.

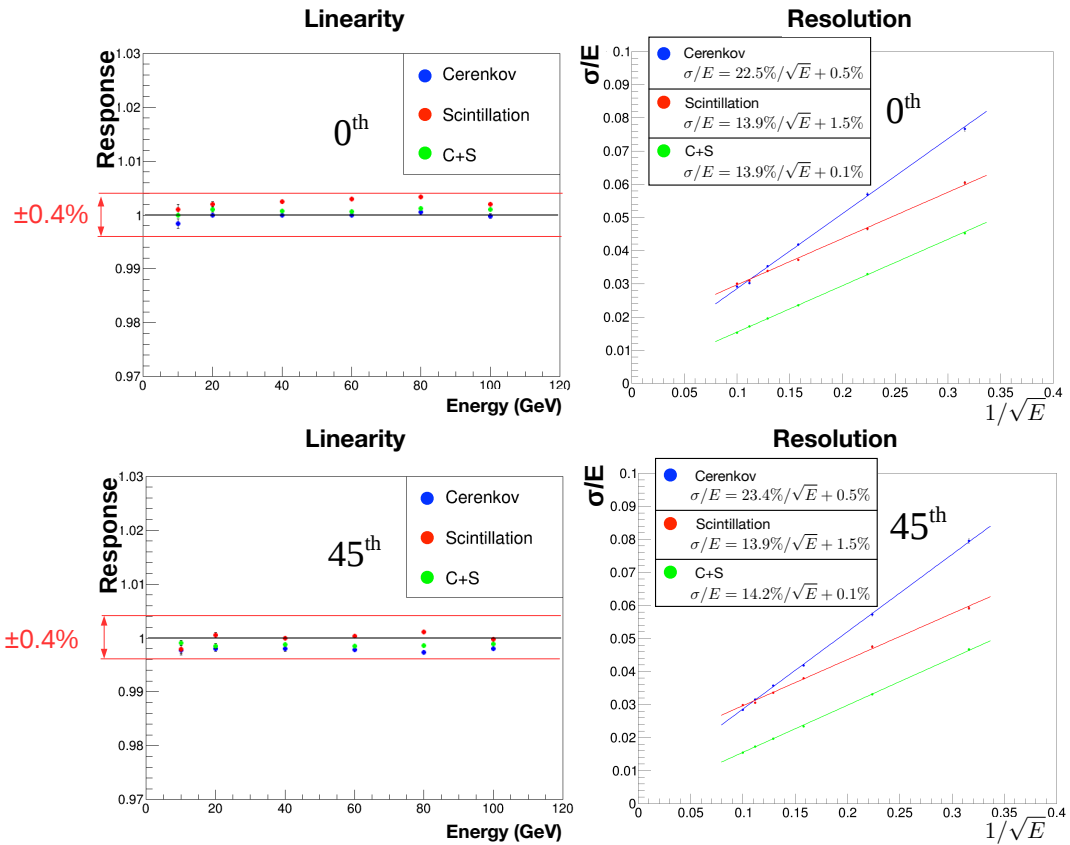


Figure 5.51: Linearity and *em* energy resolution for towers #0 (top) and #45 (bottom), in the wedge geometry (MC simulations).

These results support the statement that the hadronic energy resolution and the response to single hadrons should be constant (and appropriate) over the full barrel region. We may reasonably expect to obtain good performance over the entire 4π detector.

For the wing geometry, the results, at present, are limited to the *em* performance of few towers and the results (linearity and *em* resolution) substantially reproduce the wedge geometry ones.

5.5.6.4 Short term planning and open issues

The performance for single hadrons, jets and τ leptons has to be understood and the work has just started. For validation, the comparison with a prototype with a non-marginal hadronic shower containment, like the RD52 lead matrix, will be pursued.

For the *em* simulations, a program for the comparison with the 2017 RD52 data is ongoing. Some initial understanding of the absolute photoelectron scale for the Čerenkov light should be available in a very short time.

In general, light attenuation effects need also to be considered, for a $\sim 2 - 2.5m$ long fiber detector, that may introduce a constant term in the hadronic resolution as a function of the shower development point (late starting showers will give bigger and earlier signals).

The evaluation of advantages and disadvantages of filters (to dump the short attenuation-length components) and mirrors (to increase the number of photons that reach the photodetectors) may be relevant in this context.

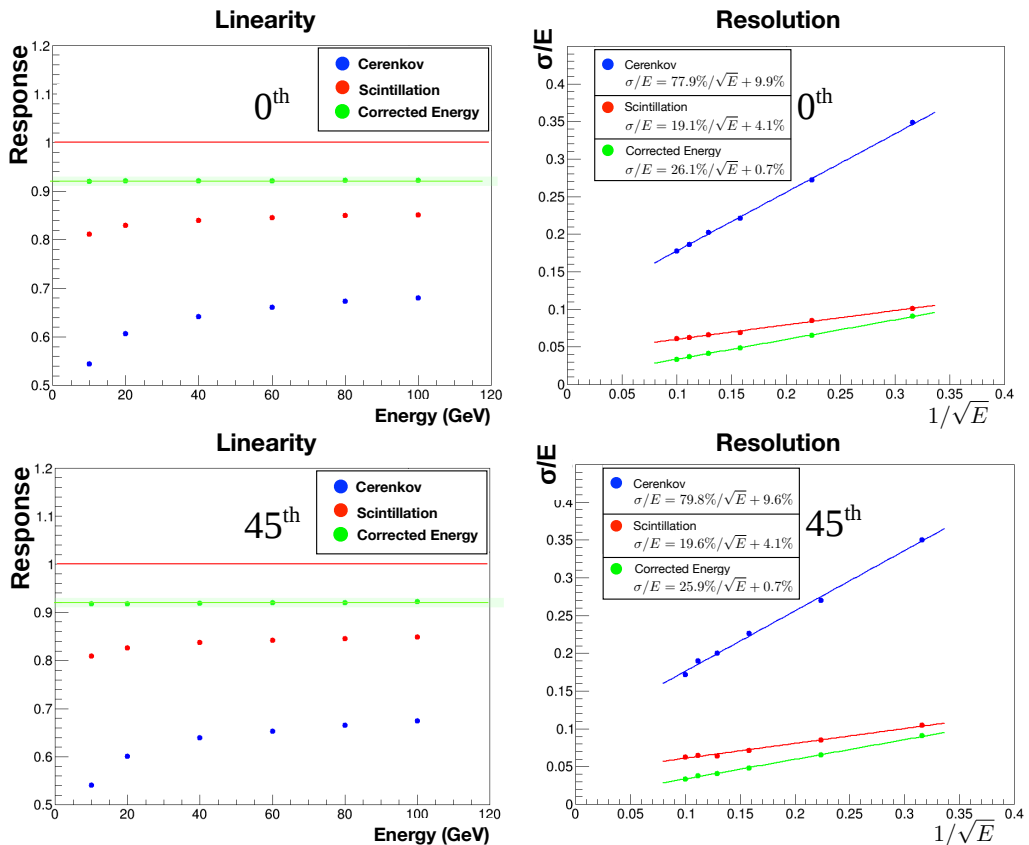


Figure 5.52: Linearity and energy resolution with pions, for towers #0 (top) and #45 (bottom), in the wedge geometry (MC simulations).

1 The effects of the integration of a preshower detector have to be evaluated and the
 2 e/π separation capability assessed and quantified, for both isolated particles and particles
 3 within jets.

4 **5.5.7 Final remarks on dual-readout calorimetry**

5 The 15-year-long experimental research program on dual-readout calorimetry of the DREAM/RD52
 6 collaboration has yielded a technology that is mature for application at CEPC. The results
 7 show that the parallel, independent, readout of scintillation and Čerenkov light, makes it
 8 possible to cancel the effects of the fluctuations of the electromagnetic fraction in hadronic
 9 showers, dominating the energy resolution of most (if not all) the calorimeters built so
 10 far. In conjunction with high-resolution em and hadronic energy measurements, excellent
 11 standalone particle-ID capability has been demonstrated as well.

12 Those results give increasing support to the conviction that a matrix of alternating
 13 scintillating and clear fibers, inserted in copper or lead strips and readout by Silicon Photo-
 14 Multipliers (SiPMs), will be able to provide performance more than adequate for the
 15 physics programs at the CEPC collider.

16 Nevertheless, there is a series of technical and physics issues that need to be solved,
 17 within the next 2-3 years in order to arrive up to the design of a realistic 4π detector. A
 18 non-exhaustive list must include:

- 19 1. The industrial machining of foils of copper, lead or some other material, with the
 20 required precision.
- 21 2. The development of a mechanical integration design.
- 22 3. The readout of the high granularity matrices of SiPM that, in order to be effective,
 23 will require the development of a dedicated Application Specific Integrated Circuit
 24 (ASIC). Possible aggregations of more fiber outputs into a single channel have also to
 25 be implemented and studied.
- 26 4. The need and, in case, the way for a longitudinally segmented calorimeter system
 27 and the performance of Particle Flow Algorithms to further boost the performance of
 28 dual-readout.
- 29 5. The development of a modular solution and the assessment, at all levels, of its perfor-
 30 mance, through beam tests of small modules and simulations. An intensive program
 31 of simulations is already ongoing for a dual-readout calorimeter system at CEPC. The
 32 response to single particles and jets is under study, in standalone configurations. The
 33 work for understanding the behavior of a 4π calorimeter integrated in a full detector,
 34 with a tracking and a magnetic system, has also started. This will include, as well, the
 35 evaluation of the combined performance with a preshower detector in front.

36 **References**

- 37 [1] J.-C. Brient, *Improving the jet reconstruction with the particle flow method: An*
 38 *introduction*, in *Calorimetry in Particle Physics*, pp. 445–451. World Scientific,
 39 2005.

- [2] CALICE Wikipage.
<https://twiki.cern.ch/twiki/bin/view/CALICE/>.
- [3] CALICE Collaboration, *Semiconductor sensors for the CALICE SiW EMC and study of the cross-talk between guard rings and pixels in the CALICE SiW prototype*, in *Proceedings CALOR'08*, vol. 160, p. 012067. 2009.
- [4] T. S. et al., *Performance study of SKIROC2/A ASIC for ILD Si-W ECAL*, in *proceeding of the International Conference on Calorimetry for the High Energy Frontier (CHEF 2017)*. 2017.
- [5] D. Grondin, J. Giraud, and J.-Y. Hostachy, *CALICE Si/W ECAL: Endcap structures and cooling system*, in *Proceedings, International Workshop on Future Linear Colliders 2016 (LCWS2016): Morioka, Iwate, Japan, December 05-09, 2016*. 2017. arXiv:1702.03770 [physics.ins-det].
<http://inspirehep.net/record/1513187/files/arXiv:1702.03770.pdf>.
- [6] V. Boudry, *SiW ECAL R&D*, in *Fourth International Workshop on Future High Energy Circular Colliders (CEPC2014)*. 2014.
<http://indico.ihep.ac.cn/event/4338/session/2/contribution/35/material/slides/0.pdf>.
- [7] CALICE Collaboration, *Design and Electronics Commissioning of the Physics Prototype of a Si-W Electromagnetic Calorimeter for the International Linear Collider*, *JINST* **3** (2008) P08001, arXiv:0805.4833 [physics.ins-det].
- [8] C. Adloff et al., *Response of the CALICE Si-W electromagnetic calorimeter physics prototype to electrons*, *Nucl. Instrum. Meth. A* **608** (2009) 372–383.
- [9] CALICE Collaboration, *A large scale prototype for a SiW electromagnetic calorimeter for a future linear collider*, in *Proceedings of International Workshop on Future Linear Colliders (LCWS11) 26-30 Sep 2011. Granada, Spain*. 2012. arXiv:1203.0249 [physics.ins-det].
- [10] V. Balagura et al., *SiW ECAL for future e^+e^- collider*, in *Proceedings, International Conference on Instrumentation for Colliding Beam Physics (INSTR17): Novosibirsk, Russia*. 2017. arXiv:1705.10838 [physics.ins-det].
<http://inspirehep.net/record/1601898/files/arXiv:1705.10838.pdf>.
- [11] CALICE Collaboration, *Latest R&D news and beam test performance of the highly granular SiW-ECAL technological prototype for the ILC*, *JINST* **13** (2018) no. 02, C02038, arXiv:Conception and construction of a technological prototype of a high-granularity digital hadronic calorimeter1802.08806 [physics.ins-det].
- [12] G. Baulieu et al., *Construction and commissioning of a technological prototype of a high-granularity semi-digital hadronic calorimeter*, *JINST* **10** (2015) no. 10, P10039, arXiv:1506.05316 [physics.ins-det].

- 1 [13] M. Bedjidian et al., *Performance of Glass Resistive Plate Chambers for a high*
 2 *granularity semi-digital calorimeter*, *JINST* **6** (2011) P02001,
 3 arXiv:1011.5969 [physics.ins-det].
- 4 [14] CALICE Collaboration, *First results of the CALICE SDHCAL technological*
 5 *prototype*, *JINST* **11** (2016) no. 04, P04001, arXiv:1602.02276
 6 [physics.ins-det].
- 7 [15] CALICE Collaboration, *Separation of nearby hadronic showers in the CALICE*
 8 *SDHCAL prototype detector using ArborPFA*, CAN-054 (2016) .
- 9 [16] CALICE Collaboration, *Resistive Plate Chamber Digitization in a Hadronic*
 10 *Shower Environment*, *JINST* **11** (2016) no. 06, P06014, arXiv:1604.04550
 11 [physics.ins-det].
- 12 [17] L. Caponetto, C. Combaret, C. de la Taille, F. Dulucq, R. Kieffer, I. Laktineh,
 13 N. Lumb, L. Mirabito, and N. Seguin-Moreau, *First test of a power-pulsed*
 14 *electronics system on a GReP detector in a 3-Tesla magnetic field*, *JINST* **7** (2012)
 15 P04009, arXiv:1111.5630 [physics.ins-det].
- 16 [18] F. Sefkow, *Prototype tests for a highly granular scintillator-based hadron*
 17 *calorimeter*, CHEF2017. <https://indico.cern.ch/event/629521/contributions/2702990/>.
- 19 [19] CALICE Collaboration, *A design of scintillator tiles read out by surface-mounted*
 20 *SiPMs for a future hadron calorimeter*, (NSS/MIC), IEEE (2014) 1–4.
- 21 [20] CALICE Collaboration, *hadronic energy resolution of a highly granular*
 22 *scintillator-steel hadron calorimeter using software compensation techniques*,
 23 *Journal of Instrumentation* **7(09)** (2012) 1–23.
- 24 [21] K. Krueger, *Software compensation and particle flow*, CHEF2017. <https://indico.cern.ch/event/629521/contributions/2703038/>.
- 26 [22] M. Bouchel et al., *Second generation Front-end chip for H-Cal SiPM readout*
 27 :SPIROC, ILC website. https://agenda.linearcollider.org/event/1354/contributions/2542/attachments/1826/3054/SPIROC_presentation_13_02_2007.pdf.
- 30 [23] R. Wigmans, *Calorimetry, Energy Measurement in Particle Physics*, vol. 168
 31 (second edition). International Series of Monographs on Physics, Oxford University
 32 Press, 2017.
- 33 [24] C. Patrignani and P. D. Group, *Review of Particle Physics*, Chinese Physics C **40**
 34 (2016) no. 10, 100001.
 35 <http://stacks.iop.org/1674-1137/40/i=10/a=100001>.
- 36 [25] D. E. Groom, *Energy flow in a hadronic cascade: Application to hadron*
 37 *calorimetry*, *Nucl. Instrum. Methods A* **572** (2007) 633–653.
- 38 [26] D. E. Groom, *Erratum to "Energy flow in a hadronic cascade: Application to*
 39 *hadron calorimetry" [Nucl. Instr. and Meth. A 572 (2007) 633-653]*, *Nucl. Instrum.*
 40 *Methods A* **593** (2008) 638.

- 1 [27] N. Akchurin et al., *Particle identification in the longitudinally unsegmented RD52*
2 *calorimeter*, Nucl. Instrum. Methods A **735** (2014) 120.
- 3 [28] N. Akchurin et al., *The electromagnetic performance of the RD52 fiber calorimeter*,
4 Nucl. Instrum. Methods A **735** (2014) 130.
- 5 [29] N. Akchurin et al., *Lessons from Monte Carlo simulations of the performance of a*
6 *dual-readout fiber calorimeter*, Nucl. Instrum. Methods A **762** (2014) 100.
- 7 [30] A. Cardini et al., *The small-angle performance of a dual-readout fiber calorimeter*,
8 Nucl. Instrum. Methods A **808** (2016) 41.
- 9 [31] R. Wigmans, *New results from the RD52 project*, Nucl. Instrum. Methods A **824**
10 (2016) 721.
- 11 [32] S. Lee et al., *Hadron detection with a dual-readout fiber calorimeter*, Nucl.
12 Instrum. Methods A **866** (2017) 76.
- 13 [33] *Letter of Intent from the Fourth Detector ("4th") Collaboration at the International*
14 *Linear Collider*, <http://www.4thconcept.org/4{L}o{I}.pdf>.
- 15 [34] S. Lee, M. Livan, and R. Wigmans, *On the limits of the hadronic energy resolution*
16 *of calorimeters*, Nucl. Instrum. Methods A **882** (2018) 148.
- 17 [35] N. Akchurin et al., *Hadron and jet detection with a dual-readout calorimeter*, Nucl.
18 Instrum. Methods A **537** (2005) 537.
- 19 [36] N. Akchurin et al., *Lessons from Monte Carlo simulations of the performance of a*
20 *dual-readout fiber calorimeter*, Nucl. Instrum. Methods A **762** (2014) 100.

CHAPTER 6

DETECTOR MAGNET SYSTEM

¹ The CEPC detector magnet is an iron-yoke-based solenoid to provide an axial magnetic
² field of 3 Tesla at the interaction point. A room temperature bore is required with 6.8 m in
³ diameter and 8.3 m in length. This chapter describes the conceptual design of magnet, in-
⁴ cluding the design of field distribution, solenoid superconducting coil, cryogenics, quench
⁵ protection, power supply and the yoke. In the end of this chapter, the R&D Section 6.5
⁶ brings up other concept options and some reach projects. The compensating magnets
⁷ designed to minimize the disturbance from the detector solenoid on the incoming and out-
⁸ going beams are briefly discussed in Section 9, and in more detail in the Accelerator CDR
⁹ Chapter 9.2 [1].

¹⁰ **6.1 Magnetic field design**

¹¹ The CEPC detector magnet follows the same design concepts of the CMS and ILD detec-
¹² tor magnets [2, 3]. The aluminium superconductor stabilisation with indirect LHe cooling
¹³ will be adopted. The self-supporting winding turn with aluminium alloy reinforcement
¹⁴ is suitable for the CEPC magnet. The conductor with reinforcement wrapped around the
¹⁵ pure aluminium as a box configuration is chosen for the magnet design and is manufac-
¹⁶ tured in the R&D project.

¹⁷ **6.1.1 Main parameters**

¹⁸ The CEPC magnet system requires a 3 T central field. The superconducting coil is de-
¹⁹ signed with 5 modules wound with 4 layers. The three middle coil modules and the two
²⁰ end coil modules are wound with 78 and 44 turns, respectively. The operating current is

15,779 A for each turn. The geometrical layout of magnet are shown in Figure 6.1. The main magnetic and geometrical design parameters are given in Table 6.1.

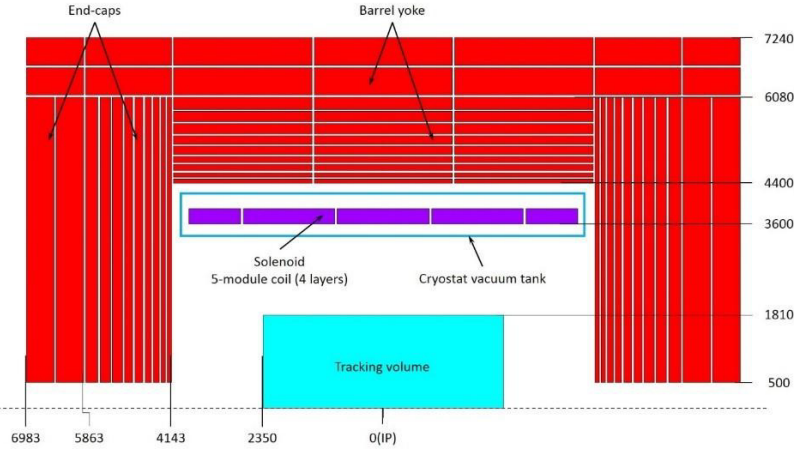


Figure 6.1: the geometrical layout of CEPC detector magnet. The simulation model consists of the superconducting coil and the iron yoke with a barrel yoke and two endcap yokes. The superconducting coil is designed with 5 modules wound with 4 layers. Eleven iron plates with 4 cm gaps form both the barrel and endcap yokes.

The solenoid central field (T)	3	Working current (A)	15779
Maximum field on conductor (T)	3.4	Total ampere-turns of the solenoid (MAT)	20.3
Coil inner radius (mm)	3600	Inductance (H)	10.5
Coil outer radius (mm)	3828	Stored energy (GJ)	1.3
Coil length (mm)	7445	Cable length (km)	30.1

Table 6.1: Main parameters of the CEPC superconducting coil

6.1.2 Magnetic field calculation

The magnetic field simulation has been calculated in 2D finite element analysis (FEA) model, with fine structure of the barrel yokes and endcap yokes. The axial magnetic force is maximum at full current; there is no iron saturation effect. The magnetic stray fields outside the iron return yokes of the detectors need to meet the requirements of the electronics, the accelerator components and the interventions for maintenance. Figure 6.2 shows the magnetic field contour of the magnet. The maximum field on NbTi cable is 3.5 Tesla. Figure 6.3 shows the stray field map of the magnet, going respectively from 50 to 250 Gauss on the center plane (beam orbit plane). The edge of 50 Gauss stray field is at 13.6 m from the beam axis and axial direction 15.8 m from the IP.

6.2 Superconducting coil system

The CEPC solenoid conductor baseline design is the box configuration, based on the self-supporting conductor design of CMS detector magnet, composed of NbTi Rutherford cable, the pure aluminum stabilizer and aluminum alloy reinforcement. The CMS conductor is fabricated by ebeam welding aluminium alloy to the coextruded high purity

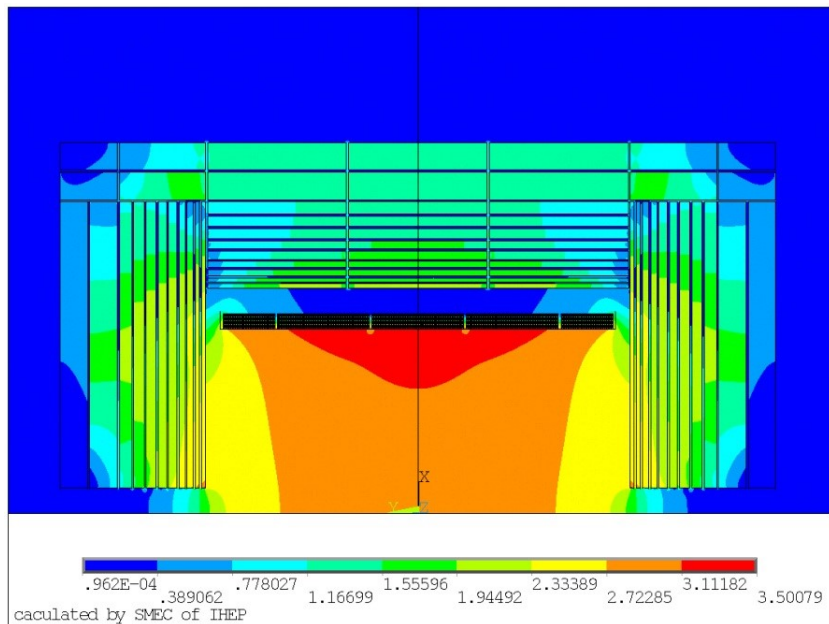


Figure 6.2: Field map of magnet in 2D FEA model. The magnetic field at IP is 3.0 T. The maximum field on superconducting cable is 3.5 T.

1 Al/superconducting cable insert. The CEPC conductor is wrapped around purity alumin-
 2 minium and aluminium alloy reinforcement with coextrusion technology. The configura-
 3 tion is shown in Figure 6.4 The Rutherford cable contains 32 NbTi strands. All magnet
 4 finite element analysis has been with this conductor with overall dimensions of 22 mm ×
 5 56 mm.

6 The coil is wound by inner winding technique on the support aluminum-alloy cylin-
 7 der, as an external supporting mandrel. The support cylinder also takes away the heat
 8 energy induced by quench. The superconducting coil in the cryostat requires cooling
 9 at liquid helium temperature. The total weight of cold mass is about 120 t. The cold
 10 mass will be indirectly cooled by a network of liquid helium (LHe) tubes. These tubes are
 11 welded to the support cylinder. The indirect cooling method is designed in a thermosiphon
 12 process. The siphon cooling circulation loop operates under a suitable filling amount 50%
 13 to 85% with high efficient heat transfer properties. In addition, it is optimized to mini-
 14 mize the temperature difference between the magnet hot spot and the cooling source. The
 15 thermosiphon cooling circuit of the coil is shown in Figure 6.5.

16 **6.3 Ancillaries (cryogenics, power supply, quench protection)**

17 **6.3.1 Cryogenics system**

18 A cryoplant with a capacity of 750W @ 4.5 K is under design for the operation of the su-
 19 perconducting facility. The cryogenic system provides the liquefaction and refrigeration
 20 at 4.5 K in varying proportions depending on the operating modes (shown in Figure 6.5),
 21 which include cooling down from 300K to 4.5K, normal operation, energy dump, warm-
 22 ing up. It also be able to extract the dynamic losses during the various magnet ramps
 23 or discharges. Helium liquefier is in a position close to the magnet compatible with the
 24 fringing field and the maintenance activities. It supplies the liquid helium to the coils and

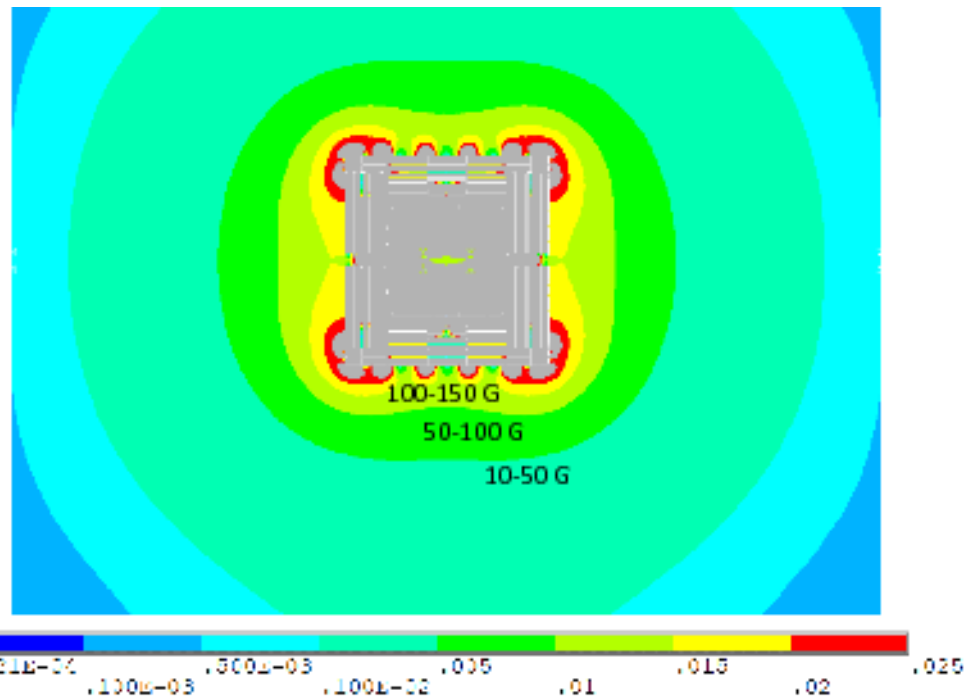


Figure 6.3: The stray field map of the magnet, going respectively from 50 to 250 Gauss on the center plane (beam orbit plane). The edge of 50 Gauss stray field is at 13.6 m from the beam axis and axial direction 15.8 m from the IP.

1 taking the helium gas return back from the coils and the power lines. The proximity cryo-
2 genics is on top of the magnet for the thermosiphon refrigerating mode. The cryogenics
3 include three parts listed as follows.

4 1. The Dewar containing a spare volume of LHe to keep the magnet at nominal field
5 in case of temporary disruption of LHe supply, and to allow the ramp down to zero field
6 keeping the magnet in superconducting state;

7 2. The valve box;

8 3. The phase separator to feed the thermosiphon of the solenoid. Depending on the
9 position of the cold box, a flexible vacuum line is used to connect the liquefier to the
10 proximity cryogenics.

11 In addition, the refrigerator is dimensioned for the acceptable cool-down time. More-
12 over, loss during ramping the magnet up and down and the loss in the current leads will
13 be taken into account for the refrigeration plant with some safety margin.

14 6.3.2 Power supply

15 A low ripple DC current-stabilized power supply, with low output voltage and high output
16 current, is requested for CEPC detector magnet. The power supply is expected to have a
17 free-wheel diode system and to be cooled with demineralized water. The main circuit of a
18 standard power supply includes 12 pulse diode rectifiers and 4 IGBT chopper units with a
19 switching frequency of 10 kHz.

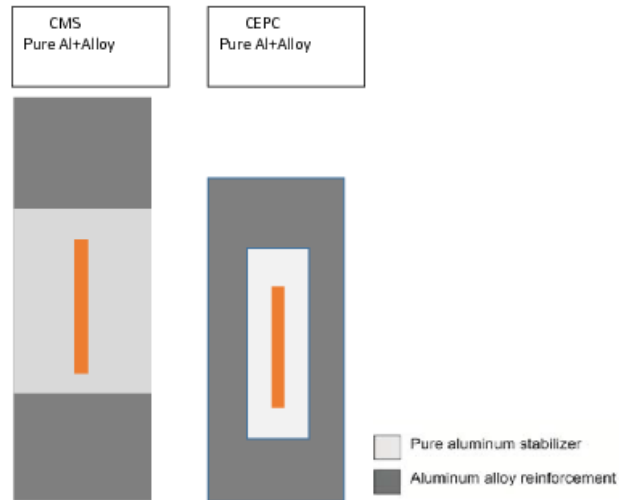


Figure 6.4: The baseline design for the CEPC solenoid conductor. The conductor is wrapped around purity aluminium stabilizer and aluminium alloy reinforcement with coextrusion technology. The Rutherford cable contains 32 NbTi strands. The overall dimensions of this conductor are 22 mm × 56 mm.

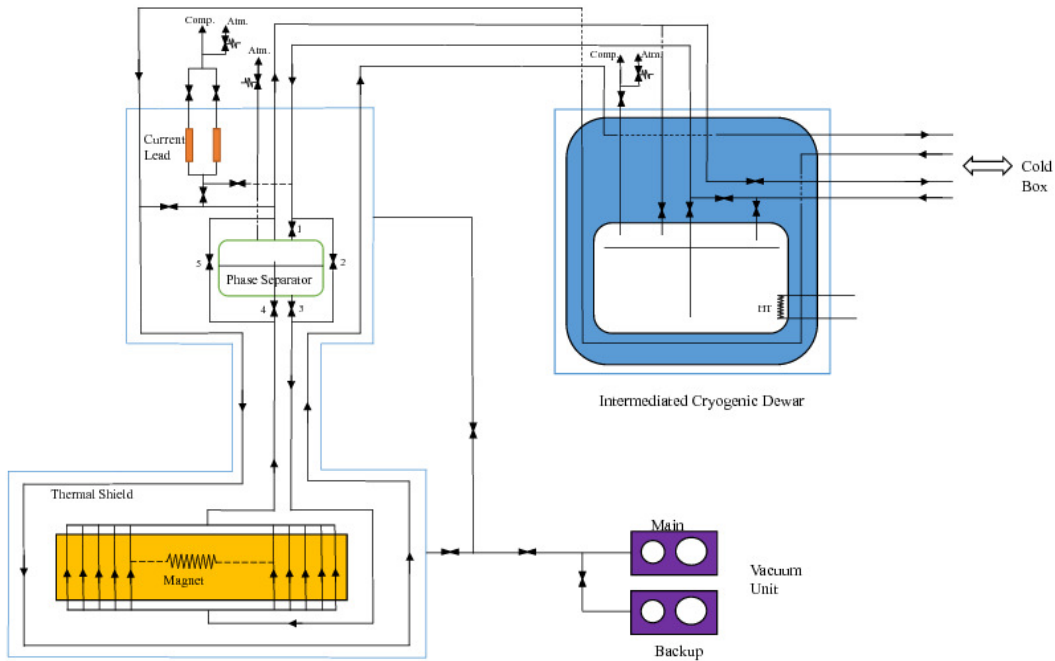


Figure 6.5: The thermosiphon cooling circuit of the superconducting coil.

1 6.3.3 Quench protection and instrumentation

- 2 Selected voltage signals from the CEPC detector magnet coil and current leads are monitored by an FPGA board for quench detection. If a quench happened, the power supply
- 3 is switched off and a dump resistor is switched into the electrical circuit, the huge stored
- 4 energy will be extracted mainly by the dump resistor and partially by the coil itself.
- 5

6.4 Iron yoke design

The iron yoke serves as the magnetic flux return and the main mechanical structure of the sub-detectors. Therefore high permeability material with high mechanical strength is required for the yoke material in account of mechanical performance and magnetic field. The gaps between yokes provide room for the muon detector, data cables, cooling pipes, gas pipes and etc. through the yoke. The yoke is divided into two main components, one cylindrical barrel yoke and two endcap yokes. The total weight of the yoke assembly is about 10,000 tons. We are studying on the yoke weight reducing. An economic solution for the yoke weight reducing has not yet been found.

The barrel yoke is a dodecagonal shape structure with a length of 8,206 mm (Figure 6.6). The outer diameter of the dodecagon and the inner diameter are 14,480 mm and 8,800 mm. The barrel yoke is subdivided along the beam axis into 3 rings, with 11 layers in each ring. Each ring of the barrel yoke is composed of 12 segments. 40 mm gap is designed between the rings and the layers for placing the muon detector and the electronics cables and services. From the inner to the outer, the layer thicknesses are 80 mm, 80 mm, 120 mm, 120 mm, 160 mm, 160 mm, 200 mm, 200 mm, 240 mm, 540 mm, 540 mm, respectively.

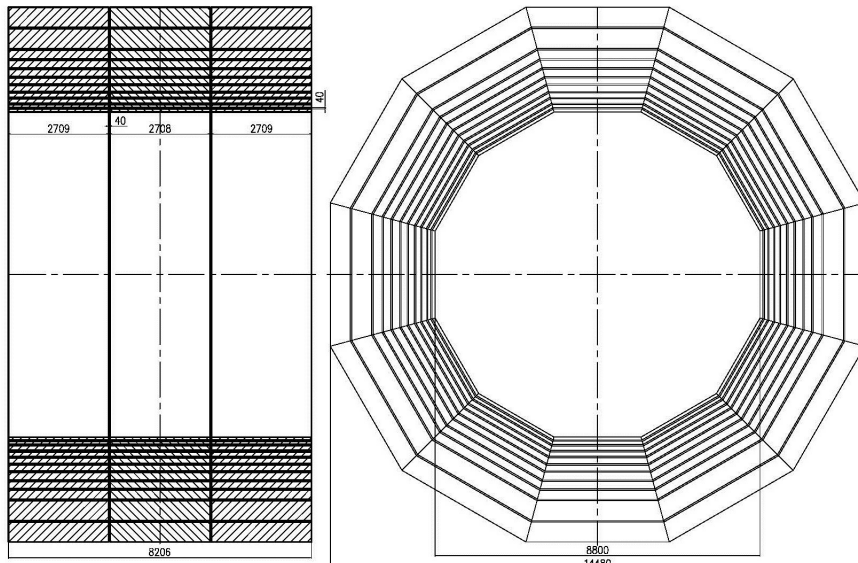


Figure 6.6: The barrel yoke of CEPC detector magnet. The barrel yoke is a dodecagonal shape structure with a length of 8,206 mm. The outer diameter of the dodecagon and the inner diameter are 14,480 mm and 8,800 mm. The barrel yoke is subdivided along the beam axis into 3 rings, with 11 layers in each ring. Each ring of the barrel yoke is composed of 12 segments. 40 mm gap is designed between the rings and the layers for placing the muon detector and the electronics cables and services. From the inner to the outer, the layer thicknesses are 80 mm, 80 mm, 120 mm, 120 mm, 160 mm, 160 mm, 200 mm, 200 mm, 240 mm, 540 mm, 540 mm, respectively.

The endcap yokes are designed to dodecagonal structure with the out diameter of 14,480 mm. Each endcap yoke will consist of 11 layers (Figure 6.7). Each endcap yoke is composed of 12 segments. The layer thicknesses are 80 mm, 80 mm, 120 mm, 120 mm, 160 mm, 160 mm, 200 mm, 200 mm, 240 mm, 540 mm, 540 mm, respectively.

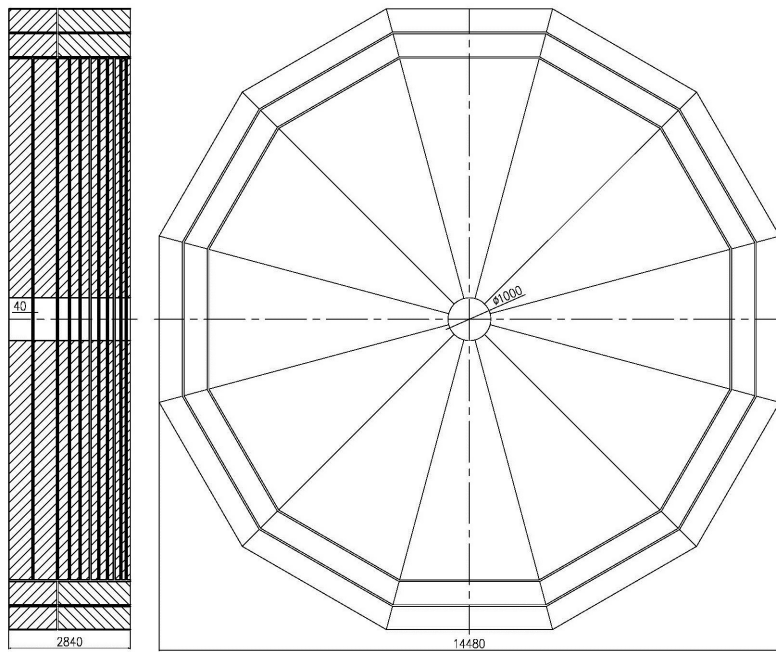


Figure 6.7: The endcap yokes of CEPC detector magnet. The endcap yokes are designed to dodecagonal structure with the out diameter of 14,480 mm. Each endcap yoke will consist of 11 layers (Fig. 6.4). Each endcap yoke is composed of 12 segments. The layer thicknesses are 80 mm, 80 mm, 120 mm, 120 mm, 160 mm, 160 mm, 200 mm, 200 mm, 240 mm, 540 mm, 540 mm, respectively.

1 6.5 Alternative designs and R&D

2 6.5.1 LTS solenoid for the IDEA detector

3 A "thin" 6 m long solenoid with an inner bore of 2.1 m radius and a field of 2 Tesla
 4 is a key element of the IDEA detector, where the calorimeter is located outside of the
 5 solenoid, allowing the maximum possible volume for tracking, but requiring maximum
 6 transparency. By "thin" we mean that the magnet should give minimal perturbation to the
 7 calorimetric measurements. The current design is mostly derived by scaling the present
 8 2 Tesla solenoid of the ATLAS detector and uses a self-supporting aluminum stabilized
 9 NbTi conductor. Preliminary engineering studies [4, 5] indicate that the coil and the cryo-
 10 stat can fit in a total thickness of 30 cm using current technology; for 0.46 radiation lengths
 11 of the coil and 0.28 radiation lengths of the cryostat or 0.16 interaction lengths at normal
 12 incidence. Up to 20% additional reduction in the overall thickness may be achieved with
 13 more R&D and engineering.

14 6.5.2 HTS solenoid for IDEA detector

15 A large HTS solenoid is being studied for the IDEA detector. The HTS solenoid is sup-
 16 posed to use YBCO stacked-tape cable as the conductor. The radiation length of single
 17 YBCO tape coated with 10 μm copper is about $0.004 X_0$. Each tape carries 700 A at 20 K.
 18 35 YBCO tapes stacked together allows 24.5 kA. These tapes are embedded in 5 mm pure
 19 aluminium. The radiation length of this YBCO stacked-tape cable is estimated to be 0.2
 20 X_0 . The radiation length of HTS coil will be less than half of the current LTS coil de-
 21 sign. If the operation temperature of the cold mass is raised to 20 K, the heat conductivity

parameters of all components are improved. In addition, the electricity consumption of cooling station is much lower than that at 4.2 K. Therefore, the YBCO stacked-tape cable and the cryogenics are brought into R&D.

6.5.3 Dual solenoid design

The dual solenoid design is presented for a conceptual option for CEPC detector magnet, which contains two series connected superconducting solenoids carrying the opposite direction current, based on FCC twin solenoid [6]. The main solenoid provides central field within the room temperature bore. The outer solenoid provides the stray field shielding and a magnetic field between the two solenoids to facilitate muon tracking. The main advantage of this dual solenoid is that the system becomes comparatively light-weight and cost saving without iron yoke. The sketch is shown in Figure 6.8.

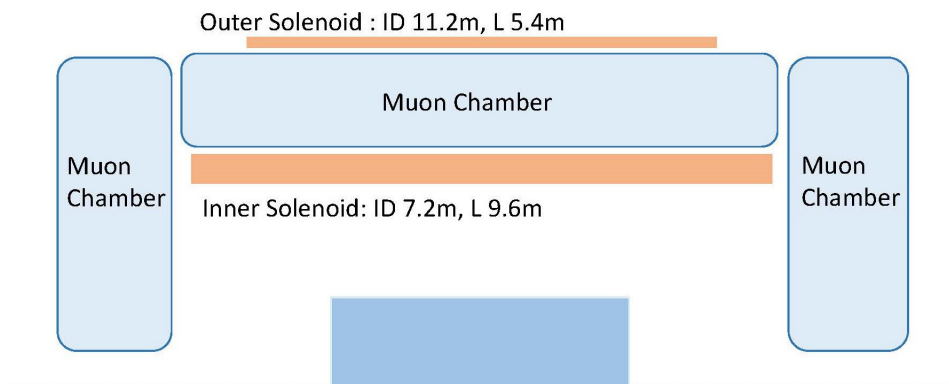


Figure 6.8: The sketch of dual solenoid design. The main solenoid provides central field within the room temperature bore. The outer solenoid provides the stray field shielding and a magnetic field between the two solenoids to facilitate muon tracking. The inner diameter of the main solenoid is 7.2 m. The inner diameter of the outer solenoid is 11.2 m.

6.5.4 Superconducting conductor

The coil is simulated with an elasto-plastic 2D FE model. Mechanical analysis requires the experimental material properties of all conductor components. We have developed a 10 m long NbTi Rutherford cable embedded inside stabilizer which provides I_c 5 kA at 4 T background magnetic field. Meanwhile we measured the material properties and the tensile stress of 10 m cable. Longer conductor with higher I_c 15 kA at 4 T background is ongoing.

6.5.5 Thermosyphon circuit

Thermosyphon principle is used to cool CEPC detector superconducting magnet by the U-shaped circuit configuration carrying LHe on the outer surfaces of the coil supporting cylinders. The thermosyphon circuit consists of helium phase separator located in an elevated position and the cooling tubes. In order to study the phase transition process of helium in the circuit, the changes of the temperature distribution and the density distri-

1 bution over the time, a 1:10 scale thermosyphon circuit will be established for simulation
2 and experiment.

3 **References**

- 4 [1] The CEPC-SPPC Study Group, *CEPC-SPPC Conceptual Design Report, Volume I -*
5 *Accelerator*, IHEP, Beijing, China, Rep. IHEP-CEPC-DR-2018-01 (2018) .
- 6 [2] H. Abramowicz et al., *The International Linear Collider Technical Design Report -*
7 *Volume 4: Detectors*, arXiv:1306.6329 [physics.ins-det].
- 8 [3] C. Collaboration, *The CMS magnet project: Technical Design Report*, CERN/LHCC,
9 1997.
- 10 [4] M. Caccia, *An International Detector for Electron-Positron Accelerator(IDEA)*,
11 Workshop on Circular Electron-Positron Colliders. Roma, May 24-26th, 2018.
- 12 [5] H. ten Kate, *Ultra-light 2T/4m bore Detector Solenoid for FCCee*, FCC Annual
13 meeting. Amsterdam, April 9-14th, 2018.
- 14 [6] M. Mentink, A. Dudarev, H. F. P. Da Silva, C. P. Berriaud, G. Rolando, R. Pots,
15 B. Cure, A. Gaddi, V. Klyukhin, H. Gerwig, et al., *Design of a 56-GJ Twin solenoid*
16 *and dipoles detector magnet system for the future circular collider*, IEEE
17 Transactions on Applied Superconductivity **26** (2016) no. 3, 1–6.

Draft-V2.0

CHAPTER 7

MUON SYSTEM

1 The muon system for a CEPC detector is designed to identify and measure muons, and
2 will be located within the solenoid flux return yoke of the whole spectrometer. Two de-
3 tector concepts are envisaged for the CEPC collider and they will likely employ different
4 muon systems. A common requirement for the muon detectors will be to identify muons
5 with very high efficiency ($\geq 95\%$) and high purity, over the largest possible solid angle
6 and down to low p_T values (≥ 3 GeV). A standalone muon momentum resolution from
7 the muon detector could be required, translating in a good position resolution along the
8 muon track which would add robustness and redundancy to the whole detector design. In
9 particular the muon system will significantly help in identifying muon produced within
10 jets, for example from b decays.

11 The muon system plays an important role in measuring physics processes involving
12 muon final states, e.g. $e^+e^- \rightarrow ZH$ with $Z \rightarrow e^+e^-$ or $\mu^+\mu^-$ and also for studying long-
13 lived particles that would decay far from the primary vertex but still within the detector.
14 In addition, the muon system compensates for leaking energetic showers and late show-
15 ering pions from the calorimeters, which could help to improve the relative jet energy
16 resolution[1].

17 In this chapter the baseline muon system design is described and then two possible
18 technologies for realizing the muon detector are presented, specifically the Resistive Plate
19 Chamber (RPC) and an innovative type of Micro Pattern Gas detector (MPGD), the μ -
20 RWELL detector. The main difference between the two technologies lies in the position
21 resolution and the cost. More layers of RPC detectors are needed to achieve a good mo-
22 mentum resolution on the muon tracks with respect to the μ -RWELL case, where 3–4
23 layers would be sufficient. In terms of rate capability both technologies are more than
24 adequate for the CEPC environment. If the requirement of a standalone muon momentum

resolution from the muon detector is relaxed, the number of layers of the RPC solution could be greatly reduced. Other gas detectors are also being considered as possible options, such as Gas Electron Multiplier (GEM), MicroMegas and Monitored Drift Tubes (MDT), although they are not described here.

7.1 Baseline Design

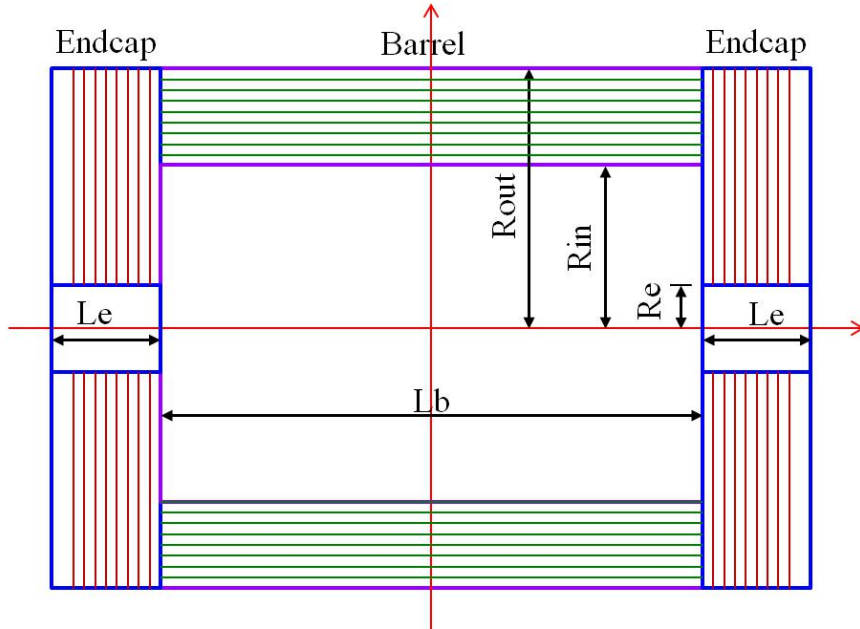


Figure 7.1: The basic layout of the muon system, subdivided in a barrel closed by two endcaps. L_b is the length of the barrel and L_e is the length of each endcap. R_{out} (R_{in}) is the outer (inner) radius of the barrel. R_e is the inner radius of each endcap.

The CEPC muon system is the outermost component of the whole detector. It is divided into barrel and endcaps, as shown in Figure 7.1. Both the barrel and endcaps consist of azimuthal segmented modules. The segmentation is constrained by the maximum sizes of the module and sensitive unit (more segments are required for a larger detector), do-decagon segmentation is selected for the baseline design of the CEPC muon system. All baseline design parameters are summarized in Table 7.1. These parameters will be further optimized together with the inner detectors, in particular the ECAL and the HCAL.

The number of sensitive layers and the thickness of the absorber (in this case iron) are two critical parameters for the muon system. For the baseline design, the total thickness of iron absorber is chosen to be 6.7λ (the nuclear interaction length of iron) distributed in 8 layers. The depth of the muon system should be sufficient to effectively reduce the pion contamination, while providing muon tracking information together with the inner tracker that can be further combined with, or independent of, the calorimeters. Gaps of 4 cm between neighboring iron layers give adequate space for installing 8 layers of sensitive detectors.

These critical parameters have been studied using a simplified simulation. Muons need a momentum larger than 2 GeV to reach the first layer of the muon chambers, and

Parameter	Possible range	Baseline
Lb/2 [m]	3.6 – 5.6	4.1
Rin [m]	3.5 – 5.0	4.4
Rout [m]	5.5 – 7.2	7.2
Le [m]	2.0 – 3.0	2.8
Re [m]	0.6 – 1.0	0.5
Segmentation in ϕ	8/10/12	12
Number of layers	3 – 10	8
Total thickness of iron	6 – 10λ ($\lambda = 16.77$ cm)	6.7λ (112 cm) (8/8/12/12/16/16/20/20) cm
Solid angle coverage	$(0.94 - 0.98) \times 4\pi$	0.98
Position resolution [cm]	$\frac{\sigma_{r\phi}}{\sigma_z} : 1.5 - 2.5$ $\sigma_z : 1 - 2$	2 1.5
Time resolution [ns]	< 10	1 – 2
Detection efficiency ($P_\mu > 5$ GeV)	92% – 99%	> 95%
Fake($\pi \rightarrow \mu$)@30GeV	0.5% – 3%	< 1%
Rate capability [Hz/cm ²]	50 – 100	~60
Technology	RPC μ RWell	RPC (super module, 1 layer readout, 2 layers of RPC)
Total area [m ²]	Barrel Endcap Total	~4450 ~4150 ~8600

Table 7.1: Design parameters of the CEPC muon system. The second column lists the possible range of parameters that could satisfy the requirements for the CEPC muon system. The last column provides the design parameters of the current baseline muon system. Further optimizations are expected in the near future and different technologies are being considered.

1 a momentum larger than 4 GeV to penetrate all 8 layers with a detection efficiency of
 2 $> 95\%$. Figure 7.2 shows the misidentification rate of pions (finding efficiency) as a
 3 function of number of the last hit muon detector layer. The misidentification rate is not
 4 sensitive to the pion momentum itself (pions with 10, 30, and 50 GeV momentum were
 5 studied), but rather to the depth of iron transversed. The fake rate decreases significantly
 6 with an increased number of layers and minimizes after 8 layers, which is the number
 7 chosen for the baseline design. These preliminary simulation studies are performed with
 8 an earlier detector geometry and simulation configuration and will undergo further study
 9 in the future. We will revisit and reoptimize the baseline parameters as described in Sec-
 10 tion 7.4.

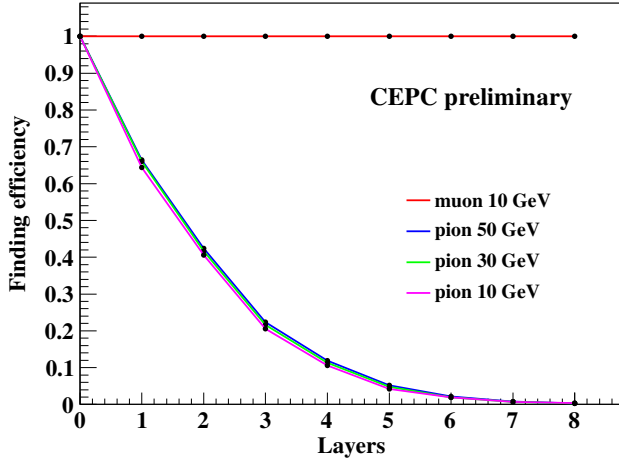


Figure 7.2: Misidentification rate of pions (finding efficiency) as a function of number of the last hit muon detector layer. Pions momenta of 10, 30 and 50 GeV is shown. Also, shown is the detection efficiency for 10 GeV muons, which should only be limited by hardware inefficiencies.

11 The solid angle coverage of the CEPC muon system should be up to $0.98 \times 4\pi$ in
 12 accordance with the tracking system. Minimum position resolutions of $\sigma_{r\phi} = 2.0$ cm
 13 and $\sigma_z = 1.5$ cm are required. The particle flow algorithm calorimetry provides very
 14 good particle identification capabilities, in particular for isolated muons, however the $>$
 15 95% ($E_\mu > 5$ GeV) detection efficiency of the muon system will provide identification
 16 redundancy and complement muon detection for most physics processes, serving also as
 17 a means for calibration of the PFA algorithms. The muon system should provide several
 18 hits each with a spatial resolution of a few cm, a time resolution of a few ns and a rate
 19 capability of 50 – 100 Hz/cm². Based on the dimensions and segmentation of the baseline
 20 design, the total sensitive area of the muon system amounts to 8600 m².

21 The baseline design of the muon system yields high efficiency ($> 95\%$) muon iden-
 22 tification with high purity (pion fake rate $< 1\%$) down to low energy (> 5 GeV). More
 23 importantly, this is independent of any object identification performance given by the PFA
 24 calorimetry alone (Section 10.2.1) and thus provides complementary information. It is
 25 particularly of interest to study the muon identification performance when muons are pro-
 26 duced in a non-isolated environment, e.g. muon inside jets, where using PFA calorimeter
 27 information to identify muons is expected to be challenging. We have performed prelim-
 28 inary studies using $e^+e^- \rightarrow ZH \rightarrow \nu\nu bb$ samples where muons are produced from b
 29 decays together with close-up jets. The average muon identification efficiency is found to

be around 80% for non-isolated muons with momentum > 10 GeV using the LICH algorithm [2] with the full calorimetry information. The purity for finding non-isolated muons is estimated to be around 95%. This performance should significantly deteriorate for lower momentum muons. On the other hand, combining both muon detector and calorimeter information in the object reconstruction and identification procedure is expected to deliver a significant improvement in performance for non-isolated muons (Section 7.4).

7.2 The Resistive Plate Chamber technology

Resistive Plate Chamber (RPC) is suitable for building large area detectors with centimeter spatial resolution. It has been applied in muon systems for experiments including BaBar [3], Belle [4], CMS [5], ATLAS [6], BESIII [7], and Daya Bay [8]. It provides a common solution with the following advantages: low cost, robustness, easy construction of large areas, large signal, simple front-end electronics, good time and spatial resolution. It is chosen as the baseline design of the CEPC muon system.

RPCs can be built with glass or Bakelite, and run in avalanche or streamer mode. Bakelite RPCs of about 1200 m^2 and 3200 m^2 were produced for the BESIII and Daya Bay muon systems, respectively. Compared with glass RPC, Bakelite RPC has the advantages of easier construction, lower density, larger cell size and lower cost, especially if the event rate is below 100 Hz/cm^2 as required by the CEPC muon system. The characteristics of Bakelite and glass RPCs are compared in Table 7.2. Further improvements are required for Bakelite RPCs, however, in terms of long-term stability, detection efficiency, readout technologies, lower resistivity ($< 10^{10}$) and higher rate capability.

Parameters	Bakelite	Glass
Bulk resistivity [$\Omega \cdot \text{cm}$]	$10^{10} \sim 10^{12}$	$> 10^{12}$
Normal		
Developing	$10^8 \sim 10^9$	
Max unit size (2 mm thick) [m]	1.2×2.4	1.0×1.2
Surface flatness [nm]	< 500	< 100
Density [g/cm ³]	1.36	2.4~2.8
Min board thickness [mm]	1.0	0.2
Mechanical performance	Tough	Fragile
Rate capability [Hz/cm ²]	Streamer Avalanche	100@92% 10K
Noise rate [Hz/cm ²]	Streamer	< 0.8 0.05

Table 7.2: Comparison of the main parameters of Bakelite and glass RPCs.

7.3 The μ -RWELL technology

The μ -RWELL is a compact, spark-protected and single amplification stage Micro-Pattern Gas Detector (MPGD). A μ -RWELL detector [9] is composed of two PCBs: a standard GEM Drift PCB acting as the cathode and a μ -RWELL PCB that couples in a unique

structure the electron amplification (a WELL patterned matrix) and the readout stages. The layout is shown in Figure 7.3(a). A standard GEM 50 μm polyimide foil is copper clad on one side and Diamond Like Carbon (DLC) sputtered on the opposite side. The thickness of the DLC layer is adjusted according to the desired surface resistivity value (50–200 $\text{M}\Omega/\square$) and represents the bottom of the WELL matrix providing discharge suppression as well as current evacuation. The foil is then coupled to a readout board.(as shown in Figure 7.3(b). A chemical etching process is then performed on the top surface of the overall structure in order to create the WELL pattern (conical channels 70 μm (50 μm) top (bottom) in diameter and 140 μm pitch) that constitutes the amplification stage. The process is shown in Figure 7.4. The high voltage applied between the copper and the resistive DLC layers produces the required electric field within the WELLs that is necessary to develop charge amplification. The signal is capacitively collected at the readout strips/pads. Two main schemes for the resistive layer can be envisaged: a *low-rate* scheme (for particles fluxes lower than 100 kHz/cm^2) based on a simple resistive layer of suitable resistivity; and an *high-rate* scheme (for a particle flux up to 1 MHz/cm^2) based on two resistive layers intra-connected by vias and connected to ground through the readout electrodes. Finally, a drift thickness of 3-4 mm allows for reaching a full efficiency while maintaining a versatile detector compactness.

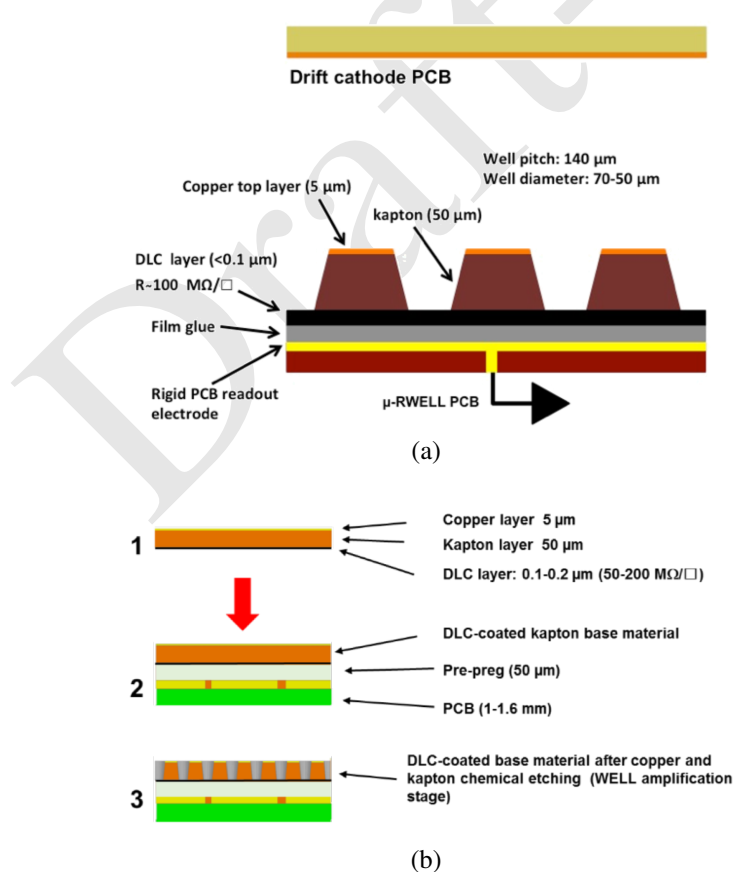


Figure 7.3: (a) Layout of a μ -RWELL detector module with the cathode and the μ -RWELL PCBs; (b) Coupling steps of the μ -RWELL PCB.

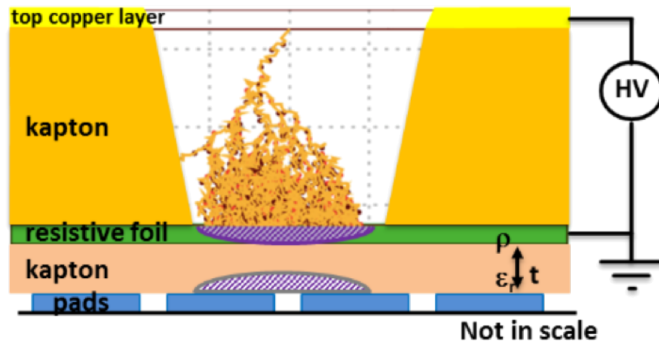


Figure 7.4: Amplification stage of a μ -RWELL detector directly coupled to the readout PCB.

1 A distinctive advantage of the proposed μ -RWELL technology is that the detector
 2 does not require complex and time-consuming assembly procedures (neither stretching
 3 nor gluing), and is definitely much simpler than many other existing MPGDs, such as
 4 GEMs or MicroMegas. Being composed of only two main components, the cathode and
 5 anode PCBs, is extremely simple to be assembled. This makes the cost of a μ -RWELL
 6 detector typically less than half the cost of a triple-GEM detector of the same size and the
 7 same strip pitch.

8 The μ -RWELL technology, especially in its *low-rate* version, is a mature solution,
 9 with whom single detectors of a 0.5 m^2 have been realized and successfully operated in
 10 the laboratory as well as in test beams. They can withstand particle rates up to a few tens
 11 of kHz/cm^2 , providing a position resolution as good as $\sim 60 \mu\text{m}$ with a time resolution of
 12 5–6 ns. The detailed results are presented in the Appendix. The requirements of a muon
 13 detector for CEPC are not as stringent and therefore can be easily and cost-effectively
 14 achieved with the μ -RWELL technology. Moreover the μ -RWELL technology is a robust
 15 solution, intrinsically safer against sparks than, for example, the widely used GEM detec-
 16 tors. The muon system could be realized by using tiles of μ -RWELL detectors of a size
 17 $50 \times 50 \text{ cm}^2$. This would make the whole muon detector very modular with components
 18 bought directly from industry. A CEPC muon detector made of μ -RWELL tiles could
 19 consist of three or four detector layers stations, each equipped with a couple of layers
 20 of μ -RWELL detectors in order to provide a very precise, of the order of 200–300 μm ,
 21 position resolution on the coordinates of a muon track.

22 7.4 Future R&D

23 The baseline conceptual design and most promising technologies for the CEPC muon sys-
 24 tem have been discussed. Future R&D requires detailed studies of different technologies
 25 and further optimization of baseline design parameters. Several critical R&D items have
 26 been identified, including:

- 27 • **Combined optimization with ECAL and HCAL:** Study and improve muon identifi-
 28 cation performance when combining both muon detector and calorimeter information.
- 29 • **Long-lived particles optimization:** Explore new physics scenario of long-lived par-
 30 ticles and exotic decays. Optimize detector parameters and technologies.

- 1 **• Layout and geometry optimization:** Detailed studies on the structure of the seg-
2 ments and modules need to be carried out to minimize the dead area and to optimize
3 the interface for routing, support and assembly. The geometry and dimensions need to
4 be optimized together with the inner detectors, in particular the ECAL and the HCAL.
- 5 **• Detector optimization:** Study aging effects, improve long-term reliability and stabil-
6 ity, readout technologies.
- 7 **• Detector industrialization:** Improve massive and large area production procedures
8 for all technologies. One example is the engineering and the following industrializa-
9 tion of the μ -RWELL technology. The engineering of the detector essentially coincides
10 with the technological transfer of the manufacturing process of the anode PCB
11 and the etching of the kapton foil to suitable industrial partners.

12 **References**

- 13 [1] CALICE Collaboration, *Construction and performance of a silicon*
 14 *photomultiplier/extruded scintillator tail-catcher and muon-tracker*, JINST **7** (2012)
 15 no. 04, P04015, [arXiv:1201.1653](https://arxiv.org/abs/1201.1653).
 16 <http://stacks.iop.org/1748-0221/7/i=04/a=P04015>.
- 17 [2] D. Yu et al., *Lepton identification at Particle Flow oriented detector for the future*
 18 e^+e^- *Higgs factories*, Eur. Phys. J. C **77** (2017) , [arXiv: 1701.07542](https://arxiv.org/abs/1701.07542)
 19 [[physics.ins-det](#)].
- 20 [3] Babar Collaboration, *The BaBar detector*, Nucl. Instrum. Meth. **A479** (2002) 1–116,
 21 [arXiv:hep-ex/0105044](https://arxiv.org/abs/hep-ex/0105044).
- 22 [4] A. Abashian et al., *The Belle Detector*, Nucl. Instrum. Meth. **A479** (2002) 117–232.
 23 KEK-PROGRESS-REPORT-2000-4.
- 24 [5] CMS Collaboration, *The CMS muon project: Technical Design Report*. Technical
 25 Design Report CMS. CERN, Geneva, 1997.
 26 <http://cds.cern.ch/record/343814>.
- 27 [6] ATLAS Collaboration, *ATLAS muon spectrometer: Technical Design Report*.
 28 Technical Design Report ATLAS. CERN, Geneva, 1997.
 29 <http://cds.cern.ch/record/331068>.
- 30 [7] Y.-G. XIE, J.-W. ZHANG, Q. LIU, J.-F. HAN, S. QIAN, N. YAO, J.-B. ZHAO,
 31 J. CHEN, and J.-C. LI, *Performance Study of RPC Prototypes for the BESIII Muon*
 32 *Detector*, Chinese Physics C **31** (2007) no. 01, 70–75.
 33 [http://cpc-hepnp.ihep.ac.cn:
 34 8080/Jwk_cpc/EN/abstract/abstract7618.shtml](http://cpc-hepnp.ihep.ac.cn:8080/Jwk_cpc/EN/abstract/abstract7618.shtml).
- 35 [8] J.-L. Xu, M.-Y. Guan, C.-G. Yang, Y.-F. Wang, J.-W. Zhang, C.-G. Lu,
 36 K. McDonald, R. Hackenburg, K. Lau, L. Lebanowski, C. Newsom, S.-K. Lin,
 37 J. Link, L.-H. Ma, and P. Viktor, *Design and preliminary test results of Daya Bay*
 38 *RPC modules*, Chinese Physics C **35** (2011) no. 9, 844.
 39 <http://stacks.iop.org/1674-1137/35/i=9/a=011>.

- [9] G. Bencivenni, R. D. Oliveira, G. Morello, and M. P. Lener, *The micro-Resistive WELL detector: a compact spark-protected single amplification-stage MPGD*, Journal of Instrumentation **10** (2015) no. 02, P02008.
[http://stacks.iop.org/1748-0221/10/i=02/a=P02008.](http://stacks.iop.org/1748-0221/10/i=02/a=P02008)

Draft-V2.0

Draft-V2.0

CHAPTER 8

READOUT ELECTRONICS, TRIGGER AND DATA ACQUISITION

The readout electronics and data acquisition (DAQ) systems for the detectors at the CEPC need to operate synchronously with the circular collider time structure for beam collisions and deliver high efficiency for recording all events without compromising on rare or yet unknown physics processes. The beam conditions and time structure are adjusted to operate in three different modes, corresponding to three different center-of-mass energies (\sqrt{s}): Higgs factory ($e^+e^- \rightarrow ZH$) at $\sqrt{s} = 240$ GeV, Z boson factory ($e^+e^- \rightarrow Z$) at $\sqrt{s} = 91.2$ GeV and W threshold scan ($e^+e^- \rightarrow W^+W^-$) at $\sqrt{s} \sim 160$ GeV. The instantaneous luminosities are expected to reach 3×10^{34} , 32×10^{34} and $10 \times 10^{34} \text{ cm}^{-2}\text{s}^{-1}$, respectively, as shown in Table 1.1. The current tentative operation plan will allow the CEPC to collect one million Higgs particles or more, close to one trillion Z boson events, and ten million W^+W^- event pairs.

In conjunction with the recording of central events, the forward luminosity monitors are required to measure Bhabha scattering events to determine the delivered integrated luminosity to a relative accuracy of 0.1% for the Higgs factory operation, and 10^{-4} for the Z line shape scan. This imposes dedicated readout capabilities to maintain the high rates of the luminosity calorimeter (LumiCal).

The following sections detail specifications for the on-detector front-end electronics and off-detector back-end electronics for the detector subsystems and their interface to the central DAQ, trigger, clock and control systems. The event builders provide data to the event filters to determine the final event selection and data storage.

1 8.1 Trigger strategy

2 The specifics of the trigger system remain to be defined. At the conceptual stage, two
 3 approaches are being considered. The first is a standard approach where trigger primitives
 4 will be based on sub-detector data and correlations will be used. The back-end electronics
 5 of the sub-detectors will include trigger hardware that will be designed in a board frame
 6 compliant to the xTCA standard providing a high level of interconnectivity. The alter-
 7 native approach is a trigger-less scheme that would provide a continuous stream of data
 8 processing, assuming a high fraction of the data is signal. Further study on the hardware
 9 trigger will be done before the technical design report and incorporated into the readout
 10 structure.

11 8.2 Readout electronics

12 The readout electronics of each detector subsystem consists of on-detector front-end elec-
 13 tronics and off-detector back-end electronics. The front-end electronics directly receive
 14 the analog signals from the sensors. These signals are fed into Application Specific Inte-
 15 grated Circuits (ASIC) to produce digital signals that are further processed by configurable
 16 front-end chips, such as digital signal processors (DSP) and field-programmable gate ar-
 17 rays (FPGA), that format and buffer the data to be sent on the data link to the back-end
 18 electronics.

19 The specific details of how the analog signals are processed to yield buffered digital
 20 data varies depending on the each detector subsystem, as described in the Chapter 4 for
 21 the vertex detector and tracking systems, Chapter 5 for the electromagnetic and hadronic
 22 calorimeters, Chapter 7 for the muon systems, and Chapter 9 for the LumiCal. A com-
 23 mon set of specifications for the readout electronics parameters are needed to ensure that
 24 the detector data from a CEPC collision collected across all subsystems can be fully as-
 25 sembled into a single event containing all measurements above threshold of all final state
 26 particles produced within the detector acceptance.

27 The most fundamental step in the readout is to provide synchronized data. This
 28 is achieved foremost by distributing phase-locked copies of the machine clock from the
 29 accelerator to the front-end systems that digitize and buffer the data. The specifications
 30 on the clock jitter depend on the level of precision required for timing measurements,
 31 where for reference the LHC clock distribution for the HL-LHC upgrade is expected to
 32 have an RMS jitter of less than 10 ps. The requirements for the digital transmission and
 33 event building are to keep the data aligned on the same clock boundary and depend on
 34 the speed of the data transmission, where transfer rates of 25 Gbps have been achieved.
 35 The standardization of the clock distribution and data links across the detector subsystems
 36 is advantageous to provide uniform performance and robust synchronization of the data
 37 links.

38 The second parameter common to all readout systems is the maximum latency for
 39 receiving a trigger decision to initiate the transfer of data from the front-end buffers to the
 40 back-end systems or from the back-end systems to the central DAQ, depending on where
 41 the data are buffered. The latency is set by the total transit time for the collision data used
 42 by the trigger to provide the data to trigger processors, to process a trigger decision, and
 43 to receive the trigger decision by the data buffers. Depending on the complexity of the
 44 triggers and internal response times of the detectors providing the data, the latency will be

1 set. With the maximum latency, the required data buffering per sub-detector will depend
 2 on the occupancy of the channels served by the same readout segment. The occupancy,
 3 channel capacity and amount of data per channel, for channels above threshold, will set the
 4 average data volume per DAQ link per trigger. The buffer needs to account for fluctuations
 5 with respect to the average to avoid buffer overrun. Control signals to monitor the data
 6 buffers and back pressure are used to throttle the trigger, as needed, to avoid data loss.
 7 Most notably, the detector data occupancies per readout segment need to model well the
 8 beam background contributions in addition to the expected occupancies from collisions.

9 The off-detector back-end readout systems will provide the data links to the trig-
 10 ger processors and the central DAQ system. Current back-end designs using Advanced
 11 Telecommunications Computing Architecture (ATCA) readout platforms are able to pro-
 12 vide a common framework for configuring the data management from different front-end
 13 systems [1, 2]. Mezzanine boards are typically implemented to allow customization of
 14 the number and types of front-end links to optimize the resources of the back-end read-
 15 out boards. The ATCA readout crates support high-speed commercial data links that can
 16 directly feed commercial network switches in the central event builder.

17 **8.3 Data Acquisition System**

18 The main task of the central DAQ system is to readout data from the electronics with
 19 the level-1 trigger decision given by trigger system, then build into a full event with data
 20 fragments from different sub-detectors and process data, such as data compression and
 21 event filter. Finally, the data are sent to permanent storage.

22 **8.3.1 Readout Data Rate Estimation**

23 The proposed CEPC detector includes seven type optional sub-detectors in the above
 24 chapters: Vertex, silicon tracker, TPC, Draft chamber, ECAL, HCAL and dual-readout
 25 calorimeter.

26 Table 8.1 shows the estimated data rate of sub-detectors of CEPC. The event rate
 27 reaches ~ 32 kHz for Z factory operation from Z boson decays and Bhabha events with
 28 the 2 Tesla solenoid option ($\mathcal{L} = 3.2 \times 10^{35} \text{ cm}^2/\text{s}$). We apply a safety factor and assume
 29 a maximum event rate of 100 kHz. TPC and drift chamber are two options of outer side
 30 tracker. Vertex and silicon tracker assume a 10 μs time readout window for occupancy.
 31 With the level-1 trigger operating at 100 kHz, the total raw data rate is about 2 TBytes/s.

32 **8.3.2 Conceptual Design Schema**

33 The current LHC experiments have up to 10^8 front-end readout channels and a maximum
 34 event building rate of 100 kHz, moving data at speeds of up to 300 GBytes/s (with an
 35 average throughput of < 200 GBytes/s required). The HL-LHC Phase-2 Upgrades reach
 36 6000 GBytes/s and average event sizes of 7.4 MBytes [1]. The proposed CEPC DAQ
 37 system has the similar requirement in terms of data throughput. Upon the reception of the
 38 data, the computing requirements for event processing at the CEPC, in terms of storage
 39 and CPU, depend on the reconstruction times and trigger algorithms. As these algorithms
 40 are evolving, the current approach is to remain as compatible as possible with the rapidly
 41 developing technologies in the computing and network markets.

	Total # channels M(10^6)	Occupancy %	Nbit /channel	# Channels readout/evt k(10^3)	Volume /evt MBytes	Data rate @100 kHz GBytes/s
Vertex	690	0.3	32	2070	8.3	830
Silicon Tracker						
Barrel	3238	0.01 ~ 1.6	32	1508	3.15	315
Endcap	1238	0.01 ~ 0.8	32	232	0.4	40
TPC	2	0.1-8	30	1375	5	500
Drift Chamber	0.056	5-10	480	?	3	300
ECAL						
Barrel	17/7.7	0.17	32	28.8/13.1	0.117/0.053	11.7/5.3
Endcap	7.3/3.3	0.31	32	22.4/10.2	0.090/0.041	9.0/4.1
AHCAL						
Barrel	3.6	0.02	32	0.72	0.0029	0.3
Endcap	3.1	0.12	32	3.72	0.015	1.5
DHCAL						
Barrel	32	0.004	2	1.28	0.00032	0.03
Endcap	32	0.01	2	3.2	0.0008	0.08
Dual Readout Calorimeter	22	0.4-1.6	64	88-352	0.704-2.8	70-280
Muon						
Barrel	4.9	0.0002	24	0.01	< 0.0001	< 0.01
Endcap	4.6	0.0002	24	0.01	< 0.0001	< 0.01

Table 8.1: CEPC DAQ Data Rate Estimation. TPC and drift chamber are options of outer side tracker.
With the level-1 trigger operating at 100 kHz, the total raw data rate is 2 TBytes/s.

Figure 8.1 shows the conceptual software architecture design of the CEPC DAQ based on the experience gained from BES III and DayaBay experiments. The DAQ system is connected with the sub-detector back-end electronics in counting rooms through commercial network switches with the TCP/IP protocol. For 2 TBytes/s data readout requirement, it need about 1600 10 Gbit or 640 25 Gbit network links. All other DAQ devices are deployed in a dedicated machine room. Event building will be performed on the online farm connected to the back-end electronics via network switches. An event filter will also run on an online farm. Each node of the online farm will process the data of one complete event at a time. The purpose of the online event processing will mainly be event classification, data quality monitoring and online filtering to reduce background events. The DAQ system will provide other common functions including run control, run monitoring, information sharing, distributed process manager, software configure, Elog, data quality monitoring, remote monitoring and so on.

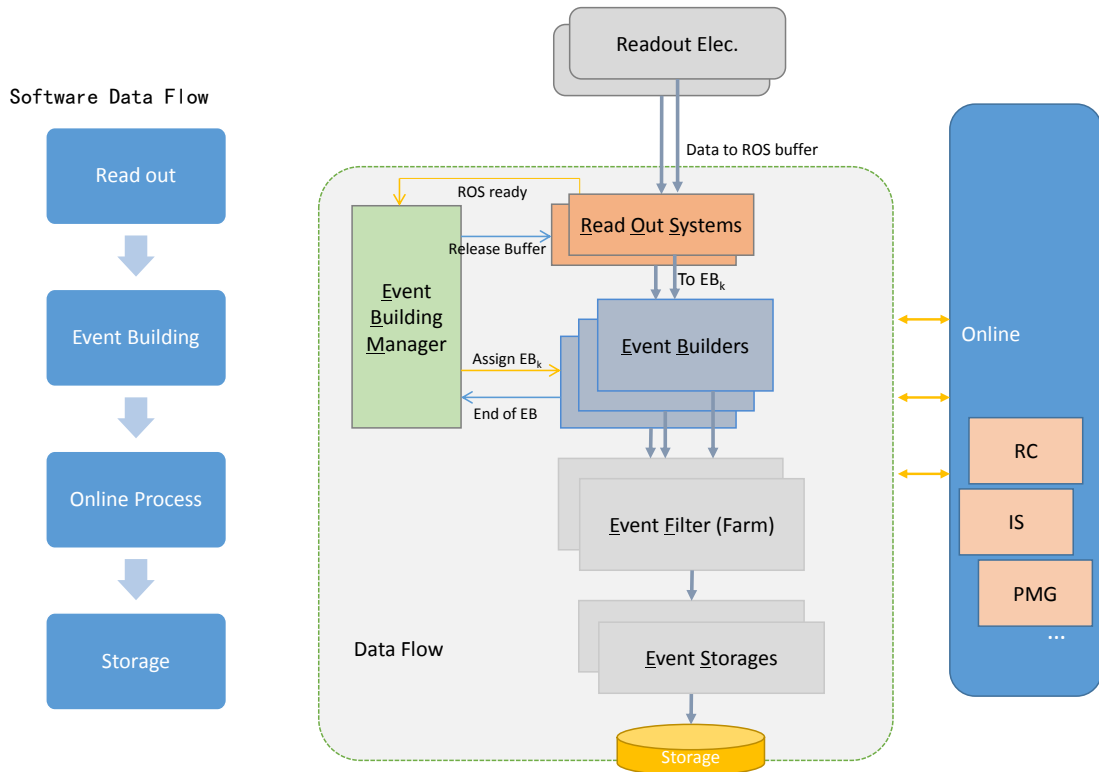


Figure 8.1: DAQ Conceptual Software Architecture Design Diagram. ROS readout data from electronics and send data to EB with EBM by data driven. After event building the event filter or software trigger will be processed at EF farm. Then the passed events will be stored at storage nodes.

There are two levels of event building in the conceptual design data flow. The first level is implemented in readout farm which reads out the data from the back-end electronics and builds into a data fragment. The second level implemented in online farm which reads out the data from readout farms and builds into a full event. The two levels of event building could function according to the BES III event building as follows [2]:

1. electronics boards send data to ROS(read out system) through network.

- 1 2. ROS receive all data slice of one event and send event ID to EBM(event building
2 manager).
- 3 3. EBM assign event ID to a free EB(event builder) node when EBM get all same event
4 ID from all ROSSs.
- 5 4. EB send data request to each ROSSs.
- 6 5. ROSSs send requested data to EB.
- 7 6. EB receive all ROSSs data fragments of one event and finish full event building, then
8 send event ID back to EBM.
- 9 7. EBM send event ID to ROSSs to clear data buffer.

10 A software trigger can be deployed in the event filter farm. Each event filter node
11 requests a full event from EBs, then sends the event data to process tasks to analyze for
12 software trigger and data quality monitoring, and then in the last step sends triggered event
13 to event storage nodes.

14 **References**

- 15 [1] J. G. Hegeman, *The CMS Data Acquisition System for the Phase-2 Upgrade*, CERN,
16 CMS-CR-2018-099 (2018) .
- 17 [2] M. Liu, J. Lang, S. Yang, T. Perez, W. Kuehn, H. Xu, D. Jin, Q. Wang, L. Li, Z. Liu,
18 et al., *ATCA-based computation platform for data acquisition and triggering in*
19 *particle physics experiments*, in *Field Programmable Logic and Applications, 2008.*
20 *FPL 2008. International Conference on*, pp. 287–292, IEEE. 2008.

CHAPTER 9

MACHINE DETECTOR INTERFACE AND LUMINOSITY DETECTORS

The Machine-Detector Interface (MDI) represents one of the most challenging tasks for the CEPC project. In general, it will have to address all common issues relevant to both the machine and detector. Topics summarized in this chapter include the interaction region, the final focusing magnets, the beam pipe, the detector radiation backgrounds and the luminosity instrumentation. Integration of all the machine and detector components in the interaction region is also briefly discussed. It is critical to achieve comprehensive understanding of MDI issues to assure the optimal performance of the machine and detector.

9.1 Interaction region

The interaction region (IR) is where both electron and positron beams are focused to small spot sizes at the interaction point (IP) to maximize the machine luminosity, and merged but subsequently separated the two beams traveling in separate storage rings. The IR layout, as illustrated in Figure 9.1, has received several necessary updates with respect to the published preliminary CDR [1], to cope with the latest double-ring design and a beam-crossing angle of 33 mrad. The two final focusing magnets, QD0 and QF1, sits inside the detector. The focal length (L^*), defined as the distance from the final focusing magnet (*i.e.* QD0) to the IP, has increased from 1.5 m to 2.2 m. This allows enlarged separation between the two single apertures of the QD0. Compensating magnets are positioned in front of the QD0 and surrounding both the QD0 and QF1 magnets. They are introduced to cancel out the detector solenoid field and minimize the disturbance on the focusing beams. Furthermore, the outer radius of the compensating magnets defines the detector acceptance to be $|\cos \theta| \leq 0.993$. The luminosity calorimeter (so called “LumiCal”), located right in front of the compensating magnets, is designed to measure the integrated

luminosity to a precision of 10^{-3} or better. Tracking disks, labeled as FTD, are designed to measure charged particle trajectories in the forward region.

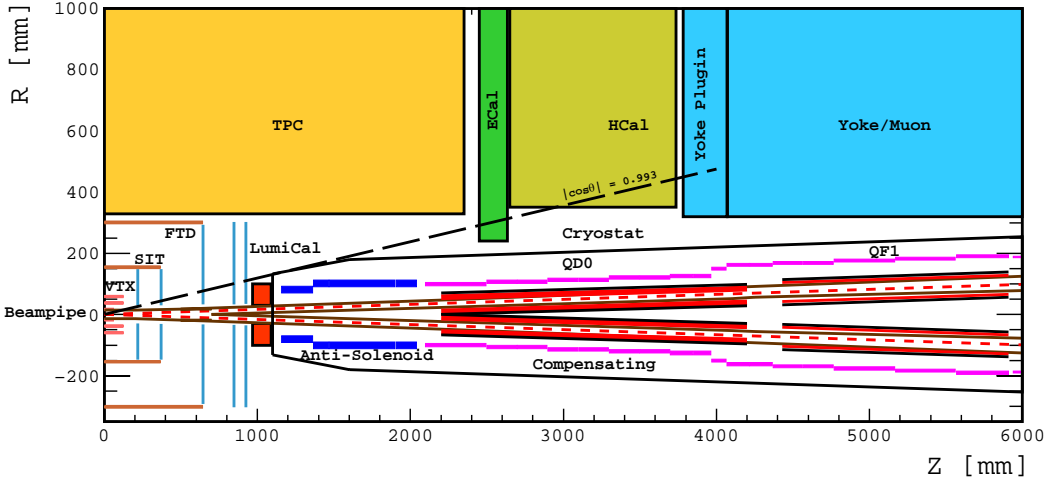


Figure 9.1: Layout of the CEPC interaction region. The two beam pipes merge into one at $|z| = 70$ cm, with the central part of $|z| = \pm 7$ cm made with Beryllium. The two final focusing magnets (QD0 and QF1) are surrounded with the screening magnets (purple lines) and with the compensating magnet (blue lines) in front. The magnets are placed inside the cryostat. The LumiCal (red) sitting in front of the cryostat provides precise luminosity measurement. Silicon tracking detectors, VTX and SIT, are in the barrel region, while FTD disks are covering the forward region.

9.2 Final focusing magnets

In the interaction region, compact high gradient quadrupole magnets are designed to focus the electron and positron beams. The two final focusing quadrupoles (QD0 and QF1), are placed inside the CEPC detector and must operate in the background field of the detector solenoid. QD0 is the quadrupole magnet close to the interaction point, with a distance of 2.2 m to the IP. It is designed as a double aperture superconducting magnet and can be realized with two layers of Cos-Theta quadrupole coil using NbTi Rutherford cables without iron yoke. It is designed to deliver a gradient field of 136 T/m and control the field harmonics in the sensitive area to be below 3×10^{-4} . Design parameters are summarized in Table 9.1. The QF1 magnet is similar to the QD0, except that there is an iron yoke around the quadrupole coil for the QF1.

Additional compensating magnets are introduced to minimize the disturbance from the detector solenoid on the incoming and outgoing beams. The compensating magnets in front of the QD0 is designed to achieve an almost zero integral longitudinal field before entering the QD0. And the compensating magnet right outside the QD0 and QF1 is necessary to screen the detector field. The magnets are based on wound of rectangular NbTi-Cu conductors. To minimize the magnet size, the compensating magnets are segmented into 22 sections with different inner coil diameters. Inside the first section, the central field reaches the peak value of 7.2 Tesla. More detailed design of the final focusing magnets and the compensating magnets can be found in [2].

Magnet	QD0	QF1
Field gradient [T/m]	136	110
Magnetic length [m]	2.0	1.48
Coil turns per pole	23	29
Excitation current [A]	2510	2250
Coil layers	2	2
Stored energy [kJ]	25.0	30.5
Inductance [H]	0.008	0.012
Peak field in coil [T]	3.3	3.8
Coil inner diameter [mm]	40	56
Coil outer diameter [mm]	53	69
X direction Lorentz force/octant [kN]	68	110
Y direction Lorentz force/octant [kN]	-140	-120

Table 9.1: Main design parameters of the two final focusing magnets, QD0 and QF1.

9.3 Beam pipe

The beam pipe design foresees several constraints. In the central region ($z = \pm 7$ cm or longer), its radius should be small enough ($r = 1.4$ cm) to allow precise measurement of track impact parameters, but still large enough not to interfere with the beam backgrounds. It shall be made with Beryllium to reduce photon conversions and hadronic interactions, but has to be rigid enough (sufficient wall thickness of ~ 500 μm) to withstand the high vacuum pressure. In the forward region, the beam pipe opens conically away from the IP to allow enough space for the beam-induced backgrounds and splits into two pipes at $|z| = 70$ cm. Beam pipe in the forward region can be built with stainless steel or copper. Bellows required for installation are located at about $|z| = 70$ cm. Additional water cooling structures need to be deployed, to control the high order mode (HOM) heating. For the beam pipe extending into the final quadrupoles, a room temperature beam pipe has been chosen because of the 4 mm gap between the beam pipe and the Helium vessel.

9.4 Detector backgrounds

Beam and machine induced radiation backgrounds can be the primary concern for the detector design [3–6]. They can cause various radiation damages to the detectors and electronic components, and degrade the detection performance or even kill the detector completely in the extreme case. During data-taking, high rate radiation backgrounds may significantly increase the detector occupancy and impair the data-taking capability of the detector. Therefore it is always desirable to characterize the potential backgrounds at the machine and detector design stage and mitigate their impacts with effective measures. Detailed Monte Carlo simulation, along with lessons and experience learned from other experiments, can serve as the basis for such studies.

The deleterious effects of the radiation backgrounds can be represented with hit density, total ionizing dose (TID), and non-ionizing energy loss (NIEL). The expected hit density can be used to evaluate the detector occupancy. TID is an important quantity for understanding surface damage effects in electronics. NIEL, represented in the 1 MeV neutron equivalent fluence, is important for understanding the bulk damage to silicon devices. The background simulation starts with either generating background particles directly in the IR (e.g. pair production) or propagating them to the region close enough to the IR (e.g. SR photons and off-energy beam particles). Particle interactions with detector components are simulated with GEANT4 [7–9]. The characterization methodology for the ATLAS detector background estimation [10] has been adopted. In the following, main radiation backgrounds originating from synchrotron radiation, beam-beam interactions, and off-energy beam particles, are discussed and their contributions are carefully evaluated. Safety factors of ten are always applied to cope with the uncertainties on the event generation and the detector simulation.

9.4.1 Synchrotron radiation

Synchrotron radiation (SR) photons are prevalent at circular machines. At the CEPC, they are mostly produced in the last bending dipole magnets and in the focusing quadrupoles inside the interaction region. The innermost tracking detectors can be sensitive to photons above 10 keV and vulnerable to high levels of soft photon radiation.¹ In order to reduce the energy and flux of SR photons that enter the straight sections, the field strength of the last bending dipole magnet has been reduced and becomes much weaker than the normal arc dipole fields. This controls the critical energy of SR photons to be below 100 keV and makes the collimation design less difficult.

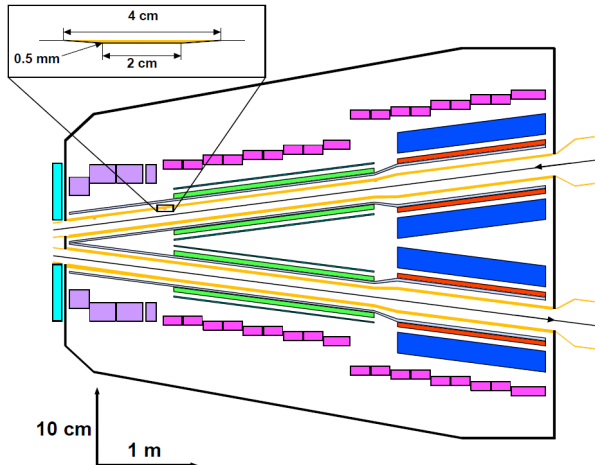


Figure 9.2: Three sets of mask tips located at $|z| = 1.51, 1.93$ and 4.2 m are introduced to suppress scattered SR photons.

The BDSim [11] software based on GEANT4 has been deployed for the detailed studies. It allows generating SR photons from the relevant magnetic elements and transports them to the region of the experimental detectors. Particular care has been taken for

¹It should be noted that the SR photon energy increases rapidly with the beam energy and additional measures might have to be introduced to allow detector operation at higher operation energies.

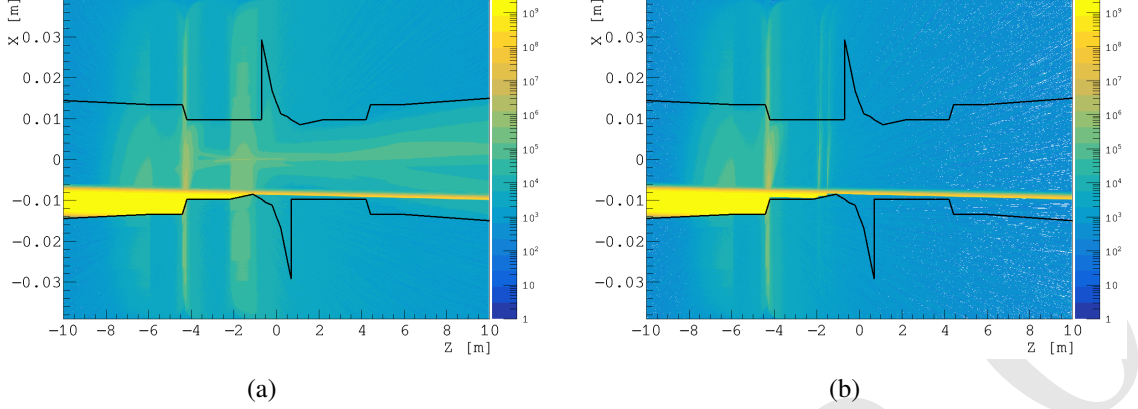


Figure 9.3: Illustration of the synchrotron photon flux formed by the upstream bending magnet on the left side and the photons scattered by the beam pipe before (a) and after (b) introducing the mask tips.

1 a realistic simulation in the tails of the beam density distributions (up to $10 \sigma_{x/y}$) and for
 2 both beam core and halo, as particles form the tails are most effective in producing back-
 3 ground particles. SR photons from the last dipole magnet form the light yellow band in
 4 Figure 9.3 and can hit the beam pipe in the interaction region. A considerable amount of
 5 them are scattered and can hit the central Beryllium beam pipe ($z = \pm 7$ cm) as shown
 6 in Figure 9.3(a). Collimators made with high- Z materials (e.g. Tungsten) and particular
 7 shapes are designed to block those scattering photons. As shown in Figure 9.2, three sets
 8 of mask tip, located at $|z| = 1.51, 1.93$ and 4.2 m along the beam pipe to the IP and as
 9 thin as 0.5 mm, are introduced to suppress such SR photons. They can effectively reduce
 10 the number of SR photons hitting the central beam pipe from nearly 40,000 to below 80.
 11 This reduction leads to a much lower power deposition in the beam pipe and allows a
 12 simplified cooling design for the beam pipe. The resulting photon flux distribution after
 13 collimation is shown in Figure 9.3(b). SR photons generated in the final focusing magnets
 14 are also carefully evaluated. They are highly forward and do not strike directly the central
 15 beam pipe unless the particles are $40 \sigma_x$ off the central orbit.

Machine Parameters	H (240 GeV)	W (160 GeV)	Z (91 GeV)
Beam energy [GeV]	120	80	45.5
Particles per bunch [10^{10}]	15	12	8
Transverse size σ_x/σ_y [μm]	20.9/0.068	13.9/0.049	6.0/0.078
Bunch length σ_z [μm]	3260	5900	8500
Emittance $\varepsilon_x/\varepsilon_y$ [nm]	12.1/0.0031	0.54/0.0016	0.18/0.004

Table 9.2: The input parameters to the GUINEA-PIG for the pair production simulation for the machine operations at $\sqrt{s} = 240, 160$ and 91 GeV.

9.4.2 Beam-beam interactions

Beamstrahlung and its subsequent process of pair production ($\gamma\gamma \rightarrow e^+e^-$) are important background at the CEPC. Due to the pinch effect in the beam-beam interaction, the trajectories of beam particles in the bunches are bent, which causes the emission of beamstrahlung photons. This process has been studied with the Monte Carlo simulation program GUINEA-PIG [12], which takes into account dynamically changing bunch effects, reduced particle energies and their impacts on the electric and magnetic fields. In addition, the simulation program has been customized to implement the external detector field for the charged particle tracking. This allows improved determination of the positions and momenta of the out-going charged particles before interfacing to the GEANT4 detector simulation. Machine parameters for operation at different energies are listed in Table 9.2, and serve as the input to the GUINEA-PIG simulation. It should be noted that compared to other consequent processes, electron-positron pair production generates most significant detector backgrounds. The processes can be categorized as:

- *Coherent Production*: e^+e^- pairs are produced via the interaction of virtual or real photons (e.g. beamstrahlung photons) with the coherent field of the oncoming bunch. Particles can be highly energetic but are dominantly produced with small angle and confined in the beam pipe. Its contribution to the detector backgrounds is negligible.
- *Incoherent Production*: e^+e^- pairs are produced through interactions involving two real and/or virtual photons. Most of the particles are confined in the beam pipe by the strong detector solenoid field. However, a small fraction of them are produced with high transverse momentum and large polar angle. The incoherent production dominates the contribution to the detector backgrounds.

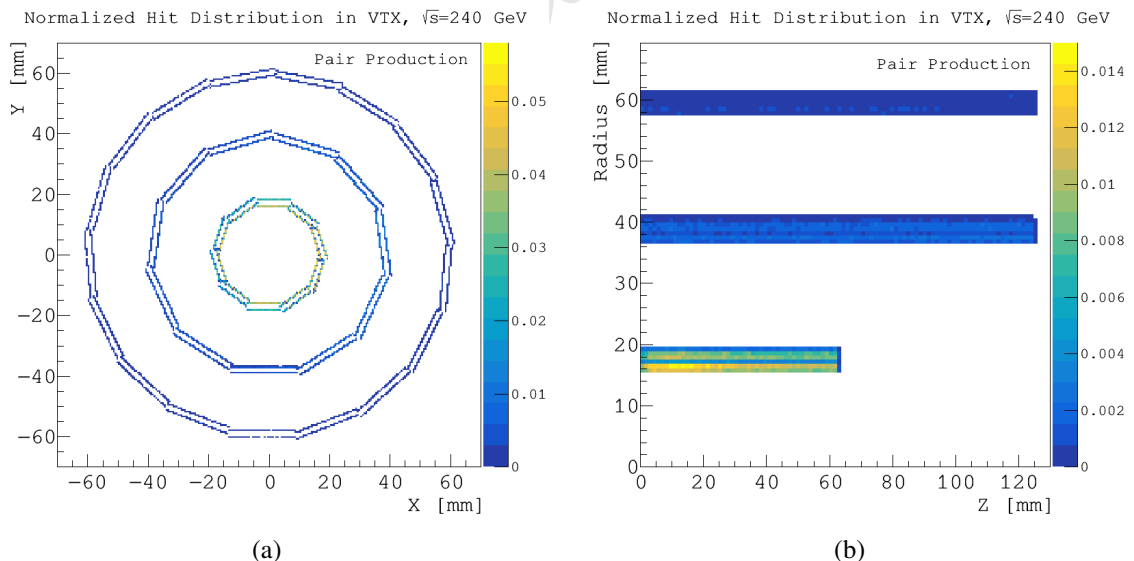


Figure 9.4: Hit distributions due to the pair production in the $x - y$ and $r - z$ planes of the vertex detector for the machine operation at $\sqrt{s} = 240$ GeV. The incoherent production dominates detector backgrounds.

As shown in Figure 9.4(a), the resulting hit distribution is nearly uniform in the ϕ -direction, even though the beam squeezing is different in the x and y directions. On

the other hand, the hit distribution is more dense in the central region as shown in Figure 9.4(b), but decreases rapidly with the increased radius, as shown in Table 9.3.

	Hit Density [hits/cm ² ·BX]	TID [kRad/year]	NIEL [1 MeV n_{eq} / cm ² ·year]
Layer 1 ($r = 1.6$ cm)	2.2	620	1.2×10^{12}
Layer 2 ($r = 1.8$ cm)	1.5	480	9.1×10^{11}
Layer 3 ($r = 3.7$ cm)	0.18	60	1.2×10^{11}
Layer 4 ($r = 3.9$ cm)	0.15	45	1.0×10^{11}
Layer 5 ($r = 5.8$ cm)	0.03	9.7	3.3×10^{10}
Layer 6 ($r = 6.0$ cm)	0.02	6.8	3.0×10^{10}

Table 9.3: Maximum hit density, total ionizing dose (TID) and non-ionizing energy loss due to the pair production ($\gamma\gamma \rightarrow e^+e^-$) at each vertex detector layer for the machine operation at $\sqrt{s} = 240$ GeV.

9.4.3 Off-energy beam particles

Circulating beam particles can lose significant amounts of energy in scattering processes. If exceeding 1.5% of the nominal energy (defined as the machine energy acceptance), scattered particles can be kicked off their orbit. A fraction of them will get lost close to or in the interaction region. They can interact with machine and/or detector components and contribute to the radiation backgrounds. There are three main scattering processes that are almost entirely responsible for the losses of beam particles, including beamstrahlung, radiative Bhabha scattering and beam-gas interaction.

Beamstrahlung events out of beam-beam interactions are generated with GUINEA-PIG. Radiative Bhabha events with small angles are generated with the BBBREM program [13]. Interactions between the beam particles and the residual gas in the beam pipe are simulated with custom code, assuming the gas pressure to be 10^{-7} mbar. The backgrounds originating from the beam-gas interaction is much smaller compared to that from the Radiative Bhabha scattering. Beam particles after interactions are tracked with SAD [14] and transported to the interaction region. Particles lost close to the interaction region, either right after the bunch crossing or after traveling multiple turns, are interfaced to detector simulation.

Backgrounds introduced by the off-energy beam particles can be effectively suppressed with proper collimation. The collimator aperture has to be small enough to stop as much as possible the off-energy beam particles, but must be sufficiently large without disturbing the beam. Four collimators are deployed in the design. APTX1 and APTX2, with an aperture size of 5 mm, are placed in the horizontal plane, and APTY1 and APTY2, with an aperture size of 1 mm, are placed in the vertical plane. All the four collimators are located in the upstream of the IP, in the range between 1700 m and 2300 m. The aperture sizes are chosen to be equivalent to $14 \sigma_x$ and $39 \sigma_y$, for being sufficiently away from the beam clearance region. Figure 9.5 shows detector backgrounds from the off-energy beam particles are reduced significantly after introducing the collimation system. As shown in Figure 9.6(a), the resulting hit distribution is maximized towards the $-x$ direction due to

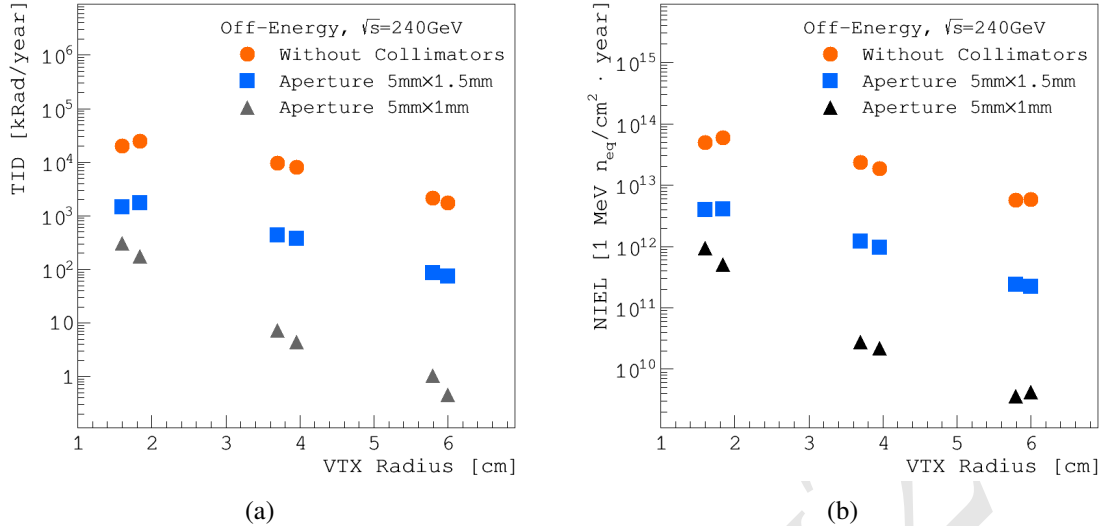


Figure 9.5: Total ionizing dose (TID) (a) and non-ionizing energy loss (NIEL) (b) caused by off-energy beam particles at each vertex detector layer are effectively reduced after introducing the two sets of collimators.

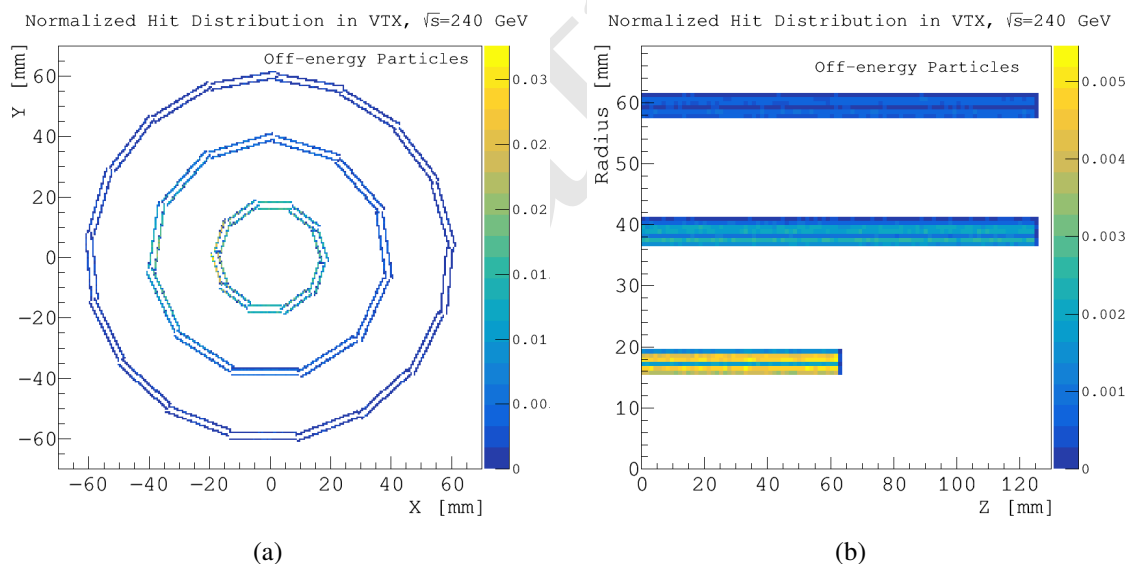


Figure 9.6: Hit distributions due to the radiative Bhabha scattering process in the $x - y$ and $r - z$ planes of the vertex detector for the machine operation at $\sqrt{s} = 240$ GeV.

¹ the nature of the off-energy beam particles that are swept away by the magnets. But along
² the z direction, the hit distribution is more or less uniform with the additional contribution
³ of the back-scattered particles by the LumiCal downstream. Although the exact locations
⁴ and shapes of the collimators are subject to further optimization as the machine design
⁵ evolves, the current design demonstrate the feasibility to control such specific background
⁶ to a sufficiently low level. For background estimation, the maximum values in the $-x$ di-
⁷ rection are taken. At the first vertex detector layer ($r = 1.6$ cm), the hit density is about

- 1 0.22 hits/cm² per bunch crossing from radiative Bhabha scattering events. The TID and
 2 NIEL are 310 kRad per year and 9.3×10^{11} 1 MeV n_{eq}/cm^2 per year, respectively.

3 9.4.4 Summary of radiation backgrounds

- 4 When operating the machine at the center-of-mass energy of $\sqrt{s} = 240$ GeV, the main de-
 5 tector backgrounds come from the pair-production. The contribution from the off-energy
 6 beam particles is nearly an order of magnitude lower. Figure 9.7 shows the hit density,
 7 TID and NIEL at different vertex detector layers, originating from the pair production,
 8 off-energy beam particles and the two combined. In addition, TID and NIEL distributions
 9 covering the silicon detectors in $r - z$ are shown in Figure 9.8.

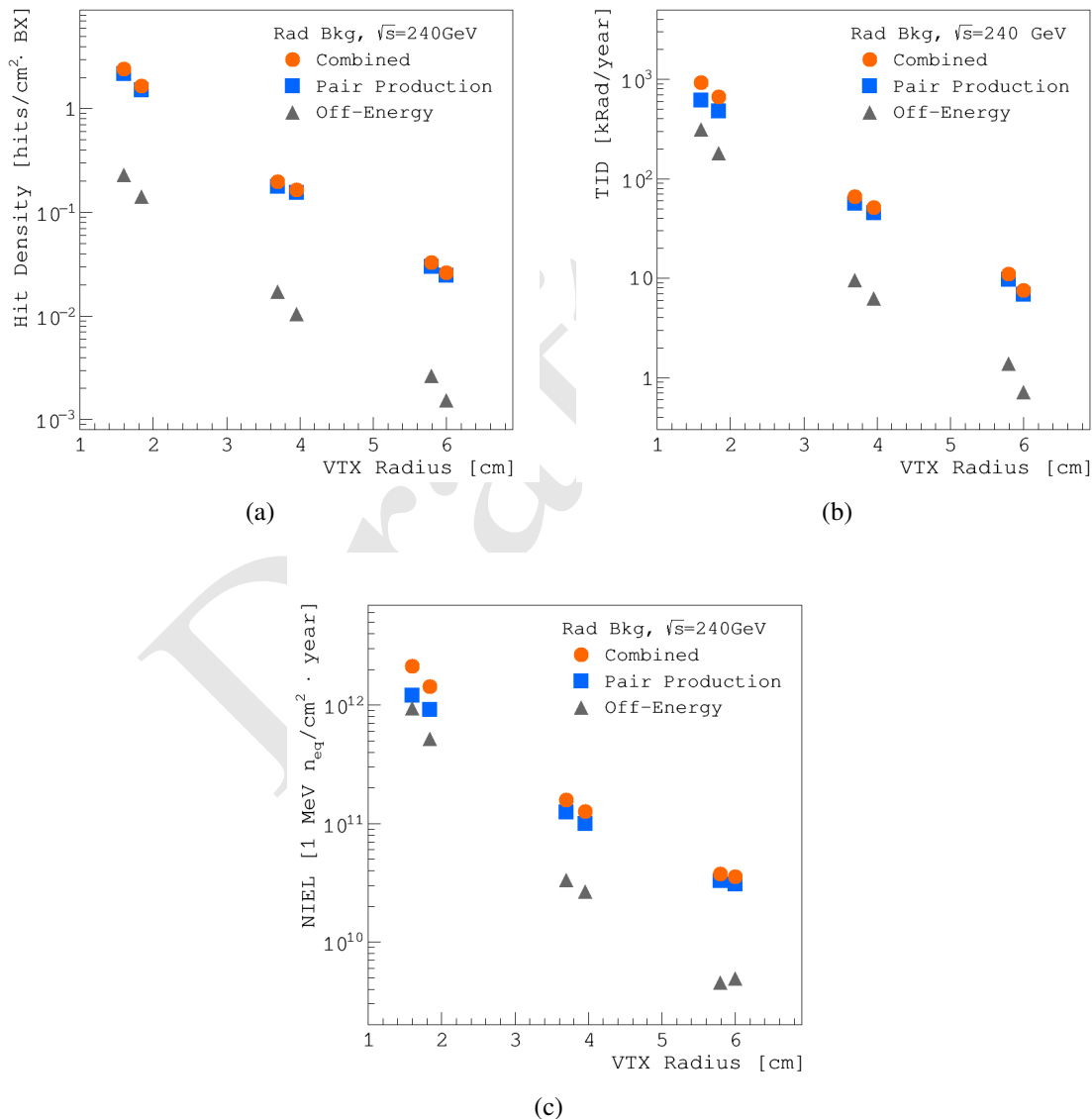


Figure 9.7: Hit density, total ionizing dose (TID) and non-ionizing energy loss (NIEL) at different vertex detector layers due to the pair production, off-energy beam particles and the two combined for the machine operation at $\sqrt{s} = 240$ GeV.

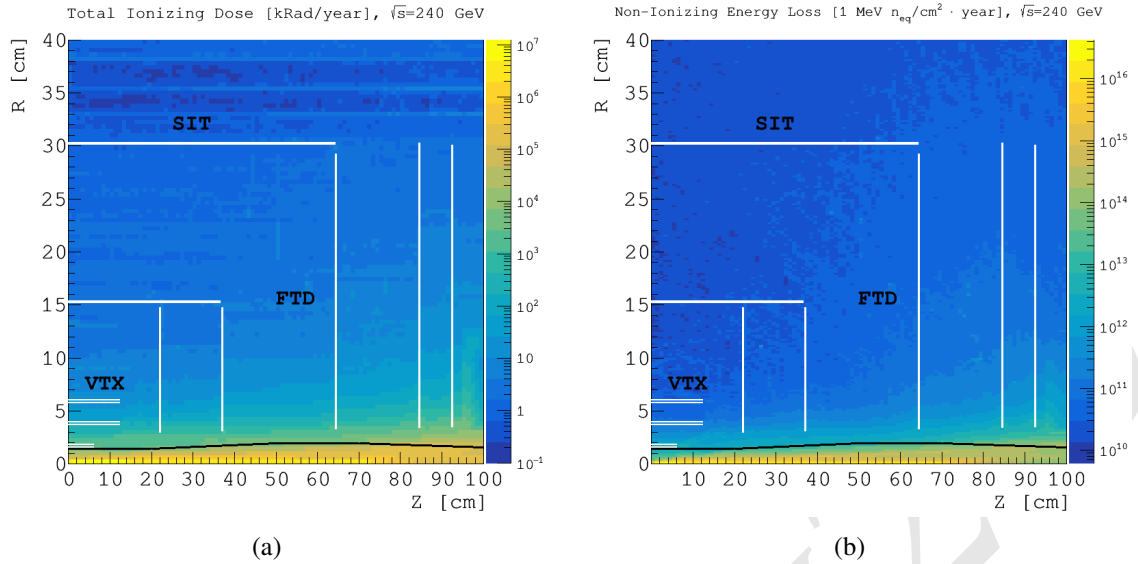


Figure 9.8: Total ionizing dose (TID) and non-ionizing energy loss (NIEL) distribution in $r - z$ for the machine operation at $\sqrt{s} = 240$ GeV. The white lines indicate the locations of the vertex detector (VTX), the forward tracking disks (FTD) and the silicon inner tracker (SIT).

At lower operation energies, *i.e.* $\sqrt{s} = 160$ GeV for W and $\sqrt{s} = 91$ GeV for Z , the background particles are usually produced with lower energies but with higher rates given the higher machine luminosities. In addition, the pair-production dominates the radiation backgrounds and contributions from other sources become negligible. The resulting radiation backgrounds at the first vertex detector layer at different operation energies are summarized in Table 9.4.

	H (240)	W (160)	Z (91)
Hit Density [hits/cm ² ·BX]	2.4	2.3	0.25
TID [MRad/year]	0.93	2.9	3.4
NIEL [10 ¹² 1 MeV n_{eq} /cm ² ·year]	2.1	5.5	6.2

Table 9.4: Summary of hit density, total ionizing dose (TID) and non-ionizing energy loss (NIEL) with combined contributions from pair production and off-energy beam particles, at the first vertex detector layer ($r = 1.6$ cm) at different machine operation energies of $\sqrt{s} = 240, 160$ and 91 GeV, respectively.

9.5 Luminosity instrumentation

The forward region of the CEPC detector will be instrumented with a luminometer (LumiCal), aiming to measure integrated luminosity with a precision of 10^{-3} and 10^{-4} in e^+e^- collisions at the center-of-mass energy of 240 GeV and at the Z pole, respectively. The precision requirements on the integrated luminosity measurement are motivated by the CEPC physics program, intended to test the validity scale of the Standard Model through precision measurements in the Higgs and the electroweak sectors with 10^6 Higgs and 10^{10-12} Z bosons. Many sensitive observables for such measurements critically depend on the uncertainty of the integrated luminosity.

Luminosity at an e^+e^- collider is best measured by counting Bhabha events of elastic e^+e^- scattering. Its theoretical uncertainty is better than 0.05% at the Z pole [15]. The scattered electrons are distributed in the forward direction with a $1/\theta^3$ dependence. The cross section of the BHLUMI [16] simulation is illustrated in Figure 9.9(a).

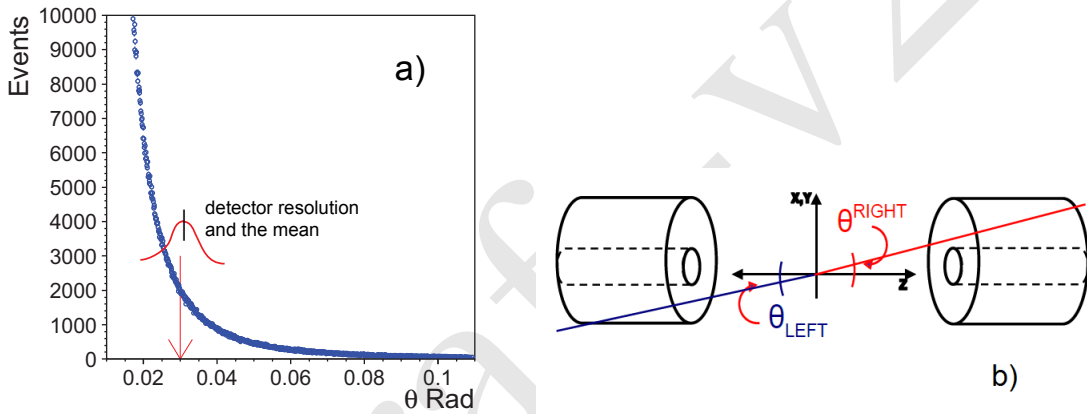


Figure 9.9: a) Distribution of scattered electrons in polar angle of the BHLUMI simulation. The Gaussian curve illustrates the detector resolution to θ measured at a given fiducial edge. The offset of the mean in measurement contributes to the systematic uncertainties. b) Bhabha events are measured preferably in the forward direction of the e^+e^- collision characterized by the back-to-back of elastic scattering and the electromagnetic shower of the electrons.

A Bhabha event is detected with a pair of scattered electrons back-to-back in direction, and the momenta of beam energy. Therefore the luminosity detector is consisted of a pair of forward calorimeters with high precision on detecting electron impact positions. The configuration is sketched in Figure 9.9(b). Bhabha events are detected in the angular coverage ($\theta_{min} < \theta < \theta_{max}$) of the forward calorimeters. The integrated luminosity (L) of the leading order calculation is

$$\sigma^{vis} = \frac{16\pi\alpha^2}{s} \left(\frac{1}{\theta_{min}^2} - \frac{1}{\theta_{max}^2} \right), \quad \mathcal{L} = \frac{1}{\epsilon} \frac{N_{acc}}{\sigma^{vis}}, \quad \frac{\Delta\mathcal{L}}{\mathcal{L}} \sim \frac{2\Delta\theta}{\theta_{min}}, \quad (9.1)$$

where ϵ is the detection efficiency. The systematic uncertainties are mostly from the precision on θ_{min} , mainly due to mechanical alignment and the detector resolution. The uncertainty propagates to the luminosity calculation is about twice in magnitude.

The dimension of the detector is favorable to have the θ_{min} as low as possible to optimize coverage of the Bhabha cross section. The luminosity detector is planned to be mounted in front of the quadrupole magnets at $z = \pm 100$ cm. With the θ_{min} of ~ 30 mrad,

1 corresponding to a radius of 30 mm to the beam pipe at $z = 100$ cm, the corresponding
 2 Bhabha cross-section, σ^{vis} , after event selection will reach ~ 50 nb. A large detector
 3 coverage of σ^{vis} is necessary for statistics required for the Z line-shape study, where the
 4 $Z \rightarrow q\bar{q}$ cross section is 41 nb. The precision for Z -pole studies reaching 10^{-4} makes a
 5 strong demand on the detector resolution. At $\theta = 30$ mrad, it corresponds to an offset of
 6 $\Delta\theta \sim 1.5 \mu\text{rad}$, which is equivalent to 1.5 μm in radius at $z = 100$ cm.

7 Several technological options for LumiCal design under study, are described in Sec. 9.5.1,
 8 with emphases on the precision of polar angle and energy reconstruction of Bhabha parti-
 9 cles scattered in the t -channel $V(V = \gamma, Z)$ exchange. The dual beam-pipe configuration
 10 with the beam-crossing at 33 mrad results to a boost to particles of e^+e^- collisions. The
 11 back-to-back characteristics of Bhabha electrons is shifted by approximately a horizontal
 12 offset of 33 mm. The impact to LumiCal design is discussed. The LumiCal together with
 13 the quadrupole magnet are inserted into the tracking volume that extended to $z = \pm 200$ cm.
 14 Shower leakage of electrons off the LumiCal to central tracker is studied by simulation,
 15 which is also discussed.

16 The LumiCal is a precision device with challenging requirements on the integrated
 17 luminosity measurement depending on the opening aperture and positioning of the Lumi-
 18 Cal. Various sources of luminosity uncertainty in this respect are reviewed in Sec. 9.5.2.
 19 Encouraging estimations on feasibility reaching the goals on the luminosity precision are
 20 presented. Detailed studies are ongoing, to include the full simulation of physics and ma-
 21 chine induced processes and of the detector itself, for various LumiCal positioning and
 22 technology choices.

23 **9.5.1 Technological and design options**

24 In the current design of the forward region, LumiCal is foreseen to cover the polar angle
 25 region between 26 mrad and 105 mrad corresponding to the detector aperture of 25 mm
 26 for the inner radius and 100 mm for the outer, at $z = \pm 100$ cm of the LumiCal front plane
 27 from the IP. The detector options shall be considered for

- 28 1. precision of the electron impact position at the $r \sim 10 \mu\text{m}$ ($1 \mu\text{m}$) level for the un-
 29 certainties on luminosity corresponding to the systematic uncertainties on luminosity
 30 of $\Delta L/L \sim 10^{-3}$ (10^{-4}) of the machine operation at the Higgs (Z -pole) energies;
- 31 2. monitoring of the detector alignment and calibration of detector position by tracking
 32 of Bhabha electrons with upstream detectors;
- 33 3. energy resolution and separation of e/γ for measurements of single photons and ra-
 34 diative Bhabha events;
- 35 4. maximum coverage and segmentation of the LumiCal to accommodate the dual beam-
 36 pipe and the beam crossing of 33 mrad;
- 37 5. minimizing shower leakage into the central tracking volume.

38 The LumiCal detector option that can reach the 1 μm precision on electron impact
 39 position is very much limited silicon detectors segmented in strips or pixels. Silicon strip
 40 detectors of 50 μm readout pitch is commonly reaching a resolution of $\sigma \sim 5 \mu\text{m}$. The
 41 uncertainty on the mean ($\bar{\sigma} = \sigma/\sqrt{n}$) would be much smaller. The selection of Bhabha
 42 events is set on a fiducial edge of θ_{min} , for example, by choosing the center region in

the gap between two silicon strips. The systematic uncertainty is therefore the number of events being selected with an uncertainty on $\bar{\sigma}$ despite the detector resolution, and would be relatively small. The uncertainty on θ_{min} is indicated by the Gaussian curve in Figure 9.9(a). The alignment of the detector position would be the major systematic requirement for an absolute precision of 1 μm .

A conceptional Luminosity detector is illustrated in Figure 9.10 for the combination of a silicon detector and a calorimeter around the beam pipe for measurement of the electron impact position and energy. The segmentation of the calorimeter is considered for the back-to-back resolution detecting a pair of Bhabha electrons, and for separation of e/γ in case of a radiative photon accompanied with the electron or from beam background. The thickness is determined for the energy resolution favorable of $> 20X_0$ for shower containment of a 50 GeV electron. The option on the calorimeter is limited by the space available. The traditional crystal or scintillator-based calorimeter will require more than 20 cm in length for $> 20X_0$. The most compact design would be a sandwiched stack of Silicon samplers with Tungsten layers of $1X_0$ (3.5 mm thick), to a total of about 10 cm that weights about 400 kg.

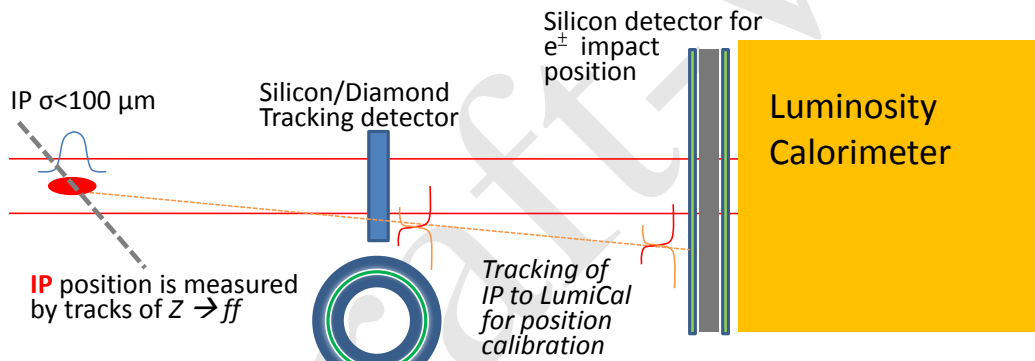


Figure 9.10: A conceptional luminosity detector combination with a upstream silicon/diamond detector for tracking Bhabha electrons to calibrate position of the luminosity detector.

The alignment precision of the front-layer Silicon detector is the most critical issue to reach 1 μm in radius for the luminosity measurement of 10^{-4} . At the 1 μm level, a monitoring system with laser alignment is required to calibrate the detector position. The θ angle of a detected electron impact position is calculated assuming an IP position measured by the beam steering and the central tracking system. The IP position relative to the luminosity detector could be limited to survey relative to the central tracking devices or beam pipe. If feasible, a tracking system on the Bhabha electrons will improve the measurement precision of the electron theta angle. This is illustrated in Figure 9.10 for the option with a ring of silicon or diamond detector mounted in front of the Luminosity detector. In this configuration, an electron track is measured with respect to the IP, the ring detector, and the LumiCal impact positions. The ring detector offers a second survey, and by extrapolation, to calibrate the LumiCal position.

The front silicon layer of the luminosity detector will measure electron impact positions to a few micron. If this will be a fine-pitch strip detector, the position is measured by strips collecting the ionization charges generated by a traversing electron. In Figure 9.11,

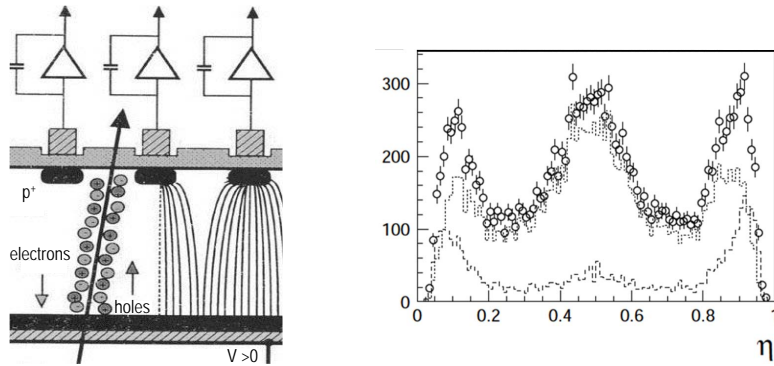


Figure 9.11: Charge collection by silicon strips is illustrated for ionization charges generated by a traversing particle. The $\eta = Q_r/(Q_r + Q_l)$ distributions are made for charge sharing to left and right strips to the impact position, for a test device with strip implementation in 25 μm pitch and the readout of every other strips in 50 μm pitch. The η distributions are also plotted for contents with charges collected by two-strip (dotted) and three-strip (dashed) cases. The middle bump corresponds to the position of the floating strip between two readout strips.

the charge sharing is illustrated for $\eta = Q_r/(Q_r + Q_l)$ with the ionization charges collected by the strips on the right (left) of the impact position. The distribution is collected for a test device having strips implanted in 25 μm pitch, and the readout in 50 μm pitch by wire bonding to every other strips. The floating strip between two readout strips attracts charges drifting towards it and results to the bump at $\eta \sim 0.5$, in particular for a wide cluster of charges collected by three strips (dotted line). The impact position of a particle is approximated by its center-of-gravity weighted on the charges between two strips. With the η distribution, the non-linear distribution can be corrected to achieve a position resolution of better than $\sim 5 \mu\text{m}$ for the readout pitch of 50 μm . With the strip detectors placed in a magnetic field, the ionization charge in the silicon wafer is drifted toward one side, and therefore the η distribution is tilted un-evenly. Without a proper correction for the η , the off-set to the true impact position can be as large as half the readout pitch.

If the luminosity detector will be a sandwiched silicon-tungsten calorimeter. The silicon wafer for shower sampling may be segmented like the case of the OPAL Lumi-Cal [17], applying 2.5 mm wide strips in circular span of 11.25°. The resolution on detection of an electron position, as well as for e/γ separation is at the 1 mm level. Assuming that the Bhabha electrons has the fiducial edge, θ_{min} , chosen at the middle between two strips, and the events are evenly divided to left and right strips without charge sharing. The systematic uncertainty to luminosity measurement is by the alignment uncertainty of the strip position of a few microns, and is not by the resolution.

Charge sharing between the gap of two-strips have been studied with prototype wafers[18] shown in Figure 9.12. The wafer dimension is $65 \times 65 \text{ mm}^2$ implemented with 2 mm wide strips and the gaps from 50 μm to 160 μm . The beam test was conducted with a set of fine-pitched strip detectors as a telescope to provide reference positions of incident electrons scattered across strips and gaps. The charge sharing for electrons in the gaps are compared for η distributions in Figure 9.12, which are found compatible for the different gap widths. Charge collection shows no loss, and are drifted toward the near strips with the η peaking at the edges. The dispelling charges in the middle of a gap is

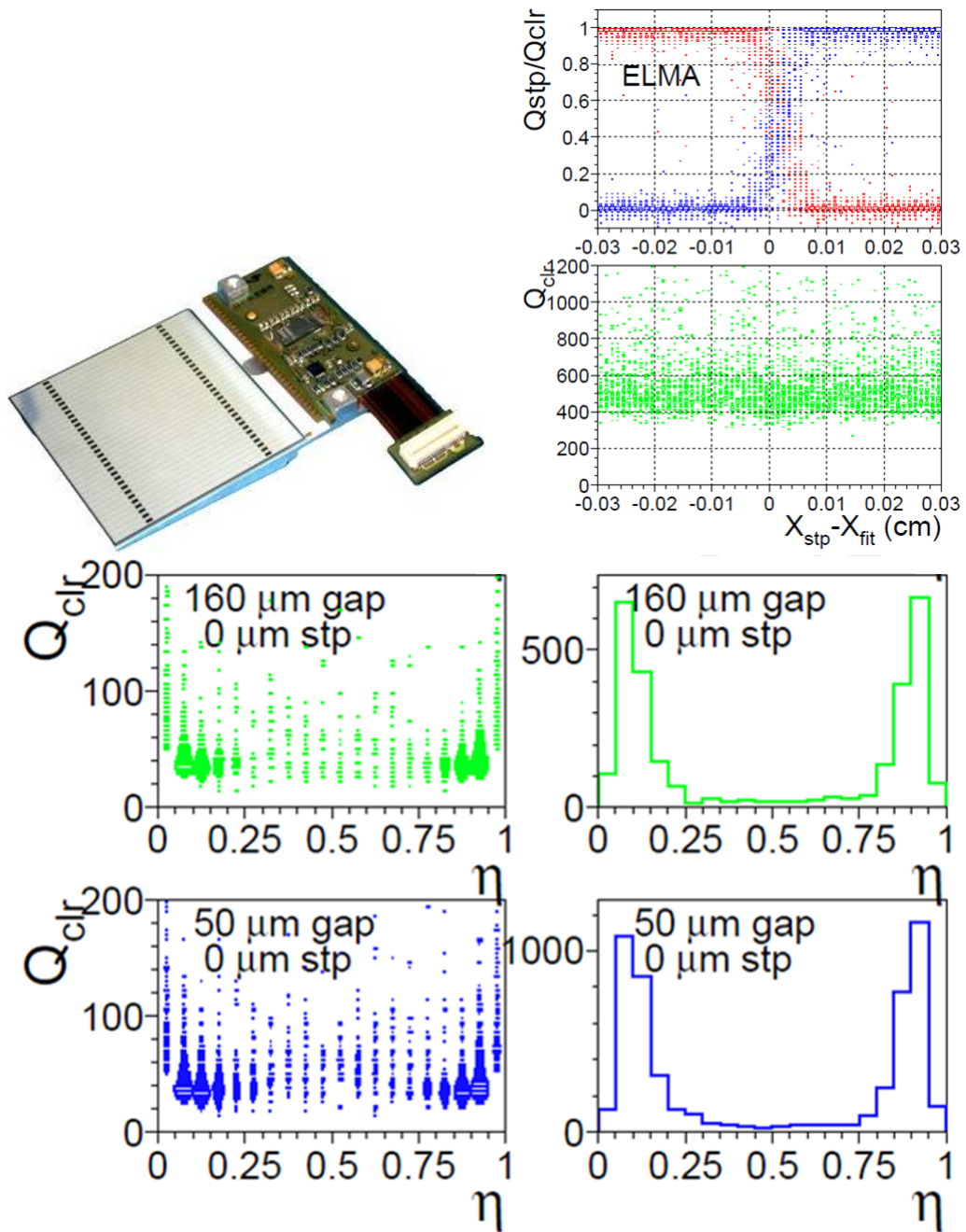


Figure 9.12: Beam tests using prototype silicon wafer of the CMS pre-shower detector (top-right) were conducted for collection of ionization charges generated by traversing particles across the gap between strips. The charge sharing by adjacent strips are plotted (top-left) to the reference impact position (X_{fit}) extrapolation of a upstream telescope). The sum strip charges is compatible to the hits on a strip. The charge sharing in $\eta = Q_r/(Q_r + Q_l)$ peaks near 0 and 1 (bottom), indicating non-linear response to the randomly distributed beam particles across the gap.

¹ difficult for detecting the position of an incident electron in the gap. But, it does divide the event fraction cleanly to the near side of the strips.

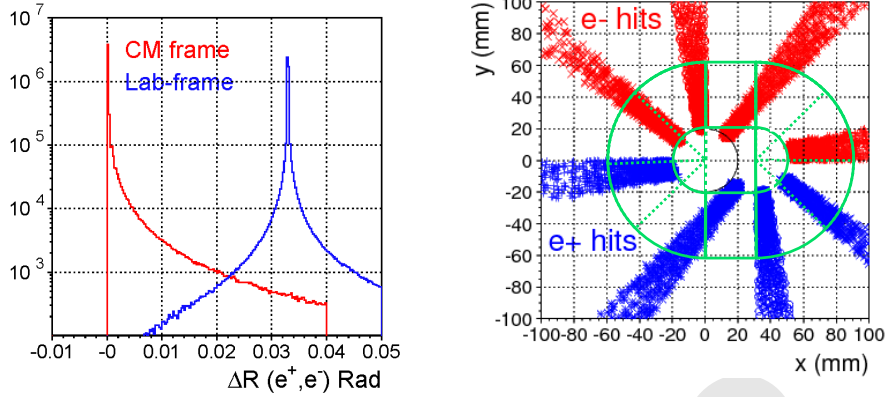


Figure 9.13: Bhabha events of BHLUMI simulation at the Z -pole are plotted for the back-to-back opening angle of scattered electron-position pairs in the Center-of-Mass and the laboratory frames (left). The impact positions on the LumiCal front face are plotted in slides of ϕ angles every 45 degrees (right). The detector coverage is illustrated in green lines indicating a beam-pipe of 20 mm, extended from beam center at $x = \pm 16.5$ mm.

1 The double ring configuration of the CEPC machine design at the interaction point
 2 has a beam crossing angle of 33 mrad. The effect to the electrons of Bhabha interaction
 3 is a boost off the accelerator ring center, by maximum 16.5 mrad in horizontal direction.
 4 The distribution is simulated with the BHLUMI program. The shift on back-to-back angle
 5 is plotted in Figure 9.13. The boost is toward $+x$ direction of the laboratory frame. The
 6 electron impact positions on the LumiCal front-layer at $z = 100$ cm are also plotted in
 7 Figure 9.13, in slices of every 45 degrees to indicate the dependence on p_T direction. The
 8 beam-pipe centers are at $x = \pm 16.5$ mm. The green lines indicate the beam-pipe area of
 9 20 mm in radius extending horizontally, and the coverage of the LumiCal in segmentation
 10 of circular and rectangular silicon wafers. The distributions of electron impact positions
 11 are illustrated for $\theta > 20$ mrad in the laboratory frame. Electrons of low scattering angles,
 12 in particular for those in $-x$ direction, are lost into beam-pipe. To have both scattered
 13 electrons and positrons detected, the corresponding θ_{min} on the horizontal axis is the
 14 beam-pipe acceptance plus 16.5 mrad. The loss of events on vertical direction is much
 15 less. With a beam pipe as indicated with $\pm y$ dimension equals radius, the horizontal boost
 16 does not lead to the loss of electrons with a larger y -position. The coverage for Bhabha
 17 events increases in favor of a smaller beam pipe opening. We shall pursue the vertical
 18 dimension to be low as possible for a total integrated Bhabha cross section of larger than
 19 50 nb.

20 The LumiCal mounted in front of the quadrupole magnet at $z = \pm 100$ cm is half
 21 way in the tracking volume of $z = \pm 200$ cm. Shower leakage of electrons at the edge of
 22 LumiCal is investigated with a GEANT simulation with parameters cross-checked with
 23 a lateral shower study [19]. The LumiCal is configured assuming a sandwiched Silicon-
 24 Tungsten calorimeter stacked in twenty decks of 2 mm air-gaps and $1X_0$ thick tungsten
 25 layers. Each air-gap has a layer of silicon wafer of 0.3 mm thick. The front layer of
 26 the LumiCal is positioned at $z = \pm 100$ cm. The geometry of the LumiCal is tested
 27 in two configurations: a TUBE with uniform inner and outer radii of 25 and 100 mm,
 28 respectively; and a CONE shape with the outer edge at a constant angle of $\arctan 0.1$

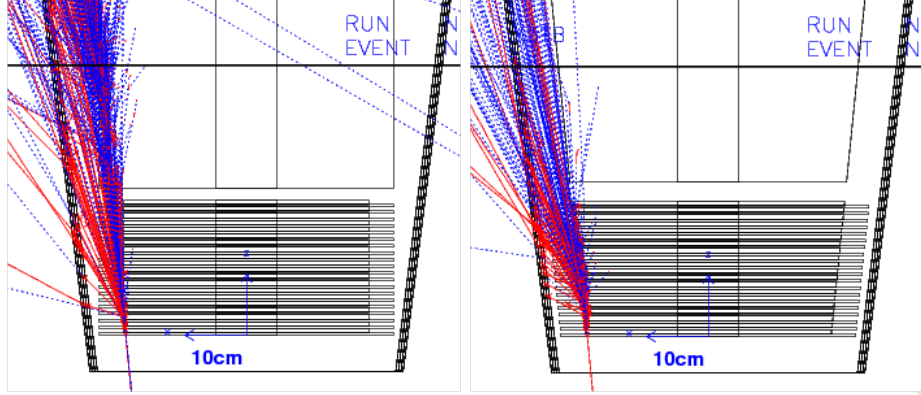


Figure 9.14: Event display of a GEANT simulation for electron shower on the LumiCal configuration stacked with 20 decks of silicon and Tungsten layers in TUBE (left) and CONE (right) shapes.

to the interaction point. The CONE shape is intended for well separated absorption of electron shower at a θ threshold. Illustrated in Figure 9.14 are the event display of the simulations. Out of the LumiCal, a 5 mm iron cone at $|\cos \theta| = 0.992$ is implemented for absorption of low energy shower secondaries traversing into the center tracking volume.

The TUBE configuration has a corner of about 5 mrad on the outer edge to the IP, where energetic shower secondaries can penetrate and leak to detector endcap region. The CONE shape allows the shower fully developed once the electron enters the calorimeter coverage. The shower leakage reaching the Fe-cone is recorded for the particle energies arriving and penetrating through. The statistics are listed in Table 9.5 for 50 GeV and 125 GeV electrons. When the shower is well contained, the leakage is just a few dozens of less than 30 MeV particles. A shower on the edge creates up to 3k secondaries into the tracking volume mostly of less than 100 MeV. The 5 mm iron layer can filter a large fraction of them, to less than 1k particles traversing through.

θ (mrad)	50 GeV electrons		125 GeV electrons	
	TUBE	CONE	TUBE	CONE
	$N_{\text{enter}} / N_{\text{pass}}$	$N_{\text{enter}} / N_{\text{pass}}$	$N_{\text{enter}} / N_{\text{pass}}$	$N_{\text{enter}} / N_{\text{pass}}$
40	15.4/5.6	13.6/5.8	38.0/16.0	35.8/14.7
90	392/155	173/76	1028/399	434/19.7
95	501/290	367/152	2389/720	937/382
98	762/216	860/284	1718/473	2176/725
99	553/140	1331/367	1102/273	3306/915

Table 9.5: Number of particles leaking out of the LumiCal outer radius (N_{enter}) and number of particles passing through the Fe-cone (N_{pass}). Two different detector designs (TUBE and CONE) and two shower energies (50 GeV and 125 GeV) are simulated. A shower on the edge creates up to 3k secondaries toward the tracking volume, which are mostly of less than 100 MeV and are filtered by the 5 mm thick Fe-cone.

9.5.2 Systematic effects

The measurement of luminosity is by counting of Bhabha events N_{Bh} detected in coincidence in the two halves of the luminosity calorimeter LumiCal. The luminosity figure is then obtained from the equation of $\mathcal{L} = N_{\text{acc}}/(\epsilon\sigma^{\text{vis}})$. The visible cross section for the Bhabha process, σ_{vis} , should be integrated over the same phase space as used for the counting of Bhabha events. The limited precision with which the experimental acceptance region is defined gives rise to a number of systematic effects. Further, other processes misidentified as Bhabha and the limited accuracy of the theoretical calculation of σ_{vis} contribute to the overall systematic uncertainty.

A generator-level study was performed to assess the effects related to the precision of the Bhabha acceptance region on Bhabha counting. An underlying assumption of the study is that the LumiCal is centered on the outgoing beam axis. This assumption is essential for data-driven control of the radial offset of LumiCal with respect to the IP, as well as for Bhabha event counting based on the mirrored asymmetric polar-angle acceptance regions on the left and right side of the detector [17] (in further text, *OPAL-style selection*). OPAL-style counting cancels out biases due to left-right asymmetries of the experimental angular acceptance. It is further assumed that for the final state particles hitting the radial region between 50 mm and 75 mm, corresponding to the detector fiducial volume (FV), shower leakage has a negligible effect on the reconstruction of the polar angle and the energy.

Bhabha event samples are generated using the BHLUMI generator [16]. Center-of-mass energy of 240 GeV is assumed, corresponding to approximately the energy of the maximum Higgs boson production cross section. The particles are generated in the range of polar angles including a ~ 7 mrad margin outside the FV to allow non-collinear final state radiation (FSR) to contribute to the events. After event generation, smearing is applied to the final particle vertices and momenta according to the nominal CEPC parameters. Additional smearing or bias is then applied according to one systematic effect at a time. Four momenta of close-by particles are summed up to account for cluster merging in LumiCal. The selection criteria to count an event consist of the OPAL-style angular selection and the requirement that the energy of both detected showers is above 50% of the nominal beam energy. The relative acceptance bias is determined as the relative difference between the Bhabha count $N_{\text{Bh},i}$ obtained with the inclusion of the considered effect i and N_{Bh} obtained with the nominal set of parameters.

Table 9.6 lists the requirements on beam delivery, MDI and LumiCal installation, needed to limit individual systematic effects in the luminosity measurement to 1×10^{-3} , such as required for the Higgs boson physics program at the CEPC. Parameters influencing the integral luminosity precision are given as follows:

- ΔE_{CM} , uncertainty of the available center-of-mass energy affecting the Bhabha cross-section,
- $E_{e+} - E_{e-}$, asymmetry of the incident beam energies resulting in a net longitudinal boost of the event,
- $\frac{\delta\sigma_{E_{\text{beam}}}}{\sigma_{E_{\text{beam}}}}$, uncertainty of the beam energy spread,
- Δx_{IP} and Δz_{IP} , radial and axial offsets of the IP w.r.t. the LumiCal,
- Beam synchronization, resulting in axial offset of the IP w.r.t. the LumiCal,

Parameter	Unit	Limit
ΔE_{CM}	MeV	120
$E_{e^+} - E_{e^-}$	MeV	240
$\frac{\delta \sigma_{E_{\text{beam}}}}{\sigma_{E_{\text{beam}}}}$		effect canceled
Δx_{IP}	mm	<1
Δz_{IP}	mm	10
Beam synchronization	ps	7
$\sigma_{x_{\text{IP}}}$	mm	1
$\sigma_{z_{\text{IP}}}$	mm	10
r_{in}	mm	10
$\sigma_{r_{\text{shower}}}$	mm	1
Δd_{IP}	μm	500

Table 9.6: Requirements on beam delivery, MDI and LumiCal installation, needed to limit individual systematic effects to $< 1 \times 10^{-3}$.

- 1 ■ $\sigma_{x_{\text{IP}}}$ and $\sigma_{z_{\text{IP}}}$, radial and axial fluctuations of the scattering position,
- 2 ■ r_{in} , inner radius of the LumiCal acceptance region,
- 3 ■ $\sigma_{r_{\text{shower}}}$, reconstruction precision of the radial shower coordinate,
- 4 ■ Δd_{IP} , uncertainty of the distance between the LumiCal halves.

5 Most requirements are technically feasible with the present state of the art of acceler-
6 ator and detector technology. The most important challenge identified is the precision
7 of the inner acceptance radius r_{in} of LumiCal. In order to keep the luminosity precision
8 of 1 per mille, r_{in} must be known to within 10 μm . The precision requirement of r_{in}
9 scales linearly with the required luminosity precision, implying a correspondingly stricter
10 requirement for the Z -pole run.

11 **9.5.3 Summary on LumiCal**

12 Instrumentation of the very forward region is very important for the realization of the
13 CEPC physics program. Several technology options are under consideration. Some of
14 them have been successfully applied at LEP or are under study for other future projects.
15 A tracker placed in front of the LumiCal can improve polar angle measurement accuracy,
16 facilitate LumiCal alignment and enable electron-photon separation. LumiCal centered on
17 the outgoing beam axis is studied for the systematic effects at the required level. Precision
18 requirements on beam delivery, MDI and LumiCal installation have been addressed by
19 simulation, and proven to be feasible with the present state-of-the-art of accelerator and
20 detector technology.

1 9.6 Detector integration

2 Both QD0 and QF1 are located inside the detector, which drastically complicates the sup-
 3 port and alignment of the detector and machine components in the interaction region. The
 4 two final focus magnets and the LumiCal will possibly be mounted on a dedicated sup-
 5 port structure, extended from a pillar outside the detector and suspended from the solenoid
 6 cryostat. They might have to be integrated together before being pushed into the inter-
 7 action region. The amount of material in front of the LumiCal must be minimized so
 8 that the high precision of the LumiCal can be maintained. This shall inevitably introduce
 9 more complexities to the detector integration. Furthermore, the shaped beam pipe and
 10 surrounded silicon detectors will possibly be supported from a structure of carbon fiber
 11 reinforced plastic, which can hang at the flanges of the field cage of the Time Projection
 12 Chamber (TPC). Significant effort is required to realize a solid mechanical design and to
 13 define a reasonable procedure for the detector and machine installation scheme.

14 References

- 15 [1] The CEPC-SPPC Study Group, *CEPC-SPPC Preliminary Conceptual Design*
 16 *Report, Volume I - Physics and Detector*, .
 17 <http://cepc.ihep.ac.cn/preCDR/volume.html>.
 18 IHEP-CEPC-DR-2015-01, IHEP-TH-2015-01, IHEP-EP-2015-01.
- 19 [2] The CEPC Study Group, *CEPC Conceptual Design Report, Volume I - Accelerator*,
 20 . IHEP-CEPC-DR-2018-01, IHEP-AC-2018-01, to be published.
- 21 [3] G. von Holtey et al., *Study of beam-induced particle backgrounds at the LEP*
 22 *detectors*, *Nucl. Instr. and Meth.* **A403** (1998) 205 – 246.
- 23 [4] P. M. Lewis et al., *First Measurements of Beam Backgrounds at SuperKEKB*,
 24 [arXiv:1802.01366 \[physics.ins-det\]](https://arxiv.org/abs/1802.01366).
- 25 [5] D. S. Denisov et al., *Machine-Related Backgrounds in the SiD Detector at ILC*,
 26 *JINST* **1** (2006) P12003, [arXiv:hep-ex/0608001 \[hep-ex\]](https://arxiv.org/abs/hep-ex/0608001).
- 27 [6] B. Dalena, J. Esberg, and D. Schulte, *Beam-induced backgrounds in the CLIC 3 TeV*
 28 *CM energy interaction region*, in *International Workshop on Future Linear*
 29 *Colliders (LCWS11) Granada, Spain, September 26-30, 2011*. 2012.
 30 [arXiv:1202.0563 \[physics.acc-ph\]](https://arxiv.org/abs/1202.0563).
- 31 [7] GEANT4 Collaboration, S. Agostinelli et al., *GEANT4: A Simulation toolkit*, *Nucl.*
 32 *Instrum. Meth.* **A506** (2003) 250–303.
- 33 [8] J. Allison et al., *Geant4 developments and applications*, *IEEE Trans. Nucl. Sci.* **53**
 34 (2006) 270.
- 35 [9] Geant4 Collaboration, M. Asai et al., *Recent developments in Geant4*, *Annals Nucl.*
 36 *Energy* **82** (2015) 19–28.
- 37 [10] S. Baranov, I. Dawson, M. Shupe, A. Nisati, M. Bosman, and V. Hedberg,
 38 *Estimation of radiation background, impact on detectors, activation and shielding*

- 1 optimization in ATLAS, 2005. ATL-GEN-2005-001, ATL-COM-GEN-2005-001,
 2 CERN-ATL-GEN-2005-001.
- 3 [11] I. Agapov, G. A. Blair, S. Malton, and L. Deacon, *BDSIM: A particle tracking code*
 4 *for accelerator beam-line simulations including particle-matter interactions*, *Nucl.*
 5 *Instrum. Meth.* **A606** (2009) 708–712.
- 6 [12] D. Schulte, *Beam-beam simulation with GUINEA-PIG*, In 5th International
 7 Computational Accelerator Physics Conference (1998) . CLIC-NOTE 387.
- 8 [13] R. Kleiss and H. Burkhardt, *BBBREM – Monte Carlo simulation of radiative*
 9 *Bhabha scattering in the very forward direction*, *Comput. Phys. Commun.* **81**
 10 (1994) 372 – 380.
- 11 [14] K. Oide and H. Koiso, *Anomalous equilibrium emittance due to chromaticity in*
 12 *electron storage rings*, *Phys. Rev.* **E49** (1994) 4474–4479.
- 13 [15] S. Jadach, *Theoretical error of luminosity cross-section at LEP*, in *Electroweak*
 14 *precision data and the Higgs mass. Proceedings, Workshop, Zeuthen, Germany,*
 15 *February 28-March 1, 2003*, pp. 85–95. 2003. [arXiv:hep-ph/0306083](https://arxiv.org/abs/hep-ph/0306083)
 16 [*hep-ph*].
- 17 [16] S. Jadach et al., *Upgrade of the Monte Carlo program BHLUMI for Bhabha*
 18 *scattering at low angles to version 4.04*, *Comput. Phys. Commun.* **102** (1997)
 19 229–251.
- 20 [17] OPAL Collaboration, G. Abbiendi et al., *Precision luminosity for Z0 line shape*
 21 *measurements with a silicon tungsten calorimeter*, *Eur. Phys. J.* **C14** (2000)
 22 373–425, [arXiv:hep-ex/9910066](https://arxiv.org/abs/hep-ex/9910066) [*hep-ex*].
- 23 [18] P. Bloch et al., *Performance Study of Non-Irradiated Prototype Silicon Preshower*
 24 *Samplers for CMS*, 2000. CMS-NOTE-2000-042.
- 25 [19] Y. Chang et al., *Lateral development of electron showers measured by silicon*
 26 *microstrip detectors*, *Nucl. Instr. and Meth.* **A388** (1997) 135 – 143.

Draft-V2.0

CHAPTER 10

SIMULATION, RECONSTRUCTION AND PHYSICS OBJECT PERFORMANCE

This chapter summarizes the expected performances of the CEPC baseline detector concept based on Monte Carlo (MC) simulation studies. Section 10.1 describes software and algorithm tools, event generation and simulation as well as the reconstruction. Section 10.2 presents the performances for identifying and measuring basic physics objects such as leptons, photons, jets and their flavors that form the building blocks of physics analyses. The results presented represent the first attempt to understand the performance of the CEPC baseline detector. They will likely improve with further studies and optimization.

10.1 Event simulation and reconstruction

The simulation of physics events and detector responses and the reconstruction of the raw detector information are vital for high energy physics experiments. Figure 10.1 shows the flow chart of the event simulation and reconstruction. In this section, the functionalities of key components of the chart are described.

10.1.1 Event simulation

For the studies of the CEPC physics performance, the Whizard [1] package is used as the main event generator to produce physics events. Collaborating with the Whizard team, a dedicated CEPC beam parametrization has been implemented in its official release. The Whizard generator is used to simulate Standard Model processes, including both the Higgs boson signal and all its SM background samples. Additionally, Madgraph [2] and Pythia [3] generators are used to produce samples from beyond Standard Model physics.

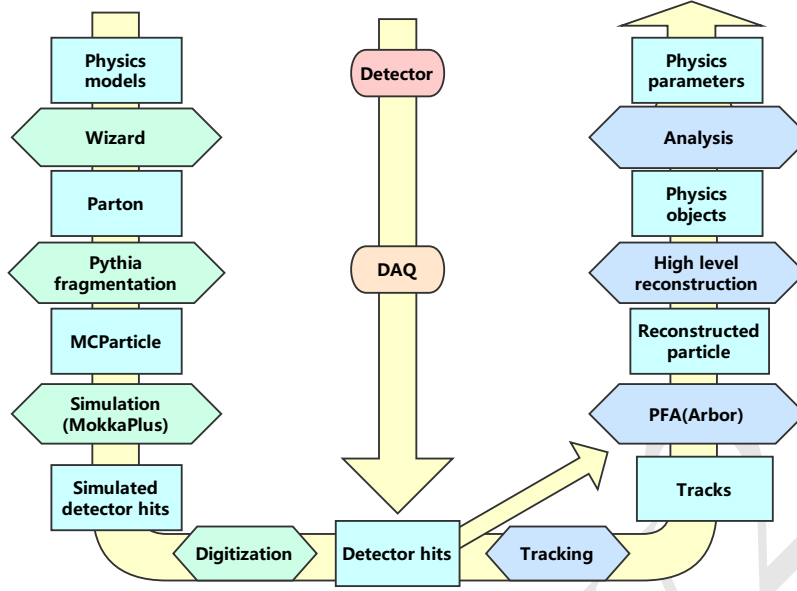


Figure 10.1: The flow chart of the CEPC simulation studies.

A GEANT4-based detector simulation framework, MokkaPlus, is used for the CEPC detector simulation. MokkaPlus is a virtual geometry constructor that compiles with the GEANT4 libraries [4] and a MySQL database [5]. It is an improved version of Mokka [6], a simulation framework used for early linear collider studies. The digitization of simulated energy deposits in the detector are performed using a general algorithm that reproduces the test beam results [7] for the calorimeter and an *ilcsoft* scheme for the tracking detectors. The parameter values of the *ilcsoft* scheme are tuned to match the CEPC detector design. In addition, a fast simulation based on the efficiency and resolution parametrization derived from the full simulation was also developed. The fast simulation is used to produce most of the background samples for studies presented in this report.

10.1.2 Event reconstruction

The event reconstruction chain starts with the track reconstruction, followed by the particle flow interpretation of tracks and calorimeter hits and finally the reconstruction of compound physics objects such as converted photons, K_S 's, τ -leptons and jets.

Tracks are reconstructed from hits in the tracking detectors by the tracking module. The module is currently based on the *Clupatra* module [8] of *ilcsoft* which has been shown to have excellent performance. A CEPC-specific tracking module with the flexibility of geometry modification is under development.

A dedicated particle flow reconstruction toolkit, ARBOR [9, 10], has been developed for the CEPC baseline detector concept. ARBOR is composed of a clustering module and a matching module. The clustering module reads the calorimeter hits and forms clusters of hits (also called branches) which are then arranged into a tree topology as illustrated in Figure 10.2 for the 3-prong decay of a τ -lepton. The matching module identifies calorime-

ter clusters with matching tracks and builds reconstructed charged particles. The remaining clusters are reconstructed into photons, neutral hadrons and unassociated fragments. From this unique list of particles, simple particles such as electrons, muons, photons, charged pions and kaons can then be identified.

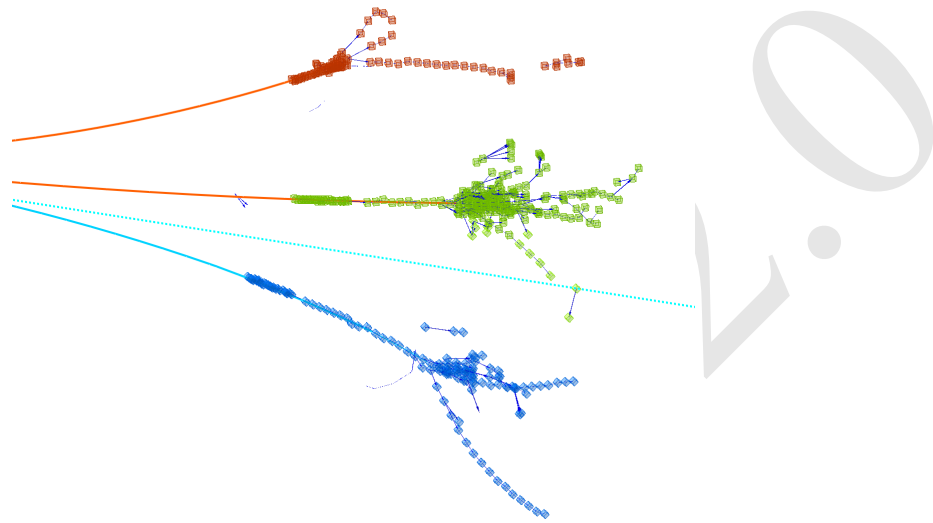


Figure 10.2: An illustration of particle flow reconstruction: the 3-prong decay of a τ -lepton from $Z \rightarrow \tau^+\tau^-$ reconstructed by the ARBOR algorithm. Three branches of calorimeter clusters correspond to the three reconstructed charged particles of the τ -lepton decay: a 5.7 GeV π^+ (red), a 27.4 GeV π^+ (green) and a 10.3 GeV π^- (blue). Also shown are lines representing Monte Carlo truth information: two π^+ 's (red), a π^- (cyan) and a $\bar{\nu}_\tau$ (cyan dashed).

The particle flow reconstruction provides a coherent interpretation of an entire physics event and, therefore, is well suited for the reconstruction of compound physics objects such as converted photons, K_S 's, τ -leptons and jets. The reconstruction of τ -leptons and jets are described in Section 10.2. CORAL, an algorithm that targets the reconstruction of converted photons, π^0 's and K_S 's, is being developed.

10.1.2.1 Track reconstruction

The CEPC baseline tracker consists of a silicon tracking system and a barrel TPC. The two subsystems play complementary roles. The silicon system provides high precision spatial point measurements whereas the TPC has more than 200 radial layers which significantly enhances the track finding performance of the detector. In addition, the silicon system includes a forward tracking system that extends the solid angle coverage of the tracker.

The performance of the CEPC tracker is studied using two samples: a single muon particle sample and an $e^+e^- \rightarrow Z \rightarrow \tau^+\tau^-$ sample at $\sqrt{s} = 91.2$ GeV. The single muon sample is used to characterize the tracking efficiency and momentum resolution for isolated tracks while the $Z \rightarrow \tau^+\tau^-$ sample, with the 3-prong decay for one of the two τ -leptons, provides a test for reconstructing closely spaced tracks.

The single muon sample covers a momentum range of 0.1 GeV to 100 GeV and the full angular range. Figure 10.3 shows the extracted efficiency and momentum resolution

as a function of the polar angle for different momentum bins. For muons in the tracking fiducial volume of $|\cos \theta| < 0.985$ and with momentum above 0.5 GeV, the reconstruction efficiency is nearly 100%. The momentum resolution reaches per mille level for the momentum range of 10–100 GeV in the barrel region. The resolution is limited by material-induced multiple scatterings at low momentum and by the magnetic field and level-arm at high momentum, consistent with the design goal outlined in Chapter 3. The τ -leptons from $Z \rightarrow \tau^+ \tau^-$ are highly boosted and can lead to three closely spaced charged particles in their 3-prong decays, see Figure 10.2. For this sample, the efficiency for reconstructing all three tracks of the τ decays is found to be close to 100% .

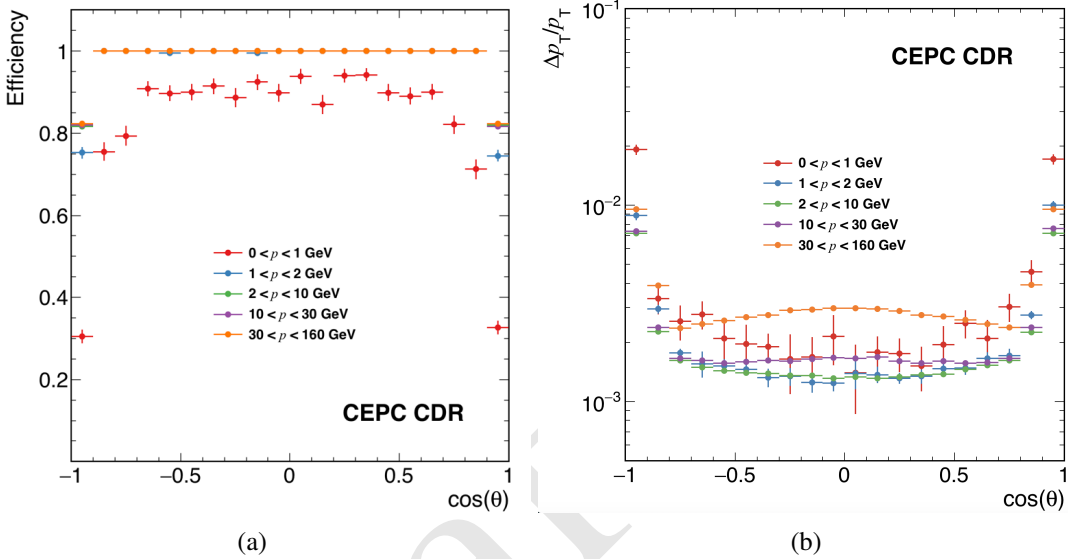


Figure 10.3: Single track reconstruction: (a) efficiency and (b) momentum resolution as a function of the cosine of the polar angle in different momentum bins.

10.1.2.2 Cluster reconstruction

The high-granular calorimeters of the CEPC baseline detector concept are well suited for reconstructing clusters of energy deposits by traversing particles. The fine segmentation allows for the reconstruction of individual particles produced in shower cascades, see Figure 10.2.

Two relevant performance measures of the cluster reconstruction are the energy collection efficiency for single neutral particles and spatial separation capability for two closely spaced neutral particles. For photons with energy above 5 GeV, ARBOR is able to collect more than 99% of the energy deposited in the calorimeter while keeping the mis-clustering rate small. Good cluster spatial separation capability is essential for the reconstruction of compound particle objects such as π^0 's and τ -leptons. Figure 10.4(a) is a demonstration of the reconstructed clusters from two closely spaced photons from a π^0 decay. The efficiencies for successfully reconstructing two photon clusters as functions of their separation at the calorimeter entry points are shown in Figure 10.4(b) for three different ECAL cell sizes. The critical distance, defined as the minimum separation at which the efficiency for reconstructing two photon clusters is 50%, is found to be 16 mm for the baseline design of ECAL cell size of $10 \times 10 \text{ mm}^2$. This corresponds to an average

¹ efficiency of 50% for reconstructing two photons as two separate clusters from a 30 GeV
² π^0 decay with equal energy.

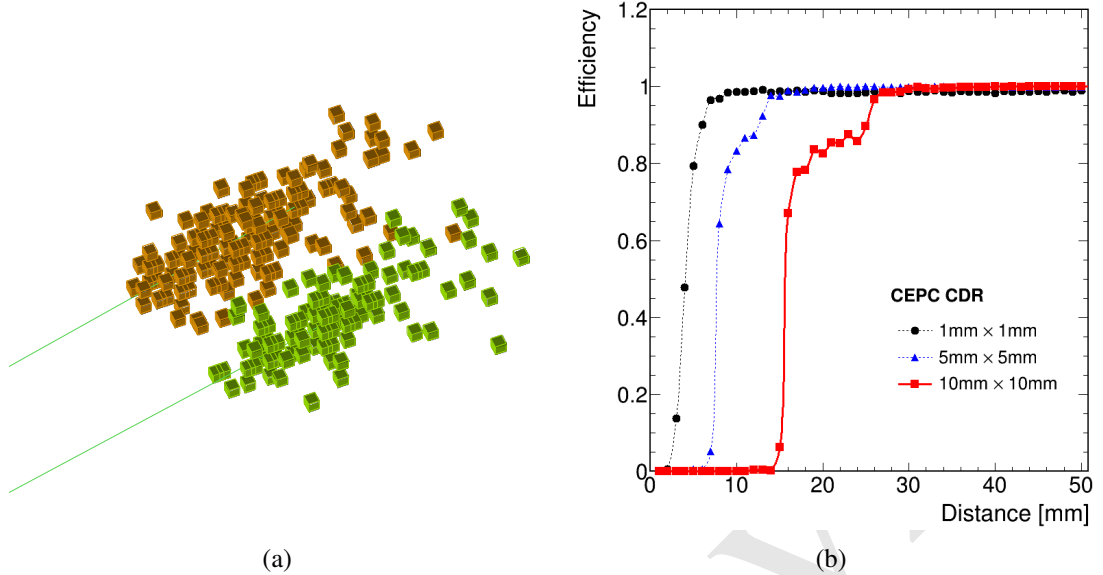


Figure 10.4: (a) Clusters of the two photons of energies of 6.2 GeV and 5.8 GeV from a 10 GeV π^0 decay reconstructed in the Silicon-Tungsten ECAL with a $10 \times 10 \text{ mm}^2$ cell size. (b) Reconstruction efficiencies of two photons as two separate clusters as functions of the distance between their calorimeter impact points for three different ECAL cell sizes. The ECAL cell size of the CEPC baseline detector is chosen to be $10 \times 10 \text{ mm}^2$. The secondary step structures in the efficiency curves reflect the finite granularity of the calorimeter.

³ 10.2 Object Identifications and Performances

⁴ Particle flow reconstruction leads to a unique list of particles from which electrons, muons,
⁵ photons, τ -leptons, and jets etc., the physics objects as they are customarily called, can
⁶ be identified or built. These objects serve as building blocks for further physics analyses
⁷ as presented in Chapter 11. In this section, their general identifications and the expected
⁸ performances are described. For analyses of specific processes, the identifications and
⁹ performances can often be improved by utilizing the unique topologies of the events under
¹⁰ study.

¹¹ 10.2.1 Leptons

¹² Leptons (ℓ , $\ell = e, \mu$)¹ are bedrocks to the CEPC physics program. $Z \rightarrow e^+e^-$ and
¹³ $Z \rightarrow \mu^+\mu^-$ decays are indispensable for electroweak measurements and for the model-
¹⁴ independent identification of the Higgs boson through the recoil mass method. A large
¹⁵ fraction of Higgs bosons decay, directly or via cascade, into final states with electrons and
¹⁶ muons.

¹⁷ The particle-flow oriented baseline detector, particularly its fine-segmented calorime-
¹⁸ ter system, provides enormous information for the lepton identification. High energy

¹Unless otherwise noted, leptons refer to electrons, muons or their antiparticles.

1 electrons and hadrons will likely induce thousands of hits whereas muons deposit little
 2 energy in the calorimeter. Electrons can be identified from their pencil-like electromagnetic
 3 shower development in ECAL matched with tracks in the tracker. Muons exhibit
 4 themselves as minimum ionizing particles in the calorimeter matched with tracks in the
 5 tracker as well as in the muon system. Moreover, the dE/dx measurements in the TPC
 6 could provide additional discrimination of electrons from muons and hadrons for energies
 7 up to 10 GeV.

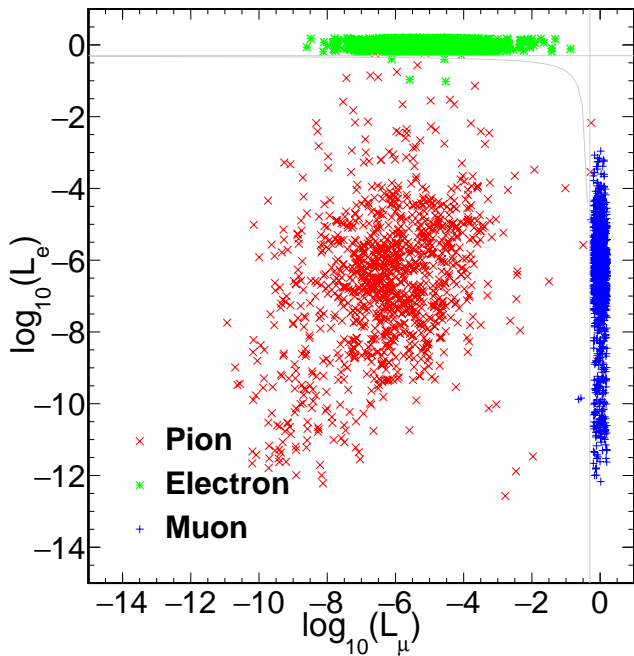


Figure 10.5: Distributions of the logarithm of e -likeliness L_e and μ -likeliness L_μ expected from 40 GeV electrons, muons and charged pions in the barrel calorimeter ($|\cos \theta| < 0.7$).

8 A lepton identification algorithm, LICH [11], has been developed and implemented
 9 in ARBOR. LICH combines more than 20 discriminating variables from the detector to
 10 build lepton-likelihoods, e -likeliness (L_e) and μ -likeliness (L_μ), using a multivariate tech-
 11 nique. Figure 10.5 compares the two-dimensional distributions of L_e and L_μ expected
 12 from single electrons, muons and charged pions, showing clear separations among these
 13 particles. For leptons above 2 GeV, an identification efficiency better than 99.5% and a
 14 mis-identification rate from hadrons smaller than 1% can be achieved. The main sources
 15 of mis-identifications are irreducible backgrounds from the $\pi^\pm \rightarrow \mu^\pm$ decays for muons
 16 and highly electromagnetic like π^\pm clusters (π^0 produced in pion-nucleon interactions)
 17 for electrons. The momentum resolution of the tracker (see Section 10.1.2.1) largely de-
 18 termines the resolutions for both electrons and muons. However, degradation of the reso-
 19 lutions is expected from Bremsstrahlung radiation, most importantly for electrons and to a
 20 lesser extent for muons. Recovering the radiation energy losses using the ECAL measure-
 21 ments should improve the resolutions. However, this is not implemented for the current
 22 studies.

23 For complex physics events, lepton identification will be affected by the limited spa-
 24 tial separation capability of the detector. For example, the efficiency for successfully
 25 identifying two leptons with opposite charges is found to be 97–98% for the $e^+e^- \rightarrow$

$ZH \rightarrow \ell^+ \ell^- H$ events. The small loss of the efficiency can be attributed to overlapping clusters in the calorimeter.

Figure 10.6 shows the reconstructed recoil mass² distributions of the $Z \rightarrow \mu^+ \mu^-$ and $Z \rightarrow e^+ e^-$ decays from the $e^+ e^- \rightarrow ZH$ process, and Figure 10.7 is the dimuon invariant mass distribution of $H \rightarrow \mu^+ \mu^-$ again from $e^+ e^- \rightarrow ZH$. The sharp peaks at the Higgs boson mass are demonstrations of excellent lepton energy/momenta and angular resolutions. The tails are due to radiation effects. The recoil mass distributions are critical for the model-independent identifications of the Higgs boson and a good dimuon mass resolution is essential for identifying $H \rightarrow \mu^+ \mu^-$ decays, see Section 11.1.

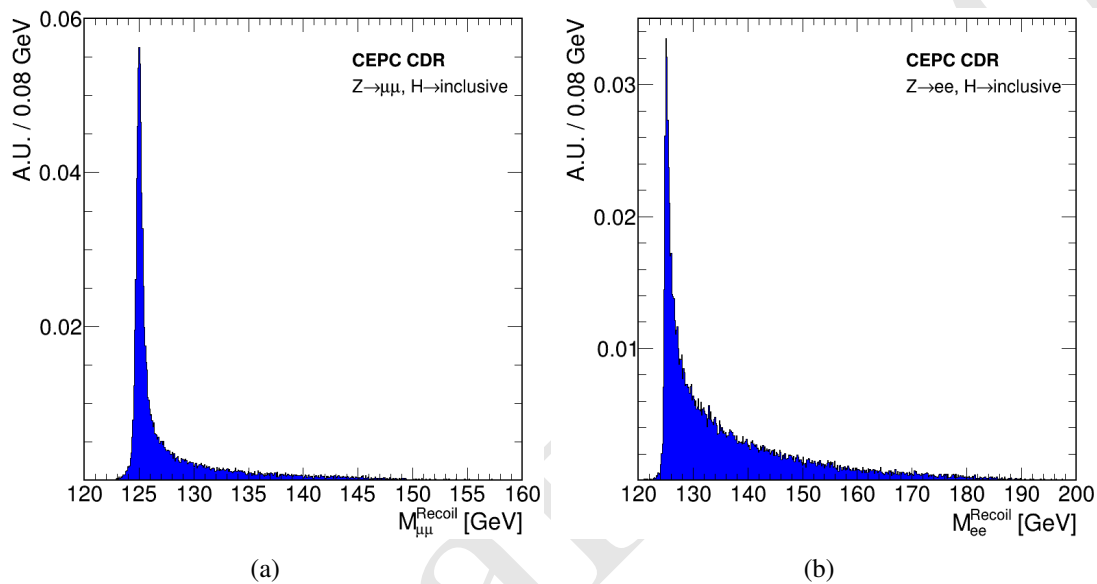


Figure 10.6: The reconstructed dilepton recoil mass distributions of $\mu^+ \mu^- H$ and $e^+ e^- H$ events, both normalized to unit area. The distributions peak strongly at the Higgs boson mass. The high-mass tails are results of radiation effects (for example the initial- and final-state radiations, the beamstrahlung and the Bremsstrahlung effects). Fit with double-sided crystal ball functions, each distribution exhibits a core width of 200–300 MeV. The $e^+ e^- H$ has a much more significant high mass tail, as the electrons have much stronger radiation effects compared to the muons.

10.2.2 Photons

Photons can be produced from either initial- and final-state radiation or decays of unstable particles. Precise photon measurements are essential, for example, for studying the $H \rightarrow \gamma\gamma$ decay and counting neutrino species. Moreover, photons are a large part of secondary particles that form jets and have an important role in the τ -lepton identification, they impact all aspects of the physics at the CEPC.

Photons have similar signatures as electrons in the calorimeter, but in general without matching tracks in the tracker. However, 5–10% of photons in the central region and $\sim 25\%$ of photons in the forward region convert to $e^+ e^-$ pairs through their interaction with the materials in front of the calorimeter. Some of these converted photons will have reconstructed matching tracks. Figure 10.8(a) shows the material in the unit of radiation

²See Section 11.1.2 for the definition.

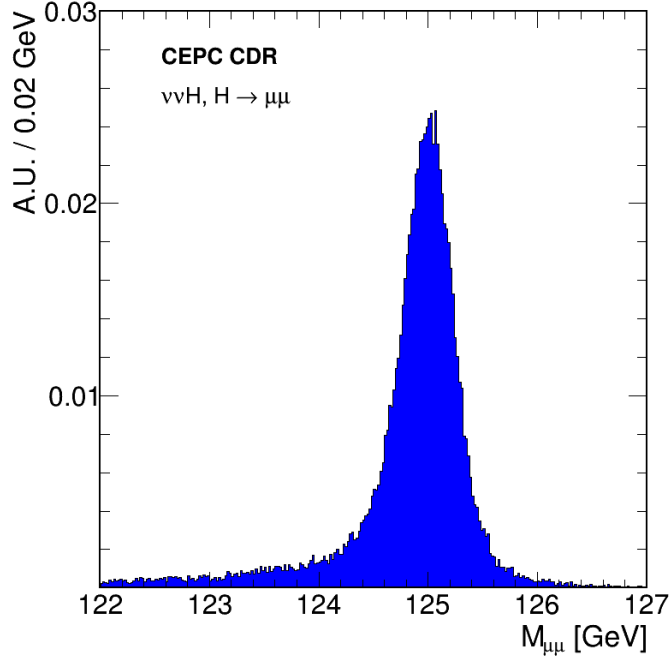


Figure 10.7: The reconstructed invariant mass distributions of dimuons from the $H \rightarrow \mu^+\mu^-$ decay produced in the $e^+e^- \rightarrow ZH$ process. The distribution shows a relative mass resolution of 0.19%.

length, and Figure 10.8(b) is the photon conversion rate at different polar angles. For unconverted photons of energies above 5 GeV, the identification efficiency is nearly 100% with more than 99% of their energy reconstructed. For the current studies, a simplistic algorithm has been used to identify converted photons. Approximately 80% of the converted photons are recovered using this algorithm. The rate of misidentifying a hadronic jet as a photon is found to be negligible.

Figure 10.9(a) compares the energy resolution of unconverted photons of the baseline detector concept with the intrinsic resolution of the calorimeter. The intrinsic resolution is obtained from MC simulation without material in front and gaps between modules and is consistent with the CALICE test beam result [12]. It represents the ultimate resolution of the detector. The material in the tracker and geometric inhomogeneities are the main causes for the degradation in the resolution of the baseline detector. These effects are currently not taken into account in the calibration. The resolution, both the sampling and constant terms, is expected to improve significantly once geometry dependent calibration is implemented. The photon energy resolution can be benchmarked using the diphoton mass distribution of the $H \rightarrow \gamma\gamma$ decay as shown in Figure 10.9(b). The width of the mass distribution is dominated by the energy resolution effect because of the narrow intrinsic Higgs boson width. The current diphoton mass resolution is approximately 2.5% compared with 1.7% of the intrinsic resolution.

10.2.3 Tau Leptons

As the heaviest lepton, τ -leptons have a unique role in studying Higgs boson physics. Leptonic decays of τ -leptons, $\tau \rightarrow e\nu\nu$ and $\tau \rightarrow \mu\nu\nu$, are indistinguishable from electrons or muons, displaced by the finite τ -lifetime. Hadronic decays of the τ -leptons appear in

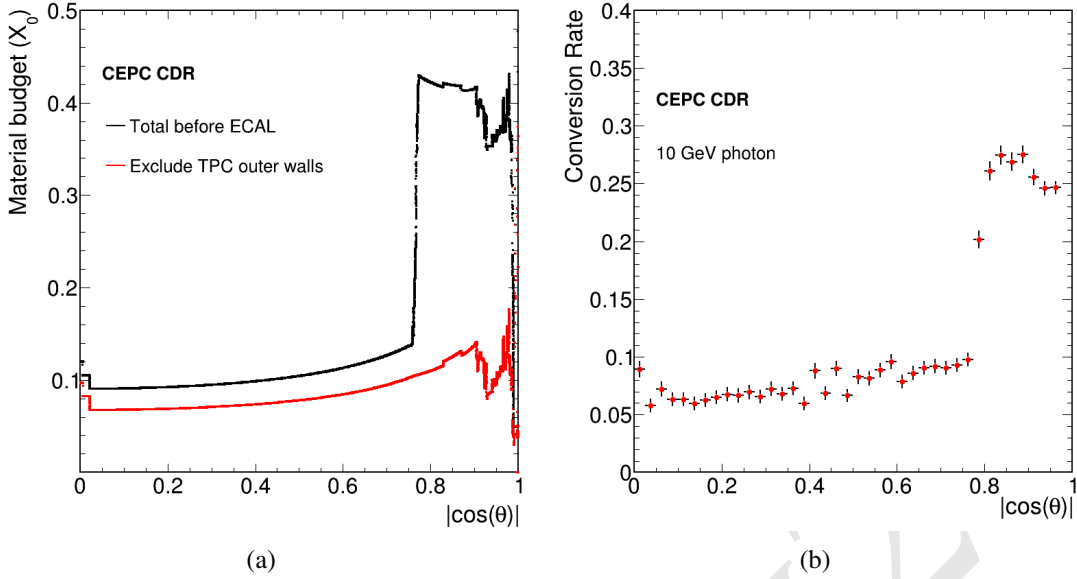


Figure 10.8: (a) The material in the unit of radiation length inside the tracker and (b) the conversion rate of 10 GeV photons for different polar angles.

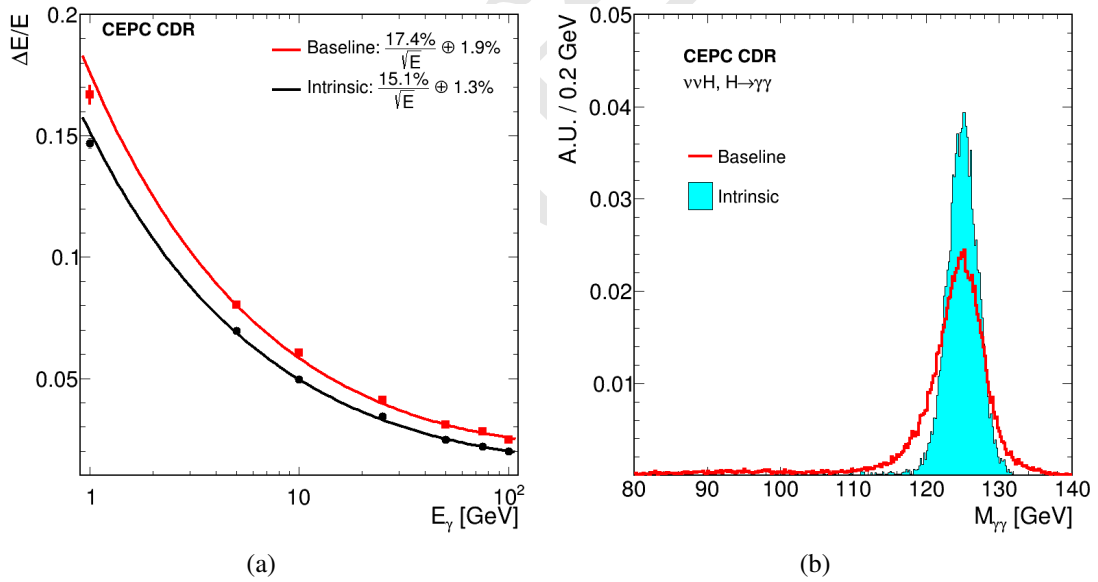


Figure 10.9: (a) The energy resolution of unconverted photons as a function of energy of the baseline detector compared with the intrinsic resolution of the calorimeter and (b) the invariant mass distribution of diphotons from the $H \rightarrow \gamma\gamma$ decay of the $e^+e^- \rightarrow ZH$ process. For the photon energy resolution, both detectors refers to single particle sample with a flat distribution in θ . The resolution of the baseline detector is expected to improve with further optimizations and geometry-dependent calibrations which should bring it closer to the intrinsic resolution of the calorimeter.

- ¹ the detector as narrow pencil-shaped hadronic jets with low particle multiplicity. A basic
- ² τ -lepton identification algorithm has been developed for hadronic decays. The algorithm
- ³ starts with a seed track with its energy above 1.5 GeV and clusters charged and neutral
- ⁴ particles in a small cone of radius of 0.15 radians around it to form the τ -lepton candidate.

The invariant mass formed by the particles in the cone is required to be in the range of 0.2–2 GeV, consistent with the τ -lepton mass. Furthermore, a discriminant variable based on the longitudinal and transverse impact parameters of the leading track is constructed and the variable is required to be consistent with the non-zero lifetime of the τ -lepton. Finally, the τ -lepton candidate is required to be isolated. The total energy in an annular cone or radius between 0.15–0.45 radians is required to be less than 8% of the τ -lepton candidate energy. The main backgrounds are hadronic jets.

Figure 10.10(a) is a graphic representation of the tau identification. The efficiency and the mis-identification rate as functions of the visible energy of the τ -lepton candidate are shown in Figure 10.10(b). The identification efficiency and mis-identification rate are currently optimized and characterized using the $e^+e^- \rightarrow ZH$ events with the $Z \rightarrow q\bar{q}$ and $H \rightarrow \tau^+\tau^-$ decays. For visible energies above 50 GeV, the efficiency is closer to 90% or higher with less than 1% mis-identification rate. The loss of efficiency is largely due to the large cone size used for the isolation requirement. Significant improvement in performance can be expected from dedicated optimization for τ -lepton identification.

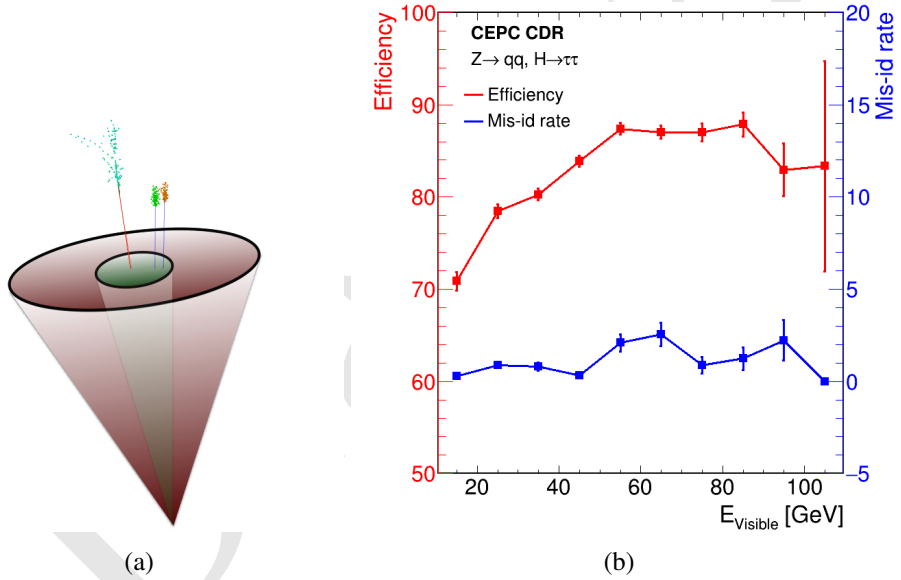


Figure 10.10: (a) Illustration of τ -lepton identification and (b) the efficiency and mis-identification rate as functions of the visible energies of τ -lepton candidates. The efficiency is measured using the $H \rightarrow \tau^+\tau^-$ decays of $e^+e^- \rightarrow ZH \rightarrow q\bar{q}\tau^+\tau^-$ events and the mis-identification rate is measured from an inclusive $e^+e^- \rightarrow q\bar{q}H$ sample for τ -lepton candidates in $|\cos(\theta)| < 0.6$.

10.2.4 Jets

The vast majority of the events produced at the CEPC have hadronic jets in their final states. For example, 70% of the Higgs bosons decay directly to a pair of jets and another 20% decay indirectly to jets through intermediate W or Z bosons. Coincidentally, about 70% of the W or Z bosons each decays to dijets. Thus the impact of jets to the CEPC physics program cannot be overstated.

Jets are formed from particles reconstructed by ARBOR using the Durham clustering algorithm [13]. The ambiguity in clustering is the leading source of uncertainty in

jet reconstruction and measurements, particularly in events with closely spaced physics objects.

Jet energies are foreseen to be calibrated through a two-step process. First, calibrations are applied to particles identified by ARBOR. While the energies of the charged particles are determined by their track momenta, the energies of neutral particles are currently calibrated using MC simulation and can be calibrated using the test beam or collision data when they are available. Approximately 35% of the jet energy is carried by neutral particles. In the second step, the jet energy are calibrated using physics events. At the CEPC, W and/or Z bosons are copiously produced and can be identified with high efficiency and purity. Thus $W \rightarrow q\bar{q}$ and $Z \rightarrow q\bar{q}$ decays serve as standard candles for the jet energy calibration. Clean samples of $WW \rightarrow \ell\nu q\bar{q}$ (ZH and WW runs), $ZZ \rightarrow \nu\bar{\nu}q\bar{q}$ (ZH run) and $Z \rightarrow q\bar{q}$ (Z pole run) can be selected. The enormous statistics allows the jet response to be characterized in detail.

Figure 10.11(a) shows energy ratios between the reconstructed jets and MC particle jets for different polar angles derived from simulated $ZZ \rightarrow \nu\bar{\nu}q\bar{q}$ events. The ratios are close to unity and thus the corrections are $< 1\%$. The jet energy resolution is shown in Figure 10.11(b) as a function of jet energy for different jet flavors. For light jets, the resolution ranges from 6% for at 20 GeV to 3.6% for at 100 GeV. The resolutions for heavy-flavor jets are poorer as expected because of neutrinos in their decays. Major factors affecting the jet energy scale and/or resolution are jet flavor composition, shower fluctuations, clustering algorithm as well as the stability and uniformity of the detector responses. Their impacts can be minimized by detailed studies and calibrations. A sub-percent level jet energy scale precision and a jet energy resolution of 3–5% for the jet energy range of 20–100 GeV should be achievable.

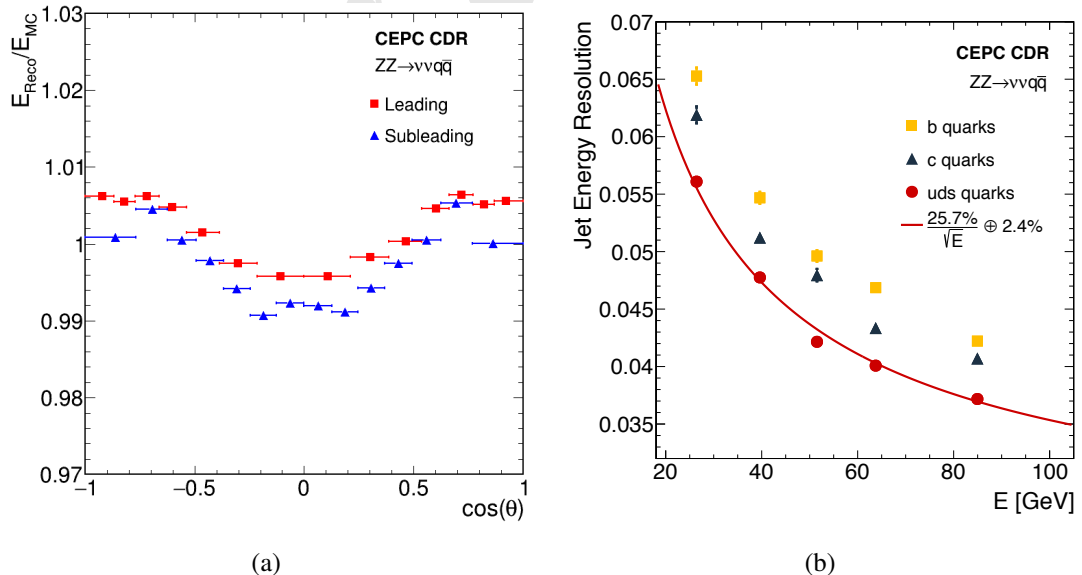


Figure 10.11: (a) The energy ratios between the reconstructed jets and MC particle jets as functions of cosine of their polar angles and (b) jet energy resolution as a function of jet energy for different jet flavor categories. These distributions are derived from simulated $ZZ \rightarrow \nu\bar{\nu}q\bar{q}$ events. The energy ratios are shown for leading and subleading jets separately.

One key jet performance measure is the ability to separate hadronic decays of W , Z and Higgs bosons. Figure 10.12(a) compares the reconstructed dijet invariant mass distributions from $W \rightarrow q\bar{q}$, $Z \rightarrow q\bar{q}$ and $H \rightarrow b\bar{b}/c\bar{c}/gg$ decays of $WW \rightarrow \ell\nu q\bar{q}$, $ZZ \rightarrow \nu\bar{\nu}q\bar{q}$ and $ZH \rightarrow \nu\bar{\nu}(b\bar{b}/c\bar{c}/gg)$ processes, respectively. Compared with $W \rightarrow q\bar{q}$, the $Z \rightarrow q\bar{q}$ and $H \rightarrow b\bar{b}/c\bar{c}/gg$ distributions have long low-mass tails. These tails are from the heavy-flavor jets as demonstrated in Figure 10.12(b) where the distributions from $H \rightarrow b\bar{b}$, $H \rightarrow c\bar{c}$ and $H \rightarrow gg$ decays are separately shown and compared. The $H \rightarrow gg$ distribution is symmetric and has the best mass resolution (at approximately 3.8%) whereas the $H \rightarrow b\bar{b}$ decay has a long asymmetric low-mass tail and therefore degraded mass resolution. The degradations in resolution and the distortions in the mass distributions for the $H \rightarrow b\bar{b}$ and $H \rightarrow c\bar{c}$ decay are expected from neutrinos produced in semi-leptonic decays of b - and c -quarks. The mass resolutions for $W \rightarrow q\bar{q}$ and $Z \rightarrow q\bar{q}$ are 4.4%, leading to an average separation of 2σ or better for the hadronic decayed W and Z bosons.

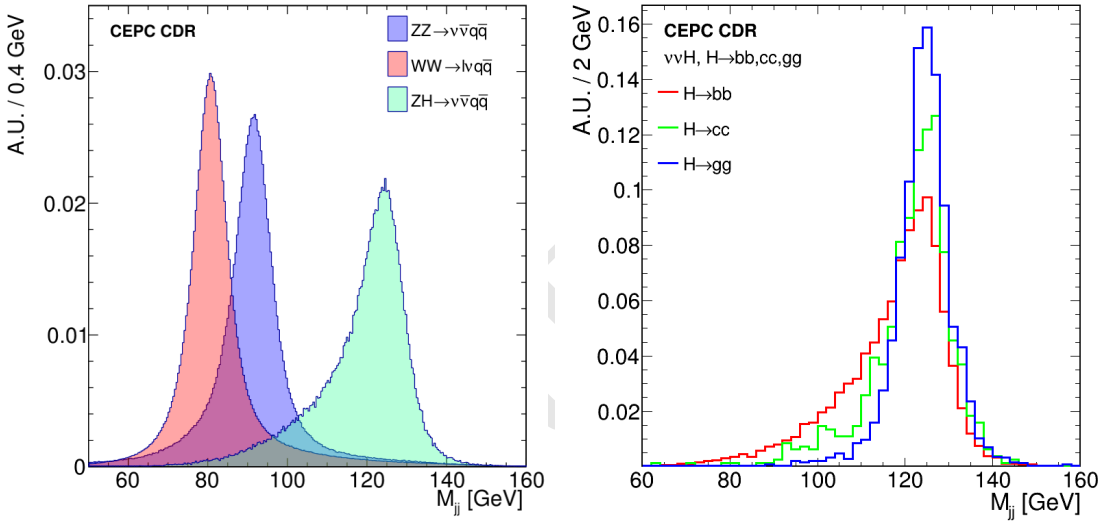


Figure 10.12: Reconstructed dijet mass distributions of (a) the $W \rightarrow q\bar{q}$, $Z \rightarrow q\bar{q}$ and $H \rightarrow b\bar{b}/c\bar{c}/gg$ decays from the $ZZ \rightarrow \nu\bar{\nu}q\bar{q}$, $WW \rightarrow \ell\nu q\bar{q}$ and $ZH \rightarrow \nu\bar{\nu}(b\bar{b}, c\bar{c}, gg)$ processes, respectively, and (b) the separate $H \rightarrow b\bar{b}$, $H \rightarrow c\bar{c}$ and $H \rightarrow gg$ decays from the $ZH \rightarrow \nu\bar{\nu}(b\bar{b}/c\bar{c}/gg)$ process. All distributions are normalized to unit area.

10.2.5 Jet flavor tagging

Identification, *i.e.* tagging, of jet flavors is essential for the measurements of the Higgs couplings and the electroweak observables at the CEPC. Heavy-flavor quarks (b and c) from W , Z or Higgs boson decays hadronize quickly to form heavy bottom and charm hadrons (B^0 , B^\pm , B_s , D^0 , D^\pm , ...). Those hadrons are short-lived and have typical decay distances of a few millimeters. Therefore, the reconstruction of their decay vertices, often referred as secondary vertices, is an important tool for tagging jet flavors. Other information such as jet and vertex mass, impact parameters and leptons inside the jets, are also frequently used to differentiate heavy-flavor jets from light-quark and gluon jets. For example, the excellent impact parameter resolution shown in Figure 4.2 can significantly improve the detector's capability for jet flavor tagging.

The jet flavor tagging is performed using LCFIPlus [14], the tagging algorithm used for linear collider studies. LCFIPlus reconstructs secondary vertices from the final-state particles identified by ARBOR. It combines more than 60 discriminant variables to calculate the b -likeliness (L_B) and c -likeliness (L_C) using a Boosted Decision Tree [15] method. Compared with the b -jet tagging, c -jet tagging is particularly challenging as charm hadrons have shorter lifetimes than bottom hadrons and therefore suffers more from light-quark and gluon jet backgrounds. Benefiting from the high precision vertex system, the CEPC detector provides reasonable separation of c -jets from other flavor jets. Figure 10.13 shows the b -jet tagging efficiencies for different rejections of background jets, measured from a $Z \rightarrow q\bar{q}$ sample of the Z pole run. For this sample, b -jets can be tagged with an efficiency of 80% and a purity of 90%. Similarly, an efficiency of 60% and a purity of 60% can be achieved for the c -jet tagging. Purities can be improved by tightening the tagging requirements at the expense of reduced efficiencies. Figure 10.14 is a demonstration of the b/c -likeliness distributions of the b , c and gluon jets from the $H \rightarrow b\bar{b}/c\bar{c}/gg$ decays, showing good separations between jets of different flavors.

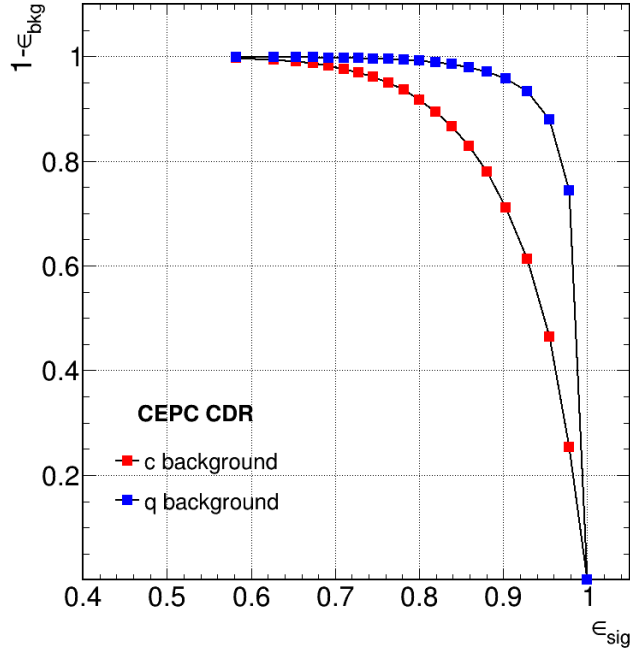


Figure 10.13: Efficiencies for tagging b -jets versus rejection of background jets, determined from an inclusive $Z \rightarrow q\bar{q}$ sample at the Z pole run.

10.2.6 Missing Energies, Momenta and Masses

Neutrinos interact weakly with the detector and for all practical purposes escape detection without traces. The same is true for the hypothesized dark matter particles. However, their existences can be inferred from detectable (“visible”) particles. The total energy and momentum of these “missing” particles, missing energy and momentum as they are usually called, can be calculated from the energies and momenta of visible particles through energy-momentum conservation. Despite of their elusive nature, neutrinos are as important as visible particles for the CEPC physics program. About 20% of the Z bosons and

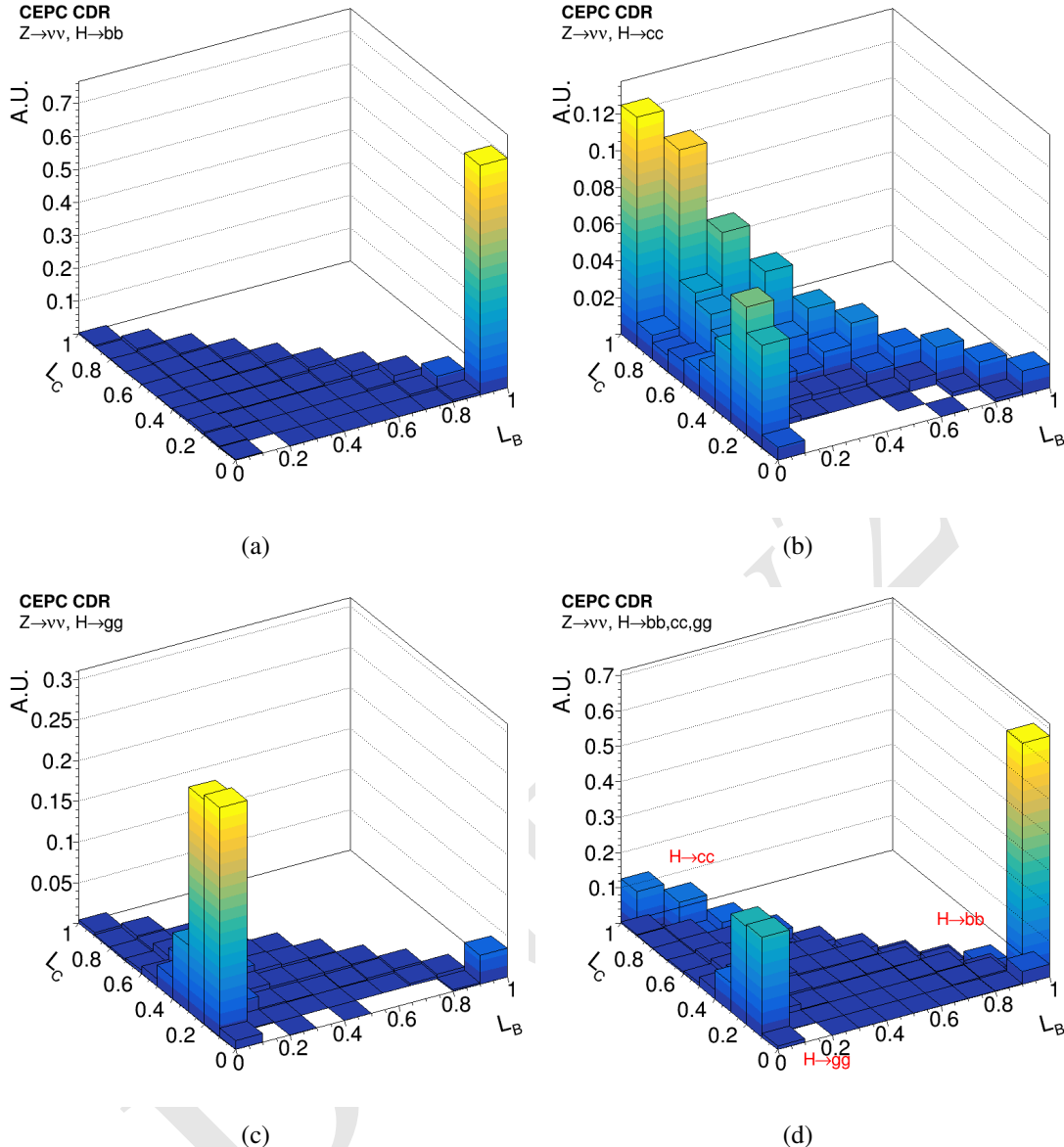


Figure 10.14: The two-dimensional distributions of b -likeliness L_B and c -likeliness L_C of jets from the $H \rightarrow b\bar{b}$, $H \rightarrow c\bar{c}$ and $H \rightarrow gg$ decays showing separately (a,b,c) and combined (d). Distributions of individual decays (a,b,c) are normalized to unit volume while the combined distribution is the sum of the three individual distributions.

¹ 30% of the W bosons decay directly into final states with neutrinos. Searching for Higgs
² boson decays to dark matter particles is a key physics goal of the Higgs factory.

The excellent energy and momentum resolutions of the CEPC baseline conceptual detector for visible particles allow for the determinations of missing energy and momentum with good precision. This is demonstrated using $e^+e^- \rightarrow ZH$ events in Figure 10.15 which shows the missing mass distributions of events from, respectively, ($Z \rightarrow q\bar{q}$, $H \rightarrow \text{inv}$) and ($Z \rightarrow \nu\bar{\nu}$, $H \rightarrow b\bar{b}/c\bar{c}/gg$) decays. The missing mass, calculated from the missing energy and momentum, is the invariant mass of the system of undetected particles. The missing mass distribution peaks at the Higgs boson mass for the $H \rightarrow \text{inv}$ decay and at the

¹ Z boson mass for the $Z \rightarrow \nu\bar{\nu}$ decay, as expected. Contributions from different jet flavors
² are shown separately. The Higgs and Z boson masses can be determined from missing
³ masses with good precision, allowing their identifications without direct detections.

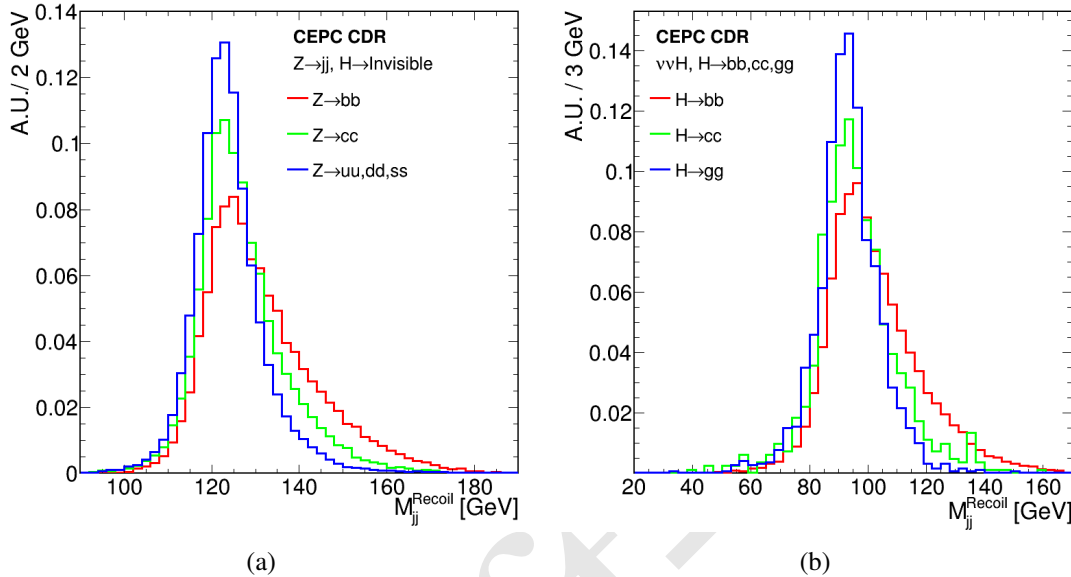


Figure 10.15: The dijet recoil mass (*i.e.*, the missing mass) distributions of $e^+e^- \rightarrow ZH$ events in the (a) $Z \rightarrow q\bar{q}$, $H \rightarrow \text{inv}$ and (b) $Z \rightarrow \nu\bar{\nu}$, $H \rightarrow b\bar{b}/c\bar{c}/gg$ decay, separately for different jet flavors. All distributions are normalized to unit area. The light-jet distribution in (a) has a Gaussian core width of approximately 6 GeV and the corresponding width of the $H \rightarrow gg$ distribution in (b) is 8 GeV.

10.2.7 Kaon Identification

Successful identification of charged kaons will greatly benefit the flavor physics program and aid in the determination of jet flavor as well as jet charge. The dE/dx information from the TPC can be used to separate kaons from pions. Assuming a relative dE/dx resolution of 5%, the measurement could lead to 2–4 σ separation of K/π for momentum between 2–20 GeV as shown in Figure 10.16.

The discriminating power of dE/dx vanishes for pions and kaons with their momenta around 1 GeV. Meanwhile, a significant portion of the charged particles has an energy smaller than 2 GeV at the CEPC. To aid the separation of these low momentum charged particles, it has been proposed to add a Time of Flight (TOF) capability with a 50 ps resolution to the detector design. The ECAL could be instrumented with a few layers of time sensitive readout to provide the TOF information. Using both the TOF and dE/dx information, a separation better than 2σ could be achieved for charged particles with momenta smaller than 20 GeV in the conservative scenario as shown in Figure 10.16(b). For the inclusive $Z \rightarrow q\bar{q}$ sample, charged kaons can be identified with an efficiency of 91% and a purity of 94%, integrated over the momentum range of 2–20 GeV.

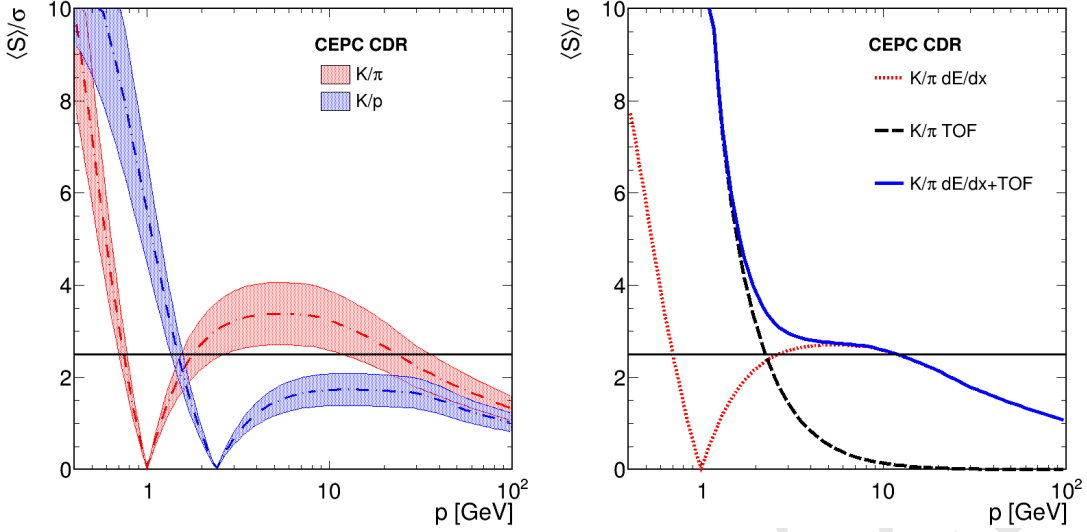


Figure 10.16: Charged particle identifications: (a) K/π and K/p separations from the dE/dx measurement in the TPC and (b) the K/π separation from both the dE/dx measurement and the proposed TOF information. The upper boundaries of the bands in (a) are the ideal separations predicted by the GEANT4 simulation while the lower boundaries correspond to conservative estimates with a 50% degradation in performance.

10.3 Summary

- Precise measurements of the Higgs boson properties and the electroweak observables at the CEPC place stringent requirements on the performance of the CEPC detector to identify and measure physics objects such as leptons, photons, τ -leptons, jets and their flavors with high efficiencies and purities as well as high precision. The performances of the CEPC baseline detector have been investigated with full simulation. Benchmark performances are described above and are briefly summarized below:
- 1 Leptons: an efficiency of $> 99.5\%$ with a mis-identification rate of $< 1\%$ for electrons and muons with momenta above 2 GeV, a relative mass resolution of 0.19% for the $H \rightarrow \mu^+ \mu^-$ decay;
 - 2 Photons: an efficiency of nearly 100% with negligible mis-identification rate from hadronic jets for photons above 5 GeV, relative mass resolution of 2.5% for the $H \rightarrow \gamma\gamma$ decay;
 - 3 τ -leptons: an efficiency of 90% or higher with a mis-identification rate of $< 1\%$ should be achievable for the identification of hadronic decays of τ -leptons from W , Z or Higgs boson decays;
 - 4 Jet energy scale and resolution: the jet energy scale can be measured with a sub-percent accuracy and a jet energy resolution of 3–5% is achievable for the energy range relevant at the CEPC, enabling a 2σ or better separation of the $W \rightarrow q\bar{q}$ and $Z \rightarrow q\bar{q}$ decays;
 - 5 Jet flavor tagging: efficiency/purity of 80%/90% for b -jets tagging and 60%/60% for c -jets tagging can be achieved for the $Z \rightarrow q\bar{q}$ sample of the Z pole run;

1 6 K^\pm identification: kaons can be separated from pions at 2σ for momentum up to
 2 20 GeV, corresponding to efficiency/purity of 95%/95% for identifying kaons in the
 3 $Z \rightarrow q\bar{q}$ sample integrated over the momentum range of 2–20 GeV.

4 Though significant progress has been made in understanding and characterizing the
 5 detector performance, the performance results can be further enhanced with improved
 6 algorithms and better calibrations. Nevertheless, the performance results as currently un-
 7 derstood are sufficient to fulfill the requirements laid out in Chapter 3 and to meet the
 8 physics analysis needs as presented in Chapter 11.

9 References

- 10 [1] W. Kilian, T. Ohl, and J. Reuter, *WHIZARD: Simulating Multi-Particle Processes at*
 11 *LHC and ILC*, *Eur. Phys. J. C* **71** (2011) 1742, [arXiv:0708.4233 \[hep-ph\]](https://arxiv.org/abs/0708.4233).
- 12 [2] J. Alwall, R. Frederix, S. Frixione, V. Hirschi, F. Maltoni, O. Mattelaer, H. S. Shao,
 13 T. Stelzer, P. Torrielli, and M. Zaro, *The automated computation of tree-level and*
 14 *next-to-leading order differential cross sections, and their matching to parton*
 15 *shower simulations*, *JHEP* **07** (2014) 079, [arXiv:1405.0301 \[hep-ph\]](https://arxiv.org/abs/1405.0301).
- 16 [3] The Pythia Group, *An Introduction to PYTHIA 8.2*, *Comput. Phys. Commun.* **191**
 17 (2015) 159–177, [arXiv:1410.3012 \[hep-ph\]](https://arxiv.org/abs/1410.3012).
- 18 [4] S. Agostinelli, J. Allison, K. Amako, et al., *Geant4 - a simulation toolkit*, *Nucl.*
 19 *Instr. and Meth. A* **506** (2003) no. 3, 250–303. [http://www.](http://www.sciencedirect.com/science/article/pii/S0168900203013688)
 20 [sciencedirect.com/science/article/pii/S0168900203013688](http://www.sciencedirect.com/science/article/pii/S0168900203013688).
- 21 [5] *MySQL*, <https://www.mysql.com/>.
- 22 [6] P. M. de Freitas and H. Videau, *Detector simulation with Mokka/Geant4: Present*
 23 *and future*, LC-TOOL-2003-010 .
- 24 [7] Y. Haddad, M. Ruan, and V. Boudry, *Software digitizer for high granular gaseous*
 25 *detector*, *JINST* **9** (2014) no. 11, C11016, [arXiv:1405.1286](https://arxiv.org/abs/1405.1286)
 26 [physics.ins-det].
- 27 [8] F. Gaede, S. Aplin, R. Glattauer, C. Rosemann, and G. Voutsinas, *Track*
 28 *reconstruction at the ILC: the ILD tracking software*, *J. Phys. Conf. Ser.* **513** (2014)
 29 022011.
- 30 [9] M. Ruan and H. Videau, *Arbor, a new approach of the Particle Flow Algorithm*, in
 31 *Proceedings, International Conference on Calorimetry for the High Energy*
 32 *Frontier (CHEF 2013): Paris, France, April 22-25, 2013*, pp. 316–324. 2013.
 33 [arXiv:1403.4784 \[physics.ins-det\]](https://arxiv.org/abs/1403.4784).
- 34 [10] M. Ruan et al., *Reconstruction of physics objects at the Circular Electron Positron*
 35 *Collider with Arbor*, *Eur. Phys. J. C* **78** (2018) no. 5, 426, [arXiv:1806.04879](https://arxiv.org/abs/1806.04879)
 36 [hep-ex].
- 37 [11] D. Yu, M. Ruan, V. Boudry, and H. Videau, *Lepton identification at particle flow*
 38 *oriented detector for the future e^+e^- Higgs factories*, *Eur. Phys. J. C* **77** (2017)
 39 no. 9, 591, [arXiv:1701.07542 \[physics.ins-det\]](https://arxiv.org/abs/1701.07542).

- [12] F. Sefkow, A. White, K. Kawagoe, R. Poschl, and J. Repond, *Experimental Tests of Particle Flow Calorimetry*, *Rev. Mod. Phys.* **88** (2016) 015003, [arXiv:1507.05893 \[physics.ins-det\]](https://arxiv.org/abs/1507.05893).
- [13] S. Catani, Y. L. Dokshitzer, M. Olsson, G. Turnock, and B. R. Webber, *New clustering algorithm for multi - jet cross-sections in e^+e^- annihilation*, *Phys. Lett.* **B269** (1991) 432–438.
- [14] T. Suehara and T. Tanabe, *LCFIPlus: A Framework for Jet Analysis in Linear Collider Studies*, *Nucl. Instrum. Meth.* **A808** (2016) 109–116, [arXiv:1506.08371 \[physics.ins-det\]](https://arxiv.org/abs/1506.08371).
- [15] J. Therhaag, *TMVA Toolkit for multivariate data analysis in ROOT*, PoS **ICHEP2010** (2010) 510.

CHAPTER 11

PHYSICS PERFORMANCE WITH BENCHMARK PROCESSES

¹ The historic discovery of a Higgs boson in 2012 by the ATLAS and CMS collaborations [1, 2] and the subsequent studies of the properties of the particle [3–9] indicate compatibility with the SM predictions at the current measurement precision. The Higgs boson appears to complete all of the particles needed to describe the SM. This possibility creates an inexplicable foundation for the SM theory, one that is elusive as to the origin and stability of the vast difference between the Planck and electroweak (EW) scales, the nature of the electroweak phase transition, whether the Higgs boson couples to dark matter, and other fundamental questions that remain to be understood. The attempt to further address those questions will involve new physics beyond the SM which could lead to deviations from SM expectations when tested with precision measurements. A circular electron positron collider will provide an unique opportunity to have precise measurements of the Higgs, W and Z properties.

¹³ The CEPC produces a huge statistics of massive SM bosons. Its physics potential is explored on two different classes of physics benchmarks, Higgs physics and precision EW physics. Using the software tools introduced in Section 10.1, the physics potential on Higgs physics is analyzed at full simulation level, see Section 11.1. The accuracies on the EW precision measurements are mainly limited by systematic errors and are estimated in Section 11.2. The synergies of these different physics measurements, the complimentarity and comparison to the HL-LHC and other high energy physics programs are discussed as well.

11.1 Higgs Boson Physics

2 The Higgs boson is responsible for the electroweak symmetry breaking. It is the only
 3 fundamental scalar particle in the Standard Model observed so far. The discovery of such
 4 a particle at the LHC is a major breakthrough on both theoretical and experimental fronts.
 5 However, the Standard Model is likely only an effective theory at the electroweak scale.
 6 To explore potential new physics at the electroweak scale and beyond, complementary
 7 approaches of direct searches at the energy frontier as well as precision measurements will
 8 be needed. The current LHC and the planned HL-LHC have the potential to significantly
 9 extend its new physics reach and to measure many of the Higgs boson couplings with
 10 precision of a few percents model-dependently.

11 At the CEPC, in contrast to the LHC, Higgs boson candidate events can be identified
 12 through a technique known as the recoil mass method without tagging its decays. There-
 13 fore, Higgs boson production can be disentangled from its decay in a model independent
 14 way. Moreover, the cleaner environment at a lepton collider allows much better exclu-
 15 sive measurement of Higgs boson decay channels. All of these give the CEPC impressive
 16 reach in probing Higgs boson properties. In this section, the results of the current CEPC
 17 simulation studies on the precision of the Higgs boson property measurements are sum-
 18 marized. In addition, potential reaches in the CP admixture of the Higgs boson are also
 19 estimated. More details can be found in Ref. [10].

20 11.1.1 Higgs boson production and decay

21 Production processes for a 125 GeV SM Higgs boson at the CEPC are $e^+e^- \rightarrow ZH$ (ZH
 22 or Higgsstrahlung), $e^+e^- \rightarrow \nu_e\bar{\nu}_e H$ ($\nu\bar{\nu}H$ or W fusion) and $e^+e^- \rightarrow e^+e^- H$ (eeH or
 23 Z fusion) as illustrated in Figure 11.1. The W and Z fusion processes are collectively
 24 referred to as vector-boson fusion (VBF) production.

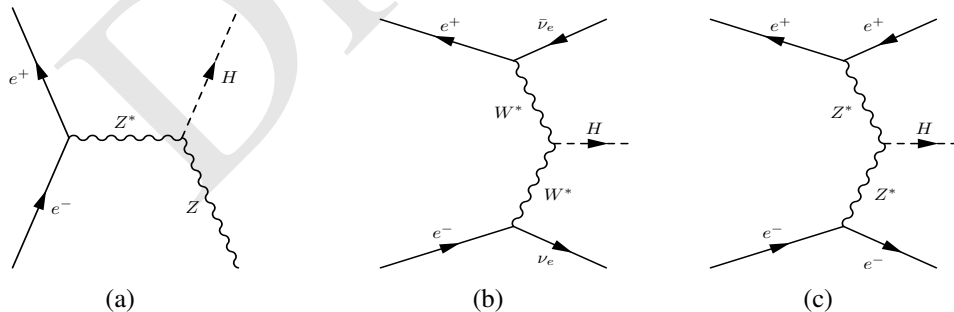


Figure 11.1: Feynman diagrams of the Higgs boson production processes at the CEPC: (a) $e^+e^- \rightarrow ZH$, (b) $e^+e^- \rightarrow \nu_e\bar{\nu}_e H$ and (c) $e^+e^- \rightarrow e^+e^- H$.

25 The total and individual cross sections for the production of a SM Higgs boson with a
 26 mass of 125 GeV as functions of center-of-mass energy are plotted in Figure 11.2 while its
 27 decay branching ratios and total width are shown in Table 11.1. As an s -channel process,
 28 the cross section of the $e^+e^- \rightarrow ZH$ process reaches its maximum at $\sqrt{s} \sim 250$ GeV,
 29 and then decreases asymptotically as $1/s$. The VBF production processes are through
 30 t -channel exchanges of vector bosons. Their cross sections increase logarithmically as

$\ln^2(s/M_V^2)$. Because of the accidental small neutral-current Zee coupling, the VBF cross section is dominated by the W fusion process.

Numerical values of these cross sections at $\sqrt{s} = 240$ GeV are listed in Table 11.2.¹ Because of the interference effects between $e^+e^- \rightarrow ZH$ and $e^+e^- \rightarrow \nu_e\bar{\nu}_e H$ for the $Z \rightarrow \nu_e\bar{\nu}_e$ decay and between $e^+e^- \rightarrow ZH$ and $e^+e^- \rightarrow e^+e^- H$ for the $Z \rightarrow e^+e^-$ decay, the cross sections of these processes cannot be separated. The breakdowns in Figure 11.2 and Table 11.2 are for illustration only. The $e^+e^- \rightarrow ZH$ cross section shown is from Figure 11.1(a) only whereas the $e^+e^- \rightarrow \nu_e\bar{\nu}_e H$ and $e^+e^- \rightarrow e^+e^- H$ cross sections include contributions from their interference with the $e^+e^- \rightarrow ZH$ process.

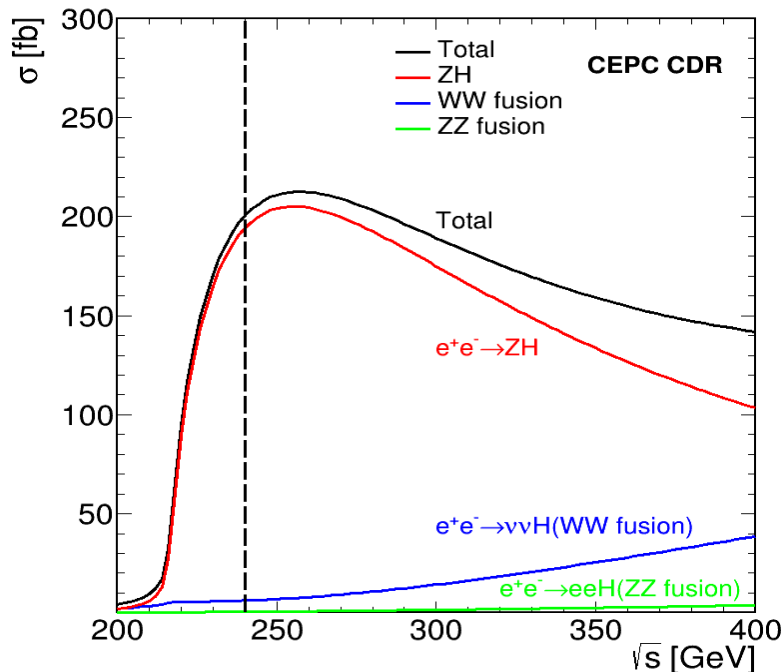


Figure 11.2: Production cross sections of $e^+e^- \rightarrow ZH$ and $e^+e^- \rightarrow (e^+e^-/\nu\bar{\nu})H$ as functions of \sqrt{s} for a 125 GeV SM Higgs boson. The vertical dashed line indicates $\sqrt{s} = 240$ GeV, the nominal energy of the CEPC Higgs factory.

The CEPC as a Higgs factory is designed to deliver a total of 5.6 ab^{-1} integrated luminosity to two detectors in 7 years. Over 10^6 Higgs boson events will be produced during this period. The large statistics, well-defined event kinematics and clean collision environment will enable the CEPC to measure Higgs boson production cross sections as well as its properties (mass, decay width and branching ratios, etc.) with precision far beyond those achievable at the LHC. Compared with hadron collisions, e^+e^- collisions are unaffected by underlying event and pile-up effects. Theoretical calculations are less dependent on higher order QCD radiative corrections. Therefore, more precise tests of theoretical predictions can be performed at the CEPC. The tagging of $e^+e^- \rightarrow ZH$ events using the invariant mass of the system recoiling against the Z boson, independent of the Higgs boson decay, is unique to lepton colliders. It provides a powerful tool for the model-independent measurements of the inclusive $e^+e^- \rightarrow ZH$ production cross section,

¹Note that the QED ISR correction for the $e^+e^- \rightarrow ZH$ channel produces a lowering of the cross section of about 20% at the nominal energy of 240 GeV.

Decay mode	Branching ratio	Relative uncertainties
$H \rightarrow b\bar{b}$	57.7%	+3.2%, -3.3%
$H \rightarrow c\bar{c}$	2.91%	+12%, -12%
$H \rightarrow gg$	8.57%	+10%, -10%
$H \rightarrow \tau^+\tau^-$	6.32%	+5.7%, -5.7%
$H \rightarrow \mu^+\mu^-$	2.19×10^{-4}	+6.0%, -5.9%
$H \rightarrow WW^*$	21.5%	+4.3%, -4.2%
$H \rightarrow ZZ^*$	2.64%	+4.3%, -4.2%
$H \rightarrow \gamma\gamma$	2.28×10^{-3}	+5.0%, -4.9%
$H \rightarrow Z\gamma$	1.53×10^{-3}	+9.0%, -8.8%
Γ_H	4.07 MeV	+4.0%, -4.0%

Table 11.1: Standard model predictions of the decay branching ratios and total width of a 125 GeV Higgs boson. These numbers are obtained from Refs. [11, 12].

$\sigma(ZH)$, and of Higgs boson decay branching ratios. Combinations of these measurements will enable to determine the total Higgs boson decay width and to extract the Higgs boson couplings to fermions and vector bosons, providing sensitive probes to potential new physics beyond the SM.

SM background processes include $e^+e^- \rightarrow e^+e^-$ (Bhabha), $e^+e^- \rightarrow Z\gamma$ (Z radiative return), $e^+e^- \rightarrow WW/ZZ$ (diboson) as well as the single boson production of $e^+e^- \rightarrow e^+e^-Z$ and $e^+e^- \rightarrow e^+\nu W^-/\bar{e}^-\bar{\nu}W^+$. Their cross sections and expected numbers of events for an integrated luminosity of 5.6 ab^{-1} at $\sqrt{s} = 240\text{ GeV}$ are shown in Table 11.2 as well. The energy dependence of the cross sections for these and the Higgs boson production processes are shown Figure 3.1. Note that many of these processes can lead to identical final states and thus can interfere. For example, $e^+e^- \rightarrow e^+\nu_e W^- \rightarrow e^+\nu_e e^-\bar{\nu}_e$ and $e^+e^- \rightarrow e^+e^-Z \rightarrow e^+e^-\nu_e\bar{\nu}_e$ have the same final state. Unless otherwise noted, these processes are simulated together to take into account interference effects for the studies presented in this report. Similar to the Higgs boson processes, the breakdowns shown in the table and figure are for illustration only.

11.1.2 Higgs boson tagging

Perhaps the most striking difference between hadron-hadron and e^+e^- collisions is that electron and positron are fundamental particle whereas hadrons are composite particles. Consequently the energy of e^+e^- collisions is known. Therefore through the energy and momentum conservation, the energy and momentum of a Higgs boson can be inferred from other particles in an event without examining the Higgs boson itself. For a Higgsstrahlung event where the Z boson decays to a pair of visible fermions (ff), the mass of the system recoiling against the Z boson, commonly known as the recoil mass, can be calculated assuming the event has a total energy \sqrt{s} and zero total momentum:

$$M_{\text{recoil}}^2 = (\sqrt{s} - E_{ff})^2 - p_{ff}^2 = s - 2E_{ff}\sqrt{s} + m_{ff}^2. \quad (11.1)$$

Process	Cross section	Events in 5.6 ab^{-1}
Higgs boson production, cross section in fb		
$e^+e^- \rightarrow ZH$	196.2	1.10×10^6
$e^+e^- \rightarrow \nu_e \bar{\nu}_e H$	6.19	3.47×10^4
$e^+e^- \rightarrow e^+e^- H$	0.28	1.57×10^3
Total	203.7	1.14×10^6
Background processes, cross section in pb		
$e^+e^- \rightarrow e^+e^-$ (Bhabha)	24.7	1.4×10^8
$e^+e^- \rightarrow q\bar{q}(\gamma)$	54.1	3.0×10^8
$e^+e^- \rightarrow \mu^+\mu^-$ (γ) [or $\tau^+\tau^-$ (γ)]	5.3	3.0×10^7
$e^+e^- \rightarrow WW$	16.7	9.4×10^7
$e^+e^- \rightarrow ZZ$	1.1	6.2×10^6
$e^+e^- \rightarrow e^+e^- Z$	4.54	2.5×10^7
$e^+e^- \rightarrow e^+\nu W^-/e^-\bar{\nu} W^+$	5.09	2.6×10^7

Table 11.2: Cross sections of Higgs boson production and other SM processes at $\sqrt{s} = 240 \text{ GeV}$ and numbers of events expected in 5.6 ab^{-1} . The cross sections are calculated using the Whizard program [13]. Note that there are interferences between the same final states from different processes after the W or Z boson decays. Their treatments are explained in the text.

¹ Here E_{ff} , p_{ff} and m_{ff} are, respectively, the total energy, momentum and invariant mass of the fermion pair. The M_{recoil} distribution should show a peak at the Higgs boson mass m_H for $e^+e^- \rightarrow ZH \rightarrow ffH$ and $e^+e^- \rightarrow e^+e^- H$ processes, and is expected to be smooth without a resonance structure for background processes in the mass region around 125 GeV. Two important measurements of the Higgs boson can be performed from the M_{recoil} mass spectrum. The Higgs boson mass can be determined from the position of the resonance in the spectrum. The width of the resonance structure is dominated by the beam energy spread (including ISR effects) and energy/momentum resolution of the detector as the natural Higgs boson width is only 4.07 MeV. The best precision of the mass measurement can be achieved from the leptonic $Z \rightarrow \ell\ell$ ($\ell = e, \mu$) decays. The height of the resonance is a measure of the Higgs boson production cross section $\sigma(ZH)$.² Through a fit to the M_{recoil} spectrum, the $e^+e^- \rightarrow ZH$ event yield, and therefore $\sigma(ZH)$, can be extracted, independent of Higgs boson decays. Higgs boson decay branching ratios can then be determined by measuring the ZH cross sections of individual Higgs boson decay modes. The recoil mass spectrum has been investigated for both leptonic and hadronic Z boson decays as presented below.

The leptonic Z decay is ideal for studying the recoil mass spectrum of the $e^+e^- \rightarrow ZX$ events. The decay is easily identifiable and the lepton momenta can be precisely measured. Figure 11.3 shows the reconstructed recoil mass spectra of $e^+e^- \rightarrow ZX$ candidates for the $Z \rightarrow \mu^+\mu^-$ and $Z \rightarrow e^+e^-$ decay modes. The analyses are based on

²For the $Z \rightarrow e^+e^-$ decay, there will be a small contribution from $e^+e^- \rightarrow e^+e^- H$ production.

the full detector simulation for the signal events and on the fast detector simulation for background events. The event selections are entirely based on the information of the two leptons, independent of the final states of Higgs boson decays. This approach is essential for the measurement of the inclusive $e^+e^- \rightarrow ZH$ production cross section and the model-independent determination of the Higgs boson branching ratios. SM processes with at least 2 leptons in their final states are considered as backgrounds. As shown in Figure 11.3, the analysis has a good signal-to-background ratio. The long high-mass tail is largely due to the initial-state radiation. Leading background contributions after the selection are from ZZ , WW and $Z\gamma$ events. Compared to the $Z \rightarrow \mu^+\mu^-$ decay, the analysis of the $Z \rightarrow e^+e^-$ decay suffers from additional and large background contributions from Bhabha and single boson production.

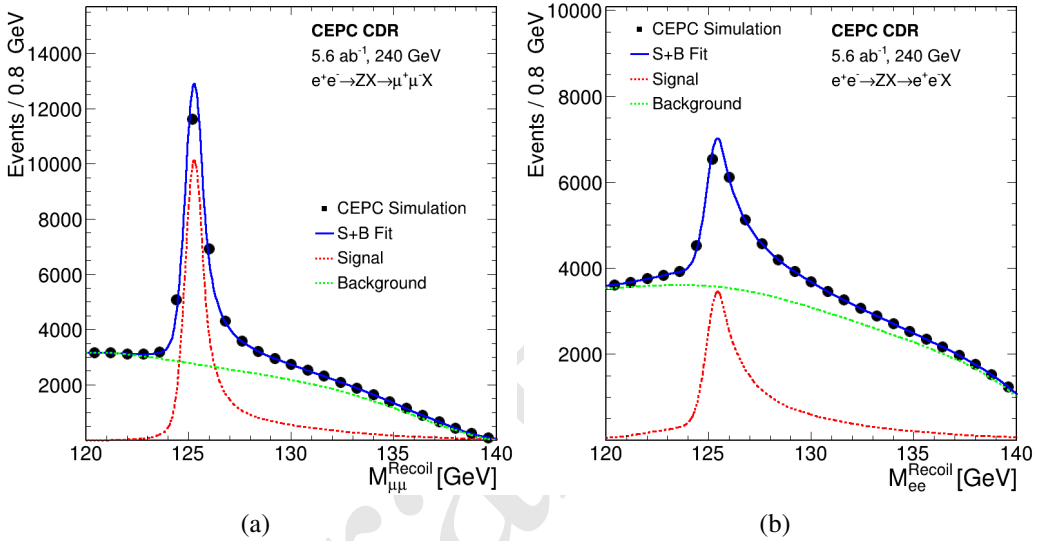


Figure 11.3: The inclusive recoil mass spectra of $e^+e^- \rightarrow ZX$ candidates of (a) $Z \rightarrow \mu^+\mu^-$ and (b) $Z \rightarrow e^+e^-$. No attempt to identify X is made. The markers and their uncertainties represent expectations from a CEPC dataset of 5.6 ab^{-1} whereas the solid blue curves are the signal-plus-background fit results. The dashed curves are the signal and background components.

The recoil mass technique can also be applied to the hadronic Z boson decays ($Z \rightarrow q\bar{q}$) of the $e^+e^- \rightarrow ZX$ candidates. This analysis benefits from a larger $Z \rightarrow q\bar{q}$ decay branching ratio, but suffers from worse jet energy resolution compared with the track momentum and electromagnetic energy resolutions. In addition, ambiguity in selecting jets from the $Z \rightarrow q\bar{q}$ decay, particularly in events with hadronic decays of the Higgs boson, can degrade the analysis performance and also introduce model dependences. Therefore, the measurement is highly dependent on the detector performance and the jet clustering algorithm. Following the same approach as the ILC study [14], an analysis based on the fast simulation has been performed. After the event selection, main backgrounds arise from $Z\gamma$'s and WW production.

11.1.3 Measurements of $\sigma(ZH)$ and m_H

The inclusive $e^+e^- \rightarrow ZH$ production cross section $\sigma(ZH)$ and Higgs boson mass m_H can be extracted from fits to the recoil mass distributions of the $e^+e^- \rightarrow ZX \rightarrow$

$(\ell^+\ell^-/q\bar{q})X$ candidates. For the leptonic $Z \rightarrow \ell\ell$ decays, the recoil mass distribution of the signal process $e^+e^- \rightarrow ZH$ (and also $e^+e^- \rightarrow e^+e^-H$ in case of the $Z \rightarrow e^+e^-$ decay) is modeled with a Crystal Ball function [15] whereas the total background is modeled with a polynomial function in the fit. As noted above, the recoil mass distribution is insensitive to the intrinsic Higgs boson width if it were as small as predicted by the SM. The Higgs boson mass can be determined with precision of 6.5 MeV and 14 MeV from the $Z \rightarrow \mu^+\mu^-$ and $Z \rightarrow e^+e^-$ decay modes, respectively. In combination, an uncertainty of 5.9 MeV can be achieved. $e^+e^- \rightarrow ZX \rightarrow q\bar{q}X$ events contribute little to the precision of the m_H measurement due to the poor $Z \rightarrow q\bar{q}$ mass resolution, but dominates the precision of the $e^+e^- \rightarrow ZH$ cross section measurement benefiting from its large statistics. A relative precision of 0.65% on $\sigma(ZH)$ is predicted from a simple event counting analysis. In comparison, the corresponding precision from the $Z \rightarrow e^+e^-$ and $Z \rightarrow \mu^+\mu^-$ decays is estimated to be 1.5% and 0.9%, respectively. The combined precision of the three measurements is 0.5%.

For the model-independent measurement of $\sigma(ZH)$, event selections independent of the Higgs boson decays are essential. However, additional selections using the Higgs boson decay information can be applied to improve the Higgs boson mass measurement. This will be particularly effective in suppressing the large backgrounds in the $Z \rightarrow e^+e^-$ and $Z \rightarrow q\bar{q}$ decay modes. This improvement is not implemented in the current study.

11.1.4 Analyses of individual Higgs boson decay modes

Different decay modes of the Higgs boson can be identified through their unique signatures, enabling the measurements of production rates for these decays. Simulation studies of the CEPC baseline conceptual detector have been performed for the Higgs boson decay modes of $H \rightarrow b\bar{b}/c\bar{c}/gg$, $H \rightarrow WW^*$, $H \rightarrow ZZ^*$, $H \rightarrow \gamma\gamma$, $H \rightarrow Z\gamma$, $H \rightarrow \tau^+\tau^-$, $H \rightarrow \mu^+\mu^-$ and $H \rightarrow \text{inv}$. The large numbers of the decay modes of the H , W and Z boson as well as the τ -lepton lead to a very rich variety of event topologies. This complexity makes it impractical to investigate the full list of final states descending from the Higgs boson decays. Instead, a limited number of final states of individual Higgs boson decay mode has been considered. In most cases, the dominant backgrounds come from SM diboson production and Z production with initial or final state radiations.

The studies are optimized for the dominant ZH process, however the $e^+e^- \rightarrow \nu_e\bar{\nu}_e H$ and $e^+e^- \rightarrow e^+e^-H$ processes are included whenever applicable. The production cross sections of individual decay mode, $\sigma(ZH) \times \text{BR}$, are extracted. Combined with the inclusive $\sigma(ZH)$ measurement, these measurements will permit the determinations of the Higgs boson decay branching ratios in a model-independent way. Main features of these studies are described below and their results are presented in Section 11.1.5.

For a SM Higgs boson with a mass of 125 GeV, nearly 70% of all Higgs bosons decay into a pair of jets: b -quarks (57.7%), c -quarks (2.9%) and gluons (8.6%). While the $H \rightarrow b\bar{b}$ decay has been observed at the LHC, the $H \rightarrow c\bar{c}$ and $H \rightarrow gg$ decays are difficult, if not impossible, to be conclusively identified even at the HL-LHC due to large backgrounds. In comparison, these three decays can be isolated and studied at the CEPC in detail. This is important as the $H \rightarrow c\bar{c}$ decay is likely the only vehicle for investigating the Higgs boson couplings to the second-generation quarks. The study considers all Z boson decay modes except $Z \rightarrow \tau^+\tau^-$. The $H \rightarrow b\bar{b}/c\bar{c}/gg$ candidates are identified through the dijet invariant mass, or the recoil mass of the visible Z boson decays, or

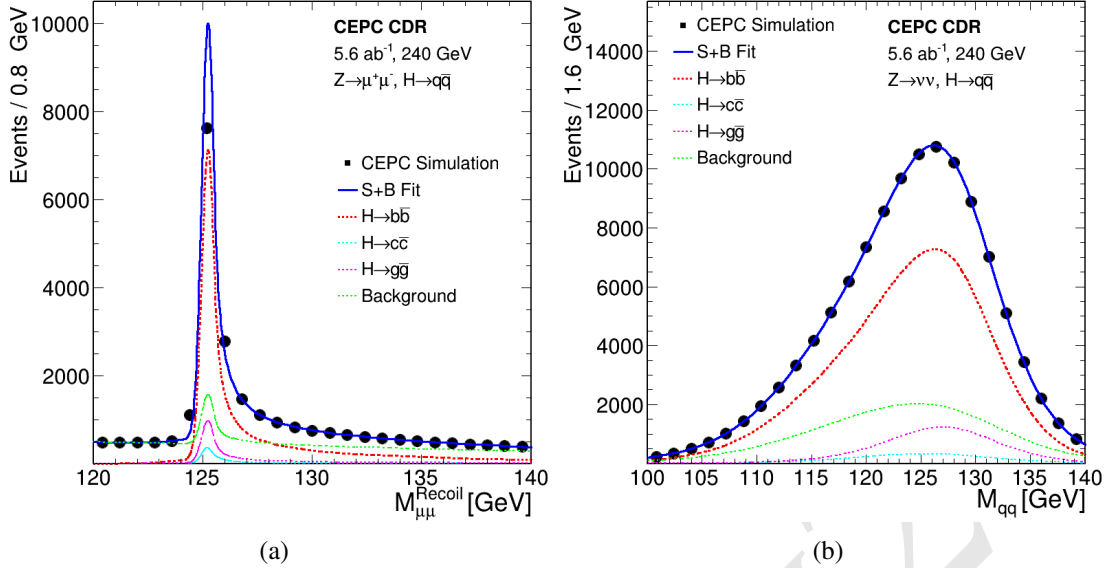


Figure 11.4: (a) $e^+e^- \rightarrow ZH$ production with $H \rightarrow b\bar{b}/c\bar{c}/gg$: distributions of (a) the recoil mass of $Z \rightarrow \mu^+ \mu^-$ and (b) the dijet invariant mass distribution for the $Z \rightarrow \nu\bar{\nu}$ decay. The markers and their uncertainties represent expectations from a CEPC dataset of 5.6 ab^{-1} whereas the solid blue curves are the signal-plus-background fit results. The dashed curves are the signal and background components. Contributions from other Higgs boson decays are included in the background.

both. Jet flavor tagging is employed to statistically separate $H \rightarrow b\bar{b}/c\bar{c}/gg$ contributions. Figure 11.4(a) shows the reconstructed recoil mass distribution of the $Z \rightarrow \mu^+ \mu^-$ decay. Compared with the distribution of inclusive Higgs boson decays shown in Figure 11.3(a), the background is significantly reduced through the identification of specific Higgs boson decay modes. Figure 11.4(b) is the dijet mass distribution of the $Z \rightarrow \nu\bar{\nu}$ decay, showing excellent signal-to-background ratio and good dijet mass resolution.

The W -fusion $e^+e^- \rightarrow \nu_e \bar{\nu}_e H$ process has a cross section of 3.2% of that of the ZH process at $\sqrt{s} = 240$ GeV in the SM. This process has been explored with the $H \rightarrow b\bar{b}$ decay mode. The analysis suffers from large backgrounds from $ZH \rightarrow \nu\bar{\nu} b\bar{b}$ as it has the same signature. However, the $\nu\bar{\nu}H$ and $Z(\nu\bar{\nu})H$ contributions can be separated through the exploration of their kinematic differences. Higgs bosons are produced with different polar angular distributions. Moreover, the recoil mass distribution of the $b\bar{b}$ system should exhibit a resonance structure at the Z boson mass for $Z(\nu\bar{\nu})H$ and show a continuum spectrum for $e^+e^- \rightarrow \nu_e \bar{\nu}_e H$. The $\nu\bar{\nu}H$ contribution is extracted through a fit to the two-dimensional distribution of the cosine of the polar angle and the recoil mass of the $b\bar{b}$ system.

The $H \rightarrow WW^*$ and $H \rightarrow ZZ^*$ decays are among the first decay modes studied at the LHC and are critical for the discovery of the Higgs boson thanks to the clean leptonic signatures of the W and Z boson decays. However due to their large backgrounds, hadronic final states of the $H \rightarrow WW^*$ and $H \rightarrow ZZ^*$ decays are out of reach at the LHC despite of their larger branching ratios than leptonic final states. This is not the case at the CEPC. In fact, most of the sensitivities to these two Higgs boson decay modes at the CEPC are expected to be from final states with one or both vector bosons decay hadronically. A number of selected final states have been studied. For $H \rightarrow WW^*$, the final states

included are $Z \rightarrow \ell\ell$, $H \rightarrow WW^* \rightarrow \ell\nu\ell\nu, \ell\nu q\bar{q}$; $Z \rightarrow \nu\bar{\nu}$, $H \rightarrow WW^* \rightarrow \ell\nu\ell\nu, q\bar{q}q\bar{q}$ and $Z \rightarrow q\bar{q}$, $H \rightarrow WW^* \rightarrow q\bar{q}q\bar{q}$. For $H \rightarrow ZZ^*$, they are $Z \rightarrow \mu^+\mu^-$, $H \rightarrow ZZ^* \rightarrow \nu\bar{\nu}q\bar{q}$ and $Z \rightarrow \nu\bar{\nu}$, $H \rightarrow ZZ^* \rightarrow \ell\ell q\bar{q}$. A combination of the recoil mass, the invariant mass of the $W \rightarrow q\bar{q}$ and $Z \rightarrow q\bar{q}$ decay as well as the leptonic decay signatures of W and Z bosons are used to identify ZH events. Some of these analyses suffer from large backgrounds as shown, for example, in Figure 11.5(a), while others are almost background free as illustrated in Figure 11.5(b).

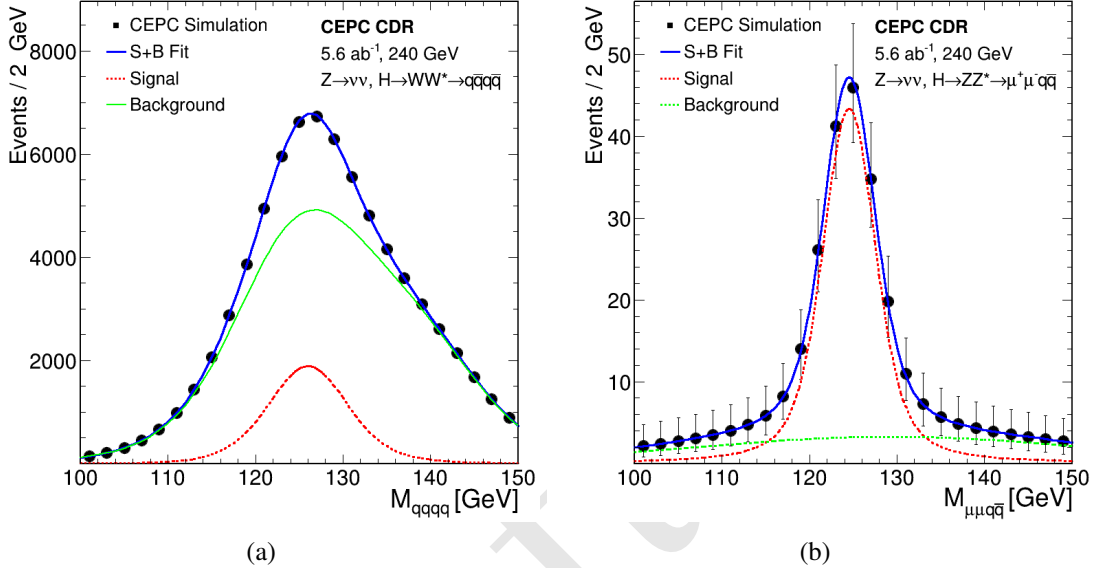


Figure 11.5: (a) $e^+e^- \rightarrow ZH$ production with $H \rightarrow WW^* \rightarrow q\bar{q}q\bar{q}$ and $Z \rightarrow \nu\bar{\nu}$: the invariant mass of the 4-jet system. (b) $e^+e^- \rightarrow ZH$ production with $H \rightarrow ZZ^* \rightarrow \mu^+\mu^-q\bar{q}$ and $Z \rightarrow \nu\bar{\nu}$: the invariant mass distribution of the dimuon and dijet system. The markers and their uncertainties represent expectations from a CEPC dataset of 5.6 ab^{-1} whereas the solid blue curves are the signal-plus-background fit results. The dashed curves are the signal and background components. Contributions from other Higgs boson decays are included in the background.

The $H \rightarrow \gamma\gamma$ and $H \rightarrow Z\gamma$ decays have small branching ratios in the SM as they proceed through W boson and top quark triangular loops. CEPC's sensitivities to these two decay modes have been examined. The $H \rightarrow \gamma\gamma$ analysis of ZH production suffers from large $e^+e^- \rightarrow (Z/\gamma^*)\gamma\gamma$ background where γ is arise from the initial and final state radiations. All Z boson decay modes other than the $Z \rightarrow e^+e^-$ decay are considered for the $H \rightarrow \gamma\gamma$ studies. The ZH production with $Z \rightarrow e^+e^-$ has additional large backgrounds from the Bhabha process. As shown in Figure 11.6(a), the $H \rightarrow \gamma\gamma$ signal is expected to appear as a resonance over a smooth background in the diphoton mass distribution. ZH production with $H \rightarrow Z\gamma$ decay will lead to events with two on-shell Z bosons and one photon. The $H \rightarrow Z\gamma$ study targeted the signal process of $ZH \rightarrow ZZ\gamma \rightarrow \nu\bar{\nu}q\bar{q}\gamma$. In this final state, the energy and momentum of the $\nu\bar{\nu}$ system can be calculated from the visible energy and momentum of the event. The mass difference between the Higgs boson candidate and the candidate of the associated Z boson can then be calculated. For signal events, this mass difference is expected to be $m_H - m_Z \sim 35 \text{ GeV}$ for correct combinations as shown in Figure 11.7(b). For background events and wrong combinations of signal events, the distribution should be smooth.

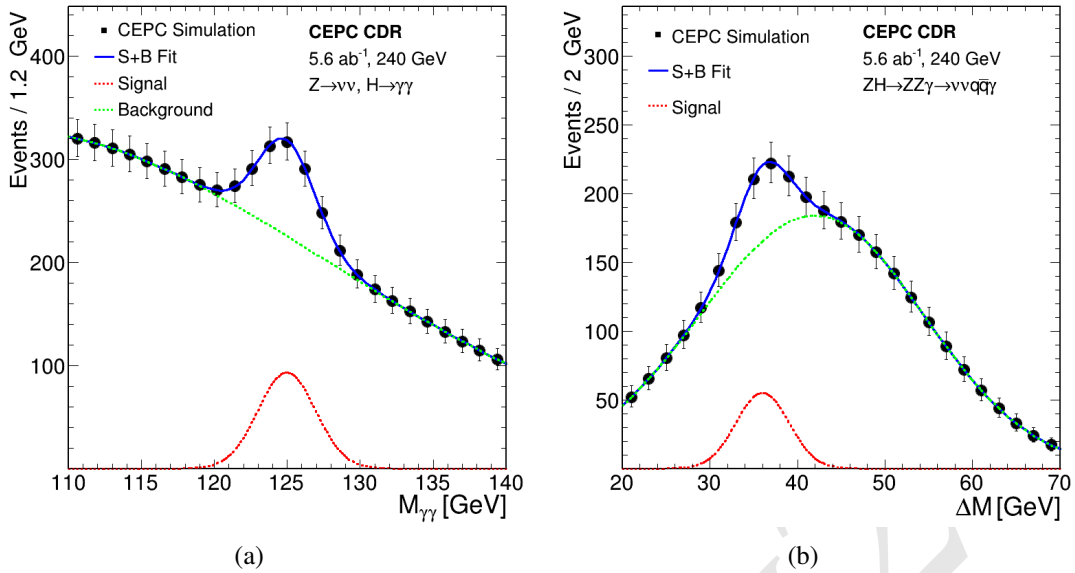


Figure 11.6: (a) $e^+e^- \rightarrow ZH$ production with $H \rightarrow \gamma\gamma$: the invariant mass distribution of the selected photon pairs for $Z \rightarrow \nu\bar{\nu}$. (b) $e^+e^- \rightarrow ZH$ production with $H \rightarrow Z\gamma$: the distribution of the mass difference between the reconstructed $Z\gamma$ and Z system. The markers and their uncertainties represent expectations from a CEPC dataset of 5.6 ab^{-1} whereas the solid blue curves are the signal-plus-background fit results. The dashed curves are the signal and background components.

Leptonic Higgs boson decays are accessible for $H \rightarrow \tau^+\tau^-$ and $H \rightarrow \mu^+\mu^-$ at the CEPC. Simulation studies of ZH production with the $H \rightarrow \tau^+\tau^-$ decay have been performed for all Z boson decay modes except $Z \rightarrow e^+e^-$. A boosted decision tree utilizing particle multiplicity and their separations is used to select ditau candidates from $H \rightarrow \tau^+\tau^-$. An impact-parameter based variable of the leading track of the ditau candidate is used as the final discriminant for the signal extraction. An example distribution of this variable for $Z \rightarrow \nu\bar{\nu}$ is shown Figure 11.7(a). Similar to $H \rightarrow \gamma\gamma$, the $H \rightarrow \mu^+\mu^-$ decay also allows the reconstruction of the Higgs boson with high resolution. The signal is expected to appear as a resonance structure at m_H over the smooth background in the dimuon mass spectrum. Good dimuon mass resolution is essential for the performance. For this study, all Z boson decay modes are considered. Figure 11.7(b) shows the dimuon mass distribution combining all Z boson decay modes.

In the SM, the Higgs boson can decay invisibly via $H \rightarrow ZZ^* \rightarrow \nu\bar{\nu}\nu\bar{\nu}$ with a branching ratio of 1.06×10^{-3} . In many extensions to the SM, the Higgs boson can decay directly to invisible particles with a significantly higher branching ratio. At the CEPC, the invisible decay of the Higgs boson ($H \rightarrow \text{inv}$) can be directly identified using the recoil mass information of the Z boson decays. The sensitivity to ZH production with $H \rightarrow \text{inv}$ is estimated for $Z \rightarrow \ell\ell$ and $Z \rightarrow q\bar{q}$ decays. The SM $H \rightarrow ZZ^* \rightarrow \nu\bar{\nu}\nu\bar{\nu}$ decay is used to model the $H \rightarrow \text{inv}$ decay in both the SM and its extension. This is made possible by the fact that the Higgs boson is narrow scalar in the SM so that the production and decay are factorized. The upper limit on the BSM contribution to $\text{BR}(H \rightarrow \text{inv})$, $\text{BR}_{\text{inv}}^{\text{BSM}}$, can then be estimated.

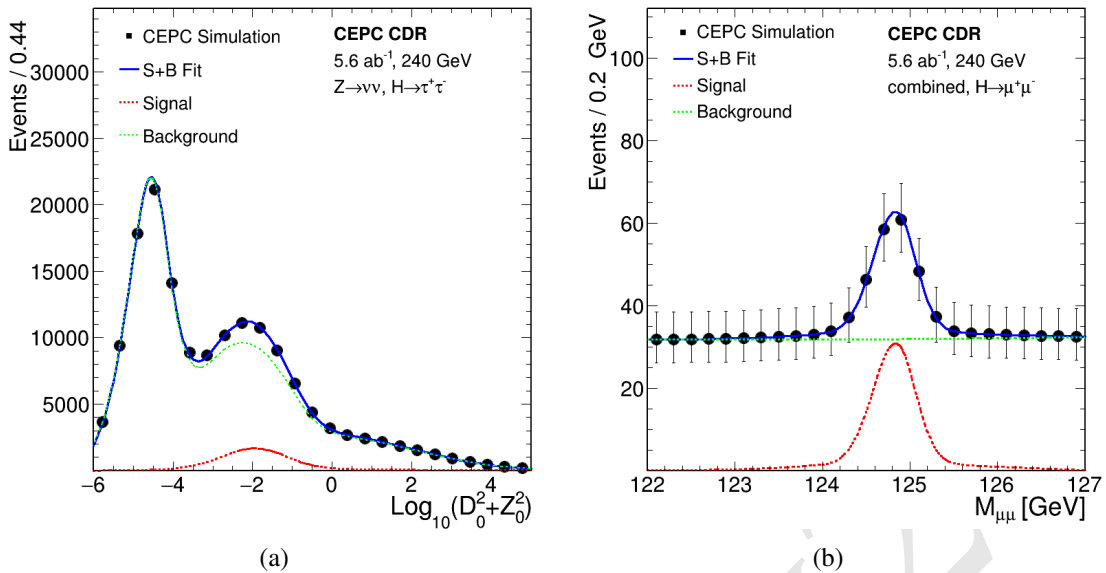


Figure 11.7: (a) $e^+e^- \rightarrow ZH$ production with $H \rightarrow \tau^+\tau^-$: the distribution of impact parameter variable of the leading track of the ditau candidates for the $Z \rightarrow \nu\bar{\nu}$ decay mode. Contributions from other Higgs boson decays are included in the background. (b) $e^+e^- \rightarrow ZH$ production with $H \rightarrow \mu^+\mu^-$: the invariant mass distribution of the selected muon pairs combining all Z boson decay modes. The markers and their uncertainties represent expectations from a CEPC dataset of 5.6 ab^{-1} whereas the solid blue curves are the signal-plus-background fit results. The dashed curves are the signal and background components.

11.1.5 Combination of individual analyses

With the measurements of inclusive cross section $\sigma(ZH)$ and the cross sections of individual Higgs boson decay mode $\sigma(ZH) \times \text{BR}$, the Higgs boson decay branching ratio, BR , can be extracted. Most of the systematic uncertainties associated with the measurement of $\sigma(ZH)$ cancels in this procedure. A maximum likelihood fit is used to estimate the precision on BRs. For a given Higgs boson decay mode, the likelihood has the form:

$$L(\text{BR}, \theta) = \text{Poisson} \left[N^{\text{obs}} \middle| N^{\text{exp}}(\text{BR}, \theta) \right] \cdot G(\theta), \quad (11.2)$$

7 where BR is the parameter of interest and θ represent nuisance parameters associated with
 8 systematic uncertainties. N^{obs} is the number of the observed events, $N^{\text{exp}}(\text{BR}, \theta)$ is the
 9 expected number of events, and $G(\theta)$ is a set of constraints on the nuisance parameters
 10 within their estimated uncertainties. The number of expected events is the sum of signal
 11 and background events. The number of signal events is calculated from the integrated
 12 luminosity, the $e^+e^- \rightarrow ZH$ cross section $\sigma(ZH)$ measured from the recoil mass method,
 13 Higgs boson branching ratio BR , the event selection efficiency ϵ . The number of the
 14 expected background events, N^b , is estimated from Monte Carlo samples. Thus

$$N^{\text{exp}}(\text{BR}, \theta) = \text{Lumi}(\theta^{\text{lumi}}) \times \sigma_{ZH}(\theta^\sigma) \times \text{BR} \times \epsilon(\theta^\epsilon) + N^b(\theta^b), \quad (11.3)$$

¹⁵ where θ^X ($X = \text{lumi}, \sigma, \epsilon$ and b) are the nuisance parameters of their corresponding
¹⁶ parameters or measurements. Even with 10^6 Higgs boson events, statistical uncertainties

¹ are expected to be dominant and thus systematic uncertainties are not taken into account
² for the current studies. Thus the nuisance parameters are fixed to their nominal values.

Property	Estimated Precision	
m_H	5.9 MeV	
Γ_H	3.1%	
$\sigma(ZH)$	0.5%	
$\sigma(\nu\bar{\nu}H)$	3.0%	

Decay mode	$\sigma(ZH) \times \text{BR}$	BR
$H \rightarrow b\bar{b}$	0.27%	0.56%
$H \rightarrow c\bar{c}$	3.26%	3.30%
$H \rightarrow gg$	1.27%	1.36%
$H \rightarrow WW^*$	0.98%	1.10%
$H \rightarrow ZZ^*$	5.09%	5.11%
$H \rightarrow \gamma\gamma$	6.84%	6.86%
$H \rightarrow Z\gamma$	15%	15%
$H \rightarrow \tau^+\tau^-$	0.82%	0.96%
$H \rightarrow \mu^+\mu^-$	17%	17%
$H \rightarrow \text{inv}$	—	< 0.30%

Table 11.3: Estimated precision of Higgs boson property measurements expected from a CEPC dataset of 5.6 ab^{-1} at $\sqrt{s} = 240 \text{ GeV}$. All precision are relative except for m_H and $\text{BR}(H \rightarrow \text{inv})$ for which Δm_H and 95% CL upper limit on $\text{BR}_{\text{inv}}^{\text{BSM}}$ are quoted respectively. The $e^+e^- \rightarrow e^+e^-H$ cross section is too small to be measured with a reasonable precision.

³ Table 11.3 summarizes the estimated precision of Higgs boson property measure-
⁴ ments, combining all studies described above and taking into account cross-feeds be-
⁵ tween different Higgs boson production processes and decay modes. For the leading
⁶ Higgs boson decay modes, namely $b\bar{b}$, $c\bar{c}$, gg , WW^* , ZZ^* and $\tau^+\tau^-$, percent level pre-
⁷ cision are expected. The best achievable statistical uncertainties for 5.6 ab^{-1} are 0.27% for
⁸ $\sigma(e^+e^- \rightarrow ZH) \times \text{BR}(H \rightarrow b\bar{b})$ and 0.5% for $\sigma(e^+e^- \rightarrow ZH)$. Even for these measure-
⁹ ments, statistics is likely the dominant source of uncertainties. Systematic uncertainties
¹⁰ from the efficiency/acceptance of the detector, the luminosity and the beam energy deter-
¹¹ mination are expected to be small. The integrated luminosity can be measured with a 0.1%
¹² precision, a benchmark already achieved at the LEP [16], and can be potentially improved
¹³ in the future. The center-of-mass energy will be known better than 1 MeV, resulting neg-
¹⁴ ligible uncertainties on the theoretical cross section predictions and experimental recoil
¹⁵ mass measurements.

11.1.6 Higgs boson width

The Higgs boson width is of special interest as it is sensitive to BSM physics in Higgs boson decays that are not directly detectable or searched for. However, the 4.07 MeV width predicted by the SM is too small to be measured with a reasonable precision from the distributions of either the invariant mass of the Higgs boson decay products or the recoil mass of the system produced in association with the Higgs boson. Unique to lepton colliders, the width can be determined from the measurements of Higgs boson production cross sections and its decay branching ratios. This is because the inclusive $e^+e^- \rightarrow ZH$ cross section $\sigma(ZH)$ can be measured from the recoil mass distribution, independent of Higgs boson decays.

Measurements of $\sigma(ZH)$ and BR's have been discussed in above. Combining these measurements, the Higgs boson width can be calculated in a model-independent way:

$$\Gamma_H = \frac{\Gamma(H \rightarrow ZZ^*)}{\text{BR}(H \rightarrow ZZ^*)} \propto \frac{\sigma(ZH)}{\text{BR}(H \rightarrow ZZ^*)} \quad (11.4)$$

Here $\Gamma(H \rightarrow ZZ^*)$ is the partial width of the $H \rightarrow ZZ^*$ decay. Because of the small expected $\text{BR}(H \rightarrow ZZ^*)$ value for a 125 GeV Higgs boson (2.64% in the SM), the precision of Γ_H is limited by the $H \rightarrow ZZ^*$ statistics. It can be improved using decay final states with expected large BR values, for example the $H \rightarrow b\bar{b}$ decay:

$$\Gamma_H = \frac{\Gamma(H \rightarrow b\bar{b})}{\text{BR}(H \rightarrow b\bar{b})} \quad (11.5)$$

$\Gamma(H \rightarrow b\bar{b})$ can be independently extracted from the cross section of the W fusion process:

$$\sigma(\nu\bar{\nu}H \rightarrow \nu\bar{\nu} b\bar{b}) \propto \Gamma(H \rightarrow WW^*) \cdot \text{BR}(H \rightarrow b\bar{b}) = \Gamma(H \rightarrow b\bar{b}) \cdot \text{BR}(H \rightarrow WW^*) \quad (11.6)$$

Thus the Higgs boson total width

$$\Gamma_H = \frac{\Gamma(H \rightarrow b\bar{b})}{\text{BR}(H \rightarrow b\bar{b})} = \frac{\Gamma(H \rightarrow WW^*)}{\text{BR}(H \rightarrow WW^*)} \propto \frac{\sigma(\nu\bar{\nu}H)}{\text{BR}(H \rightarrow WW^*)} \quad (11.7)$$

Here $\text{BR}(H \rightarrow b\bar{b})$ and $\text{BR}(H \rightarrow WW^*)$ are measured from the $e^+e^- \rightarrow ZH$ process. The limitation of this method is the precision of the $\sigma(e^+e^- \rightarrow \nu_e\bar{\nu}_e H)$ measurement.

The expected precision on Γ_H is 5.4% from the measurements of $\sigma(ZH)$ and $\text{BR}(H \rightarrow ZZ^*)$ and is 3.3% from the measurements of $\sigma(\nu\bar{\nu}H)$ and $\text{BR}(H \rightarrow WW^*)$. The former is dominated by the precision of the $\text{BR}(H \rightarrow ZZ^*)$ measurement while the latter by the $\sigma(\nu\bar{\nu}H)$ measurement. The combined Γ_H precision of the two measurements is 3.1%, taking into account correlations between the two measurements.

11.1.7 Higgs Boson Coupling Measurements

To understand the implications of the predicted measurement precision shown in Table 11.3 on possible new physics models, one would need to translate them into constraints on the parameters in the Lagrangian. This is frequently referred to as Higgs boson coupling measurement, even though this way of phrasing it can be misleading as discussed in the following.

There are different ways of presenting the constraints. Before going into CEPC results, we briefly comment on the reasons behind choices of schemes in this section. First, the goal of theory interpretation is different from analyzing actual data, where a lot of detailed work will be done to derive the extended sets of observables. Instead, obtaining a broad brushed big picture of the basic capability of the Higgs boson coupling measurement at the CEPC is the goal. Ideally, the presentation would be simple with an intuitive connection with the observables. The presentation would ideally also be free of underlying model assumptions. In addition, it would be convenient if the result presentation can be interfaced directly with higher order computations, RGE evolutions, and so on. However, achieving all of these goals simultaneously is not possible. Two of the most popular and balanced approaches are the so-called κ -framework and the Effective Field Theory (EFT) analysis. As discussed in more detail later, none of these is perfect. At the same time, neither of these is wrong as long as one is careful not to over interpreting the result. Another important aspect of making projections on the physics potential of a future experiment is that they will be compared with other possible future experiments. Hence, CEPC follows the most commonly used approaches to facilitate such comparisons.

Motivated by these arguments, in the following, CEPC presents the projections using both the κ -framework and EFT approach. In the later part of this section, Higgs physics potential beyond coupling determination will be discussed.

11.1.7.1 Coupling fits in the κ -framework

The Standard Model makes specific predictions for the Higgs boson couplings to the SM fermions, $g(Hff; \text{SM})$, and to the SM gauge bosons $g(HVV; \text{SM})$.³ In the κ -framework, the potential deviations are parametrized by

$$\kappa_f = \frac{g(Hff)}{g(Hff; \text{SM})}, \quad \kappa_V = \frac{g(HVV)}{g(HVV; \text{SM})}, \quad (11.8)$$

with $\kappa_i = 1$ indicating agreement with the SM prediction.

In addition to couplings which are present at tree level, the Standard Model also predicts effective couplings $H\gamma\gamma$ and Hgg , in terms of other SM parameters. Changes in the gluon and photon couplings can be induced by the possible shifts in the Higgs boson couplings described above. In addition, these couplings can also be altered by loop contributions from new physics states. Hence, these couplings will be introduced as two independent couplings, with their ratios to the SM predictions denoted as κ_γ and κ_g .

Furthermore, it is possible that the Higgs boson can decay directly into new physics particles. In this case, two type of new decay channels will be distinguished:

1. Invisible decay. This is a specific channel in which Higgs boson decay into invisible particles. This can be searched for and, if detected, measured.
2. Exotic decay. This includes all the other new physics channels. Whether they can be observed, and, if so, to what precision, depends sensitively on the particular final states. In one extreme, they can be very distinct and can be measured very well. In another extreme, they can be in a form which is completely swamped by the background. Whether postulating a precision for the measurement of the exotic decay or treating it as an independent parameter (essentially assuming it can not be measured

³For the discussion of coupling fits and their implications, “ H ” is used to denote the 125 GeV Higgs boson.

directly) is an assumption one has to make. In the latter case, it is common to use the total width Γ_H as an equivalent free parameter.⁴

In general, possible deviations of all Standard Model Higgs boson couplings should be considered. However, in the absence of obvious light new physics states with large couplings to the Higgs boson and other SM particles, a very large deviation ($> \mathcal{O}(1)$) is unlikely. In the case of smaller deviations, the Higgs boson phenomenology will not be sensitive to the deviations [17] κ_e , κ_u , κ_d and κ_s . Therefore, they will not be considered here and set to be their SM values.

The CEPC will not be able to directly measure the Higgs boson coupling to top quarks. A deviation of this coupling from its SM value does enter $H\gamma\gamma$ and Hgg amplitudes. However, this can be viewed as parametrized by κ_γ and κ_g already. Therefore, we will not include κ_t as an independent parameter. Hence, the following set of 10 independent parameters is considered:

$$\kappa_b, \kappa_c, \kappa_\tau, \kappa_\mu, \kappa_Z, \kappa_W, \kappa_\gamma, \kappa_g, \text{BR}_{\text{inv}}^{\text{BSM}}, \Gamma_H. \quad (11.9)$$

Several assumptions can be made that can lead to a reduced number of parameters (see also [18, 19]). It can be reduced to a 7-parameter set, by assuming lepton universality, and the absence of exotic and invisible decays (excluding $H \rightarrow ZZ^* \rightarrow \nu\bar{\nu}\nu\bar{\nu}$) [18, 20]:

$$\kappa_b, \kappa_c, \kappa_\tau = \kappa_\mu, \kappa_Z, \kappa_W, \kappa_\gamma, \kappa_g. \quad (11.10)$$

This is useful for hadron collider studies since it can not measure the Higgs boson total width with precision; it is more useful for models in which this assumption is satisfied.

There are some pros and cons of the κ -framework. κ_i s give a simple and intuitive parameterization of potential deviations. It has a direct connection with the observables shown in Table 11.3. It does cover a lot of possible modifications of the coupling. At the same time, κ -framework has its limitations. Strictly speaking, it should not be understood as modifying the SM renormalizable Lagrangian by a multiplicative factor. For instance, individual κ modifications violates gauge invariance. The higher order corrections in the κ framework is not easily defined. κ_i s do not summarize all possible effects of new physics neither. For example, in addition to the overall size, potential new physics can also introduce form factors which can change the kinematics of particles connected to a vertex. Manifestations of this effect will be seen in the discussion of the EFT approach. It is useful to pause here and compare with the EFT scheme introduced in detail in the next subsection. The EFT scheme relates κ_Z and κ_W , and further expand them into three different Lorentz structures. In addition, some of these higher dimensional HVV coupling are also in connection with κ_γ and anomalous trilinear gauge couplings. The current EFT scheme does not include important new degree of freedom $\text{BR}_{\text{inv}}^{\text{BSM}}$ and Γ_H as independent parameters. Overall, κ -framework does capture the big picture of the capability of precision Higgs boson measurement at CEPC. It is useful as long as we understand its limitation.

The LHC and especially the HL-LHC will provide valuable and complementary information about the Higgs boson properties. For example, the LHC is capable of directly measure the $t\bar{t}H$ process [21, 22]. In addition, the LHC could use differential cross sections to differentiate top-loop contributions and other heavy particle-loop contributions to

⁴Total width is a very useful parameter in understanding and deriving parameter precisions in the κ -scheme.

the Higgs boson to gluon coupling [23–26], and similarly to separate contributions from different operators to the Higgs boson to vector boson couplings [27]. For the purpose of the coupling fit in the κ -framework, the LHC with its large statistics, helps improving precision on rare processes such as Higgs to diphoton couplings. Note that a large portion of the systematics intrinsic to a hadron collider would be canceled by taking ratios of measured cross sections. For example, combining the ratio of the rates $pp \rightarrow H \rightarrow \gamma\gamma$ and $pp \rightarrow H \rightarrow ZZ^*$ and the measurement of HZZ coupling at the CEPC can significantly improve the measurement of κ_γ . These are the most useful inputs from the LHC to combine with the CEPC. Similar studies of combination with the LHC for the ILC can be found in Refs. [28–32].

	10-parameter fit		7-parameter fit	
	CEPC	+HL-LHC	CEPC	+HL-LHC
Γ_H	3.1	2.5	—	—
κ_b	1.6	1.2	1.5	1.1
κ_c	2.2	1.9	2.2	1.9
κ_g	1.6	1.3	1.6	1.2
κ_W	1.4	1.1	1.4	1.0
κ_τ	1.5	1.2	1.5	1.1
κ_Z	0.25	0.25	0.15	0.15
κ_γ	3.7	1.6	3.7	1.6
κ_μ	8.7	5.0	—	—
BR_{inv}^{BSM}	0.30	0.30	—	—

Table 11.4: Coupling measurement precision in percentage from the 7-parameter fit and 10-parameter fit described in the text for the CEPC, and corresponding results after combination with the HL-LHC. All the numbers refer to are relative precision except for BR_{inv}^{BSM} of beyond standard model for which 95% CL upper limit are quoted respectively. Some entries are left vacant for the 7-parameter fit to stress them being dependent parameter under the fitting assumptions of the 7-parameter fit scheme.

The 10-parameter fit and the 7-parameter fit for CEPC with integrate luminosity of 5.6 ab^{-1} are shown in Table 11.4. In addition, the combinations with expectations (optimistically assuming no theoretical uncertainties) from the HL-LHC from Ref. [33] are shown in the same tables as well.⁵ We assume the HL-LHC will operate at 14 TeV center-of-mass energy and accumulate an integrated luminosity of 3000 fb^{-1} .

The CEPC Higgs boson properties measurements mark a giant step beyond the HL-LHC. First of all, in contrast to the LHC, a lepton collider Higgs factory is capable of measuring the absolute width and coupling strengths of the Higgs boson. A comparison with the HL-LHC is only possible with model dependent assumptions. One of such comparison is within the framework of a 7-parameter fit, shown in Figure 11.8. Even with this set of restrictive assumptions, the advantage of the CEPC is still significant. The measure-

⁵We note here that the LHC and the CEPC have different sources of theoretical uncertainties, for detailed discussion, see Refs. [19, 20, 34–36].

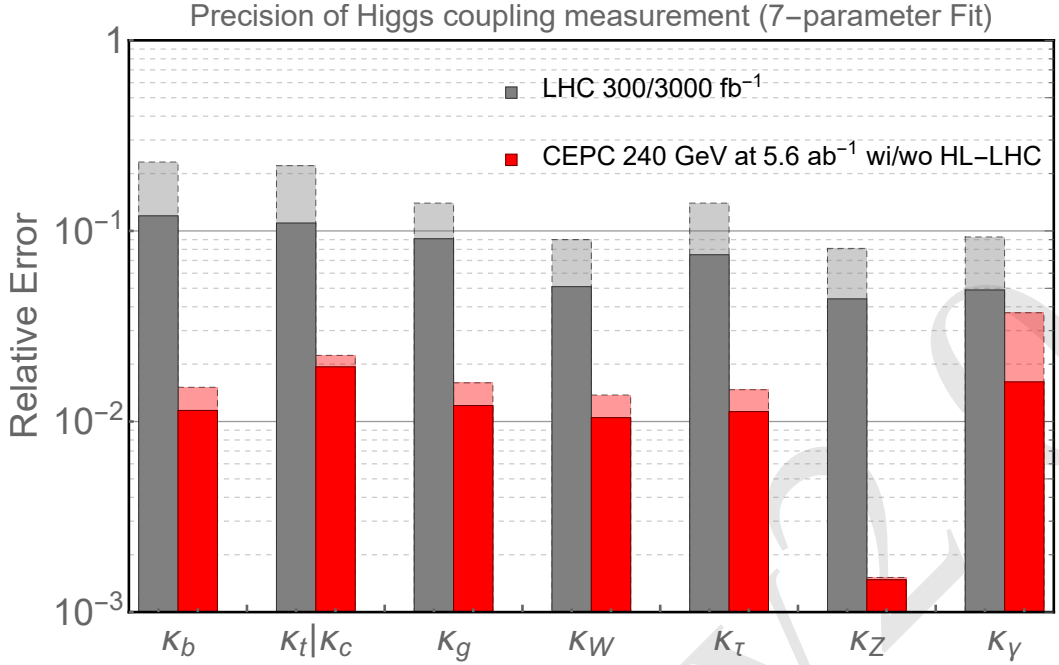


Figure 11.8: The 7 parameter fit result, and comparison with the HL-LHC [33]. The projections for the CEPC at 240 GeV with 5.6 ab^{-1} integrated luminosity are shown. The CEPC results without combination with the HL-LHC input are shown with dashed edges. The LHC projections for an integrated luminosity of 300 fb^{-1} are shown in dashed edges.

ment of κ_Z is more than a factor of 10 better. The CEPC can also improve significantly on a set of channels which suffers from large background at the LHC, such as κ_b , κ_c , and κ_g . Note that this is in comparison with the HL-LHC projection with aggressive assumptions about systematics. Such uncertainties are typically under much better control at lepton colliders. Within this 7-parameter set, the only coupling which the HL-LHC can give a competitive measurement is κ_γ , for which the CEPC's accuracy is limited by statistics. This is also the most valuable input that the HL-LHC can give to the Higgs boson coupling measurement at the CEPC, which underlines the importance of combining the results of these two facilities.

The direct search for Higgs boson decaying into invisible particles from BSM physics is well motivated, in close connection to dark sectors. The CEPC with 5.6 ab^{-1} can measure this to a high accuracy as 95% upper limit 0.30%, as shown in Table 11.4. At the same time, the HL-LHC can only manage a much lower accuracy 6–17% [20] and some improved analysis may reach 2–3.5% [37].

As discussed above, one of the greatest advantages of lepton collider Higgs boson factory is the capability of determining the Higgs boson coupling *model independently*. The projection of such a determination at the CEPC is shown in Figure 11.9. The advantage of the higher integrated luminosity at a circular lepton collider is apparent. The CEPC has a clear advantage in the measure of κ_Z . It is also much stronger in κ_μ and $\text{BR}_{\text{inv}}^{\text{BSM}}$ measurements.

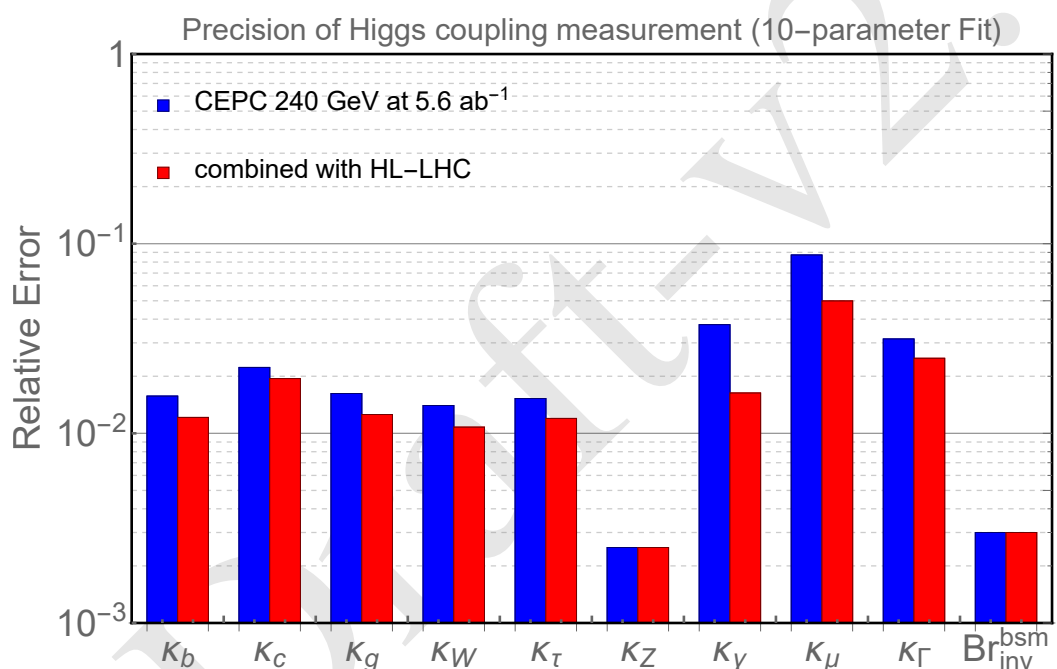


Figure 11.9: The 10 parameter fit result for CEPC at 240 GeV with 5.6 ab^{-1} integrated luminosity (blue) and in combination with HL-LHC inputs (red). All the numbers refer to are relative precision except for $\text{BR}_{\text{inv}}^{\text{BSM}}$ for which 95% CL upper limit are quoted respectively.

11.1.7.2 Effective-field-theory analysis

With the assumption that the new physics particles are heavier than the relevant energy of the Higgs factory, their effect can be characterized in the effective-field-theory (EFT) framework, in which higher dimensional operators supplement the Standard Model Lagrangian. Imposing baryon and lepton numbers conservations, all higher dimensional operators are of even dimension:

$$\mathcal{L}_{\text{EFT}} = \mathcal{L}_{\text{SM}} + \sum_i \frac{c_i^{(6)}}{\Lambda^2} \mathcal{O}_i^{(6)} + \sum_j \frac{c_j^{(8)}}{\Lambda^4} \mathcal{O}_j^{(8)} + \dots \quad (11.11)$$

The leading effects of new physics at the electroweak scale would be the dimension-six operators. To obtain robust constraints on the Wilson coefficients c_i , a global analysis is required which includes the contributions from all possible dimension-six operators. While a large number of dimension-six operators can be written down, only a subset of them contribute to the Higgs boson processes at leading order. Among these operators, some are much better constrained by other measurements. It is thus reasonable to focus on the operators that primarily contribute to the Higgs boson processes and reduce the parameter space by making appropriate assumptions, as done in many recent studies of EFT global analysis at future lepton colliders [32, 38–43]. Following these studies, the CP -violating operators as well as the ones that induce fermion dipole interactions are discarded in this analysis. At leading order, CP -violating operators do not have linear contributions to the rates of Higgs boson processes. While they do contribute to the angular observables at the leading order [44, 45], these operators are usually much better constrained by EDM experiments [46–48], though some rooms are still possible for the CP -violating couplings of Higgs boson to the heavy flavor quarks and leptons [49, 50]. The interference between the fermion dipole interactions with SM terms are suppressed by the fermion masses. The corresponding operators also generate dipole moments, which are stringently constrained especially for light fermions. For the operators that modify the Yukawa matrices, only the five diagonal ones that correspond to the top, charm, bottom, tau, and muon Yukawa couplings are considered, which are relevant for the Higgs boson measurements at CEPC.

Before presenting the projections, some brief comments on the EFT framework are in order. In comparison with the κ -framework, a significant advantage of the EFT framework is that it gives physical parametrizations of the new physics effect. EFT operators can be used directly in computations. It also allows natural inclusions of new observables, with possible correlations automatically taken into account. At the same time, the connections with experimental observables are less direct and intuitive. Sometimes, the EFT approach is referred to as model-independent. This is only accurate to a certain extent. At least, it assumes that there are no new light degrees of freedom. In practice, assumptions are often made to simplify the set of EFT operators, as also done here.

The electroweak precision observables are already tightly constrained by the LEP Z -pole and W mass measurements. The CEPC Z -pole run can further improve the constraints set by LEP, thanks to the enormous amount ($\sim 10^{11}$) of Z bosons that can be collected. The W mass can also be constrained within a few MeVs at CEPC even without a dedicated WW threshold run. Given that the expected precisions of the Z -pole observables and the W mass are much higher than the ones of Higgs boson observables, in the Higgs boson analysis, it is assumed that the former ones are perfectly constrained, which significantly simplifies the analysis. In particular, in a convenient basis all the contact

interaction terms of the form $HVf\bar{f}$ can be discarded since they also modify the fermion gauge couplings. Realistic Z -pole constraints have also been considered in recent studies [32, 41, 43], but certain assumptions (such as flavor-universality) and simplifications are made. Future studies with more general frameworks are desired to fully determine the impact of the Z -pole measurements on the Higgs boson analysis.

CEPC 240 GeV (5.6 ab^{-1})			
	uncertainty	correlation matrix	
		$\delta g_{1,Z}$	$\delta \kappa_\gamma$
$\delta g_{1,Z}$	1.2×10^{-3}	1	0.08
$\delta \kappa_\gamma$	0.9×10^{-3}		-0.42
λ_Z	1.3×10^{-3}		1

Table 11.5: The estimated constraints on aTGCs from the measurements of the diboson process ($e^+e^- \rightarrow WW$) in the semi-leptonic channel at CEPC 240 GeV with 5.6 ab^{-1} data and unpolarized beams. All angular distributions are used in the fit. Only the statistical uncertainties of the signal events are considered, assuming a selection efficiency of 80%.

The measurements of the triple gauge couplings (TGCs) from the diboson process ($e^+e^- \rightarrow WW$) play an important role in the Higgs boson coupling analysis under the EFT framework. Focusing on CP -even dimension-six operators, the modifications to the triple gauge vertices from new physics can be parametrized by three anomalous TGC parameters (aTGCs), conventionally denoted as $\delta g_{1,Z}$, $\delta \kappa_\gamma$ and λ_Z [51, 52]. Among them, $\delta g_{1,Z}$ and $\delta \kappa_\gamma$ are generated by operators that also contribute to the Higgs boson processes. At 240 GeV, the cross section of $e^+e^- \rightarrow WW$ is almost two orders of magnitude larger than the one of the Higgsstrahlung process. The measurements of the diboson process thus provide strong constraints on the operators that generate the aTGCs. A dedicated study on the TGC measurements at CEPC is not available at the current moment. A simplified analysis is thus performed to estimate the precision reaches on the aTGCs. The results are shown in Table 11.5. The analysis roughly follows the methods in Refs. [40, 53]. Only the WW events in the semi-leptonic (electron or muon) channel are used, which have good event reconstructions and also a sizable branching fraction ($\approx 29\%$). In particular, the production polar angle, as well as the two decay angles of the leptonic W , can be fully reconstructed, which contain important information on the aTGCs. The two decay angles of the hadronic W can only be reconstructed with a two-fold ambiguity. A χ^2 fit of the three aTGC parameters to the binned distribution of all five angles is performed, from which the one-sigma precisions of the three aTGCs as well as the correlations among them are extracted. A signal selection efficiency of 80% is assumed. The effects of systematics and backgrounds are not considered, assuming they are under control after the selection cuts.

Under the assumptions specified above, the contributions to the Higgs boson and diboson processes from dimension-six operators consist of a total number of twelve degrees of freedom. While all non-redundant basis are equivalent, it is particularly convenient to choose a basis in which the twelve degrees of freedom can be mapped to exactly twelve operators, while the rest are removed by the assumptions. Two such bases are considered in our analysis, one is defined by the set of dimension-six operators in Table 11.6,

$\mathcal{O}_H = \frac{1}{2}(\partial_\mu H^2)^2$	$\mathcal{O}_{GG} = g_s^2 H ^2 G_{\mu\nu}^A G^{A,\mu\nu}$
$\mathcal{O}_{WW} = g^2 H ^2 W_{\mu\nu}^a W^{a,\mu\nu}$	$\mathcal{O}_{y_u} = y_u H ^2 \bar{Q}_L \tilde{H} u_R \quad (u \rightarrow t, c)$
$\mathcal{O}_{BB} = g'^2 H ^2 B_{\mu\nu} B^{\mu\nu}$	$\mathcal{O}_{y_d} = y_d H ^2 \bar{Q}_L H d_R \quad (d \rightarrow b)$
$\mathcal{O}_{HW} = ig(D^\mu H)^\dagger \sigma^a (D^\nu H) W_{\mu\nu}^a$	$\mathcal{O}_{y_e} = y_e H ^2 \bar{L}_L H e_R \quad (e \rightarrow \tau, \mu)$
$\mathcal{O}_{HB} = ig'(D^\mu H)^\dagger (D^\nu H) B_{\mu\nu}$	$\mathcal{O}_{3W} = \frac{1}{3!}g\epsilon_{abc}W_{\mu}^{a\nu}W_{\nu\rho}^bW_{\rho}^{c\mu}$

Table 11.6: A complete set of CP -even dimension-six operators that contribute to the Higgs boson and TGC measurements, assuming there is no correction to the Z -pole observables and the W mass, and also no fermion dipole interaction. For \mathcal{O}_{y_u} , \mathcal{O}_{y_d} and \mathcal{O}_{y_e} , only the contributions to the diagonal elements of the Yukawa matrices that corresponds to the top, charm, bottom, tau, and muon Yukawa couplings are considered.

the other is the so-called "Higgs basis", proposed in Ref. [54]. In the Higgs basis, the parameters are defined in the broken electroweak phase, and can be directly interpreted as the size of the Higgs boson couplings. Different from the original Higgs basis, this analysis follows Ref. [40], with the parameters associated with the Hgg , $H\gamma\gamma$ and $HZ\gamma$ vertices normalized to the SM one-loop contributions, and denoted as \bar{c}_{gg} , $\bar{c}_{\gamma\gamma}$ and $\bar{c}_{Z\gamma}$. The parameter $\bar{c}_{gg}^{\text{eff}}$ is further defined to absorb all contributions to the Hgg vertex. These redefined parameters can be more conveniently interpreted as the precisions of the Higgs boson couplings analogous to those in the κ framework. The exact definitions of the Higgs basis and the translation to the basis in Table 11.6 can be found in the end of the section.

The estimated precisions of all the Higgs boson rate measurements in Section 11.1.5 (Table 11.3), along with the correlations among them, are included as inputs for the EFT global analysis. In addition, the angular observables of the channel $e^+e^- \rightarrow ZH$, $Z \rightarrow \ell^+\ell^-$, $H \rightarrow b\bar{b}$ are included, following the studies in Refs. [44, 45]. This channel is almost background-free after the selection cuts, with a signal selection efficiency of about 40%. For the TGC measurements, the results in Table 11.5 are used as inputs. The global χ^2 is obtained by summing over the χ^2 of all the measurements. Due to the high precision of the measurements, it is shown that for all observables, keeping only the linear terms of all EFT parameters gives a very good approximation [40]. This greatly simplifies the fitting procedure, as the total χ^2 can be written as

$$\chi^2 = \sum_{ij} (c - c_0)_i \sigma_{ij}^{-2} (c - c_0)_j, \quad \text{where } \sigma_{ij}^{-2} \equiv (\delta c_i \rho_{ij} \delta c_j)^{-1}, \quad (11.12)$$

where c_i 's are the EFT parameters, c_0 's are the corresponding central values which are zero by construction, as the measurements are assumed to be SM-like. The one-sigma uncertainties δc_i and the correlation matrix ρ can be obtained from $\sigma_{ij}^{-2} = \partial^2 \chi^2 / \partial c_i \partial c_j$.

For comparison, the reaches of the LHC 14 TeV are also considered, with a total luminosities of 300 fb^{-1} or 3000 fb^{-1} , which are combined with the diboson ($e^+e^- \rightarrow WW$) measurements at LEP as well as the LHC 8 TeV Higgs boson measurements. For the LHC 14 TeV Higgs boson measurements, the projections by the ATLAS collaboration [33] are used, while the composition of each channel is obtained from Refs. [55–59]. The constraints from the LHC 8 TeV Higgs boson measurements and the diboson measurements at LEP are obtained directly from Ref. [60]. While the LHC diboson measurements could potentially improve the constraints on aTGCs set by LEP [61], they are

not included in this analysis due to the potential issues related to the validity of the EFT [62, 63] and the TGC dominance assumption [64].

The results of the 12-parameter fit at CEPC are shown in Figure 11.10 for the Higgs basis and Figure 11.11 for the basis in Table 11.6. The results from LHC Higgs boson measurements (both 300 fb^{-1} and 3000 fb^{-1}) combined with LEP diboson measurements are shown in comparison. The results of the combination of CEPC with HL-LHC (3000 fb^{-1}) are also shown in addition to the ones of CEPC alone. In Figure 11.10, the results are shown in terms of the one-sigma precision of each parameter. The LHC results are shown with gray columns with 300 fb^{-1} (3000 fb^{-1}) in light (solid) shades, while the CEPC ones are shown with the red columns, with the CEPC-alone (combination with HL-LHC) results shown in light (solid) shades. In Figure 11.11, the results are presented in terms of the reaches of $\Lambda/\sqrt{|c_i|}$ at 95% confidence level (CL), where Λ is the scale of new physics and c_i is the corresponding Wilson coefficient for each operator, defined in Equation 11.11. Four columns are shown separately for LHC 300 fb^{-1} , LHC 3000 fb^{-1} , CEPC alone and CEPC combined with HL-LHC. The results of the global fits are shown with solid shades. The results from individual fits are shown with light shades, which are obtained by switching on one operator at a time with the rest fixed to zero.

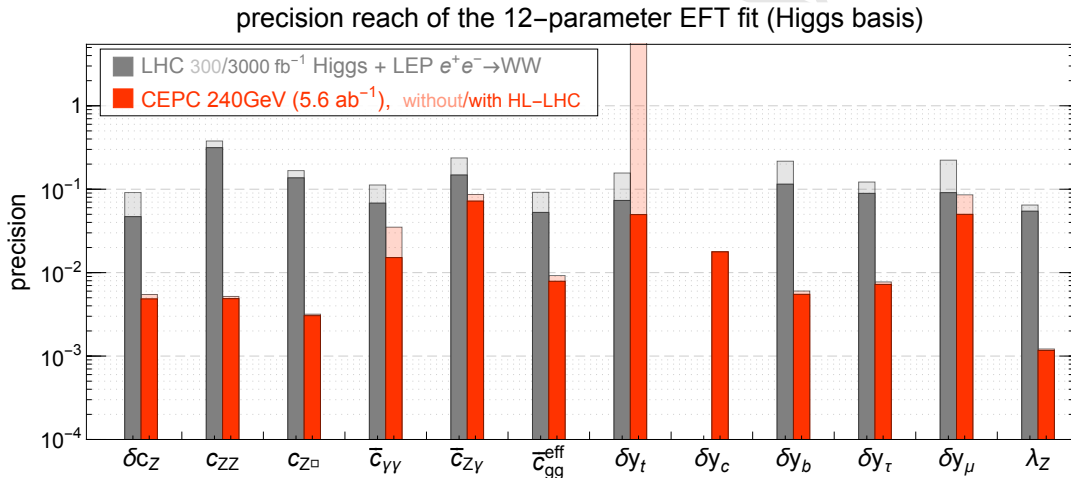


Figure 11.10: One-sigma precision reach of the twelve parameters in the Higgs basis. The first column shows the results from the LHC Higgs boson measurements with 300 fb^{-1} (light shade) and 3000 fb^{-1} (solid shade) combined with LEP diboson ($e^+e^- \rightarrow WW$) measurement. The second column shows the results from CEPC with 5.6 ab^{-1} data collected at 240 GeV with unpolarized beam. The results from CEPC alone are shown in light shades, and the ones from a combination of CEPC and HL-LHC are shown in solid shades. δy_c is fixed to zero for the LHC fits.

It is transparent from Figure 11.10 that CEPC provides very good reaches on the precisions of Higgs boson couplings, which are of one order of magnitude better than the ones at the LHC. For the parameters $\bar{c}_{\gamma\gamma}$, $\bar{c}_{Z\gamma}$ and δy_μ , the clean signal and small branching ratios of the corresponding channels ($H \rightarrow \gamma\gamma/Z\gamma/\mu\mu$) makes the HL-LHC precisions comparable with the CEPC ones. The combination with additional LHC measurements thus provides non-negligible improvements, especially for those parameters. It should be noted that, while δy_t modifies the Hgg vertex via the top loop contribution, CEPC alone could not discriminate it from the Hgg contact interaction obtained from integrating out a heavy new particle in the loop. The parameter \bar{c}_{gg}^{eff} absorbs both contributions and reflects the overall precision of the Hgg coupling. The combination with the LHC $t\bar{t}H$ measure-

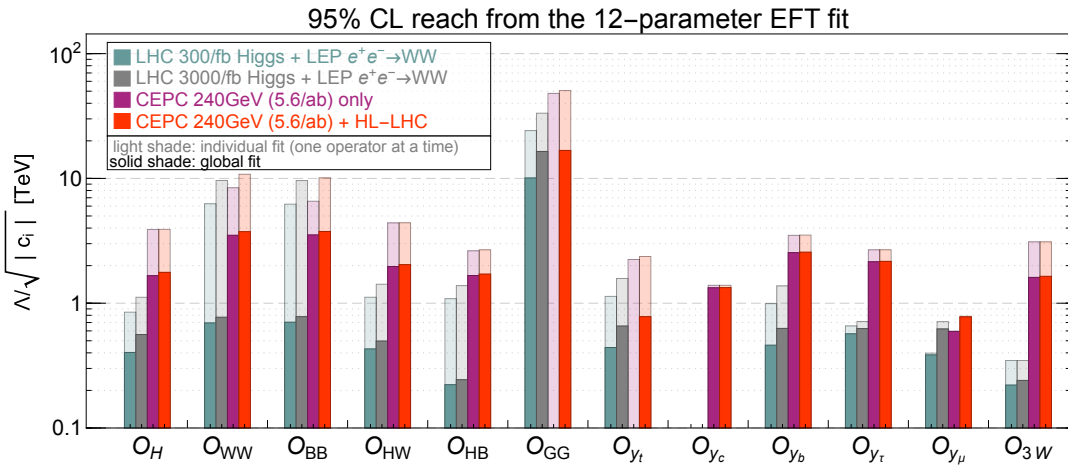


Figure 11.11: The 95% CL reach on $\Lambda/\sqrt{|c_i|}$ for the operators in the basis defined in Table 11.6. The first two columns show the results from LHC Higgs boson measurements with 300 fb^{-1} and 3000 fb^{-1} combined with LEP diboson ($e^+e^- \rightarrow WW$) measurement. The last two columns show the results from CEPC alone and the combination of CEPC and HL-LHC (3000 fb^{-1}). The results of the global fits are shown with solid shades. The results from individual fits (by switching on one operator at a time) are shown with light shades. δy_c is fixed to zero for the LHC fits.

ments could resolve this flat direction. The CEPC measurements, in turn, could improve the constraint on δy_t set by the LHC by providing much better constraints on the other parameters that contribute to the $t\bar{t}H$ process. It should also be noted that the measurement of the charm Yukawa coupling is not reported in Ref. [33], while the projection of its constraint has a large variation among different studies and can be much larger than one [65–70]. Therefore, δy_c is fixed to be zero for the LHC-only fits, as treating δy_c as an unconstrained free parameter generates a flat direction in the fit which makes the overall reach much worse. The CEPC, on the other hand, provides excellent measurements of the charm Yukawa and can constrain δy_c to a precision of $\sim 2\%$.

Regarding the reaches of $\Lambda/\sqrt{|c_i|}$ in Figure 11.11, it is also clear that CEPC has a significantly better performance than the LHC. If the couplings are naïvely assumed to be of order one ($c_i \sim 1$), the Higgs boson measurements at CEPC would be sensitive to new physics scales at multiple TeVs. While the individual reach for some of the operators at the LHC can be comparable to the ones at CEPC (*e.g.*, O_{WW} and O_{BB} from the measurement of $H \rightarrow \gamma\gamma$), the reaches of CEPC are much more robust under a global framework thanks to its comprehensive measurements of both the inclusive ZH cross section and the exclusive rates of many Higgs boson decay channels. Operators O_{GG} and O_{y_t} both contribute to the Hgg vertex. While the CEPC could provide strong constraints on either of them if the other is set to zero, they can only be constrained in a global fit if the $t\bar{t}H$ measurements at the LHC are also included. It is also important to note that the validity of EFT could be a potential issue for the LHC measurements [62]. Depending on the size of the couplings, the inferred bounds on the new physics scale Λ could be comparable with or even smaller than the energy scale probed by the LHC. The CEPC has a smaller center of mass energy and much better precisions, which ensures the validity of EFT for most new physics scenarios.

In Table 11.7, the numerical results of the global fit are presented for CEPC in terms of the one-sigma precisions of the 12 parameters and the correlations among them. The

1 results assume an integrated luminosity of 5.6 ab^{-1} at 240 GeV with unpolarized beams,
 2 both without and with the combination of HL-LHC (3000 fb^{-1}) Higgs boson measure-
 3 ments. With both the one-sigma bounds and the correlation matrix, the corresponding
 4 *chi-squared* can be reconstructed, which can be used to derive the constraints in any other
 5 EFT basis or any particular model that can be matched to the EFT. This offers a con-
 6 venient way to study the reaches on new physics models, as detailed knowledge of the
 7 experimental measurements are not required.

Higgs basis											
δc_Z	c_{ZZ}	$c_{Z\Box}$	$\bar{c}_{\gamma\gamma}$	$\bar{c}_{Z\gamma}$	$\bar{c}_{gg}^{\text{eff}}$	δy_t	δy_c	δy_b	δy_τ	δy_μ	λ_Z
0.0055	0.0052	0.0032	0.035	0.086	0.0092	—	0.018	0.0060	0.0077	0.086	0.0012
0.0048	0.0049	0.0031	0.015	0.072	0.0079	0.050	0.018	0.0055	0.0072	0.050	0.0012
$c_i/\Lambda^2 [\text{TeV}^{-2}]$ of dimension-six operators											
c_H	c_{WW}	c_{BB}	c_{HW}	c_{HB}	c_{GG}	c_{y_t}	c_{y_c}	c_{y_b}	c_{y_τ}	c_{y_μ}	c_{3W}
0.18	0.041	0.040	0.13	0.18	—	—	0.28	0.077	0.11	1.4	0.19
0.16	0.036	0.035	0.12	0.17	0.0018	0.82	0.28	0.076	0.11	0.83	0.19

Table 11.7: The one-sigma uncertainties for the 12 parameters from CEPC ($240 \text{ GeV}, 5.6 \text{ ab}^{-1}$) in the Higgs basis and the basis of dimension-six operators. For both cases, the upper (lower) row correspond to results without (with) the combination of the HL-LHC Higgs boson measurements.. Note that, without the $t\bar{t}H$ measurements, δy_t can not be constrained in a global fit, thus c_{GG} and c_{y_t} can not be resolved.

8 In the EFT framework, it is explicitly assumed that the Higgs boson total width is
 9 the sum of all the widths of its SM decay channels. This is because the EFT expansion
 10 in Equation 11.11 relies on the assumption that the new physics scale is sufficiently large,
 11 while any potential Higgs boson exotic decay necessarily introduces light BSM particles,
 12 thus in direct conflict with this assumption. One could nevertheless treat the Higgs boson
 13 total width as a free parameter in the EFT global fit and obtain an indirect constraint of
 14 it, as done in Ref. [32]. With this treatment, the CEPC could constrain the Higgs boson
 15 total width to a precision of 1.7% (1.6% if combined with HL-LHC). This result is signif-
 16 icantly better than the one from the 10-parameter coupling fit in Table 11.4 (3.4%/2.6%).
 17 The improvement is mainly because the HWW and HZZ couplings are treated as being
 18 independent in the 10-parameter coupling fit, while in the EFT framework they are
 19 related to each other under gauge invariance and custodial symmetry. It should also be
 20 noted that the Higgs boson width determined using Equation (11.4) and (11.7) explicitly
 21 assumes that the HWW and HZZ couplings are independent of the energy scale. Such
 22 an assumption is not valid in the EFT framework with the inclusion of the anomalous
 23 couplings.

24 11.1.7.3 The Higgs boson self-coupling

25 The Higgs boson self-coupling is a critical parameter governing the dynamics of the elec-
 26 troweak symmetry breaking. In the Standard Model, the Higgs boson trilinear and quadri-
 27 linear couplings are fixed once the values of the electroweak VEV and the Higgs boson
 28 mass are known. Any deviation from the SM prediction is thus clear evidence of new
 29 physics beyond the SM. The Higgs boson trilinear coupling is probed at the LHC with the
 30 measurement of the di-Higgs process, $pp \rightarrow HH$. Current bounds on the Higgs boson
 31 trilinear coupling is at the $\mathcal{O}(10)$ level, while the HL-LHC is expected to improve the pre-
 32 cision to the level of $\mathcal{O}(1)$ [71]. The prospects for extracting the Higgs boson quadrilinear
 33 coupling are much less promising, even for a 100 TeV hadron collider [72].

To measure the di-Higgs-boson processes at a lepton collider, a sufficiently large center of mass energy ($\gtrsim 400$ GeV) is required, which is likely to be achieved only at a linear collider. The CEPC, instead, can probe the Higgs boson trilinear coupling via its loop contributions to the single Higgs boson processes. This indirect approach nevertheless provides competitive reaches since the loop suppression is compensated by the high precision of the Higgs boson measurements at CEPC [73]. With a precision of 0.5% on the inclusive ZH cross section at 240 GeV, the Higgs boson trilinear coupling can be constrained to a precision of 35%, assuming all other Higgs boson couplings that contributes to $e^+e^- \rightarrow ZH$ are SM-like.⁶ While this indirect bound is comparable to the direct ones at linear colliders, it relies on strong assumptions which are only applicable to some specific models. A more robust approach is to include all possible deviations on the Higgs boson couplings simultaneously and constrain the Higgs boson trilinear coupling in a global fit. The EFT framework presented in Section 11.1.7.2 is ideal for such an analysis. Under this framework, the one-loop contributions of the trilinear Higgs boson coupling to all the relevant Higgs boson production and decay processes are included, following Ref. [42]. The new physics effect is parametrized by the quantity $\delta\kappa_\lambda \equiv \kappa_\lambda - 1$, where κ_λ is the ratio of the Higgs boson trilinear coupling to its SM value,

$$\kappa_\lambda \equiv \frac{\lambda_3}{\lambda_3^{\text{sm}}}, \quad \lambda_3^{\text{sm}} = \frac{m_H^2}{2v^2}. \quad (11.13)$$

The global fit is performed simultaneously with $\delta\kappa_\lambda$ and the 12 EFT parameters in Section 11.1.7.2. The results are presented in Table 11.8. The results for HL-LHC are also shown, which were obtained in Ref. [74] under the same global framework. For CEPC 240 GeV, the one-sigma bound on $\delta\kappa_\lambda$ is around ± 3 , significantly worse than the 35% in the $\delta\kappa_\lambda$ -only fit. This is a clear indication that it is difficult to resolve the effects of $\delta\kappa_\lambda$ from those of other Higgs boson couplings. For HL-LHC, the reach on $\delta\kappa_\lambda$ is still dominated by the di-Higgs process. However, as a result of the destructive interferences among diagrams, the di-Higgs process at LHC could not constrain $\delta\kappa_\lambda$ very well on its positive side, even with the use of differential observables [75]. The combination of HL-LHC and CEPC 240 GeV thus provides a non-trivial improvement to the HL-LHC result alone, in particular for the two-sigma bound on the positive side, which is improved from +6.1 to +2.8. This is illustrated in Figure 11.12, which plots the profiled χ^2 as a function of $\delta\kappa_\lambda$ for the two colliders.

bounds on $\delta\kappa_\lambda$	$\Delta\chi^2 = 1$	$\Delta\chi^2 = 4$
CEPC 240 GeV 5.6 ab^{-1}	[−3.0, +3.1]	[−5.9, +6.2]
HL-LHC	[−0.9, +1.3]	[−1.7, +6.1]
HL-LHC + CEPC 240 GeV	[−0.8, +1.0]	[−1.5, +2.7]

Table 11.8: The $\Delta\chi^2 = 1$ (one-sigma) and $\Delta\chi^2 = 4$ (two-sigma) bounds of $\delta\kappa_\lambda$ for various scenarios, obtained in a global fit by profiling over all other EFT parameters. The results for HL-LHC are obtained from Ref. [74].

⁶ A better precision can be obtained by also using the exclusive channels, such as $\sigma(ZH) \times \text{BR}(H \rightarrow b\bar{b})$, but would require an even stronger assumption that all Higgs boson couplings contributing to the branching ratios are also SM-like except the Higgs boson trilinear coupling.

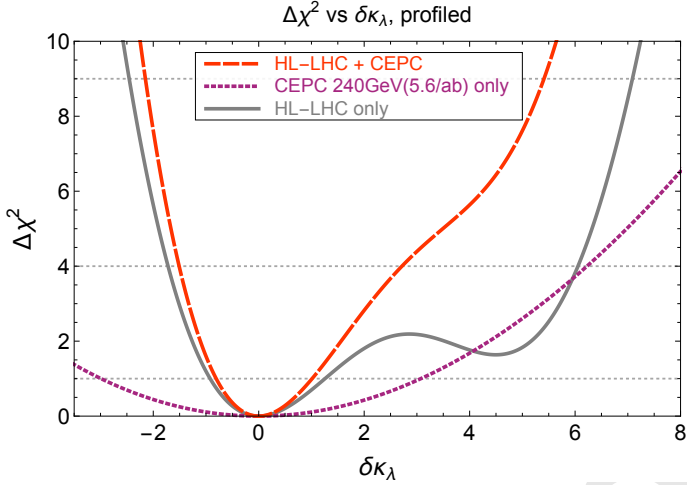


Figure 11.12: Chi-square as a function of $\delta\kappa_\lambda$ after profiling over all other EFT parameters for HL-LHC, CEPC and their combination.

11.1.7.4 Higgs and top couplings

Interactions of the Higgs boson with the top quark are widely viewed as a window to new physics beyond the Standard Model. Parametrizing effects of new physics in terms of dimension-six gauge-invariant operators modifying the Higgs-top interactions [76, 77], the Higgs-top couplings physics potential at CEPC can be evaluated [78–81]. This EFT basis enlarges the Higgs EFT considered above. Moreover, the CP violation effects in the third generation Yukawas can be reflected as the complexity of the Wilson coefficients of operator \mathcal{O}_{y_t} and \mathcal{O}_{y_b} ,

$$\Delta y_t = y_t^{\text{SM}} \left(\Re[C_{y_t}] \frac{v^3}{2m_t \Lambda^2} + i \Im[C_{y_t}] \frac{v^3}{2m_t \Lambda^2} \right) \quad (11.14)$$

$$\Delta y_b = y_t^{\text{SM}} \left(\Re[C_{y_b}] \frac{v^3}{2m_b \Lambda^2} + i \Im[C_{y_b}] \frac{v^3}{2m_b \Lambda^2} \right). \quad (11.15)$$

In this section, the effect of introducing CP phases in the Yukawa operators in Higgs boson physics are discussed. For more detailed discussion on a complete set of Higgs and Top operators, see Ref. [78]. The dominant sources of constraints are from $H \rightarrow \gamma\gamma$ and $H \rightarrow gg$ for \mathcal{O}_{y_t} , and $H \rightarrow gg$ and $H \rightarrow b\bar{b}$ for \mathcal{O}_{y_b} . Given that $H \rightarrow gg$ measurements are sensitive to both operators, a joint analysis of \mathcal{O}_{y_t} and \mathcal{O}_{y_b} will yield a significantly different result comparing to individual operator analysis. A joint analysis for these two operators in terms of Yukawa coupling strengths and the associated CP phases is performed at CEPC. The important physics cases for such considerations are highlighted.

In Figure 11.13 constraints on the top and bottom Yukawa coupling strengths and their CP phases are presented in the left panel and right panel, respectively. The 68% and 95% exclusion bands are shown in solid and dashed lines. The limits for CEPC are shown in *bright* black and magenta lines for individual operator analysis and the *bright* green and yellow shaded regions representing the 68% and 95% allowed parameter space, respectively. The *dimmed* thick black curves represent the results after turning on both operators \mathcal{O}_{tH} and \mathcal{O}_{bH} at the same time, using a profile-likelihood method profiling over other parameters. Furthermore, in the left panel the cyan band represents constraints from HL-

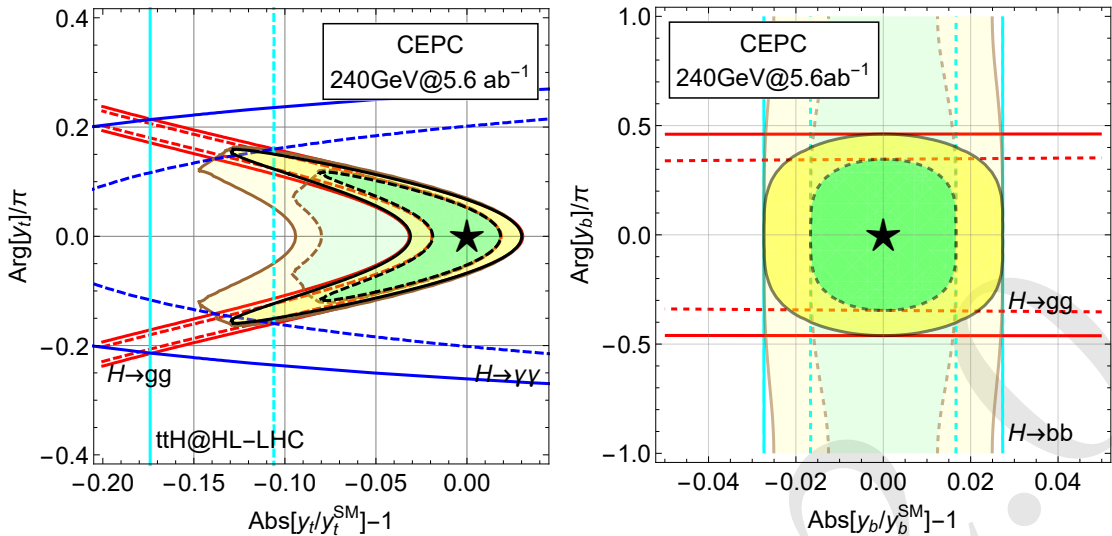


Figure 11.13: Results for analysis on C_{y_t} and C_{y_b} in the projected allowed regions for modification to top and bottom Yukawa couplings in magnitude and CP phase at 68% and 95% confidence level. The combined results for CEPC are shown in black curves. The source of individual constraints for the single operator analysis are labeled correspondingly. For a joint analysis of simultaneous appearance of both \mathcal{O}_{y_t} and \mathcal{O}_{y_b} operators, the results for CEPC are shown in the enlarged yellow (95%) and green regions (68%) with thick brown boundary lines.

1 LHC $t\bar{t}H$ measurements, red bands are constraints from CEPC $H \rightarrow gg$ measurements
2 and blue bands are constraints from CEPC $H \rightarrow \gamma\gamma$ measurements. Similarly in the right
3 panel, the cyan bands are constraints from $H \rightarrow b\bar{b}$ and the red bands are constraints from
4 $H \rightarrow gg$ at CEPC.

5 The left panel of Figure 11.13 shows that the expected sensitivity on the modification
6 in the magnitude of top Yukawa is at around $\pm 3\%$ for the single operator analysis, which
7 is relaxed to $[-9.5\%, +3\%]$ for the joint analysis allowing the bottom Yukawa and the
8 associated CP phase to vary freely, in the case of zero CP phase in the top Yukawa. The
9 phase of the top Yukawa could be constrained to be $\pm 0.16\pi$. The constraints on the phase
10 of the top Yukawa is driven by the $H \rightarrow \gamma\gamma$ measurements, where a sizable phase shift
11 will enlarge the Higgs boson to diphoton rate via reducing the interference with SM W -
12 loop. The constraints on the magnitude of the top Yukawa modification is driven by the
13 $H \rightarrow gg$ measurements due to the dominant contribution to $H \rightarrow gg$ being from top-loop.
14 Note that constraints from $H \rightarrow gg$ measurement is not entirely vertical, this is a result
15 of the different sizes of the top-loop contribution to Hgg through scalar and pseudoscalar
16 couplings. Similarly, as shown in the right panel of Figure 11.13 for the bottom Yukawa
17 magnitude modification, the constraint is $\pm 2.5\%$ and, for the bottom Yukawa CP phase,
18 the constraints changes from $\pm 0.47\pi$ to no constraint for simultaneous modification to top
19 Yukawa.

20 11.1.8 Tests of Higgs boson spin/ CP

21 The CP parity of a Higgs boson, and more generally its anomalous couplings to gauge
22 bosons in the presence of BSM physics, can be measured at the CEPC based on the
23 $e^+e^- \rightarrow Z^* \rightarrow ZH \rightarrow \mu^+\mu^- b\bar{b}$ process. It is convenient to express the anomalous cou-

pling measurements in terms of physical quantities of effective fractions of events of the anomalous contribution relative to the SM predictions as detailed in Refs. [82–84], which are invariant under independent re-scalings of all couplings.

Two of the anomalous HZZ coupling measurements are of particular interest at the CEPC: the fraction of the high-order CP -even contribution due to either SM contribution or new physics, f_{a2} , and the fraction of a CP -odd contribution due to new physics, f_{a3} . The following two types of observables can be used to measure these anomalous couplings of the Higgs bosons.

1. The dependence of the $e^+e^- \rightarrow Z^* \rightarrow ZH$ cross section on \sqrt{s} is different for different CP property of the Higgs boson [84]. Therefore, measurements of the cross section at several different energies will yield useful information about anomalous HZZ couplings. However this has non-trivial implications to the accelerator design and is not included in this study as a single value of \sqrt{s} is assumed for the CEPC operating as a Higgs boson factory.
2. Angular distributions, $\cos \theta_1$ or $\cos \theta_2$ and Φ as defined in Figure 11.14. These angles are also sensitive to interference between CP -even and CP -odd couplings. In particular forward-backward asymmetry with respect to $\cos \theta_1$ or $\cos \theta_2$ and non-trivial phase in the Φ distributions can lead to an unambiguous interpretation of CP violation.

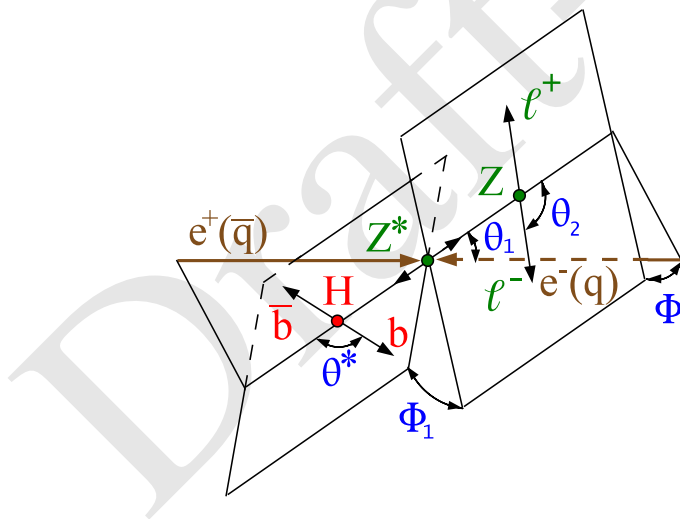


Figure 11.14: Higgs boson production and decay angles of the $e^+e^- \rightarrow Z^* \rightarrow ZH \rightarrow \mu^+\mu^- b\bar{b}$ process.

To estimate the sensitivities on the anomalous couplings, a maximum likelihood fit [84] is performed to match observed three-dimensional angular distributions to theory predictions including signal and background processes. In this likelihood fit, the signal probability density functions are from analytical predictions that are validated using a dedicated MC program, the JHU generator [82, 83], which incorporates all the anomalous couplings, spin correlations, interference of all contributing amplitudes. The background probability density function is modeled from simulation based on $e^+e^- \rightarrow ZZ \rightarrow e^+e^- b\bar{b}$ process in Madgraph [85].

Several thousand statistically-independent experiments are generated and fitted to estimate the sensitivity to f_{a2} and f_{a3} , defined as the smallest values that can be measured

with 3σ away from 0. All other parameters in the fit, including the number of expected signal and background events, are fixed. Figure 11.15 shows precision on f_{a2} and f_{a3} obtained with generated experiments. The expected sensitivity on f_{a2} and f_{a3} are 0.018 and 0.007 respectively.

The sensitivities of f_{a2} and f_{a3} are then converted to the equivalent parameters defined for the on-shell $H \rightarrow ZZ^*$ decays, f_{a2}^{dec} and f_{a3}^{dec} , in order to compare with the sensitivities from the LHC experiments as described in Ref. [84]. The corresponding sensitivities of f_{a2}^{dec} and f_{a3}^{dec} are 2×10^{-4} and 1.3×10^{-4} respectively. The much smaller values in the $f_{a2,a3}^{\text{dec}}$ are due to the much smaller $m_{Z^*}^2$ in the $H \rightarrow ZZ^*$ decay compared to the value in the $Z^* \rightarrow ZH$ production. A simultaneous fit of f_{a2} and f_{a3} can also be performed with the 68% and 95% confidence level contours shown in Figure 11.15.

Compared to the ultimate sensitivity of HL-LHC as shown in Ref. [84], the sensitivities in the f_{a2} and f_{a3} at the CEPC are a factor of 300 and 3 better. Further improvements can be achieved by exploring kinematics in the $H \rightarrow b\bar{b}$ decays, including other Z decay final states, and combining with the overall cross-section dependence of the signal with a threshold scan in \sqrt{s} .

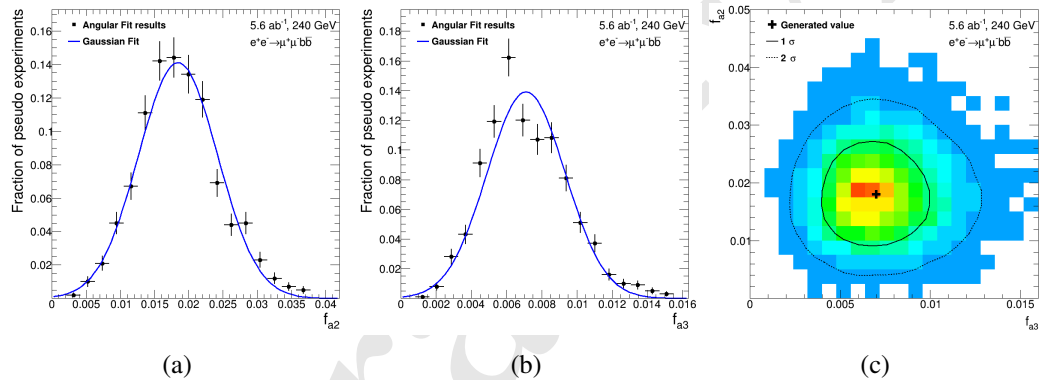


Figure 11.15: Distributions of fitted values of (a) f_{a2} and (b) f_{a3} in a large number of generated experiments. Only the parameter shown is floated in these fits. Other parameters are fixed to their SM expectations. (c) Simultaneous fit of non-zero f_{a2} and f_{a3} , with 68% and 95% confidence level contours shown.

11.1.9 Summary

Many new physics models predict Higgs boson coupling deviations at the sub-percent level, beyond those achievable at the LHC. The CEPC complements the LHC and will be able to study the properties of the Higgs boson in great details with unprecedented precision. At the CEPC, most of Higgs boson couplings can be measured with precision at a percent level or better, in particular the coupling to the Z boson can be determined with a precision of 0.25%. More importantly, the CEPC will be able to measure many of the key Higgs boson properties such as the total width and decay branching ratios model independently, greatly enhancing the coverage of new physics searches. Furthermore, the clean event environment of the CEPC will allow the identification of potential unknown decay modes that are impractical at the LHC.

This section provides a snapshot of the current studies, many of them are ongoing and more analyses are needed to fully understand the physics potential of the CEPC.

1 Nevertheless, the results presented here have already built a strong case for the CEPC as a
 2 Higgs factory. The CEPC has the potential to “undress” the Higgs boson as what the LEP
 3 has done to the Z boson, and potentially shed light on new physics.

4 11.2 W and Z Boson Physics

5 With high production cross sections and large integrated luminosity, the CEPC will reach
 6 a new level of precision for the measurements of the properties of the W and Z bosons.
 7 Precise measurements of the W and Z boson masses, widths, and couplings are critical
 8 to test the consistency of the SM [86]. In addition, many BSM models predict new cou-
 9 plings of the W and Z bosons to other elementary particles. Precise electroweak (EW)
 10 measurements performed at the CEPC could discover deviations from the SM predictions
 11 and reveal the existence of new particles that are beyond the reaches of direct searches at
 12 the current experiments.

13 Significant improvements are expected from the CEPC measurements. Table 11.9
 14 lists the expected precision from CEPC compared to achieved precision from the LEP
 15 experiments for various measurements. Details about the estimation of these uncertainties
 16 are described in this section.

Observable	LEP precision	CEPC precision	CEPC runs	CEPC $\int \mathcal{L} dt$
m_Z	2 MeV	0.5 MeV	Z pole	8 ab^{-1}
$A_{FB}^{0,b}$	1.7%	0.1%	Z pole	8 ab^{-1}
$A_{FB}^{0,\mu}$	7.7%	0.3%	Z pole	8 ab^{-1}
$A_{FB}^{0,e}$	17%	0.5%	Z pole	8 ab^{-1}
$\sin^2 \theta_W^{\text{eff}}$	0.07%	0.001%	Z pole	8 ab^{-1}
R_b	0.3%	0.02%	Z pole	8 ab^{-1}
R_μ	0.2%	0.01%	Z pole	8 ab^{-1}
N_ν	1.7%	0.05%	ZH runs	5.6 ab^{-1}
m_W	33 MeV	2–3 MeV	ZH runs	5.6 ab^{-1}
m_W	33 MeV	1 MeV	WW threshold	2.6 ab^{-1}

Table 11.9: The expected precision in a selected set of EW precision measurements in CEPC and the comparison with the precision from LEP experiments. The CEPC accelerator running mode and total integrated luminosity expected for each measurement are also listed.

17 11.2.1 Z pole measurements

18 The CEPC offers the possibility of dedicated low-energy runs at the Z pole for at least two
 19 years with a high instantaneous luminosity ($1.6 \times 10^{35} \text{ cm}^{-2}\text{s}^{-1}$). The expected integrated
 20 luminosity for CEPC Z pole runs is more than 8 ab^{-1} , and it is expected to produce about
 21 3×10^{11} Z bosons.

22 These runs allow high precision electroweak measurements of the Z boson proper-
 23 ties, such as mass, total width and partial widths, e.g. the parameters $R_b = \Gamma_{Z \rightarrow b\bar{b}} / \Gamma_{\text{had}}$

and⁷ $R_\ell = \Gamma_{\text{had}}/\Gamma_{Z \rightarrow \ell\bar{\ell}}$. It would also perform high precision measurements of the forward-backward charge asymmetry (A_{FB}), the effective weak mixing angle ($\sin^2 \theta_W^{\text{eff}}$), number of light neutrino species (N_ν), and the mass of the Z boson (m_Z). It is also possible to perform some measurements with the Z boson without these dedicated low-energy runs near or at the Z pole. For example, the direct measurement of the number of light neutrino species can be performed in ZH runs at 240 GeV.

11.2.1.1 Z mass and width measurements

The mass m_Z , together with its total width Γ_Z , is a fundamental parameter in the SM and was determined with an overall uncertainty of 2 MeV by four LEP experiments. The lineshape scan around the Z peak was performed from 87.9 GeV to 94.3 GeV. The Z mass and widths were measured by a combined fit to the hadronic and leptonic cross sections in the on-peak and off-peak datasets. Most of the m_Z information is extracted from the off-peak runs. Taking the OPAL measurement as one example, six off-peak datasets were used to complete the m_Z scan. The main uncertainty of m_Z includes the statistical uncertainty (1 MeV), and the LEP beam energy (about 1 MeV).

\sqrt{s} (GeV)	Luminosity (ab^{-1})
87.9	0.25
90.2	0.25
91.2	7
92.2	0.25
94.3	0.25

Table 11.10: The proposed five $e^+e^- \rightarrow Z$ threshold scan runs and their integrated luminosity, for a total integrated luminosity of 8 ab^{-1} .

A precision of 0.5 MeV in m_Z and Γ_Z can be achieved in CEPC measurement. The lineshape scan around the Z peak is the key for improving m_Z measurements. The LEP measurement was limited by the statistics in their off-peak runs, therefore the luminosity in Z off-peak runs plays an important role in the m_Z measurement. We propose four off-peak runs and one on-peak run in CEPC Z mass scan, as listed in Table 11.10. The expected m_Z uncertainty in CEPC due to statistics is below 0.1 MeV.

The major systematic uncertainty is beam momentum scale uncertainty. The beam momentum is expected to be measured by depolarizing resonance method, which was developed by LEP [87]. The beam momentum uncertainty in the CEPC accelerator is expected to be less than 0.5 MeV. The uncertainty in luminosity measurement is expected to be the sub-leading systematic uncertainty. As described in Section 9.5.2, this uncertainty is about 0.05% level, corresponding to about 0.1 MeV uncertainty in Z mass measurement.

Z threshold scan is also needed for Z lineshape studies. The lineshape is strongly affected by the emission of initial state photon radiation (ISR), with a shift of the peak position by about 100 MeV and a decrease of the cross section by about 25%. Moreover

⁷Here R_ℓ is defined as the ratio to any *one* charged lepton flavor, assuming lepton universality, not the ratio to the sum of all lepton flavors.

the emission of ISR creates a distortion of the shape with respect to a Breit-Wigner form, with the appearance of a typical radiative tail for $\sqrt{s} \sim 93$ GeV. An efficient way to account for ISR is to convolute a QED radiator function with the kernel cross section $\hat{\sigma}$ evaluated at the proper reduced center of mass energy, according to

$$\sigma(s) = \int_{z_0}^1 dz H(z; s) \hat{\sigma}(zs), \quad (11.16)$$

where z_0 depends on the event selection. The radiator function is known at $\mathcal{O}(\alpha^2)$ and including leading terms of $\mathcal{O}(\alpha^3 L^3)$ [88, 89], where $L = \log(s/m_e^2)$. Such calculations have been implemented in two independent codes, TOPAZO [90–93] and ZFITTER [94–96], used to estimate the impact of the residual QED uncertainty on Z mass and width at the level of 0.1 MeV [97–99]. The uncertainty on the cross sections due to QED was estimated below the 0.01% level. The kernel cross section in the SM is composed of three contributions: Z exchange, γ exchange and their interference, which are calculated perturbatively with NLO precision supplemented with higher order terms from running couplings and QCD corrections, which guarantees a theoretical uncertainty on observables at the 0.01% level. Aiming at a model-independent parameterization of the Z lineshape around the Z resonance [100], the Z exchange contribution can be parametrized in the following way

$$\begin{aligned} \sigma_{f\bar{f}}^Z &= \sigma_{f\bar{f}}^{\text{peak}} \frac{s\Gamma_Z^2}{(s - m_Z)^2 + s^2\Gamma_Z^2/m_Z^2} \\ \sigma_{f\bar{f}}^{\text{peak}} &= \frac{\sigma_{f\bar{f}}^0}{R_{\text{QED}}}, \quad \sigma_{f\bar{f}}^0 = \frac{12\pi}{m_Z^2} \frac{\Gamma_{ee}\Gamma_{f\bar{f}}}{\Gamma_Z^2}, \end{aligned}$$

where R_{QED} removes the final state QED corrections. The two contributions which are not factorizable on the Z exchange are calculated in the SM, thus introducing a dependence on the SM parameters, such as the mass of the top quark, the Higgs boson mass and the strong coupling constant. The SM model parameter dependence has been estimated at the end of LEP1 operations to be below 0.1% level, which was the target precision. After subtraction of the non-factorizable terms, the resonance parameters are extracted from the lineshape data by means of a global fit. In particular, assuming lepton universality, four quantities are extracted from the fit: m_Z , Γ_Z , R_ℓ and the hadronic peak cross section σ_h . The Z resonance parameter measurements can be directly compared with SM predictions. The latter have been completed very recently at complete two-loop electroweak accuracy, including corrections due to the top-quark Yukawa coupling up to $\mathcal{O}(\alpha_t^3)$ and mixed $\mathcal{O}(\alpha\alpha_s)$ and $\mathcal{O}(\alpha_t\alpha_s^n)$ contributions with $n = 2, 3$ and $\mathcal{O}(\alpha_t^2\alpha_s)$ terms (see Ref. [101]). This level of perturbative knowledge guarantees remaining theoretical uncertainties in the range 0.005%-0.05% for the various Z resonance parameters (including ratios of partial widths), which is, depending on the quantity, comparable or slightly larger than the projected experimental precision discussed in the following sections. Further theoretical efforts would be needed to obtain negligible theoretical systematic uncertainties.

An alternative, more model independent, approach to fit the Z lineshape data is the one proposed in Refs. [102–104], where the Z - γ interference is obtained by fitting additional parameters, j_Z^i (one for each measured $f\bar{f}$ channel), to off-peak data. At CEPC this method could be adopted at the ZH and WW threshold runs. Similar measurements were performed at LEP2 for the hadronic parameter j_Z^{had} , even if limited by the available statistics [105–108].

11.2.1.2 R_b

² The partial width of the Z boson to its individual decay channel is proportional to the
³ square of the fundamental Z -fermion couplings. The ratio of the partial widths R_b is sen-
⁴ sitive to electroweak radiative corrections from new particles. For example, the existence
⁵ of the scalar top quarks or charginos in supersymmetry could lead to a visible change of
⁶ R_b from the SM prediction.

⁷ Precise measurements of R_b have been made by LEP collaborations [109–113] and
⁸ by the SLD collaboration [114] using hadronic Z events.

⁹ Decays of b -hadrons were tagged using tracks with large impact parameters and/or
¹⁰ reconstructed secondary vertices, complemented by event shape variables. The combi-
¹¹ nation of LEP and SLD measurements yields a value of 0.21629 ± 0.00066 for R_b . The
¹² relative statistical uncertainty of R_b is above 0.2%, and systematic uncertainty is about
¹³ 0.2%.

¹⁴ A relative precision of 0.02% can be achieved for the measurement of R_b at the
¹⁵ CEPC, and it will improve the current precision in experimental measurement by one or-
¹⁶ der of magnitude. The main systematic uncertainty is due to hemisphere tag correlations
¹⁷ in $Z \rightarrow bb$ events (0.02%). The uncertainty due to hemisphere tag correlations can be re-
¹⁸duced to a level of 0.02% from the expected improvement in the b -tagging performance
¹⁹ of the CEPC detector. The improvement of b -tagging efficiency is the key to reduce this
²⁰ uncertainty, and this uncertainty becomes irrelevant in the limit of 100% b -tagging effi-
²¹cience. Due to that fact that a next-generation vertex detector will be used in the CEPC
²² detector, the b -tagging efficiency is expected to be around 70% with a b -jet purity of 95%
²³ as shown in Figure 10.13, which is about 15%–20% higher than the efficiency achieved in
²⁴ previous experiments. The uncertainty due to hemisphere tag correlations can be reduce
²⁵ to 0.02% level, which is a factor of ten lower than previous measurements.

26 11.2.1.3 The partial decay width of $Z \rightarrow \mu^+\mu^-$

²⁷ The $\mu^+\mu^-$ channel provides the cleanest leptonic final state. Combining the measurements
²⁸ from all four LEP experiments [115–118], the overall uncertainty of R_μ is 0.2%. The
²⁹ statistical uncertainty of R_μ is about 0.15%.

³⁰ A precision of 0.01% can be achieved at the CEPC. The main systematic is expected
³¹ to be the uncertainty in modeling the $Z \rightarrow \mu^+\mu^-\gamma$ events. About 2% of the $Z \rightarrow \mu^+\mu^-$
³² sample are classified as $Z \rightarrow \mu^+\mu^-\gamma$ events with a photon detected in ECAL. For this
³³ class of events, the most critical issue is to reconstruct and identify the low energy photon
³⁴ object with high efficiency. Benefiting from high granularity of CEPC EM calorimeter
³⁵ ($10 \times 10 \text{ mm}^2$ as shown in Chapter 5), we expect to have close to 100% efficiency for
³⁶ photon with $E > 5 \text{ GeV}$ as shown in Section 10.2.2. Another challenge in this measure-
³⁷ment is to reduce the systematics due to QED ISR events. Detailed studies of radiative
³⁸ events in Z off-peak runs are expected, especially the Z off-peak runs at $\sqrt{s} = 92.2 \text{ GeV}$.
³⁹ Benefiting from high statistics in Z off-peak runs ($> 1 \text{ ab}^{-1}$), the uncertainty in the mod-
⁴⁰eling uncertainty of $Z \rightarrow \mu^+\mu^-\gamma$ events can be reduced to a level of 0.01%.

41 11.2.1.4 Forward-backward asymmetry measurements at the Z pole

⁴² Another important class of measurements for the study of the chiral couplings of the
⁴³ Z boson to fermions is given by the forward-backward asymmetries in the processes

¹ $e^+e^- \rightarrow f\bar{f}$,

$$A_{FB} = \frac{\sigma_F - \sigma_L}{\sigma_L + \sigma_R}, \quad (11.17)$$

² which are optimal observables to quantify the parity violation of neutral currents. In fact,
³ the differential tree-level cross section at the Z peak, for unpolarized incoming beams and
⁴ including only the Z exchange contribution, can be written as

$$\frac{d\sigma_{f\bar{f}}}{d\cos\vartheta} = \frac{3}{8}\sigma^{tot} [1 + \cos^2\vartheta + 2\mathcal{A}_e\mathcal{A}_f \cos\vartheta], \quad (11.18)$$

⁵ where the coefficients \mathcal{A}_i can be expressed in terms of the left/right couplings $g_{L/R,i}$ or the
⁶ vectorial and axial-vector couplings g_V^i and g_A^i :

$$\mathcal{A}_f = \frac{g_{L,f}^2 - g_{R,f}^2}{g_{L,f}^2 + g_{R,f}^2} = \frac{2g_V^f g_A^f}{(g_V^f)^2 + (g_A^f)^2} = \frac{\frac{g_V^f}{g_A^f}}{1 + \left(\frac{g_V^f}{g_A^f}\right)^2} \quad (11.19)$$

⁷ In particular the last expression of Equation 11.19 shows that the observable A_{FB} gives
⁸ an information complementary to the partial widths, which are proportional to the combi-
⁹ nation $(g_V^f)^2 + (g_A^f)^2$, giving access to the linear ratio g_V^f/g_A^f . The same expression is used
¹⁰ to define the parameter $\sin^2\vartheta_{eff}^f$

$$4|Q_f| \sin^2\vartheta_{eff}^f = 1 - \frac{g_V^f}{g_A^f}, \quad (11.20)$$

¹¹ which, at tree-level, coincides with $1 - (M_W/M_Z)^2$. The relation between A_{FB} and \mathcal{A}_i at
¹² the Z pole, for unpolarized beams, is the following:

$$A_{FB}^{0,f} = \frac{3}{4}\mathcal{A}_e\mathcal{A}_f. \quad (11.21)$$

¹³ Since $\sin^2\vartheta_{eff} \sim 1/4$, \mathcal{A}_l is close to 0.1 for leptons while for quarks $\mathcal{A}_u \sim 0.7$ and $\mathcal{A}_d \sim$
¹⁴ 0.9. This, associated to the fact that the asymmetry measurements at LEP were limited
¹⁵ by statistics, implied that $A_{FB}^{0,b}$ offered the most precise determination of $\sin^2\vartheta_{eff}$. The
¹⁶ measurements have been made at SLD and LEP experiments [119–123]. $Z \rightarrow b\bar{b}$ events
¹⁷ were identified by tagging two b jets. Each event was divided into forward and backward
¹⁸ categories by the plane perpendicular to the thrust axis which contains the interaction
¹⁹ point. The combination of the LEP and SLD measurements gives a measured value of
²⁰ $A_{FB}^{b,0} = 0.1000 \pm 0.0017$. The statistical uncertainty is 1.2% and the main systematic
²¹ uncertainties come from hemisphere tag correlations for b events (1.2%) and QCD and
²² thrust axis correction (0.7%).

²³ A precision of 10^{-4} can be achieved for the measurement of $A_{FB}^{0,b}$ at the CEPC,
²⁴ improving the current precision by more than a factor of 10. The expected statistical
²⁵ uncertainty is at a level of 0.01%. The uncertainty due to hemisphere tag correlations for
²⁶ b events can be reduced to 0.1% due to excellent b -tagging performing in CEPC vertex
²⁷ detector. By selecting events with back-to-back jets event topology, the uncertainty on
²⁸ thrust axis definition due to QCD higher correlations can be reduced down to less than
²⁹ 0.1%.

1 The expected precision of the effective weak mixing angle measurement in CEPC
 2 using $Z \rightarrow b\bar{b}$ events is expected to be 0.02%. The theory uncertainty of the SM predic-
 3 tion is below the 0.01% threshold, thanks to the recent complete two-loop electroweak
 4 calculation of Ref. [124].

5 The energy dependence of the asymmetries around the Z resonance is sensitive to the
 6 interference between Z and γ exchange. It allows to measure the values of the axial-vector
 7 couplings.

8 11.2.1.5 Neutrino species counting

9 Two different methods have been used to determine the number of light neutrino species
 10 (N_ν) at LEP. The first one is the indirect method using the analysis of the Z lineshape,
 11 and it uses the data collected by the Z threshold scan runs. The Z peak scan at CEPC can
 12 improve the LEP determination of N_ν by a factor of three. The second method is a direct
 13 measurement, which is based on the measurement of the cross section for the radiative
 14 process $e^+e^- \rightarrow \nu\nu\gamma$. The second method at CEPC is supposed to use the ZH runs and
 15 improve the LEP direct determination by a factor of ten.

16 The systematic uncertainties of theoretical origin associated with the two methods
 17 are completely different: the indirect one relies on the precision calculation of the Z
 18 partial decay widths, while the direct one needs the calculation of higher order radiative
 19 corrections for the process $e^+e^- \rightarrow \nu\bar{\nu}\gamma$. Moreover the two methods use completely dif-
 20 ferent datasets, therefore they are independent and complementary. The sensitivity to new
 21 physics will be different for these two methods. In the direct method, one can measure N_ν
 22 as a function of \sqrt{s} . A deviation of N_ν from an integer value would signal the presence
 23 of new physics. Possible contributions include WIMP dark matter particles, and other
 24 weakly coupled particles such as exotic neutrinos, gravitinos, or KK gravitons in theories
 25 with large extra dimensions. Thus, when we refer to the number of neutrino species, we
 26 actually include any number of possible invisible particles other than neutrinos. The sub-
 27 process $e^+e^- \rightarrow \nu_e\bar{\nu}_e\gamma$ is particularly important because it will allow to investigate pos-
 28 sible deviations with respect to the SM in the vertex γW^+W^- , in a complementary way
 29 with respect to the W^+W^- production cross section, where both γW^+W^- and ZW^+W^-
 30 vertices appear in the matrix element.

31 **Indirect method from Z line shape** The indirect method assumes all contributions from
 32 invisible channels are coming from the $Z \rightarrow \nu\bar{\nu}$ decay, assuming that the total Z width
 33 does not receive additional contribution with respect to the SM ones. This method used
 34 the analysis of Z lineshape, subtracting the visible partial widths of the hadrons (Γ_{had}),
 35 and the partial widths of the leptons (Γ_ℓ) from the total width Γ_Z . The invisible width Γ_{inv}
 36 can be written as:

$$\Gamma_{\text{inv}} = N_\nu \Gamma_\nu = \Gamma_Z - \Gamma_{\text{had}} - 3\Gamma_\ell. \quad (11.22)$$

37 We take as our definition of the number of neutrinos $N_\nu = \Gamma_{\text{inv}}/\Gamma_\nu$, i.e. the ratio of the
 38 invisible width to the Standard Model expectation for the partial width to a single neutrino
 39 species.

40 Using the input from SM model, we can rewrite equation 11.22 as follows:

$$N_\nu = \frac{\Gamma_\ell}{\Gamma_\nu} \left(\sqrt{\frac{12\pi R_\ell}{m_Z^2 \sigma_{\text{had}}^0}} - R_\ell - 3 \right). \quad (11.23)$$

The final LEP1 result was $N_\nu = 2.9840 \pm 0.0082$ [125]. As shown in equation 11.23, the precision of N_ν depends on the the lepton partial width R_ℓ measurement, the Z mass measurement, and the hadronic cross section of the Z boson on its mass peak (σ_{had}^0). The decomposition of the error on N_ν is given by [125]

$$\delta N_\nu \simeq 10.5 \frac{\delta n_{\text{had}}}{n_{\text{had}}} \oplus 3.0 \frac{\delta n_{\text{lep}}}{n_{\text{lep}}} \oplus 7.5 \frac{\delta \mathcal{L}}{\mathcal{L}}, \quad (11.24)$$

where $\delta n_{\text{had}}/n_{\text{had}}$, $\delta n_{\text{lep}}/n_{\text{lep}}$ and $\delta \mathcal{L}/\mathcal{L}$ represent the total errors on the number of selected hadronic and leptonic events and on the luminosity determination. The symbol \oplus denotes the sum in quadrature. The final theoretical uncertainty of 0.061% [126] (0.054% [127, 128]), available at the end of LEP operation [125] for the small angle Bhabha process, reflects in a systematic uncertainty of 0.15%, i.e. $\sim 50\%$ of the total uncertainty of 0.27%, on N_ν .

The precision of 0.1% in N_ν measurement with the indirect method can be achieved in CEPC measurement, which improves the current precision by a factor of three. Benefiting from the recent development of luminosity detector technology, the uncertainty due to luminosity can be reduced to 0.05%. The theoretical uncertainty of predictions for the small angle Bhabha process can be reduced, conservatively, to 0.05% or below, mainly due to the recent progress in the evaluation of the hadronic contribution to the photon vacuum polarization [129–131]. This uncertainty can be pushed down even further, close to the 0.01% scale, once the NNLO QED predictions are matched to higher order soft/collinear contributions.

Direct method using $e^+e^- \rightarrow \nu\bar{\nu}\gamma$ events The direct method is based on the process $e^+e^- \rightarrow \nu\bar{\nu}\gamma$, whose cross section is proportional to N_ν , with the typical signature in the detector of only one photon with energy $E_\gamma = (s - m_Z^2)/(2\sqrt{s})$. The most precise direct N_ν measurements at LEP were carried out by the L3 collaboration and Delphi collaboration. By combining the direct measurements at LEP, the current experimental result is $N_\nu = 2.92 \pm 0.04$. The statistical uncertainty of N_ν in the previous measurement is 1.7%. The main systematic uncertainty from the L3 measurement includes the uncertainty in single photon trigger efficiency (0.6%), and photon identification efficiency (0.3%), and the uncertainty in identifying the converted photons (0.5%). The systematic uncertainty of theoretical origin is due to the knowledge of higher order radiative corrections to the process $e^+e^- \rightarrow \nu\bar{\nu}\gamma$, within the SM. At LEP an uncertainty at the percent level was achieved through complete tree-level matrix elements for $e^+e^- \rightarrow \nu\bar{\nu}\gamma$ and $e^+e^- \rightarrow \nu\bar{\nu}\gamma\gamma$, properly combined with higher orders initial state multiphoton radiation [132]. The bulk of the electroweak corrections were accounted for through running couplings on top of the tree-level matrix elements or through $\mathcal{O}(\alpha)$ corrections to $Z\gamma$ production [132–137]. A first calculation including one-loop electroweak corrections appeared in Ref. [138], with an estimated uncertainty of the order of 1%.

An overall precision of 0.2% can be achieved for the direct measurement of N_ν at CEPC, and it will improve the current precision by a factor of 10. Due to the excellent performance of the CEPC inner tracker, the uncertainty due to converted photons' selection efficiency is expected to be negligible. The granularity of the CEPC EM calorimeter is expected to be 10 to 100 times better than the detectors at LEP. Therefore photons can be identified with high purity with loose EM shower shape based selection. The uncertainty of photon efficiency can be reduced to less than 0.05%. On the theoretical side, the con-

trol of electroweak corrections should be moved to the two-loop level, in addition to the matching to higher order QED corrections. Given the recent progress in the calculation of NNLO corrections for $2 \rightarrow 3$ processes at the LHC, the program looks feasible. It would be also worth to investigate the ratio $\sigma(e^+e^- \rightarrow \nu\bar{\nu}\gamma)/\sigma(e^+e^- \rightarrow \mu^+\mu^-\gamma)$, where (large) part of the ISR radiative corrections are expected to cancel, provided the luminosity allows enough statistics for the process $e^+e^- \rightarrow \mu^+\mu^-\gamma$.

11.2.2 Measurement of the W boson mass

In e^+e^- collisions, W bosons are mainly produced in pairs, through the reaction $e^+e^- \rightarrow W^+W^-$. At threshold, $\sqrt{s} \sim 2m_W$, the cross section of this process is very sensitive to m_W , providing a natural method for the measurement of this parameter. At center-of-mass energies above the W^+W^- production threshold, m_W can be determined from the peak of the invariant mass distribution of its decay products. Both methods are very complementary : while the former requires an accurate theoretical prediction of the W^+W^- production cross section as a function of m_W and a precise determination of the collider luminosity, the latter mostly relies on a good resolution in the reconstruction of the hadronic invariant mass, and a precise control of the detector calibration.

Both methods have been used at LEP. With only about 40 pb^{-1} collected by the four LEP experiments at $\sqrt{s} \sim 161.3 \text{ GeV}$ and given the low cross section at threshold, the former is limited by a significant statistical uncertainty of about 200 MeV. The final state reconstruction method exploited the full LEP2 dataset, about 2.6 fb^{-1} collected between $\sqrt{s} \sim 161.3 \text{ GeV}$ and 206 GeV, and achieved a total uncertainty of 33 MeV. While this measurement used both the $W^+W^- \rightarrow \ell\nu qq$ and $W^+W^- \rightarrow qqqq$ channels, the fully hadronic channel is limited by uncertainties in the modeling of hadronization and interactions between the decaying W bosons, and the semi-leptonic final state dominates the precision of the final result.

Accounting for results from the CDF and D0 experiments at the TeVatron, and from ATLAS at the LHC, the present world-average value of m_W has an uncertainty estimated between 12 and 13 MeV. The uncertainty is expected to fall below 10 MeV when including final LHC measurement results. A natural goal for CEPC is thus to reach a precision well below 5 MeV, making optimal use of W^+W^- cross section data around $\sqrt{s} \sim 161 \text{ GeV}$, and of the final state invariant mass distributions at $\sqrt{s} \sim 240 \text{ GeV}$. The achievable precision of both methods is described below.

Determination of m_W and Γ_W from the W^+W^- production cross section

In this section, the possibility of extracting the W boson mass and width from the production cross section is explored. The study assumes a total integrated luminosity of $L = 3.2 \text{ ab}^{-1}$, which can be collected in one year, assuming an instantaneous luminosity of 2.5 ab^{-1} . For this study, the GENTLE program version 2.0 [139] is used to calculate σ_{WW} as a function of the center-of-mass energy, m_W and Γ_W . The behavior of the cross section as a function of the center-of-mass energy, \sqrt{s} , is illustrated in Figure 11.16.

The statistical sensitivity of the measurement is optimized in the following way:

- the total integrated luminosity is shared between one, two or three values of \sqrt{s} ;
- in the two-point scenario, a three-dimensional optimization is performed, scanning both values \sqrt{s} in steps of 100 MeV, and the fraction of integrated luminosity spent at each point in steps of 5%;

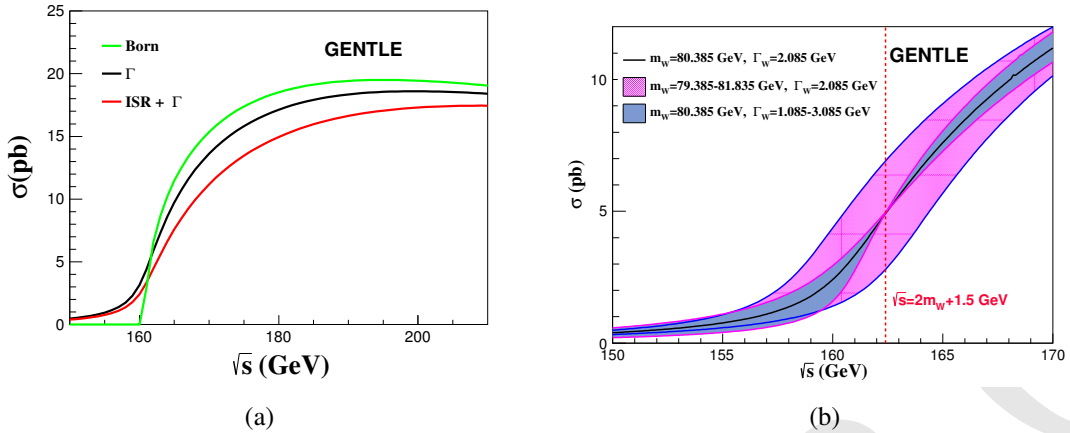


Figure 11.16: W^+W^- production as a function of \sqrt{s} , (a) at Born level, including finite width effects, and including initial state radiation corrections; and (b) for a range of values of m_W and Γ_W .

- in the three point scenario, a corresponding five-dimensional optimization is performed.

Sources of systematic uncertainties can be categorized as correlated or uncorrelated between measurements at different values of \sqrt{s} . The following sources are considered:

- Uncorrelated sources: this category includes the uncertainties associated with the beam energy calibration, and the beam energy spread. For the former, an uncertainty of 0.5 MeV is assumed, and the latter can be controlled to 1%, at each value of \sqrt{s} ;
- Correlated sources: this category includes the uncertainties from the integrated luminosity, the detection efficiency, the purity, and the theoretical W -pair cross section. It is assumed that these sources sum up to a total relative uncertainty of 2×10^{-4} on the ratio between measured and predicted cross sections.

The result of the statistical optimization leads to a three-point scenario, with most of the data collected at energies of 157.5 and 162.5 GeV. Another run at energy of 172 GeV is also needed for $\alpha_S(m_W)$ measurement. A summary of given in Table 11.11. The final measurement uncertainties, assuming this optimal scenario and systematic uncertainties are described above, are collected in

Table 11.12. We conclude that an uncertainty of about 1 MeV can be achieved for m_W , and 3 MeV for Γ_W . Both m_W and Γ_W are expected to be dominated by statistical uncertainties. The major systematic uncertainty for m_W measurement is expected to be the uncertainty in beam energy calibration, while the Γ_W measurement is significantly affected by the beam energy spread.

Determination of m_W by kinematic reconstruction

According to LEP experience, the fully hadronic final state is limited by systematic uncertainties that are difficult to control using data. The present section therefore concentrates on the semi-leptonic final states, where one W boson decays to an electron or a muon, while the other decays hadronically. An estimate of the m_W measurement potential is presented based on $WW \rightarrow \ell\nu qq$ events ($\ell = e, \mu$), and the potential of hadronic Z boson decays to calibrate the measurement of the hadronic invariant mass is evaluated.

\sqrt{s} (GeV)	Luminosity (ab $^{-1}$)
157.5	0.5
161.5	0.2
162.5	1.3
172.0	0.6

Table 11.11: The proposed $e^+e^- \rightarrow W^+W^-$ threshold scan runs and their integrated luminosity, for a total integrated luminosity of 2.6 ab^{-1} .

Observable	m_W	Γ_W
Source	Uncertainty (MeV)	
Statistics	0.8	2.7
Beam energy	0.4	0.6
Beam spread	–	0.9
Corr. syst.	0.4	0.2
Total	1.0	2.8

Table 11.12: Dominant systematic uncertainties in the measurement of m_W and Γ_W , using the production cross section at threshold at CEPC.

The W^+W^- cross section at $\sqrt{s} = 240 \text{ GeV}$ is about 17 pb. For an integrated luminosity of 5.6 ab^{-1} , this corresponds to a sample of about 95×10^6 W boson pairs, and 28×10^6 $WW \rightarrow \ell\nu qq$ events. For ZZ production, the cross section is about 1 pb, yielding about 5.6×10^6 Z boson pairs, and 1.6×10^6 $ZZ \rightarrow \nu\bar{\nu}q\bar{q}$ events. While the Z boson mass is more precisely known than m_W and the $Z \rightarrow q\bar{q}$ resonance provides a useful check of the detector calibration, the sample is small compared to the $W \rightarrow q\bar{q}$ one, and the presence of heavy quarks in Z boson decays has to be accounted for when deriving constraints on the hadronic response in W events.

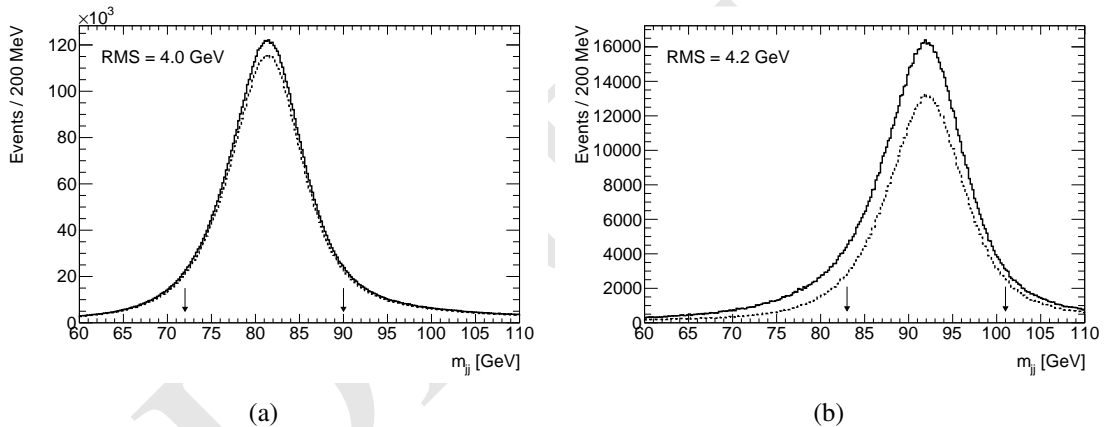
W^+W^- event selection criteria will require the presence of one reconstructed electron or muon with energy greater than 10 GeV, and missing transverse momentum greater than 10 GeV. The invariant mass of all reconstructed final state particles should exceed 50% of the center-of-mass energy; the hadronic system, *i.e.* the set of all particles excluding the selected lepton, is clustered into two jets and its invariant mass distribution is used to probe the W boson mass. A b -tag veto can be applied to enrich the selected samples in light-quark decays, and reduce the systematic differences between the W and Z boson samples. In the $\mu\nu q\bar{q}$ channel, the efficiency of these criteria is 71.3%, as shown in Table 11.13. Corresponding selection efficiencies for $ZZ \rightarrow \nu\bar{\nu}q\bar{q}$ events are shown in Table 11.14. The corresponding hadronic invariant mass distributions are shown in Figure 11.17. After these selections, backgrounds are expected to be small and play a negligible role in the measurement.

Given the large expected statistics, the availability of the $e\nu qq$ channel and the good resolution in the invariant mass distribution, the statistical sensitivity of the m_W measure-

Selection	Efficiency (%)	Nb. of events
$E_\mu > 10 \text{ GeV}, \cos(\theta_\mu) < 0.995$	85.4	11.9×10^6
$p_T^{\text{miss}} > 10 \text{ GeV}$	82.0	11.5×10^6
$m_{\text{vis}} > 0.5 \times \sqrt{s}$	75.6	10.6×10^6
$b\text{-tag score} < 0.5$	71.3	10.0×10^6

Table 11.13: Efficiency of the event selection criteria in the $WW \rightarrow \mu\nu qq$ channel.

Selection	Efficiency (%)	Nb. of events
Missing Energy $> 35 \text{ GeV}$	69.9	1.12×10^6
$m_{\text{vis}} > 0.2 \times \sqrt{s}$	66.4	1.06×10^6
$b\text{-tag score} < 0.5$	50.1	0.80×10^6

Table 11.14: Efficiency of the event selection criteria in the $ZZ \rightarrow \nu\nu qq$ channel.**Figure 11.17:** Dijet invariant mass distributions for (a) $WW \rightarrow \mu\nu qq$ events, without and with a b -jet veto cut, and correspondingly for (b) $ZZ \rightarrow \nu\nu qq$ events. The RMS of the distributions are quoted for the interval indicated by the arrows.

ment is better than 1 MeV. Using the $ZZ \rightarrow \nu\nu qq$ sample alone, the detector calibration can be checked to about 6 MeV. Further calibration samples can be extracted from radiative return events ($e^+e^- \rightarrow Z\gamma$). In addition, runs at $\sqrt{s} = 91.2 \text{ GeV}$ will be required for general detector alignment, monitoring and calibrations; these runs will provide copious samples of hadronic Z boson decays that will further constrain the hadronic calibration. Combining all information, the statistical precision of the calibration samples will match that of the W boson decays.

The statistical sensitivity can be further enhanced using kinematics fits, constraining the reconstructed lepton and jet momenta to match the known center of mass energy ($\sum_i E_i = \sqrt{s}$) and total event momentum ($\sum_i \vec{p}_i = \vec{0}$). This method was routinely used at LEP, gaining a factor of about 3 in the statistical precision, at the expense of an explicit de-

pendence of the measurement on the beam energy. Given the expected statistical precision at CEPC, this refinement seems unnecessary here. In these conditions, the beam energy calibration, and initial state radiation are expected to contribute less than 1 MeV to the measurement uncertainty. Further significant sources of systematic uncertainty include the lepton momentum scale, which can be reduced using Z boson decays as discussed above, and the modeling of hadronization. The latter can be strongly reduced using measurements of rates and distributions of identified particles, in both Z and W boson decays.

The primary sources of uncertainty are summarized in Table 11.15, comparing LEP and CEPC. A total uncertainty at the level of 3 MeV seems reachable.

Collider	LEP	CEPC
\sqrt{s} (GeV)	180–203	240
$\int \mathcal{L} dt$	2.6 fb^{-1}	5.6 ab^{-1}
Channels	$\ell\nu qq, qqqq$	$\ell\nu qq$
Source		Uncertainty (MeV)
Statistics	25	1.0
Beam energy	9	1.0
Hadronization	13	1.5
Radiative corrections	8	1.0
Detector effects	10	1.5
Total	33	3.0

Table 11.15: Dominant systematic uncertainties in the measurement of m_W using direct reconstruction, as achieved at LEP, and expected at CEPC.

11.2.3 Oblique Parameter

Using the estimated experimental capabilities of CEPC, we carry out a fit to determine the sensitivity of CEPC to the oblique electroweak parameters S and T [140, 141]. We omit the parameter U that is often included in fits as it arises from a dimension-8 operator in theories with a weakly coupled Higgs boson [142], and so is expected to be much smaller than S and T which arise at dimension 6. In the electroweak fit we treat the following five well-measured observables as parameters, from which the Standard Model prediction for all of the other observables may be computed:

$$\alpha_s(m_Z^2), \Delta\alpha_{\text{had}}^{(5)}(m_Z^2), m_Z, m_t, m_H. \quad (11.25)$$

Of these parameters, CEPC is expected to significantly improve our knowledge of m_Z . The primary power of CEPC is in improving the precision of measurements of other observables, including m_W and $\sin^2\theta_{\text{eff}}^\ell$, which may be derived from these parameters. Readers interested in more background information may find a thorough and up-to-date review of the status of electroweak precision in Ref. [143].

The inputs to the fit are listed in Table 11.16. Notice that we have performed the fit directly using forward-backward asymmetry parameters $A_{\text{FB}}^{0,f}$ as inputs, rather than

Observable	Value	Exp. Uncertainty	Th. Uncertainty
$\alpha_s(m_Z^2)$	0.1185	1.0×10^{-4} [36]	1.5×10^{-4}
$\Delta\alpha_{\text{had}}^{(5)}(m_Z^2)$	276.5×10^{-4}	4.7×10^{-5} [144]	–
m_Z [GeV]	91.1875	0.0005	–
m_t [GeV] (pole)	173.34	0.6 [145]	0.25 [146]
m_H [GeV]	125.14	0.1 [144]	–
m_W [GeV]	80.358617 [147]	0.001	1.4×10^{-3}
$A_{\text{FB}}^{0,b}$	0.102971 [124, 148]	1.0×10^{-4}	8.3×10^{-5}
$A_{\text{FB}}^{0,\mu}$	0.016181 [148]	4.9×10^{-5}	2.6×10^{-5}
$A_{\text{FB}}^{0,e}$	0.016181 [148]	8.1×10^{-5}	2.6×10^{-5}
Γ_Z [GeV]	2.494682 [101]	0.0005	2×10^{-4}
$R_b \equiv \Gamma_b/\Gamma_{\text{had}}$	0.2158459 [101]	4.3×10^{-5}	7×10^{-5}
$R_\ell \equiv \Gamma_{\text{had}}/\Gamma_\ell$	20.751285 [101]	2.1×10^{-3}	1.5×10^{-3}
$\Gamma_{Z \rightarrow \text{inv}}$ [GeV]	0.167177 [101]	8.4×10^{-5}	–

Table 11.16: Inputs to the CEPC fit. Numbers in bold are expected experimental uncertainties from CEPC measurements. Other entries reflect anticipated uncertainties at the time of CEPC operation. The numbers in the “Value” column for the first five parameters are current measurements; those below the horizontal line give the Standard Model calculated value as a function of the five parameters. Theory uncertainties are future projections assuming complete 3-loop calculations, based on estimates in Refs. [147–150].

the derived quantities $\sin^2 \theta_{\text{eff}}^f$ that were used in earlier work [151, 152]. The forward-backward asymmetries more directly reflect the experimental measurements; on the other hand, theoretical predictions are often expressed in terms of the effective weak mixing angles [124, 148]. They are related through the asymmetry parameters A_f :

$$A_f = \frac{1 - 4|Q_f| \sin^2 \theta_{\text{eff}}^f}{1 - 4|Q_f| \sin^2 \theta_{\text{eff}}^f + 8|Q_f|^2 \sin^4 \theta_{\text{eff}}^f}, \quad (11.26)$$

$$A_{\text{FB}}^{0,f} = \frac{3}{4} A_e A_f. \quad (11.27)$$

1 There is an extensive literature on the computation of the S and T dependence of ob-
2 servables (e.g. [140, 141, 153]); a convenient tabulation of the results may be found in
3 Appendix A of [154]. Assembling these results, we obtain a prediction of the observables
4 in terms of the five input parameters, S , and T . In the fit we compute a profile likelihood,
5 floating the five parameters to obtain the maximum likelihood for given S and T .

The fit is performed following [151] (which in turn relied on [155–157]): in constructing a likelihood we treat experimental uncertainties as Gaussian but theory uncertainties as a flat prior, leading to an effective χ^2 function

$$\chi_{\text{mod}}^2 = \sum_j \left[-2 \log \left(\operatorname{erf} \left(\frac{M_j - O_j + \delta_j}{\sqrt{2}\sigma_j} \right) - \operatorname{erf} \left(\frac{M_j - O_j - \delta_j}{\sqrt{2}\sigma_j} \right) \right) - 2 \log \left(\sqrt{2\pi}\sigma_j \right) \right], \quad (11.28)$$

6 with M_j the measured value, O_j the prediction for the observable, σ_j the experimental
7 uncertainty, and δ_j the theory uncertainty.

8 Our estimates of theory uncertainties assume that full three-loop computations of
9 the parametric dependence of observables in the Standard Model will be completed. The
10 remaining uncertainties are estimated based on [147–150]. In the case of the W mass
11 measurement, an uncertainty of 1 MeV from the computation of the near-threshold WW
12 cross section is added in quadrature with the estimated four-loop theory uncertainty in the
13 observable itself.

14 The results of the fit are depicted in Figure 11.18. Solid contours are 68% confidence
15 level curves, meaning $\Delta\chi_{\text{mod}}^2 = 2.30$; the dashed contour is 98% C.L. ($\Delta\chi_{\text{mod}}^2 = 6.18$).
16 For clarity we have assumed that the measured central values will precisely agree with
17 Standard Model predictions. In particular, the contour depicting current constraints is
18 artificially displaced to be centered at the origin, though it accurately reflects the size
19 of the uncertainties in current data. From the figure, we see that the results of CEPC will
20 significantly shrink the error bars on the S and T parameters relative to currently available
21 data.

By fixing $T = 0$ or $S = 0$, we can also obtain the projected one-parameter 68% C.L. bounds on S and T . As one-parameter fits these correspond to $\Delta\chi_{\text{mod}}^2 = 1.0$. We obtain:

$$|S| < 3.6 \times 10^{-2} \text{ (current), } 7.9 \times 10^{-3} \text{ (CEPC projection),} \quad (11.29)$$

$$|T| < 3.1 \times 10^{-2} \text{ (current), } 8.4 \times 10^{-3} \text{ (CEPC projection).} \quad (11.30)$$

22 Thus CEPC will achieve about a factor of 4 additional precision on both of the electroweak
23 oblique parameters.

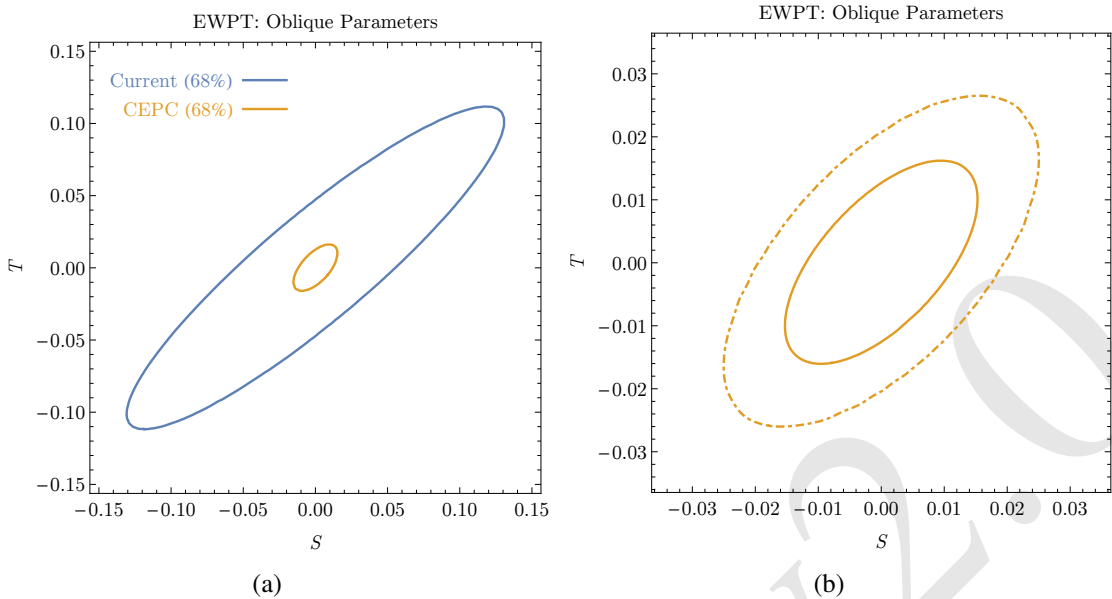


Figure 11.18: CEPC constraints on the oblique parameters S and T . (a):comparison of CEPC projection (orange) to current constraints (blue). Contours are 68% confidence level. (b): a closer look at the CEPC fit, showing 68% confidence level (solid) and 95% confidence level (dashed).

References

- [1] ATLAS Collaboration, *Observation of a new particle in the search for the Standard Model Higgs boson with the ATLAS detector at the LHC*, *Phys. Lett. B* **716** (2012) 1, [arXiv:1207.7214 \[hep-ex\]](#).
- [2] CMS Collaboration, *Observation of a new boson at a mass of 125 GeV with the CMS experiment at the LHC*, *Phys. Lett. B* **716** (2012) 30, [arXiv:1207.7235 \[hep-ex\]](#).
- [3] ATLAS Collaboration, *Measurements of Higgs boson production and couplings in diboson final states with the ATLAS detector at the LHC*, *Phys. Lett. B* **726** (2013) 88–119, [arXiv:1307.1427 \[hep-ex\]](#). [Erratum: *Phys. Lett.B*734,406(2014)].
- [4] ATLAS Collaboration, *Evidence for the spin-0 nature of the Higgs boson using ATLAS data*, *Phys. Lett. B* **726** (2013) 120–144, [arXiv:1307.1432 \[hep-ex\]](#).
- [5] CMS Collaboration, *Observation of a new boson with mass near 125 GeV in pp collisions at $\sqrt{s} = 7$ and 8 TeV*, *JHEP* **1306** (2013) 081, [arXiv:1303.4571 \[hep-ex\]](#).
- [6] CMS Collaboration, *Evidence for the direct decay of the 125 GeV Higgs boson to fermions*, *Nature Phys.* **10** (2014) , [arXiv:1401.6527 \[hep-ex\]](#).
- [7] CMS Collaboration, *Constraints on the spin-parity and anomalous HVV couplings of the Higgs boson in proton collisions at 7 and 8 TeV*, *Phys. Rev. D* **92** (2015) no. 1, 012004, [arXiv:1411.3441 \[hep-ex\]](#).

- [8] ATLAS, CMS Collaboration, *Combined Measurement of the Higgs Boson Mass in pp Collisions at $\sqrt{s} = 7$ and 8 TeV with the ATLAS and CMS Experiments*, *Phys. Rev. Lett.* **114** (2015) 191803, [arXiv:1503.07589 \[hep-ex\]](https://arxiv.org/abs/1503.07589).
- [9] ATLAS, CMS Collaboration, *Measurements of the Higgs boson production and decay rates and constraints on its couplings from a combined ATLAS and CMS analysis of the LHC pp collision data at $\sqrt{s} = 7$ and 8 TeV*, *JHEP* **08** (2016) 045, [arXiv:1606.02266 \[hep-ex\]](https://arxiv.org/abs/1606.02266).
- [10] F. An, Y. Bai, C. Chen, X. Chen, Z. Chen, J. Guimaraes da Costa, and Z. Cui, *Precision Higgs Boson Physics at the CEPC*, TBD (2018).
- [11] LHC Higgs Cross Section Working Group, *Handbook of LHC Higgs Cross Sections: 1. Inclusive Observables*, [arXiv:1101.0593 \[hep-ph\]](https://arxiv.org/abs/1101.0593).
- [12] LHC Higgs Cross Section Working Group, *Handbook of LHC Higgs Cross Sections: 2. Differential Distributions*, [arXiv:1201.3084 \[hep-ph\]](https://arxiv.org/abs/1201.3084).
- [13] W. Kilian, T. Ohl, and J. Reuter, *WHIZARD: Simulating Multi-Particle Processes at LHC and ILC*, *Eur. Phys. J.* **C71** (2011) 1742, [arXiv:0708.4233 \[hep-ph\]](https://arxiv.org/abs/0708.4233).
- [14] Y. Haddad, *Feasibility of a minimum bias analysis of $e^+e^- \rightarrow ZH \rightarrow q\bar{q} + X$ at a 250 GeV ILC*, [arXiv:1404.3164 \[hep-ph\]](https://arxiv.org/abs/1404.3164).
- [15] M. Oreglia, *A Study of the Reactions $\psi' \rightarrow \gamma\gamma\psi$* , SLAC-R-0236 (1980).
<http://www.slac.stanford.edu/cgi-wrap/getdoc/slac-r-23\6.pdf>.
- [16] ALEPH, DELPHI, L3, OPAL, LEP Electroweak Collaboration, *Electroweak Measurements in Electron-Positron Collisions at W-Boson-Pair Energies at LEP*, *Phys. Rept.* **532** (2013) 119, [arXiv:1302.3415 \[hep-ex\]](https://arxiv.org/abs/1302.3415).
- [17] J. Gao, *Probing light-quark Yukawa couplings via hadronic event shapes at lepton colliders*, *JHEP* **01** (2018) 038, [arXiv:1608.01746 \[hep-ph\]](https://arxiv.org/abs/1608.01746).
- [18] LHC Higgs Cross Section Working Group, *LHC HXSWG interim recommendations to explore the coupling structure of a Higgs-like particle*, [arXiv:1209.0040 \[hep-ph\]](https://arxiv.org/abs/1209.0040).
- [19] LHC Higgs Cross Section Working Group, *Handbook of LHC Higgs Cross Sections: 3. Higgs Properties*, [arXiv:1307.1347 \[hep-ph\]](https://arxiv.org/abs/1307.1347).
- [20] S. Dawson, A. Gritsan, H. Logan, J. Qian, C. Tully, et al., *Working Group Report: Higgs Boson*, [arXiv:1310.8361 \[hep-ex\]](https://arxiv.org/abs/1310.8361).
- [21] CMS Collaboration, *Search for the associated production of the Higgs boson with a top-quark pair*, *JHEP* **1409** (2014) 087, [arXiv:1408.1682 \[hep-ex\]](https://arxiv.org/abs/1408.1682).
- [22] ATLAS Collaboration, *Search for $H \rightarrow \gamma\gamma$ produced in association with top quarks and constraints on the Yukawa coupling between the top quark and the Higgs boson using data taken at 7 TeV and 8 TeV with the ATLAS detector*, *Phys. Lett.* **B740** (2015) 222, [arXiv:1409.3122 \[hep-ex\]](https://arxiv.org/abs/1409.3122).

- [23] A. Banfi, A. Martin, and V. Sanz, *Probing top-partners in Higgs+jets*, JHEP **1408** (2014) 053, [arXiv:1308.4771 \[hep-ph\]](https://arxiv.org/abs/1308.4771).
- [24] A. Azatov and A. Paul, *Probing Higgs couplings with high p_T Higgs production*, JHEP **1401** (2014) 014, [arXiv:1309.5273 \[hep-ph\]](https://arxiv.org/abs/1309.5273).
- [25] C. Grojean, E. Salvioni, M. Schlaffer, and A. Weiler, *Very boosted Higgs in gluon fusion*, JHEP **1405** (2014) 022, [arXiv:1312.3317 \[hep-ph\]](https://arxiv.org/abs/1312.3317).
- [26] M. Buschmann, C. Englert, D. Goncalves, T. Plehn, and M. Spannowsky, *Resolving the Higgs-Gluon Coupling with Jets*, Phys. Rev. **D90** (2014) 013010, [arXiv:1405.7651 \[hep-ph\]](https://arxiv.org/abs/1405.7651).
- [27] J. Ellis, V. Sanz, and T. You, *Complete Higgs Sector Constraints on Dimension-6 Operators*, JHEP **1407** (2014) 036, [arXiv:1404.3667 \[hep-ph\]](https://arxiv.org/abs/1404.3667).
- [28] T. Han, Z. Liu, and J. Sayre, *Potential Precision on Higgs Couplings and Total Width at the ILC*, Phys. Rev. **D89** (2014) 113006, [arXiv:1311.7155 \[hep-ph\]](https://arxiv.org/abs/1311.7155).
- [29] M. Klute, R. Lafaye, T. Plehn, M. Rauch, and D. Zerwas, *Measuring Higgs Couplings at a Linear Collider*, Europhys. Lett. **101** (2013) 51001, [arXiv:1301.1322 \[hep-ph\]](https://arxiv.org/abs/1301.1322).
- [30] M. E. Peskin, *Estimation of LHC and ILC Capabilities for Precision Higgs Boson Coupling Measurements*, [arXiv:1312.4974 \[hep-ph\]](https://arxiv.org/abs/1312.4974).
- [31] K. Fujii et al., *Physics Case for the 250 GeV Stage of the International Linear Collider*, [arXiv:1710.07621 \[hep-ex\]](https://arxiv.org/abs/1710.07621).
- [32] T. Barklow, K. Fujii, S. Jung, R. Karl, J. List, T. Ogawa, M. E. Peskin, and J. Tian, *Improved Formalism for Precision Higgs Coupling Fits*, Phys. Rev. **D97** (2018) no. 5, 053003, [arXiv:1708.08912 \[hep-ph\]](https://arxiv.org/abs/1708.08912).
- [33] ATLAS Collaboration, *Projections for measurements of Higgs boson signal strengths and coupling parameters with the ATLAS detector at a HL-LHC*, ATL-PHYS-PUB-2014-016 (2014).
<http://cds.cern.ch/record/1956710>.
- [34] A. Denner, S. Heinemeyer, I. Puljak, D. Rebuzzi, and M. Spira, *Standard Model Higgs-Boson Branching Ratios with Uncertainties*, Eur. Phys. J. **C71** (2011) 1753, [arXiv:1107.5909 \[hep-ph\]](https://arxiv.org/abs/1107.5909).
- [35] L. G. Almeida, S. J. Lee, S. Pokorski, and J. D. Wells, *Study of the standard model Higgs boson partial widths and branching fractions*, Phys. Rev. **D89** (2014) 033006, [arXiv:1311.6721 \[hep-ph\]](https://arxiv.org/abs/1311.6721).
- [36] G. P. Lepage, P. B. Mackenzie, and M. E. Peskin, *Expected Precision of Higgs Boson Partial Widths within the Standard Model*, [arXiv:1404.0319 \[hep-ph\]](https://arxiv.org/abs/1404.0319).
- [37] C. Bernaciak, T. Plehn, P. Schichtel, and J. Tattersall, *Spying an invisible Higgs boson*, Phys. Rev. **D91** (2015) 035024, [arXiv:1411.7699 \[hep-ph\]](https://arxiv.org/abs/1411.7699).

- [38] J. Ellis and T. You, *Sensitivities of Prospective Future $e+e-$ Colliders to Decoupled New Physics*, **JHEP** **03** (2016) 089, [arXiv:1510.04561 \[hep-ph\]](https://arxiv.org/abs/1510.04561).
- [39] J. Ellis, P. Roloff, V. Sanz, and T. You, *Dimension-6 Operator Analysis of the CLIC Sensitivity to New Physics*, [arXiv:1701.04804 \[hep-ph\]](https://arxiv.org/abs/1701.04804).
- [40] G. Durieux, C. Grojean, J. Gu, and K. Wang, *The leptonic future of the Higgs*, **JHEP** **09** (2017) 014, [arXiv:1704.02333 \[hep-ph\]](https://arxiv.org/abs/1704.02333).
- [41] T. Barklow, K. Fujii, S. Jung, M. E. Peskin, and J. Tian, *Model-Independent Determination of the Triple Higgs Coupling at e^+e^- Colliders*, [arXiv:1708.09079 \[hep-ph\]](https://arxiv.org/abs/1708.09079).
- [42] S. Di Vita, G. Durieux, C. Grojean, J. Gu, Z. Liu, G. Panico, M. Riembau, and T. Vantalon, *A global view on the Higgs self-coupling at lepton colliders*, **JHEP** **02** (2018) 178, [arXiv:1711.03978 \[hep-ph\]](https://arxiv.org/abs/1711.03978).
- [43] W. H. Chiu, S. C. Leung, T. Liu, K.-F. Lyu, and L.-T. Wang, *Probing 6D operators at future e^-e^+ colliders*, **JHEP** **05** (2018) 081, [arXiv:1711.04046 \[hep-ph\]](https://arxiv.org/abs/1711.04046).
- [44] M. Beneke, D. Boito, and Y.-M. Wang, *Anomalous Higgs couplings in angular asymmetries of $H \rightarrow Z\ell^+\ell^-$ and $e^+e^- \rightarrow HZ$* , **JHEP** **11** (2014) 028, [arXiv:1406.1361 \[hep-ph\]](https://arxiv.org/abs/1406.1361).
- [45] N. Craig, J. Gu, Z. Liu, and K. Wang, *Beyond Higgs Couplings: Probing the Higgs with Angular Observables at Future e^+e^- Colliders*, **JHEP** **03** (2016) 050, [arXiv:1512.06877 \[hep-ph\]](https://arxiv.org/abs/1512.06877).
- [46] S. M. Barr and A. Zee, *Electric Dipole Moment of the Electron and of the Neutron*, **Phys. Rev. Lett.** **65** (1990) 21–24. [Erratum: Phys. Rev. Lett. 65, 2920 (1990)].
- [47] J. Fan and M. Reece, *Probing Charged Matter Through Higgs Diphoton Decay, Gamma Ray Lines, and EDMs*, **JHEP** **06** (2013) 004, [arXiv:1301.2597 \[hep-ph\]](https://arxiv.org/abs/1301.2597).
- [48] ACME Collaboration, *Order of Magnitude Smaller Limit on the Electric Dipole Moment of the Electron*, **Science** **343** (2014) 269–272, [arXiv:1310.7534 \[physics.atom-ph\]](https://arxiv.org/abs/1310.7534).
- [49] Y. T. Chien, V. Cirigliano, W. Dekens, J. de Vries, and E. Mereghetti, *Direct and indirect constraints on CP-violating Higgs-quark and Higgs-gluon interactions*, **JHEP** **02** (2016) 011, [arXiv:1510.00725 \[hep-ph\]](https://arxiv.org/abs/1510.00725). [JHEP02,011(2016)].
- [50] R. Harnik, A. Martin, T. Okui, R. Primulando, and F. Yu, *Measuring CP violation in $h \rightarrow \tau^+\tau^-$ at colliders*, **Phys. Rev.** **D88** (2013) no. 7, 076009, [arXiv:1308.1094 \[hep-ph\]](https://arxiv.org/abs/1308.1094).
- [51] K. Hagiwara, S. Ishihara, R. Szalapski, and D. Zeppenfeld, *Low-energy effects of new interactions in the electroweak boson sector*, **Phys. Rev.** **D48** (1993) 2182–2203.

- [52] G. Gounaris et al., *Triple gauge boson couplings*, in *AGS / RHIC Users Annual Meeting Upton, New York, June 15-16, 1995*, pp. 525–576. 1996.
 $\text{arXiv:hep-ph/9601233 [hep-ph]}$. [525(1996)].
- [53] L. Bian, J. Shu, and Y. Zhang, *Prospects for Triple Gauge Coupling Measurements at Future Lepton Colliders and the 14 TeV LHC*, *JHEP* **09** (2015) 206,
 $\text{arXiv:1507.02238 [hep-ph]}$.
- [54] A. Falkowski, *Higgs Basis: Proposal for an EFT basis choice for LHC HXSWG*, LHCHXSWG-INT-2015-001 (2015) .
 $\text{https://cds.cern.ch/record/2001958}$.
- [55] ATLAS Collaboration, *Projections for measurements of Higgs boson cross sections, branching ratios and coupling parameters with the ATLAS detector at a HL-LHC*, ATL-PHYS-PUB-2013-014 (2013) .
 $\text{https://cds.cern.ch/record/1611186}$.
- [56] ATLAS Collaboration, *HL-LHC projections for signal and background yield measurements of the $H \rightarrow \gamma\gamma$ when the Higgs boson is produced in association with t quarks, W or Z bosons*, ATL-PHYS-PUB-2014-012 (2014) .
 $\text{https://cds.cern.ch/record/1741011}$.
- [57] ATLAS Collaboration, *Update of the prospects for the $H \rightarrow Z\gamma$ search at the High-Luminosity LHC*, ATL-PHYS-PUB-2014-006 (2014) .
 $\text{https://cds.cern.ch/record/1703276}$.
- [58] ATLAS Collaboration, *Prospects for the study of the Higgs boson in the VH(bb) channel at HL-LHC*, ATL-PHYS-PUB-2014-011 (2014) .
 $\text{https://cds.cern.ch/record/1740962}$.
- [59] ATLAS Collaboration, *Studies of the VBF $H \rightarrow \tau_l\tau_{had}$ analysis at High Luminosity LHC conditions*, ATL-PHYS-PUB-2014-018 (2014) .
 $\text{https://cds.cern.ch/record/1956732}$.
- [60] A. Falkowski, M. Gonzalez-Alonso, A. Greljo, and D. Marzocca, *Global constraints on anomalous triple gauge couplings in effective field theory approach*, *Phys. Rev. Lett.* **116** (2016) no. 1, 011801, $\text{arXiv:1508.00581 [hep-ph]}$.
- [61] A. Butter, O. J. P. Éboli, J. Gonzalez-Fraile, M. C. Gonzalez-Garcia, T. Plehn, and M. Rauch, *The Gauge-Higgs Legacy of the LHC Run I*, *JHEP* **07** (2016) 152,
 $\text{arXiv:1604.03105 [hep-ph]}$.
- [62] R. Contino, A. Falkowski, F. Goertz, C. Grojean, and F. Riva, *On the Validity of the Effective Field Theory Approach to SM Precision Tests*, *JHEP* **07** (2016) 144,
 $\text{arXiv:1604.06444 [hep-ph]}$.
- [63] A. Falkowski, M. Gonzalez-Alonso, A. Greljo, D. Marzocca, and M. Son, *Anomalous Triple Gauge Couplings in the Effective Field Theory Approach at the LHC*, *JHEP* **02** (2017) 115, $\text{arXiv:1609.06312 [hep-ph]}$.
- [64] Z. Zhang, *Time to Go Beyond Triple-Gauge-Boson-Coupling Interpretation of W Pair Production*, *Phys. Rev. Lett.* **118** (2017) no. 1, 011803,
 $\text{arXiv:1610.01618 [hep-ph]}$.

- [65] ATLAS Collaboration, *Search for the Standard Model Higgs and Z Boson decays to $J/\psi\gamma$: HL-LHC projections*, ATL-PHYS-PUB-2015-043 (2015) .
<http://cds.cern.ch/record/2054550>.
- [66] G. T. Bodwin, F. Petriello, S. Stoynev, and M. Velasco, *Higgs boson decays to quarkonia and the $H\bar{c}c$ coupling*, Phys. Rev. **D88** (2013) no. 5, 053003, [arXiv:1306.5770](https://arxiv.org/abs/1306.5770) [hep-ph].
- [67] G. Perez, Y. Soreq, E. Stamou, and K. Tobioka, *Constraining the charm Yukawa and Higgs-quark coupling universality*, Phys. Rev. **D92** (2015) no. 3, 033016, [arXiv:1503.00290](https://arxiv.org/abs/1503.00290) [hep-ph].
- [68] I. Brivio, F. Goertz, and G. Isidori, *Probing the Charm Quark Yukawa Coupling in Higgs+Charm Production*, Phys. Rev. Lett. **115** (2015) no. 21, 211801, [arXiv:1507.02916](https://arxiv.org/abs/1507.02916) [hep-ph].
- [69] F. Bishara, U. Haisch, P. F. Monni, and E. Re, *Constraining Light-Quark Yukawa Couplings from Higgs Distributions*, [arXiv:1606.09253](https://arxiv.org/abs/1606.09253) [hep-ph].
- [70] L. M. Carpenter, T. Han, K. Hendricks, Z. Qian, and N. Zhou, *Higgs Boson Decay to Light Jets at the LHC*, Phys. Rev. **D95** (2017) no. 5, 053003, [arXiv:1611.05463](https://arxiv.org/abs/1611.05463) [hep-ph].
- [71] ATLAS Collaboration, *Study of the double Higgs production channel $H(\rightarrow b\bar{b})H(\rightarrow \gamma\gamma)$ with the ATLAS experiment at the HL-LHC*, ATL-PHYS-PUB-2017-001, CERN, Geneva, Jan, 2017.
<https://cds.cern.ch/record/2243387>.
- [72] R. Contino et al., *Physics at a 100 TeV pp collider: Higgs and EW symmetry breaking studies*, CERN Yellow Report (2017) no. 3, 255–440, [arXiv:1606.09408](https://arxiv.org/abs/1606.09408) [hep-ph].
- [73] M. McCullough, *An Indirect Model-Dependent Probe of the Higgs Self-Coupling*, Phys. Rev. **D90** (2014) 015001, [arXiv:1312.3322](https://arxiv.org/abs/1312.3322) [hep-ph].
- [74] S. Di Vita, C. Grojean, G. Panico, M. Riembau, and T. Vantalon, *A global view on the Higgs self-coupling*, JHEP **09** (2017) 069, [arXiv:1704.01953](https://arxiv.org/abs/1704.01953) [hep-ph].
- [75] A. Azatov, R. Contino, G. Panico, and M. Son, *Effective field theory analysis of double Higgs boson production via gluon fusion*, Phys. Rev. **D92** (2015) no. 3, 035001, [arXiv:1502.00539](https://arxiv.org/abs/1502.00539) [hep-ph].
- [76] J. A. Aguilar-Saavedra, *A Minimal set of top anomalous couplings*, Nucl. Phys. **B812** (2009) 181–204, [arXiv:0811.3842](https://arxiv.org/abs/0811.3842) [hep-ph].
- [77] J. A. Aguilar-Saavedra, *A Minimal set of top-Higgs anomalous couplings*, Nucl. Phys. **B821** (2009) 215–227, [arXiv:0904.2387](https://arxiv.org/abs/0904.2387) [hep-ph].
- [78] Z. Liu, I. Low, and L.-T. Wang, *Higgs-Top Interactions at Future Circular e^+e^- Colliders*, TBD .

- [79] G. Li, H.-R. Wang, and S.-h. Zhu, *Probing CP-violating $h\bar{t}$ coupling in $e^+e^- \rightarrow h\gamma$* , *Phys. Rev.* **D93** (2016) no. 5, 055038, [arXiv:1506.06453 \[hep-ph\]](https://arxiv.org/abs/1506.06453).
- [80] E. Vryonidou and C. Zhang, *Dimension-six electroweak top-loop effects in Higgs production and decay*, [arXiv:1804.09766 \[hep-ph\]](https://arxiv.org/abs/1804.09766).
- [81] G. Durieux, *Precision constraints on the top-quark effective field theory at future lepton colliders*, PoS **DIS2017** (2018) 088, [arXiv:1708.09849 \[hep-ph\]](https://arxiv.org/abs/1708.09849).
- [82] Y. Gao, A. V. Gritsan, Z. Guo, K. Melnikov, M. Schulze, and N. V. Tran, *Spin determination of single-produced resonances at hadron colliders*, *Phys. Rev.* **D81** (2010) 075022, [arXiv:1001.3396 \[hep-ph\]](https://arxiv.org/abs/1001.3396).
- [83] S. Bolognesi, Y. Gao, A. V. Gritsan, K. Melnikov, M. Schulze, N. V. Tran, and A. Whitbeck, *On the spin and parity of a single-produced resonance at the LHC*, *Phys. Rev.* **D86** (2012) 095031, [arXiv:1208.4018 \[hep-ph\]](https://arxiv.org/abs/1208.4018).
- [84] I. Anderson et al., *Constraining anomalous HVV interactions at proton and lepton colliders*, *Phys. Rev.* **D89** (2014) no. 3, 035007, [arXiv:1309.4819 \[hep-ph\]](https://arxiv.org/abs/1309.4819).
- [85] J. Alwall, P. Demin, S. de Visscher, R. Frederix, M. Herquet, F. Maltoni, T. Plehn, D. L. Rainwater, and T. Stelzer, *MadGraph/MadEvent v4: The New Web Generation*, *JHEP* **09** (2007) 028, [arXiv:0706.2334 \[hep-ph\]](https://arxiv.org/abs/0706.2334).
- [86] J. Erler, S. Heinemeyer, W. Hollik, G. Weiglein, and P. Zerwas, *Physics impact of GigaZ*, *Phys.Lett.* **B486** (2000) 125–133, [arXiv:hep-ph/0005024 \[hep-ph\]](https://arxiv.org/abs/hep-ph/0005024).
- [87] L. Arnaudon, B. Dehning, P. Grosse-Wiesmann, R. Jacobsen, M. Jonker, J. P. Koutchouk, J. Miles, R. Olsen, M. Placidi, R. Schmidt, J. Wenninger, R. Assmann, and A. Blondel, *Accurate determination of the LEP beam energy by resonant depolarization*, *Zeitschrift für Physik C Particles and Fields* **66** (Mar, 1995) 45–62. <https://doi.org/10.1007/BF01496579>.
- [88] S. Jadach, M. Skrzypek, and B. F. L. Ward, *Is there a better way of exponentiating QED corrections?*, *Phys. Lett.* **B257** (1991) 173–178.
- [89] G. Montagna, O. Nicrosini, and F. Piccinini, *The QED radiator at order α^3* , *Phys. Lett.* **B406** (1997) 243–248, [arXiv:hep-ph/9611463 \[hep-ph\]](https://arxiv.org/abs/hep-ph/9611463).
- [90] G. Montagna, F. Piccinini, O. Nicrosini, G. Passarino, and R. Pittau, *On a semianalytical and realistic approach to e^+e^- annihilation into fermion pairs and to Bhabha scattering within the minimal Standard Model at LEP energies*, *Nucl. Phys.* **B401** (1993) 3–66.
- [91] G. Montagna, F. Piccinini, O. Nicrosini, G. Passarino, and R. Pittau, *TOPAZ0: A Program for computing observables and for fitting cross-sections and forward - backward asymmetries around the Z^0 peak*, *Comput. Phys. Commun.* **76** (1993) 328–360.

- [92] G. Montagna, O. Nicrosini, G. Passarino, and F. Piccinini, *TOPAZO 2.0: A Program for computing deconvoluted and realistic observables around the Z^0 peak*, *Comput. Phys. Commun.* **93** (1996) 120–126, [arXiv:hep-ph/9506329 \[hep-ph\]](https://arxiv.org/abs/hep-ph/9506329).
- [93] G. Montagna, O. Nicrosini, F. Piccinini, and G. Passarino, *TOPAZO 4.0: A New version of a computer program for evaluation of deconvoluted and realistic observables at LEP-1 and LEP-2*, *Comput. Phys. Commun.* **117** (1999) 278–289, [arXiv:hep-ph/9804211 \[hep-ph\]](https://arxiv.org/abs/hep-ph/9804211).
- [94] D. Yu. Bardin, M. S. Bilenky, T. Riemann, M. Sachwitz, and H. Vogt, *Dizet: A Program Package for the Calculation of Electroweak One Loop Corrections for the Process $e^+e^- \rightarrow f^+f^-$ Around the Z^0 Peak*, *Comput. Phys. Commun.* **59** (1990) 303–312.
- [95] D. Yu. Bardin et al., *ZFITTER: An Analytical program for fermion pair production in e^+e^- annihilation*, [arXiv:hep-ph/9412201 \[hep-ph\]](https://arxiv.org/abs/hep-ph/9412201).
- [96] D. Yu. Bardin, P. Christova, M. Jack, L. Kalinovskaya, A. Olchevski, S. Riemann, and T. Riemann, *ZFITTER v.6.21: A Semianalytical program for fermion pair production in e^+e^- annihilation*, *Comput. Phys. Commun.* **133** (2001) 229–395, [arXiv:hep-ph/9908433 \[hep-ph\]](https://arxiv.org/abs/hep-ph/9908433).
- [97] D. Bardin and G. Passarino, *Results of the working group on precision calculations for the Z resonance*, in *Proceedings, 8th J.A. Swieca Summer School on Particles and Fields: Rio de Janeiro, Brazil, February 5-18, 1995*, pp. 17–41. 1995.
- [98] D. Yu. Bardin, M. Grunewald, and G. Passarino, *Precision calculation project report*, [arXiv:hep-ph/9902452 \[hep-ph\]](https://arxiv.org/abs/hep-ph/9902452).
- [99] D. Yu. Bardin and G. Passarino, *The standard model in the making: Precision study of the electroweak interactions*. 1999.
- [100] A. Borrelli, M. Consoli, L. Maiani, and R. Sisto, *Model Independent Analysis of the Z Line Shape in e^+e^- Annihilation*, *Nucl. Phys.* **B333** (1990) 357–379.
- [101] I. Dubovsky, A. Freitas, J. Gluza, T. Riemann, and J. Usovitsch, *Complete electroweak two-loop corrections to Z boson production and decay*, [arXiv:1804.10236 \[hep-ph\]](https://arxiv.org/abs/1804.10236).
- [102] A. Leike, T. Riemann, and J. Rose, *S matrix approach to the Z line shape*, *Phys. Lett.* **B273** (1991) 513–518, [arXiv:hep-ph/9508390 \[hep-ph\]](https://arxiv.org/abs/hep-ph/9508390).
- [103] S. Kirsch and T. Riemann, *SMATASY: A program for the model independent description of the Z resonance*, *Comput. Phys. Commun.* **88** (1995) 89–108, [arXiv:hep-ph/9408365 \[hep-ph\]](https://arxiv.org/abs/hep-ph/9408365).
- [104] T. Riemann, *S-matrix Approach to the Z Resonance*, *Acta Phys. Polon.* **B46** (2015) no. 11, 2235, [arXiv:1610.04501 \[hep-ph\]](https://arxiv.org/abs/1610.04501).
- [105] ALEPH Collaboration, *Four jet final state production in e^+e^- collisions at center-of-mass energies of 130 GeV and 136 GeV*, *Z. Phys.* **C71** (1996) 179–198.

- [106] DELPHI Collaboration, *Measurement and interpretation of fermion pair production at LEP energies from 130 GeV to 172 GeV*, *Eur. Phys. J.* **C11** (1999) 383–407.
- [107] L3 Collaboration, *Determination of γ/Z interference in e^+e^- annihilation at LEP*, *Phys. Lett.* **B489** (2000) 93–101, [arXiv:hep-ex/0007006 \[hep-ex\]](https://arxiv.org/abs/hep-ex/0007006).
- [108] OPAL Collaboration, *Tests of the standard model and constraints on new physics from measurements of fermion pair production at 130 GeV to 172 GeV at LEP*, *Eur. Phys. J.* **C2** (1998) 441–472, [arXiv:hep-ex/9708024 \[hep-ex\]](https://arxiv.org/abs/hep-ex/9708024).
- [109] G. Durieux, *Precision constraints on the top-quark effective field theory at future lepton colliders*, *PoS DIS2017* (2018) 088, [arXiv:1708.09849 \[hep-ph\]](https://arxiv.org/abs/1708.09849).
- [110] L3 Collaboration, *Measurement of R_b and $Br(b \rightarrow \ell\nu X)$ at LEP using double tag methods*, *Eur. Phys. J.* **C13** (2000) 47–61, [arXiv:hep-ex/9909045 \[hep-ex\]](https://arxiv.org/abs/hep-ex/9909045).
- [111] OPAL Collaboration, *A Measurement of R_b using a double tagging method*, *Eur. Phys. J.* **C8** (1999) 217–239, [arXiv:hep-ex/9810002 \[hep-ex\]](https://arxiv.org/abs/hep-ex/9810002).
- [112] DELPHI Collaboration, *A Precise measurement of the partial decay width ratio $R_b^0 = \Gamma_{b\bar{b}}/\Gamma_{\text{had}}$* , *Eur. Phys. J.* **C10** (1999) 415–442.
- [113] ALEPH Collaboration, *A Measurement of R_b using mutually exclusive tags*, *Phys. Lett.* **B401** (1997) 163–175.
- [114] SLD Collaboration, *Measurement of the branching ratio of the Z^0 into heavy quarks*, *Phys. Rev.* **D71** (2005) 112004, [arXiv:hep-ex/0503005 \[hep-ex\]](https://arxiv.org/abs/hep-ex/0503005).
- [115] OPAL Collaboration, *Precise determination of the Z resonance parameters at LEP: 'Zedometry'*, *Eur. Phys. J.* **C19** (2001) 587–651, [arXiv:hep-ex/0012018 \[hep-ex\]](https://arxiv.org/abs/hep-ex/0012018).
- [116] DELPHI Collaboration, *Cross-sections and leptonic forward backward asymmetries from the Z^0 running of LEP*, *Eur. Phys. J.* **C16** (2000) 371–405.
- [117] L3 Collaboration, *Measurements of cross-sections and forward backward asymmetries at the Z resonance and determination of electroweak parameters*, *Eur. Phys. J.* **C16** (2000) 1–40, [arXiv:hep-ex/0002046 \[hep-ex\]](https://arxiv.org/abs/hep-ex/0002046).
- [118] ALEPH Collaboration, *Measurement of the Z resonance parameters at LEP*, *Eur. Phys. J.* **C14** (2000) 1–50.
- [119] SLD Collaboration, *Direct measurements of $A(b)$ and $A(c)$ using vertex/kaon charge tags at SLD*, *Phys. Rev. Lett.* **94** (2005) 091801, [arXiv:hep-ex/0410042 \[hep-ex\]](https://arxiv.org/abs/hep-ex/0410042).
- [120] ALEPH Collaboration, *Measurement of $A^b(FB)$ using inclusive b hadron decays*, *Eur. Phys. J.* **C22** (2001) 201–215, [arXiv:hep-ex/0107033 \[hep-ex\]](https://arxiv.org/abs/hep-ex/0107033).
- [121] OPAL Collaboration, *Measurement of the b quark forward backward asymmetry around the Z^0 peak using an inclusive tag*, *Phys. Lett.* **B546** (2002) 29–47, [arXiv:hep-ex/0209076 \[hep-ex\]](https://arxiv.org/abs/hep-ex/0209076).

- [122] DELPHI Collaboration, *Determination of $A^b(FB)$ at the Z pole using inclusive charge reconstruction and lifetime tagging*, *Eur.Phys.J.* **C40** (2005) 1–25, [arXiv:hep-ex/0412004 \[hep-ex\]](https://arxiv.org/abs/hep-ex/0412004).
- [123] L3 Collaboration, *Measurement of the $e^+e^- \rightarrow Z \rightarrow b\bar{b}$ forward–backward asymmetry and the B_0 anti- B_0 mixing parameter using prompt leptons*, *Phys.Lett.* **B448** (1999) 152–162.
- [124] I. Dubovsky, A. Freitas, J. Gluza, T. Riemann, and J. Usovitsch, *The two-loop electroweak bosonic corrections to $\sin^2 \theta_{\text{eff}}^b$* , *Phys. Lett.* **B762** (2016) 184–189, [arXiv:1607.08375 \[hep-ph\]](https://arxiv.org/abs/1607.08375).
- [125] S. Schael et al., *Precision electroweak measurements on the Z resonance*, *Phys.Rept.* **427** (2006) 257–454, [arXiv:hep-ex/0509008 \[hep-ex\]](https://arxiv.org/abs/hep-ex/0509008).
- [126] B. F. L. Ward, S. Jadach, M. Melles, and S. A. Yost, *New results on the theoretical precision of the LEP / SLC luminosity*, *Phys. Lett.* **B450** (1999) 262–266, [arXiv:hep-ph/9811245 \[hep-ph\]](https://arxiv.org/abs/hep-ph/9811245).
- [127] G. Montagna, M. Moretti, O. Nicrosini, A. Pallavicini, and F. Piccinini, *Light pair corrections to small angle Bhabha scattering in a realistic set up at LEP*, *Phys. Lett.* **B459** (1999) 649–652, [arXiv:hep-ph/9905235 \[hep-ph\]](https://arxiv.org/abs/hep-ph/9905235).
- [128] G. Montagna, M. Moretti, O. Nicrosini, A. Pallavicini, and F. Piccinini, *Light pair correction to Bhabha scattering at small angle*, *Nucl. Phys.* **B547** (1999) 39–59, [arXiv:hep-ph/9811436 \[hep-ph\]](https://arxiv.org/abs/hep-ph/9811436).
- [129] F. Jegerlehner, *Variations on Photon Vacuum Polarization*, [arXiv:1711.06089 \[hep-ph\]](https://arxiv.org/abs/1711.06089).
- [130] C. M. Carloni Calame, *Selected topics in electroweak physics at future e^+e^- colliders*, 2017. CEPC Workshop, Wuhan, China.
- [131] S. Jadach, *QED calculations for Bhabha luminometer*, 2006. FCAL Workshop at INP-PAN, Cracow, Poland.
- [132] G. Montagna, M. Moretti, O. Nicrosini, and F. Piccinini, *Single photon and multiphoton final states with missing energy at e^+e^- colliders*, *Nucl. Phys.* **B541** (1999) 31–49, [arXiv:hep-ph/9807465 \[hep-ph\]](https://arxiv.org/abs/hep-ph/9807465).
- [133] Y. Kurihara, J. Fujimoto, T. Ishikawa, Y. Shimizu, and T. Munehisa, *Event generator for the single photon and double photon emission associated with neutrino pair production*, *Comput. Phys. Commun.* **136** (2001) 250–268, [arXiv:hep-ph/9908422 \[hep-ph\]](https://arxiv.org/abs/hep-ph/9908422).
- [134] A. Jacholkowska, J. Kalinowski, and Z. Was, *Higher order QED corrections to $e^+e^- \rightarrow \nu\bar{\nu}\gamma$ at LEP-2*, *Eur. Phys. J.* **C6** (1999) 485–491, [arXiv:hep-ph/9803375 \[hep-ph\]](https://arxiv.org/abs/hep-ph/9803375).
- [135] S. Jadach, B. F. L. Ward, and Z. Was, *The Monte Carlo program KORALZ, for the lepton or quark pair production at LEP / SLC energies: From version 4.0 to version 4.04*, *Comput. Phys. Commun.* **124** (2000) 233–237, [arXiv:hep-ph/9905205 \[hep-ph\]](https://arxiv.org/abs/hep-ph/9905205).

- [136] S. Jadach, B. F. L. Ward, and Z. Was, *The Monte Carlo program KORALZ, version 4.0, for the lepton or quark pair production at LEP / SLC energies*, *Comput. Phys. Commun.* **79** (1994) 503–522.
- [137] S. Jadach, B. F. L. Ward, and Z. Was, *The Monte Carlo program KORALZ, version 3.8, for the lepton or quark pair production at LEP / SLC energies*, *Comput. Phys. Commun.* **66** (1991) 276–292.
- [138] D. Bardin, S. Jadach, T. Riemann, and Z. Was, *Predictions for anti-nu nu gamma production at LEP*, *Eur. Phys. J.* **C24** (2002) 373–383, [arXiv:hep-ph/0110371 \[hep-ph\]](https://arxiv.org/abs/hep-ph/0110371).
- [139] D. Yu. Bardin, J. Biebel, D. Lehner, A. Leike, A. Olchevski, and T. Riemann, *GENTLE/4fan v. 2.0: A Program for the semianalytic calculation of predictions for the process $e+ e- \rightarrow 4f$* , *Comput. Phys. Commun.* **104** (1997) 161–187, [arXiv:hep-ph/9612409 \[hep-ph\]](https://arxiv.org/abs/hep-ph/9612409).
- [140] M. E. Peskin and T. Takeuchi, *A New constraint on a strongly interacting Higgs sector*, *Phys. Rev. Lett.* **65** (1990) 964–967.
- [141] M. E. Peskin and T. Takeuchi, *Estimation of oblique electroweak corrections*, *Phys. Rev.* **D46** (1992) 381–409.
- [142] J. Wudka, *Effective Lagrangians (for electroweak physics)*, in *4th Mexican Workshop on Particles and Fields Yucatan, Mexico, October 25-29, 1993*, pp. 61–106. 1994. [arXiv:hep-ph/9405206 \[hep-ph\]](https://arxiv.org/abs/hep-ph/9405206).
- [143] J. Erler and F. Ayres, *Electroweak Model and Constraints on New Physics*, Particle Data Group review . <http://pdg.lbl.gov/2014/reviews/rpp2014-rev-standard-model.pdf>.
- [144] M. Baak, J. Cuth, J. Haller, A. Hoecker, R. Kogler, et al., *The global electroweak fit at NNLO and prospects for the LHC and ILC*, [arXiv:1407.3792 \[hep-ph\]](https://arxiv.org/abs/1407.3792).
- [145] CMS Collaboration, *Projected improvement of the accuracy of top-quark mass measurements at the upgraded LHC*, CMS-PAS-FTR-13-017, CERN, Geneva, 2013. <https://cds.cern.ch/record/1605627>.
- [146] J. Erler, *Status of Precision Extractions of α_s and Heavy Quark Masses*, *AIP Conf. Proc.* **1701** (2016) 020009, [arXiv:1412.4435 \[hep-ph\]](https://arxiv.org/abs/1412.4435).
- [147] M. Awramik, M. Czakon, A. Freitas, and G. Weiglein, *Precise prediction for the W boson mass in the standard model*, *Phys. Rev.* **D69** (2004) 053006, [arXiv:hep-ph/0311148 \[hep-ph\]](https://arxiv.org/abs/hep-ph/0311148).
- [148] M. Awramik, M. Czakon, and A. Freitas, *Electroweak two-loop corrections to the effective weak mixing angle*, *JHEP* **0611** (2006) 048, [arXiv:hep-ph/0608099 \[hep-ph\]](https://arxiv.org/abs/hep-ph/0608099).
- [149] A. Freitas, K. Hagiwara, S. Heinemeyer, P. Langacker, K. Moenig, M. Tanabashi, and G. W. Wilson, *Exploring Quantum Physics at the ILC*, in *Proceedings, 2013 Community Summer Study on the Future of U.S. Particle Physics: Snowmass on*

- 1 *the Mississippi (CSS2013): Minneapolis, MN, USA, July 29-August 6, 2013.* 2013.
2 arXiv:1307.3962 [hep-ph].
3 [https://inspirehep.net/record/1242667/files/arXiv:
4 1307.3962.pdf](https://inspirehep.net/record/1242667/files/arXiv:1307.3962.pdf).
- 5 [150] A. Freitas, *Higher-order electroweak corrections to the partial widths and
6 branching ratios of the Z boson*, JHEP **04** (2014) 070, arXiv:1401.2447
7 [hep-ph].
- 8 [151] J. Fan, M. Reece, and L.-T. Wang, *Possible Futures of Electroweak Precision: ILC,
9 FCC-ee, and CEPC*, JHEP **09** (2015) 196, arXiv:1411.1054 [hep-ph].
- 10 [152] CEPC-SPPC Study Group, CEPC-SPPC Preliminary Conceptual Design Report.
11 1. Physics and Detector (2015).
12 <http://cepc.ihep.ac.cn/preCDR/volume.html>.
- 13 [153] C. Burgess, S. Godfrey, H. Konig, D. London, and I. Maksymyk, *Model
14 independent global constraints on new physics*, Phys.Rev. **D49** (1994) 6115–6147,
15 arXiv:hep-ph/9312291 [hep-ph].
- 16 [154] M. Ciuchini, E. Franco, S. Mishima, and L. Silvestrini, *Electroweak Precision
17 Observables, New Physics and the Nature of a 126 GeV Higgs Boson*, JHEP **08**
18 (2013) 106, arXiv:1306.4644 [hep-ph].
- 19 [155] A. Hocker, H. Lacker, S. Laplace, and F. Le Diberder, *A New approach to a global
20 fit of the CKM matrix*, Eur.Phys.J. **C21** (2001) 225–259,
21 arXiv:hep-ph/0104062 [hep-ph].
- 22 [156] H. Flacher, M. Goebel, J. Haller, A. Hocker, K. Monig, et al., *Revisiting the
23 Global Electroweak Fit of the Standard Model and Beyond with Gfitter*,
24 Eur.Phys.J. **C60** (2009) 543–583, arXiv:0811.0009 [hep-ph].
- 25 [157] R. Lafaye, T. Plehn, M. Rauch, D. Zerwas, and M. Duhrssen, *Measuring the Higgs
26 Sector*, JHEP **0908** (2009) 009, arXiv:0904.3866 [hep-ph].

Draft-V2.0

CHAPTER 12

FUTURE PLANS AND R&D PROSPECTS

Since the release of the pre-CDR, the main effort of the CDR has been focusing on exploring different concepts of the detector design. In addition to a baseline detector optimized from ILD with 3T magnetic field, two alternative detectors are also proposed. One with a full-silicon tracker and another one with a drift chamber under 2T magnetic field. The baseline concept detector is used to evaluate the physics potential of the 240 GeV CEPC accelerator.

For the next TDR phase more in-depth studies will be carried out for both detector and physics. For tracking, thorough investigation of silicon based material and processes will be performed on vertex, silicon tracker. Sub-module level studies will also be achieved for most tracking components including TPC and drift chamber. For calorimetry, prototypes for silicon-tungsten and scintillator-tungsten ECAL, different prototypes for PFA-HCAL, and characters of dual-readout calorimeter will be studied comprehensively. The R&D work of magnet will include longer conductor, large HTS solenoid and helium phase transition. For muon system, optimization and industrialization will be the focus. Attention will be made to follow the ongoing improvement of data communication and processing technologies of to be used for future CEPC DAQ system. For MDI, studies such as interaction region layout optimization and background models validation will be explored. In-situ calibration and advanced reconstruction algorithm will be addressed for the physics objects performance.

To be consolidated and updated.

1 **12.1 Tracking**2 **12.1.1 Vertex**

3 As the inner most layers, the vertex detector has to fulfill the most demanding requirements imposed by the physics program. To meet these requirements of single-point resolution, low material budget, fast readout, low power consumption and radiation tolerance, coherent R&D activities have to be pursued:

- 7 ▪ Enhancement of density, radiation hardness and ultra-light module assembling.
- 8 ▪ Explore smaller production line for TowerJazz and LAPIS in conjunction with the NpD (Nano-particle deposition) technique.
- 10 ▪ Improve the charge collection efficiency of the TowerJazz process by N-type implant
- 11 ▪ Improve the radiation hardness and low power design for SOI process.
- 12 ▪ Sensor thinning for CMOS and SOI.
- 13 ▪ Detailed designs for mechanical supports to enable cooling, cabling and power con-
14 servation.

15 **12.1.2 Silicon tracker**

16 Placed outside the vertex detector and after the TPC, the silicon tracker forms the complete
17 tracking system of CEPC. The silicon tracker is designed to have low material budget
18 and high tracking efficiency. With preliminary studies, several critical R&D items are
19 identified for the next TDR phase:

- 20 ▪ Alternative pixelated strip sensors with CMOS technologies;
- 21 ▪ p⁺-on-n silicon microstrip sensors with slim-edge structure;
- 22 ▪ Front-end electronics with low power consumption and low noise, fabricated with
23 CMOS technologies of small feature size;
- 24 ▪ Efficient powering with low material budget and CO₂ cooling techniques;
- 25 ▪ Lightweight but robust support structure and related mechanics;
- 26 ▪ Detector layout optimization, in particular in the forward region.

27 **12.1.3 TPC**

28 Time Projection Chambers is considered as the baseline central tracker for the CEPC
29 tracking system. Modularized design with gas amplification and readout pad optimization
30 have been investigated. The low power consumption electronics and ion backflow (IBF)
31 are also considered. The future R&D consists:

- 32 ▪ Hybrid structure TPC detector module,
- 33 ▪ Laser calibration and alignment system.

12.1.4 Full-silicon tracker

2 To demonstrate a viable option for CEPC under the same detector boundary conditions of
 3 the baseline design, the TPC is replaced with a full-silicon tracker (CEPC-FST) layout.
 4 A second approach is used to fulfill the CEPC tracking volume with the ILC-SID tracker
 5 to achieve better momentum resolution. To explore the full potential of the all silicon
 6 tracker, possible improvements are:

- 7 ▪ Optimize the layout for better performance and lower cost based on satisfy mechanics.
 8 ▪ Study physical performance and find out which physics processes are suitable for
 9 evaluation.

12.1.5 Drift Chamber tracker

11 The drift chamber tracker is another option to provide good tracking, high precision mo-
 12 mentum measurement and excellent particle identification by cluster counting.

- 13 ▪ Final layout optimization of the full tracking system, which, besides the drift chamber,
 14 includes the vertex detector and the silicon micro-strip detector layers (the silicon
 15 wrapper, as indicated in Figure 3.11).
 16 ▪ Studies for a non-flammable gas mixture alternative to He/Isobutane 90/10.
 17 ▪ Particle identification performance with cluster counting, to be assessed in beam tests
 18 of realistic drift chamber prototypes.
 19 ▪ Full length (> 4 m) prototypes to establish limits of the wires electrostatic stability.

12.2 Calorimetry

21 Two technology options respectively based on the Particle Flow Algorithm (PFA) con-
 22 cept and the dual-readout concept are both being explored for the design of the CEPC
 23 calorimetry system. The PFA approach aims to develop both a high-granularity electro-
 24 magnetic calorimeter (ECAL) and a high-granularity hadronic calorimeter (HCAL) that
 25 are capable of measuring individual particles in a jet, while the dual-readout approach
 26 aims for a combined and homogeneous calorimeter with excellent performance for both
 27 electromagnetic and hadronic particle showers.

12.2.1 PFA-ECAL

28 The CEPC ECAL is required to have a good intrinsic energy resolution for precise energy
 29 measurement of electrons and photons, as well as excellent shower imaging capability
 30 that would allow to identify photons from close-by showers, reconstruct detailed prop-
 31 erties of a shower and distinguish electromagnetic showers from hadronic ones very ef-
 32 fectively. Extensive and focused R&D will be conducted on developing a tungsten-based
 33 high-granularity sampling calorimeter with either silicon or scintillator as active medium
 34 to address the above requirements for the CEPC ECAL. Future study work towards com-
 35 pletion of a TDR will involve detector design optimization and critical common R&D in
 36 view of the CEPC experimental conditions, particularly the continuous operation mode

imposed by the CEPC accelerator, and a great deal of prototyping for the two ECAL technology options.

- Design optimization and common R&D
 - Optimization of primary detector parameters with full detector simulation.
 - Thermal studies of detector and electronics components using both simulation and experiment.
 - Cooling design based on the above studies and prototyping.
- Silicon-Tungsten ECAL
 - Full characterization of a physics Silicon-Tungsten ECAL prototype using its existing test beam data.
 - Development of a technological prototype to address power, cooling and front-end electronics issues.
 - Design of detector modules. Development of technology for fabricating large-size detector modules.
- Scintillator-Tungsten ECAL
 - Development of a SiPM-scintillator coupling scheme that allows very large dynamic range.
 - Development of technology of fabricating high-quality scintillator strips with required fine structures.
 - Design, construction and characterization of a small-size physics prototype.
 - Development of a technological prototype to address power, cooling and front-end electronics issues.
 - Design of detector modules. Development of technology for fabricating large-size detector modules.

12.2.2 PFA-HCAL

The future plans of HCAL include R&D on new gaseous detector technology for PFA-HCAL, design, construction and characterization of various prototypes.

- DHCAL based on RPC, Test beams and performance study
- MRPC with better time resolution (about 50 ps)
- THGEM with very compact structure and stable operation
- AHCAL based on scintillator + SiPM, prototype design and construction, performance study

12.2.3 Dual-readout calorimeter

Concerning the dual-readout calorimeter, a 3-year R&D program is being pursued in order to address and clarify the following issues:

- absorber material choice, current candidates are lead, brass and iron;
- machining and assembly procedure for modules of $\sim 10 \times 10 \text{ cm}^2$ cross section;
- development of a modular, projective solution for a 4π calorimeter concerning both the construction of single modules and the design and construction of a full detector;
- identification of adequate solid-state photo-sensors in order to independently optimize both Čerenkov and scintillation light detection (with respect to PDE, linearity, dynamic range and cross-talk performance);
- readout granularity (i.e. identify the optimal fiber grouping into a single readout channel);
- identification of a tailored front-end electronics, likely composed by an ASIC and an FPGA chip, in order to extract in real time both charge and time information (in principle, a time resolution of 100 ps should allow to identify the shower starting point inside the calorimeter with a precision of about 6 cm);
- particle ID performance with Particle Flow Algorithms, with and without a longitudinal segmentation;
- development and validation of full and fast simulations of both test beam modules and an integrated 4π detector;
- assessment of the performance for the most relevant physics channels (such as W , Z , H decays).

12.3 Magnet

A detector superconducting solenoid with 3.0T central field is chosen for this CDR for feasibility reasons. It makes full cancellation to avoid disturbance to the beam with technologies in coming years. For the TDR phase, the following R&D work will be conducted:

- Longer conductor with higher I_c : A 10 m long NbTi Rutherford cable embedded inside stabilizer have been developed, which provides I_c 5 kA at 4T background magnetic field. In the future, a longer conductor with higher I_c 15 kA at 4 T background is in our R&D plan. Meanwhile the measurement of the material properties and the tensile stress of the cable will be a necessary part for the structural simulation of the solenoid coil and the conductor development.
- YBCO stacked-tape cable and the cryogenics: A large HTS solenoid concept is proposed for the IDEA detector. The HTS solenoid is supposed to use YBCO stacked-tape cable as the conductor. The operation temperature of the cold mass is raised to 20K. Therefore, the YBCO stacked-tape cable and the cryogenics are brought into R&D.

- 1:10 scale thermosyphon circuit model: In order to study the phase transition process of helium in the circuit, the changes of the temperature distribution and the density distribution over the time, a 1:10 scale thermosyphon circuit will be established for simulation and experiment.

12.4 Muon system

Located within the solenoid flux return yoke, the muon system is required to identify muons with very high efficiency. Both Resistive Plate Chamber (RPC) and Micro Pattern Gas detector (MPGD) are considered in CDR. Future R&D requires detailed studies of different technologies and further optimization of baseline design parameters. Several critical R&D items have been identified, including:

- Long-lived particles optimization: Explore new physics scenario of long-lived particles and exotic decays. Optimize detector parameters and technologies.
- Layout and geometry optimization: Detailed studies on the structure of the segments and modules need to be carried out to minimize the dead area and to optimize the interface for routing, support and assembly.
- Detector optimization: Study aging effects, improve long-term reliability and stability, readout technologies.
- Detector industrialization: Improve massive and large area production procedures for all technologies.

12.5 DAQ

New technologies will emerge before the CEPC DAQ system has to be built. Attention will be made to follow and explore the ongoing improvement of the data communication and processing technologies. In particular the following areas will be addressed:

- The high speed and low latency communication technology should be the key point for data readout.
- A high efficient data flow distribution schema is another key point for data dispatching on a huge computing farm. There the data are concentrated, re-formatted, possibly zero-suppressed, assembled full event and filtered.
- Online software trigger and data compression algorithm should be study and provided by physics. But the implementation of the data processing inside online farm is DAQ scope.

12.6 Machine detector interface

Machine-Detector Interface (MDI) represents one of the most challenging topics in which both the accelerator and detector will be covered. The interaction region (IR) has to focus both electron and positron beams to small spot sizes to maximize the machine luminosity. The following R&D will be carried out during the next TDR phase:

- ¹ ▪ Interaction region layout re-design/optimization
- ² ▪ Background models validation with experimental data, e.g. SuperKEKB/Belle II
- ³ ▪ Beam pipe design together with SR photon protection, HOM absorber and cooling if
⁴ needed
- ⁵ ▪ Installation scheme that involves both LumiCal and final focusing magnets
- ⁶ ▪ Prototyping R&D on LumiCal, and demonstration of alignment of desired precision
⁷ with laser and optical devices.

⁸ **12.7 Simulation, reconstruction and object performance**

⁹ Offline algorithms such as simulation, reconstruction and calibrations play important role
¹⁰ in maximizing the potential of the CEPC detector. The performances of physics objects
¹¹ depend on the performance of these algorithms. Though basic understanding of their
¹² performances has been achieved and documented in this report, more need to be done
¹³ to optimize existing algorithms and to develop new ones with the goal to improve their
¹⁴ performance for physics analyses. Future work thus includes

- ¹⁵ ▪ keeping up the offline software with the detector design optimization;
- ¹⁶ ▪ developing calibration methods including in-situ calibrations;
- ¹⁷ ▪ developing sub-detector digitization algorithms;
- ¹⁸ ▪ characterizing in details the detector performances such as photon and jet energy res-
¹⁹ olutions;
- ²⁰ ▪ improving identifications of particles such as τ -leptons and photons, particularly con-
²¹ verted photons;
- ²² ▪ developing Bremsstrahlung photon recovery algorithms to improve the energy mea-
²³ surements of electrons and muons;
- ²⁴ ▪ studying advanced reconstruction algorithms and pattern recognitions;
- ²⁵ ▪ understanding and controlling theoretical uncertainties.

²⁶ **12.8 Physics**

²⁷ The goal of the physics study in the future is to strengthen the physics case for the CEPC.

²⁸ The physics case for the CEPC summarized in the CDR covers the main physics
²⁹ motivations. Several case studies, based on some of the most prominent new physics sce-
³⁰ narios, are presented. In the future, such studies need to be expanded to include more new
³¹ physics scenarios and take into account new developments. Some of the projections, such
³² as Higgs boson and Z exotic decays, precision QCD measurements, and flavor physics
³³ both at the Higgs boson factory and Z factory, are based on simple simulation and extrap-
³⁴ olation. They can benefit from more detailed and realistic simulation.

Another major direction for the future is the development of state of art Monte Carlo tools, which implements the most precise calculation available and is capable of making both inclusive and differential predictions.

Higgs boson physics is the primary physics target for the CEPC. The studies presented in the CDR gives a leading order assessment of the capability of CEPC in measuring the properties of the CEPC. In this area, there are a few improvements and updates which can be done at the next stage. First of all, the analyses of many Higgs boson decay channels for current studies are extrapolated from CEPC_v1 setup. New analyses based on full simulated samples with the most updated geometry in future are expected. The studies now are classified with different Higgs boson decay modes. An updated analyses categorizing events according to different final state particles are worthwhile to be explored. In addition, some further optimizations can be implemented for the future analyses, e.g. classifying events with variant S/B ratio instead of simply applying cuts to further improve the sensitivity. Further more, some fundamental systematics can be taken into account for the future study. Most of the information used in the physics studies in the CDR are inclusive rates. On the other hand, differential information can be useful in increasing the sensitivity to potential new physics effects. It deserves more detailed study. More Higgs boson rare decay channels, such as those sensitive to the Higgs boson coupling to the strange quark, should be included in the study.

The electroweak precision measurement is an important component of the CEPC physics program. The most important factor is the estimate of systematical error. More realistic detector effect need to be taken into account. Some of the projections, such as the precision in Z mass measurement, should be assessed once more detailed design of the accelerator has been made. The results should also be updated when more accurate theoretical computation and estimate of the theoretical error become available.

References

- [1] CEPC project website. <http://cepc.ihep.ac.cn>.
- [2] The CEPC-SPPC Study Group, *CEPC-SPPC Preliminary Conceptual Design Report, Volume II - Accelerator*, 2015.
<http://cepc.ihep.ac.cn/preCDR/volume.html>.
IHEP-CEPC-DR-2015-01, IHEP-AC-2015-01.
- [3] The ATLAS Collaboration, G. Aad et al., *Observation of a new particle in the search for the Standard Model Higgs boson with the ATLAS detector at the LHC*, *Phys. Lett. B* **716** (2012) 1–29, [arXiv:1207.7214 \[hep-ex\]](https://arxiv.org/abs/1207.7214).
- [4] The CMS Collaboration, S. Chatrchyan et al., *Observation of a new boson at a mass of 125 GeV with the CMS experiment at the LHC*, *Phys. Lett. B* **716** (2012) 30–61, [arXiv:1207.7235 \[hep-ex\]](https://arxiv.org/abs/1207.7235).

CHAPTER 13

SUMMARY

Draft-V2.0

Draft-V2.0

APPENDIX A

HTS SOLENOID CONCEPT FOR IDEA DETECTOR

2 A large HTS solenoid is being studied for the IDEA detector. The HTS solenoid is sup-
3 posed to use YBCO stacked-tape cable as the conductor. The radiation length of single
4 YBCO tape coated with 10 μm copper is about $0.004 X_0$. Each tape carries 700 A at 20
5 K. 35 YBCO tapes stacked together allows 24.5 kA. These tapes are embedded in 5 mm
6 pure aluminum. The radiation length of this YBCO stacked-tape cable is estimated to be
7 $0.2 X_0$. The radiation length of HTS coil will be less than half of the current LTS coil de-
8 sign. If the operation temperature of the cold mass is raised to 20 K, the heat conductivity
9 parameters of all components are improved. In addition, the electricity consumption of
10 cooling station is much lower than that at 4.2 K. Therefore, the YBCO stacked-tape cable
11 and the cryogenics are brought into R&D.

A.1 Radiation length of YBCO superconductor

13 The second generation HTS YBCO tape is chosen as the superconducting wire. YBCO:
14 Yttrium Barium Copper Oxide, $\text{YBa}_2\text{Cu}_3\text{O}_7$, $T_c=90$ K, tape, produced by coating method
15 (CCC - coated conductor composite): using chemical deposition or physical coating meth-
16 ods coating a layer of YBCO superconducting film on the hastelloy substrate.

17 Figure A.1 shows the architecture of YBCO superconductor from Shanghai Super-
18 conductor Technology Company. The thickness of single tape is about 65 μm , its critical
19 tensile stress is larger than 400 Mpa.

20 The inner radius of the HTS solenoid coil is 2.2 m. The length is 6 m. The operation
21 temperature of the cold mass is raised to 20 K. The coil is supposed to use YBCO stacked-
22 tape cable as the conductor. Each cable contains 35 tapes with 700 A at 20 K. There are

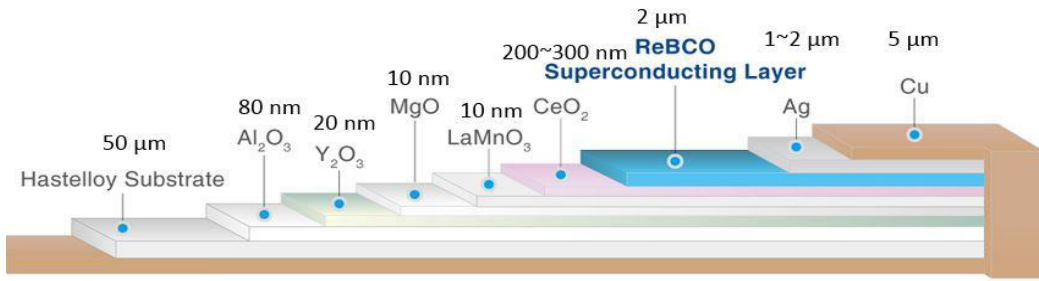


Figure A.1: YBCO: Yttrium Barium Copper Oxide, $\text{YBa}_2\text{Cu}_3\text{O}_7$, $T_c=90$ K, tape, produced by coating method (CCC - coated conductor composite): using chemical deposition or physical coating methods coating a layer of YBCO superconducting film on the hastelloy substrate. Different layers of the YBCO tape can be seen in the picture (different companies have different layers, this picture is the product of Shanghai Superconductor Technology Company).

- ¹ 500 winding turns per layer. The cable carries 24500 A. These tapes are embedded in 5 mm pure aluminum, shown in Figure A.2
- ²

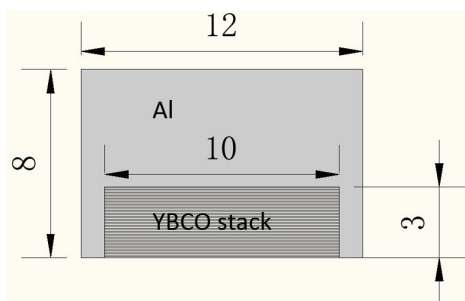


Figure A.2: Schematic diagram of YBCO cable including support (unit mm)

³ The radiation length of single YBCO tape coated with 10 μm copper is about 0.004
⁴ X_0 . These tapes are embedded in 5 mm pure aluminum. The radiation length of this
⁵ YBCO stacked-tape cable is estimated to be 0.2 X_0 . The radiation length of HTS coil will
⁶ be less than half of the current LTS coil design. The radiation thickness of each material
⁷ is listed in Table A.1. The total radiation thickness of the cable is listed in Table A.2.

R&D

- ⁸ I) YBCO cable research. Develop YBCO stack cable and study its performance.
- ⁹ II) Study the quench detection, transmission and protection of the HTS coil.
- ¹⁰ III) Prototype HTS coil development.
- ¹¹

Material	Thickness,X(mm)	Radiation,X ₀ (mm)	X/X ₀	Material Ratio
Cu	0.01	14.36	0.0007	17.97%
Fe	0.05	17.57	0.0028	73.41%
Ag	0.002	8.543	0.0002	6.04%
YBa ₂ Cu ₃ O ₇	0.002	20	0.0001	2.58%
MgO	0.00000001	78.28	0	0%
Al ₂ O ₃	0.00000008	70.38	0	0%
CeO ₂	0.0000003	16.54	0	0%
Total, X _{tot}			0.0039	100%

Table A.1: Radiation thickness of Single YBCO tape

Material	Thickness,X(mm)	Radiation,X ₀ (mm)	X/X ₀	Material Ratio
Cu	0.01	14.36	0.0007	17.97%
Fe	0.05	17.57	0.0028	73.41%
Ag	0.002	8.543	0.0002	6.04%
YBa ₂ Cu ₃ O ₇	0.002	20	0.0001	2.58%
MgO	0.00000001	78.28	0	0%
Al ₂ O ₃	0.00000008	70.38	0	0%
CeO ₂	0.0000003	16.54	0	0%
Support cylinder, Al	5	88.97	0.0562	28.26%
Glass/polyimide/epoxy	2	286	0.0070	3.52%
Total, X _{tot}			0.1989	100%

Table A.2: Radiation thickness of 35 layers YBCO cable, contains 5 mm Al support and 2mm Glass/polyimide/epoxy.

Draft-V2.0

Glossary

- ² **DCH** drift chamber 177
- ³ **Escape electron** ionization energy of an electron from the argon K-shell 157
- ⁴ **GEM** Gas Electron Multiplier 150, 157
- ⁵ **GEM-MM** hybrid Gas Electron Multiplier and Micro-Mesh Gaseous Structure 150, 157,
⁶ 158, 159
- ⁷ **IBF** ion backflow 151, 157
- ⁸ **MicroMegas** Micro-Mesh Gaseous Structure 150, 157
- ⁹ **MPGD** micro-pattern gaseous detector 147, 148, 149, 150, 157
- ¹⁰ **MPWC** multi-wire proportional chamber 156
- ¹¹ **TPC** Time Projection Chamber 147